5th European Lidar Conference

Scientific contributions

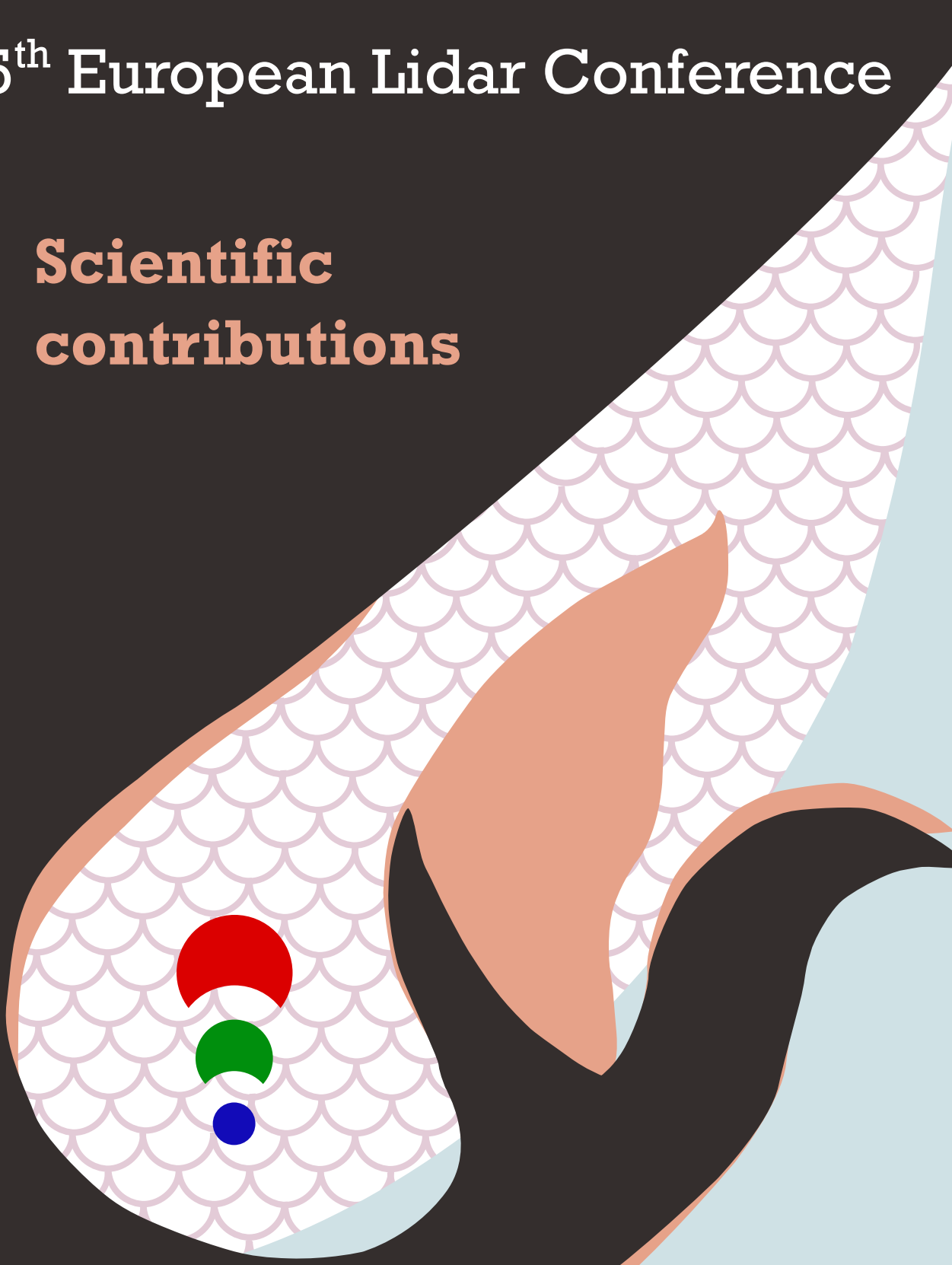

Warsaw, Poland

10-12 September 2025

5th European Lidar Conference ELC2025

Scientific contributions

UNIVERSITY OF WARSAW | INSTITUTE OF GEOPHYSICS

FACULTY OF PHYSICS
UNIVERSITY OF WARSAW

licel

Warsaw, Poland

10-12 September 2025

Scientific reviewers

Albert Ansmann
Nicolae Ajtai
Salvadore Amoruso
Arnoud Apituley
Holger Baars
Dimitris Balis
Livio Belegante
Daniele Bortoli
Adolfo Comeron
Paolo Di Girolamo
Davide Dionisi
Tanja Dreischuh
Ronny Engelmann
Ann Mari Fjaeraa
Volker Freudenthaler
Alexander Geiss
Giovanni Giuliano
José Luis Gómez-Amo
Silke Gross
Juan Luis Guerrero-Rascado
Cedric Jamet
Lucja Janicka
Mikka Kompula
Rodanthi Mamouri
Franco Marenco
Eleni Marinou
Giovanni Martucci
Lucia Mona
Anca Nemuc
Doina Nicolae
Jens Reichardt
Michael Sicard
Iwona Stachlewska
Iwona Stachlewska
Horatiu Stefani
Dominika Szczepanik
Camelia Talianu
Georgios Tzeremes

Book editors

Lucja Jancka
Dominika Szczepanik
Iwona Stachlewska

Graphic design

Łukasz Sobola

Table of contents

Lidar technology and advances

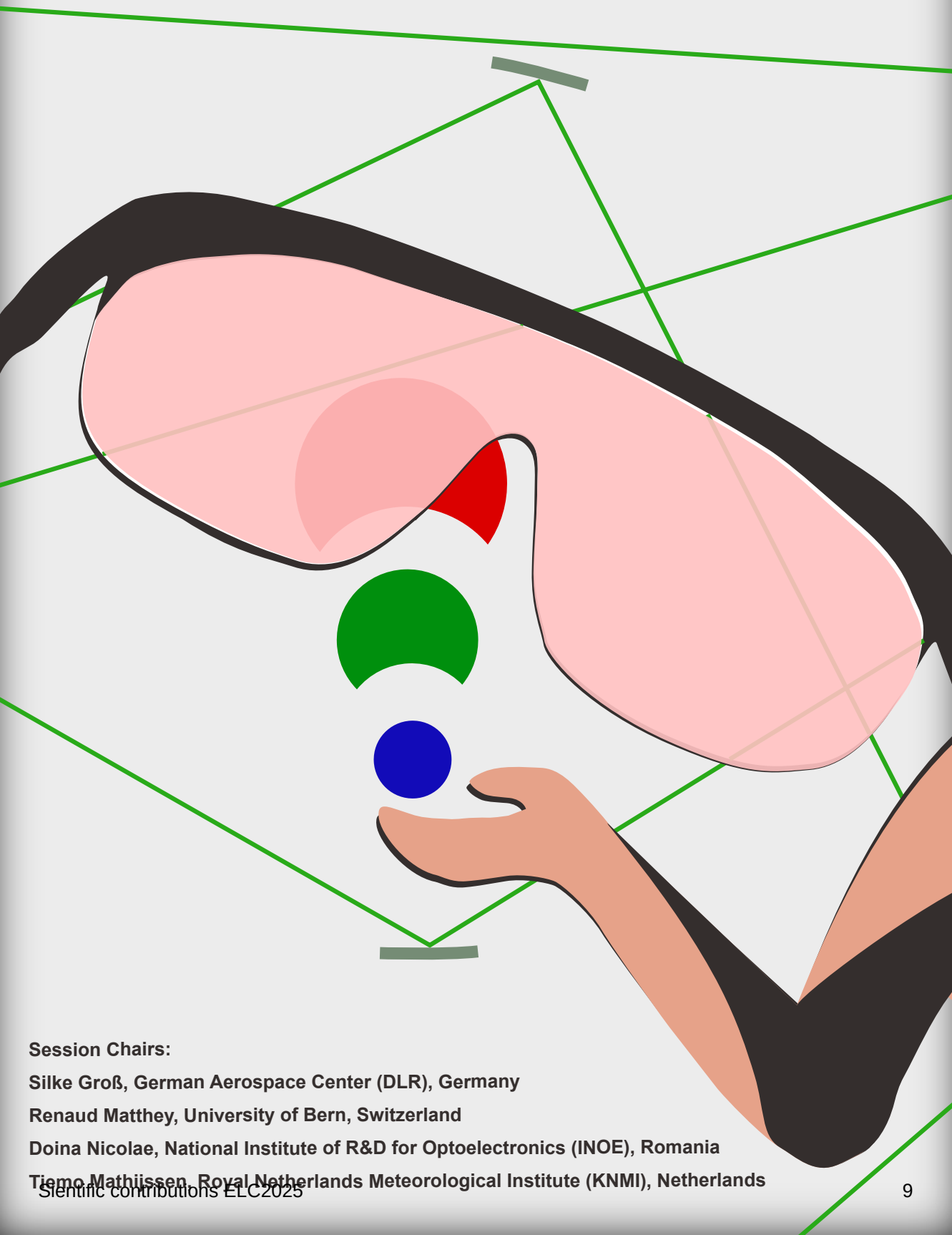

Session Chairs:

Silke Groß, German Aerospace Center (DLR), Germany

Renaud Matthey, University of Bern, Switzerland

Doina Nicolae, National Institute of R&D for Optoelectronics (INOE), Romania

Tiemo Mathijssen, Royal Netherlands Meteorological Institute (KNMI), Netherlands

Design Considerations for a Bistatic Camera Lidar

***John E. Barnes*[1]** *and Nimmi C. P. Sharma*[2]

(1) BJE Environmental Optics, 127 S Hoover, Louisville, Colorado, USA
(2) Central Connecticut State University, Department of Physics and Engineering Physics, 1615 Stanley Street, New Britain, CT 06050 U.S.A.

Corresponding author: barnesbje@gmail.com

Abstract

The bistatic camera lidar is compared to traditional backscatter lidar for profiling aerosols in the atmosphere. Two disadvantages of the bistatic approach are a loss of signal to noise, limiting the bistatic approach to twilight and nighttime conditions, and a loss of altitude resolution in the upper troposphere and stratosphere. Advantages of the bistatic technique over traditional lidar include simplicity and lower cost of the equipment, ease of optical alignment, and high-resolution data (less than 1.0 meter) starting at the ground with no overlap function. The ground capability allows direct comparisons to surface in-situ aerosol measurements. Additionally, the stars in the camera images can be used to calculate Aerosol Optical Depth (AOD) with no additional equipment or calibration. This AOD is obtained at the same wavelength, time, and location as the camera lidar altitude profile.

Introduction

The bistatic approach to profiling atmospheric quantities with altitude predates lasers. A searchlight [1], [2] was first used in 1953 to get molecular density in the mesosphere by scanning a telescope up and down the beam from a distance. With the advent of continuous wave (CW) lasers, more precise measurements could be made [3][4][5][6] with the same scanning telescope and photomultiplier tube sensor. A CCD camera was used for qualitative measurements [7][8] in 1996 and 1999. In the early 2000s the technique was made rigorously quantitative at Mauna Loa Observatory in Hawaii (USA) [9][10] by using a wide-angle lens that could image the entire laser from the ground to the zenith. This required no scanning of the beam greatly simplifying the technique. The analysis followed the standard lidar method of subtracting a molecular signal from the raw signal and normalizing to an upper altitude range with an assumed aerosol/molecular scattering ratio.

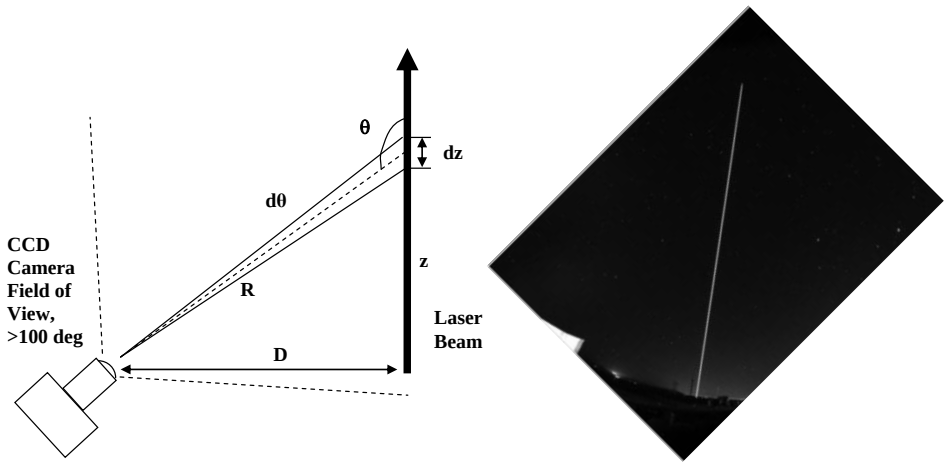

Figure 1. a) Camera Lidar Geometry: CCD camera detector is located D meters from laser transmitter (typically ~ 50 to 200 m), Each image pixel views a variable altitude segment, dz, of the beam with constant angular field of view, dΘ, at changing scattering angle Θ and altitude z. b) Raw data image

The basic lidar equation has a challenging dependance of 1/altitude^2. This results in the signal changing many orders of magnitude from low altitudes to top altitudes measured. Experimentally this means the relatively large low-altitude signal must be measured, followed by a weak high-altitude signal a millisecond later. This requires accurate, linear, fast electronics and a pulsed laser. An extremely important difference in the basic camera lidar equation to the lidar, is that with the proper optics this 1/altitude^2 dependence cancels out [9]. This cancelation results in a much smaller dynamic range (3-4 orders) needed for the CCD camera detector. In the following sections the distinctions of the bistatic camera lidar technique to be considered when implementing a system are summarized.

Optical considerations

CCD cameras have continually evolved over the past two decades. The sensitivity, noise, and readout electronics have improved substantially. The camera lidar uses a relatively simple camera. Desired characteristics are cooling to reduce dark noise, a simple shutter for long exposures (few minutes or less), and a larger CCD chip size. Some cameras have an anti-blooming feature which drains off electronic charge from a filled pixel. This is not wanted for camera lidar since it might perturb the linear response.

Adding to the simplicity of the camera lidar equipment is that the electronics needed are contained in the camera. The image is continuously acquired during the integration period. Non-linearity may occur when the electric charge in a pixel nears its limit, so it is best to adjust integration time so pixels stay below 90% capacity [11].

The lenses used by the authors have been commercial “Fisheye” lenses. The desired function that maps angles to pixels is the “equidistant fisheye” [12] This mapping function sets the angle mapped to a pixel, as you go out from the center of the image, to be constant (Figure 1, $d\Theta$).

Also very important is that the transmission of the lens is constant across the angular range. All the commercial lenses tested by the authors have shown very good angular mapping and constant transmission, but this is something to be verified when using new equipment. Note that most fisheye lenses have a field of view of 180 or 185 degrees. The camera lidar only needs accuracy in mapping and transmission over the central 100 degrees.

Table 1 shows four of the camera lidars used by the authors since the first measurements in 2000. The ST cameras were made by the Santa Barbara Instrument Group [13].

Table 1. Evolution of camera lidar systems. Relative Collection Efficiency is the improvement in signal compared to the first Kinoptics lens.

Camera	CCD Width (mm)	CCD Height (mm)	Fisheye Lens	Focal Length (mm)	F#	100 deg image size (mm)	Relative Collection Efficiency
ST-237	4.7	3.6	Kinoptics	1.98	4	3.46	1
Apogee	10.2	10.2	Coastal Optics	4.88	5.2	8.52	3.5
ST-1603	13.8	9.2	Sigma	8	3.5	13.96	21
STF-8300	17.96	13.52	Sigma	10	2.8	17.45	51

The lenses paired with the cameras are also listed. The image size for the fisheye lenses is given by Θ * Focal Length where Θ is in radians. Θ is usually around 90 degrees to image the ground to the zenith. But there must be extra pixels at the ends of the beam for the analysis so 100 degrees is used in the table. So, the camera CCD size must be larger than the image size. The progression to larger CCDs can be seen in the table. Imaging the beam on the diagonal is often preferred.

There is a tradeoff between the field-of-view of a lens and the effective optical diameter. This diameter is focal length / F#. For the STF-8300 lens the optical diameter is 3.57 mm, or a telescope area of 10.0 mm^2.

This area is much smaller than the physical size of the fisheye lens, in contrast with the entire telescope diameter collecting light in a traditional lidar. The fisheye lens can be thought of as directing a bundle of rays to an individual pixel. The rest of the lens doesn't contribute to the signal. This can easily be demonstrated by blocking parts of the lens and noticing the image remains the same in the selected direction.

Table 1 shows the improvement of the optical collection efficiency since the first lens used. The current system using the STF-8300 camera collects 51 times as much signal. The restriction in the fisheye lens is due to the insertion of a small aperture in the lens, which is needed to get the focusing, transmission, and image quality. An optimal lens for the camera lidar would be a fisheye designed for only a 100 degree field-of-view. This should significantly improve the throughput, but unfortunately there is not a commercial market to justify its development.

An additional consideration of the optical system is the use of the interference filter for the laser wavelength. The transmission of filters is specified for perpendicular incidence. The transmission falls off as the angle of incidence decreases [14] which occurs in the more extreme angles imaged by the lens. With the current Sigma lens (f.l. 10 F#2.8) the filter FWHH is limited to 10 nm to keep the transmission constant.

Mechanical and Placement

The camera/lens detection system is angled at 45 degrees to center the laser beam. The current camera has plenty of room for the image so alignment is quite simple; as long as the beam is not near the edges of the image it should be analyzable. For smaller camera CCDs, fine adjustment might be needed to position the beam. The moon can interfere with taking data so facing the camera North (South in southern hemisphere) can be helpful. Bright lights in the image can also be a problem, but as mentioned in the previous section a light may be blocked near the lens, in some cases, without affecting the image of the beam.

Analysis

The data image captured by the CCD camera detector is shown in Figure 1b. The ground appears on the bottom right of the image and the laser beam, imaged from the side from ground to zenith in a two minute exposure, is visible along the diagonal. The brightness of the beam at each pixel depends on the aerosol and molecular scattering at the scattering altitude imaged in that pixel. The altitude of the scatterers for the system is determined from geometry rather than by the pulse timing used in traditional lidar systems. Since the angular field of view in the system is constant, the altitude resolution, dz, changes with altitude. Thus most pixels in the beam represent lower altitudes. The resolution is excellent in the near-ground region where most aerosols reside, and becomes coarser as altitude increases. There is no overlap function to deal with as in traditional lidar. The image also captures stars in the background. Prior to analysis a dark frame from the cooled CCD camera for the same exposure time is subtracted from the data image.

To determine the intensity at each altitude bin from the image, the beam is fit with a polynomial from four initial points selected along the beam in the image. The perpendicular to the beam is then computed at each bin and pixels are interpolated along the perpendicular to construct a fitting array. The array is then fit to a function consisting of a Gaussian plus a constant. The area under the Gaussian is interpreted as the signal at that altitude, and the constant represents the sky background. The fitting process is shown in Figure 2a for a beam that is aligned along the columns of the CCD pixels and for a beam that is not aligned with the columns (as in our typical data).

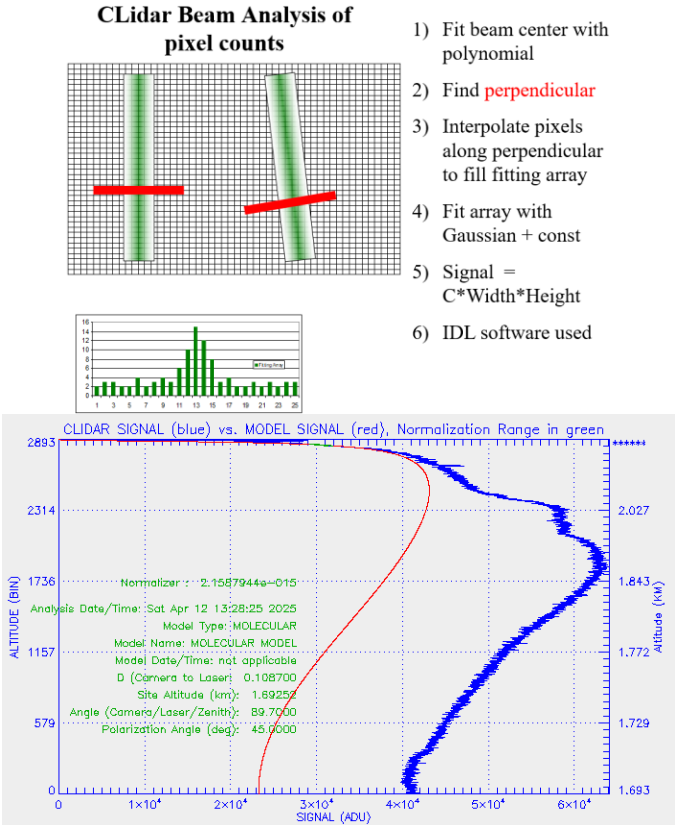

Figure 2. a) Gaussian fit schematic, b) Normalization

Since the signal contains both aerosol and molecular scattering, to remove the molecular scattering the signal is normalized to match a molecular model at a range of altitudes for which aerosol scattering is assumed to be negligible, as is done in the traditional lidar method. Here the signal also depends on the polarization angle. In many experiments, a quarter wave plate is used in the laser transmitter to turn the linearly polarized light into circularly polarized light so that it mimics unpolarized light over the duration of the exposure. It is also possible to normalize the model to a set aerosol to molecular ratio.

A sample altitude vs signal profile is shown in Figure 2b. The molecular model (red) is matched to the signal (blue) in the normalization range (green). Note that while the vertical scale is linear in bin it is non-linear in altitude. The data go all the way to the ground level as the example shown is from the National Oceanic and Atmospheric Administration's test site at Table Mountain, Colorado, USA where ground level is 1693 meters above sea level. The molecular scattering is then subtracted from the signal. An aerosol scattering phase function is assumed since the side scatter detected is sensitive to the relative scattering efficiency at the scattering angle from which the given altitude is viewed. The aerosol scattering phase function can be taken from phase functions derived for general aerosol classes either from CALIPSO space-based data [15] or from inversions of data from nearby ground-based sites in NASA's Aerosol Robotic Network (AERONET). The signal is corrected for transmission. With the assumption of a single scattering albedo, the measured side-scatter, converted to total scatter, is converted to aerosol extinction. Extinction can then be integrated to derive Aerosol Optical Depth (AOD).

The sensitivity of the derived vertical extinction profile to the aerosol scattering phase function has been demonstrated in experiments which employed two cameras at differing distances from the laser, each

viewing the same altitude segment of the atmosphere at the same time but from different scattering angles [16]. While traditional lidar uses one point on the aerosol phase function (at 180 degrees) to determine the extinction to backscatter ratio, Camera Lidar views the beam from the side and thus uses the range of angles from 90 degrees (near the ground) to 180 degrees (near zenith) on the phase function. Utilization of phase functions which do not completely capture the scattering behavior of the actual aerosols present can lead to differences in the derived aerosol extinction profiles from the two detectors, highlighting the need for improved phase function measurements. An integrating polar nephelometer on the ground at the experiment site would provide a direct measurement of the aerosol scattering phase function for low altitude aerosols, and such an instrument is under development. The dual camera method can also be used to constrain the aerosol phase function in the boundary layer by forcing the extinctions from the two detectors to match.

Starphotometry

If a measurement of the Aerosol Optical Depth (AOD) is available it is a very useful constrain on the integrated lidar or camera lidar profile. The two determine an average extinction to backscatter ratio, which often has to be assumed. The AOD is normally measured with sun photometry which requires an additional well-calibrated instrument, and only gets measurements during the daytime. By using stars [17] in the camera lidar images, the AOD can be measured at the same wavelength, time, and location as the aerosol profile with no additional equipment. In addition, pairs of stars can be used with astronomers' stellar observations, which doesn't require calibration [18]. The variety of types of stars is a complication, and reliable algorithms are being developed.

Improvements

When using a pulsed laser for the light source, as with a lidar, a significant reduction in background light can be achieved by blocking the camera in between laser shots. The background light can be the dominate noise source especially in urban locations. A system was constructed [10] that used an optical chopper between the lens and the camera. The laser was part of the NOAA Mauna Loa Observatory lidar running at 30 Hz repetition rate. The chopper was designed to be open for about 1 millisecond when the laser fired and closed for the other 32 milliseconds, reducing the background light by a factor of 32. It was synchronized with the laser with a 140 meter cable, which could be nuisance in many locations. But a simple solution is to have two readily available and inexpensive Global Positioning System (GPS) receivers, at the camera and the laser. Both would be synchronized to the very accurate 1 pulse per second GPS timing signal.

The authors are investigating fabricating an interference filter on a curved surface, allowing a narrower FWHH and substantially reducing the background light. An Imaging Polar Nephelometer is being developed to directly measure the Aerosol Phase Function (APF). This would be an extremely useful measurement since most APFs are calculated from assumed aerosol properties, not directly measured.

Conclusions

The camera lidar has unique features for measuring boundary layer aerosols. The capability of measuring all the way to the ground at high resolution complements traditional lidar, and allows direct comparisons with in-situ instruments. Adding a camera/lens detector to a traditional lidar could be very useful. The simplicity and lower-cost are attractive to researchers in developing countries, and those at undergraduate institutions.

References

[1] Elterman, L., A series of stratospheric temperature profiles obtained with the searchlight technique, J. Geophys. Res. 58, 519–530, 1953.

[2] Antuña-Marrero, Juan-Carlos , Mann, Graham W. Barnes, John , Calle, Abel , Dhomse, Sandip S., Cachorro Revilla, Victoria E., Deshler, Terry, Zhengyao, Li , Sharma, Nimmi and Elterman, Louis, The recovery and re-calibration of a 13-month aerosol extinction profiles dataset from searchlight observations from New Mexico, after the 1963 Agung eruption, Atmosphere, 15, no. 6: 635. https://doi.org/10.3390/atmos15060635, 2024.

[3] Reagan, J. A., Byrne, D. M. and Herman, B. M., Bistatic lidar: a tool for characterizing atmospheric particulates. Part 1. The remote sensing problem, IEEE Trans. Geosci. Remote Sens. GE-20, 229–235, 1982.
[4] Reagan, J. A., Byrne, D. M. and Herman, B. M., Bistatic lidar: a tool for characterizing atmospheric particulates. Part 2. The inverse problem, IEEE Trans. Geosci. Remote Sens. GE-20, 236–243, 1982.
[5] Parameswaran, K., Rose, K. O., and Krishna Murthy, B. W., Aerosol characteristics from bistatic lidar observations, J. Geophys. Res. 89D, 2541–2552, 1984.
[6] Devera, P. C. S. and Raj, P. E., Remote sounding of aerosols in the lower atmosphere using a bistatic cw helium-neon lidar, J. Aerosol Sci. 20 1, 37–44, 1989.
[7] Meki, K., Yamaguchi, K., Li, X., Saito, Y. and Nomura, A., Range-resolved bistatic imaging lidar for the measurement of the lower atmosphere, Opt. Lett. 21**,** 1318–1320, 1996.
[8] Lin, J., Mishima, H., Kubota, Y., Kobayashi, F., Kawahara, T.,
Saito, Y., Nomura, A., Yamaguchi, K. and Morikawa, K., Bistatic imaging lidar measurements in the lower atmosphere, Rev. Laser Eng. 27**,** 827–834, 1999.
[9] Barnes, John E., Bronner, Sebastian, Beck, Robert and Parikh, N. C., Boundary Layer Scattering Measurements with a Charge-Coupled Device
Camera Lidar, Applied Optics, 42, no. 15, 2647-2652, 2003.
[10] Barnes, John E., Sharma, N. C. Parikh, and Kaplan, Trevor B., Atmospheric aerosol profiling with a bistatic imaging lidar system, Applied Optics, 46, no. 15, 2922-2929, 2007.
[11] Howell, Steve B., Handbook of CCD Astronomy, Cambridge University Press, 2006
[12] Wikipedia, https://en.wikipedia.org/wiki/Fisheye_lens
[13] https://diffractionlimited.com/
[14] https://andovercorp.com/optical-bandpass-filters-fundamentals/
[15] Omar, Ali H., Winker, David M., Kittaka, Chieko, Vaughan, Mark A., Liu, Zhaoyan, Hu, Yongxiang , Trepte, Charles R., Rogers, Raymond R., Ferrare, Richard A., Lee, Kam-Pui, Kuehn, Ralph E. and Hostetler, Chris A., The CALIPSO Automated Aerosol Classification and Lidar Ratio Selection Algorithm, Journal of Atmospheric and Oceanic Technology, 26, 1994-2014, DOI: 10.1175/2009JTECHA1231.1, 2009.
[16] , Farinsky, Meg, Garcia, Gabriel E., Sharma, Nimmi C.P., Kabir, Amin, Barnes, John E., Odhiambo, George, Zaldivar, Johnjairo and Masi, Tessa E., Two Camera Setup in Bistatic Camera Lidar for Atmospheric Sensing Applications, SPIE Defense & Commercial Sensing: Laser Radar Technologies and Applications XXX, Orlando, Florida, April 13-17, 2025.
[17] Leiterer, U., et al., 1995: A new star photometer developed for spectral aerosol optical thickness measurements in Lindenberg, Beitr. Phys. Atmosph., 68, 133-141.
[18] Perez-Ramirez, D. et al., Development and calibration of a star photometer to measure the aerosol optical depth: smoke observations at a high mountain site, Atmos. Environ., 42, 2733-2738 (2008).

Dual-Field-of-View Depolarization approach using the Polly^{XT} Raman Lidar: Characterization of aerosol-cloud interactions in the semi-arid climate of Cyprus.

C. Chrysostomou[1,2], *C. Jimenez*[3], *R. E. Mamouri*[1,2], *A. Nisantzi*[1,2], *D. Hadjimitsis*[1,2], *and A. Ansmann*[3]

(1) Eratosthenes Centre of Excellence, Franklin Roosevelt 82, 3012, Limassol, Cyprus
(2) Department of Civil Engineering and Geomatics, Cyprus University of Technology, Archiepiskopou Kyprianou 30, 3036, Limassol, Cyprus
(3) Leibniz Institute for Tropospheric Research (TROPOS), Permoserstraße 15, 04318, Leipzig, Germany

Corresponding author: constantinos.chrysostomou@eratosthenes.org.cy

Introduction

Aerosols are a key parameter when referring to atmospheric studies or advanced climate research. Their role in influencing Earth's energy balance or the formation, lifetime and evolution of clouds has long been studied, but no clear conclusion on their contribution to climate forcing has yet emerged. This leaves us with high uncertainties in both the aerosol-radiation interactions (ARI), as well as in aerosol-cloud interactions (ACI). The latter one especially, exhibits one of the largest uncertainties among all the forcing parameters. According to the Fifth Assessment Report (AR5) of IPCC, the radiative forcing of aerosol-cloud interactions was estimated as -0.45 W/m^2 with uncertainties ranging from -1.2 to 0 W/m^2, whereas the last report (AR6) of IPCC refined these numbers to -0.7 ± 0.5 W/m^2, highlighting in both cases that these values rely on moderate and not high confidence [1], [2]. This last statement showcases how important it is for extensive, detailed, and in-depth studies of these interactions to be conducted now more urgently than ever, as these significant uncertainties arise due to the incomplete understanding of how clouds develop during certain aerosol and weather conditions.

The novel Dual-Field-of-View (DFOV) polarization lidar approach, developed by C. Jimenez et al., 2020, comes as a competent solution to the aforementioned challenges [3]. This method works just by using lidar's data and is able to provide crucial information about the microphysical properties of liquid-water, or even, mixed phase clouds. Properties such as the Cloud Droplet Number Concentration (N_d), their effective radius (R_e), the cloud extinction coefficient (α), and the Liquid Water Content (LWC). Additionally, by using products like the quasi backscatter coefficient and by implementing Doppler Lidar's data, the cloud condensation nuclei (CCN) concentration and the vertical wind below the cloud base can be retrieved, and therefore, the influence of certain type of aerosols and their concentration in relation also to the behavior of the wind, can yield to an unprecedent view of aerosol-cloud interactions.

In this study, data acquired by the Cyprus Atmospheric Remote-Sensing Observatory (CARO) National Facility of the Eratosthenes Centre of Excellence, and more precisely by the Polly^{XT} Raman Lidar and the Halo Photonics (Snoopy) Doppler Lidar, are used to analyze cases of liquid-water or mixed-phase clouds in Limassol. By applying the DFOV Depolarization approach on these cases, cloud properties are able to accurately be retrieved for the first time in the region of Eastern Mediterranean, Middle East and Northern Africa (EMMENA), further contributing to ACI studies.

Methodology

The lidar instrument used is part of the third generation of Polly^{XT} systems and it is installed within a dedicated container at the facility. It functions autonomously and operates continuously, whereby using a diode-pumped laser it is able to emit linearly polarized light at three wavelengths – 1064 nm, 532 nm, and 355 nm – at a pulse repetition rate of 100 Hz, while at the same time it measures the nitrogen Raman signals as it is equipped with channels for the wavelengths of 387, 407, and 607 nm. Fig. 1 below presents the setup of the instrument, depicting all the channels and specifying which ones belong to the far-range receiver, which ones to the near-range one, and the channels that measure the cross-polarized backscattered light (noted with the symbol ⊥) [4, 5].

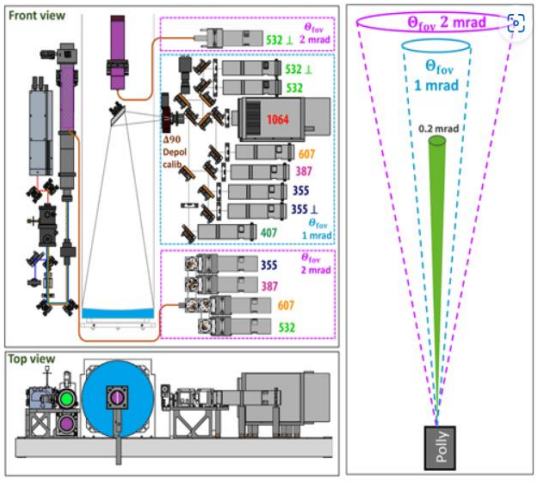

Figure 1. Scheme of the optical setup of the 3rd generation Polly^{XT} Raman lidar as used in [5].

The DFOV polarization lidar method works by using the depolarization ratios of two different FOVs of the 532 nm channels. This is necessary, as the narrower FOV channels (θ_{in} = 1 mrad) look at a slightly different area of the cloud than the wider ones (θ_{out} = 2 mrad), therefore two perspectives are created, whereby comparing the two signals, the multiple scattering effects caused by the cloud droplets can be separated, and the retrieval of clouds' properties becomes possible [5]. As a first step, cloudy days are studied and after necessary signal corrections, the cloud base height (z_{bot}) is estimated with a temporal resolution of 3 minutes, followed then by the calculation of the DFOV ratio by dividing the integrated depolarization ratio of the inner FOV 532 nm signals (δ_{in}) to the integrated depolarization ratio of the outer FOV 532 nm signals (δ_{out}) between z_{bot} and a reference height inside the cloud (z_{ref}) as can be seen below in Eq. 1.

$$\bar{\delta}_{rat}\,(z_{bot}, z_{ref}) = \frac{\bar{\delta}_{in}(z_{bot}, z_{ref})}{\bar{\delta}_{out}(z_{bot}, z_{ref})} \quad (1)$$

Next, the droplet effective radius (R_e), cloud extinction coefficient (α), the cloud droplet number concentration (N_d), and the liquid water content (w_l) are then calculated as follows:

$$R_e\,(z_{ref}) = R_0 + R_1 \times \bar{\delta}_{rat} + R_2 \times \bar{\delta}_{rat}^2 + R_3 \times \bar{\delta}_{rat}^3 \quad (2)$$

$$\alpha\,(z_{ref}) = a_0(R_e, z_{bot}) + a_1(R_e, z_{bot}) \times \bar{\delta}_{in} + a_2(R_e, z_{bot}) \times \bar{\delta}_{in}^2 \quad (3)$$

$$N_d\,(z_{ref}) = \frac{1}{2\pi k}\alpha(z_{ref})R_e^{-2}(z_{ref}) \quad (4)$$

$$w_l\,(z_{ref}) = \frac{2}{3}\rho_w\alpha(z_{ref})R_e(z_{ref}) \quad (5)$$

where, R_0, R_1, R_2, and R_3 are polynomial coefficients that depend on the lidar instrument setup, $a_0(R_e, z_{bot})$, $a_1(R_e, z_{bot})$, and $a_2(R_e, z_{bot})$ are coefficients derived from polynomial regression analysis for the given z_{bot}, $R_e\,(z_{ref})$ and $\bar{\delta}_{in}$, and ρ_w is the liquid-water density. k parameter is described as the cubic power of the ratio of the volume mean droplet radius (R_V) to the effective radius, as follows:

$$k = \frac{R_V^3}{R_e^3} \quad (6)$$

All the above equations are described in detail in the referenced paper number [3].

In addition, for those same days, the lidar product of the quasi backscatter coefficient (β^{quasi}) and the vertical wind obtained from the Doppler Lidar are used, with the first one serving as an approximation of the particle backscatter coefficient, which through the POLIPHON [6] method analysis, CCN concentration can be estimated.

Results and Discussion

In the figures below, the atmospheric conditions, the input parameters, as well as the retrieved parameters of this method are presented. As an example, February 21st, 2025, is used as low-level clouds were identified, while the CCN concentration, and the vertical wind information were available throughout the day. On each time-height plot, black or white dots represent the height of the cloud base.

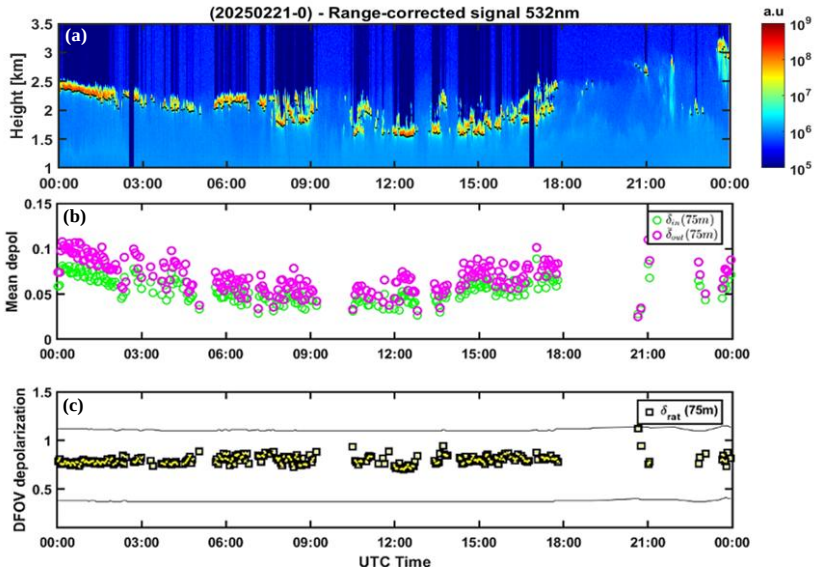

Figure 2. Plots of the input parameters for the DFOV method. Plot (a) shows the range-corrected 532 nm far-range signal, (b) the integrated depolarization ratios from the inner FOV (green) and the outer FOV (pink) 532 nm channels, and (c) the ratio of the DFOV depolarization ratios for each cloud base point (black lines indicate the boundaries of the acceptable values, based on the z_{bot} and the $R_e(z_{ref})$).

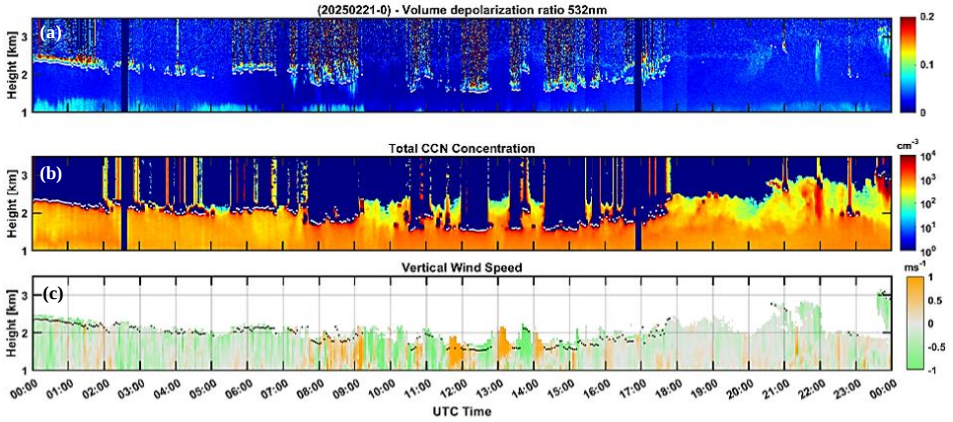

Figure 3. Time-height plots of (a) the volume depolarization ratio at 532 nm of the inner FOV, (b) the total CCN concentration, and (c) the vertical wind for that day.

At first glance, the errorbar plots (c) and (d) of Fig. 4 present an inversely proportionate behaviour as expected. The alteration, however, of the N_d isn't easily interpretable as it relies on both the vertical wind behaviour and the CCN concentration, the type of which also plays an important role in cloud formation processes.

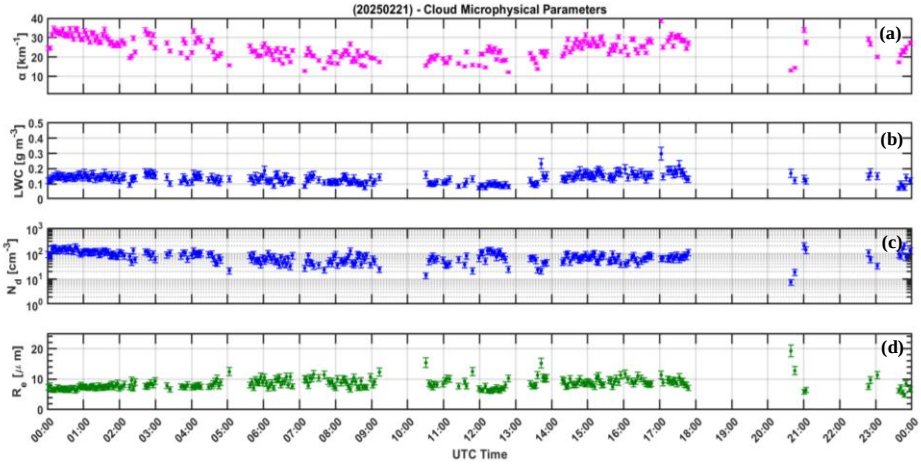

Figure 4. Plot (a) shows the Cloud Extinction Coefficient, (b) the Liquid-Water Content, (c) the Cloud Droplet Number Concentration, and (d) the droplet Effective Radius. The error bars are plotted for all retrieved cloud parameters at z_{ref}.

Conclusions

Continuous and systematic observations and analysis of diverse atmospheric scenarios are needed to capture the variability and complexity of these processes. As of now, a clear conclusion cannot be drawn as to how and how much each parameter affects the characteristics of the clouds, but by combining all the provided information and by extending the analysis, a detailed quantification of Aerosol-Cloud Interactions becomes possible with accurate results. Moreover, next steps include the retrieval of the average vertical wind, the CCN concentration, and the aerosol extinction coefficient for some meters below the cloud base, while the concentration of specific aerosol types, and therefore, their influence on clouds can be estimated.

Acknowledgements

This study has been supported by the EXCELSIOR project under Grant Agreement No 857510, funding from the EU Horizon 2020, the Government of the Republic of Cyprus, and the Cyprus University of Technology. The authors also acknowledge the support received by ATARRI Horizon Europe Widespread Twinning Project under the Grant Agreement No 101160258.

References

[1] Boucher, O. et al.: Clouds and aerosols, in: Climate Change 2013: The Physical Science Basis, Contribution of Working Group I to the Fifth Assessment Report of the Intergovernmental Panel on Climate Change, edited by: Stocker, T. F., Qin, D., Plattner, G.-K., Tignor, M., Allen, S. K., Boschung, J., Nauels, A., Xia, Y., Bex, V., and Midgley, P. M., Cambridge University Press, Cambridge, United Kingdom and New York, NY, USA, 2013.

[2] Forster, P. et al.: The Earth's energy budget, climate feedbacks, and climate sensitivity, in: Climate Change 2021: The Physical Science Basis, Contribution of Working Group I to the Sixth Assessment Report of the Intergovernmental Panel on Climate Change, edited by: Masson-Delmotte, V., Zhai, P., Pirani, A., Connors, S. L., Péan, C., Berger, S., Caud, N., Chen, Y., Goldfarb, L., Gomis, M. I., Huang, M., Leitzell, K., Lonnoy, E., Matthews, J. B. R., Maycock, T. K., Waterfield, T., Yelekçi, O., Yu, R., and Zhou, B., Cambridge University Press, Cambridge, United Kingdom and New York, NY, USA, pp. 923–1054, https://doi.org/10.1017/9781009157896.009, 2021.

[3] Jimenez, C. et al.: The dual-field-of-view polarization lidar technique: a new concept in monitoring aerosol effects in liquid-water clouds – theoretical framework, Atmos. Chem. Phys., 20, 15247–15263, https://doi.org/10.5194/acp-20-15247-2020, 2020.

[4] Engelmann, R. et al.: The automated multiwavelength Raman polarization and water-vapor lidar PollyXT: the neXT generation, Atmos. Meas. Tech., 9, 1767–1784, https://doi.org/10.5194/amt-9-1767-2016, 2016.

[5] Jimenez, C. et al.: The dual-field-of-view polarization lidar technique: a new concept in monitoring aerosol effects in liquid-water clouds – case studies, Atmos. Chem. Phys., 20, 15265–15284, https://doi.org/10.5194/acp-20-15265-2020, 2020.

[6] Mamouri, R.-E. and Ansmann, A.: Potential of polarization lidar to provide profiles of CCN- and INP-relevant aerosol parameters, Atmos. Chem. Phys., 16, 5905–5931, https://doi.org/10.5194/acp-16-5905-2016, 2016.

New capabilities for Fluorescence Lidar Observations at CIAO Observatory

Benedetto De Rosa[1], *Jens Reichardt*[2], *Giuseppe D'Amico*[1], *Aldo Amodeo*[1], *Nikolaos Papagiannopoulos*[1], *Michail Mytilinaios*[1], *Lucia Mona*[1]

(1) Consiglio Nazionale delle Ricerche-Istituto di Metodologie per l'Analisi Ambientale CNR-IMAA, 85050 Potenza, Italy
(2) Deutscher Wetterdienst (DWD), Meteorologisches Observatorium Lindenberg, Am Observatorium 12, 15848, Tauche OT Lindenberg, Germany

Corresponding author: benedetto.derosa@cnr.it

Introduction

Since 1993, atmospheric aerosol study based on multi-wavelength Raman lidar observations is one of the main research activities carried out at CNR-IMAA Atmospheric Observatory (CIAO). Over the years, the observatory contributed to better understanding the role of various types of atmospheric aerosols, including dust, biomass burning aerosol, and volcanic ash in different atmospheric processes. In particular, CIAO operates the POtenza Lidar for Particle Observation (POLPO) capable to measure aerosol depolarization ratio and backscatter coefficient at three different wavelengths (355, 532 and 1064nm) and the aerosol extinction coefficient at 355 and 532nm. Even though this experimental set-up allows quite complete characterization of atmospheric aerosols we have decided to further expand our observational capabilities by integrating POLPO together with an additional lidar system capable of performing fluorescence measurements.

Despite fluorescence-based techniques have been already used in several fields of environmental sciences, lidar applications for atmospheric aerosol studies have been traditionally focused mainly on elastic and Raman scattering techniques.

Consequently, fluorescence played only a minor role in lidar applications and it has often been treated as secondary, despite its potential to add a new dimension to aerosol characterization.

The first truly quantitative aerosol fluorescence spectra were reported by [1] using RAMSES, the Raman lidar for atmospheric moisture sensing, operated by the German Meteorological Service. Thanks to its unique design, RAMSES can measure absolute calibrated fluorescence spectra in a wide spectral interval ranging from UVA to VIS. Such observations clearly demonstrated the RAMSES added value in improving traditional aerosol classification.

Making advantage of these studies we plan to set-up a new fluorescence lidar at CIAO. We will firstly fully calibrate the spectrometer used for fluorescence measurements and secondly, we will perform the first aerosol fluorescence observations at CIAO.

Methodology

The CIAO lidar for fluorescence measurements will be set-up in a laboratory located within a thermally insulated container. This laboratory is equipped with a 10 Hz injection-seeded Nd:YAG laser source emitting the fundamental 1064 nm and the second and third harmonic at 532 nm and 354.7 nm respectively. The atmospheric backscattered light can be collected by two telescopes optimized to detect the signal coming from the near and far range. The far range telescope is designed with a 400 mm primary mirror diameter in classical Cassagrain configuration (F#10) while the near range one has a 200 mm primary mirror (F#5).

The facility allows to have quite high flexibility regarding the selection of the spectral analysis to be done on the light collected by the two mentioned telescopes. Thanks to a modular structure it is possible to set-up different detection scenarios according to the specific observational needs.

The set-up that will be used to perform fluorescence measurements is shown in Fig. 1. The collimated light beam coming out from the telescope (near or far range one) is first spectrally filtered by the modules A and B and finally the UVA fluorescence spectrum is measured by a spectrometer coupled via an optical fiber. Additionally, a mechanical shutter (SH) is located prior to the module A in order to have the possibility to

block completely the atmospheric radiation from the telescope (useful to calibrate the spectrometer with an external lamp). To prevent the strong elastic signals backscattered at the three laser wavelengths from entering the spectrometer the following actions are taken:

- Fundamental and second-harmonic generation light is effectively suppressed by a combination of dichroic beam splitters module and a beam dump. This is a fundamental prerequisite for accurate measurements of fluorescence spectra in the VIS region. In this particular study, however, we are not interested in considering visible and infrared spectral regions.
- Laser radiation at 355nm (the only one sent into the atmosphere) is suppressed by the module A containing a dichroic beam splitter reflecting the 355nm wavelength and transmitting the spectral region 365 – 600nm. The reflected radiation is properly dumped to avoid unwanted back reflections.

As vibrational-rotational Raman bands of oxygen and nitrogen molecules are extremely intense in comparison to Raman scattering by other specimens, or (mineral) fluorescence they should be suppressed as well to avoid spill-over effect in the detector. This is done by the module B containing another dichroic mirror reflecting approximately 95% (and subsequently dumping) only the spectral region where the rovibrational Raman bands of molecular oxygen and nitrogen are located.

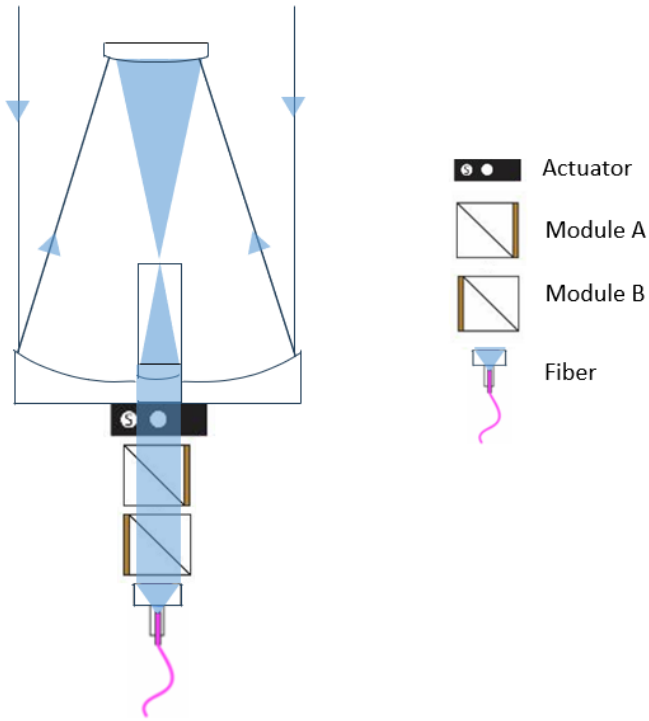

Figure 1. The optical setup adopted for the fluorescence measurements. It includes a Classical Cassegrain telescope, actuators for the insertion and removal of shutters, module A and module B, and the optical fiber used for signal collection.

The filtered signal is coupled into a fiber-fed Shamrock A-SR-750-A spectrometer (focal length 750 mm, f/9.7), equipped with interchangeable gratings (300 gr/mm for emission overview over a wide spectral range spectral, 1200 gr/mm for high resolution measurements and 2400 gr/mm for higher resolution UV measurements). The main characteristics are reported in table.

Table 1. Grating grooves, spectral coverage and full width half maximum (FWHM).

Grating grooves (mm^-1)	Spectral coverage (nm)	FWHM (nm)
300	138.3	8.7
1200	32.1	2.0
2400	14.3	0.9

Finally, the Licel Multispectral Lidar Detector based on a multi-anode, metal channel dynode photomultiplier allows simultaneous detection of multiple spectrometer wavelengths. A total of 32 photocathode elements together with 32 single photon counting systems provide 2-dimendional spectral and range resolved lidar signals.

Discussion

Before performing fluorescence measurements with the mentioned experimental set-up a calibration of the spectrometer is needed. For this purpose, a 6035 Spectral Calibration Lamp, which produces well characterized narrow and intense spectral lines from the excitation of argon gas and mercury vapor, will be directly sent into the spectrometer by an additional optical fiber. During the calibration the lidar system will be operated in standard mode, with the exception that atmospheric return signals will be blocked to prevent background interference by closing the shutter SH.

Subsequently, the relative intensity response of the spectrometers will be determined by either calibrated LEDs where applicable [3], or using solar background measurements in combination with radiative transfer model calculations. The absolute calibration of the spectral response will follow the well-established water-vapor Raman technique. This will include the correction for differential light extinction as described by [1]. For clouds, the particle extinction coefficient will be assumed to be wavelength-independent. In the case of aerosol layers, Ångström exponents derived from POLPO or co-located spectral radiometer measurements will be used to describe the wavelength dependence extinction.

After the instrument calibration, the operational measurement phase will begin. The location of CIAO observatory is particularly well-suited for fluorescence observations. Located in a rural area and surrounded by extensive oak forests, the site is often affected by local biomass burning events during the summer season [2]. These fires, typically occurring within a few kilometers from the station, frequently produce smoke plumes that remain confined within the planetary boundary layer (PBL), especially under stable atmospheric conditions.

The implementation of fluorescence detection will complement traditional elastic and Raman lidar observations, adding a new dimension to the characterization of these events. Fluorescence spectra of atmospheric aerosols, as presented by [3] have shown that biomass burning aerosols (BBA) exhibit broad and nearly symmetric fluorescence spectra, typically centered between 505 and 518 nm. Figure 2 shows an example of a lidar observation of a fire that occurred on 16 July 2024 approximately 1 km from the observatory, highlighting the potential of the upgraded system to resolve both vertical and spectral features of the plume.

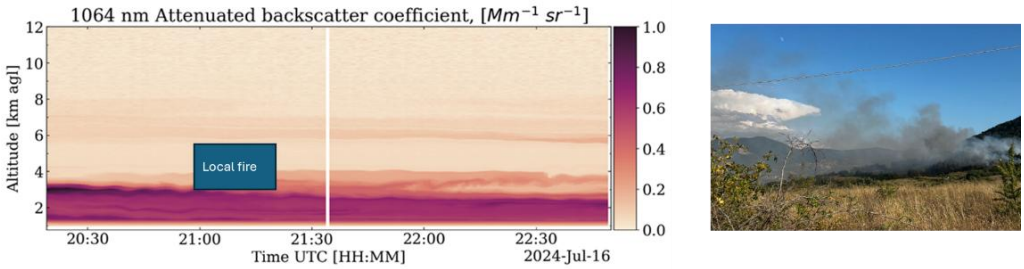

Figure 2. Temporal evolution of attenuated backscatter coefficient at 1064 nm obtained with the POLPO systems on 16 July 2024 from 20:19 to 22:50 UTC. On the right we report an image of the local fire captured by the lidar

Dust aerosol events, especially Saharan dust outbreaks, have also been a recurring subject of study at our observatory. These events have been routinely tracked using elastic backscatter and depolarization measurements. In particular, the lidar POLPO provides measurements of depolarization at 355, 532 and 1064 nm. Recent studies suggest that even mineral dust—previously assumed to be weakly fluorescent—can exhibit detectable fluorescence features, often attributed to quartz or other silicate components. This opens new research avenues in identifying mineralogical content within dust layers using fluorescence spectra. Finally, given the presence of bioaerosols in our area, simultaneous measurements can be performed with the pollen instrument. SwisensPoleno Jupiter latest generation of optical particle measurement systems for real-time measurement and monitoring of bioaerosols.

Conclusions

By expanding our lidar capabilities to include fluorescence detection, we expect to gain key insights into aerosol source attribution, mixing state, and atmospheric processing. In particular, the ability to distinguish between dust, smoke, and potentially bioaerosols based on spectral fluorescence signatures represents a major advancement. The upcoming absolute calibration campaign in June will ensure quantitative retrievals and spectral accuracy. The results of this effort, along with our first case studies of aerosol fluorescence measurements, will be presented at ELC2025.

Acknowledgements

The authors acknowledge the IR0000032 – ITINERIS, Italian Integrated Environmental Research Infrastructures System (D.D. n. 130/2022 - CUP B53C22002150006) Funded by EU -Next Generation EU PNRR- Mission 4 “Education and Research” - Component 2: “From research to business” – Investment 3.1: “Fund for the realisation of an integrated system of research and innovation infrastructures” and ATMO-ACCESS (Access to Atmospheric Research Facilities) Funded in the frame of the programme H2020-EU.1.4.1.2 – Grant Agreement n. 101008004 – (1 April 2021 – 31 March 2025). The authors also acknowledge the Joint Research Unit ACTRIS-Italy funded by the Italian Ministry of University and Research.

References

[1] Reichardt, J.: Cloud and aerosol spectroscopy with Raman lidar, J. Atmos. Ocean. Tech., 31, 1946–1963, https://doi.org/10.1175/JTECH-D13-00188.1, 2014.

[2] De Rosa, B., Amato, F., Amodeo, A., D’Amico, G., Dema, C., Falconieri, A., ... & Mona, L. (2022). Characterization of extremely fresh biomass burning aerosol by means of lidar observations. Remote Sensing, 14(19), 4984.

[3] Reichardt, J., Behrendt, O., and Lauermann, F.: Spectrometric fluorescence and Raman lidar: absolute calibration of aerosol fluorescence spectra and fluorescence correction of humidity measurements, Atmos. Meas. Tech., 16, 1–13, https://doi.org/10.5194/amt-16-1-2023, 2023.

[4] Reichardt, J., Lauermann, F., and Behrendt, O.: Fluorescence spectra of atmospheric aerosols, EGUsphere [preprint], https://doi.org/10.5194/egusphere-2024-3928, 2024.

From Peaks to Seas: Introducing the DECIPHER and LAMP Measurement Campaigns

M. Di Paolantonio[1], *D. Dionisi*[1], *G.L. Liberti*[1], *G. Giuliano*[1], *L. Masi*[1,2], *D. Summa*[3], *A. Rajput*[4], *G. Doglioni*[4], *L. Giovannini*[4], *D. Zardi*[4,5], *and P. Di Girolamo*[6]

(1) Institute of Marine Sciences (ISMAR), National Research Council (CNR), Rome, Italy
(2) "Parthenope" University of Naples, Naples, Italy
(3) Institute of Methodologies for Environmental Analysis (IMAA), National Research Council (CNR), Tito Scalo, Italy
(4) Department of Civil, Environmental and Mechanical Engineering (DICAM), University of Trento, Trento, Italy
(5) Center Agriculture Food Environment (C3A), University of Trento, Trento, Italy
(6) Department of Health Sciences (DISS), University of Basilicata, Potenza, Italy

Corresponding author: marco.dipaolantonio@artov.ismar.cnr.it

Introduction

Understanding the complex interactions between atmospheric processes and the Earth's surface requires precise, high-resolution observations across diverse geographical environments. From rugged alpine terrains to open marine settings, the ability to capture vertical and temporal variations in atmospheric constituents is vital for improving weather prediction models and climate projections. In this context, Raman lidar technology has emerged as a powerful remote sensing tool, capable of delivering detailed measurements of aerosols, clouds, temperature, and water vapor with fine spatial and temporal resolution.

This work presents two recent atmospheric field campaigns, DECIPHER (Disentangling Mechanisms Controlling Atmospheric Transport and Mixing Processes Over Mountain Areas at Different Space- and Time-scales) and LAMP (Lidar-based Atmospheric Measurement at Pianosa), which together span a unique range of environmental conditions, from alpine areas to marine-influenced zones. Central to both efforts is the MARCO system (Micro-pulse Atmospheric optical Radar for Climate and weather Observations), a compact, transportable Raman lidar developed by the University of Basilicata. MARCO's advanced capabilities in measuring backscatter, extinction, depolarization, temperature and water vapor profiles enable atmospheric profiling in challenging field conditions.

MARCO Lidar System

Figure 1: System MARCO (left) next to the University of Trento wind lidar (right) during the DECIPHER campaign.

MARCO is a compact and easily transportable Raman lidar system based on a micro-pulse laser source, developed by the Lidar Group of the University of Basilicata in 2022 [1]. MARCO is an advanced instrument that enables the acquisition of vertical profiles of the backscatter and extinction coefficients of atmospheric particulate matter and clouds, the aerosol depolarization ratio, temperature, and the mixing ratio of atmospheric water vapor. Housed in a sealed and rugged container with a fused-silica window (Figure 1), it is capable of operating in all weather conditions and can be remotely operated with 24/7 measurement capabilities. The technical characteristics are listed below (Table 1). The overall small volume (<3 m^3), weight (750 kg) and power consumption (~900 W) translates into the possibility of considerably simplifying the logistics and costs associated with the transportation and deployment of the system.

Table 1. Technical specifications of MARCO lidar system.

Laser	Nd:YAG
Power/Energy	250 μJ / 5 W @ 354.7 nm
Frequency	20 kHz
Beam divergence	< 0.3 mrad
Reception channels	Elastic total, ∥ and ⊥ @ 354.7 nm Ro-vib. Raman N_2 @ 386.7 nm Ro-vib. Raman H_2O @ 407.5 nm Rotational Raman (Low J) @ 354.3 nm and (High J) @ 352.9 nm
Telescope diameter	406 mm (f/8)
Field of view	0.31 mrad (FWHM)
Full overlap	~ 500 m
Detector	Photomultiplier modules (Hamamatsu H10721P-210)
Filter bandwidths	0.2–0.5 nm
Vertical sampling	15 m (analog & photon counting)
Vertical resolution	15 m - 150 m
Temporal resolution	3 s - 30 min
Acquisition system	16 Bit 40 MHz analog acquisition, 800 MHz photon counting

DECIPHER

The measurement campaign DECIPHER, funded by the Italian Ministry of University and Research and organized by the University of Trento, is part of the international TEAMx (multi-scale Transport and Exchange processes in the Atmosphere over Mountains – programme and eXperiment) program [2].

The project aims at improving the understanding of: i) processes controlling the exchange of momentum, energy and substances between the Earth surface and the atmosphere over mountains; ii) transport processes across a variety of scales, including turbulent mixing and removal by precipitation scavenging, and evaluating how accurately these are represented in numerical models used for weather prediction and climate simulation. Field measurements have and will be performed with multiple instruments during Summer/Autumn 2024 and 2025 at two selected target areas representative of two different mountain situations: the isolated peak of Col Margherita (Eastern Italian Alps) and an extended slope on Monte Baldo (Central Italian Alps).

As already anticipated above, the first part of the measurement campaign took place at Passo Valles, Trento, Italy (Lat: 46,338469 N, Lon: 11.799588 E, Elev: 2032 m a.s.l.) between July 27th and October 29th 2024, with the system MARCO being deployed (Figure 1) near Col Margherita CNR-ISP observatory [3], next to the wind lidar (Leosphere WINDCUBE 100s) of the University of Trento and a weather station managed by Meteotrentino.

The synergic use of the set of deployed instruments (e.g., applied to measurements of vertical profiles of latent and sensible heat fluxes) will allow for performing measurements of fundamental importance for a comprehensive understanding of alpine meteorological phenomena and the characterization of atmospheric turbulent properties.

The measurements are particularly effective for the purposes of the DECIPHER project. Specifically, they will contribute to understanding the mechanisms that control atmospheric transport and mixing processes in

mountain areas at different spatial and temporal scales, characterizing turbulent processes in the atmospheric boundary layer on mountain slopes, and, in general, surface-atmosphere exchange processes.

Figure 2 shows the temporal evolution of the backscattering coefficient of aerosols and clouds, as well as the mixing ratio of water vapor for a selected case study.

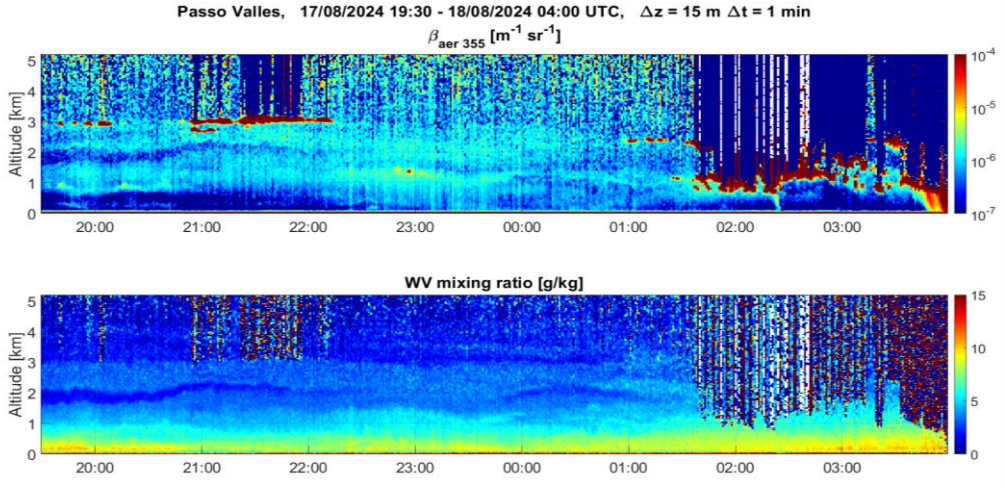

Figure 2: Temporal evolution of the backscattering coefficient of aerosols and clouds, and water vapor mixing ratio for a selected case study during the DECIPHER field campaign (August 17th-18th 2024).

LAMP

On December 17th 2024, MARCO was installed at the BRP-CNR (Base Ricerca Pianosa – Italian National Research Council) in Pianosa, Tuscan Archipelago, Italy (Lat: 42.584896 N, Lon: 10.097097 E, Elev: 17 m a.s.l.) as part of the LAMP project. This project, organized by the Institute of Marine Sciences (ISMAR-CNR), aims to characterize marine aerosols and monitor atmospheric water vapor to better understand the interactions between marine aerosols and cloud formation [4], as well as to study extreme precipitation events in the Mediterranean [5].

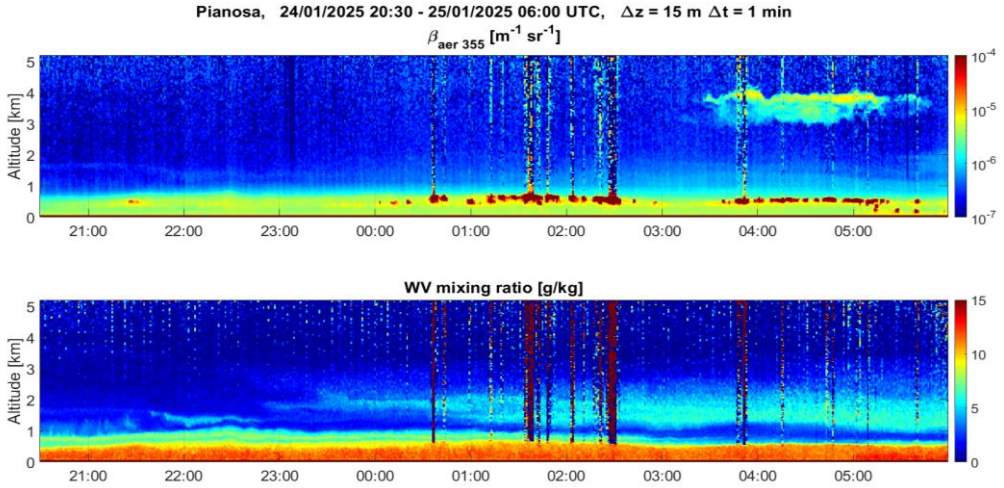

Figure 3: Test measurements carried out during the night between January 24th and 25th 2025 in the LAMP field campaign. The graph shows the temporal evolution of the backscattering coefficient of aerosols and clouds, as well as the mixing ratio of water vapor.

The island of Pianosa was chosen as the ideal site for the installation of the lidar system due to its geographical characteristics: small size, limited human activity, and absence of complex topography. These conditions allow for the acquisition of background measurements of marine aerosol and the study of its interaction with continental aerosols under different atmospheric circulation scenarios. Moreover, the CNR base in Pianosa is in a favourable position for monitoring atmospheric water vapor and studying intense precipitation in the Mediterranean. The collected measurements will contribute to the validation of models and satellite products (e.g., EarthCARE). The project also represents the first planned step toward the potential future permanent installation of a multispectral scanning lidar system, integrated into the international ACTRIS observation network.

Activation, testing, and calibration of the lidar system took place from January 21th to 28th, 2025 (Figure 3), and the system will remain active, carrying out continuous measurements for a full year.

Conclusions

Preliminary results from the DECIPHER and LAMP campaigns highlight the versatility and scientific value of the MARCO lidar system in capturing key atmospheric processes across different environments. From high-altitude alpine regions to remote Mediterranean islands, MARCO has proven to be capable of delivering high-resolution, continuous observations that will contribute to advance our understanding of aerosol dynamics, water vapor transport, and surface-atmosphere exchange. Collected data is currently being analyzed and will be used in detailed case studies and comparisons with EarthCARE profiles. Specific case studies will be illustrated at the Conference.

Acknowledgments

The project DECIPHER was funded by the European Union under NextGenerationEU. PRIN 2022 Prot. n. 2022NEWP4J_001.

We acknowledge the support of B. Raco, scientific coordinator of BRP-CNR. We also thank F. Sartori and P. Scarfiello for their assistance with the logistics of the DECIPHER campaign, and S. Trifirò and R. Scaccia for their support with the logistics of the LAMP campaign.

References

1. Di Girolamo, P.; Franco, N.; Di Paolantonio, M.; Summa, D.; Dionisi, D. Atmospheric Thermodynamic Profiling through the Use of a Micro-Pulse Raman Lidar System: Introducing the Compact Raman Lidar MARCO. *Sensors* **2023**, *23*, 8262, doi:10.3390/s23198262.
2. Disentangling Mechanisms Controlling Atmospheric Transport and Mixing Processes over Mountain Areas at Different Space- and Timescales (DECIPHER) Available online: https://www.teamx-programme.org/projects/DECIPHER/ (accessed on 4 October 2024).
3. CNR-ISP Col Margherita Observatory Available online: https://www.isp.cnr.it/index.php/en/research/other-activities/col-margherita (accessed on 4 October 2024).
4. Cairo, F.; Di Liberto, L.; Dionisi, D.; Snels, M. Understanding Aerosol–Cloud Interactions through Lidar Techniques: A Review. *Remote Sensing* **2024**, *16*, 2788, doi:10.3390/rs16152788.
5. Flamant, C.; Chazette, P.; Caumont, O.; Di Girolamo, P.; Behrendt, A.; Sicard, M.; Totems, J.; Lange, D.; Fourrié, N.; Brousseau, P.; et al. A Network of Water Vapor Raman Lidars for Improving Heavy Precipitation Forecasting in Southern France: Introducing the WaLiNeAs Initiative. *Bull. of Atmos. Sci.& Technol.* **2021**, *2*, 10, doi:10.1007/s42865-021-00037-6.

A methodology to measure the GHK factors using atmospheric regions where the volume linear depolarization ratio is known. Challenges and limitations.

N. Siomos[1], *V. Freudenthaler*[1]

(1) Meteorologisches Institut, Ludwig-Maximilians-Universität München, Munich, Germany

Corresponding author: nikolaos.siomos@lmu.de

Introduction

Polarization lidar measurements are of great importance for the characterization of the atmospheric aerosol composition and are often applied in inversion algorithms to determine the concentration of non-spherical particles (e.g. [1]). The main targets of such measurements are the volume and particle linear depolarization ratio (VLDR and PLDR, respectively). A major challenge in measuring the VLDR profile is introduced by cross-talk effects which can originate from: non-ideal optics in the lidar transceiver, misalignment of those optics with respect to the analyzer, and also due to impurities in the emitted laser beam. [2] has introduced a methodology to account for such systematic errors. This technique, commonly referred to as "GHK correction", is generally adopted within the Aerosol Clouds and Trace Gases Research Infrastructure (ACTRIS). It is applied on the lidar systems of the network if the polarization properties of the transceiver optics and of the laser beam are known. While some ACTRIS systems already fulfill these requirements, this is not generally the case due to the following reasons. First, the polarizing properties of transceiver optics such as dichroic beam-splitters, partial reflective mirrors, protective windows, and high power laser mirrors might be unknown or they are only partially known. Quite often there is also no possibility to measure them in the laboratory. Second, the eigenaxis of each of the receiver optics must be accurately aligned, either parallel or perpendicular to the eigenaxis of the analyzer. This is important in order to avoid introducing retardation-related cross-talks. If the optics are not properly aligned at the manufacturing stage of the lidar then it can be very challenging to do so afterwards. And third, the state of polarization of the emitted laser beam must be known. Achieving this experimentally is challenging due to the high power of the laser.

In this study, we present a methodology for measuring the GHK factors directly from lidar measurements. The technique is, in principle, applicable to any aerosol lidar system and relies on measurements in at least three atmospheric regions where the VLDR is known.

Methodology

According to [2], the ratio of the signal intensities I_R and I_T measured in the reflected and transmitted channel R and T, respectively, is linked to the atmospheric polarization parameter a through Eq. 1.

$$\frac{1}{\eta}\frac{I_R}{I_T} = \frac{G_R + aH_R}{G_T + aH_T} \quad (1), \qquad \eta = \frac{\eta^*}{K} \quad (2)$$

The G_R, G_T, H_R, and H_T terms represent cross-talk effects in the R and T channels. The calibration factor η accounts for the different opto-electronical amplification in channels R and T. It is connected to the gain ratio η^* of the R and T channels recorder during the polarization calibration measurement. Cross-talk effects can be also present during the polarization calibration measurement. These are expressed with factor K. By substituting Eq. 2 to Eq. 1 and performing some algebraic computations we end up with Eq. 3 and 4.

$$\delta_c \frac{K G_T}{G_R} + a\delta_c \frac{K H_T}{G_R} - a\frac{H_R}{G_R} = 1 \quad (3), \qquad \delta_c = \frac{1}{\eta^*}\frac{I_R}{I_T} \quad (4)$$

The calibrated ratio δ_c is defined in Eq. 4 as the ratio of the R and T signals divided by the gain ratio η^* At this point we will split the parameters of Eq. 3 into two groups, the cross-talk related factors X_1, X_2, and X_3, and the non cross-talk related factors $A_{i,1}, A_{i,2}, A_{i,3}$. These are defined in Eq. 5-10.

$$A_{i,1} = \delta_{c,i} \quad (5), \qquad A_{i,2} = a_i\delta_{c,i} \quad (6), \qquad A_{i,3} = a_i \quad (7),$$

$$X_1 = \frac{KG_T}{G_R} \text{ (8)}, \qquad X_2 = \frac{KH_T}{G_R} \text{ (9)}, \qquad X_3 = -\frac{H_R}{G_R} \text{ (10)}$$

The index *i* in Eq. 5-7 denotes measurements of δ_c in atmospheric layers with different a values. There is no restriction as to when these measurements, and the corresponding polarization calibration, are performed (e.g. simultaneously or consecutively). By substituting Eq. 5-10 to Eq. 3 we end up with Eq. 11.

$$A_{i,1}X_1 + A_{i,2}X_2 + A_{i,3}X_3 = 1 \text{ (11)}$$

Equation 11 describes a linear system of equations which can be solved towards the X_1, X_2, and X_3 factors (e.g. with the linear least squares method) if the calibrated ratio $\delta_{c,i}$ is measured in at least three atmospheric layers where a_i is known. Solving the system with less than three known a_i values is meaningless because it will be under-determined, resulting to an infinite number of solutions.

Once the X_1, X_2, and X_3 factors are retrieved, they can be applied to calculate the VLDR (δ_V) using Eq. 62 from [2], which can be reformed to Eq. 12 by replacing the GHK factors with X_1, X_2, X_3 and δ_c.

$$\delta_V = \frac{\delta_c(X_1+X_2)-(1-X_3)}{(1+X_3)-\delta_c(X_1-X_2)} \text{ (12)}$$

Challenges and limitations

A major challenge of the technique is that the VLDR, measurant of a, is actually the target of polarization lidar measurements. In most cases, a is only known within aerosol-free regions. The molecular linear depolarization ratio (MLDR) can be calculated in such regions from the transmission of the narrow-band interference filter (IF) of the polarization channels, the emitted laser wavelength, and the atmospheric temperature (e.g. [3], [4]). Interference filters are commonly used to suppress background photons and unwanted laser lines. Using IFs with different characteristics modifies the molecular a values without affecting any other polarization-related parameter of the lidar system.

The central wavelength of the IF of an elastic channel is typically close to the corresponding emitted wavelength. The MLDR of an elastic IF will range between the Cabannes and the full Rayleigh values (i.e. 0.00363 and 0.0143 at 532 nm according to [3]) depending on the filter bandwidth. Narrow filters, which suppress all of the Stokes (S) and anti-Stokes (O) RR lines, will produce MLDR values close to Cabannes value. Broad IFs, which allow all RR lines from the S and O branches to be transmitted, would produce an MLDR close to the Rayleigh one. All intermediate bandwidths will produce values between these two extremes. By using three elastic IFs, it is, in principle, possible to produce three well-defined values of a in aerosol free regions. Then, the corresponding calibrated ratios could be measured per filter and would be applied to solve Eq. 11. The accuracy requirements of this approach are described in the next section.

The elastic IFs produce generally small MLDR values. In order to achieve larger values, the highly depolarized Raman lines of Nitrogen (N_2) and Oxygen (O_2) have to be targeted. Interference filters made for rotational Raman applications isolate part of the pure RR spectrum from either the Stokes or the anti-Stokes branch. The pure RR lines of N_2 and O_2 are highly depolarized with a constant MLDR of 0.75 [5]. Using a RR IF instead of an elastic one for the polarization channels would, ideally, result to a MLDR of exactly 0.75. This is difficult to achieve in practice, because most RR filters are not designed to operate at 0° angle of incident (AOI). For larger AOIs, the transmission of the p and s polarizations is no longer exactly the same, leading to diattenuation. Then, the exact MLDR value is difficult to calculate because the AOI-dependence of the diattenuation is generally not available. More accurate values of the corresponding MLDR should be measured directly by mounting the RR IF on a well-calibrated lidar.

An alternative to the RR approach is to use the vibrational Raman (VR) lines of N_2 or O_2. This results to MLDR values of 0.0940 and 0.1952 from the full ro-vibrational spectrum of N_2 and O_2, respectively. Using narrow-band IFs to isolate the central VR line, instead, results to an MLDR of 0.0265 and 0.0628 for N_2 and

O_2, respectively. These values were computed using the ARC (Algorithm for Rayleigh and Raman Calculations) software [6] (publicly available here https://github.com/nikolaos-siomos/ARC) based on the equations from [4]. The advantage of this approach is that VR IFs are designed for 0° AOI and diattenuation is no longer a problem. A technical difficulty, though, is that the radiation of the VR lines that reaches the polarization channels is already attenuated by ~1-2 orders of magnitude in most Raman lidar systems as most photons are already directed to a dedicated Raman channel by a dichroic beam-splitter. In addition, it is also questionable whether the X_1, X_2, and X_3 factors are the same in the Raman shifted wavelength. This approach cannot be applied to 1064 nm channels as the VR lines are naturally quite weak and are also located in a spectral region where the CO_2 and water vapor absorption is not negligible.

Finally, the most straightforward way to determine the atmospheric parameter a is to use co-located measurements from a well calibrated lidar system. A similar approach has already been presented by [7] using a neighboring system. The main drawback of using a co-located reference system is that transportation is certainly costly and also not always possible.

Uncertainty of the retrieval and discussion

In this section, we will discuss and compare the uncertainty requirements for solving Eq. 11 based on the aforementioned approaches for determining the atmospheric parameter a at least three times. The following cases are examined: a) use of three elastic IFs, one targeting the Cabannes line, one targeting the full Rayleigh spectrum and one intermediate filter b) use of two elastic IFs and one RR IF, c) use of one elastic IF and two VR IFs targeting the O_2 Cabannes line and the full ro-vibrational spectrum of O_2, d) use of a reference lidar, e) use of one elastic IF, one VR IF targeting the full ro-vibrational spectrum of O_2, and one RR IF. The MLDR values of case c) are very similar to the VLDR of depolarizing aerosol layers measured with a reference lidar. Consequently. the uncertainties of cases c) and d) will be provided together. All related a_i values and corresponding uncertainties, converted to VLDR ($\delta_{v,i}$) for better understanding, are provided in Table 1 per case.

Table 1. VLDR uncertainty introduced by the GHK correction due to uncertainties in a_i and $\delta_{c,i}$. Four different methods are applied to determine a_i (converted to $\delta_{v,i}$) in three atmospheric regions.

Method to determine a_i		3 Elastic IFs	2 Elastic and 1 RR IFs	1 Elastic and 2 VR IFs or Reference lidar measurements	1 Elastic, 1 RR, 1 VR IF
VLDR converted from a_i and uncertainty	$\delta_{v,1}$	0.004 ± 1E-6	0.004 ± 0.0001	0.004 ± 0.0001	0.004 ± 0.0001
	$\delta_{v,2}$	0.010 ± 1E-6	0.75 ± 0.01	0.07 ± 0.001	0.75 ± 0.01
	$\delta_{v,3}$	0.014 ± 1E-6	0.014 ± 0.0001	0.19 ± 0.001	0.19 ± 0.001
$\delta_{c,i}$ relative uncertainty		0.001 %	0.1 %	0.1 %	1 %
Target VLDR		Target VLDR Uncertainty (Max Absolute Bias)			
0		<1E-05	<0.002	<0.001	0.010
0.1		<0.002	0.014	<0.002	0.014
0.2		0.006	0.024	<0.002	0.023
0.3		0.013	0.030	0.008	0.029
0.4		0.023	0.032	0.018	0.029
0.5		0.036	0.030	0.033	0.029

The uncertainty of the retrieved X_1, X_2, and X_3 factors depends on the uncertainties of a_i and $\delta_{c,i}$. We have assumed that the uncertainty of the calibrated ratio is affected only by random measurement errors when recording the R and T signals and the gain ratio η^*. We analyzed the case of a system with an analyzer which separates the beam in one co-polar (p) and one cross-polar (s) component. Without loss of generality, we assumed that the cross-polar component is recorded in channel R. For such a setup in an ideal lidar transceiver the values of X_1, X_2, and X_3 are all unity. In our simulations, we variate all three X factors from 0.5 to 1.5 (~9000 combination in total). These combinations corresponds to non-ideal systems where the X_1,

X_2, and X_3 will be retrieved including uncertainties. We assume a_i is known within three atmospheric regions and simulate the $\delta_{c,i}$ values the lidar would measure in those three regions adding uncertainties to both parameters. Then, we solve Eq. 11 to retrieve X_1, X_2, and X_3 including errors. In the last step, we apply the GHK correction to target VLDR values ranging from 0 to 0.5 and simulate the corresponding uncertainty due to errors in the retrieved X factors. The uncertainty of δ_{c_i} is the measured relative standard error in our simulations. The uncertainty of a_i is the expected maximum absolute bias. We have simulated the effect that different combinations of the a_i and $\delta_{c,i}$ uncertainties have on the target VLDR retrieval. Table 1 provides a summary of those simulations. In all four cases, the a_i and $\delta_{c,i}$ uncertainties have been selected so that the VLDR error does not exceed 0.02 (0.04) when performing the GHK correction to aerosol layers with target VLDR smaller than 0.3 (0.5).

According to Table 1, it is obvious that relying solely on elastic IFs for the retrieval of the X_1, X_2, and X_3 factors is not possible. The required a_i and $\delta_{c,i}$ uncertainties are unrealistically small, indicating that the system of Eq. 11 is ill-posed when only small a_i values are provided.

Using a RR IF and two elastic IFs results in a retrieval of the X factors that is far less sensitive to the a_i and $\delta_{c,i}$ uncertainties. An error of the RR MLDR up to 0.01 can be well tolerated. This is a realistic demand, given that the RR MLDR has to be verified experimentally .

Using two VR IFs (or reference lidar measurements) and one elastic IF has similar uncertainty demands with the RR method. An MLDR uncertainty of 0.001 is easily achievable for AOIs close to 0°. The target VLDR error is improved compared to the RR method for VLDR values smaller than 0.3. It has been assumed that the X_1, X_2, and X_3 values are the same between the elastic and the Raman shifted wavelength. This has to be verified before applying the VR method. The benefit of using co-located lidar measurements is that this assumption is not needed and also no exchanging of IFs is necessary.

The least demanding method in terms of uncertainty is using one elastic, one RR, and one O_2 VR IFs. The a_i uncertainty requirement can be easily met for all three IFs and the $\delta_{c,i}$ uncertainty is also less demanding (1 %) compared to the other methods. The limitations of the VR method apply also here.

Acknowledgements

This project/ receives funding from the European Union's Horizon 2020 research and innovation programme under grant agreements No 871115. ACTRIS-D is funded by the German Federal Ministry for Education and Research (BMBF) under grant agreements 01LK2001A-K & 01LK2002A-G.

References

[1] R. E. Mamouri and A. Ansmann, "Fine and coarse dust separation with polarization lidar," *Atmospheric Measurement Techniques*, vol. 7, no. 11, pp. 3717–3735, 2014, doi: 10.5194/amt-7-3717-2014.

[2] V. Freudenthaler, "About the effects of polarising optics on lidar signals and the Δ90 calibration," *Atmos. Meas. Tech.*, vol. 9, no. 9, pp. 4181–4255, Aug. 2016, doi: 10.5194/amt-9-4181-2016.

[3] A. Behrendt and T. Nakamura, "Calculation of the calibration constant of polarization lidar and its dependency on atmospheric temperature," *Opt. Express*, vol. 10, no. 16, p. 805, Aug. 2002, doi: 10.1364/OE.10.000805.

[4] M. Adam, "Notes on Temperature-Dependent Lidar Equations," *Journal of Atmospheric and Oceanic Technology*, vol. 26, no. 6, pp. 1021–1039, Jun. 2009, doi: 10.1175/2008JTECHA1206.1.

[5] C.-Y. She, "Spectral structure of laser light scattering revisited: bandwidths of nonresonant scattering lidars," *Appl. Opt.*, vol. 40, no. 27, p. 4875, Sep. 2001, doi: 10.1364/AO.40.004875.

[6] N. Siomos *et al.*, Rotational Raman scattering through narrow-band interference filters: investigating uncertainties using a new Rayleigh scattering code developed within ACTRIS, *in the proceedings of the 30th International Laser Radar Conference*. S.l.: Springer International PU, 2023.

[7] A. Papetta *et al.*, "Lidar depolarization characterization using a reference system," *Atmospheric Measurement Techniques*, vol. 17, no. 6, pp. 1721–1738, 2024, doi: 10.5194/amt-17-1721-2024.

CE710-LIFE fluorescence lidar: first results at ATOLL, Lille, France

***I. E. Popovici*[1,2]**, *I. Veselovskii*[3], *Q. Hu*[1], *W. Boissière*[1], *T. Podvin*[1], *G. Dubois*[1], *R. Loisil*[1], *P. Goloub*[1], *J. Vieira*[2], *C. Vinciguerra*[2], *S. Victori*[2]

(1) Univ. Lille, CNRS, UMR 8518 - LOA - Laboratoire d'Optique Atmosphérique, F-59000 Lille, France
(2) R&D Department, CIMEL Electronique, 75011 Paris, France
(3) Prokhorov General Physics Institute, Moscow, Russia

Corresponding author: i-popovici@cimel.fr

Introduction

Fluorescence techniques for aerosol studies have been in use since the 1970s [1], primarily employing lasers and optical systems in low-pressure laboratory chambers for in situ measurements. Early applications of laser-induced fluorescence (LIF) targeted trace gases like the OH radical, VOCs, and NO_2 [2–5], but were limited to controlled environments without vertical atmospheric profiling. These foundational studies demonstrated the potential of fluorescence for aerosol classification. Fluorescence lidar systems now enable vertical chemical identification of aerosols [6], enhancing our understanding of aerosol properties, distribution, and their climatic impact, and helping to reduce current uncertainties [7].

Fluorescence lidars detect particles containing UV-excitable organic compounds, including bioaerosols (pollen, fungal spores), combustion-related particles, SOAs, organic-rich marine aerosols, and mineral dust coated with biological material. They use measurements of backscatter, depolarization, spectral extinction, and fluorescence to distinguish aerosol types. Two main detection methods exist: spectrometer-based systems, offering detailed spectral resolution but with greater complexity and size [8], and optical filter-based systems, which are more suitable for real-time and operational applications due to their simplicity and effective wavelength separation [9–11]. The following describes the development of a new fluorescence lidar using the optical filter-based detection approach.

Methodology

The CE710-LIFE (*Laser Induced Fluorescence Explorer*) lidar (Fig. 1b) was developed through the collaboration of scientists at LOA (Laboratoire d'Optique Atmosphérique), lidar experts at PIC (Prokhorov General Physics Institute) and CIMEL lidar manufacturing company, within the framework of AGORA-Lab CNRS Labcom. The system has been operating since October 2024 at the ATOLL (Atmospheric Observations in LiLle) ACTRIS NF (National Facility) in Lille, France. This novel high-power fluorescence lidar, unique in Europe, can probe the atmosphere up to 30 km of altitude (elastic backscattering) and thus access the properties of atmospheric particles by exploiting elastic, Raman and enhanced fluorescence profiles at several wavelengths in the UV-VIS-NIR, an innovation that shows promising results for better knowledge and classification of atmospheric particles vertically.

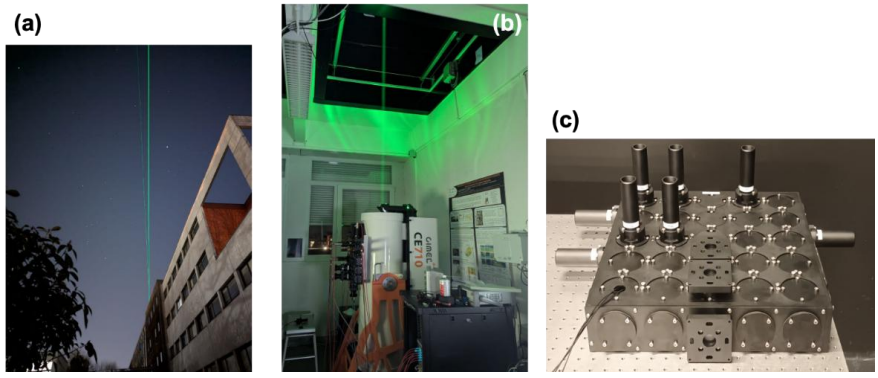

Figure 1. CE710-LIFE lidar at ATOLL ACTRIS NF, Lille, France: a) view of LILAS and LIFE beams by night, scattering through the atmosphere, b) installation of CE710-LIFE lidar at ATOLL, c) view of the modular 5x5 "Lego-like" light analysis system (analyzer) of the CE710-LIFE lidar

The CE710-LIFE lidar is composed of the following parts: i) a Lumibird Merion MW 9-100 tripled Nd:YAG laser, with a pulse energy of 260 mJ at 355 nm, operating at 100 Hz, ii) a 40 cm diameter Newton carbon-fiber telescope, iii) a Beam Expander (BE) allowing the separation of 355 nm emission-only for dedicated spectral fluorescence studies, and a double-branch (355 nm and 532 nm,1064 nm) for regular operation, iv) a 15-channels-capacity Licel acquisition system (electronic bay) and v) a "Lego-like" receiving module (Fig. 1c), allowing modular configurations of up to 15 channels using dichroic mirrors, interference filters and polarizing beamsplitters (PBS). The full overlap of LIFE lidar is reached at 500 m altitude. Motorized mirrors are integrated on the emission part, for remote control of the alignment. The polarization calibration is also controllable and programmable by software and pre-trigger is included to ensure precise synchronization of measurements.

The system detects elastic backscattering at 355 nm, 532 nm, 1064 nm, N_2 Raman backscattering at 387 nm, 408 nm water vapor channel, and 530 nm Rotational Raman channels and is planned to integrate the 353 nm and 1056 nm rotational Raman channels. The system also has 3 depolarization channels at 355 nm, 532 nm and 1064 nm and a fluorescence channel at 466 nm. Additionally, the lidar enables to perform CO_2 Raman measurements. An interference filter with a width of 0.3 nm (produced by Alluxa) was centered at 371.7 nm wavelength to select CO_2 Raman line with a frequency shift of 1285 cm^{-1}. The filter's peak transmission is approximately 80%, with specified suppression of 355 nm and 532 nm radiation of greater than 12 orders. The initial configuration of LIFE system is similar to LILAS multi-wavelength Raman fluorescence lidar [12], part of ACTRIS/EARLINET, configuration chosen for comparison reasons and evaluation of performances. The modular analyzer will allow ease of change between different channels configuration, one of future configurations including 5 fluorescence channels (423-641 nm).

In Fig. 1a, two laser beams can be seen. The one on the left corresponds to LILAS lidar, the one on the right corresponds to CE710-LIFE lidar. For comparison, LIFE emits 26 W of light per second, while LILAS emits 2.6 W of light per second, making LIFE appear ~10 times brighter than LILAS system.

The CE710-LIFE lidar is a state-of-the-art research lidar dedicated to fluorescence studies and will serve as a tool to improve our future models of ACTRIS compliant high-power CE710 lidar series at CIMEL. The purpose of the manufacturing LIFE lidar was also to develop a modular research-oriented ACTRIS compliant system, that would allow both scientific and industrial evolutions for future lidar systems.

Results and Discussion

Figure 2 presents backscatter coefficient (Fig. 2a) and fluorescence backscatter (Fig. 2b) measurements performed by CE710-LIFE lidar on the night of 5-6 April 2025 at Lille, France.

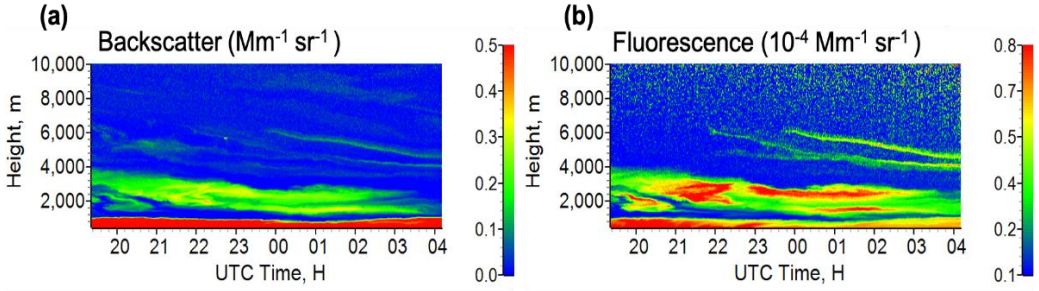

Figure 2. Spatio-temporal distribution of aerosol parameters on the night of 5-6 April 2025 at ATOLL, Lille, France. (a) Aerosol backscatter coefficient at 532 nm (β_{532}) and (b) fluorescence backscattering at 466 nm (β_F)

The backscatter measurements (Fig. 2a) present 3 main categories of layers: the PBL, from surface (400 m on the figure) up to 1100 m, with a homogeneous structure, a ~2000 m thick layer between 1200 m and 4000 m, and thin layers up to 10 000 altitude AGL. The fluorescence measurements (Fig. 2b) allow to discriminate the species present inside these layers: the strong fluorescence of the layers between 2000 m

and 4000 m altitude and for the thin layers up to 10 000 indicate the presence of organic particles in these layers. The low depolarization (<0.07 at 1064 nm) for these layers and the altitude of these layers (free troposphere, clear separation from PBL) suggests the presence of non-depolarizing (spherical) particles with organics content, indicating the presence of long-range transported smoke. Back-trajectories performed for this night indicate passage of air masses over wildfires in eastern US. A strong fluorescence (organics presence) is also observed for the PBL during night (19:30-23:30 UTC), stronger than that in the beginning of the day (0-4 UTC), suggesting different aerosol types in the PBL.

Profiles averaged along the whole time series (19:20-04:15) of backscatter coefficient at 532 nm, of fluorescence backscatter at 466 nm and the CO_2 concentrations derived from the 371 nm channel are presented in Fig. 3. The highest backscatter is observed in the PBL (0.8 $Mm^{-1}sr^{-1}$ at 500 m) and backscatter up to 0.2 $Mm^{-1}sr^{-1}$ is observed for the smoke layer between 1200 and 3500 m altitude. A very strong fluorescence is observed for the smoke layer at 1200-3500 m altitude (0.55 $*10^{-4}$ $Mm^{-1}sr^{-1}$ at 2500 m), close to the one observed for the pollutants in the boundary layer (0.7 $*10^{-4}$ $Mm^{-1}sr^{-1}$ at 500 m).

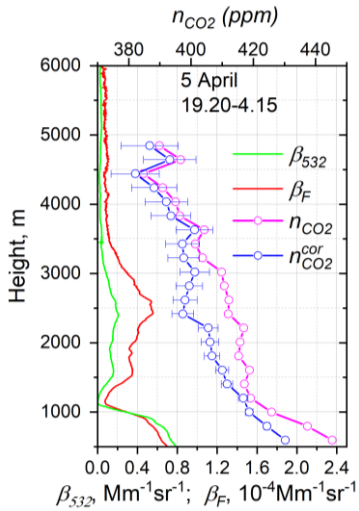

Figure 3. Profiles on 5-6 April 2025 for the period 19:20-04:15 UTC measured by CE710-LIFE lidar at ATOLL, Lille, France: aerosol backscatter at 532 nm (β_{532}), fluorescence backscattering at 466 nm (β_F), CO_2 concentration profile (n_{CO2}) and corrected CO_2 concentration profile (n_{CO2}^{cor})

Additionally, the possibility of CO_2 profiling was demonstrated. Fig. 3 shows concentration of CO_2 (n_{CO2}) measured on 5 April 2025 with 200 m resolution. The aerosol fluorescence penetrates within the CO_2 Raman channel, causing an enhancement of the observed signal and as a first step, the fluorescence signal at 466 nm channel is used to correct this contribution. The profile corrected for fluorescence impact (n_{CO2}^{cor}) is shown in Fig. 3 with blue symbols. For the episode considered, the fluorescence backscattering is quite low (below 0.6 $Mm^{-1}sr^{-1}$) and the corresponding contribution is below 10 ppm. At the moment, CO_2 measurements are not calibrated and results are given in arbitrary units. Still, Fig. 3 clearly demonstrates decrease of CO_2 concentration with height.

Conclusions and perspectives

This paper presents the description and first results of the first prototype of CIMEL high-power multi-wavelength fluorescence lidar called CE710-LIFE. It is the first step towards the manufacturing of industrial fluorescence lidars, proving the use of such high-quality and modular systems for aerosol research and discretization of aerosol types. The first results of the high-power fluorescence CE710-LIFE show the performances of such system to profile fluorescence up to 8 000 -10 000 m altitude by night (compared to 4 000 – 6 000 m achieved by LILAS), the interest of exploring spectral fluorescence using the 5-wavelengths

fluorescence channels and the potential to profile trace gases, such as CO_2, field that is yet to be explored by lidars systems.

While CE710-LIFE lidar is designed for high-end research on aerosol fluorescence, using a high-power UV laser, plans for a more compact, automatic, modular CE710 lidar are under way. The perspectives for CIMEL are to make use of the lessons-learnt on this high-performance system to propose affordable and automatic solutions, including the fluorescence solution and its quality, to lidar users.

Acknowledgements

CE710-LIFE lidar was funded by OBS4CLIM EQUIPEX project (ANR-11-EQPX-0010). The authors want to thank University of Lille, CNRS, SNO PHOTONS ACTRIS/EARLINET, ACTRIS and CaPPA Labex and CDP AREA projects. The CaPPA project (Chemical and Physical Properties of the Atmosphere) is funded by the French National Research Agency (ANR) through the PIA (Programme d'Investissement d'Avenir) under contract « ANR-11-LABX-0005-01 » and by the Regional Council « Hauts-de-France » and the « European Funds for Regional Economic Development » (FEDER).

References

[1] Gelbwachs, J. and Birnbaum, M.: Fluorescence of atmospheric aerosols and lidar implications. Appl. Opt., 12(10), 2442–2447, https://doi.org/10.1364/AO.12.002442, 1973

[2] Holland, F. et al.: In Situ Measurement of Tropospheric OH Radicals by Laser-Induced Fluorescence—A Description of the KFA Instrument, Journal of the Atmospheric Sciences, 52 (19), 3393-3401,1995

[3] Faloona, I.C. et al.: A Laser-induced Fluorescence Instrument for Detecting Tropospheric OH and HO2: Characteristics and Calibration. Journal of Atmospheric Chemistry 47, 139–167, https://doi.org/10.1023/B:JOCH.0000021036.53185.0e, 2004

[4] St. Clair, J. M. et al.: CAFE: a new, improved nonresonant laser-induced fluorescence instrument for airborne in situ measurement of formaldehyde, Atmos. Meas. Tech., 12, 4581–4590, https://doi.org/10.5194/amt-12-4581-2019, 2019

[5] Javed, U. et al.: Laser-induced fluorescence-based detection of atmospheric nitrogen dioxide and comparison of different techniques during the PARADE 2011 field campaign, Atmos. Meas. Tech., 12, 1461–1481, https://doi.org/10.5194/amt-12-1461-2019, 2019

[6] Veselovskii, I. et al.: Combining Mie–Raman and fluorescence observations: a step forward in aerosol classification with lidar technology, Atmos. Meas. Tech., 15, 4881–4900, https://doi.org/10.5194/amt-15-4881-2022, 2022

[7] IPCC (2021). Climate Change 2021: The Physical Science Basis. Contribution of Working Group I to the Sixth Assessment Report of the Intergovernmental Panel on Climate Change. Cambridge University Press. https://doi.org/10.1017/9781009157896, 2021

[8] Reichardt, J. et al.: Spectrometric fluorescence and Raman lidar: absolute calibration of aerosol fluorescence spectra and fluorescence correction of humidity measurements, Atmos. Meas. Tech., 16, 1–13, https://doi.org/10.5194/amt-16-1-2023, 2023

[9] Veselovskii, I. et al.: Mie–Raman–fluorescence lidar observations of aerosols during pollen season in the north of France, Atmos. Meas. Tech., 14, 4773–4786, https://doi.org/10.5194/amt-14-4773-2021, 2021

[10] Veselovskii, I. et al.: Fluorescence lidar observations of wildfire smoke inside cirrus: a contribution to smoke–cirrus interaction research, Atmos. Chem. Phys., 22, 5209–5221, https://doi.org/10.5194/acp-22-5209-2022, 2022

[11] Veselovskii, I. et al.: Multiwavelength fluorescence lidar observations of smoke plumes, Atmos. Meas. Tech., 16, 2055–2065, https://doi.org/10.5194/amt-16-2055-2023, 2023

[12] Hu, Q. et al.: Long-range-transported Canadian smoke plumes in the lower stratosphere over northern France, Atmos. Chem. Phys., 19, 1173–1193, https://doi.org/10.5194/acp-19-1173-2019, 2019

POLIS1064 – A polarization Raman lidar with state-of-the-art recorders for minimizing analogue signal distortions

M. Haimerl [1], *N.Siomos*[1], *V. Freudenthaler* [1], *F. Duran*[2], *B. Stein*[2], *B. Mielke*[2], *A. Louridas*[3], *G. Georgousis*[3], *A.Hafiz*[4], *I.S. Stachlewska*[4]

(1) Ludwig-Maximilians-Universität, Meteorological Institute, Theresienstraße 37, 80333 Munich, Germany
(2) Licel GmbH, Gustav-Meyer-Allee 25, 13355 Berlin, Germany
(3) Raymetrics S.A., Spartis 32, Metamorfosi 14453, Greece
(4) University of Warsaw, Faculty of Physics, Institute of Geophysics, L.Pasteura 5 02-093, Warsaw, Poland
Corresponding author: m.haimerl@lmu.de

Introduction

Multi-wavelength lidar measurements are essential for aerosol remote sensing as they can provide additional information on the aerosol size and type. Such measurements are commonly performed using the fundamental of an Nd:YAG laser at 1064nm and the first two harmonics at 532nm and 355 nm. It is known that signal detection in the near infrared is challenging due to limitations in the dynamic range and quantum efficiency of the detectors. While photon-counting detection is possible with photo-multipliers (PMT), e.g. Hamamatsu R3236 and H12694A, their thermo-electric cooling system is rather bulky. An alternative is given by avalanche photo-diodes (APD) which offer higher quantum efficiency at 1064 nm, solves the size limitations and should offer a better dynamic range. For APDs, signal amplification is needed, hence, any noise and analogue distortions introduced to measured signals are also amplified. This limits dynamic range by introducing artifacts, e.g.in the far range where lidar signals are highly attenuated by the atmosphere. [1]

Here, we discuss a novel series of APDs developed by Licel GmbH under the scope of minimizing the APDs susceptibility to noise and analogue distortions. These new APDs are part of a newly designed reference lidar system (POLIS1064, see Figure 1) by CARS-LMU (Center of Aerosol Remote Sensing – Ludwig-Maximilians University) and developed by Raymetrics S.A. in the frame of the ACTRIS (Aerosol, Clouds, and Trace Gases Research Infrastructure).

Methodology

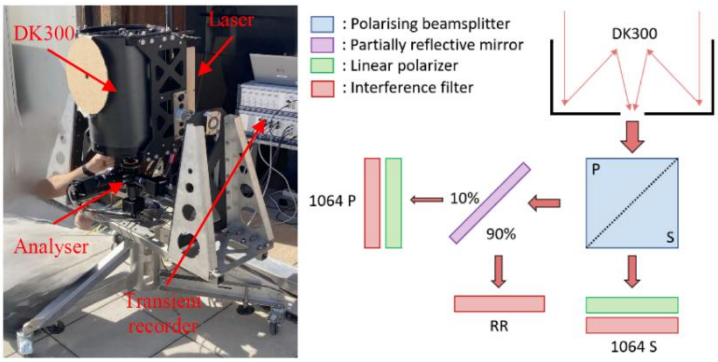

Figure 1. Left: Picture of the new lidar system. Laser: Innolas Spitlight EvoS, rep. rate 100 Hz and 120mJ pulse energy. Telescope: Dall-Kirkham with 300 mm diameter and 1500 mm focal length (DK300). Right: Schematic of the detection box after the telescope. A polarizing beam splitter separates cross (S) and parallel (P) polarisation. A partially reflective mirror further separates the P polarization in two parts, reflecting 90% of the signal to the rotational Raman (RR) channel. Cleaning linear polarisers are installed in front of each polarisation channel followed by interference filters.

As a mobile reference lidar, POLIS1064 was designed in a way that it can be transported under minimal effort. In that sense, assembling and disassembling must be simple and should not introduce any misalignment to optical components. One of the main advances of our POLIS1064 are the new APDs. In contrast to PMTs, APDs suffer from a comparably lower internal signal gain, thus amplification of the collected signal is needed. As a consequence, all electric distortions at the input side of the amplifier get amplified along with the signal and make APDs more susceptible to electric interferences compared to PMTs

operating in analogue mode. Major sources of signal interspersions in lidars are ground-loops and radio-frequency electromagnetic induction. These can originate e.g., by the electronics of the laser power supplies, or other radio-frequency radiators and even from external devices plugged to the same electric power phase.

To reduce the influence of these distortions, two new developments were introduced by Licel GmbH. First, the analogue-digital converter was implemented into the APD detector head assembly after the pre-amplifier to provide better shielding through the detector housing and avoid AC coupled interspersion through cables. Second, the APD power supply was isolated and a filter stage for the protected earth connection was set.

During the development of the new APDs, extensive tests of the different versions of the APD electronic modules developed by Licel GmbH were done to assess the effectiveness of reducing the electronic distortions in APD signals. For these tests we were using the ESA Mobile Raman Lidar (EMORAL) [3] detection line at 1064 nm. Four different versions of the Licel electronic modules were used; the profiles of measured dark signal (1 minute average 100 shots acquisition, total of 10 profiles) of each version are plotted in Figure 2. To evaluate the performance of the new APDs used at POLIS1064, we performed a 1 hour dark-signal-measurement over with 10 s averages of 1000 shots. A shutter at the opening of the detection box ensured that no light would reach the detectors. After aligning the lidar by means of an alignment camera we performed measurements to see the performance of the whole new system. The distance of full overlap of the system is 300 m, verified by a telecover test.

Results and Discussion

APD dark measurements

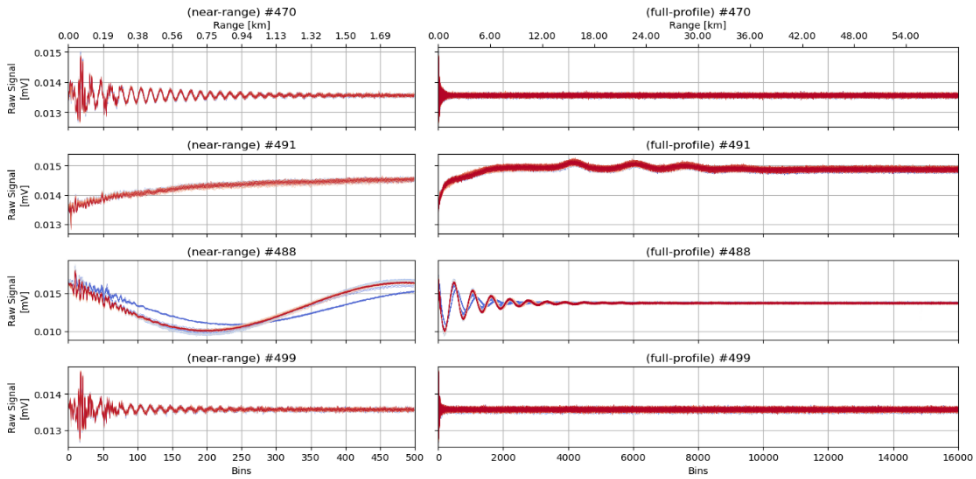

Figure 2. Dark signal profiles for different versions of Licel APD electronic modules tested in the EMORAL lidar. Numbers #470, #488, #491, #499 indicate different modifications of the electronic setup of APD and transient recorder.

The dark signals from version #470 (initial module installed in EMORAL) look good on full profile (right plot) but have fine distortions at near range (left plot) that persist up to bin 400 (1.5km). These are the distortions that we want to reduce using the new Licel modules, particularly from bin 100 (375m, close to where EMORAL full overlap is completed). Version #491 successfully removed the fine scale distortions but introduced ascending slope in near-range and wavy structures in far-range. Version #488 also reduced the fine distortions significantly but added low frequency distortions with periodically decaying-amplitude observed till bin 5000 (18.75km). Results from #499 (currently used in EMORAL) show great improvement by limiting fine distortions up to bin 260 (975m) and reducing its amplitude at bin 100 to approximately a half of that observed by #470. The version proposed for POLIS1064, will be also tested in EMORAL in May 2025 at Licel GmbH.

In Figure 3, we depict the dark signal measurement with a 10 μs pre-trigger range. The Q-switch trigger pulse appears at ~1024 range bin. The other features are interspersions in the beginning of the pre-trigger

range which originate due to charging of the power capacitors for the laser diodes. This was confirmed by the laser manufacturer [2]. The signal baseline shifts with time, decreasing by ~0.2 mV within one hour. This shift could occur due to warming of electronics in the transient recorders. Changes in the baseline are not particularly alarming, as the background is normally removed while analysing the signals.

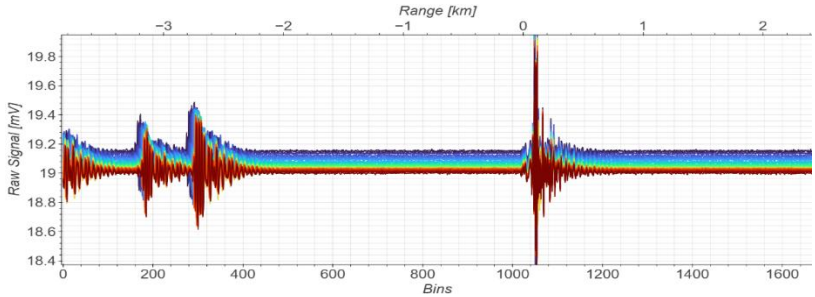

Figure 3. Raw dark signal plotted over range bins and range in km against the raw signal amplitude in mV. Each line displayed corresponds to 1 minute averages. Negative ranges correspond to the pre-trigger region.

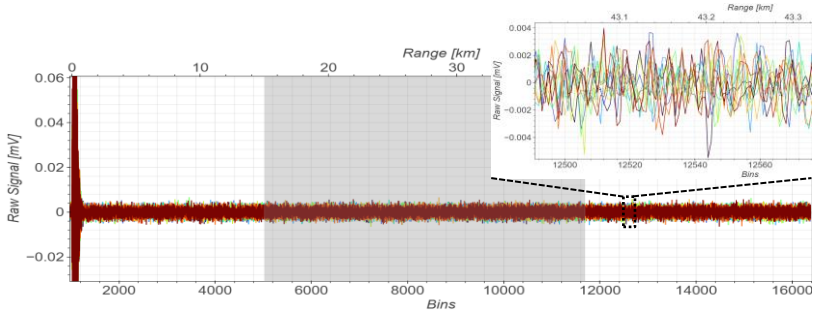

Figure 4. Close-up of the measured dark signal between 0 km and 50 km. Another close-up between 43 km and 43.3 km is added for visual inspection of the noise.

The interspersions in the pre-trigger range do not seem to introduce ringing. Statistical analysis performed between 15 – 35 km, after removing the background (see Figure 4), shows a Gaussian distribution of noise according to the Shapiro-Wilk test that confirms the absence of low frequency distortions in the signal. The standard deviation is 8.76 µV, corresponding to 1000 shot-averages and a high voltage of 300 V. As a result, the noise-per-bin-per shot should be on the order of 280 µV. This is in agreement with the laboratory tests performed by Licel GmbH without a laser operating; they found the noise-per-bin-per shot in the order of 220 µV when applying a high voltage of 345 V.

Rayleigh measurement (10.04.2025)

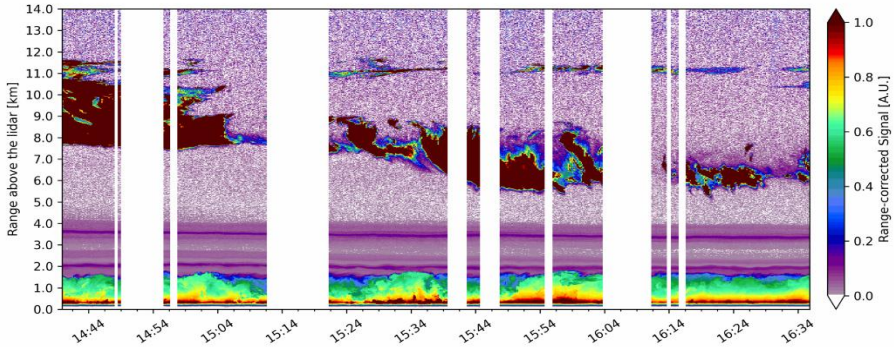

Figure 5. Quick-look plot of range corrected lidar signal of the 1064 S channel recorded on 10.04.2025. Cirrus clouds are above 5 km. Gaps occur due to laser shut-downs during airplane overpasses. Time is CEST (+2 UTC).

The quick-look in Figure 5, shows multiple aerosol layers starting in the boundary layer and reaching up to 4 km. Cirrus structures are visible initially with a base at 7.8 km and they continuously descend down to 5.4 km during the following 1,5 hours. From 15:20 CET on, another elevated thin cirrus cloud appears at ~11 km.

The 1064 P signal can be seen in Figure 5. The Rayleigh fit test seems successful up to 15.2 km, despite the multiple aerosol and cirrus layers. The layer-like structures visible above 12 km might be due to stratospheric aerosols. The depolarization ratio (not shown) indicates that those are stratospheric aerosols but to draw firm conclusions more measurements have to be performed in cleaner conditions and nighttime. Signal induced distortions or ringing could be observed. For brevity the 1064 S and 1064 RR channels are not shown here, however, theý show comparably good results. The Rayleigh fit test analysis and quick-looks were produced with the open-source Python code ATLAS (Automated Lidar Analysis Software) [4].

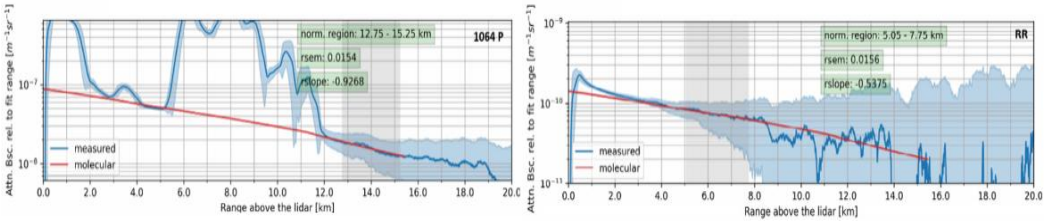

Figure 6. Lidar signal at 1064 P channel and Rayleigh backscatter signal (red) calculated from local radiosonde data (Oberschleissheim, 10868 WMO, 12:00 UTC). The range-corrected signals (blue) measured on 10.04.2025 normalized to Rayleigh profile. Blue shadows indicate the corresponding standard deviation per range bin.

Conclusions

The preliminary analysis of the first measurements of POLIS1064 looks very promising. The analogue signal issues, that have been for years limiting the retrieval of aerosol lidar products at 1064 nm, might have finally been overcome. Of course, this has to be verified by intercomparisons with other 1064 systems, especially the ones used in the ACTRIS. Aerosol-free regions, even under the presence of aerosol layers and cirrus, could be detected during daytime up to 15 km for the 1064 P channel. The newly developed APDs from Licel GmbH, a key factor for the improved performance, showed no obvious signal distortions, such as low frequency distortions and ringing in the far range of the lidar profile, according to the dark measurement. Again, we show a preliminary analysis of the first measurements of a completely new system. The polarisation analysis will follow soon. Nighttime measurements and comparisons with other similar lidar systems are already planned and will be performed in the near future.

Acknowledgements

This project receives funding from the European Union's Horizon research and innovation programme under grant agreement No. 871115. ACTRIS-D is funded by the German Federal Ministry for Education and Research (BMBF) under grant agreements 01LK2001A-K & 01LK2002A-G. The tests of Licel GmbH APD electronic modules were done at the ACTRIS-PL facility of the University of Warsaw within "APD Ground Loop Prevention (AGLP)" the EC-funded Trans-National Access in ATMO-ACCESS project (GA no.101008004). ACTRIS-PL is funded by the Ministry of Science and Higher Education of Poland under grant agreement 2024/WK/04. We thank Opto-Electronics section (TEC-MME) at the European Space Research and Technology (ESTEC) of the European Space Agency (ESA) for providing the ESA Mobile Raman Lidar EMORAL that was developed within non-commercial scientific collaboration of University of Warsaw (UW), Ludwig Maximilian University of Munich (LMU), and Raymetrics S.A. within "Technical assistance for Polish Radar and Lidar Mobile Observation System (POLIMOS)" funded by ESA-ESTEC (4000119961/16/NL/FF/mg).

References

[1] Weitcamp, C. and Eloranta, E.E.: Lidar Range resolved optical remote sensing of the atmosphere, Springer 2005.
[2] Rapp, S.; Innolas GmbH, personal communication, 24 February 2025.
[3] Stachlewska, I.S., et al.: EMORAL—Mobile Mie-Raman Lidar with Fluorescence, Polarization and Water Vapor Observational Capabilities for Satellite Cal/Val Field Campaigns. In: Singh, U.N., Tzeremes, G., Refaat, T.F., Ribes Pleguezuelo, P. (eds) Space-based Lidar Remote Sensing Techniques and Emerging Technologies. LIDAR 2023. Springer Aerospace Technology. Springer, Cham. https://doi.org/10.1007/978-3-031-53618-2_21.
[4] Siomos, N.: ATLAS v0.5.0, Opensource Python code, URL: https://github.com/nikolaos-siomos/ATLAS .

LUCE: A Pioneering Lidar Mission for Earth Sciences

Paolo Di Girolamo[1], *Davide Dionisi[2], Marco Di Paolantonio[2], Donato Summa[3], Simone Lolli[3], Giuseppe D'Amico[3], Lucia Mona[3], Rosalia Santoleri[4], Simona Zoffoli[4], Francesco Tataranni[4], Sara Venafra[4], Arianna Rinaldi[4], Raffaele Votta[4], Roberto Luciani[4], Matteo Picchiani[4], Francesco Longo[4], Valentina Sacchieri[5], Francesco Coppola[5], Pasquale Ferrara[5], Peter Coppo[5], Alessandro Perna[5], Guglielmo Landi[5], Emanuele Capuano[5], Gianluca Aroldi[5], Matteo Burresi[5], Paolo Mosciarello[5], Luca Zerilli[5], Alberto Cosentino[5], Antonio Dattoli[6], Yongxiang Hu[7], Chris A. Hostetler[7], Tyler Thorsen[7], John Smith[7], Mark Vaughan[7], Jason Tackett[7], Brian Getzewich[7], Michael J. Behrenfeld[8], Scott Braun[9], Bob Holz[10], Gerald "Jay" Mace[11], Hal Maring[12], Laura Lorenzoni[12], Stephen R. Hall[7], Charles R. Trepte[7]*

(1) Department of Health Sciences, School of Engineering, University of Basilicata, 85100 Potenza, Italy
(2) Institute of Marine Sciences, Italian National Research Council, 00133 Rome, Italy
(3) Institute of Methodologies for Environmental Analysis, Italian National Research Council, 85050 Tito Scalo, Italy
(4) Italian Space Agency, 00133 Rome, Italy
(5) Leonardo S.p.A, Italy
(6) TMC Europa, Italy
(7) NASA Langley Research Center, MS 475, Hampton, VA, USA
(8) Oregon State University, Corvallis, OR, USA
(9) NASA Goddard Space Flight Center, Greenbelt, MD, USA
(10) University of Wisconsin-Madison, Madison
(11) University of Utah,
(12) NASA Head Quarters, DK000, Washington, MD, USA

Corresponding author: paolo.digirolamo@unibas.it

Abstract

The LUCE mission, formerly Cloud and Aerosol Lidar for Global Scale Observations of the OceanLand-Atmosphere System (CALIGOLA), is an advanced multi-purpose space lidar mission, exploiting elastic (Rayleigh-Mie), depolarized, Raman and fluorescent lidar echoes from atmospheric and ocean constituents, with a focus on atmospheric and oceanic observation aimed at characterizing the Ocean-EarthAtmosphere system and the mutual interactions within it. This mission has been conceived by the Italian Space Agency (ASI) with the aim to provide the international scientific community with an unprecedented dataset of geophysical parameters capable of increasing scientific knowledge in the areas of atmospheric, aquatic, terrestrial, cryospheric and hydrological sciences. The Italian Space Agency is partnering with NASA on this exciting new space lidar mission. The mission is planned to be launched in the time frame 2031-2032, with an expected lifetime of 3-5.

Exploiting the three Nd:YAG laser emissions at 354.7, 532 and 1064 nm and the elastic (Rayleigh-Mie), depolarized, Raman and fluorescent lidar echoes from atmospheric and ocean constituents, CALIGOLA will carry out multi-wavelength profile measurements of the backscatter, extinction and fluorescent coefficient and the depolarization ratio of atmospheric and ocean particles. These measurements will enable determinations of the microphysical and dimensional properties of atmospheric aerosols and clouds and their typing. Measurements of ocean optical properties will document phytoplankton seasonal and interannual dynamics and will improve understanding on marine biogeochemistry, the global carbon cycle, and responses of plankton ecosystems to climate variability. One specific measurement channel at 685 nm will be dedicated to fluorescence measurements from atmospheric aerosols and marine chlorophyll for the purpose of aerosol typing and the characterization of phytoplankton nutrient stress and primary production. CALIGOLA will provide accurate measurements of small-scale variability in earth surface elevation, primarily associated with variations in the ice and snow, terrain, and terrestrial vegetation height (e.g., forest canopies).

Phase A studies, commissioned by the Italian Space Agency to Leonardo S.p.A. and focusing of the technological feasibility of the laser source and the receiver, were conducted from October 2022, while Phase A/B1 activities for the payload, platform, and end-to-end system started in March 2025. Scientific studies in support of the mission are ongoing, commissioned by the Italian Space Agency to University of

Basilicata (KO: November 2021) and ISMAR-CNR (KO: September 2023). In September 2023, NASALARC initiated a pre-formulation study to assess the feasibility of a possible contribution to the CALIGOLA mission focused on development of the detection system and sampling chain and the implementation of data down link capabilities. The pre-formulation study ended in September 2024, and, after a successful Mission Concept Review, a phase A/formulation study started in January 2025, aimed to support activities in preparation of the System Requirements Review, which will likely take place in Autumn 2025. This presentation will provide details on current status and future steps of this groundbreaking multidisciplinary lidar mission.

Newest 18-channel PollyNET lidar with Rotational Raman, Fluorescence, and three-wavelength depolarization measurement capabilities

R. Engelmann[1], *B. Heese, A. Skupin, D. Althausen, H. Baars, C. Jimenez, B. Gast, M. Radenz, P. Seifert*

(1) Institute for Tropospheric Research (TROPOS), Permoserstraße 15, 04318 Leipzig, Germany

Corresponding author: ronny@tropos.de

Introduction

The lidar network PollyNET [1] with its meanwhile 15 operational automatic multiwavelength high-power Raman lidars [2] is operational since about 20 years. During this time, lidar technology, lasers, and measurement requirements advanced based on scientific needs. The latest addition to PollyNET is an 18-channel system with the ability to measure triple wavelength depolarization [3,4], fluorescence [5,6], water vapor, and cloud droplet parameters by the dual-field-of-view polarization method [7].

The lidar system

The new lidar system is based on the Polly-XT lidar described in [2]. The telescope diameters of 300 mm for far range and 50 mm for near range (N/R) receivers, internal beam path, optical carbon-fiber board, most beam splitters, interference filter design, and detection system (photon counting PMTs, Hamamatsu, H10721P-110) remain unchanged. The laser source is a 100 Hz, diode-pumped system (Innolas, DPSS-250) with pulse energies of 100 mJ at 1064 nm and 532 nm, respectively, and 50 mJ at 355 nm wavelength. A triple-wavelength beam expander increases the laser beam diameter to 40 mm and reduces the full-width beam divergence to <0.2 mrad. The photon counting data acquisition system is an in-house development based on a design from Holger Linné which is known as the CNT80 system. Table 1 summarizes the detection channels. The signal detection at 1064 nm is performed with two photon-counting PMTs (Hamamatsu, R3236) which are cooled to < -20 °C in specially designed chiller.

Table 1. Overview of the 18 receiver channels of the newest Polly lidar generation. Most other system parameters agree with [2].

Laser wavelength	Channel name	IF center, nm	IF bandwidth, nm
354.72 nm	O_2/N_2 rot. Raman	353.8	0.85
	Elastic, total	354.72	1.0
	Elastic, cross polarized	354.72	1.0
	N_2 rot./vibr. Raman	386.69	0.3
	WV rot./vibr. Raman	407.48	1.0
	Fluorescence	465.42	44.0
	N/R elastic N/R	354.72	1.0
	N/R N_2 rot./vibr. Raman	386.69	0.3
532.07 nm	O_2/N_2 rot. Raman	530.12	2.25
	Elastic, total	532.08	1.0
	Elastic, total (high)	532.08	1.0
	Elastic, cross polarized	532.08	1.0
	N_2 rot./vibr. Raman	607.4	0.3
	N/R elastic, total	532.08	1.0
	N/R N_2 rot./vibr. Raman	607.4	0.3
	N/R elastic, cross pol.	532.08	1.0
1064.15 nm	Elastic, total	1064.15	1.0
	Elastic, cross polarized	1064.15	1.0

First Measurement Example

The lidar was switched-on on 11 April 2025 for the first time. After minor alignment procedures the system was set into 24-h measurement mode. Figure 1 shows the automatically derived profiles from the PollyNET website. In this first test, it can be seen that the particle linear depolarization ratio at three

wavelengths agree very well in the cirrus at 10-12 km altitude. A different smoothing length of the automatic algorithm at 355 nm is most likely responsible for the difference observed at the cloud boundaries.

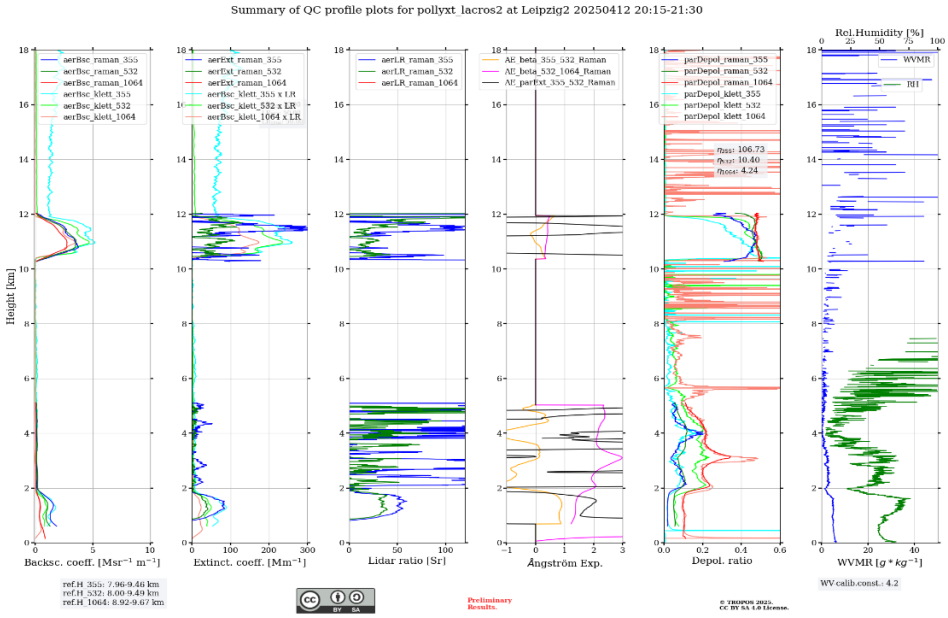

Figure 1: Fully-automatic retrieved multiwavelength data from PollyNET for the test measurement on 12 April, 20:15 to 21:30 UTC (https://polly.tropos.de/lidarproduct/47417122). The results are preliminary and also contain irrelevant "noisy" data points. The PollyNET data evaluation scheme follows the methods presented in [1] (Here, the lidar ratio used for the backscatter-times-lidar-ratio extinction product was set to 50 sr. Hence, the discrepancies in the cirrus).

Figure 2 shows one of the first fluorescence measurements with a Polly lidar. Also shown is a simultaneous measurement with the Leipzig Raman lidar MARTHA [5]. MARTHA has an 80-cm telescope and approx. 400 to 500 mJ of pulse energy at 355 nm wavelength. Therefore, the Polly data are noisier. However, it could be shown, that also fluorescent particles, especially within the planetary boundary layer and lower free troposphere can be detected at nighttime.

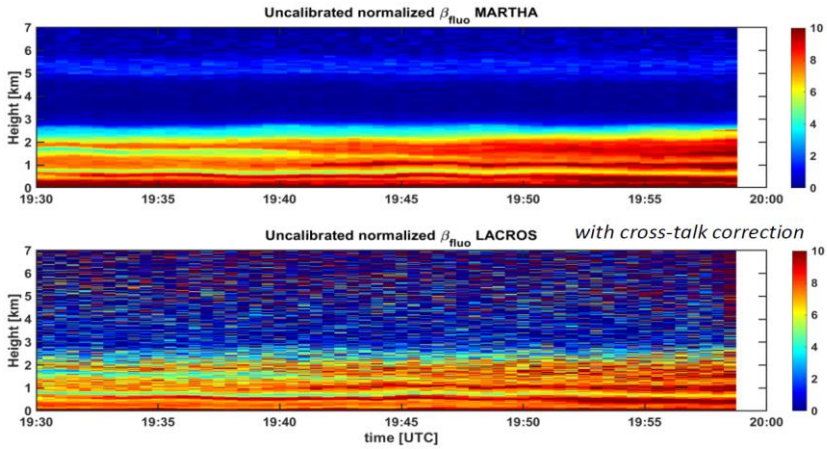

Figure 2: Comparison of the uncalibrated fluorescence backscatter of the Leipzig Raman lidar MARTHA [5] (top) and the new Polly system (LACROS, bottom) on 14 April 2025.

It was noticed during the comparison of the fluorescent backscatter of Polly and MARTHA that the data measured with Polly showed a cross-talk like behavior. Figure 3 shows averaged profiles (30 min) for both lidar systems for the time period presented in Fig. 2. The uncorrected profile (green, Fig. 3) shows less contrast and an increased fluorescence between 3 and 5 km height with respect to the profile derived from MARTHA (blue) which led to the assumption of a cross-talk effect. The calibration of the fluorescence backscatter from MARTHA underwent several steps in the past [5]. For simplicity, the Polly data shown here were calibrated to the MARTHA data at an altitude above the planetary boundary layer.

The beam splitters (HR355-500/HT>500), HT355-407/HR>420) and interference filters (two stacked filters to increase the sideband suppression ratio) in MARTHA and Polly are identically, i.e., of the same type. Therefore, the cross-talk possibly does not originate from too low suppression of the elastic signals. The only significant difference with respect to cross talk between the Polly and MARTHA setup is the laser energy distribution between 532 and 355 nm. In Polly, this energy ratio is 2:1 while in MARTHA it is approx. 1:3. In conclusion, it might be that the anti-Stokes vibration rotation Raman line from Nitrogen (at about 473 nm) which stems from the 532 nm laser beam is added to the fluorescence signal. This assumption has to be further investigated. However, a rough cross-talk correction using the 607-nm signal improved the comparison between the fluorescence backscatter from MARTHA and Polly greatly. For the comparison in Fig. 3, 3 % of the 607 nm signal have been subtracted from the fluorescence signal. This approach is far from ideal, as it will not be constant over time. For example, a change of the energy distribution of the laser will affect this correction. Also, the different atmospheric transmission at 473 and 607 nm is not considered. A more suitable solution would probably be an extra notch filter to suppress the 473 nm line.

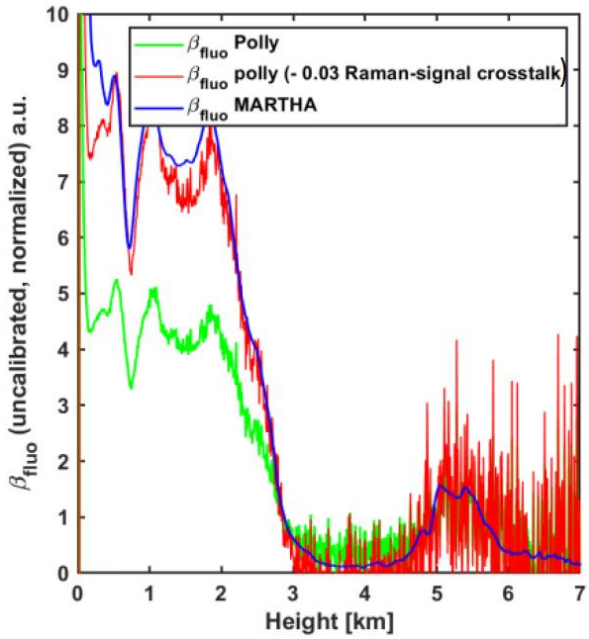

Figure 3: Fluorescence backscatter measured with Polly (green) and measured with MARTHA (blue) for a 30-min period (c.f. Fig. 2). After a simple cross-talk correction of the Polly data (red) the profiles agree. The noise is, however, much larger for the Polly data as telescope area and laser energy are together are a factor of approx. 70 smaller for Polly than for MARTHA.

Conclusions

A new Polly lidar with 18 channels has been introduced. For the first time, fluorescence has been measured with such a PollyNET system. It could be shown, that for at least the planetary boundary layer and lower free troposphere can be monitored during nighttime. Especially, pollen and smoke identification can be further improved by this new addition. Nevertheless, several aspects of this work are still ongoing and require further attention. For example, the observed cross-talk with, most likely, the anti-Stoked vibration rotation Raman line from 532 nm at 473 nm wavelength needs to be investigated. Such an effect also means that also MARTHA might be subject to cross-talk effect. In the past, they might just have been to small to be noticed.

Also, the use of the 44 nm wide filter at 465 nm wavelength is quite risky. In an automatic Polly system that is operating 24/7 it is absolutely crucial to switch-off this detector during daytime to avoid detector damage. While this procedure is momentarily performed by a computer script, it does not ensure reliable operation if, e.g., there is a computer issue (update, power break, crash, etc).

The use of rotational Raman filters at 354 and 530 nm, respectively, is also new for the multiwavelength PollyNET systems. It the past it could be shown that in this way an Angström exponent could be derived from a single-wavelength lidar by comparing the vibration rotation Raman signal with the pure rotational Raman signal [8]. In this sense, these channels shall improve the measurement of the particle extinction and backscatter coefficients and improve data quality especially in low-aerosol concentration cases.

This new lidar system is currently part of the Leipzig Aerosol and Cloud Remote Observations System (LACROS) and on the way to be installed at the southern tip of New Zealand, at Invercargill airport. As part of the GO-SOUTH-2 campaign it is planned to investigate aerosol and clouds in the Southern Ocean for one to two years.

Acknowledgements

Many thanks go to all PollyNET members that are putting lots of effort in keeping the lidar network alive. Partly in system maintenance, partly in improving data evaluation routines, and mostly in publishing scientific articles with the use of PollyNET data. This is what keeps us going!

This work was financed by the German Federal Ministry of Education and Research (BMBF) under the FONA Strategy “Research for Sustainability” (ACTRIS-D, grant no. 01LK2001A).

References

[1] Baars, H. et al.: *An overview of the first decade of PollyNET: an emerging network of automated Raman-polarization lidars for continuous aerosol profiling*, Atmos. Chem. Phys., 16, 5111–5137, https://doi.org/10.5194/acp-16-5111-2016, 2016.

[2] Engelmann, R. et al.: *The automated multiwavelength Raman polarization and water-vapor lidar PollyXT: the neXT generation*, Atmos. Meas. Tech., 9, 1767–1784, https://doi.org/10.5194/amt-9-1767-2016, 2016.

[3] Haarig, M. et al: *First triple-wavelength lidar observations of depolarization and extinction-to-backscatter ratios of Saharan dust*, Atmos. Chem. Phys., 22, 355–369, https://doi.org/10.5194/acp-22-355-2022, 2022.

[4] Haarig, M. et al.: *Discussion of the spectral slope of the lidar ratio between 355 nm and 1064 nm from multiwavelength Raman lidar observations*, EGUsphere [preprint], https://doi.org/10.5194/egusphere-2025-449, 2025.

[5] Gast, B. et al.: *Invisible aerosol layers: improved lidar detection capabilities by means of laser-induced aerosol fluorescence*, Atmos. Chem. Phys., 25, 3995–4011, https://doi.org/10.5194/acp-25-3995-2025, 2025.

[6] Veselovskii, I. et al: *Combining Mie–Raman and fluorescence observations: a step forward in aerosol classification with lidar technology*, Atmos. Meas. Tech., 15, 4881–4900, https://doi.org/10.5194/amt-15-4881-2022, 2022.

[7] Jimenez, C. et al.: *The dual-field-of-view polarization lidar technique: a new concept in monitoring aerosol effects in liquid-water clouds – case studies*, Atmos. Chem. Phys., 20, 15265–15284, https://doi.org/10.5194/acp-20-15265-2020, 2020.

[8] Malollari, G. et al.: *Ångström exponent impact on the aerosol optical properties obtained from vibrational-rotational Raman lidar observations*, EGUsphere [preprint], https://doi.org/10.5194/egusphere-2025-1386, 2025.

High spatial resolution of lidar signals - how far can we get?

I.S. Stachlewska[1], *M. Winkowski[1], A. Hafiz[1], A. Adamovic[2], V. Kurtenoks[2], N. Tihomorskis[3], V. Stepanovs[2], A. Aboltins[2,3], P. Razmajevs[2], N. Adamovitch[2]*

(1) University of Warsaw, Faculty of Physics (UW), Pasteura 5, 02-093, Warsaw, Poland
(2) Eventech Ltd, Pulka iela 3, Riga, LV-1007, Latvia
(3) Riga Technical University, 6A Kipsalas Street, Riga LV-1048 Latvia
Corresponding author: iwona.stachlewska@fuw.edu.pl;

Introduction

An extensive testing of different Eventech Ltd. devices, which implement their metrological expertise, was carried out using one of the atmospheric lidars at the Warsaw Observatory Station (ACTRIS facility) of the University of Warsaw. Main goal was to adapt the Eventech Ltd. devices to enable lidar measurements and to assess the effectiveness of increasing the temporal resolution of lidar data in photon-counting mode. After the initial testing with the Eventech Stream Time Tagger 7 Series (ESTT 704), necessary changes were identified and implemented in the new device Eventech Photon Counter (EPC) prototype. The ETR was then tested and achieved the spatial resolution of 0.375 m could be obtained, that is one order of magnitude better than any classical lidar avaliable within the EARLINET/ACTRIS.

Instrument

We used the ESA Mobile Raman Lidar (EMORAL), the official EarthCARE mobile calibration/validation reference lidar [1]. The EMORAL uses Nd-YAG laser, (SpitLight 400, InnoLas) operating at 1064 nm (112 mJ), linearly polarized 532 nm (103 mJ), and linearly polarized 355 nm (128 mJ), with repetition rate of 10Hz, and pulse length 5-7 ns. To collect the lidar signals the Cassegrain telescope with primary mirror of 300 mm and adjustable field of view (2-3.6 mrad) is used. The collected signal is folded to the Wavelength Separation Unit (WSU) that comprises 9 channels: 5 elastic Mie channels (1064 nm, 532 nm -s, -p, and 355 nm -s , -p); 3 vibrational Raman channels (N_2 at 387 nm and 607 nm and H_2O at 407 nm), and broadband fluorescence channel centered at 470 nm with a bandwidth of 100nm. Lidar uses for detection several 16 bits transient recorders (TR40-160, Licel GmbH) to simultaneously record analogue and photon-counting signals with the spatial resolution of 3.75 m. The instrument was inter compared with the ACTRIS-CARS reference lidar at the National Institute for R&D for Optoelectronics (INOE), Romania in May 2024 and was found to meet all technical requirements issued by CARS.

Figure. 1. The EMORAL lidar transceiver unit manufactured by Raymetrics S.A. comprises the classical lidar detection with 9 TR40-160 manufactured by Licel GmbH used as a reference.

Methodology

The experiment attempted to perform lidar detection using the Eventech time tagger device (ESTT), and later EPC, by feeding the signal (output of photomultiplier tube, as well as the trigger signal from the laser) directly into the device. The ESTT and EPC devices precisely tag the interval time between its inputs with high temporal resolution. The signal was measured simultaneously with the classical lidar detection chain to have direct comparison of the registered data.

In this way, we compared signals detected with the ESTT and EPC device to the classical lidar detection chain - the Licel transient recorders, which are used not only in the EMORAL lidar but also in a great number of the lidars within EARLINET/ACTRIS and even airborne lidars, e.g. the Airborne Mobile Aerosol Lidar (AMALi) designed for research in the Arctic research, where the range-resolution of data collected during the flight , especially matters as it translates to the horizontal resolution [2].

The EMORAL lidar channels at 532 nm (-s, -p) PMT outputs were used for collecting lidar data, whereas the trigger was connected to both using a simple passive splitter. Several simultaneous measurements were done: initial tests, comparison of the daytime/nighttime signals, comparisons of the signals with/without clouds. Due to intense communication between scientists from University of Warsaw and Eventech Ltd, subsequent, increasingly refined versions of software and time tagger devices were created.

Results and Discussion

Initial tests were done to establish the proper setup for installation of the device to EMORAL, that also included configuring the setting of ESTT and EPC.

It resulted in several important outcomes. To be able to collect backward-scattered lidar signal correctly, an additional high-pass filter was required before feeding the PMT signal to ESTT and EPC. It was also crucial to find the proper threshold value in signal input, to be able to collect data with good signal to noise ratio.

The initial measurements showed that ESTT and EPC collected lidar-like signal but with distortions in the detection channel to which it was connected, due to initially used passive BNC splitter for the PMT and the trigger signals (ground loops and consequently electronic noise propagation). Also, the line impedance was not matched and signal amplitude was reduced when passive splitting was used. This was eliminated by optically splitting the received backscatter signal at 532 nm by rotating the wavelength separation unit of 45° and using separate, independent 532 -s and -p channels.

We notice also that signals vary (in the altitude axis) depending on the trigger threshold. Because the ESTT and EPC device measures the time elapsed from the trigger to the detected PMT pulse (time is then converted into distance), the moment of trigger occurrence is crucial for the measurement. Ideally, the trigger signal would be a rectangular with a vertical slope. In reality, it does not have rectangular shape and slope is not infinitely steep but increases over a finite time. Therefore, assuming that the ESTT and EPC is triggered by the rising edge of the signal (in the case of the falling edge, it will be exactly the opposite) and depending on the measurement trigger threshold, the measured time will increase (or decrease). The slower the trigger signal increases the greater the effect. To overcome this, we used an internal reflection pulse to synchronize the signals in a similar way that the so-called “zero-bin” measurement is done for the lidar systems within the EARLINET/ACTRIS to assure high quality of the derived lidar data products (one of the obligatory QA operational tests).

After eliminating the aforementioned concerns, the direct, simultaneous comparison of data measured by the EPC device (red) and the TR40-160 lidar detection system (black) installed in EMORAL was done.

The result is shown in Fig. 2. During the measurement a cloud peak at ~1750 m was clearly visible. Additional subplots of Fig 2 present the data collected in the near (left) and far (right) field. Lidar signal shown was collected for 5 minutes integration time.

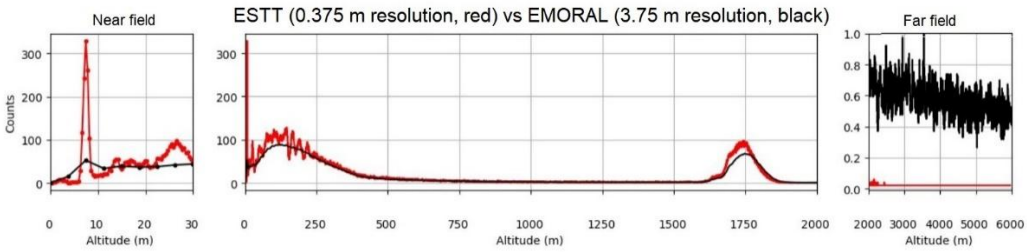

Figure. 2. Comparison between the high spatial resolution of the EPC, Eventech (red) and the classical lidar detection TR40-160, Licel (black) including near and far field (5 min average).

The core goal of the experiment was to observe and evaluate the differences in how EPC and TR40-160 register signal within the cloud regime. The details of data measured in cloud are depicted in Fig. 3 zoomed to clearly see the cloud structures.

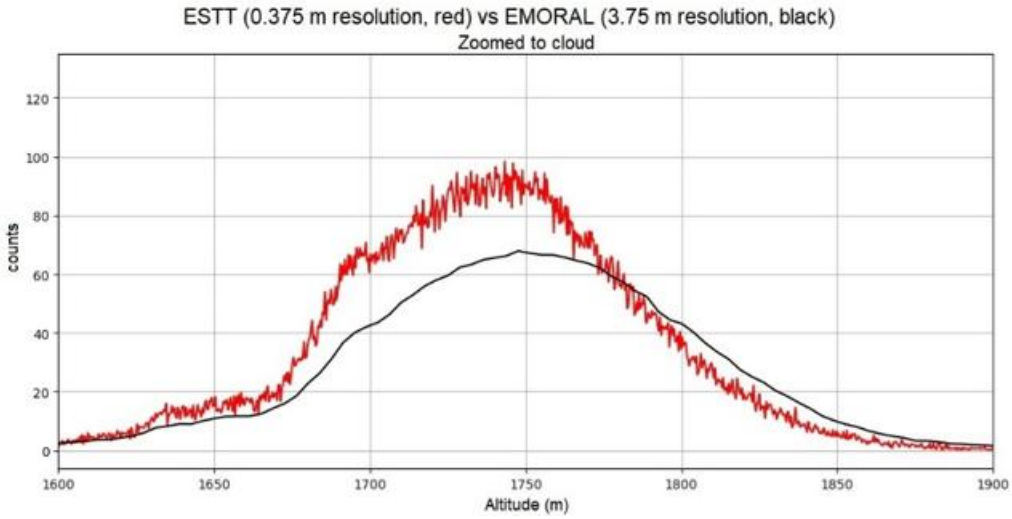

Figure. 3. Direct comparison between high resolution EPC and TR40-160 (typical solution used in the EARLINET/ACTRIS lidar systems) with zoomed cloud structures.

Moreover, additional extensive tests for both daytime and night-time measurements (with and without clouds), not shown here for brevity, indicate a high level of agreement between data collected from the EPC device and the TR40-160 lidar detection. The added value of the EPC is clearly in increased spatial resolution and signal sensitivity.

Conclusions

After a series of tests with ESTT and modifications, the research team from the University of Warsaw and experts from Eventech Ltd. came up with the adapted EPC device, now able to directly measure lidar signals.

Measurements carried out both during the day and at night showed high agreement with the typical lidar detection system (here with TR40-160, Licel GmbH). The achieved measurement spatial resolution is of an order of magnitude higher (0.375 m) with the adapted EPC detection module.

In this way, we show the potential of the EPC device to be a great addition to the currently existing classical lidar detection chain, i.e. the Licel transient recorders, which are used not only in the EMORAL lidar but also in a great number of the lidars within EARLINET/ACTRIS, as well for airborne lidars.

The Airborne Mobile Aerosol Lidar (AMALi, [2]) designed for research in the Arctic research uses the single-shot data acquisition system developed by Licel. In the airborne measurements the range-resolution of data collected during the flight but also the temporal-resolution especially matter, note that the latter translates to the horizontal resolution of the airborne lidar profiles.

For the near future we are planning to use the EPC device for comparative studies with other types of the lidar detection systems used within the EARLINET/ACTRIS. Specifically, we plan to use it with the detection modules of the PollyXT lidars [3] gathered within worldwide observational lidar network POLLYNET coordinated by the Leibniz Institute for Tropospheric Research (TROPOS). The PollyXT lidars use the open-source, field programmable gate array (FPGA) based photon-counting signal detection [4] that was initially developed at Max-Planck Institute in Hamburg (MPI-Hamburg) for free-use in lidar community, especially within EARLINET. The PollyXT lidars make a great use of this technology providing measurements of the lidar signals up to ~40 km with range resolution of 7.5 m, pre-trigger of 256 bins, at frequency > 800 MHz. One of the very first next-generation POLLYNET systems (PollyXT-UW lidar) was built in a collaborative effort of TROPOS and University of Warsaw, and it is in operation since July 2013 as a core instrument at the Warsaw Observatory Station (ACTRIS facility).

It is obviously expected that the additional signal detection with the optimized EPC and the PollyXT detection will bring even more added value (due to much finer spatial resolution, 0.375 m vs 7.5 m, respectively) but there is one more aspect of interest. The collected EPC data in the case of the PollyXT-UW lidar can be used for the comparative study and performance tests for detection channels of the large-size (diameter of 30 cm) and also the small-size (5 cm) Newtonian telescopes, the latter designed for the near reage observations.

In the case of classical aerosol lidar, this technique opens up new perspectives for measuring signals with high resolution and sensitivity, which can be an advantage especially for the detection of weak signals (Raman detection and derivation of the aerosol extinction profiles in near field), as well as for measurements of thin aerosol layers. Moreover, other lidar applications need such a high range resolution, e.g. ocean lidars, turbulence lidars.

Acknowledgements

The extensive tests of the Eventech LTD time tagger modules was done within project “Testing Eventech Timestamps for Lidar Applications (ETTLA)” as a part of the Trans-national Access program (TNA) within the EC-funded ATMO-ACCESS grant no.: 101008004.

We thank Opto-Electronics section (TEC-MME) at the European Space Research and Technology (ESTEC) of the European Space Agency (ESA) for providing the ESA Mobile Raman Lidar EMORAL that was developed within non-commercial scientific collaboration of University of Warsaw (UW), Ludwig Maximilian University of Munich (LMU), and Raymetrics S.A. within “Technical assistance for Polish Radar and Lidar Mobile Observation System (POLIMOS)” funded by ESA-ESTEC Contract no. 4000119961/16/NL/FF/mg.

References

[1] Stachlewska, I.S., Georgoussis G., Freudenthaler V., Hafiz A., Poczta P., Louridas A., Wang D., Janicka Ł., Siomos N., Karasewicz M., Fortuna R., Kokkalis P., Amiridis V., Byčenkienė S., Drzeniecka-Osiadacz A., Belegante L., Nicolae D., Tzeremes G., Ribes P., Schüttemeyer D. (2024). EMORAL—Mobile Mie-Raman Lidar with Fluorescence, Polarization and Water Vapor Observational Capabilities for Satellite Cal/Val Field Campaigns. In: Singh, U.N., Tzeremes, G., Refaat, T.F., Ribes Pleguezuelo, P. (eds) Space-based Lidar Remote Sensing Techniques and Emerging Technologies. LIDAR 2023. Springer Aerospace Technology. Springer, Cham. https://doi.org/10.1007/978-3-031-53618-2_21.

[2] Stachlewska, I. S., Neuber, R., Lampert, A., Ritter, C., and Wehrle, G.: AMALi – the Airborne Mobile Aerosol Lidar for Arctic research, Atmos. Chem. Phys., 10, 2947–2963, https://doi.org/10.5194/acp-10-2947-2010, 2010.

[3] Engelmann, R., Kanitz, T., Baars, H., Heese, B., Althausen, D., Skupin, A., Wandinger, U., Komppula, M., Stachlewska, I.S., Amiridis, V., Marinou, E., Mattis, I., Linné, H., and Ansmann, A.: The automated multiwavelength Raman polarization and water-vapor lidar PollyXT: the neXT generation, Atmos. Meas. Tech., 9, 1767–1784, https://doi.org/10.5194/amt-9-1767-2016, 2016.

[4] Linné H. (2012) Max-Planck Institute in Hamburg; priv.comm.on FPGA-based lidar signal detection.

Mapping of the water vapor structure of the tropical and sub-tropical Atlantic using airborne DIAL measurements during the PERUSION campaign

M. Wirth[1], *S. Groß*[1],

(1) German Aerospace Center (DLR), Institute of Atmospheric Physics, Münchener Str. 20, 82234 Wessling, Germany
Corresponding author: martin.wirth@dlr.de

Introduction

In many important respects climate and weather rely heavily on the distribution of water vapour in the atmosphere. In terms of climate change, water vapour leads to the largest feedback, as it more than doubles the surface warming from atmospheric CO_2 [1]. In the tropics, lower tropospheric water vapour is the best predictor of vertical motion and precipitation, thus making it central for understanding tropical weather, the climate of the tropics, and tropical climate change [2,3], as well as cloud feedbacks [4]. Apart from balloon-borne soundings, of which there are very few over the ocean, there is presently no operational standard measurement to determine how water vapour is distributed in the vertical in the troposphere. Passive sounders from satellites are, owing to their broad weighting functions, relatively blind to differences in the structure of the lower troposphere, as demonstrated by comparisons with highly resolved soundings [5, 6]. Currently the only proven technique capable of profiling water vapour with high horizontal and vertical resolution over lager areas is the DIAL technique [7], as implemented in the *Water Vapour Experiment in Space* (WALES) airborne demonstrator [8]. This instrument was flown during the PERCUSION (Persistent EarthCARE under flight studies of the ITCZ and organized convection) mission in August and September 2024 onboard the German research aircraft HALO. We will give an overview of the mission and show selected examples of the humidity structure within the ITCZ and its subtropical surroundings.

Methodology

In August and September 2024 PERCUSION took place as part of a network of campaign activities called ORCESTRA (Organized Convection and EarthCARE Studies over the Tropical Atlantic). PERCUSION is an airborne mission using the German research aircraft HALO. It is an initiative of German research institutes and universities (led by the Max-Planck-Institute for Meteorology and DLR) and had two main objectives:

(1) To test factors hypothesized to influence the organization of deep maritime convection in the tropics and the influence of organized convection on the large-scale environment.

(2) To establish confidence in EarthCARE by validating the EarthCARE measurements and data.

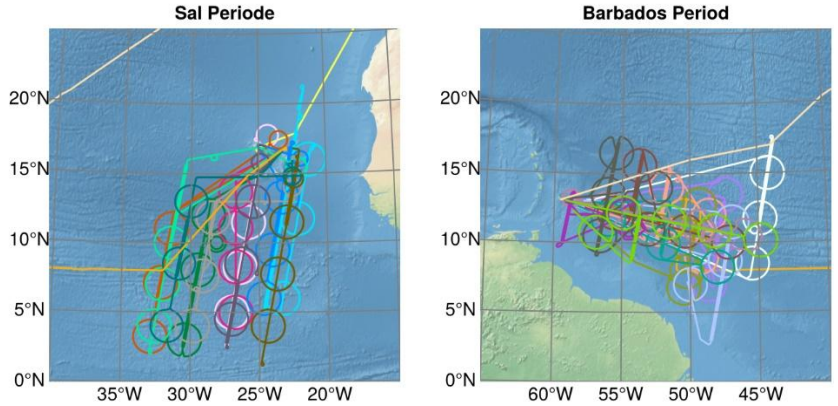

Figure 1. Flight tracks of the HALO research aircraft during the PERCUSION campaign out of Sal (left) and Barbados (right). The straight thick lines indicate direct underpasses under the EarthCARE satellite.

HALO measurements were carried out of two locations (Figure 1): In August 2024 we performed measurements out of Sal (Cape Verde) to target marine aerosol, Saharan dust and biomass burning aerosol as well as shallow to deep convective clouds and the ITCZ. In September 2024 measurement flights out of Barbados took place to address different kinds of cloud and aerosol situations. There was also a third campaign period solely devoted to EarthCARE validation which operated out of Oberpfaffenhofen, Germany, but results from these flights are not considered in the following. To achieve the objectives listed above, we planned our flights in a way, that they included at least one EarthCARE underpass in each research flight, but also probed larger regions of the ITCZ.

During PERCUSION, HALO was equipped with an EarthCARE-like payload acting as airborne aerosol and cloud observatory [9]. One of the key instruments during the PERCUSION campaign was the WALES demonstrator lidar system. It is a combined airborne differential absorption lidar (DIAL) and HSRL system developed and built at the DLR Institute of Atmospheric Physic [8]. It measures profiles of backscatter ratio at 532 nm and 1064 nm, and depolarization ratio at 532 nm. In addition, it is equipped with an HSRL channel at 532 nm using an iodine filter. But as the primary data product WALES measures water vapor using the DIAL principle with four wavelengths in the 935 nm wavelength region.

Results and Discussion

During the August and September periods of the PERCUSION campaign altogether 25 HALO research flights were carried out addressing different aerosol and cloud situations. In the following we will focus on two examples, first the transfer flight to Sal which took place on 9. August 2024 as an example of a Saharan air layer (SAL) case and on 14. September a flight towards the ITCZ that shows the modification of the tropical humidity structure by deep convection.

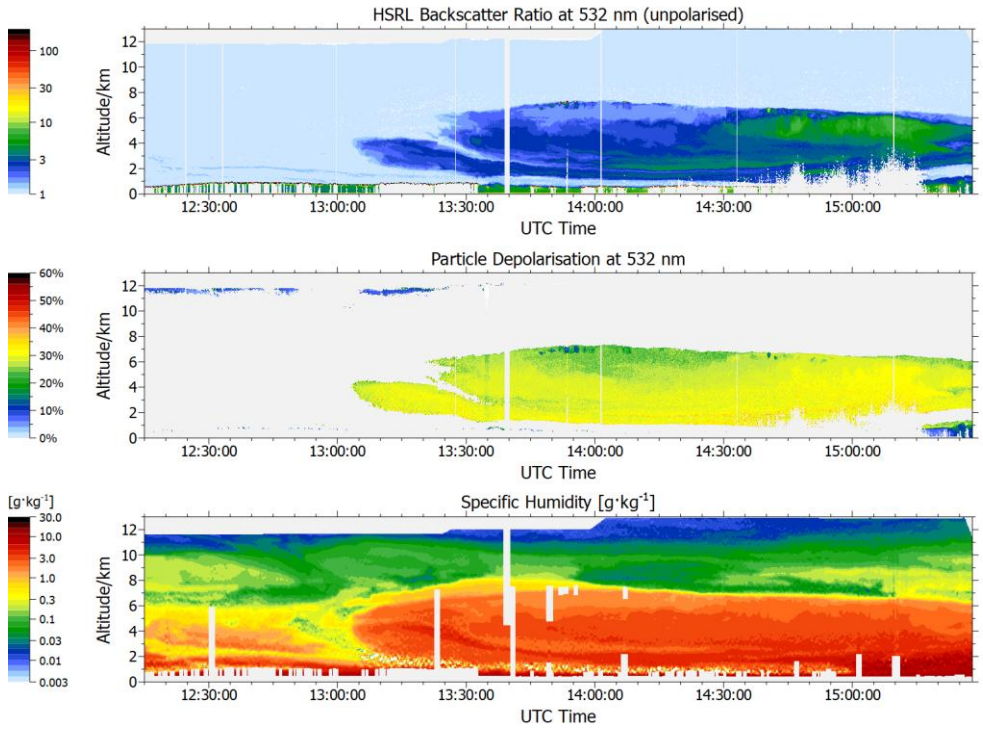

Figure 2. Two dimensional curtains of backscatter ratio, particle depolarization and humidity data as measured by the WALES system on 9. August 2024 on the transfer fight to Sal.

Figure 2 shows curtains of backscatter ratio, particle depolarization and humidity data as measured by the WALES system on 9. August 2024 on the transfer fight to Sal. Shown is the section from the Spanish coast (12:15 UTC) over the subtropical Atlantic until the begin of the descent to Sal (15:28 UTC). Clearly visible is a layer with scattering properties typical for Saharan dust which was accompanied by high humidity values and a characteristic strong humidity drop at the upper boundary. A recent study [10] has shown that the high stability of the Saharan dust layer during long range transport can to a large part be attributed to radiative effects which mainly come from the water vapor and to a much lower part from the aerosol. Crucial in this case is the steep drop of humidity at the upper boundary which favors a radiatively generated inversion. The water vapor not only stabilizes the dust layer but has also consequences on the formation of convection below. In contrast to the case investigated in [10], here the layer is not separated from the marine boundary layer. So, these measurements provide an excellent dataset to extend the previous studies about radiative effects on stability and convection within the Atlantic sub-tropical region to so far uncovered scenarios.

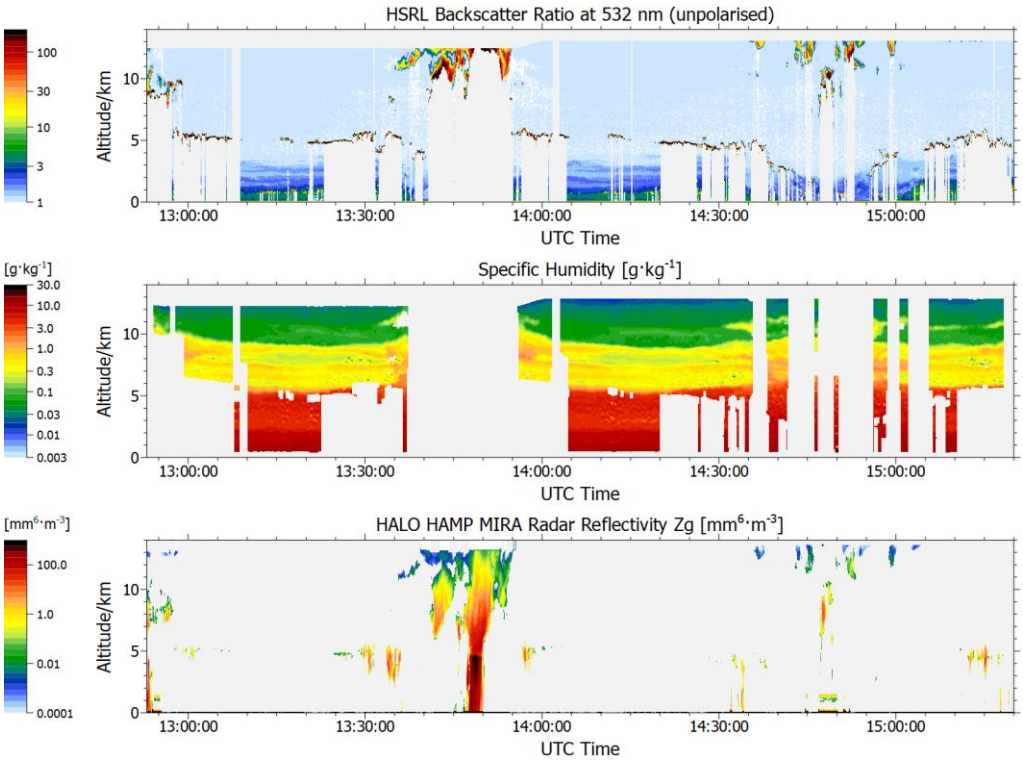

Figure 3. Time-height cross-section of the WALES backscatter (upper panel), humidity (middle panel) and radar reflectivity data (lower) on the 14 September 2024.

The second case presented is linked to a moistening of the middle and upper tropical troposphere by out flow from convective towers. The data shown in Figure 3 was collected on a flight from Barbados which overpassed and then surrounded a high reaching convective system with a strongly precipitation core as can be seen from the radar data. The HALO aircraft was not able to fly above the cloud top and no water vapor data could be retrieved directly above the system due to severe detector overload and high optical thickness. But what clearly can be seen are layers of humidity linked to the convective system with values of 1-3 g/kg at 8 km altitude which is about 10 times higher than the typical background humidity at this level. These layers are then transported over longer ranges and determine the structure of the humidity field within and in the surrounding of the ITCZ, long after the convection has stopped.

Conclusions

Airborne measurements with an airborne water vapor DIAL as part of an EarthCARE-like payload have been carried out during the PERCUSION campaign. Bedsides the validation of EarthCARE products these flights provided the opportunity to investigate the humidity structure of the tropical and sub-tropical troposphere and its relation to aerosol transport and cloud formation. Having a long-range and high-altitude aircraft gives the unique possibility to probe these remote regions, especially over the ocean, where observational density is particularly sparse. We showed two cases out 25 available data sets as a starting point for the discussion on how to further evaluate these measurements to investigate (i) the coupling of deep convection to its environment and the factors influencing the genesis of tropical storms; (ii) the controls on the distribution of shallow convection, the intensity of cloud feedbacks and thus climate sensitivity.

While such case studies provide excellent opportunities to investigate these coupling mechanisms, they are of course not sufficient to quantity the overall impact on the weather and climate system. To answer these question long-term and global measurements of this kind would be necessary. The final goal of the development of the WALES airborne demonstrator is to show by measurements like this that a space-borne water vapour DIAL – preferably extended by aerosol channels – is the missing component of the Earth observation system to bring our understanding of the coupling processes listed above to the next level.

Acknowledgements

This work was financed by the ESA project GIVEair (EarthCARE: Give Airborne with Radar, Lidar – HALO EC-TOOC and Home-Base) under ESA Contract No. 4000145500/24/NL/SC, and has received funding from Horizon Europe programme under Grant Agreement No 101137680 via project CERTAINTY (Cloud-aERosol inTeractions & their impActs IN The earth sYstem). Furthermore, this work has been supported by the DLR internal funding within the MABAK project (Innovative Methoden zur Analyse und Bewertung von Veränderungen der Atmosphäre und des Klimasystems).

References

1. Stevens, B. and Bony, S. (2013): Physics Today, 66(6), 29. doi:10.1063/PT.3.2009
2. Bretherton, C. S., Peters, M. E. and Back, L. E. (2004): Journal of Climate, 17(7), 1517–1528. doi: 10.1175/1520-0442(2004)017<1517:RBWVPA>2.0.CO;2
3. Peters, O., and Neelin, J. D. (2006): Nature Physics, 2(6), 393–396. doi:10.1038/nphys314
4. Sherwood, S. C., Bony, S. and Dufresne, J.-L. (2014): Nature, 505(7481), 37–42. doi:10.1038/nature12829
5. Stevens, B., Brogniez, H., Kiemle, C., Lacour, J.-L., Crevoisier, C. and Kiliani, J. (2017): Surveys in Geophysics, 38: 1371-1397. doi:10.1007/s10712-017-9420-8
6. Schröder, M., et al. (2017): GEWEX Water Vapor Assessment (G-VAP); WCRP Report 16/2017, https://www.wcrp- climate.org/WCRP-publications/2017/WCRP-Report-16-2017-GVAP-v1.3_web.pdf
7. Nehrir, A.R., Kiemle, C., Lebsock, M.D. et al. (2017): Surveys in Geophysics 38: 1445–1482. doi:10.1007/s10712-017-9448-9
8. Wirth, M., Fix, A., Mahnke, P., Schwarzer, H., Schrandt , F. and Ehret, G. (2009):, Applied Physics B: Lasers and Optics, 96, 1, 201-213. doi:10.1007/s00340-009-3365-7
9. Stevens B. et al. (2021): ESSD 13(8): 4067-4119, https://doi.org/10.5194/essd-13-4067-2021
10. Gutleben, M., Groß S., Wirth M. and Mayer B., ACP, (2020), https://doi.org/10.5194/acp-20-12313-2020

Telecover tests for ceilometers of type CHM

A. Geiß[1], *F. Wagner*[2], *I. Mattis*[2], *N. Siomos*[1]

(1) Ludwig-Maximilians-Universität München, Meteorological Institute, 80333 Munich, Germany
(2) Deutscher Wetterdienst (DWD), Meteorological Observatory, Hohenpeißenberg, 82383, Germany
Corresponding author: alexander.geiss@lmu.de

Introduction

Automatic low-power lidars and ceilometers (ALCs) have recently gained attention for quantitative aerosol profiling due to their low cost, minimal maintenance, and eye-safe, single-wavelength operation [1,2]. When well-calibrated and quality-controlled, they enable aerosol monitoring with high spatial and temporal resolution, supporting air quality assessments and the detection of elevated layers such as Saharan dust or volcanic ash. Deployed in networks, they provide large-scale regional and continental coverage.

However, performance varies significantly between ALC models, requiring model-specific calibration procedures. ACTRIS (www.actris.eu) addresses this by standardizing the operation, monitoring, and calibration of these instruments.

A key part of this effort is the evaluation of near-range optical alignment and overlap performance, where system misalignments have the strongest impact [3,4]. The telecover test compares signals from different telescope quadrants to detect deviations caused by laser tilt, misalignment, or optical imperfections. Since clean-air conditions, i.e. aerosol free, for calibration are not available in the near range, the test serves as a vital tool for diagnosing uncertainties in signal overlap. This study presents telecover measurements on two Lufft (now Ott-Hydromet) CHM15k and one CHM8k instrument to assess their optical alignment (see Figure 1).

Figure 1. Left: Lufft CHM8k (red) and Lufft CHM15k (blue) on the rooftop of the Meteorological Institute of LMU Munich. Right: Inside view of the CHM15k showing the laser optical module (LOM) with the laser on the left axis and the telescope on the right axis (see arrows).

Methodology

The CHM15k and the CHM8k (see Figure 1), differ significantly in their specifications, area of application and also in their price, but are both built together in a bi-axial configuration (see Figure 1 right). The CHM15k, which was the first model on the market, uses a Nd:YAG Class 1M microchip and operates at a wavelength of 1064 nm whereas the CHM8k uses an InGaAs laser diode and operates at a wavelength of 905 nm and with significantly less laser power (see Table 1 for details). Their maximum range is specified as 10 km and 15 km for the CHM8k and CHM15 respectively. The larger field of view of the CHM8k enables a lower full overlap range of approx. 800m compared to the CHM15k with approx. 1500m (for both

models device dependent). A device-specific overlap function is determined by the manufacturer, applied to the data and provided on request. Compared to the CHM8k, the CHM15k has the advantage of better performance in the far field, which is achieved by the higher laser power, better background suppression and an avalanche photodiode (APD) in photon counting instead of analogue detection. Since the amplification of the APD is temperature-dependent, maintaining a thermally stable environment for the receiver unit is essential, particularly for models like the CHM15k, which incorporate active thermal stabilization. In the CHM15k, this is achieved through a double-shell housing design that enables controlled airflow to heat or ventilate the unit depending on ambient conditions, and keeping the APD at a constant operating temperature of 25 °C by using a Peltier element in addition. Furthermore, the design of the ceilometers also offers protection from external factors such as solar radiation, wind, precipitation, and dirt. In contrast, the CHM8k model does not include this level of thermal stabilization.

Table 1. Lufft (OTT Hydromet) CHM8k and CHM15 key parameters.

Parameter	**CHM8k**	**CHM15k**
Optical design	biaxial	biaxial
Laser	InGaAs laser diode	Nd:YAG Class 1M microchip
Wavelength	905 nm	1064 nm
Pulse repetition rate	8 kHz	5-7 kHz
Pulse length	100 ns	1 ns
Pulse energy	<2 µJ (typ. 1.6)	7-9 µJ
Peak laser power	~20 W	~8000 W
Average laser power	~16 W	~50 W
Filter Bandwidth	25 nm	1 nm
Laser divergence	<0.5 mrad	0.33 mrad
Telescope FOV	1.1 mrad	0.45 mrad
Detection type	APD analog	APD photon counting
Measurement range	0-10 km	0-15 km
Range resolution (set)	5 m (15 m default)	5 m (15 m default)
Temporal resolution (set)	2-600 s (30 s default)	2-600 s (30 s default)
Overlap height (from manufacturer)	50% at ~280 m	50% at ~450 m

At the Meteorological Institute of the Ludwig-Maximilians-Universität in Munich (48.148° N, 11.573° E, 539 m altitude), an ALC-unit testbed as part of the ACTRIS Centre for Aerosol remote sensing (CARS) is deployed. The operation of different ALCs from different manufacturers together in this testbed allows a direct comparison of their performance as well as the development and application of necessary corrections and calibrations. However, due to the optical configuration, the telecover test can only be easily applied to the bi-axial Lufft devices, which is more difficult with the predominantly co-axial systems of the other manufacturers (Vaisala and Campbell). Two CHM15k and one CHM8k are operated with a temporal and vertical resolution of 15 s and 15 m, respectively.

Typically, a template is used for the telecover test that covers three quadrants of the telescope, allowing measurements from only one quadrant at a time, namely North (the quadrant facing the laser), South (the quadrant facing away from the laser), and East or West (the lateral quadrants) [3,4]. Each quadrant is measured for a specified duration, and the template is rotated accordingly to measure the other quadrants. To minimize the influence of atmospheric variability during the measurement period, these tests should be conducted under stable conditions and repeated in multiple runs.

Performing the telecover test in the conventional manner would require opening the inner housing each time to reposition the template for the CHM ceilometers. This procedure disrupts the thermal stability of the system and is particularly impractical when multiple measurement cycles are done. To address this, a

custom-designed, 3D-printable tool was developed as a CAD model (see Figure 2), specifically tailored to the geometry of Lufft ALCs. This device enables fully automated coverage of the telescope quadrants using a stepper motor which rotates the template. The measurement times are stored on the Raspberry Pi Pico microcontroller that controls the system, allowing for efficient and straightforward post-processing and analysis.

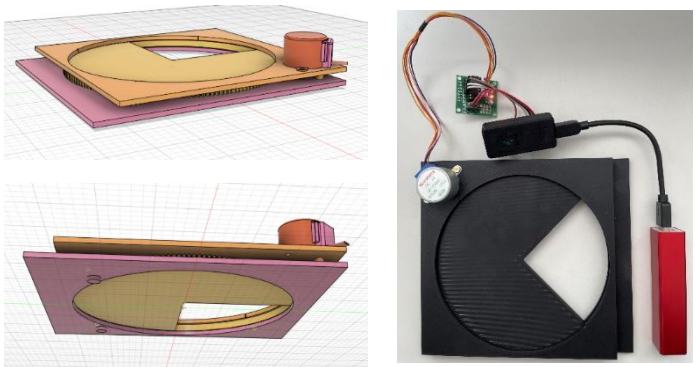

Figure 2. Left: CAD model of the automatic telecover tool for Lufft ALCs (top and bottom view). Right: 3D-printed tool with motor driver, Raspberry Pi Pico and power bank.

For a first telecover measurement, five consecutive cycles were performed, with each quadrant measured for five minutes. To ensure a sufficient signal-to-noise ratio up to the full-overlap height, where signal normalization is required in the analysis, the measurement was conducted after sunset, thereby avoiding solar background radiation.

Results and Discussion

In Figure 3, the profiles of the normalized range corrected signals averaged over all same quadrants are shown. Each quadrant signal is normalized in a region in the height of full overlap which is marked in gray. The correction with the overlap function from the manufacturer which is applied in the firmware was removed.

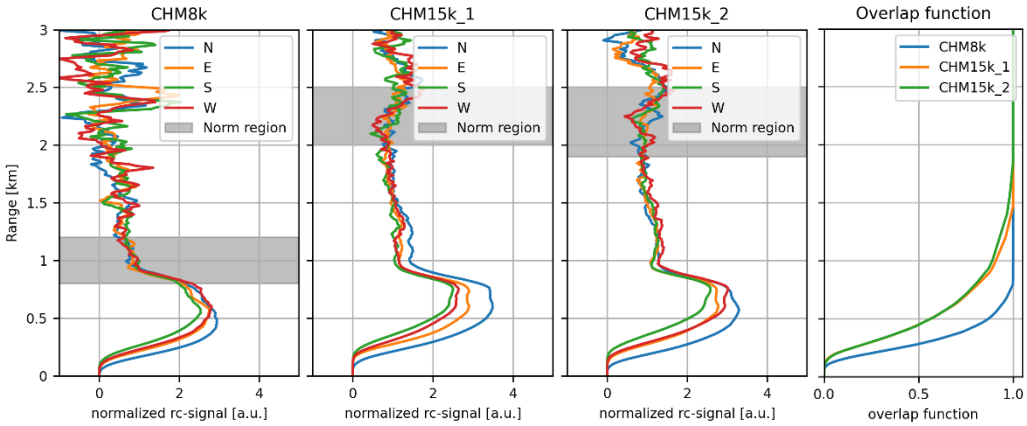

Figure 3. Profiles of the normalized range corrected signal without overlap correction of the three ALCs averaged for all four quadrants North, East, South and West. For comparison, the overlap functions provided by the manufacturer are plotted (right panel).

For all three devices, the normalized signals are highest in the North quadrant, with the maximum at the shortest range. In contrast, the South quadrant shows the lowest signal strength and a maximum at the largest

distance. The East and West quadrants lie in between. This shows that full overlap is reached first in the North quadrant and last in the South quadrant, as expected.

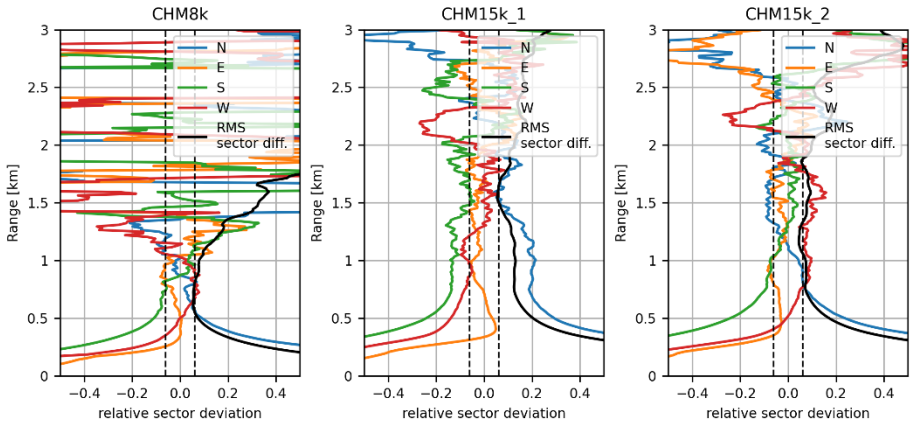

Figure 4. Profiles of the relative quadrant deviations from the mean normalized signal over all quadrants. The root mean square of the quadrant differences is shown in black. Relative deviation of 6% is marked with black dashed lines.

To better estimate the full-overlap range, Figure 4 shows the relative deviation of the quadrant signals from the mean over all quadrants, along with the corresponding RMS. Full overlap is assumed where both the deviation and RMS reach a minimum. This occurs at approximately 600 m for the CHM8k and 1.5 km for CHM15k_1, with a marked RMS decrease already at 800 m. For CHM15k_2, the RMS minimum appears at 1.2 km, with a noticeable drop from 780 m. These results align well with the manufacturer's overlap functions, which indicate full overlap at 800 m (CHM8k), 1.46 km (CHM15k_1), and 1.8 km (CHM15k_2). At 90 % overlap, the values are 600 m for the CHM8k and around 1 km for both CHM15k systems. It should be noted that the accuracy of the telecover test for ceilometers requires further investigation.

Conclusions

Determining the full overlap area and the alignment of a lidar is an essential part of quality control. The telecover test used for this can be applied to bi-axial ALCs such as the Lufft CHM models. The measurement data obtained from two CHM15k and one CHM8k using a self-developed 3D-printed tool show results that correspond well with the overlap functions provided by the manufacturer. Further comparisons with the same device types over a longer period of time should reveal possible differences between the devices as well as the long-term stability of the overlap range.

Acknowledgements

This work was carried out by the ALC unit of the Centre for Aerosol Remote Sensing (CARS) within ACTRIS. It is funded by the German Federal Ministry of Education and Research (BMBF, grant no. 01LK2002D) and the Federal Ministry for the Environment, Nature Conservation, Nuclear Safety and Consumer Protection (BMUV).

References

[1] Wiegner, M., Geiß, A.: Aerosol profiling with the Jenoptik ceilometer CHM15kx. Atmos. Meas. Tech. 5, 1953–1964, 2012

[2] Wiegner, M., Madonna, F., Binietoglou, I., Forkel, R., Gasteiger, J., Geiß, A., Pappalardo, G., Schäfer, K., Thomas, W.: What is the benefit of ceilometers for aerosol remote sensing? An answer from EARLINET. Atmospheric Measurement Techniques 7, 1979–1997, 2014

[3] Freudenthaler, V., Linné, H., Chaikovski, A., Rabus, D., and Groß, S.: EARLINET lidar quality assurance tools, Atmos. Meas. Tech. Discuss. [preprint], https://doi.org/10.5194/amt-2017-395, 2018

[4] ACTRIS CARS-AHL: High Power Lidar – Standard Quality Assurance Procedures for NF operation, https://www.actris.eu/sites/default/files/inline-files/QAPs-CARS-Jan2024-v01-rev12.pdf, 2024

Comparative Analysis of Fluorescence Lidar Measurements using 44 nm and 100 nm Interference Filters: A Case Study of a Saharan Dust Event over Thessaloniki

G. Peletidou[1], *K.A. Voudouri*[2,1], *K.Michailidis*[1], *C. Biskas*[1], *D.Balis*[1]

(1) Aristotle University of Thessaloniki, Department of Physics, 54124 Thessaloniki, Greece
(2) National Observatory of Athens, Institute for Astronomy, Astrophysics, Space Applications and Remote Sensing, 15236 Athens, Greece

Corresponding author: gpeletid@auth.gr

Introduction

Thessaloniki's lidar system (THELISYS) is part of the multitype ground-based instruments that belong to the Laboratory of Atmospheric Physics (LAP), located in the Physics Department of the Aristotle University of Thessaloniki, Greece (40.63°N, 22.96°E; 60m a.s.l.). The instrument is part of the European Aerosol Research Lidar Network (EARLINET; https://www.earlinet.org/index.php?id=earlinet_homepage) [1], providing quality-assured aerosol products since 2001 [2]. THELISYS multiwavelength Raman depolarization system (3β+2α+1δ) was upgraded and further equipped with two additional channels for calculating the vertical distribution of fluorescence capacity of the aerosols and the water vapor mixing ratio. A detailed description of the lidar system is given in [3].

Thessaloniki is an urban station in the Eastern Mediterranean where various types of aerosols coexist, making it an ideal location for aerosol classification studies and for evaluating the effectiveness of different aerosol typing algorithms [4]. The fluorescence capacity is a parameter useful for aerosol typing, as different types of aerosols, i.e., dust, smoke, pollen, and other organic particles [5] exhibit unique fluorescence emission spectra. In lidar instruments, the bandpass central wavelength (CW) and full width at half maximum (FWHM) are selected according to the fluorescence emission spectrum of the molecule of interest. In this study, we investigate how the selection of interference filters with FWHM values of 100 nm and 44 nm affects the retrieval of fluorescence lidar products and assess their impact on aerosol classification based on fluorescence capacity.

Methodology

THELISYS was upgraded in 2023 with the addition of a fluorescence channel (Fig. 1a). When the excitation wavelength is 355 nm, the primary portion of the emission spectrum typically falls within the 400–650 nm range [6]. The aerosol fluorescence backscatter coefficient was derived from the ratio of the fluorescence signal (P_F) to the nitrogen Raman signal (P_R), following [5]. The efficiency of the fluorescence with respect to elastic scattering can be derived by the fluorescence capacity,

$$G_F = \frac{\beta_F}{\beta_{355}} \ . \quad (1)$$

Initially, a 100 nm FWHM interference filter centered at 470 nm was used to isolate a segment of the fluorescence spectrum. However, due to differences in interference filters, the results were not directly comparable with those obtained in Lille [7] and Leipzig [8]. For better consistency, a 44 nm FWHM interference filter centered at 466 nm (Fig. 1b) was added at THELISYS, to be comparable to these systems. However, to achieve broader comparability of fluorescence measurements across different lidar setups it is preferable to use spectral fluorescence capacity, as introduced by [9]. In order to compare the fluorescence capacity and the florescence backscatter coefficient considering the characteristics of 100 nm and 44 nm FWHM interference filters, we assume the fluorescence capacity at 44 nm based on the following equation:

$$G_{F,44nm} = G_{F,100nm}\left(\frac{44}{100}\right). \quad (2)$$

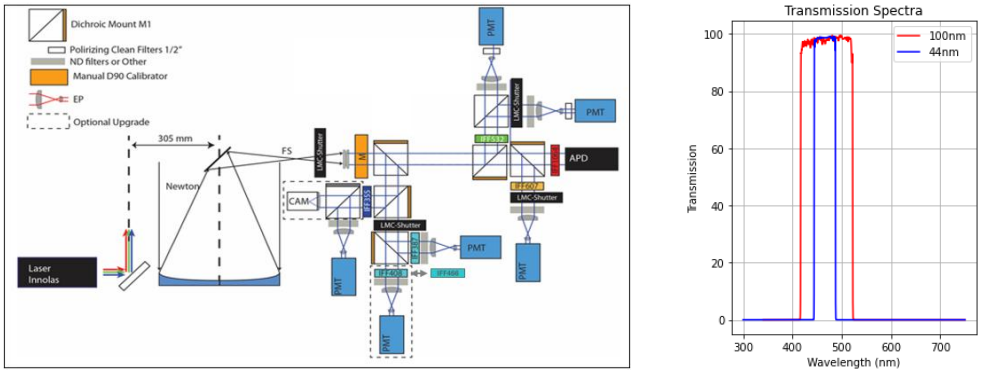

a) b)

Figure 1. a) Thessaloniki's Lidar System design after the upgrade. b) Transmission spectra of the 100 nm-wide (centered at 470 nm) and 44 nm-wide (centered at 466 nm) interference filters used in THELISYS.

Results and Discussion

Initial measurements with the THELISYS fluorescence lidar system began in April 2024 using the 100 nm interference filter. In March 2025, the 44 nm interference filter was installed, to allow comparative analysis.

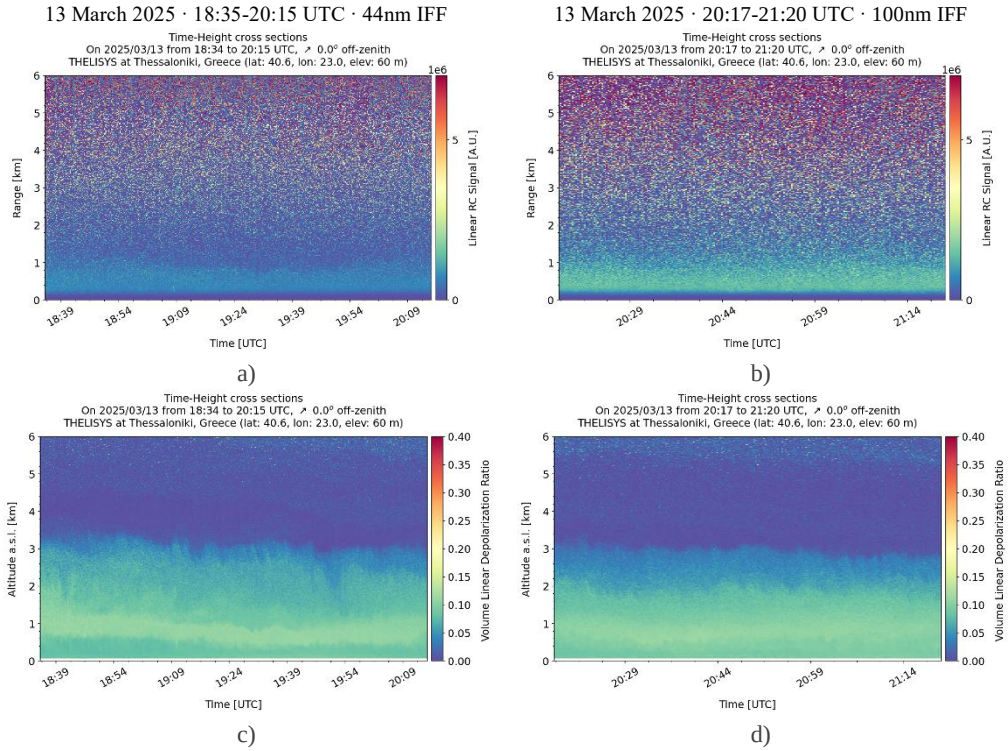

Figure 2. Height-time distributions of range-corrected glue lidar signals at 466 nm for 44 nm filter (a) and 100 nm (b) and volume linear depolarization ratio (VLDR) at 532 nm for 44 nm filter (c) and 100 nm (d) on 13 March 2025.

A case study on 13 March 2025 is presented. An extreme dust event, the first in 2025, passed over Thessaloniki, providing an opportunity to compare the performance of the two interference filters. The fluorescence range corrected glue signal for the first measurement (18:35–20:15 UTC) used the 44 nm filter and the second measurement (20:17–21:20 UTC) used the 100 nm filter are shown (Fig. 2). The aerosol layer was present within the boundary layer (below 3 km). This layer exhibited a high depolarization ratio and a low Ångström exponent, which are indicative of dust presence. HYSPLIT trajectories also confirmed that the air mass originated from the Sahara (not shown here).

The quicklooks of the fluorescence range-corrected signal using 44 nm and 100 nm filters show notable differences, with a stronger signal observed in the second case, which impacts the retrieval of fluorescence optical products. The time-averaged profiles of fluorescence capacity, fluorescence backscatter coefficient, and particle depolarization ratio are presented (Fig. 3). Across the fluorescence parameters, only minor differences are observed between the two different interference filters. Based on literature, the fluorescence capacity of dust layers typically ranges between $0.1 \times 10^{-4} - 0.5 \times 10^{-4}$ [10]. The values observed here range between $0.5 \times 10^{-4} - 0.7 \times 10^{-4}$ (Fig. 3a).

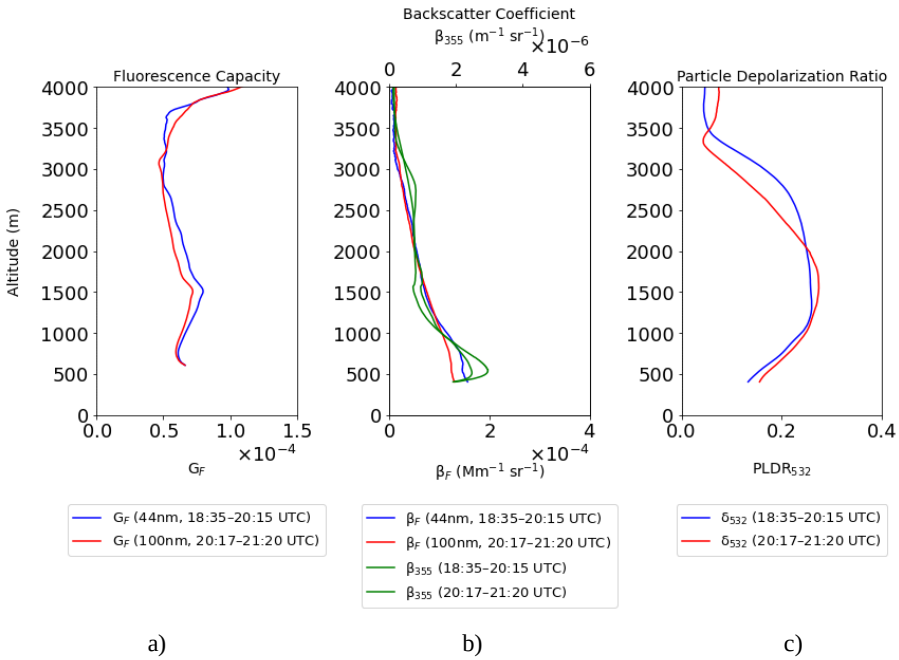

a) b) c)

Figure 3. Vertical profiles of the fluorescence capacity (a), the fluorescence and aerosol backscatter coefficients (b) for measurements with 44 nm and 100 nm filters and the particle depolarization ratio (c).

Conclusions

The study investigates the impact of interference filters with different FWHM in fluorescence lidar measurements for effective aerosol characterization. By comparing the 44 nm and 100 nm FWHM interference filters during a Saharan dust event (i.e., 13 March 2025) over Thessaloniki, the results showed minor differences in the measured spectral fluorescence capacity and spectral fluorescence backscatter coefficient. These findings underscore the need for standardizing the fluorescence capacity for aerosol characterization within EARLINET to improve data comparability and the aerosol typing schemes.

Acknowledgements

KV acknowledges the financial support by the PANGEA4CalVal project (Grant Agreement 101079201) funded by the European Union, and the CERTAINTY project (Grant Agreement 101137680) funded by the Horizon Europe program.

References

[1] Pappalardo, G., et. al.: EARLINET: towards an advanced sustainable European aerosol lidar network. Atmospheric Measurement Techniques, 7(8), 2389–2409. https://doi.org/10.5194/amt-7-2389-2014 , 2014.

[2] Siomos, N., et. al.: Are EARLINET and AERONET climatologies consistent? The case of Thessaloniki, Greece, Atmos. Chem. Phys., 18, 11885–11903, https://doi.org/10.5194/acp-18-11885-2018 , 2018.

[3] Michailidis, Optical and Microphysical Properties of Atmospheric Aerosols Based on Ground-Based and Satellite Remote Sensing Techniques (Doctoral dissertation), available at:10.26262/heal.auth.ir.351349, 2023.

[4] Voudouri, K. A, et. al.: Comparison of two automated aerosol typing methods and their application to an EARLINET station, Atmos. Chem. Phys., 19, 10961–10980, https://doi.org/10.5194/acp-19-10961-2019 , 2019.

[5] Veselovskii, I., et. al.: Combined use of Mie–Raman and fluorescence lidar observations for improving aerosol characterization: feasibility experiment, Atmos. Meas. Tech., 13, 6691–6701, https://doi.org/10.5194/amt-13-6691-2020 , 2020.

[6] Pan, Y.-L., et. al.: Single-particle laser-induced-fluorescence spectra of biological and other organic-carbon aerosols in the atmosphere: Measurements at New Haven, Connecticut, and Las Cruces, New Mexico, J. Geophys. Res., 112, D24S19, https://doi.org/10.1029/2007JD008741 , 2007.

[7] Veselovskii, I., et. al.: Mie–Raman–fluorescence lidar observations of aerosols during pollen season in the north of France, Atmos. Meas. Tech., 14, 4773–4786, https://doi.org/10.5194/amt-14-4773-2021 , 2021.

[8] Gast, B., et. al.: Invisible aerosol layers: improved lidar detection capabilities by means of laser-induced aerosol fluorescence, Atmos. Chem. Phys., 25, 3995–4011, https://doi.org/10.5194/acp-25-3995-2025 , 2025.

[9] Papadogiannaki, S., et al.: Comparative modeling approaches for predicting Olea and Quercus pollen seasons in Thessaloniki, Greece. Sci Rep 15, 12215, https://doi.org/10.1038/s41598-025-92259-3 , 2025

[10] Veselovskii, I., et. al.: Combining Mie–Raman and fluorescence observations: a step forward in aerosol classification with lidar technology, Atmos. Meas. Tech., 15, 4881–4900, https://doi.org/10.5194/amt-15-4881-2022 , 2022.

Development of an Optical Lab for Lidar Applications (OLALA)

E. Semwal[1], *M. Haarig*[1], *M. Hartmann*[1], *R. Engelmann*[1], *D. Althausen*[1], *T. Oppermann*[1], *H. Wex*[1]

(1) Leibniz Institute for Tropospheric Research (TROPOS), Permoserstr.15, 04318 Leipzig, Germany
Corresponding author: semwal@tropos.de

Introduction

Mineral dust aerosol, primarily originating from arid and semi-arid regions through wind erosion, is one of the most abundant types of natural aerosols in the atmosphere, which can be easily transported over long distances and influence atmospheric processes far from its source. Mineral dust is an important contributor to Earth's radiation budget and also plays a key role in cloud formation by serving as cloud condensation nuclei and ice nucleating particle, thereby impacting precipitation patterns and cloud lifetimes [1]. Therefore, a better understanding of scattering properties of mineral dust particles is essential for understanding their impact on climate change and atmospheric dynamics.

Active remote sensing using both ground-based and satellite-borne lidar systems provides continuous, vertically resolved measurements of the optical properties of atmospheric constituents in the exact backscattering direction. One of the most critical optical parameters retrieved from polarization-sensitive lidar is the depolarization ratio, which quantifies the degree to which linearly polarized light becomes depolarized after scattering by aerosol particles [2], [3]. This parameter has been extensively used in aerosol classification, as it is highly sensitive to particle shape. Non-spherical particles typically yield high depolarization ratios, whereas spherical particles produce values near zero [4]. Mineral dust, in particular, exhibits elevated depolarization ratios due to its highly irregular, non-spherical morphology, making it distinguishable from other aerosol types in lidar observations.

To derive the microphysical properties of mineral dust from the measured signals, inversion algorithms based on scattering models are essential. However, the intrinsic geometric complexity of mineral dust particles poses a significant challenge for accurate mathematical representation in scattering models. Although complex optical models have been developed in the past few decades [5], [6], they are often limited by the lack of robust datasets for validation and constraint. Field measurements are frequently used for model comparison [7], [8], yet these are associated with large uncertainties due to the heterogeneity of aerosol mixtures and limited knowledge of essential parameters such as particle size distribution, refractive index, and hygroscopicity. Therefore, laboratory studies at the interface between optical modelling and remote sensing are strongly required to fill this gap.

A New Scattering Laboratory: OLALA

The primary objective of the OLALA (Optical Lab for Lidar Applications) research group is to deepen the fundamental understanding of the optical backscattering properties of mineral dust, which is essential for accurate global aerosol monitoring using active remote sensing techniques from both ground-based and satellite platforms. To support this goal, a state-of-the-art scattering laboratory is currently being established at the Leibniz Institute for Tropospheric Research. This facility aims to generate a robust dataset on the 180° scattering characteristics of size selected natural mineral dust particles at typical lidar wavelengths of 355nm, 532nm and 1064nm. Laboratory measurements at sideward scattering angles [9], [10] are available in literature. However, measurement at exactly 180° scattering direction by mineral dust are extremely rare. Previous lab studies by [11], [12], [13] have contributed valuable insights, although, none have simultaneously addressed the key aspects of 180° backscattering, size-segregated dust samples, and the triple-wavelength configuration commonly used in lidar systems.

Our laboratory investigations will yield detailed information on particle size, shape, and refractive index through supplementary microscopic analyses, providing essential input parameters for optical particle shape modeling. Overall, these studies will play a critical role in validating remote sensing retrievals, improving theoretical models, and enhancing our overall understanding of the dust particle especially with regard to its spectral behavior.

Experimental Setup

Our experimental setup is divided in two main parts, Optical setup and Microphysical setup, which are described below:

1. Optical Setup

Designing the optical setup involves addressing two primary challenges. The first is achieving measurements at an exact 180° backscattering angle, and the second is effectively minimizing background stray light. To address the angular precision, careful alignment and positioning of optical components guided by advanced ray-tracing simulations using Zemax software was implemented. To mitigate stray light interference, a lock-in amplifier was employed. This device utilizes phase-sensitive detection to isolate weak signals from noisy backgrounds, thereby enhancing measurement accuracy.

The optical setup consists of three parts: an emitter system, receiver system and data acquisition system. A fiber pigtailed continuous wave (cw) laser at 532nm (Cobolt, Huebner Photonics) is used as the light source in emitter section. In contrast to atmospheric lidars that typically utilize pulsed lasers, our setup employs a continuous-wave (CW) laser, chosen for its consistent and stable output over time, which results in an improved signal-to-noise ratio. The receiver part consists of a pinhole of diameter 3mm which acts as a field stop and limits the scattering angle to 180° ± 0.2°. Behind the pinhole a polarizing beam splitter cube is placed (PBS251/M, Thorlabs) that captures the backscattered light and divides it into two orthogonal polarization components relative to the polarization plane of the emitted laser beam. An interference filter followed by a plano-convex lens of focal length 150mm (LA4874- A, Thorlabs) and a pinhole of diameter 1mm, are placed in front of the PMT detectors. The output of PMT is connected to the lock-in amplifier (SE1022D, Saluki Technology) for data visualization and recording. A block diagram of current setup is shown in figure below (Fig.1). The Δ90 approach [14] will be implemented for characterization of the two detection channels.

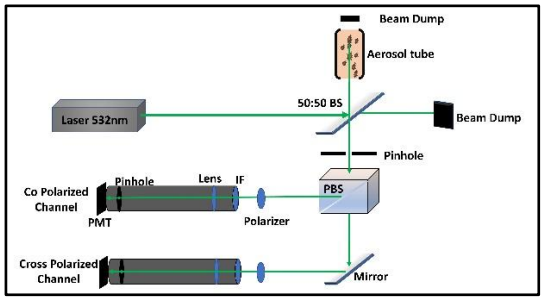

Figure 1. Optical Setup

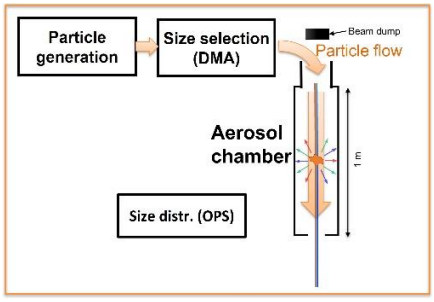

Figure 2. Particle generation setup

2. Microphysical Setup

The microphysical setup has three main parts: (i) Particle generation (wet and dry dispersion), (ii) size selection, and (iii) an aerosol chamber: (i) A custom aerosol generation enables the generation of wet or dry dispersed aerosol particles. In the case of wet dispersion, the aerosol is additionally fed through a dryer section. (ii) the polydisperse aerosol goes through a neutralizer and is then fed into a Differential Mobility Analyzer (DMA) to select only aerosol particles of a certain size. (iii) The now monodisperse aerosol then goes into the aerosol chamber, which consists of a 1-meter-long vertically oriented laminar flow tube (flow rate: 1 LPM) with an inner diameter of 0.7 in. From the top of the flow tube a 1 m long beam dump section extends (no particles flow through this section). To minimize stray light from internal reflections, all inner surfaces of the tube have been be coated with matte black paint.

The total particle concentration entering the aerosol chamber is monitored with a Condensation Particle Counter (CPC) and at the exit of the flow tube an Optical Particle Sizer (OPS) records the

concentration and size distribution of the aerosol particles. Figure 2 shows a simple block diagram for particle generation and measurement unit.

Results and Discussion

To test the working of our setup, we started with sodium chloride (NaCl) particles. NaCl particles are also non-spherical but have a less complex structure. Under low humidity atmospheric conditions, the NaCl in droplets crystallizes into cubes with rounded edges when dried. This cubic shape results in an enhanced depolarization ratio. This behavior has been observed under atmospheric conditions as has been shown by lidar observations at Barbados [16]. Figure 3 shows the variation in co and cross polarized signal on introducing 250nm NaCl particles inside the aerosol chamber. A distinct and substantial increase in signal intensity across both channels is observed, strongly indicating the non-spherical nature of the salt particles.

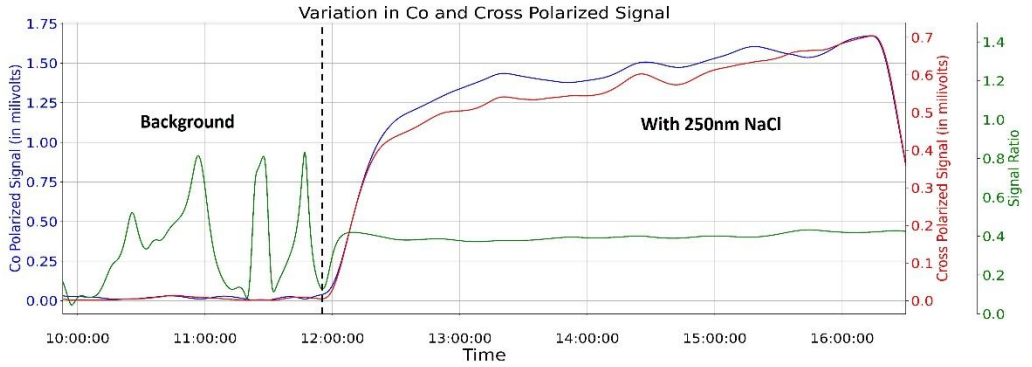

Figure 3. Shows the increase in co polarized and cross polarized signal on introducing the 250nm NaCl particles in the aerosol tube at 11:50 local time

The 250nm size represents the aerodynamical diameter which is measured by the differential mobility analyzer.

Outlook

Calibration efforts are currently underway. We intend to perform measurements with readily available standard materials such as NaCl, ammonium sulfate ($(NH_4)_2SO_4$), polystyrene latex spheres (PSL) and Arizona Test Dust with sizes ranging from 200 nm to 800 nm in diameter, before starting with natural dust samples from various deserts around the globe.

After gaining experience from the single wavelength setup, we intend to extend the setup to cover the full triple-wavelength (355, 532 and 1064nm) capabilities for linear polarization and circular polarization, enabling ellipsometry measurements of mineral dust particles. These results will lead to a better understanding of the spectral slope of the depolarization ratio of mineral dust which was observed in the atmosphere [17], [18], [19]. Optical modelling still struggles in reproducing the spectral patterns of the depolarization ratio for mineral dust. Therefore, the laboratory developments are strongly linked to modelling efforts to incorporate the findings in current scattering models of irregularly shaped particles.

Acknowledgements
The Leibniz Junior Research Group OLALA is funded by the Leibniz Association (J128/2022).

References
[1] IPCC. Intergovernmental Panel for Climate Change: the physical science basis. Contribution of Working Group I to the Fifth Assessment Report: Cambridge University Press; 2013.

[2] S. P. Burton et al., “Aerosol classification using airborne High Spectral Resolution Lidar measurements – methodology and examples,” Atmos Meas Tech, vol. 5, no. 1, pp. 73–98, 2012, doi: 10.5194/amt-5-73-2012.
[3] M. I. Mishchenko, I. V Geogdzhayev, and P. Yang, “Expansion of tabulated scattering matrices in generalized spherical functions,” J Quant Spectrosc Radiat Transf, vol. 183, pp. 78–84, 2016, doi: https://doi.org/10.1016/j.jqsrt.2016.05.015.
[4] I. M. Mishchenko, D. T. Larry, and A. L. Andrew, Scattering, absorption, and emission of light by small particles. Cambridge University Press., 2000.
[5] J. Gasteiger et al., “Modelling lidar-relevant optical properties of complex mineral dust aerosols,” Tellus B, vol. 63, no. 4, pp. 725–741, 2011, doi: 10.1111/j.1600-0889.2011.00559. x.
[6] M. Saito, P. Yang, J. Ding, and X. Liu, “A Comprehensive Database of the Optical Properties of Irregular Aerosol Particles for Radiative Transfer Simulations,” J Atmos Sci, vol. 78, no. 7, pp. 2089–2111, 2021, doi: 10.1175/JAS-D-20-0338.1.
[7] S. Kong, K. Sato, and L. Bi, “Lidar Ratio–Depolarization Ratio Relations of Atmospheric Dust Aerosols: The Super-Spheroid Model and High Spectral Resolution Lidar Observations,” Journal of Geophysical Research: Atmospheres, vol. 127, no. 4, Feb. 2022, doi: 10.1029/2021JD035629.
[8] M. Saito and P. Yang, “Advanced Bulk Optical Models Linking the Backscattering and Microphysical Properties of Mineral Dust Aerosol,” Geophys Res Lett, vol. 48, no. 17, p. e2021GL095121, 2021, doi: https://doi.org/10.1029/2021GL095121.
[9] O. Muñoz, F. Moreno, D. Guirado, D. D. Dabrowska, H. Volten, and J. W. Hovenier, “The Amsterdam–Granada Light Scattering Database,” J Quant Spectrosc Radiat Transf, vol. 113, no. 7, pp. 565–574, 2012, doi: https://doi.org/10.1016/j.jqsrt.2012.01.014.
[10] J. C. Gómez Martín et al., “On the application of scattering matrix measurements to detection and identification of major types of airborne aerosol particles: Volcanic ash, desert dust and pollen,” J Quant Spectrosc Radiat Transf, vol. 271, p. 107761, 2021, doi: https://doi.org/10.1016/j.jqsrt.2021.107761.
[11] T. Sakai, T. Nagai, Y. Zaizen, and Y. Mano, “Backscattering linear depolarization ratio measurements of mineral, sea-salt, and ammonium sulfate particles simulated in a laboratory chamber,” Appl. Opt., vol. 49, no. 23, pp. 4441–4449, Aug. 2010, doi: 10.1364/AO.49.004441.
[12] E. Järvinen et al., “Laboratory investigations of mineral dust near-backscattering depolarization ratios ,” Journal of Quantitative Spectroscopy and Radiative Transfer , vol. 178, pp. 192–208, 2016, doi: http://dx.doi.org/10.1016/j.jqsrt.2016.02.003.
[13] A. Miffre, D. Cholleton, C. Noël, and P. Rairoux, “Investigating the dependence of mineral dust depolarization on complex refractive index and size with a laboratory polarimeter at 180.0 lidar backscattering angle,” Atmos Meas Tech, vol. 16, no. 2, pp. 403–417, 2023, doi: 10.5194/amt-16-403-2023.
[14] V. Freudenthaler, “About the effects of polarising optics on lidar signals and the Δ90 calibration,” Atmos Meas Tech, vol. 9, no. 9, pp. 4181–4255, Aug. 2016, doi: 10.5194/amt-9-4181-2016.
[16] M. Haarig et al., “Dry versus wet marine particle optical properties: RH dependence of depolarization ratio, backscatter, and extinction from multiwavelength lidar measurements during SALTRACE,” Atmos Chem Phys, vol. 17, no. 23, pp. 14199–14217, 2017, doi: 10.5194/acp-17-14199-2017.
[17] M. Haarig et al., “Triple-wavelength depolarization-ratio profiling of Saharan dust over Barbados during SALTRACE in 2013 and 2014,” Atmos Chem Phys, vol. 17, no. 17, pp. 10767–10794, 2017, doi: 10.5194/acp-17-10767-2017.
[18] M. Haarig et al., “First triple-wavelength lidar observations of depolarization and extinction-to-backscatter ratios of Saharan dust,” Atmos Chem Phys, vol. 22, no. 1, pp. 355–369, 2022, doi: 10.5194/acp-22-355-2022.
[19] Q. Hu et al., “The characterization of Taklamakan dust properties using a multiwavelength Raman polarization lidar in Kashi, China,” Atmos Chem Phys, vol. 20, no. 22, pp. 13817–13834, 2020, doi: 10.5194/acp-20-13817-2020.

Design and Implementation of a Near-Range Telescope for ACTRIS Lidar Systems Compliant with NF Performance Criteria

***L.Belegante*[1]**, *D. Nicolae*[1], *G. Ciocan*[1], *C. Radu*[1], *J. Vasilescu*[1], *A. Nemuc*[1], *V. Nicolae*[1], *A. Tilea*[1], *A. M. Dandocsi*[1]

[(1)]National Institute of Research and Development for Optoelectronics INOE 2000, Atomistilor Street 409, Magurele, Ilfov Romania. [(2)] Faculty of Physics, University of Bucharest, Magurele, Atomistilor 405, Romania[)]

Corresponding author: victor.nicolae@inoe.ro

Introduction and Motivation

Accurate characterization of the lower planetary boundary layer (PBL) is essential for understanding aerosol dynamics, air quality, and atmospheric mixing processes. However, conventional lidar configurations often suffer from limited overlap performance at short ranges, restricting the retrieval of reliable data in the lowest atmospheric layers. To address this limitation, ACTRIS (Aerosol, Clouds and Trace Gases Research Infrastructure) guidelines recommend the implementation of a dedicated near-range (nr) telescope as part of the aerosol high-power lidar system, enabling robust observations down to a few hundred meters above ground level. This capability is critical for National Facilities aiming to meet the minimum performance criteria outlined by the Centre for Aerosol Remote Sensing (CARS), especially in capturing key ACTRIS variables such as the planetary boundary layer height and near-surface backscatter profiles. A near-range telescope enhances the lidar's ability to resolve the vertical structure of aerosols within the PBL, thus supporting improved synergy with sun/sky photometers and contributing to high-quality climatological datasets, special event monitoring, and satellite validation efforts.

Beyond extending lidar observations into the lowest atmospheric layers, the integration of a near-range telescope offers critical operational and scientific advantages. Technically, it facilitates the accurate assessment of the full-overlap height, enabling routine monitoring of alignment, optical stability, and potential system degradation over time - a requirement for quality assurance in ACTRIS-labelled National Facilities. Scientifically, the near-range module enhances the detection of atmospheric constituents that are predominantly confined to the lower planetary boundary layer, such as primary biological aerosol particles (PBAPs) like pollen or insect swarms [1], and anthropogenic or biogenic particles associated with seasonal agricultural activities. Additionally, it improves the capability to capture low-altitude resuspension events, such as urban/suburban dust uplift, a phenomenon driven by wind and vehicular turbulence that typically does not exceed 100–200 m above ground level. These processes are often undetectable by conventional far-range lidar channels due to their limited sensitivity at low altitudes. Thus, the near-range telescope is essential not only for meeting ACTRIS compliance thresholds, but also for broadening the scientific scope of lidar-based observations, particularly in studies of air quality and urban boundary layer dynamics.

Methodology

The primary driver in the design of the near-range telescope is the stringent overlap constraint imposed by the ACTRIS National Facilities (NF) minimal requirements. These requirements demand that lidar systems achieve full overlap at or below a defined lower boundary - typically 200 m - to enable high-quality observations within the lower planetary boundary layer. The overlap condition is governed by two distinct but interdependent factors. First, the geometrical overlap, which refers to the physical intersection between the emitted laser beam and the telescope's field of view, must be carefully optimized through optical and mechanical alignment to ensure efficient signal collection starting from low altitudes. Second, the optical overlap is constrained by the transmission properties of the interference filters (IFF) used in the detection chain. These filters exhibit angular sensitivity that causes a wavelength shift in the transmitted spectrum as the angle of incidence increases. This effect can degrade filter performance at low altitudes where the incoming radiation enters the telescope at higher angles, particularly in narrowband channels. In conclusion, the optical overlap is the range-dependent efficiency with which the lidar receiver collects backscattered light based on angular-dependent transmission properties of optical components As such, both overlap components must be simultaneously addressed in the design phase to meet ACTRIS standards and to ensure

that useful signal is collected starting from 200 m or lower without introducing significant transmission losses. The optical setup of the near-range telescope is based on a lens-based configuration, employing a primary lens with a diameter of 76.2 mm and a wide field of view (FoV) of 2 mrad full angle, specifically chosen to optimize signal collection from low altitudes. Initial performance tests were conducted using a 532.072 nm laser emission line, with future extensions planned for 354.71 nm, to support multi-wavelength operation as required by ACTRIS protocols. The focal length of 392.2 mm was selected based on the availability of commercial optical components and was found to satisfy both the optical and mechanical integration constraints of the lidar system. A critical design consideration was the aperture size at the focal plane - set to 0.8 mm diameter - which allows sufficient optical access to simplify the alignment procedure during telescope assembly and integration. The choice of a longer focal length thus represents a balance between maintaining a wide FoV for effective geometrical overlap and ensuring alignment flexibility without compromising signal quality or inducing vignetting in the collected beam. The alignment was performed by precisely adjusting the axes of the receiving telescope relative to the laser emission axes using high-precision alignment screws of 127 threads per inch resolution, resulting in an alignment accuracy of 0.84 mrad per revolution for a lever arm length of 237 mm.

Results and Discussion

To evaluate and optimize the geometrical overlap performance of the near-range telescope, a series of simulations were conducted using realistic lidar configuration parameters. The lateral separation between the optical axis of the telescope and that of the laser beam was set to 100 mm, reflecting a typical alignment constraint in compact multi-channel lidar systems. The laser beam was modeled with a 7 mm diameter and a total divergence (full angle) of 0.4 mrad, ensuring a sufficiently collimated profile for both near and far field operations. In order to achieve optimal overlap without introducing optical losses in the far-range detection channels, a laser tilt of 0.5 mrad toward the telescope axis was introduced. This value was selected to align the laser emission with the telescope field of view in such a way that full geometrical overlap is reached at the targeted near-field range while preserving signal integrity at higher altitudes. These parameters formed the basis of the optical simulations used to determine the field of view and overlap performance of the telescope. Figure 1 shows the results of the geometrical overlap simulation based on the described setup. The figure illustrates the projected paths of the laser beam and the telescope's field of view, with the overlap region marked by the intersection of the two. The green lines represent the laser beam boundaries, while the blue lines indicate the telescope's acceptance angle. The red dashed line marks the outermost limit of the telescope FoV, and the yellow point denotes the altitude where full geometrical overlap is achieved - defined as the lowest height at which the entire laser beam cross-section is fully enclosed within the telescope's FoV. For the simulated configuration, this overlap altitude was found to be approximately 150 m, in agreement with the ACTRIS NF minimum requirement. The simulation confirms that the chosen parameters (2 mrad FoV, 0.5 mrad laser tilt, 100 mm separation) allow for efficient signal collection in the lower PBL without compromising alignment or far-field performance.

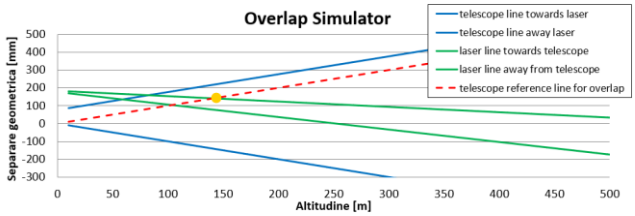

Figure 1. Geometrical overlap simulation for the near-range telescope configuration.

Cost constraints: The design of the near-range telescope was also influenced by practical cost constraints, aiming to deliver a technically compliant solution within a limited budget suitable for ACTRIS NF. The total manufacturing cost of the telescope system was approximately 4500€, with around 2000€ allocated for the optomechanical components (including the telescope body and mechanical mounts), 1500€ for the

optical elements (lenses and filters), and an additional 1000€ for alignment support hardware and precision manual adjusters. Beyond the telescope assembly, further investment is necessary for the detection and data acquisition components, specifically the photomultiplier tube (PMT) module and associated acquisition electronics, which are estimated in a range of 2000 - 10000€. The overall configuration thus represents a cost-effective and modular solution, capable of being integrated into existing lidar systems while meeting the NF performance criteria defined by ACTRIS. The optical layout of the near-range telescope, shown in Figure 2a, illustrates the full design chain from beam collection to image reduction. The beam collector section consists of a 75 mm diameter achromatic lens paired with a 25 mm achromatic lens, configured to efficiently collect and collimate the backscattered radiation entering through the 76.2 mm telescope aperture. To ensure compatibility with the small sensitive area of the photodetector, the system includes a beam reducer, composed of a plano-convex lens assembly designed to compress the beam footprint. This optical reduction not only matches the signal geometry to the detector size but also minimizes the range-dependent displacement of the image on the active area - an effect particularly relevant when switching between near-field and far-field returns. The optical configuration was optimized to achieve minimal aberration across the full field of view and to ensure stable focus across a broad altitude range. Figure 2b illustrates the simulated projection of the optical signal onto the detector's sensitive area for both near-range (0.2 km, shown in blue) and far-range (15 km, shown in green) returns. The optical system was optimized such that both image footprints remain well-aligned within the detector's active region (5 mm diameter), ensuring efficient signal collection across the full altitude range.

Figure 2. A. Optical design of the near-range telescope, including the beam collector (achromatic lenses) and beam reducer for image size adjustment and alignment stability. B. Simulated image projection on the detector's sensitive area for near-range (0.2 km, blue) and far-range (15 km, green) returns, showing minimal displacement across altitude.

The interference filter (IFF) was positioned between the image collector and the beam reducer, a location selected to minimize the angle of incidence of the incoming radiation and thus reduce wavelength-dependent transmission losses. The primary filter used in the telescope is a 0.6 nm full-width at half maximum (FWHM) module, chosen to balance spectral selectivity with angular tolerance at the target wavelength of approximately 532 nm. To evaluate performance limits, additional simulations were performed for a narrower 0.3 nm FWHM filter. Optical simulations based on the current telescope geometry show that the maximum angle of incidence for radiation collected from the near range (0.2 km) is approximately 7.5 mrad, while for the far range (15 km), the angle is significantly smaller, around 2.8 mrad. As shown in Figure 3, for the narrower 0.3 nm FWHM filter, this angular deviation induces a central wavelength shift of 0.054 nm at 532 nm, resulting in a transmission loss to 91.4% of the filter's peak value. In contrast, the broader 0.6 nm filter exhibits a smaller transmission loss of only 2.2%, maintaining 97.8% transmission under the same conditions. These results confirm the suitability of the 0.6 nm filter for this optical configuration, providing sufficient angular tolerance to support both near- and far-range signal collection without spectral distortion.

Extended tests were conducted to evaluate the signal-to-noise ratio (SNR) performance of the near-range (NR) telescope under both daytime and nighttime operating conditions. The study also included a comparative analysis between the signal strength and derived optical products obtained from the NR channel and those from the standard far-range channel. These comparisons were performed for both day and night scenarios to assess the consistency and complementarity of the two systems. Additionally, a Rayleigh fit quality assurance (QA) test was used to evaluate the alignment stability of the far-range channel. To further support alignment validation, a dedicated camera-based setup was employed for real-time monitoring and adjustment during system integration.

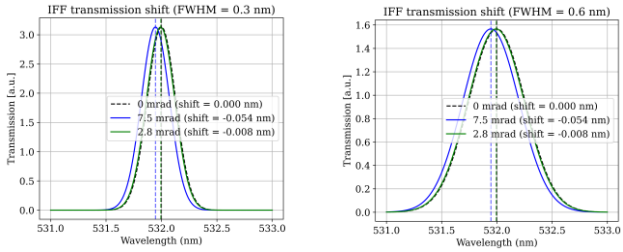

Figure 3. Simulated transmission loss of interference filters at 532 nm as a function of incidence angle. For a 7.5 mrad angle, the 0.3 nm FWHM filter shows 91.4% transmission due to a 0.054 nm spectral shift, while the 0.6 nm FWHM filter retains 97.8% transmission under the same conditions.

Figure 4 presents a representative comparison of the particle backscatter coefficient at 532 nm, averaged over a 30-minute daytime period, showing the retrievals obtained using the NR telescope optimized for far range retrievals, in comparison with those from a 400 mm Cassegrain telescope. This test was deliberately conducted under a worst-case scenario - during daytime, when background noise is highest and SNR is lowest - to critically assess the NR telescope's performance. The results demonstrate strong consistency between the two channels in the region of overlap, confirming both the optical alignment and the retrieval quality of the NR telescope.

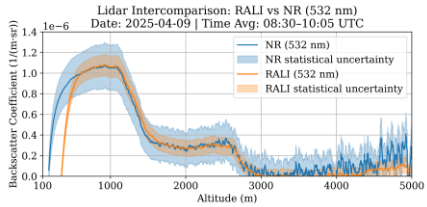

Figure 4. Comparison of 532 nm particle backscatter coefficient profiles retrieved from the near-range (NR) telescope and the reference RALI lidar (09:30–10:00 UTC, April 2025). NR telescope optimized for far range to check signal quality for upper altitudes. The comparison indicates the real full overlap height of the Reference telescope (600 m).

The 30-minute averaged daytime profiles show a strong agreement in the backscatter coefficient retrieved from the near-range (NR) telescope and the reference RALI system at 532 nm, including in the overlap region and extending well beyond 2.5 km altitude. This agreement confirms the effective alignment and stability of the NR telescope, as well as the quality of the retrieved optical products during daytime operation. Although increased noise is visible at higher altitudes in the NR channel due to its reduced aperture and shorter focal length, the core aerosol layer is consistently resolved. Even stronger consistency and signal fidelity were observed during nighttime conditions, where the improved signal-to-noise ratio enhances the overlap in retrievals - these results will be presented during the conference.

Conclusions:

These results confirm that the NR channel can provide reliable daytime retrievals, with even better agreement observed during nighttime operation (results shown during the conference). This low-cost near-range telescope has demonstrated added value in the context of ACTRIS-compliant lidar systems. Beyond enabling reliable aerosol retrievals in the lower planetary boundary layer, it proved instrumental in assessing the full-overlap height of the far-range channels. The data obtained from the NR channel provided critical insight into the incomplete overlap regions of the far-range, enabling improved operation of the system.

Acknowledgements

This work is supported by the Core Program within the Romanian National Research Development and Innovation Plan 2022-2027, carried out with the support of MCID, project no. PN 23-05, the ATMO-ACCESS H2020 Grant Agreement no. 101008004, the CARGO-ACT HEU Grant Agreement no. 101132093, and through the ACTRIS ERIC and CARS Cooperation Agreement / 25 April 2023.

References

[1] Bohlmann, S., et al. (2021). Lidar depolarization ratio of atmospheric pollen at multiple wavelengths. Atmospheric Chemistry and Physics, 21, 7083–7097. https://doi.org/10.5194/acp-21-7083-2021

Recent advances from the observational platform lidar at Atmospheric Rome joinT supersitE (ARTE)

G. Giuliano[1], *D. Dionisi*[1], *M. Di Paolantonio*[1], *L. Masi*[1,2], *A. Riciniello*[3], *G.L. Liberti*[1]

(1) Italian National Research Council, Institute of Marine Sciences, (CNR-ISMAR), 00133 Rome, Italy
(2) "Parthenope" University of Naples, 80133 Naples, Italy
(3) "Sapienza" University of Rome, 00185 Rome, Italy

Corresponding author: giovanni.giuliano@cnr.it

Introduction

In this work we describe and present the latest advances in the remote sensing capabilities provided by the multi-telescope Rayleigh-Mie-Raman (RMR) lidar system at the Italian National Facilities ARTE in Rome Tor Vergata CNR site (41.84224°N, 12.64734°E). The research activities are carried out in the framework of both national and international networks of high power lidar-based national facilities (NFs) such as the European Research Infrastructure ACTRIS, EARLINET, NDACC and within the validation of satellite data such as Earth Cloud, Aerosol and Radiation Explorer (EarthCARE).

Since the original system, developed in the mid-90s [1] to study mainly geophysical variables in the mid/upper atmosphere [2-4], major system upgrades have been performed within the Italian Integrated Environmental Research Infrastructures System (ITINERIS) project, which provides access to essential environmental data and services for the study of current and future environmental challenges. The upgrades included the implementation of new lidar acquisition channels, thus improving the observation capacity of the ARTE NF.

Technological solutions

The system, shown in Figure 1, is mounted in two stacked containers. The receiver is based on a multiple telescope configuration, which allows a wide atmospheric altitude range to be sampled. The main features are air-conditioned rooms to keep the operating temperature stable and thus reduce the detrimental thermal effects on the optomechanical components (laser crystals, optical filters, PMTs, etc.), laser beams enclosed in black plastic tubes to reduce diffuse reflections, and laser electronics located away from the receiver to minimize EM interference.

The optimization of the alignment between the laser beams and the telescopes is achieved with a semi-automated mapping procedure that controls the signal acquisition and the 3D servo motors which move the multi-wavelength separation unit mounted above the telescope around its focal point [5]. Since the planning activities in the context of international networks include both day and night sessions, with the aim of studying several aerosol observation scenarios, specific hardware-based solutions and custom packages based on different softwares (NI LabVIEW, Python, MATLAB) have been developed for remote instrument control, motorized roof, visual inspection via webcam, data acquisition and processing.

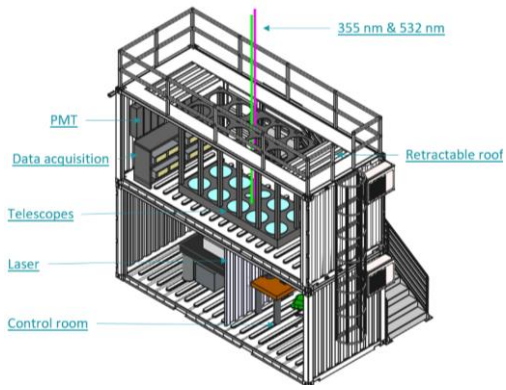

Figure 1. LIDAR at ARTE NF: details about the housing containers.

The emitter is a high-energy Nd:YAG 10 Hz laser with an energy output optimized for the investigation of the UV Raman scattering, so pulse energies are approximately 450 mJ at 355 nm and 240 mJ at 532 nm. Among the 11 Newtonian f/3 telescopes summarized in Table 1, this work focuses on the upgrade activities carried out on the 150 mm and 300 mm diameter telescopes.

Table 1. Telescope characteristics.

Telescope	**#1**	**#2**	**#3**
Type	Array of nine	Single	Single
Diameter (mm)	500 (each)	300	150
Focal length (mm)	1500	900	450
FOV (mrad)	0.5	0.9	1.8
Full overlap (m)	From 4000 to 8000	< 1000	< 300

Table 2 gives an overview of the acquisition configuration with 7 additional channels and details of the type of acquisition mode (analog or photon counting), the full width at half maximum of the interference filter and the model of the new Hamamatsu modules installed. The upgraded design of the optical system for the 150 and 300 mm telescopes results in an increased number of detection channels, from five to twelve (summarized below) and with the inclusion of polarization channels to achieve the minimum configuration 1β + 1α + 1δ at 355 nm detailed in the ACTRIS Aerosol Remote Sensing Observational Platform ACTRIS guidelines [6].

Table 2. Overview of the upgraded acquisition channels at ARTE NF.

	Previous CH#	New CH#	Tele ⌀ (mm)	λ (nm)	Type	Acq. mode (LICEL)	IF FWHM (nm)	PMT model
ACTRIS	N/A	1	150	354,7	Elastic transmitted	A	0,5	H10721P-110-01
	N/A	2		354,7	Elastic reflected	PC	0,5	H10721P-210-01
	N/A	3		386,7	N_2 Raman	A	0,3	H10721P-210-01
	N/A	4		407,5	H_2O Raman	PC	0,3	H10721P-210-01
	1	5		532,1	Elastic	A	1,0	H10721P-113-01
	N/A	6		607,6	N_2 Raman	A	1,0	H10721P-210-01
	8	7	300	354,7	Elastic transmitted	A + PC	0,5	H10721P-110-01
	N/A	8		354,7	Elastic reflected	PC	0,5	H10721P-210-01
	4	9		386,7	N_2 Raman	A + PC	0,3	H10721P-210-01
	5	10		407,5	H_2O Raman	PC	0,3	H10721P-210-01
	2	11		532,1	Elastic	A + PC	1,0	H10721P-113-01
	N/A	12		607,6	N2 Raman	A + PC	1,0	H10721P-210-01
Medium-high atmosphere	3	13	8 x 500	532,1	Elastic			
	6	14		386,7	N_2 Raman			
	7	15		407,5	H_2O Raman			
Troposphere (32-channel PMT with a 750 mm spectrograph) - To be installed	N/A	16 - 47	1 x 500	350 - 650	Aerosol fluorescence			

Results and Discussion

Figure 2 shows an example of lidar measurements from the upgraded RMR lidar system, acquired between 17:40 UTC - 6 March and 15:30 UTC - 7 March 2025. The figure displays the time evolution of selected elastic and Raman channels, among those listed in Table 1. Each profile was acquired with an integration time of 60 seconds and a vertical resolution of 3.75 m. The plots in Figure 2 were generated with the Automated Lidar Analysis Software (ATLAS) software [7].

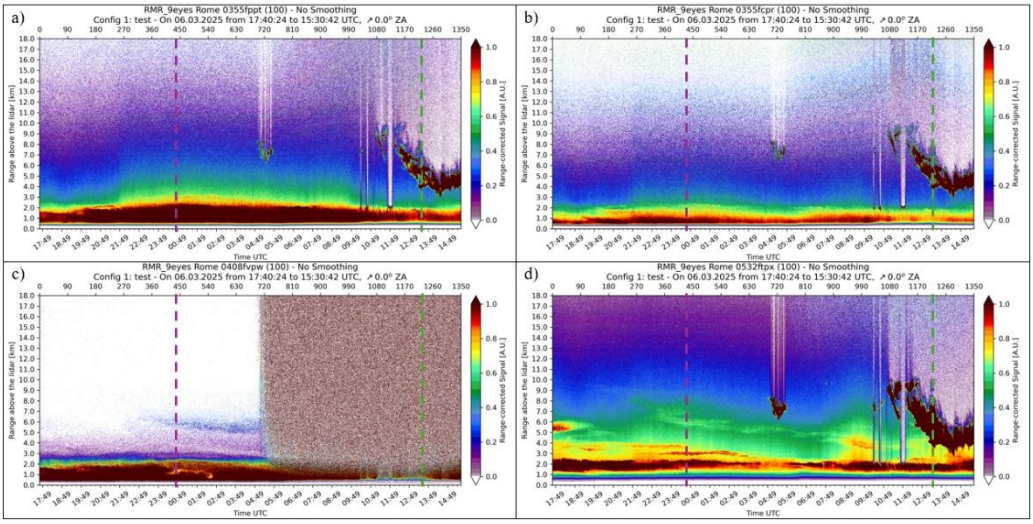

Figure 2. Contour plots of range corrected signal for the following far range (300 mm telescope) photon counting channels: a) 354.7 nm transmitted, b) 354.7 nm reflected, c) 407.5 nm total and d) 532.1 nm total. The dashed lines show the overpasses' time.

During the above acquisition time, two EarthCARE overpasses, each with a duration of 23 seconds, occurred within a 100 km radius from the lidar as shown in Figure 3. The first, ascending orbit 4389 with a distance to mid-swath of 53.8 km, on March 7th 2025 between 00:44:44 and 00:45:07 UTC, while the second between 13:29:44 and 13:30:07 UTC, descending orbit 4397 with a distance to mid-swath of 52.5 km. The presented lidar data are currently being analyzed and will be used for detailed case studies and comparisons with publicly available EarthCARE profiles.

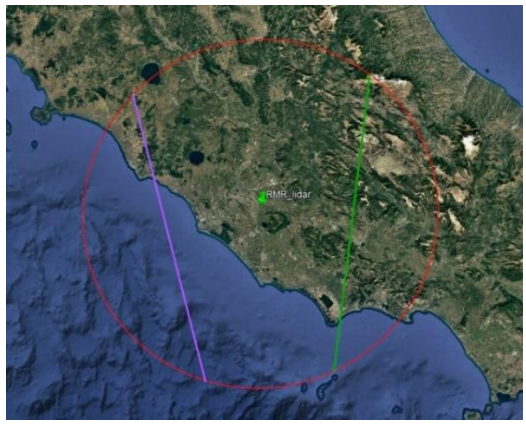

Figure 3. EarthCARE orbits (purple) 4389 at 00:45:07 UTC and (green) 4397 at 13:30:07 UTC on March 7th 2025. The red circle is centered at the ARTE NF lidar and with a 100 km radius.

The raw lidar data were converted to the NetCDF format required by EARLINET Single Calculus Chain (SCC) [8] to retrieve the elastic backscatter products for the 300 mm telescope for the following channels: 355 nm transmitted, 355 nm reflected and 532 nm. The results are summarized in Figure 4 for the EarthCARE overpasses described above. These profiles are calibrated using data from model, and future actions include the use of radiosonde data from the nearby WMO station 16245 LIRE Pratica Di Mare (41.65°N, 12.43°E).

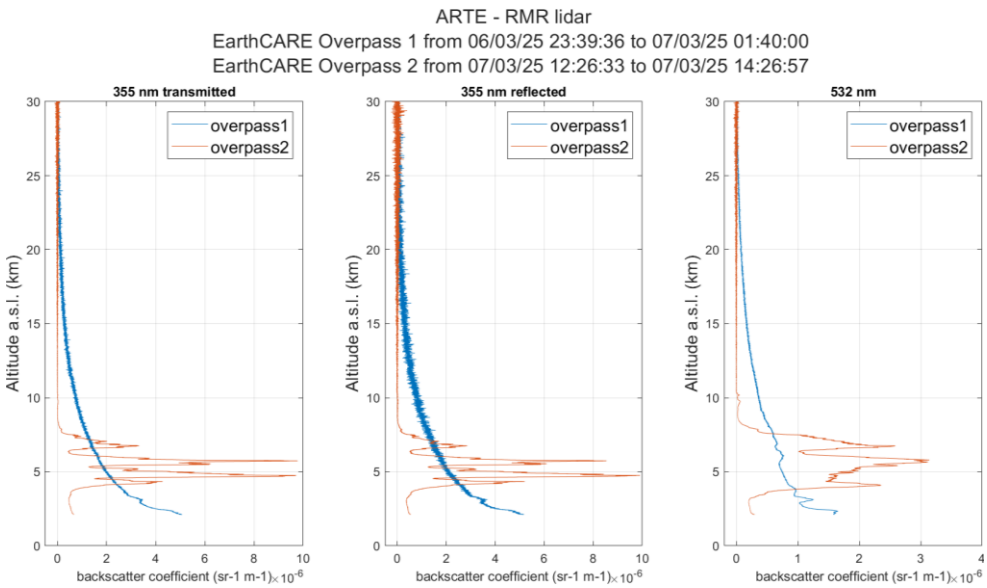

Figure 4. Aerosol backscatter coefficients calculated with the SCC for the two EarthCARE overpasses.

Conclusions

By upgrading the system with new acquisition channels, increasing the spectral information, the vertical sampling and introducing the polarization capabilities, further enhanced research and scientific applications are possible. A few examples are the analysis of the influence of aerosol in the troposphere and in the upper troposphere and lower stratosphere (UTLS) on the measurement of the water-vapour mixing ratio and the identification of the particle type with the polarization lidar technique. As described above, the system is actively involved in satellite Cal/Val tasks within the EarthCARE lidar satellite mission. Planned activities of the improved instrumental configuration at ARTE NF involve a synergistic field campaign in the coming months with two mobile lidars to extend the measurement capabilities down to the ground level, as well as aerosol fluorescence measurement using a 32-anode PMT detector.

Acknowledgements

This project was supported by IR0000032 – ITINERIS, Italian Integrated Environmental Research Infrastructures System (D.D. n. 130/2022 - CUP B53C22002150006) Funded by EU - Next Generation EU PNRR- Mission 4 “Education and Research” - Component 2: “From research to business” - Investment 3.1: “Fund for the realisation of an integrated system of research and innovation infrastructures”.

References

[1] Congeduti, F., Marenco, F., Baldetti, P., Vincenti, E., "The multiple-mirror lidar ‘9-eyes'", J. Opt. A: Pure Appl. Opt. 1, 185 (1999).

[2] Dionisi, D., Congeduti, F., Liberti, G.L., Cardillo, F. "Calibration of a multichannel water vapor Raman lidar through noncollocated operational soundings: optimization and characterization of accuracy and variability", JTECH 27.1, 108-121 (2010).

[3] Dionisi, D., Keckhut, P., Hoareau, C., Montoux, N., Congeduti, F., “Cirrus crystal fall velocity estimates using the Match method with ground-based lidars: first investigation through a case study”, AMT, 6, 457–470 (2013).

[4] Dionisi, D., Keckhut, P., Liberti, G. L., Cardillo, F., Congeduti, F., “Midlatitude cirrus classification at Rome Tor Vergata through a multichannel Raman–Mie–Rayleigh lidar”, ACP, 13, 11853–11868 (2013).

[5] Di Paolantonio, M., Dionisi, D., Liberti, G. L., "A semi-automated procedure for the emitter-receiver geometry characterization of motor-controlled lidars", AMT, 15, 1217-1231 (2022).

[6] “Guidelines and recommendations for the candidate ACTRIS Aerosol Remote Sensing Observational Platforms”, version 02, rev. 01 (2022).

[7] https://github.com/nikolaos-siomos/ATLAS

[8] D'Amico, G., Amodeo, A., Baars, H., Binietoglou, I., Freudenthaler, V., Mattis, I., Wandinger, U., Pappalardo, G., "EARLINET Single Calculus Chain–overview on methodology and strategy." AMT, 8, 4891-4916 (2015).

Boosting Wind Velocity Availability in a Six-Beam Doppler Lidar

M. Manami[1,2], *G. Léa*[2], *J. Mann*[1], *M. Sjöholm*[1], *G. Gorju*[2]

(1) Technical University of Denmark (DTU), Department of Wind and Energy Systems, Roskilde, Denmark

(2) Lumibird SA, Lidar Division, Lannion, France

Corresponding author: manami@dtu.dk

Introduction

The Doppler Beam Swinging (DBS) technique is widely recognized as a reliable method for reconstructing wind velocity profiles using coherent Doppler lidars [1], [2]. However, in commercial pulsed lidars, wind velocity availability is often restricted by requiring all individual beams to have valid measurements. Under the current filtering approach, a complete scan is typically discarded if even one beam does not meet a specified signal-to-noise ratio (SNR) threshold. This approach of performing the DBS leads to reduced overall wind velocity availability, especially at higher altitudes. The current study suggests a simple approach to improve wind velocity availability in pulsed lidar systems by optimizing the number of beams used in the DBS algorithm. The effectiveness of the proposed method is demonstrated through a field experiment conducted at the Østerild test site, where the Streamline Beam6X HALO Photonics system from Lumibird [3] is validated against a collocated RISØ P2546A cup anemometer [4] mounted on the Light Mast North at a height of 244 m, serving as reference instruments.

Methodology

The DBS method in pulsed lidar closely resembles the velocity-azimuth display (VAD) technique, which was developed by Lhermitte and Atlas [5] and Browning and Wexler [6]. In both approaches, the lidar measures the mean Doppler velocity on the cone base above the instrument (so-called conical scan). However, in DBS, there are typically only a few beams, that doesn't need to have the same elevation angle, as opposed to the VAD method where the beam is rotating with a constant elevation angle. Assuming the wind field is horizontally homogeneous and stationary within a given range gate, the full wind vector can be derived by minimizing the square differences between the measured radial velocities and the projection of the wind vector onto the known unit vectors in the direction of the lidar beams:

$$\chi^2 = \sum_{i=1}^{N} \frac{\left(\boldsymbol{u}_o \boldsymbol{r}_i^T - u_{ri}\right)^2}{\sigma_{ri}^2}, \tag{1}$$

where $\boldsymbol{u}_o = (u_o, v_o, w_o)$ denotes the mean wind velocity vector to be found, N is the number of beams, u_{ri} is the measured radial velocity, σ_{ri} represents the associated measurement uncertainty, and $\boldsymbol{r}_i$ is a unit vector in the direction of the lidar beam, which is defined by [7]:

$$\boldsymbol{r}_i = (\sin\phi_i \cos\theta_i,\ \sin\phi_i \sin\theta_i,\ \cos\phi_i), \tag{2}$$

where ϕ_i is the zenith angle, and θ_i is the azimuth angle. In this classical method, all individual beams must have valid measurements in order to perform DBS, otherwise the complete scan will be discarded. The present study investigates a simple approach using the DBS method with fewer beams in scenarios where

not all beams meet the required SNR. With the proposed technique, availability of wind velocity measurements is expected to improve. This hypothesis is assessed by comparing the different combinations of DBS beams to a well-calibrated, mast-mounted cup anemometer during a measurement campaign at the Østerild test site. In addition to the internal lidar filtering based on SNR and sum of squared residuals for the solution of Equation (1), referred to hereafter as Filter A, further filtering was applied in our analysis, consistent with the approach used in the DTU calibration report for the Lumibird Beam6X lidar [8]. Additional filtering includes:

B) Lidar availability: only 10-minute intervals with at least 75% of all possible complete scans were considered, ensuring the representativeness of the 10-minute mean wind speeds.

C) Wind direction: the westerly sector between 240° and 300° was used to avoid interference from nearby structures, based on direction measurements from reference heights closest to each lidar level.

D) Wind speed: only 10-minute mean wind speeds between 4–16 m/s were considered, matching the valid range for standard cup anemometers.

The DTU calibration report [8] includes an additional filter to account for temperature and icing effects, specifically excluding data collected when temperatures dropped below 2 °C. However, this filter was not applied in our preliminary analysis. To validate and certify the estimated mean wind speeds, the linear regression slope between the filtered lidar wind speed and the cup anemometer should fall within the range of 0.98 to 1.02. Additional details regarding the field experiment are provided in the following section.

Field Experiment

The field experiment was conducted at the Danish National Test Station for Large Wind Turbines in Østerild, Northern Jutland, Denmark. The Streamline Beam6X HALO Photonics lidar from Lumibird (see Figure 1) was installed 10 meters west of the Light Mast North during the experiment. Radial wind velocities from the lidar system, collected between October 13, 2023, and January 9, 2024, are selected for this analysis. The Beam6X lidar features a pulse width of 150 ns, a laser power of 20 μJ, a pulse repetition frequency of 10 kHz, and its acquisition board is sampling data at a rate of 50 MHz. The azimuth angles of the six beams relative to the lidar instrument are -0.1°, 71.5°, 143.05°, 215.45°, 287.8°, and 0°, with corresponding elevation angles of 59.85°, 59.3°, 59.9°, 60.6°, 60.5°, and 90°, respectively. This system provides a minimum measurement range of 40 m and a maximum range of 500 m, with a measurement every 3 meters of range. Due to reduced wind velocity availability at higher altitudes, the cup anemometer at 244 m is selected for comparison with the proposed DBS methods, as it is the highest available cup on the Light Mast North. The next section presents the preliminary analysis of wind velocity availability using different beam combinations in DBS for the lidar range gate at 243.4 m, closest to the reference cup anemometer.

Figure 1. The installed unit of Streamline Beam6X HALO Photonics lidar from Lumibird at the Østerild test site.

Analysis and Results

In our analysis, the DBS is applied for all 42 combinations of at least three of the 6 beams, and the accuracy of the estimated velocity is compared against the cup anemometer by calculating the slope and correlation coefficient, R^2, of the linear regression. As an example, Table 1 presents the preliminary analysis of wind velocity availability, applying the DBS method for 4 different beam combinations. The availability of wind velocity is expressed as the ratio between the number of valid scans for each combination to the total number of 1170500 unfiltered scans at a height of 243.5 m. Additional filters introduced in the DTU validation certificate, including lidar availability (Filter B), wind direction (Filter C), and wind speed (Filter D), are also included before the comparison of the accuracy with the cup as a reference instrument. The comparison results indicate that using fewer beams leads to higher availability, achieving up to a 6.12% increase compared to the current method in Beam6X lidars, which utilize all 6 beams for DBS. In terms of accuracy, a combination of three beams offers nearly the same level of precision as using all six, with only 0.11 m/s deterioration in root mean squared error (RMSE) of the wind speed estimation. These initial analyses show promising results for improving availability of wind velocity at high altitudes.

Table 1. Availability of wind velocity and accuracy of different beam combinations. Filter A is according to SNR applied in the DSB method, Filter B is based on minimum lidar availability in 10-minute periods, Filter C is related to wind direction and considers a wake-free sector, and Filter D is the valid range of wind speed from cup anemometer.

Beam Combination	Filter A		Filter B	Filter C	Filter D	Slope	R^2	RMSE
	Valid scans	Availability	10-min average	10-min average	10-min average	10-min average	10-min average	10-min average
	[-]	[%]	[-]	[-]	[-]	[-]	[-]	[m/s]
1-2-3	1092357	93.32	11657	2102	1209	0.989	0.994	0.23
1-2-3-4	1053644	90.02	11398	2087	1204	0.998	0.997	0.16
1-2-3-4-5	1029394	87.94	10820	1816	1196	1.001	0.998	0.12
1-2-3-4-5-6	1020665	87.20	10554	1711	1188	1.001	0.998	0.12

Conclusions

This study investigates a technique for improving wind velocity availability of a lidar at high altitudes using the DBS method. The proposed approach simply employs the DBS method with fewer beams in situations where not all beams have available measurements above the required SNR threshold. A preliminary evaluation of the proposed methodology at 244m height indicates that employing combinations of fewer beams in the DBS technique can yield significantly higher data availability compared to the standard six-beam configuration. Notably, a three-beam combination demonstrated an availability increase from 87% to 93%, while maintaining an excellent RMSE of 0.23 m/s for wind speed estimation compared to a reference cup anemometer. These initial findings serve as a proof of concept, highlighting the potential for further optimization and refinement.

Acknowledgments

This project has received funding from the European Union's Horizon Europe research and innovation program under the Marie Skłodowska-Curie grant agreement No 101119550. The authors acknowledge Jesper Grossmann Hansen, Ginka Georgieva Yankova, Valur Aðalsteinsson Vestmann, Allan Djernes Blaabjerg, and other contributors from the Testing and Calibration (TAC) section of DTU Wind and Energy Systems for performing field experiments and collecting the required datasets. Contributions from Poul Hummelshøj and Hans-Juergen Kirtzel (Metek Nordic Aps) are also acknowledged.

References

[1] V. Lehmann and W. Brown, "Radar Wind Profiler," in *Springer Handbook of Atmospheric Measurements*, T. Foken, Ed., Cham: Springer International Publishing, 2021, pp. 901–933. doi: 10.1007/978-3-030-52171-4_31.

[2] M. F. van Dooren, "Doppler Lidar Inflow Measurements," in *Handbook of Wind Energy Aerodynamics*, B. Stoevesandt, G. Schepers, P. Fuglsang, and Y. Sun, Eds., Cham: Springer International Publishing, 2022, pp. 717–750. doi: 10.1007/978-3-030-31307-4_35.

[3] HALO Photonics by the Lumibird group, "Beam6x Wind sciences." Accessed: Apr. 08, 2025. [Online]. Available: https://halo-photonics.com/lidar-systems/beam-6x/

[4] T. Friis Pedersen, "Characterisation and classification of RISØ P2546 cup anemometer," Denmark. Forskningscenter Risoe, Risoe-R No. 1364(EN), 2003.

[5] R. M. Lhermitte and D. Atlas, "Precipitation motion by pulse Doppler radar. Preprints," in *Ninth Weather Radar Conf, Kansas City, MO, Amer. Meteor. Soc.*, 1961.

[6] K. A. Browning and R. Wexler, "The Determination of Kinematic Properties of a Wind Field Using Doppler Radar," *Journal of Applied Meteorology*, vol. 7, no. 1, 1968, doi: 10.1175/1520-0450(1968)007<0105:tdokpo>2.0.co;2.

[7] A. Sathe and J. Mann, "A review of turbulence measurements using ground-based wind lidars," *Atmos Meas Tech*, vol. 6, no. 11, pp. 3147–3167, 2013, doi: 10.5194/amt-6-3147-2013.

[8] J. G. Hansen and G. G. Yankova, "Calibration of Ground-Based Lidar Beam6X-205," DTU Wind Energy LC I-243 (EN)-R0, Roskilde, Denmark, 2024.

A New advanced solution for high power lidar systems: the CLASS dual mode acquisition board

G. Di Donfrancesco[1], *S. Spinosa*[2], *M. Manzo*[2], *G. Passeggio*[1,3], *A. Boselli*[1,4], *X. Wang*[5], *F. Casertano*[1] *and G. Maresca*[1]

(1) ALA Advanced Lidar Applications s.r.l., Corso Meridionale 39, 80143 Naples, Italy
(2) University of Naples Federico II, Department of Physics, Complesso Universitario di Monte Sant'Angelo Via Cinthia, 80126 Naples, Italy
(3) INFN-Istituto Nazionale di Fisica Nucleare, Sez. Napoli, Complesso Universitario di Monte Sant' Angelo, via Cinthia, 80126 Naples, Italy
(4) Consiglio Nazionale delle Ricerche - Istituto di Metodologie per l'Analisi Ambientale, 85050 Potenza, Italy
(5) School of Remote Sensing and Information Engineering, Wuhan University, Wuhan 430079, China

Corresponding author: g.didonfrancesco@alasystems.it

Introduction

The application of LIDAR (LIgth detection And Ranging) technology to atmospheric monitoring is now mature enough to carry out routinely day and night multi-wavelength polarization measurements aiming to detect and characterize atmospheric aerosol particles in space and time.

LIDAR devices are made of several components working together to give a high level of accuracy of measured atmospheric parameters. That is the reason why LIDARs in the main international research infrastructure ACTRIS (Aerosol Cloud and Trace gases Research InfraStructure) [1], need periodic inspection of their optical and electronic components, to reach and maintain the required highest standard of quality. Generally, in order to test the LIDAR performances, intercomparison measurement campaigns using reference systems must be carried out within the CARS (Centre for Aerosol Remote Sensing) providing operational support to the ACTRIS National Facility using aerosol instrumentation for the atmospheric remote sensing.

The electronic related to the acquisition of a detected signal plays an important role in the improvement of LIDAR systems for atmospheric remote sensing. The spanning of the atmospheric LIDAR signals over many decades often requires the simultaneous use of both analog and photon-counting detections during the same measurement. However, there are very few systems which provide the simultaneous acquisition of the same signal in both analog and photon counting regimes. Lidar-specific acquisition systems, considered as benchmark for performance and reliability, are normally configured as modules, with the ability to acquire a channel in both photon-counting and analog regime, for which a mounting in racks is provided. Although this aspect may be of minor importance in the development of a fixed lidar, it becomes critical, and in some case prohibitive, for applications involving small, portable systems, installed on board of vehicles, aircraft, UAV, balloon etc.

Thanks to ever-increasing performances offered by FPGA (Field Programmable Gate Array) electronics and by Analog-to-Digital Converters (ADC), both detection schemes can be realized on a single electronic board able to manage even more sources simultaneously.

A new acquisition board (CLASS- Configurable Lidar Acquisition SyStem) has been recently designed and developed by ALA Advanced Lidar Applications s.r.l. [2] (**Figure 1**). The board can acquire up to 5 channels both in photon-counting/analog modes simultaneously and it is completely independent of PCs or rack-mounted requirements. In addition, the small dimension of the new CLASS acquisition board and its working parameters (see **Table 1**) allows miniaturization and reduced requirements in terms of isolation, power supply and thermalization of the lidar device, extending the working conditions also on board of vehicles, aircraft, UAV, balloon etc.

Figure 1. The new CLASS board with (on the left) and without (on the right) enclosure.

Table 1. Main specifications of the CLASS acquisition board

General Specification	
Modules	Up to 5
PC communications	USB, Ethernet
Typical power consumption	0.6A @ 24V
Operating temperature	-40°C to 70°C
Board size and weight	(150x120x21) cm / 300g
Module Specification	
Input connector	2 SMA (signal and trigger)
Input impedance and coupling	50 Ω - DC (signal) / >1 kΩ - DC (trigger)
Photon-counting channel	
Min. pulse width input	2 ns
Max. pulse rate input	Typ. >500 MHz
Discrim. threshold	SW selectable (-250, +2500) mV, step 0.2 mV
Dwell fifo size	SW selectable (10, 1000) ns, step 10 ns
Max. fifo / pre-trigger size	16k samples both
Analog channel	
AD converter resolutions	10 ns – 14 bit
AD ENOB	10.9
Analog filtering	35 MHz
Input gain	HW selectable (1 to 16)
Input offset	SW selectable (-2.5 to +2.5) V
Max. Vp-p input	1.5 V
Dwell fifo size	SW selectable (10, 1000) ns, step 10 ns
Max. fifo / pre-trigger size	16k samples both

We explored the capabilities of the CLASS acquisition board in analog and digital regimes by means of experimental tests performed in laboratory.

Methodology

In order to evaluate the CLASS board performances, tests were carried out using simulated signals from an electronic synthetic echo, generated by charging/discharging a capacitor on a green led circuit (Pulse Repetition Rate = 2 kHz), with the emitted light attenuated by a ND filter and acquired by a Hamamatsu H10721P-210 photomultiplier. The maximum output voltage of the exponentially decreasing signal is about 80 mV at 50 Ω load.

20 averaged acquisitions of 60 kshots each of such repetitive signal were performed with the CLASS board, recording data simultaneously in both analog and photon-counting modes. The acquisition set-up was: 100ns of bin width (both analog and digital), discriminator level -4.5 mV, analog signal gain 10, ADC resolution 100 MHz / 14 bit, analog filtering at 35 MHz.

Results and Discussion

The Figure 2 shows, on the left plot, the glued profile (at 10 km) between the analog and photon-counting signals acquired with the CLASS board in the laboratory test with the simulated lidar signals, averaged on the entire set of acquisitions (1.2 Mshots). It highlights as the analog signal spans over more than 5 decades with a good signal-to-noise ratio with respect to the photon-counting signal, that shows a maximum averaged counting rate of 75 MHz (DC coupling). On the right side of the figure, the relative deviation of both the analog and photon-counting signals of one acquisition (60 kshots) from the profiles averaged over 20 acquisitions (1.2 Mshots) is shown. The photon-counting (red curve) and the analog (green curve) relative deviations remain both comparable up to approximately 25 km (both mainly dominated by the shot noise), showing the linearity of the analog acquisition and its low noise performance, compared to the digital acquisition. Beyond 25 km of altitude, as the signal weakens, analog electronic noise becomes dominant with respect to the digital noise, leading to a fast increasing of inconsistencies between analog and photon-counting signals.

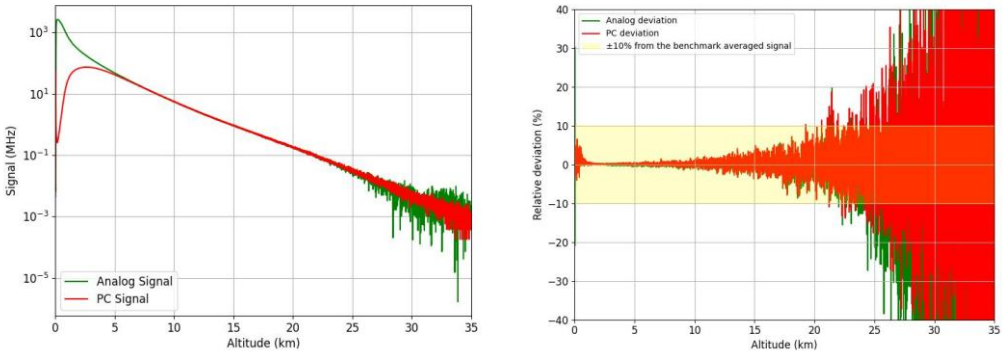

Figure 2. On the left, the scaled analog and photon-counting signals acquired with the CLASS board using simulated lidar signals (average 1.2 Mshots); on the right, the relative deviation of the analog (green) and photon-counting (red) signals (average of 60 kshots) from the total signals (average of 1.2 Mshots).

Conclusions

The new CLASS acquisition board was tested in laboratory with a simulated lidar signal, comparing the CLASS performances in analog regime with respect to the digital one. The aim was to demonstrate that the CLASS board has both high-level performances (mandatory for a lidar acquisition system), and the characteristics of size, weight, power supply, communication etc. requested in the design of compact lidars

portable or even airborne on small aircraft, balloons or drones. The obtained results confirm the analog acquisition of CLASS shows same performances of the digital acquisition for photon rate as low as 10 kHz.

As next step, in the frame of ITINERIS-ACTRIS Pilot National Access Program, the access to CARS-CNR CIAO calibration center will allow us in summer 2025 to test the CLASS board with real measured lidar data, comparing the CLASS performances with a LICEL acquisition device (Transient Digitizer TR40-16bit-3U).

Acknowledgements

This work was supported by CIR01_00015 "PER-ACTRIS-IT" – Volto al rafforzamento del capitale umano nell'ambito della compagine di progetto di PER-ACTRIS-IT and by EU - Next Generation EU Mission 4, Component 2 - CUP B53C22002150006 - Project IR0000032 – ITINERIS - Italian Integrated Environmental Research Infrastructures System.

References

[1] Laj, P. et al. *Aerosol, Clouds and Trace Gases Research Infrastructure–ACTRIS, the European research infrastructure supporting atmospheric science*, B. Am. Meteorol. Soc., 105, E1098–E1136, https://doi.org/10.1175/BAMS-D-23-0064.1, 2024.

[2] Spinosa S., et al., *An innovative system for the simultaneous acquisition of analog and photon counting lidar signals*. Società Italiana Fisica, 2023.

Characterization of atmospheric aerosol particles by combination of multi-wavelength Raman and spectroscopic lidar techniques

S. Fernández-Carvelo[1,2], *A. Yadav*[3], *B. Tatarov*[3], *P. Ortiz-Amezcua*[1,2], *A. del Águila*[1,2], *J.A. Bravo-Aranda*[1,2], *D. Müller*[3] *and L. Alados-Arboledas*[1,2]

(1) Andalusian Institute for Earth System Research (IISTA), University of Granada, Granada, 18006, Spain
(2) Department of Applied Physics, University of Granada, Granada, 18071, Spain
(3) Department of Physics, Astronomy and Mathematics, University of Hertfordshire, College Lane, Hatfield, UK
Corresponding author: solfcarvelo@ugr.es

Introduction

Atmospheric aerosol particles play a crucial role in the Earth's energy balance, highlighting its impact on human health and the environment. However, quantifying and identifying atmospheric aerosol particles remains a significant challenge due to its properties are highly variable on a spatial and temporal scale. Lidar technology has become a key approach for profiling the atmospheric components providing vertically resolved information with a high spatial resolution. In recent years, Raman and other advanced lidar techniques have become the preferred choice, as they provide valuable additional information, particularly for chemical characterization and trace gas detection [1] with can help to improve aerosol typing methodologies using both extensive and intensive optical properties, including depolarization, backscatter, extinction coefficients, lidar ratios and Ångström exponents from multi-wavelength lidar systems [2, 3]. The combination of advanced lidar techniques, such as multi -wavelength nitrogen/oxygen/water vapour Raman, fluorescence and high spectral resolution lidar with mathematical inversion algorithms today allows for temporally and vertically resolved observations of aerosol optical and microphysical properties on a routine basis [4-6]. The integration of spectroscopy methods into multiwavelength Raman lidar technique offers a great opportunity to take a step forward in atmospheric monitoring, leading to a more comprehensive characterizing of atmospheric processes, deepening the Raman-shifted lidar signals caused by specific chemical components.

Instrumentation and Methodology

The experimental result in this study were taken by Dual-LMRD lidar system (Raymetrics S.A., Greece), named ALHAMBRA, which is currently operational at the University of Granada (UGR) urban station in Granada, Spain (37.164° N, 3.605° W), as part of the AGORA (Andalusian Global Observatory of the Atmosphere). The lidar system is able to obtain backscattering coefficient vertical profiles at 3 wavelengths - 1064nm, 532nm, 355nm (3β), three vertical profiles of extinction coefficients at the same three wavelengths (3α), two depolarization (2δ) at 532nm and 355 nm, water vapor (ω) at 407 nm with pumping wavelength of 355 nm and fluorescence (φ) spectra for pumping of 355nm. The system is part of ACTRIS (Aerosol, Clouds and Trace Gases Research Infrastructure) and EARLINET (European Aerosol Research Lidar Network; data.earlinet.org).

Figure 1 shows a general scheme of ALHAMBRA dual system (more details can be found in the study in preparation (Fernández-Carvelo et al., [8]). The near-field sub-system under biaxial configuration, focusses on the atmospheric boundary layer (ABL) and is equipped with elastic and N_2 vibrational Raman channels. Far-field sub-system (coaxial configuration) reaches until upper troposphere/lowest stratosphere. It is equipped with elastic and N_2 rotational Raman channels (elements labelled '2' in figure 1). The two sub-systems also include water vapor detection (ω) at 408 nm and depolarization capabilities (δ) at 532 and 355 nm. Besides, it includes fluorescence capabilities (φ) through two different approaches: broadband interference filter in near-field subsystem (Semrock 470/100 nm BrightLine® single-bandpass filter with 100nm bandwidth) and spectrometer measurements in far-field subsystem (elements labelled '1' in figure 1).

GENERALIFE is the spectroscopic lidar subsystem that is based on a HORIBA 1250M spectrometer (https://www.horiba.com/int/scientific/ products/detail/action/show/Product/1000m-series-1587/) with tunable entrance slit as dispersive instrument, a 32-channel multi-spectral lidar detector (Licel,

https://licel.com/SP32.html) optimized for UV detection. The subsystem is coupled via optical fiber to ALHAMBRA, offering an alternative approach to atmospheric monitoring. It features the possibility of using different interchangeable diffraction gratings (https://www.horiba.com/int/scientific/products/custom-spectroscopy-solutions/spectrometers-and-monochromators/grating-calculator/), each offering spectral ranges and resolutions suitable for different specific applications. By selecting the appropriate grating and entrance slit size of the spectrometer, the spectral window and spectral resolution can be controlled to achieve optimal efficiency and spectral resolution of the measurements [1]. Table 1 summarises the main features of the system where features used in this study are highlighted.

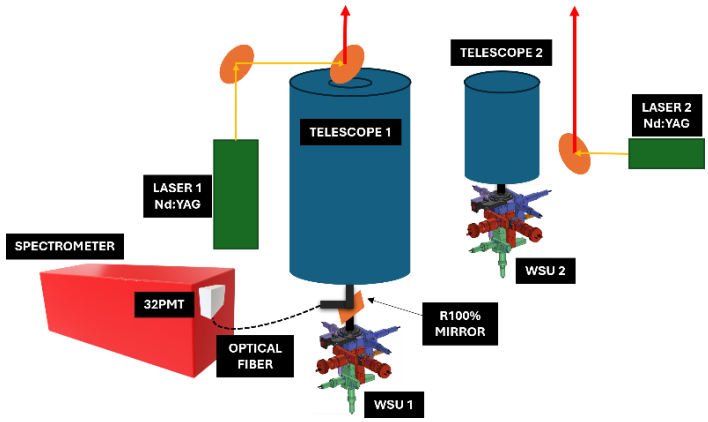

Figure 1. Scheme of the ALHAMBRA dual multiwavelength Raman Lidar + GENERALIFE spectrometer developed by AGORA and University of Granada.

Table 1. Summary of key features of the ALHAMBRA system: specifications for far-field observations (center textbox), near-field observations (right), and the GENERALIFE system (left).

HORIBA 1250m imaging spectrometer	
Elements	Characteristics
32-multi anode PMT detector (SP-32)	Focal length: 1250 mm
	Range: 0-1500nm
	Resolution: 0.006nm
Diffraction gratings	1200 g/mm 20nm of range Resolution: 0.62nm
	600 g/mm 40nm of range Resolution: 1.25nm
	300 g/mm **80nm of range** **Resolution: 2.5nm**

Far-field module	
Elements	Characteristics
Nd-YAG Laser	**200 mJ energy pulse**
	10Hz frecuency
	1064.14, 532.07 and **354.71 nm**
Telescope	Cassegrain: Diameter: 400 mm Focal length: 4000 mm
WSU 1 channels	Elastic: 1064 [t], 532 [t] and 355[p+s] nm
	N_2 rotational Raman: 1064 (1056), 532 (530.2) and 355 (353.9) nm
	Water vapor detection at 408 (407.51) nm
FoV	2.5mrad

Near-field module	
Elements	Characteristics
Nd-YAG Laser	80 mJ energy/pulse
	20Hz frecuency
	1064.14, 532.07 and 354.71 nm
Telescope	Cassegrain: Diameter: 200 mm Focal length: 1000 mm
WSU 2 channels	Elastic: 1064 [t], 532 [p+s] and 355 [p+s] nm
	N_2 vibrational Raman: 532 (607.45) and 355 (387.71) nm
	Water vapor detection at 408 (407.51) nm
	Fluorescence detection at 470 nm
FoV	1.125mrad

When GENERALIFE is coupled to ALHAMBRA, only 355 nm was emitted (emission at 532nm and 1064nm were suppressed), allowing for a better separation of the spectra rises by pumping from 355 and 532 nm. For the experimental data presented in this work the spectrometer grating was set to 300 g/mm with a 500µm entrance slit. An Ultra-Narrow Bandpass Filter, 355 nm central wavelength, 2 nm FWHM and OD6 blocking (Alluxa AUA-UNBP-355-2-OD6) with a slight tilt was used to suppress elastic scattering.

As demonstrated by previous studies [9, 10], accurately determining the overlap function is essential for reliable aerosol profiling, especially in the near-field range, where signal variations arise from

misalignments between the emitted laser beam and the receiver's field of view. Given our focus on the lower layers of the troposphere, the overlap functions of both ALHAMBRA and GENERALIFE were retrieved, and the corresponding signals were properly corrected.

Results and Discussion

Figure 2a displays 355nm range-corrected signal (RCS) from the ALHAMBRA's NF module (dark blue) and from GENERALIFE with (cyan) and without (purple) overlap correction. Figure 2b and 2c show the same profiles for 387 and 408 nm. The presence of two clouds around 4 and 8 km a.g.l. can be seen in Figure 2a. It is worth noting that decay in 387 nm where the first cloud is detected due to attenuation.

For the spectrometer profiles (purple line), a full overlap between laser beam and field of view is achieved above 1500 m, which coincides with the expected one for coaxial lidar systems such as the ALHAMBRA far-field subsystem. In contrast, the near-field subsystem (blue line) reaches full overlap below 200 m. As demonstrated the study in preparation (Fernández-Carvelo et al., [8]), by exploiting integrative methodologies between both subsystems, we can provide an overlap-corrected version of the spectrometer profiles (cyan line), enabling accurate information retrieval close to the surface.

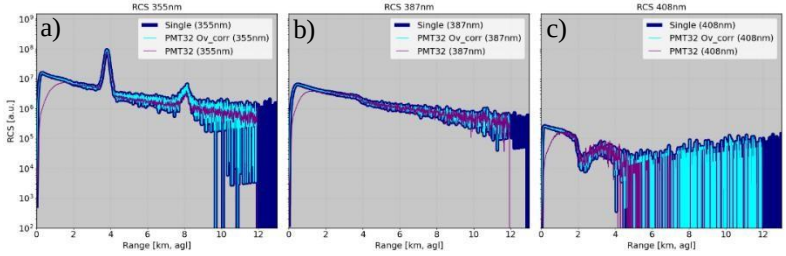

Figure 2. 20-minute average on March 7, 2025, at 20:30 p.m. Elastic RCS (a.u.) at 355 nm (left), VR at 387 nm (center), and VR at 408 nm (right). Each plot shows in dark blue the single PMT (near-field Raman lidar subsystem), in purple the 32-PMT RCS, and in cyan the overlap-corrected 32-PMT RCS.

Figure 3 shows three spectra examples from three different days (D1, D2 and D3) at four altitudes ranges corresponding where the elastic 355 nm signal was blocked (D1), partially captured (D2) and fully detected (D3) using the elastic suppression filter, for optimization of spectral accuracy (indicated by the first observed peak). All of them correspond to 20-minute averages, obtained after applying a 20-bin binning average across different vertical layers. In blue, spectra without the elastic contribution (the first large peak in orange and green in the upper center image). The second and third large peaks correspond to Nitrogen (N2) and Oxygen (O_2) signals, respectively, while the fourth peak is related to water vapor detection (H_2O). Depending on the selected height layer and the composition of air molecules and particles at that level, the signal intensity associated with each component varies. A slight shift between the selected channels is also observed, which points to the need for regular calibration to minimize potential wavelength detection offsets.

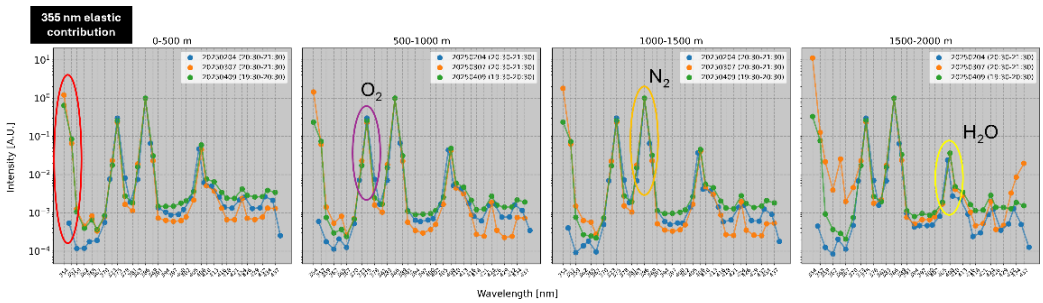

Figure 3. 32-PMT spectrum taken from three different dates and situations in terms of elastic averaged over 72000 shots (60 minutes).

Conclusions

The integration of the advanced GENERALIFE Spectroscopic lidar subsystem with the ALHAMBRA multi-wavelength Raman lidar system and provides a powerful tool for the more detailed characterization of atmospheric particles in terms of, e.g., their chemical composition. This will allow for a more comprehensive description of aerosol particles, e.g., in terms of their optical and microphysical properties. Additionally, the flexibility of GENERALIFE lidar subsystem configuration, using interchangeable diffraction gratings, enhances spectral resolution and range coverage, which optimize measurement accuracy under varying atmospheric conditions. These advancements represent a significant step forward in atmospheric monitoring, providing more comprehensive and precise characterization of atmospheric processes, and improving our understanding of atmospheric aerosols.

Acknowledgements

This work is part of the Spanish national projects PID2023-151668OB-I00 MICIU/AEI/10.13039/501100011033 “ERDF A way of making Europe", PID2020-120015RB-100 MICIU/AEI/10.13039/501100011033, PID2022-142708NA-I00 MICIU/AEI/10.13039/501100011033 “ ERDF A way of making Europe", PID2023-151817OA-I00 MICIU/AEI/10.13039/501100011033 “ERDF A way of making Europe", strategic network RED2022-134824-E MICIU/AEI/10.13039/501100011033, ATMO-ACCESS grant agreement No 101008004, Scientific Unit of Excellence: Earth System (UCE-PP2017-02). P. Ortiz-Amezcua is funded by the European project ATMO ACCESS - Solutions for Sustainable Access to Atmospheric Research Facilities (Ref. 101008004). A. del Águila is part of Juan de la Cierva programme through grant no. JDC2022-048231-I and funded by MCIN/AEI/10.13039/501100011033 and by European Union “NextGenerationEU”/PRTR". Sol Fernández-Carvelo received funding from the Spanish Ministry of Research and Innovation (Agencia Estatal de Investigación), grant PRE2021-098351 (co-funded by the European Social Fund Plus). This work has been developed in the frame of our activities within ACTRIS.

References

[1] Tatarov, B., and Müller, D.: *LITES: rotational Raman spectra of air molecules measured by high-resolution-spectroscopy lidar*, Optics Letters, Vol. 46, No. 20, doi.org/10.1364/OL.420070 , 2021.

[2] Belegante, L. et al.: Retrieval of the boundary layer height from active and passive remote sensors: Comparison with a NWP model, *Acta Geophys.*, 62, 276–289, https://doi.org/10.2478/s11600-013-0167-4, 2013.

[3] del Águila, A.et al.: Aerosol type classification with machine learning techniques applied to multiwavelength lidar data from EARLINET, *EGUsphere [preprint]*, doi:10.5194/egusphere-2025-269, 2025.

[4] Sugimoto, N., Huang, Z., Nishizawa, T., Matsui, I., and Tatarov, B.: *Fluorescence from atmospheric aerosols observed with a multi-channel lidar spectrometer*, Optics Express, Vol. 20, Issue 19, pp. 20800-20807, doi:10.1364/OE.20.020800, 2012.

[5] Reichard, J., Behrendt, O., and Lauermann, F.: *Fluorescence spectra of atmospheric aerosols*, Optics Express, Vol. 20, Issue 19, pp. 20800-20807, doi:10.5194/egusphere-2024-3928, 2024.

[6] Huang, Z., Wang, Y., Zhou, T., Ji, Y., Bi, J., Shi, J., Wen, H., and Huang, J.: *Raman-Polarization-Fluorescence Spectroscopic Lidar for Real-Time Detection of Humic-like Substance Profiles*, Environmental Science & Technology, Occurrence, Fate, and Transport of Contaminants in Indoor Air and Atmosphere, doi: 10.1021/ACS.EST.5C00028/ASSET/IMAGES/LARGE/ES5C00028_0008.JPEG, 2025.

[7] Navas-Guzmán, F., Bravo-Aranda, J.A., Guerrero-Rascado, J.L., Granados-Muñoz, M.J. and Alados-Arboledas, L., *Statistical analysis of aerosol optical properties retrieved by Raman lidar over Southeastern Spain*, Tellus B: Chemical and Physical Meteorology, 65:1, 21234, doi:10.3402/tellusb.v65i0.21234, 2013.

[8] Fernández-Carvelo, S., Ortíz-Amezcua, P., del Águila, A., Bravo-Aranda, J.A. and Alados-Arboledas, L., (in preparation**.** *Near-to-far range overlap retrival for integration of spectroscopic methodology integration into Raman lidar technique*. Manuscript in preparation.

[9] Wandinger U., and Ansmann A., *Experimental determination of the lidar overlap profile with Raman lidar*, Appl. Opt. 41, 511-514, doi:10.1364/AO.41.000511, 2002.

[10] Comerón, A., Muñoz-Porcar, C., Rodríguez-Gómez, A., Sicard, M., Dios, F., Gil-Díaz, C., Oliveira, D.C.F.S. and Rocadenbosch, F., *An explicit formulation for the retrieval of the overlap function in an elastic and Raman aerosol lidar*, Atmospheric Measurement Techniques, 1985, doi:10.5194/amt-16-3015-2023 , 2023.

First calibration results from a new rotational Raman lidar for thermodynamic profiling at the CIAO atmospheric observatory

M. Mytilinaios[1], *B. De Rosa*[1], *A. Amodeo*[1], *G. D'Amico*[1], *N. Papagiannopoulos*[1], *M. Rosoldi*[1], *I. Gandolfi*[1], *F. Marra*[1], *G. Cosimato*[1], *O. Soupiona*[2], *G. Tsaknakis*[2], *L. Mona*[1]

(1) Consiglio Nazionale Delle Ricerche, Istituto di Metodologie per l'Analisi Ambientale (CNR-IMAA), 85050, Tito Scalo, Potenza, Italy
(2) Raymetrics S.A., Spartis 32, 14452, Metamorphosis, Athens, Greece

Corresponding author: michail.mytilinaios@cnr.it

Introduction

The lidar laboratory at the CNR-IMAA Atmospheric Observatory (CIAO; 40.60° N, 15.72° E, 760 m a.s.l.) in Potenza, Southern Italy, is part of the ACTRIS Centre for Aerosol Remote Sensing (CARS) [1], and it supports multiple lidar configurations. In November 2024, a new rotational Raman (RR) lidar was installed to provide continuous high-resolution profiles of atmospheric temperature (T) and water vapor mixing ratio (WVMR), with good accuracy from approximately 1 km above sea level up to the lower stratosphere, during both day and night. The RR lidar complements a suite of advanced instruments at CIAO for remote and in-situ atmospheric observations, including multi-wavelength Raman lidars, photometers, wind lidar, cloud radar, microwave radiometer, ceilometers, and regular radiosoundings [2]. Together, they support long-term, high-quality measurements of aerosol, cloud, and thermodynamic properties throughout the troposphere and stratosphere.

The system is based on an amplified pulsed Nd:YAG laser operating at 10 Hz, emitting at 1064, 532, and 355 nm. Only the 355 nm radiation is transmitted to the atmosphere with a pulse energy of 300 mJ. A coaxial configuration ensures full overlap around 200 m above ground (~1 km a.s.l.). The receiver includes a 400 mm aperture Cassegrainian telescope (F# 10) and a wavelength separation unit (WSU) splitting incoming light into several channels: elastic backscatter at 354.73 nm; pure-rotational Raman signals at 355.2 nm (RR1, Low J) and 356.3 nm (RR2, High J); and vibrational Raman (VR) signals of N_2 at 387 nm (nighttime only) and of H_2O at 408 nm. An ultra-narrowband filter centered at 407.8 nm (FWHM = 0.3 nm) allows water vapor profiling during daylight (Fig. 1).

Methodology

The temperature profile *T(z)* is retrieved using the Eq. 1:

$$T(z) = \frac{b}{a - lnQ(z)} \quad (1)$$

where

$$Q(z) = \frac{S_{RR2}(z)}{S_{RR1}(z)} \quad (2)$$

is the ratio of the two RR signals, and *a* and *b* are calibration parameters primarily dependent on the system's optical and detection characteristics; however, these parameters can also be affected by varying atmospheric conditions. This method provides temperature retrievals with an uncertainty typically ≤ 1 K, within the temperature range of 180 – 285 K [3].

For the retrieval of the water vapor mixing ratio profile *WVMR(z)*, the Eq. 3 is used:

$$WVMR(z) = C \cdot \frac{S_{H2O}(z)}{S_{REF}(z)} \quad (3)$$

where S_{H2O} is the VR signal of water vapor at 408 nm, and S_{REF} is a reference signal. During nighttime measurements, the VR signal of N_2 at 387 nm is typically used as reference, whereas during daytime we use the RR1 signal. The calibration constant *C* depends on the system's characteristics and on the signal pair selected for the retrieval [4].

The calibration parameters *a*, *b*, and *C* are obtained by comparing the lidar-derived T and WVMR profiles with those measured from simultaneous and collocated radiosoundings. At CIAO, radiosondes are typically launched three times per week—two at night and one during the day—as part of the GRUAN network [5]. This regular schedule enables calibration of the lidar system under various atmospheric

conditions (e.g., day vs. night, clear-sky vs. dust events, etc.) and supports a robust statistical analysis of the calibration parameters.

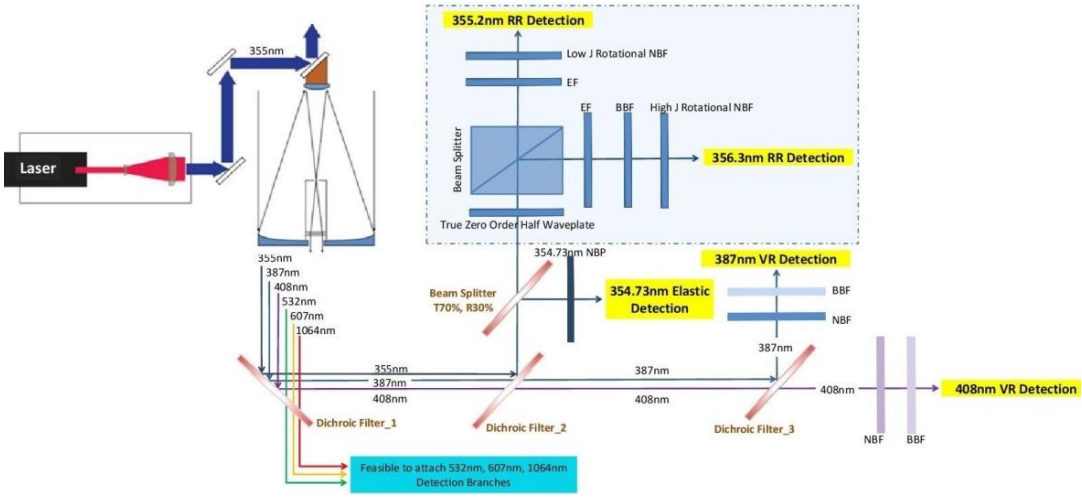

Figure 1. Experimental setup of the rotational Raman lidar system of the lidar laboratory at CIAO. NBF: Narrow Band Filter, BBF: Broad Band Filter, EF: Edge Filter, and NBP: Narrow Bandpass Filter

Here, we present first calibration results for two commonly occurring atmospheric scenarios in our measurements: (i) daytime observations under clear-sky conditions and (ii) nighttime observations during Saharan dust outbreaks. Only lidar measurements performed simultaneously with radiosoundings and under cloud-free conditions were considered. Although the RR lidar operates at a temporal resolution of 1 minute, the lidar profiles were averaged over intervals of at least 40 minutes to reduce statistical noise. While longer averaging improves the signal-to-noise ratio, excessively long periods should be avoided, as radiosondes drift from the launch site and may sample different atmospheric conditions. For the same reason, the vertical range used for calibration should also be limited—particularly for water vapor, which is more variable. Based on these considerations, we selected three clear-sky daytime cases for scenario (i), and two nighttime dust events for scenario (ii).

Results and Discussion

Figure 2 (left) shows one of the three measurements for scenario (i), in which the daytime observation from 12 December 2024 was calibrated against a radiosonde. The lidar-derived water vapor profile agrees well with the radiosonde data up to 4 km, but becomes noisy at higher altitudes due to solar background. The temperature profile also matches the radiosonde well up to 6 km, but discrepancies appear above that altitude. These differences may result from the radiosonde drifting away from the lidar site and sampling regions with different temperatures. The large deviations observed below 1 km are attributed to incomplete overlap between the laser beam and the telescope field of view.

Figure 2 (right) shows one of the two measurements for scenario (ii), specifically the dust event on 10 April 2025. As this is a nighttime observation, the lower sky background significantly improves the signal-to-noise ratio. The WVMR profile follows the radiosonde closely up to 7 km but becomes noisy at higher altitudes with low humidity. In contrast, the temperature profile appears stable both temporally and spatially. Even though the lidar profiles were averaged over a 180-minute interval, the T shows excellent agreement with the radiosonde up to 12 km.

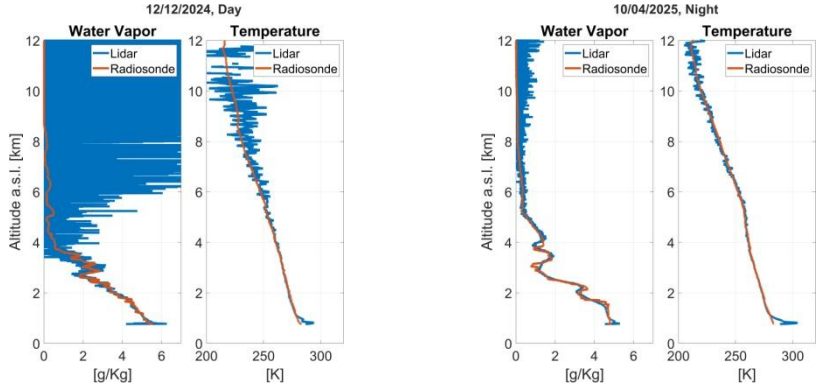

Figure 2. Left: Mean WVMR and T lidar profiles (blue) retrieved between 11:47 and 12:44 UTC on 12 December 2024, calibrated against a radiosonde (orange) launched at 12:05 UTC. Right: WVMR and T profiles averaged over the intervals 18:02–19:02 UTC and 18:02–21:03 UTC, respectively, compared with a radiosonde launched at 18:06 UTC on 10 April 2025.

Additionally, for this dust event, Fig. 3 presents quicklooks of WVMR and the cross-polarized signal at 532 nm from the fixed multi-wavelength Raman lidar at CIAO. The cross-polarized channel is sensitive to aspherical particles (e.g., dust), allowing for the identification of dust layers in the atmosphere. Enhanced WVMR layers coincide with these dust layers, suggesting a possible link between water vapor enhancement and the hygroscopicity of dust particles. Additional cases will be analyzed to further investigate this relationship.

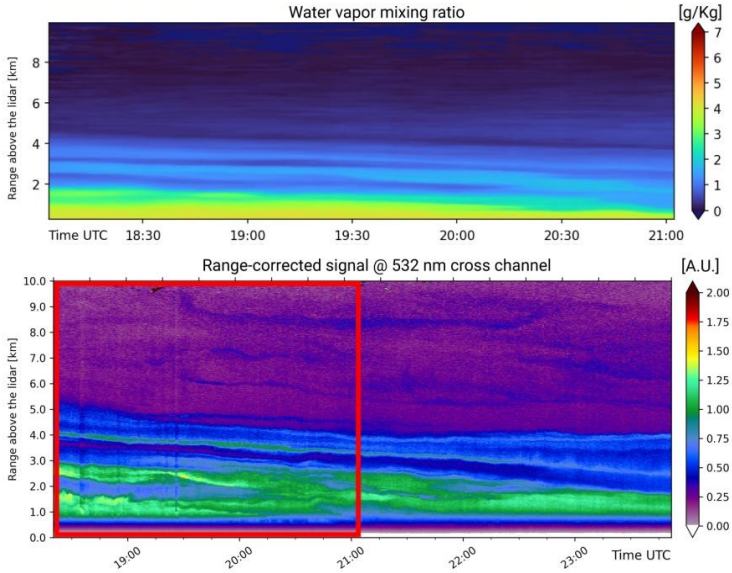

Figure 3. Top: WVMR retrieved by the rotational Raman lidar and calibrated using a radiosounding (temporal resolution: 2 min, vertical resolution 60 m). Bottom: Cross-polarized signal at 532 nm measured by the Potenza Lidar for Particle Observation (POLPO), the fixed multi-wavelength Raman lidar at CIAO for aerosol monitoring (temporal resolution: 1 min, vertical resolution 3.75 m). The red frame indicates the time interval common to both measurements.

Finally, Table 1 summarizes the mean and standard deviation of the calibration parameters under both atmospheric scenarios. Although the number of cases is limited, the results suggest that nighttime dust conditions lead to reduced variability in the calibration parameters, particularly for the calibration constant *C*. If confirmed by a larger statistical dataset, this could support the use of pre-determined calibration values for similar conditions when radiosoundings are not available, maintaining relatively low uncertainty.

Table 1. Statistical summary of the calibration parameters *a*, *b*, and *C* under different atmospheric conditions. Values are shown as mean ± standard deviation (relative error).

Condition	*a*	*b*	*C*	Number of cases
Day, Clear sky	1.93 ± 0.33 (17 %)	546 ± 84 (15 %)	30.55 ± 1.78 (6 %)	3
Night, Dust	1.49 ± 0.14 (10 %)	436 ± 39 (10 %)	35.75 ± 0.10 (0.3 %)	2

Conclusions

This study assesses the performance of the new rotational Raman lidar and the stability of its calibration constants under different atmospheric conditions. It also aims to enable accurate retrievals of T and WVMR profiles when no collocated radiosoundings are available, using statistically derived constants from past datasets. Our results so far indicate that nighttime conditions yield more stable and reliable measurements. Even with limitations due to atmospheric conditions, the RR lidar offers valuable continuous observations at a fixed location, unlike radiosoundings. Combined with other instruments at CIAO, the RR lidar also contributes to studies on aerosol microphysical and optical properties, such as hygroscopic growth and reflectivity, key factors in aerosol radiative forcing.

Future upgrades will include the integration of a spectrometer into the lidar's WSU for detecting UV and visible fluorescence spectra. Details are presented in the ELC2025 abstract "New capabilities for fluorescence lidar observations at CIAO observatory" by De Rosa et al. (#31_S1).

Acknowledgements

The CNR-IMAA authors acknowledge the IR0000032 – ITINERIS, Italian Integrated Environmental Research Infrastructures System (D.D. n. 130/2022 - CUP B53C22002150006) Funded by EU -Next Generation EU PNRR-Mission 4 "Education and Research" - Component 2: "From research to business" – Investment 3.1: "Fund for the realisation of an integrated system of research and innovation infrastructures" and ATMO-ACCESS (Access to Atmospheric Research Facilities) Funded in the frame of the programme H2020-EU.1.4.1.2 – Grant Agreement n. 101008004 – (1 April 2021 – 31 March 2025). They also acknowledge the Joint Research Unit ACTRIS-Italy funded by the Italian Ministry of University and Research.

References

[1] ACTRIS, CARS, https://www.actris.eu/topical-centre/cars, last access: 19/05/2025.

[2] Laurita, T. et al.: *CIAO observatory main upgrade: building up an ACTRIS compliant aerosol in-situ laboratory*, Atmos. Meas. Tech. Discuss. [preprint], https://doi.org/10.5194/amt-2024-57, in review, 2024.

[3] Behrendt, A.: *Temperature measurements with Lidar*, in: *LIDAR: range-resolved optical remote sensing of the atmosphere*, edited by: Weitkamp, C., Springer, Springer series in optical sciences, 102, 2005.

[4] Wandinger, U.: *Raman Lidar*, in: *LIDAR: range-resolved optical remote sensing of the atmosphere*, edited by: Weitkamp, C., Springer, Springer series in optical sciences, 102, 2005.

[5] Rosoldi, M.: *GRUAN site report for Potenza*, https://www.gruan.org/gruan/editor/documents/meetings/icm-15/doc/doc_521_SiteReport_POT_2022-2023.pdf, last access: 19/05/2025, 2024.

Upgrade of the MeteoSwiss Raman lidar RALMO for depolarisation measurements

R. Matthey[1,2], *G. Martucci*[2], *A. Haefele*[2], *V. Wittwer*[3], *A. Murk*[1]

(1) Institute of Applied Physics and Oeschger Centre for Climate Change Research, University of Bern, 3012 Bern, Switzerland
(2) Federal Office of Meteorology and Climatology, MeteoSwiss, 1530 Payerne, Switzerland
(3) Laboratoire Temps-Fréquence, Université de Neuchâtel, 2000 Neuchâtel, Switzerland

Corresponding author: renaud.matthey@unibe.ch

Introduction

The RAman Lidar for Meteorological Observations (RALMO) of the MeteoSwiss station in Payerne (Switzerland) was developed to continuously and routinely profile tropospheric water vapor [1] and tropospheric temperature [2] during day and night. Aerosol backscattering and extinction coefficients can be retrieved from the Raman channel data acquired by the instrument, which has been part of the European Aerosol Lidar Network EARLINET. However, the lidar was lacking depolarisation measurement capability. To remedy to this scientific limitation and for Payerne station to fulfil the ACTRIS requirements for aerosol remote sensing, RALMO has been upgraded and complemented by a depolarisation receiver. In this communication, we report on the design and implementation of this receiver and on first results.

Lidar description

The RALMO temperature observations are based on the temperature dependence of the intensities of pure rotational Raman (PRR) lines of nitrogen and oxygen molecules, while ro-vibrational Raman scattering from water vapor and nitrogen molecules is used to retrieve the water vapor mixing ratio. To ensure daytime operation, the lidar operates in the UV spectral region, where molecular scattering is high and solar background low. The excitation laser emits linearly polarised 355-nm pulses of 300 mJ (long-term average value) at a regime of 30 Hz. The laser beam is expanded to a spot of 15-cm diameter. The composite lidar receiver comprises four mirrors of 30-cm diameter each, symmetrically disposed around the beam expander, and fibre-coupled to grating polychromators (see Figure 1). Four long-pass (razor) edge filters, with cut-off wavelength of 364 nm, are installed in front of the optical fibre inputs placed at the focal points of the four mirrors. They reflect the 355-nm radiation and allow the longer wavelengths associated to the ro-vibrational Raman channels of nitrogen (387 nm) and water vapor (407 nm) pass through, which are then isolated and detected in the H_2O polychromator for further evaluation of the water vapor profile. For two of the telescopes, T1 and T4, the edge filter is tilted by 9° with respect to the incident angle; the reflected 355-nm signal is collected by another optical fibre and sent to the temperature polychromator, which separates several PRR spectral lines and isolates the elastically backscattered component (molecular Cabannes line and aerosol Mie scattering line), to retrieve the temperature and the total backscatter ratio profiles. For T2 and T3, the edge filter tilt angle is 0°; the 355-nm signal is not used and gets lost. An additional "near-range" (NR) fibre in installed in one of the telescopes (T3). Laterally displaced from the primary fibre, it collects more signal from ranges

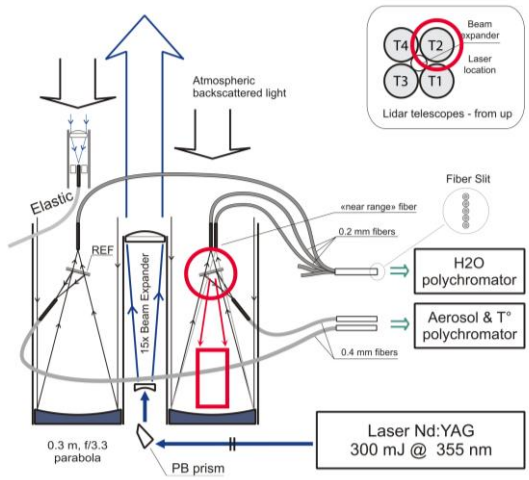

Figure 1. Diagram of RALMO lidar transceiver optics. The four telescopes are numbered T1 to T4. The depolarisation receiver (shown in red) is installed in T2. PB: Pellin-Broca (prism); REF: long-pass razor edge filter. See text for detailed explanations.

close to the lidar to retrieve the water vapor content in the near range with larger signal-to-noise and, hence, higher precision. The setup is completed by a 1-inch refractor for total elastic signal in case overlap correction for aerosol evaluation reveals necessary. Data acquisition of the signals from the H_2O and temperature polychromators is performed by a transient recorder (analogue and photon-counting modes) and a photon-counting card, respectively. Further details on the RALMO instrument can be found in [1-3].

Depolarisation receiver concept

The implementation of the depolarisation measurement capability to RALMO needed to obey several requirements. It should not impair the RALMO main purpose of temperature and water vapor profiling; the transmitter system could not be modified; changes in the receiver system should not alter any part that might affect the measurements; the initial RALMO configuration should be easily recovered; RALMO needs to comply with ACTRIS standards. As a first consequence, the Δ90° calibration method [3] had to be implemented in the reception part. To dispose of polarisation-unperturbed signals, optical signals from fibres could not be used. The adopted solution lies in the exploitation of the unused 355-nm light reflected by the long-pass edge filter in telescope T2 by a dual-channel depolarisation receiver operating in free space. The receiver was designed to be installed in a single frame to be fixed to the overall structure of the lidar, above the T2 collecting mirror. The intervention on the original lidar setup is limited to the mechanical installation of this additional frame, without requiring any changes to other parts of RALMO.

The schematics of the depolarisation receiver is shown in Figure 2. The light collected by the mirror of T2 and focused on the fibre falls on a 1-inch plano-convex lens (LPEF) positioned at a distance from the fibre corresponding to its focal length (50 mm). Suitable optical coatings were designed and deposited on this lens using an ion-beam sputtering machine by the Laboratoire Temps-Fréquence at the University of Neuchâtel (UniNE). The front-surface optical coating acts as a long-pass edge filter, similarly to the initial razor edge filter placed just in front of the fibre input (REF), while an anti-reflection coating was deposited on the back surface. Thus, the lens collimates the signal at 355 nm backward and lets the ro-vibrational signals pass through. The REF is maintained for reversibility to the initial configuration. A plano-concave lens (L1) compensates for the presence of the LPEF lens, so the optical path between the collecting mirror and the Raman signal fibre remains the same in presence of the depolarisation receiver. The 355-nm collimated beam is further focused on a pinhole acting as field stop (FS) to limit the solar background, and recollimated. A half-wave plate (HWP) is used both for calibration purpose and as a tool to align the polarisation axis of the polarisation analyser with the laser polarisation. A quarter-wave plate (QWP) can be introduced to balance the retardance of the bundle of converging rays travelling from the T2 collecting mirror when reflected by the LPEF lens, to increase the precision of the depolarisation measurements. High background rejection is ensured by a thermally controllable ultra-narrow interference filter (< 0.5 nm). The optical signal is then divided into co- and cross-polarised components and further polarisation-cleaned by thin-film polarisers (TFPs) operating at 45° incidence angles, designed and produced by UniNE. Using TFPs reduce transmission losses and avoid ghost images. The two orthogonal optical signals are injected into optical fibres and guided to detectors placed away from the receiver.

The depolarisation receiver is assembled from modules associated to the individual functionalities. They are mounted in a 60-mm cage system along four rods (6-mm diameter) that hangs along the telescope axis, as shown in Figure 3. This configuration minimises the incident angle of the rays converging from the T2 mirror on the LPEF lens (8.5° for the external rays of a *f*/3.3 mirror). Therefore, change of polarisation induced by non-normal incidence is kept minimal. As a drawback, this configuration reduces the signal collected by the mirror due to partial shadowing by the receiver (equivalent surface of a 7.5-cm diameter circle). The modules are positioned longitudinally along the receiver to limit their obstruction to the rays reflected by the collecting mirror to the rods. The losses due to the presence of the receiver in terms of signal collected by the Raman signal fibre is estimated to 1/3 (0.3 due to shadowing and obstruction and 0.03 due to the losses by the LPEF lens and the L1 compensating lens.

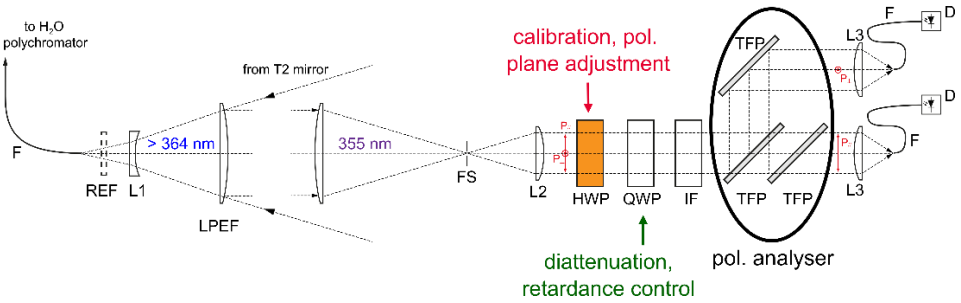

Figure 2. Schematics of the depolarisation receiver. D: detector; F: (multimode) fibres; FS: field stop; HWP: half-wave plate; IF: interference filter; L: lens; LPEF: long-pass edge filter lens; QWP: quarter-wave plate; REF: razor edge filter; TFP: thin-film polariser. The collecting mirror is not drawn but is on the right of the schematics. The setup is shown horizontally for illustration purpose; it is physically vertical.

Performance evaluation of the polarisation analyser

The lowest depolarisation ratio detectable by the receiver is ultimately limited by the performance of the polarisation analyser. To evaluate its polarisation extinction ratio (PER, transmitted light intensity in the desired polarisation state to the transmitted light intensity in the undesired polarisation state), part of the laser beam was extracted at the laser output using a Brewster window and redirected onto a test bench, where the polarisation analyser was installed, after its polarisation was cleaned by a TPF to ensure highly linear polarisation probing state. A HWP in front of the analyser allowed to control the direction of polarisation. The intensity ratio between the signals in the cross- and co-polarised channels was determined for different angles of the HWP around the minimum transmission in each channel. A PER as low as 0.06%, and even 0.04% for minimum transmission in the co-planar channel was retrieved. Using an additional QWP in front of the HWP and optimizing manually the angle of the two retarders, allowed to reach PER values of 0.03%, limited by the laser-induced electronic noise affecting the measurement device (oscilloscope). For comparison, the linear depolarisation ratio (LDR) of the molecular atmosphere Cabannes line at 355 nm is 0.4%, that is 10x larger than the intrinsic PER of the polarisation analyser.

First atmospheric measurements

After installation of the depolarisation receiver in the lidar setup, its optical elements were adjusted and aligned. Two examples of first atmospheric records are shown in Figure 4. They represent the range-corrected signal of the co-polarised channel, as detected in analogue mode. The first case illustrates the nighttime signature from two layers of optically dense broken clouds. Despite short integration time, 4 s, and high spatial resolution, 12 m, the molecular atmosphere below the first layer at 4.2 km is clearly visible. The second case corresponds to several layers of optically thin clouds. The measurement was performed during daytime; the sun disk was visible through the clouds at that time.

So far, atmospheric signatures at the output of the cross-polarised channel do not correspond to the expectations, pointing to problems in the alignment of the

Figure 3. (*Left*) Depolarisation receiver once installed above the collecting mirror (not visible). (*Right*) Imaging camera setup: (*up*) custom assembled lens; (*down*) camera (grey mate housing above the USB3 connector) with custom lens fixed over it, the whole setup being positioned, in this case, below the pinhole P to image it.

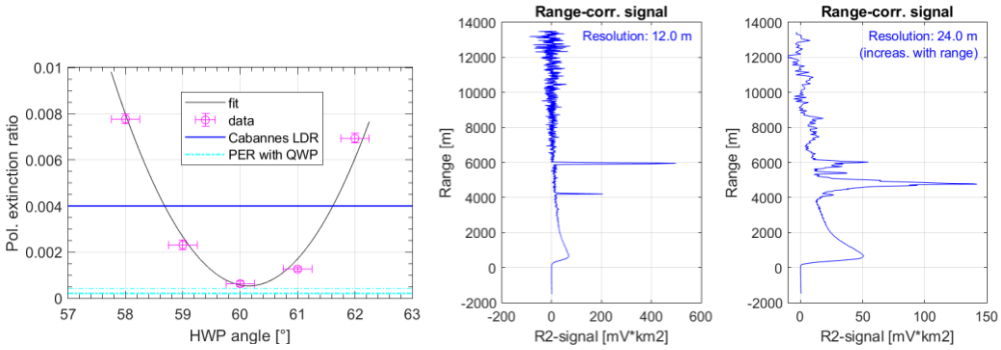

Figure 4. (*Left*) Signal ratio for the polarisation analyser in function of the angle of the half-wave plate (HWP) controlling the probing laser polarisation direction. See main text for explanation. (*Middle*) 4-s measurement of two layers of broken optically thick clouds, at 4.2 km and 6 km (nighttime, co-polarised channel signal, 12-m range resolution). (*Right*) 35-s measurement of optically thin clouds expending from 4 km to 9 km (daytime, co-polarised channel signal, range resolution: 24 m up to 6 km, 48 m up to 9 km, 72 m above).

receiver, such as beam clipping and undesired reflections. As the eye is not sensitive to 355-nm radiation and an alignment-supporting laser in the visible does not help because its beam would not be reflected by the LPEF lens, a low-cost small USB camera operating at 355 nm, and that can be positioned at various locations in the receiver, was purchased to help fine-tuning the receiver alignment, an on-going activity. A custom lens was assembled, since no sufficiently small lenses compatible with both the camera and its use in the receiver seemed available off-the-shelf. An illustration of the usage of the camera setup in the receiver is presented in Figure 3.

Conclusions

To complement and extend the primary RALMO capabilities of profiling the temperature and the water vapor content throughout the troposphere to aerosol and cloud depolarisation characterisation, a two-channel depolarisation receiver has been developed and installed in the lidar. The receiver was conceived in such a way that its installation (and removal) does not alter the original instrument setup, nor affect its performances significantly. The intrinsic extinction ratio of the polarisation analyser was evaluated to be ten times lower than the depolarisation ratio of the molecular atmosphere Cabannes line, auguring the ability to characterise quite low depolarising aerosol layers. First atmospheric measurements were carried out. They show that the receiver operates mostly correctly. However, its alignment shall be improved to reach scientifically sounding depolarisation measurements. It is hoped that this goal will be eased and met by using a small camera setup assembled to be placed at different locations in the receiver.

Acknowledgements

This work has been supported by MeteoSwiss and by the ACTRIS (Aerosols, Clouds and Traces Gases Research Infrastructure) Switzerland implementation grant, which is funded by the Swiss State Secretariat for Education, Research and Innovation (SERI).

References

[1] Brocard, E., Philipona, R., Haefele, A., Romanens, G., Mueller, A., Ruffieux, D., Simeonov, V., and Calpini, B.: *Raman Lidar for Meteorological Observations, RALMO – Part 2: Validation of water vapor measurements*, Atmos. Meas. Tech., 6, 1347–1358, https://doi.org/10.5194/amt-6-1347-2013, 2013.

[2] Martucci, G., Navas-Guzmán, F., Renaud, L., Romanens, G., Gamage, S., Hervo, M., Jeannet, P., and Haefele, A.: *Validation of pure rotational Raman temperature data from the Raman Lidar for Meteorological Observations (RALMO) at Payerne*, Atmos. Meas. Tech., 14, 1333–1353, https://doi.org/10.5194/amt-14-1333-2021, 2021.

[3] Freudenthaler, V.: *About the effects of polarising optics on lidar signals and the Δ90 calibration*, Atmospheric Meas. Tech. 9(9), 4181–4255, 2016.

Side-by-Side Intercomparison of Water Vapor Profiles from the Vaisala DIAL and Purple Pulse Raman Lidar

H. Vogelmann[1], *J. Speidel*[1], *M. Posyniak*[1], *A. Wieser*[2], *G. Hölzer*[3], *A. Gohm*[3]

(1) Karlsruhe Institute of Technology, KIT - Campus Alpin, Garmisch-Partenkirchen, Germany
(2) Karlsruhe Institute of Technology, KIT IMK-TRO, Karlsruhe, Germany
(3) University of Innsbruck, Inssbruck, Austria

Corresponding author: vogelmann@kit.edu

Introduction

Accurate profiling of atmospheric water vapor is essential for understanding boundary layer processes, cloud formation, and weather prediction. Ground-based lidar systems provide continuous vertical measurements of humidity with high temporal and spatial resolution. This study presents a side-by-side intercomparison of two advanced lidar systems for water vapor profiling: the ***Vaisala Differential Absorption Lidar (DIAL)*** and the ***Purple Pulse Raman Lidar (PPLS)***. The campaign was part of the larger TEAMx project and preparation for the TEAMx main observation campaign in 2025 [1]. This pre-campaign aims to evaluate the consistency, strengths, and limitations of each system's measurement capabilities under a variety of atmospheric conditions as well as daylight and night darkness.

Methodology

The **Vaisala DIAL DA10**[1], a commercial turn-key system optimized for autonomous operation, operates in the near-infrared at ~910 nm from laser diodes with an output of roughly 50 mW at a pulse rate of 8 kHz. For measuring water vapor it uses a pair of fixed wavelengths, one online, partially absorbed by water vapor, and one offline with minimal absorption. Unlike traditional narrow-linewidth DIAL systems, the Vaisala DIAL uses a broader emission spectrum, which overlaps multiple absorption features. Consequently, its retrieval algorithm integrates over the spectral band yielding an effective absorption coefficient. The system is optimized for stable, autonomous operation with long-term reliability. Water vapor profiles are typically averaged over **longer integration periods (~20 minutes)** to reduce statistical noise and improve retrieval stability, making the system suitable for continuous monitoring and data assimilation.

In contrast, the **Purple Pulse Raman Lidar** is a research-grade cutting-edge technology with a focus on science. The measurement principle is based on the detection of vibrational Raman return from water vapor at ~407 nm, two rotational Raman returns from air molecules close to 355 nm and elastic backscatter at 355 nm. The retrievals are based on the ratio of these signals, providing profiles of the water vapor mixing ratio, air temperature and aerosol backscatter ratio. The high-power diode pumped Nd:YAG Laser (DPSS) at 355 nm with an output of up to 20 W (at 200 Hz pulse rate) together with analog and photon-counting detection and high optical throughput, enables **rapid temporal sampling (~10 s)**, which allows for capturing short-lived and high-frequency atmospheric structures, particularly in the boundary layer.

During the campaign (July 2024 to September 2024), both systems were located side-by-side at the University of Innsbruck and operated continuously to observe a range of meteorological conditions, including clear skies, cloud passages, and diurnal variability including daylight and night darkness. Although both systems rely on different physical principles and operate at different wavelengths, the intercomparison seeks to evaluate their agreement in water vapor profile structure, responsiveness to atmospheric changes, and practical considerations for deployment in research and operational settings.

Results and Discussion

The analysis will focus on comparing vertical coverage, sensitivity to atmospheric variability, temporal resolution, and retrieval / calibration robustness under varying solar backgrounds and aerosol loads.
Preliminary observations suggest complementary capabilities: the Raman lidar's rapid profiling suits

process studies and boundary layer dynamics, while the DIAL system provides smoother, low-noise retrievals ideal for meteorological analysis and monitoring.

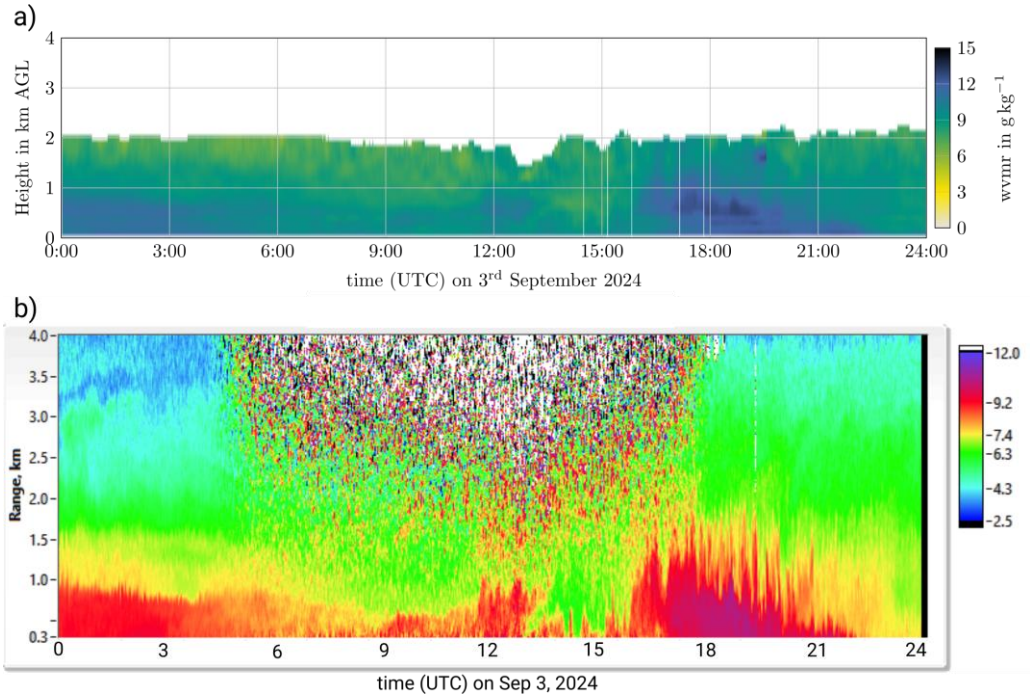

Figure 1. Water vapor mixing ratio recorded side-by-side at Innsbruck with the Vaisala DIAL DA10 (a) and the PPLS Raman lidar (b) during a warm and convective summer day (Sep 3, 2024).

Fig. 1 shows a representative example for this instrument intercomparison. While the Vaisala DIAL's range is restricted to roughly 2 km above ground (although the boundary layer height was between 3.5 and 4 km on this day), the PPLS lidar's range goes further up except the time of maximum daylight and shows humidity structures at the mixing layer (Fig 1b, left, > 3km). Furthermore, the capability of the PPLS lidar for resolving short-term variability linked to convective or even turbulent dynamics is much better compared to the Vaisala system. But, in contrast to the Vaisala DIAL, the PPLS retrieval, at its current state, does not provide valid humidity data from the first 300 m above ground.

Conclusions

This intercomparison is part of a broader effort to characterize the performance of water vapor lidar technologies and to inform their use in future field campaigns and observation networks. First results, including quantitative comparison and radiosonde validation, will be presented at the conference.

Acknowledgements

The authors thank the University of Innsbruck for hosting the lidar systems during the campaign as well as the funding from Helmholtz (HGF) and KIT within in the project "Inside Clouds".

References

[1] The TEAMx-PC22 Alpine field campaign – Objectives, instrumentation, and observed phenomena
Pfister, L. Gohm, A.; Kossmann, M.; Wieser, A., Babić, N.; Handwerker, J.; Wildmann, N.; **Vogelmann, H.**; Baumann-Stanzer, K.; Alexa, A.; Lapo, K.; Paunović, I.; Leinweber, R.; Sedlmeier, K.; Lehner, M.; Hieden, A.; Speidel, J.; Federer, M.; Rotach, M.,.2024, Meterol. Zeitschr., Vol. 33 No. 3 (2024), p. 199 – 228
https://doi.org/10.1127/metz/2024/1214
[2] https://www.vaisala.com/en/products/weather-environmental-sensors/atmospheric-profiling/dial-atmospheric-profiler-da10
[3] https://www.purplepulselidar.com

Lidar algorithms and data products

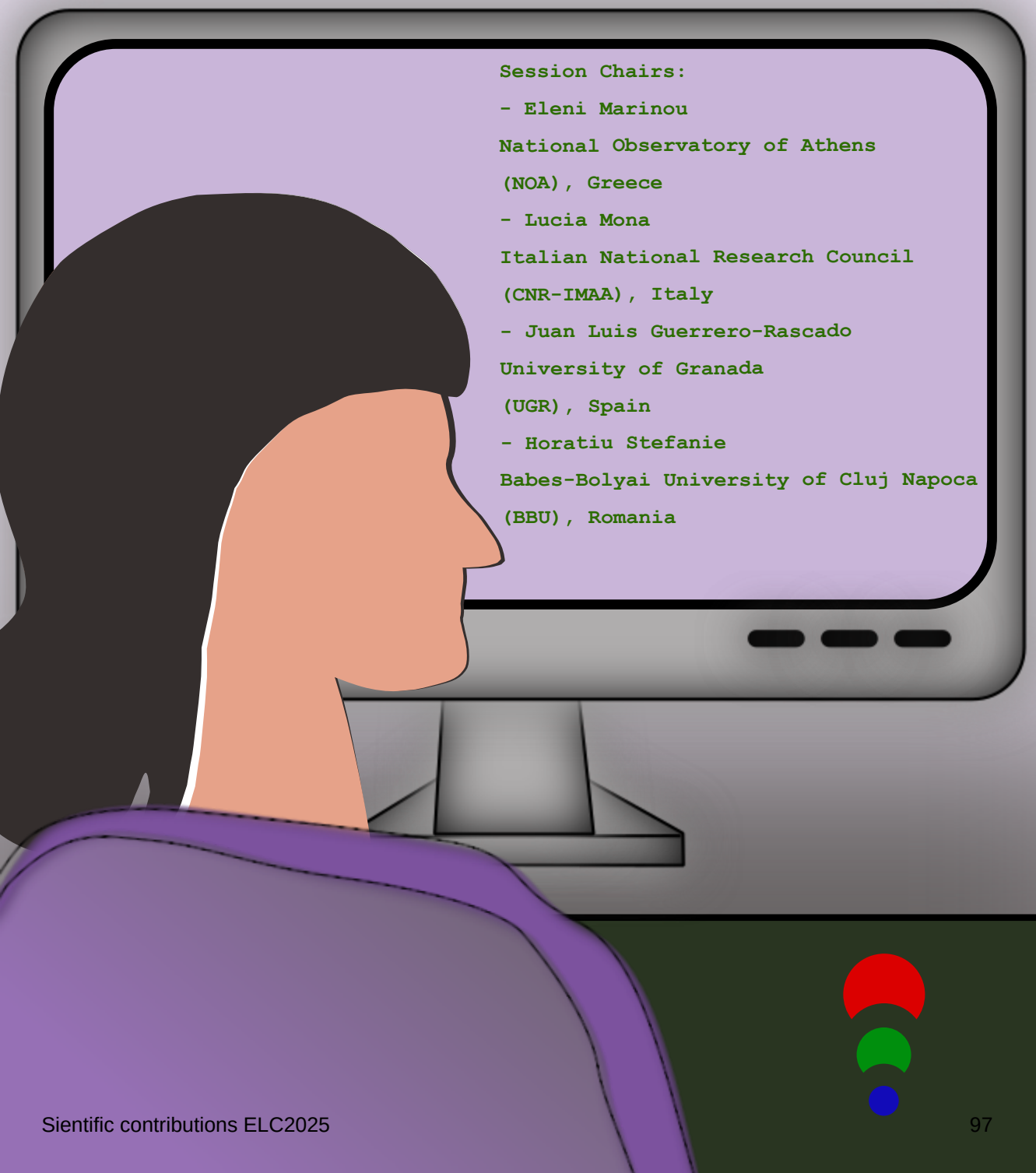

A Generalized Lidar Retrieval Algorithm for Mineral Dust Using Scattering Models Accounting for Particle Non-Sphericity

***Y. Chang*[1]**, *Q. Hu*[1], *M. Saito*[2], *A. Lopatin*[3], *C. Chen*[4,5], *T. Podvin*[1], *I. Veselovskii*[6], *F. Ducos*[1], *G. Dubois*[1], *O. Dubovik*[1], *and P. Goloub*[1]

(1) Univ. Lille, CNRS, UMR 8518–LOA–Laboratoire d'Optique Atmosphérique, Lille 59650, France
(2) Department of Atmospheric Science, University of Wyoming, Laramie 82071, WY, USA
(3) GRASP–SAS, Remote Sensing Developments, Lille 59650, France
(4) Anhui Institute of Optics and Fine Mechanics, Hefei Institutes of Physical Science, Chinese Academy of Sciences, Hefei 230031, China
(5) Key Laboratory of Optical Calibration and Characterization, Anhui Institute of Optics and Fine Mechanics, Chinese Academy of Sciences, Hefei 230031, China
(6) Prokhorov General Physics Institute of the Russian Academy of Sciences, Moscow, Russia

Corresponding author: yuyang.chang@univ-lille.fr

Introduction

Mineral dust dominates global aerosol by mass and imposes significant impacts on the Earth radiation budget, ecosystem dynamics and human health. State-of-the-art multi-wavelength Mie-Raman-depolarization lidar systems uniquely provide height-resolved optical profiles of dust aerosols from ultraviolet to near-infrared spectra, allowing a continuous monitoring of their vertical distributions. Nevertheless, sufficient estimates of dust radiative effects need further knowledge of dust microphysical properties such as the volume size distribution (VSD) and complex refractive index (CRI), which are challenging to be retrieved from the lidar optical measurements due to the following reasons. Firstly, for a long time, there had been a lack of particle scattering models that precisely describe the backscattering properties of non-spherical particles. The spherical model widely adopted by aerosol transport models produces the backward scattering peak which is not observed in laboratory measurements of non-spherical dust ensembles. The spheroidal model employed by AERONET sunphotometer retrieval performs well on mimicking forward and side scattering of irregular particles, while it also encounters difficulties in the backward direction due to the deterioration of computational accuracy[1]. The irregular-hexahedral (IH) model recently proposed by [2] exhibits encouraging potentials in dust backscattering simulation, but there is a lack of direct applications to the inversion of lidar measurements, as well as comparisons of the retrieval results with those obtained with the spherical or spheroidal models so as to better understand the strengths and limitations of this new particle shape model. Secondly, the sensitivity of lidar measurements to large aerosol particles, which ensures accurate microphysical retrievals and behaves differently for different scattering models, still needs a better understanding.

This study aims to address the aforementioned issues thanks to the Basic Algorithm for Retrieval of Aerosol with Lidar (BOREAL) algorithm which allows to calculate aerosol optical properties and retrieve microphysical properties based on different scattering models[3,4]. Both retrievals from synthetic optical properties and real lidar measurements are conducted to evaluate the performances of the three testing scattering models – the spherical, spheroidal and IH models under different combinations of spectral extinction coefficient (α), backscattering coefficient (β) and particle linear depolarization ratio (PLDR, δ). In this abstract, we present some representative results of this study after a brief description of the algorithmic principles.

Methodology

The BOREAL algorithm was developed for the retrieval of aerosol VSD and CRI from lidar measurements, as well as the calculation of total volume concentration (V_t), effective radius (r_{eff}) and single-scattering albedo (SSA) from the retrieval with efficiency and automaticity. An online GUI of BOREAL for single-fast retrievals is at https://boreal.loa.univ-lille.fr. Compared to other lidar-aerosol retrieval algorithms based on constrained linear inversion (e.g., [5]), BOREAL allows for simultaneous retrieval of VSD and CRI, which greatly simplifies the determination of the solution space. Furthermore, it enables to simultaneously consider the measurements and a priori constraints weighted by their covariance

matrices, which is particularly useful for lidar measurements since the extinction and backscattering coefficients can differ by an order in magnitude. Here we recap on its main principle whereas a detailed algorithmic implementation can be found in [3,6]. For an aerosol optical property, y, measured with lidar, the relationship with the microphysical properties can be expressed as

$$y(\lambda, m_{\mathrm{R}}, m_{\mathrm{I}}) = \int_{r_{\min}}^{r_{\max}} k_y(\lambda, m_{\mathrm{R}}, m_{\mathrm{I}}, r) \frac{\mathrm{d}V(r)}{\mathrm{d}r} \mathrm{d}r\,, \tag{1}$$

where k_y is the corresponding kernel function and $\frac{\mathrm{d}V(r)}{\mathrm{d}r}$ the VSD; m_{R} and m_{I} represent the real and imaginary parts of the CRI, λ the measurement wavelength and r the volume-equivalent radius of a single particle. Note that y can refer to α or β, while δ should be calculated from

$$\delta(\lambda, m_{\mathrm{R}}, m_{\mathrm{I}}) = \frac{P_{11,\pi}(\lambda, m_{\mathrm{R}}, m_{\mathrm{I}}) - P_{22,\pi}(\lambda, m_{\mathrm{R}}, m_{\mathrm{I}})}{P_{11,\pi}(\lambda, m_{\mathrm{R}}, m_{\mathrm{I}}) + P_{22,\pi}(\lambda, m_{\mathrm{R}}, m_{\mathrm{I}})}, \tag{2}$$

where $P_{11,\pi}$ and $P_{22,\pi}$ are the backward phase matrix elements of which the relationships with the aerosol microphysical properties can be expressed as the form of Eq. (1).

If we apply a discretization strategy to VSD and assume the Gaussian distribution of the measurement error, then the microphysical state vector $\mathbf{x} = [\mathbf{v}^T, \mathbf{m}^T]^T$ ($\mathbf{v}$ is the vector representation of VSD under the discretization strategy and $\mathbf{m} = [m_{\mathrm{R}}, m_{\mathrm{I}}]^T$) can be retrieved by minimizing the following cost function:

$$\Psi(\mathbf{x}) = [\mathbf{y} - \mathbf{K}(\mathbf{m})\mathbf{v}]^T \mathbf{C}_{\mathbf{y}}^{-1} [\mathbf{y} - \mathbf{K}(\mathbf{m})\mathbf{v}] + \gamma^2 (\mathbf{H}\mathbf{v})^T (\mathbf{H}\mathbf{v}) + [\mathbf{m}_{\mathrm{a}} - \mathbf{m}]^T \mathbf{C}_{\mathbf{m}}^{-1} [\mathbf{m}_{\mathrm{a}} - \mathbf{m}], \tag{3}$$

where the first term in the right-hand side represents the fitting to the measurement vector weighted by the measurement covariance matrix $\mathbf{C}_{\mathbf{y}}$, while the second and third terms represent the smoothing constraint on VSD and the a priori constraint on CRI, respectively. In the smoothing constraint term, $\mathbf{H}$ is the differential operator and γ is the scaler Lagrange multiplier for adjusting the weight of the constraint; in the a priori constraint term, $\mathbf{m}_{\mathrm{a}}$ and $\mathbf{C}_{\mathbf{m}}$ denote the a priori value and a priori covariance of $\mathbf{m}$, respectively. The minimization procedure is implemented by Levenberg-Marquardt iteration. After the VSD and CRI are retrieved, the V_{t} and r_{eff} are calculated from the retrieved VSD and SSA is calculated combining the scattering model. The aforementioned process is repeated for a series of inversion windows that define the interval between $r_{\min}$ and $r_{\max}$ to derive a family of individual solutions. Then a bunch of selection criteria are applied to identify qualitied individual solutions, of which the mean and standard deviation are output as the final solution to the retrieval.

Simulation and Sensitivity Study

Figures 1-2 present comparisons of lidar-related optical properties simulated with the spherical, spheroidal and IH models, respectively. Detailed descriptions about these scattering models and the integration into BOREAL can be found in [1,2,7]. The comparisons show that both α and its spectral variation (i.e., extinction Angstrom exponent, EAE) have limited sensitivities to particle shape and CRI, while β behaves in a contrast way. In particular, the β of spherical particles is apparently stronger than those of non-spherical particles. The spectral variations of the lidar ratios (LRs) and PLDRs (δ) indicate the optical properties of spheroidal and IH particles gradually differ from each other as the size parameter increases; moreover, the steady increase of δ with the size parameter as $r_{\mathrm{eff}} < 1$ μm for both spheroidal and IH particles suggests that spectral PLDR measurements contain useful information on particle size retrieval. Further comparisons show that the IH model produces dust optical properties more consistent with published lidar measurements for $r_{\mathrm{eff}} > 1$ μm, a typical range for coarse-mode dust particles[7].

Synthetic retrievals by inverting the optical properties simulated with the non-spherical models from a series of predefined VSDs and CRIs were performed in order to evaluate BOREAL's retrieval accuracy under various circumstances. Table 1 summarizes the retrieval results when traditional 3β (β at 355, 532 and 1064 nm) + 2α (α at 355 and 532 nm) data and 3β + 2α + 3δ (δ at 355, 532 and 1064 nm) data are inverted, respectively. The statistics of the retrieval accuracy are shown for three r_{eff} ranges. It can be seen

that the retrieval quality declines with the increase of particle size, whereas the incorporation of 3δ to the traditional ($3\beta + 2\alpha$) data greatly improves the retrieval accuracy. Compared to the spheroidal model, the contribution of the spectral PLDR measurements to the retrieval accuracy is more manifest in the IH model[7]. It is also important to observe that ignoring particle non-sphericity (i.e., inverting the synthetic measurements by the spherical model) severely underestimates m_R and overestimates m_I, as a result of canceling the backscattering enhancement of the spherical particle assumption (Fig. 1a), which has already been widely observed in previous lidar-dust retrievals[5].

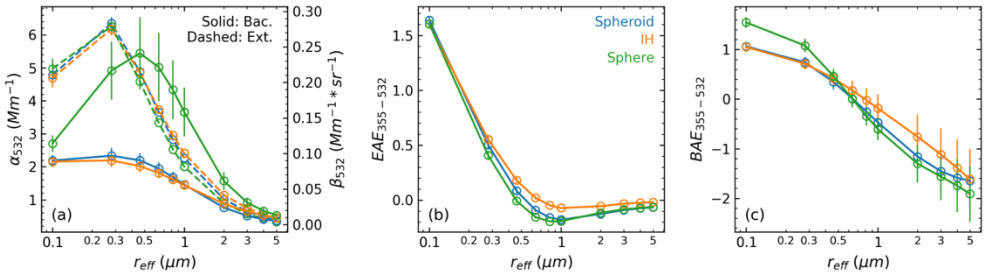

Figure 1. Lidar-related optical properties simulated with the spheroidal (blue), IH (orange) and spherical (green) models as functions of r_{eff} for varying CRIs. (a) Extinction (α, dashed lines) and backscattering (β, solid lines) coefficients at 532 nm. (b) Extinction Angstrom exponent over 355-532 nm ($EAE_{355-532}$). (c) Backscattering Angstrom exponent over 355-532 nm ($BAE_{355-532}$). The VSDs are parameterized by the lognormal distribution. The CRIs vary from 1.4 to 1.6 for the real part (m_R) and from 0.001 to 0.009 for the imaginary part (m_I). The markers and error bars represent the mean and 1 standard deviation of the spread results due to the variation of the CRIs, respectively.

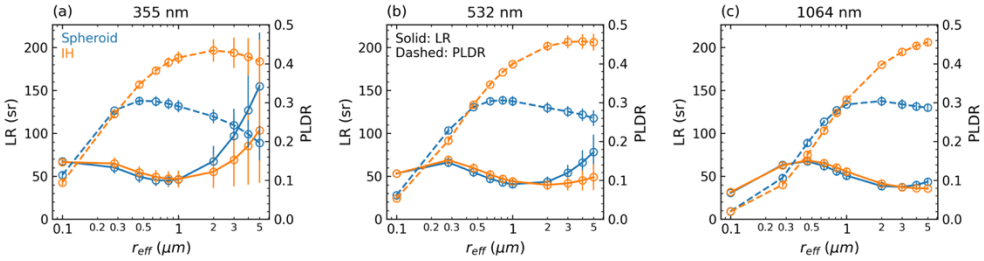

Figure 3. LRs and PLDRs simulated with the spheroidal and IH models at (a) 355 nm, (b) 532 nm, and (c) 1064 nm. The VSDs and CRIs for the calculation are the same as those in Fig. 3.

Table 1. Retrieval errors when inverting synthetic optical data simulated with the IH and spheroidal ("Sphd") models using different retrieval setups – (Sph, 3+2): inverting ($3\beta + 2\alpha$) with the spherical model, (IH/Sphd, 3+2): inverting ($3\beta + 2\alpha$) with the IH/spheroidal model, (IH/Sphd, 3+2+3): inverting ($3\beta + 2\alpha + 3\delta$) with the IH/spheroidal model. Statistical results (mean ± std) are derived for three r_{eff} range groups – G1: 0.5-1 μm, 1-2 μm and 2-5 μm.

		Opt. data simulated with IH			Opt. data simulated with Sphd		
Retrieval setup		**Sph, 3+2**	**IH, 3+2**	**IH, 3+2+3**	**Sph, 3+2**	**Sphd, 3+2**	**Sphd, 3+2+3**
r_{eff} G1	$\epsilon(V_t)$ (%)	-8±20	-16±13	-3±2	-7±20	-13±12	-7±4
	$\epsilon(r_{eff})$ (%)	-18±16	-14±12	-2±2	-12±17	-11±11	-5±4
	$\epsilon(m_R)$ (*10^{-3})	-74±59	30±27	5±7	-68±59	26±25	7±5
	$\epsilon(m_I)$ (*10^{-3})	7.0±7.8	2.2±1.6	0.8±0.5	7.0±7.5	2.4±1.9	1.2±0.5
r_{eff} G2	$\epsilon(V_t)$ (%)	-38±17	-32±16	-14±7	-39±19	-29±15	-25±10
	$\epsilon(r_{eff})$ (%)	-45±14	-29±16	-13±7	-40±17	-25±14	-22±9
	$\epsilon(m_R)$ (*10^{-3})	-58±63	42±36	-1±5	-48±67	29±29	8±6
	$\epsilon(m_I)$ (*10^{-3})	10.3±8.9	2.8±1.8	0.5±0.3	14.3±11.5	3.5±2.6	2.2±1.3
r_{eff} G3	$\epsilon(V_t)$ (%)	-72±9	-63±14	-41±11	-80±10	-67±13	-63±12
	$\epsilon(r_{eff})$ (%)	-75±8	-61±14	-39±11	-79±10	-63±14	-60±13
	$\epsilon(m_R)$ (*10^{-3})	-48±65	54±54	-6±16	-7±82	30±37	23±19
	$\epsilon(m_I)$ (*10^{-3})	23.1±16.7	9.5±11.0	1.9±1.3	51.0±30.2	19.6±15.8	17.2±13.7

Next, BOREAL combined with the three scattering models were applied to retrieve two real dust cases observed by LILAS, a multi-wavelength Mie-Raman-depolarization-fluorescence lidar developed by the Laboratoire d'Opqitue Atmosphérique (LOA) and capable of deriving $3\beta + 2\alpha + 3\delta$ profiles for aerosol study[8]. The results confirm the findings from the simulation that significant retrieval difference between the spheroidal and IH models are not expected when $(3\beta + 2\alpha)$ are inverted, while the use of the spherical model largely underestimates m_R and overestimates m_I. With 3δ included, the IH model tends to derive higher m_R and m_I than the spheroidal model to cancel the PLDR enhancement caused by the IH particle assumption. Further comparisons with the corresponding AERONET retrievals and historical in situ and laboratory measurements show smaller r_{eff} and larger SSA retrieved with BOREAL, while the IH model generally performs better than the spheroidal model[7].

Conclusions

Three particle shape models – spherical, spheroidal and IH models are integrated into the BOREAL algorithm for mineral dust retrieval from lidar measurements. For the first time, differences in optical properties among the models as well as their influences on retrieval results are analyzed. Both simulations and real data applications demonstrate the significance of incorporating spectral PLDR measurements and the superiority of the IH model in dust microphysical retrievals. Further comparisons of the retrieval results with co-located independent observations are needed for a closure validation. Based on this study, the IH model will be integrated into the BOREAL online platform (currently, only the spherical and spheroidal models are available) and we suggest using δ measurements for mineral dust retrieval.

Acknowledgements

This research has been supported by the French National Research Agency (ANR) through the PIA (Programme d'Investissement d'Avenir) under contract "ANR-11-LABX-0005-01", the Hauts-de-France regional council and the European Funds for Regional Economic Development (FEDER) and the ANR (ANR-21-ESRE-0013) through the OBS4CLIM project.

References

[1] Dubovik O, Sinyuk A, Lapyonok T, Holben BN, Mishchenko M, Yang P, Eck TF, Volten H, Muñoz O, Veihelmann B, van der Zande WJ, Leon J-F, Sorokin M, Slutsker I. Application of spheroid models to account for aerosol particle nonsphericity in remote sensing of desert dust. J Geophys Res Atmospheres 2006;111. https://doi.org/10.1029/2005JD006619.

[2] Saito M, Yang P, Ding J, Liu X. A Comprehensive Database of the Optical Properties of Irregular Aerosol Particles for Radiative Transfer Simulations. J Atmospheric Sci 2021;78:2089–111. https://doi.org/10.1175/JAS-D-20-0338.1.

[3] Chang Y, Hu Q, Goloub P, Veselovskii I, Podvin T. Retrieval of Aerosol Microphysical Properties from Multi-Wavelength Mie–Raman Lidar Using Maximum Likelihood Estimation: Algorithm, Performance, and Application. Remote Sens 2022;14:6208. https://doi.org/10.3390/rs14246208.

[4] Chang Y, Hu Q, Goloub P. Retrieval of Aerosol Properties from Multiwavelength Raman Lidar Data Based on Maximum Likelihood Estimation. In: Sullivan JT, Leblanc T, Tucker S, Demoz B, Eloranta E, Hostetler C, Ishii S, Mona L, Moshary F, Papayannis A, Rupavatharam K, editors. Proc. 30th Int. Laser Radar Conf., Cham: Springer International Publishing; 2023, p. 833–9. https://doi.org/10.1007/978-3-031-37818-8_107.

[5] Veselovskii I, Dubovik O, Kolgotin A, Lapyonok T, Di Girolamo P, Summa D, Whiteman DN, Mishchenko M, Tanré D. Application of randomly oriented spheroids for retrieval of dust particle parameters from multiwavelength lidar measurements. J Geophys Res Atmospheres 2010;115. https://doi.org/10.1029/2010JD014139.

[6] Chang Y. Retrieval of height-resolved aerosol components using high performance multiwavelength Raman-depolarization-fluorescence lidar. phdthesis. Université de Lille, 2023.

[7] Chang Y, Hu Q, Goloub P, Podvin T, Veselovskii I, Ducos F, Dubois G, Saito M, Lopatin A, Dubovik O, Chen C. Retrieval of microphysical properties of dust aerosols from extinction, backscattering and depolarization lidar measurements using various particle scattering models. EGUsphere 2024:1–42. https://doi.org/10.5194/egusphere-2024-2655.

[8] Hu Q, Wang H, Goloub P, Li Z, Veselovskii I, Podvin T, Li K, Korenskiy M. The characterization of Taklamakan dust properties using a multiwavelength Raman polarization lidar in Kashi, China. Atmospheric Chem Phys 2020;20:13817–34. https://doi.org/10.5194/acp-20-13817-2020.

Assessment of ATLID Level 2A aerosol products using ACTRIS/EARLINET observations

C.-A. Papanikolaou[1], *P. Guma' Claramunt*[1], *N. Papagiannopoulos*[1], *M.Mytilinaios*[1], *B. De Rosa*[1], *A. Amodeo*[1], *H. Baars*[2], *E. Marinou*[3], *D. Nicolae*[4], *L. Mona*[1]

(1) Consiglio Nazionale Delle Ricerche, Istituto di Metodologie per l'Analisi Ambientale (CNR-IMAA), 85050, Tito Scalo, Potenza, Italy
(2) Leibniz Institute for Tropospheric Research (TROPOS), Leipzig, 04318, Germany
(3) IAASARS, National Observatory of Athens, Athens, Greece
(4) National Institute of Research and Development for Optoelectronics, Magurele, Ilfov, Romania
Corresponding author: christinaannapapanikolaou@cnr.it

Introduction

ATLID (Atmospheric LIDAR) is an HSRL (high-spectral-resolution lidar) on board the EarthCARE (Earth Cloud Aerosol Radiation Explorer) satellite that was launched on 28 May 2024. It is a linearly polarized lidar, with three-channels – a parallel (or co-polar) Mie channel, a Rayleigh channel, and a perpendicular (or cross-polar) channel – operating at 355 nm [1].

The well-established ACTRIS (Aerosol, Clouds and Trace Gases Research Infrastructure) and EARLINET (European Aerosol Research Lidar Network) [2] lidar stations provide reference measurements of aerosol properties, which are critical for validating ATLID products. Intensive preparation activities were performed in the framework of an ATMO-ACCESS pilot project so that the consortium was well prepared for correlative measurements as soon as ATLID was in measurement mode. The extensive geographic and temporal coverage of ACTRIS/EARLINET stations, alongside their long-term and quality-assured measurements, makes these stations well-suited for facilitating intercomparisons across Europe and beyond.

This study aims to validate the aerosol optical properties—backscatter (b_{aer}) and extinction (a_{aer}) coefficients, lidar ratio (LR), and particle linear depolarization ratio (PLDR) at 355 nm—retrieved by ATLID A-AER, A-EBD, and A-TC Level 2A products, mainly from AC and AD baselines. These results will be compared with corresponding Level 1 and Level 2 products from the EARLINET database, utilizing data from various ground-based stations.

Methodology

Initially, the data were collected from 11 August 2024 to 26 March 2025, incorporating EarthCARE overpasses along with corresponding measurements from 16 ACTRIS/EARLINET stations (Figure 1, Table 1). The analysis focused on overpasses occurring within a maximum distance of 100 km from the EarthCARE footprint, while the ground-based data used, were within a ±1.5-hour window relative to the satellite overpass.

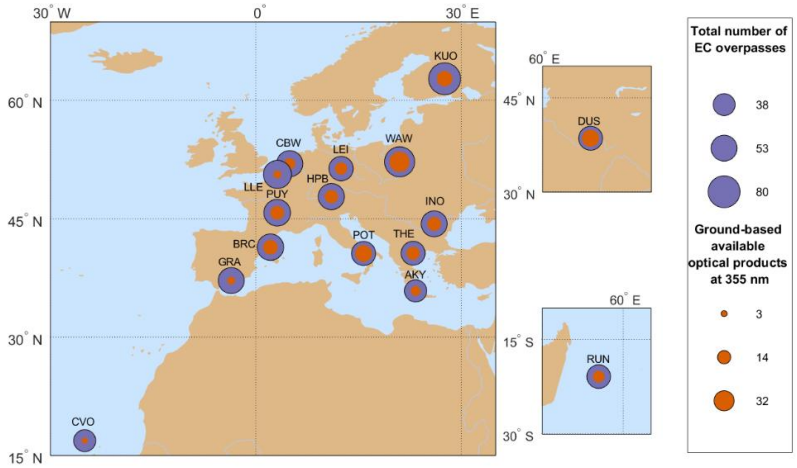

Figure 1. Spatial distribution of ACTRIS/EARLINET stations with the total number of EarthCARE overpasses (outer circle area) and the available related optical products at 355 nm (inner circle area).

Table 1. Stations used in this analysis, along with their corresponding 3-letter code, institution, and coordinates.

Code	Institute	Coordinates	Code	Institute	Coordinates
AKY	National Observatory of Athens – NOA (Antikythera, Greece)	35.8600 N, 23.3100 E, 193 m	KUO	Finnish Meteorological Institute (FMI), Atmospheric Research Centre of Eastern Finland, (Kuopio, Finland)	62.7333 N, 27.5500 E, 190 m
BRC	Universitat Politecnica de Catalunya (Barcelona, Spain)	41.3930 N, 2.1200 E, 115 m	LEI	Leibniz Institute for Tropospheric Research, (Leipzig, Germany)	51.3500 N, 12.4330 E, 125 m
CBW	KNMI - Royal Netherlands Meteorological Institute (Cabauw, Netherlands)	51.9700 N, 4.9300 E, 0 m	LLE	Lille 1 University - Science and Technology (Lille, France)	50.6117 N, 3.1417 E, 60 m
CVO	Leibniz Institute for Tropospheric Research, (Mindelo, Capo Verde)	16.8778 N, -24.9954 E, 30 m	PUY	Observatoire de Physique du Globle (OPGC-LaMP) (Puy de Dôme, France)	45.7610 N, 3.1110 E, 420 m
DUS	Leibniz Institute for Tropospheric Research, (Dushanbe, Tajikistan)	38.5594 N, 68.8561 E, 864 m	POT	Consiglio Nazionale delle Ricerche - Istituto di Metodologie per l'Analisi Ambientale (CNR-IMAA) (Potenza, Italy)	40.6000 N, 15.7200 E, 760 m
GRA	Andalusian Institute for Earth System Research, University of Granada (IISTA-CEAMA) (Granada, Spain)	37.1640 N, -3.6050 E, 680 m	RUN	French National Centre for Scientific Research (CNRS) - University of Reunion Island (Reunion Island, France)	-20.9020 N, 55.4850 E, 84 m
HPB	DWD Meteorological Observatory Hohenpeissenberg (Hohenpeissenberg, Germany)	47.8019 N, 11.0119 E, 974 m	THE	Aristotle University of Thessaloniki, (Thessaloniki, Greece)	40.6300 N, 22.9500 E, 50 m
INO	National Institute of R&D for Optoelectronics (INOE) (Magurele, Romania)	44.3480 N, 26.0290 E, 93 m	WAW	University of Warsaw, Faculty of Physics (Warsaw, Poland)	52.2100 N, 20.9800 E, 112 m

Among the 16 stations, the number of overpasses in the data collection period ranges from 38 (CVO) to 80 (KUO), with the availability of related optical products available at 355 nm from the ground-based lidar ranging from 3 (CVO) to 32 (WAW) overpasses. Notably, stations such as DUS, POT and WAW show a higher fraction of available optical products, while CVO and LLE exhibit the lowest. Unfavorable weather conditions, e.g., low clouds in Cabo Verde, are one of the reasons for the low fraction. ATLID data quality was ensured through a screening process and then horizontally averaged within a radius around each ground-based station, defined by the minimum distance to the satellite orbit.

The screened and averaged data were then compared with ACTRIS/EARLINET ground-based lidar products at 355 nm (Level 1 and 2), following the latest Quality Control Procedures (Version 4.0; https://www.earlinet.org/). These comparisons included the key parameters such as b_{aer}, a_{aer}, LR, and PLDR.

Results

A case study of 9 March 2025 over Potenza station, with a minimum distance of 49.35 km from the EarthCARE orbit is shown in Figure 2. For the horizontal averaging in this case, we used a 100km radius around the station and averaged the corresponding samples within, using the AD baseline products.

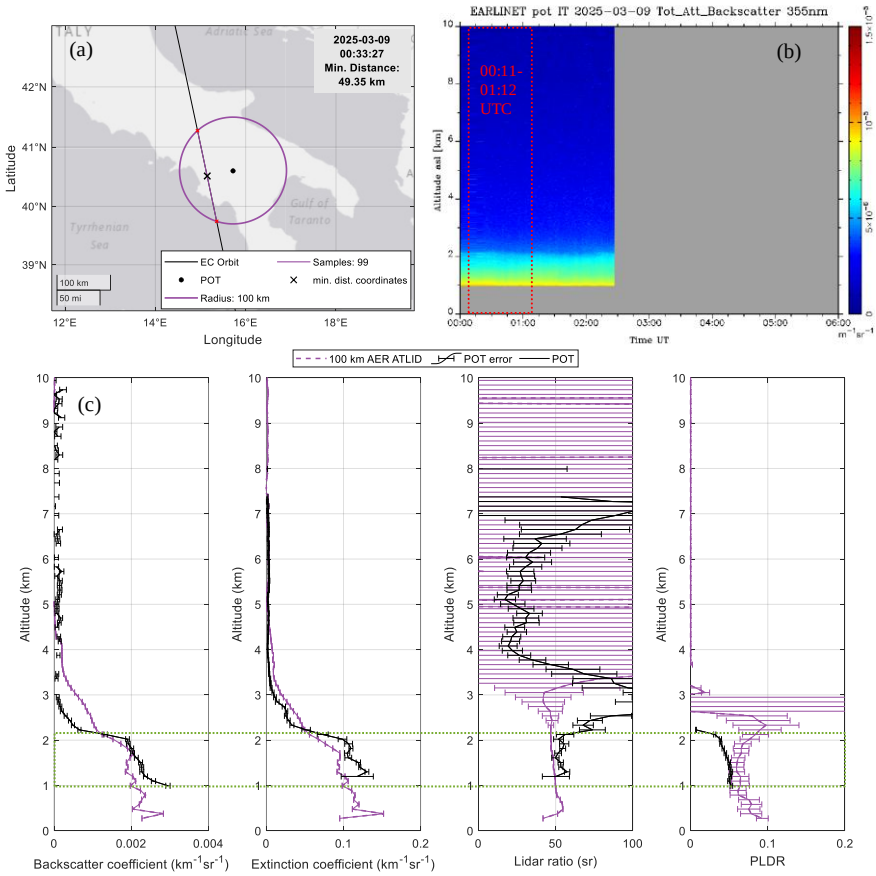

Figure 2. (a) Map of the satellite overpass, showing the minimum distance to the ground station and the radius used for horizontal averaging (100km). (b) Time evolution of the total attenuated backscatter from the ground-based lidar station measurement. (c) Comparison of the vertical distribution of A-AER (purple) and POT ground-based (black) aerosol optical properties.

Figure 3 presents the probability density histograms for each variable, derived from both A-AER and ground-based data, within the 1 to 2.1 km altitude range (a.s.l.) for the case study on 9 March 2025, over the Potenza station. A reasonable agreement is observed, particularly for b_{aer} and a_{aer}, where both A-AER and POT values exhibit similar ranges and distribution shapes, though A-AER values are generally lower than the ground measurements. The A-AER LR distribution shows lower values compared to the ground-based LR data, while a significant divergence is evident for PLDR, where A-AER reports higher values, contrasting with the very low and stable PLDR values observed by the ground station.

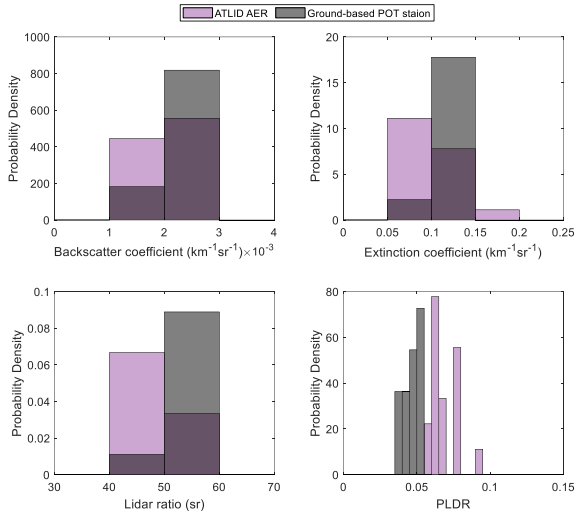

Figure 3. Distribution of aerosol optical properties' values for the A-AER product (purple) and POT ground-based data (gray) within the aerosol layer (between 1.0 and 2.1 km altitude a.s.l.).

This comparative methodology is applied to all stations on a profile-by-profile basis.

Discussion

The overall findings, using all 16 stations comparison (not shown here), show a good agreement between ATLID and ground-based lidar particularly for baer and aaer. This agreement is stronger during nighttime observations, while during daytime, agreement appears to be at good levels, particularly for minimum distances close to 5 km. However, discrepancies tend to increase as the distance grows. Pronounced differences in PLDR have been observed, particularly when ground-based lidars measure low PLDR values, ATLID often reports higher values. This discrepancy in low PLDR scenarios should be further investigated, while we should also validate PLDR measurements during Saharan dust events. It's also important to consider the baseline when analyzing these differences as they have been associated with AD and AC baselines. To enhance the accuracy of the analysis, the AE and AF baselines should be used, to include the latest updates related to the PLDR.

Acknowledgements

This study is supported by the project on Strengthening human capital of ACTRIS Italy Research infrastructure-PER-ACTRIS-IT (project code no. CIR01_00015, no. 2595—CUP: B58I20000220001). We also acknowledge the IR0000032—ITINERIS, Italian Integrated Environmental Research Infrastructures System (D.D. no. 130/2022—CUP B53C22002150006) funded by the EU—Next Generation EU PNRR-Mission 4 "Education and Research"—Component 2: "From research to business"—Investment 3.1: "Fund for the realization of an integrated system of research and innovation infrastructures" and the European Commission under the Horizon 2020 – Research and Innovation Framework Programme, through the ATMO-ACCESS Integrating Activity under grant agreement No 101008004. We also acknowledge the PANGEA4CalVal project (Grant Agreement 101079201) funded by the European Union and ACTRIS-D supported by the German Federal Ministry of Education and Research (BMBF) under the FONA Strategy "Research for Sustainability" (grant no. 01LK2001A). Additionally, we extend our gratitude to the Principal Investigators of the ACTRIS/EARLINET stations for their efforts in establishing and maintaining the observational data used in this research.

References

[1] Donovan, D.P., et al.: The EarthCARE Lidar Cloud and Aerosol Profile Processor (A-PRO): 2024, 5301–5340, doi.org/10.5194/amt-17-5301-2024

[2] Pappalardo, et al.: EARLINET: Towards an Advanced Sustainable European Aerosol Lidar Network. *Atmos. Meas. Tech.* 2014, *7*, 2389–2409, doi.org/10.5194/amt-7-2389-2014.

Validation of EarthCARE L2a products using ground-based PollyNET lidar measurements at Cabo Verde, Tajikistan, Germany and on the Atlantic Ocean

***H. Baars*[1]**, *H. Gebauer*[1], *A. A. Floutsi*[1], *J. Hofer*[1], *M. Haarig*[1], *L. König*[1], *R. Engelmann*[1], *A. Skupin*[1], *G.H. Müller*[1], *U. Wandinger*[1] *David P. Donovan*[2], *G.-J. Zadelhoff*[2]

(1) Leibniz Institute for Tropospheric Research (TROPOS), Leipzig, Germany
(2) Royal Netherlands Meteorological Institute (KNMI), De Bilt, the Netherlands

Corresponding author: baars@tropos.de

Introduction

The Earth Cloud Aerosol and Radiation Explorer (EarthCARE) is a satellite mission implemented by the European Space Agency (ESA) in cooperation with the Japan Aerospace Exploration Agency (JAXA), aiming to measure vertical profiles of aerosol, cloud, and precipitation properties together with radiative fluxes [1]. This Earth Explorer Mission was launched in May 2024 and observes the atmosphere using a high-spectral resolution lidar (HSRL), a Doppler cloud radar, a multi-spectral imager and a broadband radiometer. It can, thus, be considered as a space-based equivalent of an ACTRIS aerosol and cloud remote sensing observatory. ACTRIS is the European Aerosol, Clouds and Trace Gases Research Infrastructure.

The atmospheric lidar (ATLID) on board of EarthCARE is a polarization HSRL operating at a wavelength of 355 nm. It is the first time that the lidar ratio and the depolarization ratio can be measured simultaneously and directly from space at this wavelength. Being a novel instrument in space, extensive validation activities for the instrument (Level 1 data), but also for the derived products (Level 2 data), are needed.

The Leibniz-Institute for Tropospheric Research (TROPOS) is intensively involved in the EarthCARE Cal/Val activities and operates (mobile) ground-based multiwavelength-Raman lidar systems (PollyXT, [2]) around the globe in the framework of PollyNET ([3]).

In this presentation, case-study-based Cal/Val results will be shown. In particular, the focus will be on L1 and L2a products of ATLID [4].

Methodology

For the validation work, we will focus on overpasses for the tropical site of Mindelo, Cabo Verde, the mid-altitude site of Leipzig, Germany and the Central Asian site of Dushanbe, Tajikistan. Furthermore, we utilize direct underpasses of the research vessel Meteor with a PollyXT aboard during cruise M207 in the tropical Atlantic in January and February 2025. All four facilities belong to ACTRIS and participated in the ATMO ACCESS pilot for EarthCARE validation. While the setup of the used PollyXT instruments slightly differ (e.g. [2], [5]), they all have the capabilities to observe particle backscatter, particle extinction and particle depolarization ratio at 355 nm – the wavelength of EarthCARE's HSRL ATLID.

Direct comparison of the aerosol optical properties (backscatter and extinction coefficients, and depolarization ratio at 355 nm, which are measured with ATLID and with PollyXT) are being made with the ESA Level-2 products available, namely the A-AER and A-EBD products [6], and A-ALD [7] at different resolutions. Exemplarily, a case study from Cabo Verde is discussed in the following.

The measurement site is located at Mindelo, on the Cabo Verde Islands in the eastern tropical Atlantic. The aerosol conditions at Mindelo are typically characterized by the presence of geometrically and optically thick lofted layers of Saharan dust between June and September and a mixture of dust and biomass burning aerosol between November and March. Cloud occurrence in the planetary boundary layer (PBL) below 2 km is very common and cloud formation at the top of the dust layer can sometimes be observed [5].

Results and Discussion

Figure 1 shows EarthCARE ATLID Level 1 observation for orbit frame 02866A on 29 November 2024. The frame covers the tropical Atlantic region from 22.5°S to 22.5°N. The excellent signal quality of ATLID, shown up to 30 km altitude, is obvious.

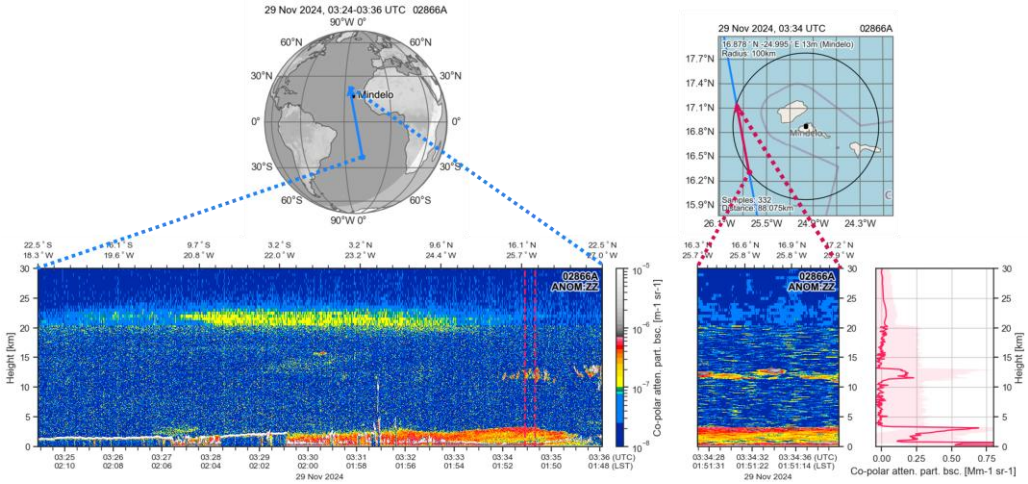

Figure 1. EarthCARE observations on 29 Nov 2024 by means of the co-polar attenuated backscatter coefficient at 355 nm (Baseline ZZ). Left: whole frame, Center: Zoom around the overpass near Mindelo, Right: averaged signal according to the zoom.

From these Level 1 products, i.e., the attenuated backscatter coefficient, one can already identify a low cloud deck (top at 1.5 km) south of the equator with clear sky above. Close to the equator up to about 20°N an intense dust plume reaching up to 4 km height was observed with occasional cloud occurrence. In the stratosphere, a prominent feature extending from 20 to 25 km was observed, which was identified as an aerosol layer related to the Ruang volcanic eruption. At around 16.5° N, EarthCARE passed close by the ground-based ACTRIS station at Cabo Verde. A zoom of the Level 1 products close to Mindelo is shown in Fig. 1 as well. Next to the prominent dust layer, also Cirrus clouds were present above 10 km. The mean ATLID signals of this nighttime overpass falling in the radius of 100 km around Mindelo are shown in Fig. 1, right panels.

For the validation of the Level 2 products for the overpass around Mindelo, the EarthCARE products (A-AER and A-EBD) are averaged to fall within 100 km around the Mindelo ground site and are then compared to reference observations made with PollyXT (0312 to 0412 UTC). The result is shown in Fig. 2 for the particle backscatter coefficient, the particle extinction coefficient, the lidar ratio and the particle depolarization ratio.

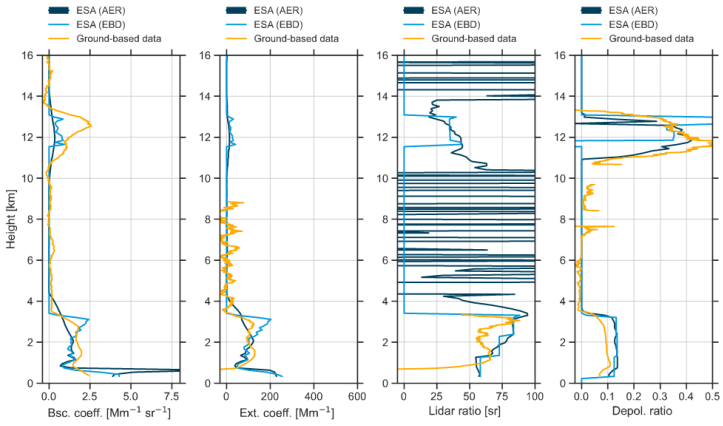

Figure 2. Vertical profiles of two ATLID products (A-AER and A-EBD, Baseline ZZ) and the ground based PollyXT lidar for 4 geophysical quantities during direct colocation.

We used the respective geophysical quantities form the EarthCARE A-AER and A-EBD products (low resolution). In general, good agreement between the results from the two instruments is found. Both capture the dust layer up to 3.5 km altitude well in terms of the particle backscatter coefficient. EarthCARE detected low clouds below 1 km altitude, which were not sampled by the ground-based measurements. The disagreement below 1 km does not represent an instrument issue but simply reflect a representativeness mismatch, which is a general challenge in the validation studies using ground-based profilers [8]. The ice cloud centered at 12 km is also more prominent in the reference observations, but might be also attributed to spatial inhomogeneity. Having a look at the intensive aerosol properties, one sees a reasonable agreement in the dust layer. The lidar ratio is slightly overestimated by the two ATLID products compared to PollyXT and for A-EBD it exhibits a step-wise evolution from the top of the dust layer towards the marine boundary layer below. This is a consequence of the averaging procedure in A-EBD, which is partly based on the A-FM (feature mask, [9]) and is performed layer-wise. Nevertheless, all three products report relatively high values of 75 sr at the top of the dust layer, decreasing towards the marine boundary layer. Note that for the ground reference, only far-range observations are shown and, thus, the extinction coefficient is affected by overlap effects in the lowermost 1 km (merging procedures are currently under way). Concerning the depolarization ratio, a discrepancy between the ground-reference and the ATLID products is observed. Despite this fact, it also becomes obvious that this is not a pure dust layer, but one which is mixed with another aerosol type as the depolarization ratio is below 15 %. In the cirrus cloud however, a reasonable agreement is found with values of around 40% for the ATLID products and 40 to 50 % for PollyXT. The cross-polar channel of ATLID was suffering from an incorrect offset correction in the previous baselines (as discussed in the recent EarthCARE workshop), but a correction was implemented with the baseline shown here (ZZ which is equivalent to AE but was processed offline). This substantially improved the results but still needs further refinement.

One important issue discussed during the latest EarthCARE workshop, was the different resolutions of the ATLID products. A-EBD provides optical properties at three different along-track resolutions, i.e., ‘High’ (1 km), ‘Medium’ and ‘Low’ resolution (~100 km). The smoothing is partly depended on the output of the A-FM results, which are also available at these three resolutions. In Fig. 3, the Level 2 Products are presented similarly to Fig. 1, but for A-AER and for A-EBD corresponding to the 3 different smoothing modes (1 km, 40 km and 100 km). While overall the results look similar, differences can also be found. We will further investigate these differences and present the results at the conference.

Conclusions

First validation results of EarthCARE ATLID products show promising results with an excellent signal quality of EarthCARE. Nevertheless, as discussed during recent validation activities (ESA/JAXA workshops), calibration and correction procedures are continuously improved. Also, the variety, diversity and complexity of EarthCARE products challenges validation efforts. Furthermore, also products from JAXA retrieved with an independent processing chain, will become available and need validation. Based on case studies, we validate key aspect of the ATLID products especially with respect to its different resolutions by ground-based PollyNET lidars and emphasize the potentials and limitations of the products at different resolutions

Disclaimer. The present work includes preliminary data (not fully calibrated/validated and not yet publicly released) of the EarthCARE ESA mission developed in collaboration with JAXA. The analysis has been performed in the context of the EarthCARE Validation Team and of the ATLID Integrated Commissioning Team.

Acknowledgements

This project is supported by the European Commission under the Horizon 2020 – Research and Innovation Framework Programme, through the ATMO-ACCESS Integrating Activity under grant agreement No 101008004. This research has been supported by the German Federal Ministry of Education and Research (BMBF) (grant no. 01LK2001A) and by German Federal Ministry for Economic Affairs and Energy (BMWi) (grant no. 50EE2403A under the FONA Strategy “Research for Sustainability”.

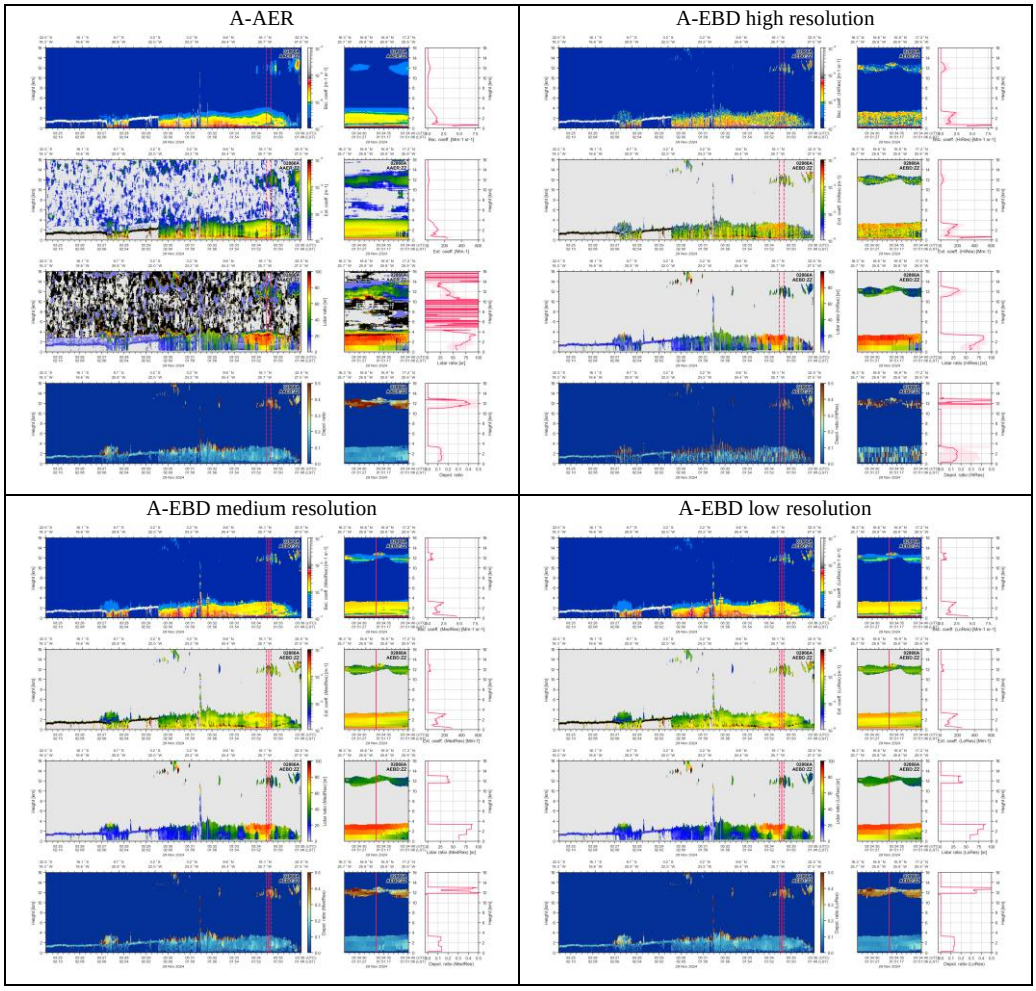

Figure 3. Overview of the ATLID Level2 products at different resolutions (Baseline ZZ).

References

[1] Wehr, T., et al.: The EarthCARE mission – science and system overview, Atmos. Meas. Tech., https://doi.org/10.5194/amt-16-3581-2023, 2023.

[2] Engelmann, R., et al.: The automated multiwavelength Raman polarization and water-vapor lidar PollyXT: the neXT generation, Atmos. Meas. Tech., https://doi.org/10.5194/amt-9-1767-2016, 2016.

[3] Baars, H. et al, An overview of the first decade of PollyNET: an emerging network of automated Raman-polarization lidars for continuous aerosol profiling, Atmos. Chem. Phys., https://doi.org/10.5194/acp-16-5111-2016, 2016.

[4] Eisinger, M., et al.: The EarthCARE mission: science data processing chain overview, Atmos. Meas. Tech., https://doi.org/10.5194/amt-17-839-2024, 2024.

[5] Gebauer, H., et al.: Tropospheric sulfate from Cumbre Vieja (La Palma) observed over Cabo Verde contrasted with background conditions: a lidar case study of aerosol extinction, backscatter, depolarization and lidar ratio profiles at 355, 532 and 1064 nm, Atmos. Chem. Phys., https://doi.org/10.5194/acp-24-5047-2024, 2024

[6] Donovan, D. P., et al.: The EarthCARE lidar cloud and aerosol profile processor (A-PRO): the A-AER, A-EBD, A-TC, and A-ICE products, Atmos. Meas. Tech., https://doi.org/10.5194/amt-17-5301-2024, 2024.

[7] Wandinger, U. et al.: Cloud top heights and aerosol layer properties from EarthCARE lidar observations: the A-CTH and A-ALD products, Atmospheric Measurement Techniques, https://doi.org/10.5194/amt-16-4031-2023, 2023

[8] Amiridis, V., et al.: Best Practice Protocol for the validation of Aerosol, Cloud, and Precipitation Profiles (ACPPV) (Version 2). Zenodo. https://doi.org/10.5281/zenodo.15025627, 2025.

[8] van Zadelhoff, G.-J., et al.: Detection of aerosol and cloud features for the EarthCARE atmospheric lidar (ATLID): the ATLID FeatureMask (A-FM) product, Atmos. Meas. Tech., https://doi.org/10.5194/amt-16-3631-2023, 2023.

Evaluation of the EarthCARE aerosol classification scheme using ACTRIS/EARLINET observations.

K.A Voudouri[1], *N. Papagiannopoulos*[2], *H. Baars*[3], *A. A. Floutsi*[3], *M. Haarig*[3], *H. Gebauer*[3], *U. Wandinger*[3], *C.-A. Papanikolaou*[2] , *P. Gumà-Claramunt*[2], *L. Mona*[2], *D. Nicolae*[4], *M. Tsichla*[1], *P. Paschou*[1], *D. Donovan*[5], *A. Apituley*[5], *D. Gouveia*[5], *G. D' Amico*[2], *D. Balis*[6], *L. Alados-Arboledas*[7], *A. del Águila*[7], *S. Fernández-Carvelo*[7], *M. Sicard*[8], *D. Gantois*[8], *F. Marenco*[9], *A. Papetta*[9], *M. Kezoudi*[9], *K. Fragkos*[9], *P. Freville*[10], *J.-L. Baray*[10], *A. Rodriguez*[11], *A. Comeron*[11], *C. Muñoz-Porcar*[11], *M. Filioglou*[12], *M. Komppula*[12], *V. Amiridis*[1], *E. Marinou*[1]

(1) National Observatory of Athens (NOA), Athens, Greece,
(2) Consiglio Nazionale delle Ricerche – Istituto di Metodologie per l'Analisi Ambientale (CNR-IMAA), Italy
(3) Leibniz Institute for Tropospheric Research (TROPOS), Leipzig, Germany,
(4) National Institute of Research & Development for Optoelectronics (INOE), Magurele, Romania,
(5) Royal Netherlands Meteorological Institute, De Bilt, Netherlands,
(6) Laboratory of Atmospheric Physics, Physics Department, Aristotle University of Thessaloniki, Thessaloniki, Greece,
(7) Andalusian Institute for Earth System Research (IISTA-CEAMA), Granada, Spain,
(8) Laboratoire de l'Atmosphère et des Cyclones (LACy), UMR 8105 CNRS, Université de La Réunion, Météo-France, Saint-Denis de la Réunion, France,
(9) Climate and Atmosphere Research Center (CARE-C), The Cyprus Institute, Nicosia, Cyprus,
(10) OPGC, UAR833, CNRS, Université Clermont Auvergne, Clermont-Ferrand, 63100, France,
(11) CommSensLab, Dept. of Signal Theory and Communications, Universitat Politècnica de Catalunya (UPC), Barcelona, Spain,
(12) Finnish Meteorological Institute, KUOPIO

Corresponding author: kavoudou@noa.gr

Introduction

Aerosol typing plays an important role in identifying aerosol sources, monitoring environmental events, and mitigating impacts. Understanding the origin and characteristics of aerosols is essential to detect aerosol hazards, issue early warnings and minimize their potential impact on climate, air quality, and public health.

To date, several aerosol typing schemes have been developed within ACTRIS (Aerosol, Clouds and Trace Gases Research Infrastructure) and EARLINET (European Aerosol Research Lidar Network; data.earlinet.org) and provide the predominant aerosol type or aerosol mixture in the atmospheric column [1-5]. Similarly, aerosol classification from space lidars offers global coverage and can either be used complementary in retrievals or radiative-closure assessments.

The ESA-JAXA EarthCARE satellite mission, launched in May 2024, provides vertical profiles of aerosols, clouds, and precipitation properties, along with radiative fluxes. Equipped with a high spectral resolution ATmospheric LIDar (ATLID), a Doppler Cloud Profiling Radar (CPR), a MultiSpectral Imager (MSI), and a BroadBand Radiometer (BBR), EarthCARE is designed to advance aerosol characterization via synergistic usage of the aforementioned sensors. As a High Spectral Resolution Lidar (HSRL), ATLID provides a feature mask based solely on aerosol-intensive properties, without relying on assumptions, as CALIPSO.

Methodology

Many EARLINET stations are actively measuring during EarthCARE overpasses when the satellite's footprint lies within a 100 km radius from the ground station, making correlative measurements from August 2024 to present. Ground based measurements from ACTRIS/ EARLINET ([6]; data.earlinet.org) include particle backscatter coefficient, particle extinction coefficient, and particle depolarization ratio profiles. The ACTRIS/EARLINET database has been used for developing aerosol typing algorithms based on type-dependent intensive optical properties [1-5]. The most common intensive optical parameters used for **aerosol-typing** are the *lidar ratio*, the *particle depolarization ratio*, and the *Ångström exponent (or Color ratio)*. Depending on the availability of the particle linear depolarization ratio and the quality of the provided lidar profiles, the derived typing within EARLINET can be either of high or low resolution. In the high-resolution typing of NATALI classification for example, 14 aerosol types can be distinguished (i.e.,

Continental, ContinentalPolluted, Dust, Maritime/CC, Smoke, Volcanic, Coastal, CoastalPolluted, ContinentalDust, ContinentalSmoke, DustPolluted, MaritimeMineral, MixedDust and MixedSmoke). In the low-resolution typing, five predominant aerosol types can be provided (i.e., Dust, ContinentalPolluted, Smoke, Continental, and Maritime), either pure or mixed.

EarthCARE, which is a 355-nm lidar, makes use of two intensive properties: the particle depolarization ratio and particle lidar ratio (L2 products) to assign an aerosol type [7]. EarthCARE's ATLID classification scheme defines ten aerosol types, with classification made at two resolution levels: low and medium. The typing is based on the size, composition, and optical characteristics of the observed aerosols. The types are as follows: Dust, Sea_salt, Continental_Pollution, Smoke, Dusty_smoke, Dusty_mix, Stratospheric_Ash, Stratospheric_Sulfate, Stratospheric_Smoke, Unknown (Aerosol Target has a very low probability (no class assigned)). Therefore, EarthCARE's aerosol classification assessment requires comparison with ACTRIS/EARLINET classification schemes.

In this study we selected cases with various atmospheric conditions to evaluate the EarthCARE aerosol classification scheme by assessing its performance through ACTRIS/EARLINET profiles and the predominant aerosol types identified by the different network's algorithms. The ground-based observations from the following 12 stations are included in this evaluation: Antikythera (AKY), Potenza (POT), Leipzig (LEI), Bucharest (INO), Cabauw (CBW), Thessaloniki (THE), Granada (GRA), La Reunion (RUN), Clermont-Ferrand (PUY), Barcelona (BRC), Cyprus CAO Nicosia (NCS), Kuopio (KUO). These stations cover a diverse range of aerosol conditions, including dust-dominated regions (e.g., NCS, GRA), urban/industrial sites (e.g., BRC, POT, CBW), marine environments (e.g., RUN) and mixed or background sites (e.g., AKY, KUO).

In total 283 measurements have been performed during EarthCARE overpasses above these stations. In the following, we consider only the collocated measurements related to overpasses within a 100 km radius from the station, and time differences within 1.5 hours are used to ensure the aerosol homogeneity. Also, we ensure that both the ground-based station and the satellite observed the same air masses. Last, we will take into account cases with distances over 100 km during intense aerosol episodes such as desert dust intrusions.

The EarthCARE lidar aerosol profile processor (A-PRO; [8]): the A-AER, A-EBD, A-TC, mainly from AC and AD baselines, and L1 and L2 nighttime EARLINET quality-assured measurements are used for the aerosol classification evaluation.

Results and Discussion

In the following, the atmospheric scene on 6 March 2025, during EarthCARE overpass over the PANGEA Antikythera station is presented. EarthCARE time-height cross sections and the intercomparison of the EC A-EBD and A-TC (all baseline AC, low resolution) products are presented in Figure 1. Aerosol layers as seen from the ground-based lidar were present in the boundary layer, along with 2 elevated layers at 1-3 km and 3-7.5 km. The aerosol layer was also detected by ATLID at 50 km radius from the site.

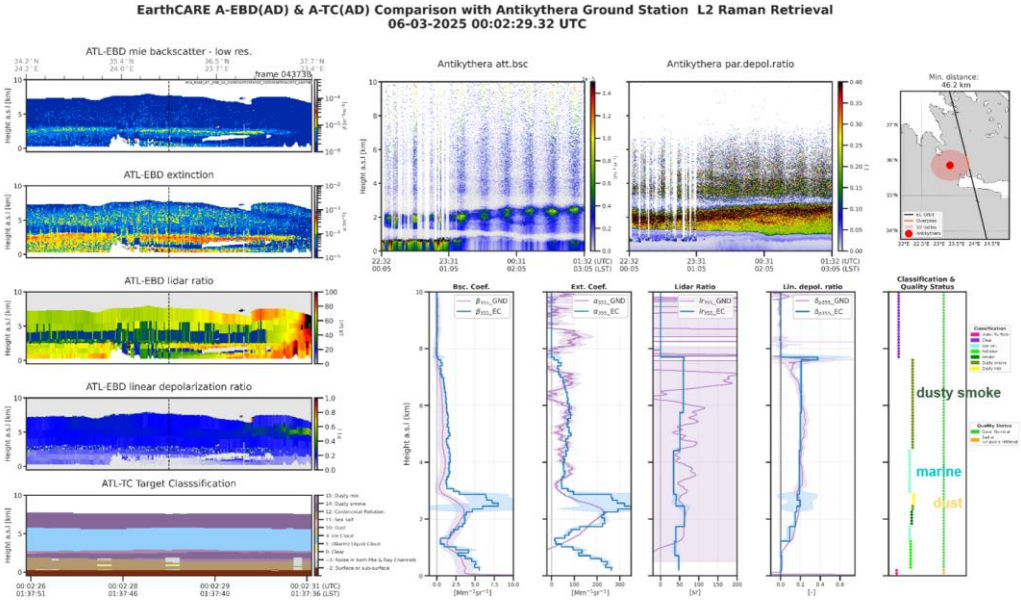

Figure 1. EarthCARE L2 A-EBD (AC) case study intercomparison. Left column: EarthCARE products, 3 right top panels: Antikythera measurements and overpass from station, 5 right lower panels: Product intercomparisons (EC: EarthCARE, GND: Antikythera measurements).

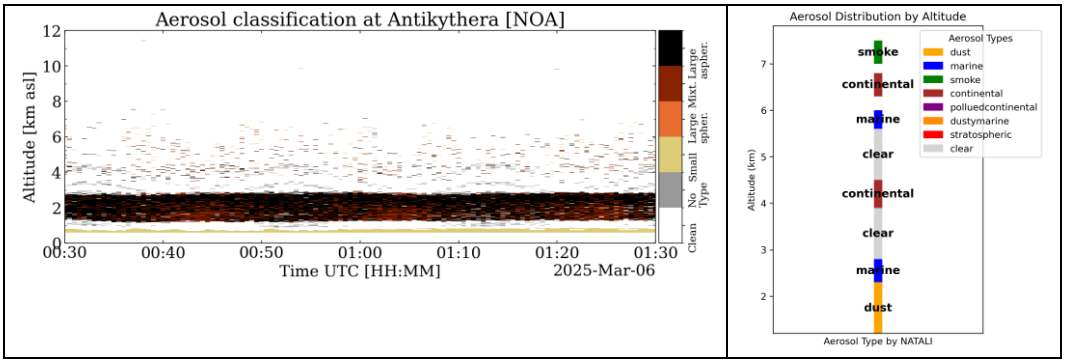

Figure 2. PollyXT target classification (left) and NATALI classification (right) of the same day above Antikythera .

The layer at around 2 km is labelled by A-TC as Dust (Figure 1 right), and the layers above it as Marine and Dusty Smoke. The same layer is characterized by the ground-based lidar following the methodology of [9] as large aspherical (i.e, dust-like aerosol; Figure 2 right), and NATALI types it as dust (Figure 2 left).

Conclusions

A preliminary evaluation of EarthCARE's aerosol classification by comparing with independent ground-based lidar measurements is presented herein. The assessment of the EarthCARE aerosol type accuracy is made under different atmospheric conditions (e.g., dust, smoke, pollution, marine aerosols).

Key points for validating the EarthCARE aerosol classification scheme, aligned with the Best Practice Protocol for the validation of Aerosol, Cloud, and Precipitation Profiles (ACPPV) project (https://zenodo.org/records/15025627) are the following:

Different smoothing of the EarthCARE A-EBD (Aerosol Extinction Backscatter Discrimination) and A-AER (Aerosol Absorption and Extinction Retrieval) products can impact the identification of aerosol layers and, ultimately, the classification of the aerosol types.

Low or medium resolution on ATLID classification scheme can also affect the A-TC product.

Consistency must be ensured for the atmospheric layer geometrical boundaries (wavelength/derivative method, etc.,).

A first step towards the classification validation is the validation of the L2 products that were used in the classification scheme. This will provide valuable information on misclassification reasons.

Intercomparison with a different aerosol typing scheme that uses the same (or different) L2 input parameters can be applied. However, this becomes difficult due to the different nomenclatures and classifications used in the different aerosol typing schemes [10].

Since aerosol typing is usually applied to atmospheric features, a consistency check between the feature identification algorithms shall be performed.

A consolidated evaluation strategy together with a thorough assessment considering all collocated cases at different stations will be presented in the coming ELC2025. Moreover, we will consider comparing collocated measurements during daytime overpasses, taking advantage of the methodology presented in Figure 2 and, for example, collocated sunphotometer observations. Last, UAV in situ observations from the Cyprus Atmospheric Observatory (CAO) of the Cyprus Institute will be explored in the assessment of EarthCARE's aerosol classification.

Acknowledgements

This research was financially supported by the PANGEA4CalVal project (Grant Agreement 101079201) funded by the European Union, and the CERTAINTY project (Grant Agreement 101137680) funded by the Horizon Europe program. The authors also acknowledge ITINERIS, Italian Integrated Environmental Research Infrastructure System (IR0000032, D.D. n. 130/2022—CUPB53C22002150006). We acknowledge EARLINET and ACTRIS aerosol remote sensing teams for the provision of datasets, and for scientific support.

References

[1] Nicolae, D., et al., A neural network aerosol-typing algorithm based on lidar data, Atmos. Chem. Phys., 18, 14511–14537, https://doi.org/10.5194/acp-18-14511-2018, 2018.

[2] Papagiannopoulos, N., et al., An automatic observation-based aerosol typing method for EARLINET, Atmos. Chem. Phys., 18, 15879– 15901, https://doi.org/10.5194/acp-18-15879-2018, 2018.

[3] Floutsi, A. A., et al., DeLiAn – a growing collection of depolarization ratio, lidar ratio and Ångström exponent for different aerosol types and mixtures from ground-based lidar observations, Atmos. Meas. Tech., 16, 2353–2379, https://doi.org/10.5194/amt-16-2353-2023, 2023.

[4]Floutsi, A. A., et al., HETEAC-Flex: an optimal estimation method for aerosol typing based on lidar-derived intensive optical properties, Atmos. Meas. Tech., 17, 693–714, https://doi.org/10.5194/amt-17-693-2024, 2024.

[5] del Águila, A., et al., Aerosol type classification with machine learning techniques applied to multiwavelength lidar data from EARLINET, EGUsphere [preprint], https://doi.org/10.5194/egusphere-2025-269, 2025.

[6] Pappalardo. G., et al., EARLINET: towards an advanced sustainable European aerosol lidar network. Atmospheric Measurement Techniques, 7(8), 2389–2409. https://doi.org/10.5194/amt-7-2389-2014, 2014.

[7] Wandinger, U., et al., HETEAC – the Hybrid End-To-End Aerosol Classification model for EarthCARE, Atmos. Meas. Tech., 16, 2485–2510, https://doi.org/10.5194/amt-16-2485-2023, 2023.

[8] Donovan, D. P., van Zadelhoff, G.-J., and Wang, P.: The EarthCARE lidar cloud and aerosol profile processor (A-PRO): the A-AER, A-EBD, A-TC, and A-ICE products, Atmos. Meas. Tech., 17, 5301–5340, https://doi.org/10.5194/amt-17-5301-2024, 2024.

[9] Baars, H., Seifert, P., Engelmann, R., and Wandinger, U.: Target categorization of aerosol and clouds by continuous multiwavelength-polarization lidar measurements, Atmos. Meas. Tech., 10, 3175–3201, https://doi.org/10.5194/amt-10-3175-2017, 2017.

[10] Voudouri, K. A., et al., Comparison of two automated aerosol typing methods and their application to an EARLINET station. Atmospheric Chemistry and Physics, 19(16), 10961–10980. https://doi.org/10.5194/acp-19-10961-2019. 2019.

Using the ground-based ESA eVe reference lidar for the validation of Aeolus and EarthCARE lidar products.

P. Paschou[1], *E. Marinou*[1], *K. A. Voudouri*[1,2], *N. Siomos*[3], *A. Gkikas*[4], *J. von Bismarck*[5], *T. Fehr*[5], *and V. Amiridis*[1]

(1) Institute for Astronomy, Astrophysics, Space Applications, and Remote Sensing, National Observatory of Athens, I. Metaxa and Vas. Pavlou str., 15236, Penteli, Greece,
(2) Physics Department, Aristotle University of Thessaloniki, University campus, 54124, Thessaloniki, Greece
(3) Ludwig Maximilian University of Munich, Geschwister-Scholl-Platz 1, 80539, Munich, Germany
(4) Research Centre for Atmospheric Physics and Climatology, Academy of Athens, 79 Vas. Sofias str., 11521, Athens, Greece
(5) European Space Agency (ESA/ESTEC), Keplerlaan 1, 2201 AG, Noordwijk, The Netherlands

Corresponding author: pepaschou@noa.gr

Introduction

The eVe lidar is the ESA's ground-based lidar system for providing reference measurements on aerosol and thin clouds optical properties for the calibration and validation (cal/val) of ESA satellite missions. The eVe lidar is a combined linear/circular polarization lidar with Raman capabilities that operates at 355 nm and derives the profiles of the particle backscatter and extinction coefficients, the lidar ratio, and the linear and circular depolarization ratios [1]. In brief, the lidar is implemented in a dual-laser/dual-telescope configuration where two lasers are used for the interleaved emission of linearly and circularly polarised light at 355 nm and two telescopes are used for the collection of the backscattered lidar signals and the optical separation and detection of the co- and cross-polar components of the elastically (355 nm) backscattered signals and the inelastically (387 nm) backscattered signals from both linear and circular polarization emission. Moreover, the lidar can be rotated to perform lidar measurements using different pointing geometries allowing eVe simultaneously reproduce the operation of any lidar system that uses linearly (e.g traditional polarization lidars; ATLID onboard EarthCARE mission) or circularly (e.g. ALADIN lidar onboard Aeolus mission) polarized emission, facilitating the cal/val activities of the ALADIN and ATLID lidar products onboard the Aeolus (2018-2023; [2]) and EarthCARE (2024-today; [3]) satellite missions, respectively, with direct comparisons on the polarization sensitive lidar products without using the theoretical relationship between linear and circular depolarization ratios [4, 5]. For Aeolus, a few studies were performed focusing mainly on the validation of the particle backscatter coefficient retrieved from different versions of the Standard Correct Algorithm (SCA) above European sites [6 – 8]. Overall, good performance of the of the Aeolus L2A particle backscatter coefficient has been reported with mean biases up to 0.37 $Mm^{-1}sr^{-1}$ in absolute values and root mean square errors up to 1.7 $Mm^{-1}sr^{-1}$. The performance of the SCA retrievals is decreased at the lowermost bins, inside the Planetary Boundary Layer (PBL), due to contamination from surface return signals in the Aeolus profiles and/or the increased Signal-to-Noise Ratio levels close to the surface, the Aeolus coarser horizontal resolution compared to the ground-based lidars and the spatiotemporal inhomogeneous conditions of the boundary layer. Nevertheless, the above studies use linear polarization lidar products and lack extended comparisons for all Aeolus L2A products (including extinction coefficient and lidar ratio profiles) and from other Aeolus algorithms such as the MLE (Maximum Likelihood Estimation) and the AEL–PRO which became available in later versions of the Aeolus L2A algorithms release. In this work we present the results from the validation study on the particle optical properties from the Aeolus mission using direct circular polarization lidar observations from eVe reference lidar. Furthermore, we discuss the main components of the eVe lidar upgrade for delivering ground-reference linear polarization lidar measurements tailored for the validation of the ATLID lidar products onboard the EarthCARE mission which is an ongoing activity for the EarthCARE cal/val teams after the mission launch on May 2024.

Methodology

For the validation of the Aeolus aerosol products (i.e. the Aeolus Level 2A products), the eVe lidar has been deployed in the ASKOS campaign [9, 10] which is the ground-based component of the Joint Aeolus Tropical Atlantic Campaign in Cabo Verde (summer 2021 and 2022). During ASKOS, targeted linear/circular depolarization measurements were performed with eVe lidar during the nearest Aeolus overpass from the ASKOS site every Friday evening, while eVe was pointing at 37.6^{o} off-zenith towards the Aeolus track in order to reproduce the Aeolus measurements from the ground [2]. In total, 14 collocated eVe – Aeolus measurements were collected under multiple aerosol conditions such as pure dust, marine and dust mixtures, and volcanic mixtures with marine and dust aerosols [10]. The collocation criteria comprise a spatial collocation of 100 km maximum distance between the nearest Aeolus overpass from the ASKOS location and a temporal window of 3 hrs centred at the Aeolus overpass time.

For these 14 collocated eVe measurements with Aeolus, the profiles of the Aeolus like particle backscatter coefficient and Aeolus like lidar ratio have been retrieved from eVe additionally to the routine eVe products (i.e. particle extinction and backscatter coefficients, lidar ratio, and depolarization ratios). The Aeolus like profiles are the ground-based lidar products harmonized with the Aeolus Level 2A products while considering the misdetection of the cross-polar component of the backscattered light from Aeolus (Appendix A in [1]). As such, for the comparison of the eVe profiles with the corresponding Aeolus L2A profiles, the eVe profiles of the particle extinction coefficient, the Aeolus like particle backscatter coefficient, and the Aeolus like lidar ratio were used as the reference. The Aeolus L2A products that are used in the validation study have been obtained from the reprocessed Aeolus dataset with the latest available version (Baseline 16) of the three Aeolus algorithms, the Standard Correct Algorithm (SCA), the Maximum Likelihood Estimation (MLE), and the AEL-PRO.

Results and Discussion

A statistical analysis has been performed using the 14 eVe – Aeolus collocations to evaluate the overall performance of Aeolus during the ASKOS period. The eVe profiles that are used in the analysis have been obtained under cloud-free nighttime conditions and have been rescaled to the Aeolus binning resolution. Similarly, the cloud contaminated bins have been removed from the Aeolus L2A profiles based on the cloud flag product from SCA algorithm aiming for cloud-free Aeolus profiles from SCA, MLE and AEL-PRO while using a common cloud masking approach. Then, for each Aeolus L2A product, the vertically resolved biases (bias = Aeolus - eVe) have been calculated and sorted into eight altitude classes. For each class, the mean bias and the standard deviation have been calculated and presented in figures 1 and 2 for the Aeolus particle backscatter and extinction coefficients respectively. The mean bias corresponds to the systematic error of the given Aeolus product which can be used to identify regions where Aeolus over or underestimates the measured parameter, and the standard deviation corresponds to the random error of the given Aeolus product which depend on the noise level in the data and/or the natural atmospheric variability since the ground-based and satellite lidars may not probing the same air mass [11].

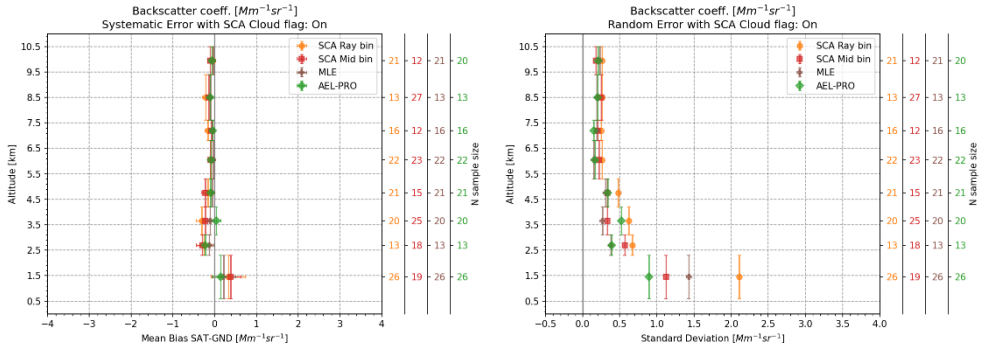

Figure 1. Systematic and Random error of the Aeolus particle backcatter coefficient from SCA (–Rayleigh and –Mid bin resolution), MLE, and AEL-PRO as a function of eight altitude classes using the Aeolus-like backscsatter coefficient from eVe lidar as reference. The x-error bars in the systematic error (mean bias) subplot correspond to the standard error of the mean, while the y-error bars correspond to the classes' boundaries (0.6, 2.3, 3.1, 4.2, 5.3, 6.8, 7.6, 9.4, 10.5 km). The secondary y-axis indicates the sample size N per class for each algorithm.

The statistics for the backscatter coefficient (Fig. 1) indicate decrease of the errors (random and systematic) with increase of altitude, reflecting improved performance in higher altitudes as already reported in [6 – 8]. In the 2.3 – 5.3 km range where the dust particles mostly reside during ASKOS [10], the systematic errors reached values up to -0.31 $Mm^{-1}sr^{-1}$ (SCA–Rayleigh bin), -0.3 $Mm^{-1}sr^{-1}$ (SCA–Mid), -0.13 $Mm^{-1}sr^{-1}$ (MLE), and -0.22 $Mm^{-1}sr^{-1}$ (AEL–PRO), indicating slight underestimation of the co-polar backscatter coefficient from Aeolus with corresponding random error values up to 0.6 $Mm^{-1}sr^{-1}$ for the SCA, and 0.4 $Mm^{-1}sr^{-1}$ for the MLE and 0.5 $Mm^{-1}sr^{-1}$ for the AEL–PRO. However, the random errors increased significantly in the lower atmospheric layers, particularly in the 0.6 – 2.3 km range, where the standard deviation reached the 2 $Mm^{-1}sr^{-1}$ for the SCA–Rayleigh, the 1.1 $Mm^{-1}sr^{-1}$ for the SCA–Mid bin, the 1.4 $Mm^{-1}sr^{-1}$ for the MLE, and the 0.9 $Mm^{-1}sr^{-1}$ for the AEL–PRO.

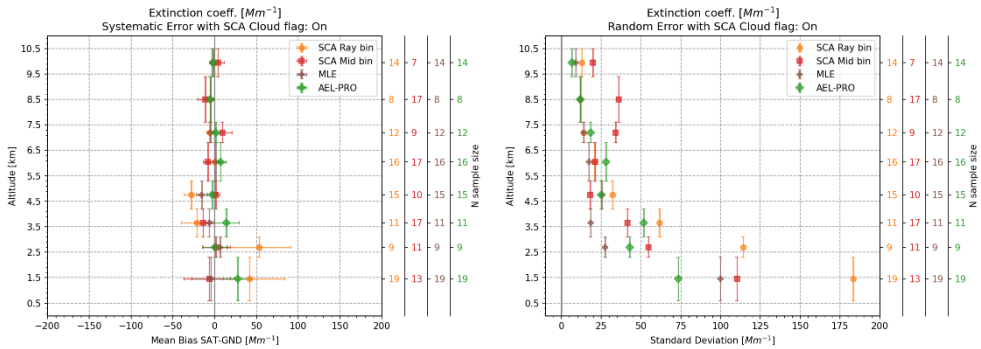

Figure 2. Same as Figure 1 but for the Aeolus particle extinction coefficient.

The extinction coefficient (Fig. 2) exhibits larger discrepancies and variability compared to the backscatter coefficient due to the noisier retrievals from Aeolus. In the 0.6 – 2.3 km range, the random errors reached values up to 178 Mm^{-1} (SCA–Rayleigh), 106 Mm^{-1} (SCA–Mid), 97 Mm^{-1} (MLE), and 72 Mm^{-1} (AEL–PRO), while in the rest altitude classes the random errors reduced to 12 Mm^{-1} (SCA–Rayleigh), 18 Mm^{-1} (SCA–Mid), 9 Mm^{-1} (MLE), and 6 Mm^{-1} (AEL–PRO). The MLE algorithm demonstrated the most consistent performance with random errors ranging from 9 to 26 Mm^{-1}, while the SCA algorithms showed larger overall error variations, from 12 to 108 Mm^{-1}.

Furthermore, the statistics for the lidar ratio (not shown here) demonstrate that this Aeolus L2A product is the noisiest one, with errors compounded in both systematic and random metrics. However, the MLE demonstrates improved performance with random errors up to 30 sr, followed by the AEL–PRO with 45 sr in the heights where the aerosols are more frequently detected (2.3 – 5.3 km). Moreover, the discrepancies between eVe and Aeolus profiles generally increase in lower altitudes reflecting the higher atmospheric variability (e.g. PBL inhomogeneities) that is typically encountered in lower altitudes as well as the greater aerosol loads at lower altitudes that lead to enhanced laser beam attenuation for Aeolus (i.e. higher noise levels).

Additional to the calculation of the mean bias and standard deviation in each altitude class, the root mean square error has been calculated which is indicative of the overall magnitude of error (not shown here). For all L2A products, the overall and random errors have similar values in all classes, with their differences to be in the second decimal place for the backscatter and extinction coefficients and by few steradians for the lidar ratio, indicating that the overall error is primarily driven by random variability rather than systematic bias.

Conclusions and Future Plans

The ESA's reference system, eVe lidar, is combined linear/circular polarization lidar with Raman capabilities designed to provide ground truth measurements of the particles' (aerosols and thin clouds) optical properties for the cal/val of the ESA satellite missions of Aeolus and EarthCARE. The validation study on the Aeolus L2A products using the eVe-Aeolus comparisons from the collocated measurements during the ASKOS campaign reveal that the Aeolus co-polar backscatter coefficient is the most accurate L2A product with overall errors up to 2 $Mm^{-1}sr^{-1}$, followed by the noisier particle extinction coefficient with overall errors up to 183 Mm^{-1}. The larger discrepancies for the Aeolus co-polar backscatter and extinction coefficients from the eVe reference profiles are observed in lower altitudes where the aerosol load is larger. The Aeolus co-polar lidar ratio is the noisiest L2A product with the largest discrepancies from the corresponding eVe profiles. Moreover, the results underline the strengths of the MLE and AEL–PRO algorithms while the SCA algorithm could be further improved, particularly in the retrieval of the extinction and lidar ratio products. The MLE algorithm demonstrates consistent performance, reducing both systematic and random errors, closely followed by the AEL–PRO algorithm which performs well particularly in the extinction coefficient retrievals. For SCA, the –Mid bin profiles outperform the corresponding –Rayleigh bin reflecting the reduction of the bias and noise levels in the L2A profiles when averaging the values from two consecutive height bins in SCA–Rayleigh bin profiles that is implemented to obtain the SCA–Mid bin profiles. The systematic errors in all algorithms are overshadowed by the random errors concluding that the discrepancies between eVe and Aeolus profiles are driven by the variability in atmospheric conditions and the inherent noise in Aeolus profiles, especially at lower altitudes where the aerosol layers reside.

Currently the eVe lidar is under upgrade to be optimized for the cal/val of ATLID lidar onboard the EarthCARE satellite mission. The upgraded eVe lidar design will incorporate the hardware and software elements that will allow eVe to provide ground-based reference measurements of the optical properties of aerosols and thin clouds according to the ACTRIS standards for quality assured and controlled (QA/QC) lidar observations that would meet the requirements for the EarthCARE cal/val, while focusing on new capabilities for measurements on the multiple scattering effects in the lidar signals. The main components of the upgrade aim to further enhance eVe's measuring capabilities by including the profiling of water vapor mixing ratio and extending the retrieval of the particle extinction coefficient towards daytime conditions. Moreover, the lidar will be upgraded to allow the retrieval of particle extinction coefficient and linear depolarization ratio while implementing the dual-FOV technique [12, 13]. After the upgrade, the eVe lidar will perform targeted measurements during the nearest EarthCARE overpasses from eVe's location for the validation of the ATLID L2A products.

Acknowledgements

This work was financially supported by the PANGEA4CalVal project (Grant Agreement 101079201) funded by the European Union and the "Best practice protocol for validation of Aerosol, Cloud, and Precipitation Profiles" ESA project (ACPV; Contract no. 4000140645/23/I-NS). The ASKOS campaign was funded by an ESA project (Contract no. 4000131861/20/NL/IA) and the acquired dataset can be accessed via https://evdc.esa.int/publications/askos-campaign-dataset/. The eVe lidar upgrade and the deployment for the cal/val of EarthCARE products are funded by an ESA project (Contract no. 4000146416/24/NL/FFi).

References

[1] P. Paschou et al., "The eVe reference polarisation lidar system for the calibration and validation of the Aeolus L2A product," Atmos. Meas. Tech., vol. 15, no. 7, pp. 2299–2323, 2022.

[2] O. Reitebuch, "The Spaceborne Wind Lidar Mission ADM-Aeolus," U. Schumann, Ed., Berlin, Heidelberg: Springer Berlin Heidelberg, pp. 815–827, 2012.

[3] T. Wehr et al., "The EarthCARE mission - science and system overview," Atmos. Meas. Tech., vol. 16, no. 15, pp. 3581–3608, 2023.

[4] M. I. Mishchenko and J. W. Hovenier, "Depolarization of light backscattered by randomly oriented nonspherical particles," Opt. Lett., vol. 20, no. 12, p. 1356, 1995.

[5] G. Roy and N. Roy, "Relation between circular and linear depolarization ratios under multiple-scattering conditions," Appl. Opt., vol. 47, no. 35, pp. 6563–6579, 2008.

[6] H. Baars et al., "Californian Wildfire Smoke Over Europe: A First Example of the Aerosol Observing Capabilities of Aeolus Compared to Ground‐Based Lidar," Geophys. Res. Lett., vol. 48, no. 8, 2021.

[7] J. Abril-Gago et al., "Statistical validation of Aeolus L2A particle backscatter coefficient retrievals over ACTRIS/EARLINET stations on the Iberian Peninsula," Atmos. Chem. Phys., vol. 22, no. 2, pp. 1425–1451, 2022.

[8] A. Gkikas et al., "First assessment of Aeolus Standard Correct Algorithm particle backscatter coefficient retrievals in the eastern Mediterranean," Atmos. Meas. Tech., vol. 16, no. 4, pp. 1017–1042, 2023.

[9] P. Paschou et al., "eVe Lidar Measurements during the ASKOS/JATAC Campaign," Environ. Sci. Proc. 2023, Vol. 26, Page 168, vol. 26, no. 1, p. 168, 2023.

[10] E. Marinou et al., "An Overview of the ASKOS Campaign in Cabo Verde," Environ. Sci. Proc. 2023, Vol. 26, Page 200, vol. 26, no. 1, p. 200, 2023.

[11] B. A. Walther and J. L. Moore, "The concepts of bias, precision and accuracy, and their use in testing the performance of species richness estimators, with a literature review of estimator performance," Ecography (Cop.)., vol. 28, no. 6, pp. 815–829, 2005.

[12] C. Jimenez et al., "The dual-field-of-view polarization lidar technique: a new concept in monitoring aerosol effects in liquid-water clouds – theoretical framework," Atmos. Chem. Phys., vol. 20, no. 23, pp. 15247–15263, 2020.

[13] J. Reichardt, "On the Shapes and Sizes of Cirrus Particles Causing Specular Reflections in Lidar Signals," EPJ Web Conf., vol. 237, p. 08015, 2020.

Machine Learning Techniques for the Estimation of Aerosol Particle Depolarization Ratio at 355 nm from ACTRIS-EARLINET

A. V. Dandocsi[1,2], *S. Nicolae*[1,2], *G. Ciocan*[1,3], *D. Nicolae*[1]

(1) National Institute of Research and Development for Optoelectronics INOE 2000, Atomistilor Street 409, Magurele, Ilfov Romania

(2) National University of Science and Technology POLITEHNICA Bucharest, Splaiul Independentei 313, Bucharest, Romania

(3) Faculty of Physics, University of Bucharest, Magurele, Atomistilor Street 405, Romania

Corresponding author: andrei.dandocsi@inoe.ro

Introduction

Atmospheric aerosols remain one of the least understood and complex contributors to climate forcing [1]. To understand how they influence weather patterns, air quality and public health, it is essential to closely analyze their properties and behaviour. Therefore, quality-assured ground-based data regarding the vertical distribution of aerosol properties is needed, as it provides crucial insights into aerosol layering and transportation. The European Aerosol Research Lidar Network (EARLINET) [2] has 33 active stations distributed over Europe and Central Asia, with different type of lidar measurement instrumentation [3]. Since some instruments lack the capability to retrieve aerosol particle depolarization ratios at 355 nm — a key requirement for EarthCARE Cal/Val studies — this study explores the possibility of converting the more commonly available 532 nm depolarization ratio measurements, which is more common for EARLINET lidar systems, using machine learning regression techniques and the spectral information provided by the aerosol backscatter coefficients at 1064, 532 and 355 nm.

Methodology

Data used in this study were collected from the EARLINET database, Level 2, meaning fully quality assured. In the first step, the profiles were filtered based on the vertical step of the altitude, retaining at first only the files in which the differences between the altitude values were equal for all three wavelengths (355, 532, and 1064 nm). For profiles that did not exhibit a clear alignment, interpolation methods were applied to bring them to a common set of altitudes. Following alignment, the dataset was further filtered to retain only data within a physically meaningful altitude range — specifically between 1 km and 12 km — where aerosol signal retrievals are typically more reliable, including for cirrus clouds. Further filtering was applied to remove physically irrelevant values of the aerosol particle depolarization ratios at 355 nm and 532 nm, respectively (e.g. values above 0.5). Finally, for each valid profile, the input features — including altitude, backscatter coefficients, and their associated uncertainties at all three wavelengths — and the output variable, defined as the 355 nm particle depolarization ratio, were extracted to build the dataset used for training and testing. While the overall approach is designed to be applicable for multiple EARLINET stations that provide the required parameters, this abstract presents detailed results using observations from the Observatoire de Physique du Globe de Clermont-Ferrand (OPGC-LaMP) as a case study, where data covering 2 years was used. For the training step, we utilized several machine learning algorithms to predict the target variable. These models include Random Forest, XGBoost, and Multi-Layer Perceptron Regressor (MLPR). The data were split into training and testing sets at the profile level, ensuring that profiles used for testing were completely independent from those used in training. For instance, the dataset was split into 80% training and 20% testing. Additionally, multiple data splitting strategies were explored (e.g. random train-test splits and cross-validation).

Results and Discussion

The performance of the XGBoost model was evaluated using data collected between 2023 and 2024 from the OPGC-LaMP station, which operates a COPLid (CO-PDD lidar) [4]. The model achieved a coefficient of determination (R^2) of 0.815, indicating a strong correlation between the predicted and actual values. Additionally, the Mean Squared Error (MSE) was calculated to be 0.0009, demonstrating low prediction error. The Mean Absolute Error (MAE) was found to be 0.0198, which further suggests that the

model's predictions are consistently close to the true values. The Random Forest model achieved an R^2 of 0.683, indicating a moderate correlation between the predicted and actual values of the aerosol particle depolarization ratio at 355 nm. The Mean Squared Error (MSE) was calculated to be 0.0015, while the Mean Absolute Error (MAE) was found to be 0.0259, suggesting that while the model performed well, it exhibited slightly higher errors compared to the XGBoost model. Similarly, the MLPR model was evaluated using a grid search approach to identify the optimal hyperparameter combination. Different configurations, such as hidden layer sizes, activation functions, and regularization parameters, were tested to optimize the model's performance. This model was trained using scaled data to enhance convergence and model efficiency. The results showed that the MLPR model achieved an R^2 of 0.8436, demonstrating a strong correlation between the predicted and actual values, a MAE of 0.0196 and a MSE of 0.0008, indicating that the model's predictions were very close to the true values. An example of the model's performance on data can be seen in Figure 1.

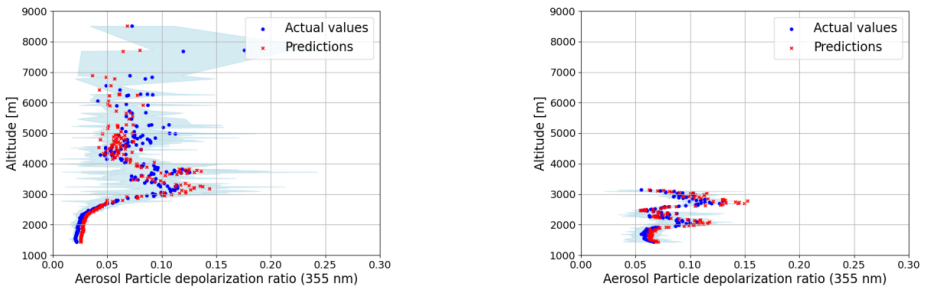

Figure 1. Prediction of aerosol particle depolarization ratio at 355 nm: an example of MLP Regressor applied to two profiles, using Clermont-Ferrand data, with light blue representing the uncertainty.

The approach proposed in this study is tested on stations that measure backscatter coefficients at all three wavelengths and depolarization ratios at both 355 nm and 532 nm. This enables a more robust and generalizable model training, based on richer input data. Moreover, efforts are directed towards training models on data from one station and testing them on another station with similar aerosol characteristics. This provides valuable insights into the transferability and applicability of machine learning models across different EARLINET sites.

Conclusions

This study explores a machine learning-based approach for estimating the 355 nm aerosol particle depolarization ratio from the more commonly available 532 nm lidar data. Results obtained demonstrate promising performance, suggesting that such models could offer a practical solution to help standardize data analysis across stations with different lidar setups. This methodology lays the groundwork for future cross-station applications and supports ongoing efforts in improving ground-based support for satellite missions like EarthCARE.

Acknowledgements

The work was financed by Smart Growth, Digitization and Financial Instruments Program (POCIDIF) 2021-2027, Action 1.3 Integration of the national RDI ecosystem in the European and international Research Space, project "Supporting the operation of facilities in Romania within the ACTRIS ERIC research infrastructure", SMIS code 309113 and supported by the Core Program within the Romanian National Research Development and Innovation Plan 2022-2027, carried out with the support of MCID, project no. PN 23-05 the ATMO-ACCESS H2020 Grant Agreement no. 101008004 and the the CARGO-ACT HEU Grant Agreement no. 101132093.We acknowledge ACTRIS and National Research Council of Italy for providing the data set which is available for download from https://data.earlinet.org.

References

[1] Nicolae, V. et al., "A multi-year analysis of aerosol properties using the calibrated multi-wavelength polarisation lidar in Măgurele," *Journal of Optoelectronics and Advanced Materials*, vol. 25, pp. 176–190, Apr. 2023.

[2] Livio, B. et al., "Lessons learnt during the first Quality Assurance exercise of the ACTRIS high-power lidars," *Journal of Optoelectronics and Advanced Materials*, vol. 26, pp. 422–432, Oct. 2024.

[3] Papanikolaou, C.-A. et al., "Large-Scale Network-Based Observations of a Saharan Dust Event across the European Continent in Spring 2022," *Remote Sensing*, vol. 16, no. 17, p. 3350, Sep. 2024, doi: 10.3390/rs16173350.

[4] Peyrin, F. et al., "Original and Low-Cost ADS-B System to Fulfill Air Traffic Safety Obligations during High Power LIDAR Operation," *Sensors*, vol. 23, no. 6, p. 2899, Mar. 2023, doi: 10.3390/s23062899.

A correlation study between ground-based lidar systems from the ACTRIS-EARLINET network and L2A data from the ATLID instrument

***S. Nicolae*[1,2], *G.Ciocan*[1,3], *D. Nicolae*[1], *A.M. Dandocsi*[1], *A.V.Dandocsi*[1, 2]**

(1) National Institute of Research and Development for Optoelectronics INOE 2000, Atomistilor Street 409, Magurele, Ilfov, Romania
(2) National University of Science and Technology POLITEHNICA Bucharest, Splaiul Independentei 313, Bucharest, Romania
(3) Faculty of Physics, University of Bucharest, Magurele, Atomistilor 405, Romania

Corresponding author: stefan.nicolae@inoe.ro

Introduction

The joint-venture ESA and JAXA EarthCARE satellite mission aims to provide new insights into cloud and aerosol properties and their effects on the global climate, by using four new instruments onboard of the orbiting platform [1].

ATLID is a high spectral resolution atmospheric backscatter Light Detection and Ranging (LIDAR) instrument onboard the EarthCARE satellite, which emits laser pulses at 355nm and measures backscattered light with a ~60cm diameter telescope, in high spectral resolution [2]. Photons are separated by a high spectral-resolution etalon filter to determine aerosol optical depth. To classify aerosols, ATLID separates and measures the co- and cross-polarized particle scattering contributions on dedicated channels. The mission requires the instrument to detect thin clouds and aerosols with extinction coefficients as low as 0.05 km-1 and a faint backscatter signal level of 8 10^{-7} m^{-1} x sr^{-1}, with a vertical resolution of less than 300 m, and horizontal integration of less than 10 km.

In order to provide the community with relevant atmospheric information, the raw signal measured by the instrument has to be processed, resulting in final aerosol properties. Multiple outputs are produced. The level 1b data products specify the instrument's performance. Level 1b products are attenuated backscatter signals from Rayleigh, Mie, and depolarization channels at 0-40 km altitude. Products must be completely geo-localized. Level 2 data products combine geophysical data from Level 1b with additional information, such as meteorological data. In this paper we used the L2a (i.e. obtained from a single instrument's measurements) ATLID-Extinction Backscatter and Depolarization (A-EBD) product [3], [4].

In order to ensure high quality data is being provided to researchers, calibration and validation (Cal/Val) activities are taking place to cross-validate the results produced by the ATLID instrument and its various processors with correlative measurements from ground-based lidars. EARLINET (European Aerosol Research Lidar Network) has been operating in Europe since 2000, providing the scientific community with the most comprehensive database of vertically resolved aerosol optical parameters in Europe. The EARLINET data can be used for a variety of purposes, including model evaluation and assimilation, full use of satellite data, research into aerosol long-range transport mechanisms, and monitoring of special events such as volcanic eruptions, large forest fires, and dust outbreaks.

EARLINET's QA/QC program allows for the determination of the uncertainty of signals at all wavelengths individually as well as their ratios (lidar ratio, linear depolarisation ratio) over the entire detection range from 200 m to 15 km, which serves as the foundation for error estimation of the final lidar products. Techniques have been developed to indirectly determine contributions from various error sources in the lidar system. These systems are undergoing continuous quality assurance testing, to provide good quality, reliable and inter-comparable data products [5].

In this study, a comparison between the L2a EBD data from the ATLID instrument and ground-based data obtained from the EARLINET network [6] is presented, highlighting the correlation between the measurements performed with the different instruments. The effect of the satellite overpass distance on the correlation between the two is also studied.

Methodology

In this study, the EarthCARE overpasses over the EARLINET stations are obtained through the ESA Online Dissemination Service (OADS) [7], by sequentially querying the database for each site's location. Satellite data which intersect a radius of 200 km in the vicinity of the site are downloaded, along with the ground-based measurements for each period of time in which a satellite overpass is present. The ground-based data is obtained from the EARLINET database, utilising the REST API offered as a means of harvesting data [8].

For the purpose of dataset quality, EarthCARE data was filtered in accordance with the following criteria:

- Data filtering according to *extended_data_quality_status* variable (only values of "0", meaning confirmed good data, are kept).
- Data filtering to exclude negative data points for strictly non-negative physical parameters.
- Data filtering to exclude point which have an uncertainty higher than 10 times the measured value.

High uncertainties are expected in the EarthCARE data, as this study looks at the high horizontal resolution profiles provided in the A-EBD files, corresponding to about 140 m horizontal resolution. The short integration time has a significant impact on the signal-to-noise ratio of the lidar profiles measured, however for the purpose of this study we accepted datasets with a high relative uncertainty in order not to filter out too many data points. Statistical analysis is performed on the medium- and low-resolution products offered by the A-EBD processor.

All ground-based data is re-gridded to the native EarthCARE grid (100 m vertical resolutions for altitudes lower than 20.2 km, and 500 m for altitudes up to 40 km), using a weighted binning approach. An example of such a re-grid is shown in Figure 1, presented for a 30-minute averaged particle backscatter coefficient profile. With the re-gridding, data measured by the ground-based lidar and ATLID level 2 data is directly comparable, bin by bin.

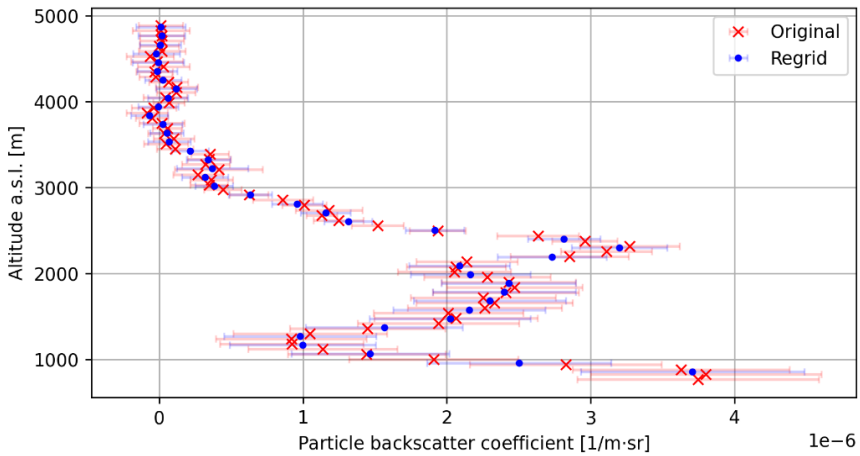

Figure 1 - Example of regridded ground-based data compared to the original measurement

Results and Discussion

Preliminary results show good correlation between the ATLID instrument measurements and ground-based lidar measurements. The comparison is shown in figures 2, 3 and 4, for the particle backscatter coefficient, the particle extinction coefficient and the particle linear depolarization ratio, respectively.

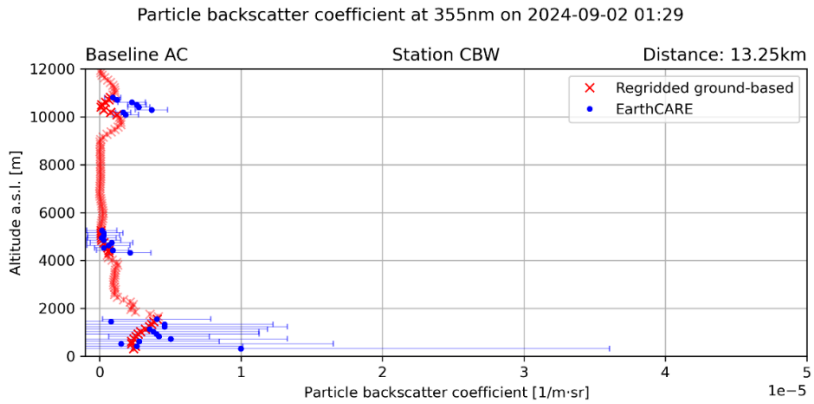

Figure 2 - Example of particle backscatter coefficient from ground-based lidar at Cabauw, Netherlands station collocated with EarthCARE ATLID measurement

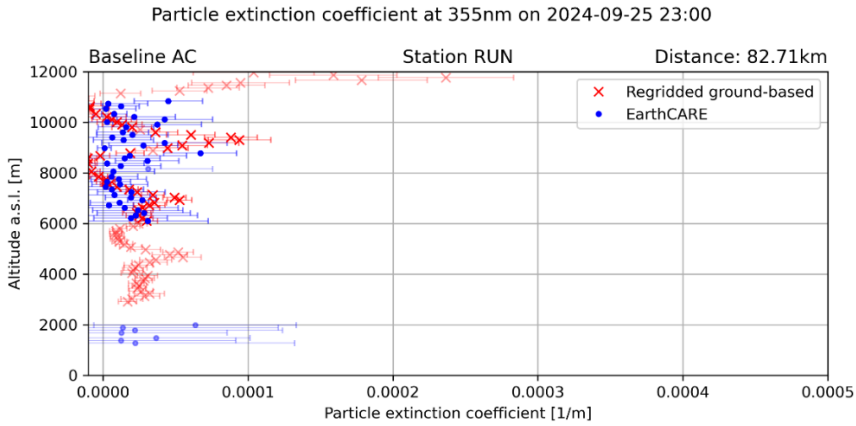

Figure 3 - Example of particle backscatter coefficient from ground-based lidar at Observatoire de Physique de l'Atmosphère de La Réunion (OPAR), Saint-Denis site, La Reunion, France station collocated with EarthCARE ATLID measurement

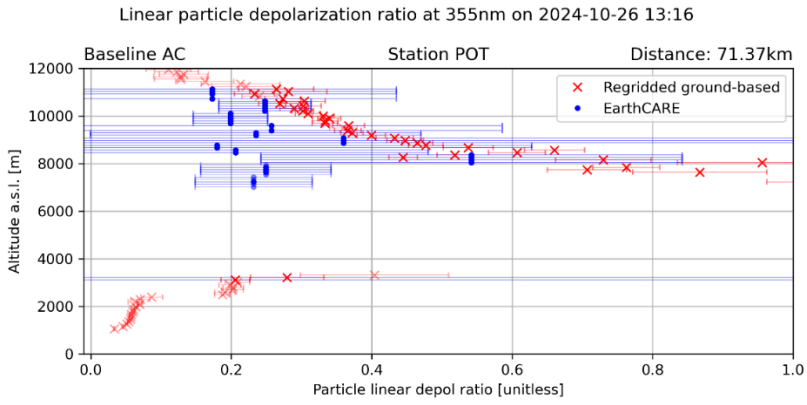

Figure 4 - Example of particle backscatter coefficient from ground-based lidar at Potenza, Italy station collocated with EarthCARE ATLID measurement

This study further includes the statistical correlation measures between the ground-based measurements and ATLID data (not shown), for which all overpasses on all EARLINET stations were used. The "overpass distance"-dependent correlation coefficients are derived, providing insights on the importance of good spatio-temporal collocations of the ground-based and satellite measurements, also dependent on the specifics of the site and its geographical surroundings (flat terrain, mountain or seaside area). These coefficients are useful as a guideline for proper spatio-temporal collocation of ground-based and EarthCARE data.

Conclusions

Preliminary results show a good qualitative correlation between ATLID and ground-based lidar measurement, particularly in terms of the detection of similar aerosol layer heights, alongside the layers having similar properties. Having looked at the high horizontal-resolution ATLID data, which features a lower signal-to-noise ratio than the low- and medium-resolution data, associated uncertainties are significant. Thus, stating that the agreement is good requires a deeper analysis, especially regarding other possible factors that can contribute to the disagreement between the two data sources, such as improper spatio-temporal collocation or other forms of unwanted biases in the data.

Acknowledgements

This work was financed by the Core Program within the Romanian National Research Development and Innovation Plan 2022-2027, carried out with the support of MCID, project no. PN 23-05, the ATMO-ACCESS H2020 Grant Agreement no. 101008004, and by the European Commission under the Horizon Europe – Research and Innovation Framework Programme, through the PANORAMA project under grant agreement No 101182795.

In this work we used data from European Space Agency, 2025, "EarthCARE ATLID EBD Level 2A", (version AE) doi: https://doi.org/10.57780/eca-5ff79cd and the ACTRIS-EARLINET Open Access Database (link: https://data.earlinet.org/)

References

[1] "EarthCARE." Accessed: Apr. 14, 2025. [Online]. Available: https://www.esa.int/Applications/Observing_the_Earth/FutureEO/EarthCARE
[2] "ATLID Overview." Accessed: Apr. 14, 2025. [Online]. Available: https://earth.esa.int/eogateway/instruments/atlid
[3] D. P. Donovan and G.-J. van Zadelhoff, "Product Definition Document (PDD)".
[4] D. P. Donovan, G.-J. Van Zadelhoff, and P. Wang, "The EarthCARE lidar cloud and aerosol profile processor (A-PRO): the A-AER, A-EBD, A-TC, and A-ICE products," *Atmos. Meas. Tech.*, vol. 17, no. 17, pp. 5301–5340, Sep. 2024, doi: 10.5194/amt-17-5301-2024.
[5] L. Belegante, C. Talianu, A. Nemuc, V. Nicolae, G. Ciocan, F. Toanca, O. Tudose, C. Radu, and D. Nicolae, "Lessons learnt during the first Quality Assurance exercise of the ACTRIS high-power lidars," *JOURNAL OF OPTOELECTRONICS AND ADVANCED MATERIALS*, vol. 26, no. 9–10, pp. 422–432, Sep. 2024.
[6] "EARLINET." Accessed: Apr. 14, 2025. [Online]. Available: https://earlinet.eu/
[7] "ESA EarthCARE Online Dissemination Service." Accessed: Apr. 14, 2025. [Online]. Available: https://ec-pdgs-dissemination2.eo.esa.int/oads/access/collection/EarthCAREL2InstChecked
[8] "Database." Accessed: Apr. 14, 2025. [Online]. Available: https://www.earlinet.org/index.php?id=125

The EARLINET Single Calculus Chain Module for the Retrieval of Optical Products at Multiple Wavelengths – Update on ELDAmwl

I. Mattis[1], *V. Jaenisch* [2], *G. D'Amico*[3], *P. Gumà-Claramunt*[3], *C. Dema*[3], *V. Freudenthaler*[4]

(1) Deutscher Wetterdienst, Meteorologisches Observatorium Hohenpeißenberg, Germany
(2) inqbus Scientific Computing GmbH, Burggen, Germany
(3) Consiglio Nazionale delle Ricerche - Istituto di Metodologie per l'Analisi Ambientale (CNR-IMAA), Potenza, Italy
(4) Ludwig-Maximilians-Universität, Meteorologisches Institut, München, Germany

Corresponding author: ina.mattis@dwd.de

Introduction

The EARLINET Single Calculus Chain (SCC) is an automated, publicly accessible tool for processing lidar data, operational for over a decade. It integrates specialized modules for pre-processing, cloud screening, optical property retrieval, layer detection, and visualization [1], [2]. The current module for the optical retrievals "EARLINET Lidar Data Analyzer" (ELDA) retrieves and optimizes optical properties (backscatter/extinction coefficients, depolarization ratios) independently for each wavelength. ELDA is currently replaced by a new module ELDAmwl which retrieves all optical products at all wavelengths on the same output grid with a common quality assurance module in a synergistic way.

Currently, ELDAmwl is running on the SCC development server where it can be tested by voluntary users. A first user group was trained on setting up an ELDAmwl configuration during a CARS webinar.

The ELDAmwl software prioritizes high modularity and expandability [3]. New improved modules for the calibration of backscatter retrievals and for the calculation of lidar constants have been introduced in [4]. Here, we are going to report about the structure of the new output file format and the new module for internal quality control of individual products and all products together.

General aspects of ELDAmwl

ELDAmwl is written in Python, using well established packages like *SQLalchemy* for the database interface, *Xarray* for handling NetCDF files and as internal data containers, *Sphinx* for automatically generating API documentation from in-code comments, unittest for automated testing. ELDAmwl has a plugin structure which allows for flexible adding new or replacing existing calculus modules. Versioning of the code and cooperation between several developers is organized with *Git*. The code is publicly available at https://github.com/actris-scc/ELDAmwl.git.

The user can define two grids for temporal averaging and vertical smoothing. One grid is meant for products which are retrieved with high resolution (e.g. backscatter coefficients), the other one for products with low resolution (e.g. lidar ratios). The user can define, which product shall be derived with low resolution or high resolution or both resolutions in parallel. The grids are part of the SCC configuration of the ELDAmwl and are applied to all measurements which are analyzed with the same configuration.

The internal workflow is as follows:

1. Read from *SCC database* what to do. Which products shall be derived with which parameters?
2. Read pre-processed signals which were generated by the SCC module *ELPP*
3. Prepare the signals for further retrievals. E.g.,
    - Temporal averaging
    - Correction for Rayleigh transmission,
    - Combining cross and parallel polarized components to total signals
4. Calculate basic products. Basic products are directly derived from the signals, those include:
    - Particle backscatter coefficients
    - Particle extinction coefficients

- Volume linear depolarization ratio (VLDR)

5. Calculate derived products. Derived products are those, which are derived from previously derived basic products, like:
    - Lidar ratio
    - Particle linear depolarization ratio (PLDR)
    - Angstrom exponent
6. Perform quality control of individual products and all of them together (see below)
7. Generate one output file with all results (see below)

The new ELDAmwl module for quality control

The quality control in ELDAmwl is applied at different levels from tests of individual data points to multi-product tests. Each test attaches a binary flag to the data points, profiles, or products. Those flags can be added without loosing the information of individual flag values.

1. Individual data points of basic and derived products are inspected and flagged concerning
    a. Data points below the full overlap or above the maximum altitude. These ranges can be enlarged due to vertical smoothing
    b. too large errors. Data points are flagged if their absolute and relative uncertainties are above thresholds. If only one threshold is exceeded, the point is still valid.
    c. negative data points are flagged if the data and their range of uncertainty are negative. The range of uncertainty is defined as the calculated uncertainty multiplied with a flexible factor which can be set by SCC operators. Currently, the factor is 2.
    d. Data points outside a valid data range. Most geophysical quantities have to be positive, but some have also maximum values, e.g. VLDR or PLDR cannot be larger than 0.5. data points above the maximum value are handled in the same way as negative data points
    e. aerosol free layers. Some geophysical properties are not defined in altitude regions without aerosol particles, e.g. particle lidar ratio or particle linear depolarization ratio. In order to decide which altitude ranges have too few particles, ELDAmwl calculates or estimates the backscatter ratio at 532nm and uses thresholds of this quantity for the decision.
    f. flag isolated data points. After performing all the previous tests, it can happen that single data points or small groups of data points without valid neighbors remain unflagged. A point is considered “single” if it and its directly adjacent valid neighbors do not cover a vertical range of at least 100m or half of the corresponding vertical resolution. Figure 1 illustrates this test. For this measurement example, there are adjacent valid data points up to 4km height and three small patches of valid points between 6 and 9km height. After performing the test, the two patches between 6 and 8km are considered too small. They are flagged with value 1024 (marked with dark cyan line). Only the regions of valid points below 4km and between 8 and 9km height are large enough to pass the test.
2. Products are derived for several time slices (profiles) with the same parameters, but the retrievals are calculated independently. Therefore, individual profiles are checked and flagged concerning
    a. too many negative data points or data points outside the valid data range.

b. too large integral values. This test is important in case of elastic backscatter retrievals and in order to detect cloud contamination.

3. If all profiles of an individual product are flagged during the previous step, the complete product retrieval is marked as failed.
    a. If the failed product is a basic product, all corresponding derived products are marked as failed, too. In addition, if the failed product is a VLDR and the corresponding backscatter is calculated from cross and parallel polarized signal components, we have to assume that this backscatter is failed, too.
    b. If products of intensive aerosol properties are out of the valid data range, the corresponding basic products are flagged. In an iterative approach, ELDAmwl will remove the basic product with most tags until no failed derived products remain.

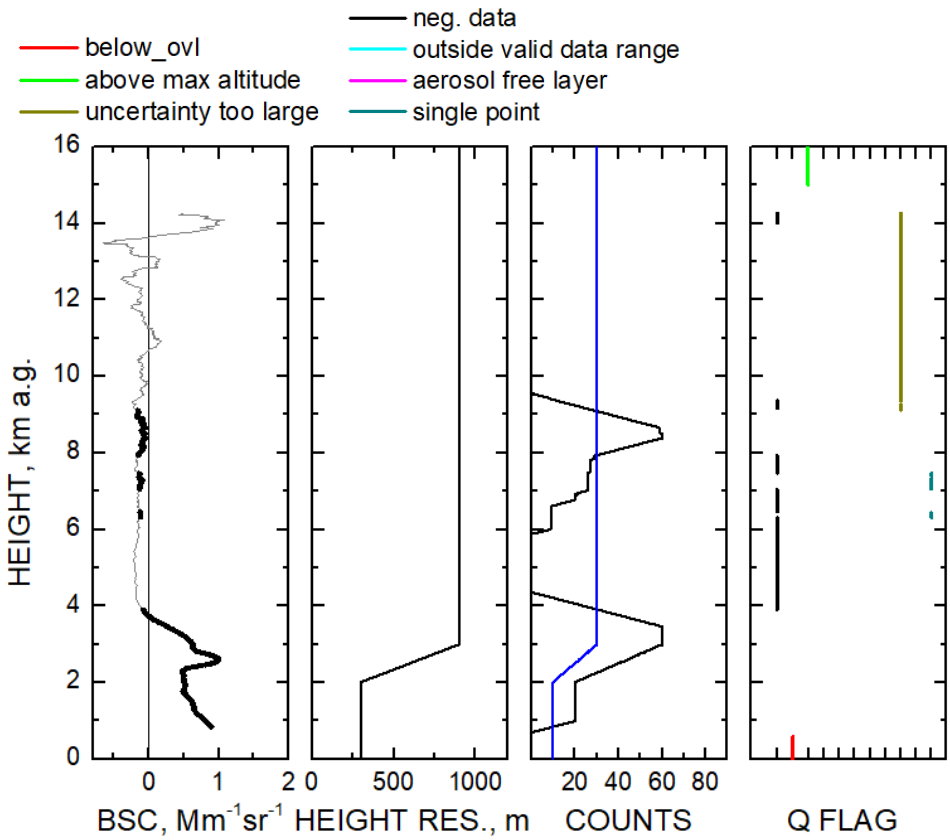

Figure 1. Illustation of detecting single data points. Left panel: the backscatter profile after tests a-e with valid data points in bold and invalid data points as thin line. Second panel: corresponding height resolution, third panel: number of valid neighbors (black) and minimum required number of valid neighbors depending on vertical resolution (blue). Right panel: quality flags.

The new output file format

All retrieved optical products and all relevant meta information for traceability are written into one output file per measurement. The output file format is NetCDF. The file structure was tested for compatibility with CF convention CF 1.8. The filename is consistent with the filename convention of all other SCC modules. It contains the station id, type of product, start and end time of the data, measurement id, the processing SCC module and its version. Each file consists of three groups.

1. ***highres_products***: contains all basic and derived products which were derived with high resolution and their related coordinates (wavelength, time, time_bounds, altitude, vertical_resolution) together with the corresponding cloud mask. Each geophysical property (e.g. particle backscatter coefficient or lidar ratio) is provided as 3-dimentional matrices (wavelength, time, level) for the data itself, for the retrieved uncertainties, and for the quality flags. All geophysical properties in this group have the same dimensions and coordinates. Thus, all properties can be easily used together. In addition, each product has a link to the corresponding meta data in the third group, e.g., *backscatter_meta_data* (wavelength) = ['/meta_data/backscatter_355', '/meta_data/backscatter_532', '/meta_data/backscatter_1064'].
2. ***lowres_products***: same as above, but for all products which were derived with low resolution
3. ***meta_data***: while the first groups are designed for the needs of end users, this group is meant for expert users and machine based analysis. It contains sub groups for each product, e.g. "*backscatter_1064*". Therein are input parameters and settings of the corresponding retrieval, e.g., *retrieval_method* = 1 (= elastic backscatter), *evaluation_algorithm* = 0 (= Klett / Fernald), *error_retrieval_method* = 0 (= Monte-Carlo), *assumed_particle_lidar_ratio* as function of time and level. Those parameters guarantee traceability and allow the analysis of data quality on expert level and by automated routines.

Conclusion and outlook

The development of ELDAmwl has made further progress. The latest version is currently tested at the SCC development server. Nevertheless, we need more test measurements from a variety of different lidar systems to make sure that ELDAmwl is operating stable before it can be released on the operational server. Next steps are the implementation of routines for the handling of signals from different telescopes and numerical optimization of calculation performance.

Acknowledgements

The quality control module was developed during a TNA visit at CIAO, IT (OBS) facility which was supported by the ATMO-ACCESS project (ATMO-TNA-3--0000000105). ATMO-ACCESS was supported by the European Commission under the Horizon 2020 – Research and Innovation Framework Programme, H2020-INFRAIA-2020-1, Grant Agreement number: 101008004.

References

[1] D'Amico, G., Amodeo, A., Baars, H., Binietoglou, I., Freudenthaler, V., Mattis, I., Wandinger, U., Pappalardo, G.: *EARLINET Single Calculus Chain – overview on methodology and strategy*, AMT, 8, 4891–4916, 2015.

[2] Mattis, I., D'Amico, G., Baars, H., Amodeo, A., Madonna, F., Iarlori, M., *EARLINET Single Calculus Chain – technical – Part 2: Calculation of optical products*, AMT, 9, 3009–3029, 2016.

[3] Mattis, I.: *New developments in the SCC: multiwavelength product (ELDAmwl)*, ACTRIS week, 26-28 October 2020

[4] Mattis, I., V. Jaenisch, G. D'Amico, P. Gumà-Claramunt, C. Dema, V.Freudenthaler: *The EARLINET Single Calculus Chain Module for the Retrieval of Optical Products at Multiple Wavelengths – Update on ELDAmwl*, Book of abstracts, European Lidar Conference 2023, Cluj-Napoca, Romania, 2023.

Stationary and Mobile Lidars for Validation of ATLID in Urban and Rural Environment

A. Hafiz[1], *D.M. Szczepanik*[1], *I.S. Stachlewska*[1]

(1) University of Warsaw, Faculty of Physics, Institute of Geophysics, (UW), Pasteura 5, 02-093, Warsaw, Poland

Corresponding author: Afwan.hafiz@fuw.edu.pl

Introduction

The EarthCARE (Earth Cloud Aerosol and Radiation Explorer) satellite mission is carried out by the collaboration of ESA (European Space Agency) and JAXA (Japan Aerospace Exploration Agency). EarthCARE has several instruments dedicated to profiling Earth's atmosphere. Among them, the high-spectral resolution atmospheric lidar ATLID provides profiles of backscattering, extinction, and depolarization ratio at 355 nm [1]. Thanks to the EarthCARE Cal/Val Pilot of the ATMO-ACCESS project, both the PollyXT-UW lidar at the Warsaw Observatory Station (WOS; ACTRIS facility offered for TNA access) of the Institute of Geophysics, Faculty of Physics, University of Warsaw, and the ESA Mobile Raman Lidar (EMORAL) were deployed for the calibration and validation activities.

The primary focus of these effort was to compare the L2-ATLID and the SCC-derived EMORAL and PollyXT-UW data products [2], [3], [4]. Both ground-based lidars operate with 3 wavelengths (λ) pulsed-laser simultaneously (355mn, 532nm, and 1064nm). Both can retrieve optical profiles of 3 backscattering coefficients at all wavelengths, 2 extinction coefficients and depolarization ratios at both 355nm and 532 nm ($3\beta+2\alpha+2\delta$). We discuss the results of a case study focusing on the Cal/Val for a special case of simultaneous measurements taken in urban (Warsaw PollyXT-UW; 52.21°N, 20.98°E) and rural (Ojrzanów, EMORAL; (52.011°N, 20.735°E) environments on 13-14 December 2024 during clear sky conditions for the nighttime overpass of EarthCARE over Poland.

Methodology

We performed comparison for collocation measurement based on the criteria that the single satellite track is close enough to the Warsaw stationary site (< 30 km; much more strict than EarthCARE Cal/Val Pilot rule of < 100 km) [3], placed the mobile facility in a rural environment in a close vicinity of that overpass (< 5 km), the distance of the two ground-based locations had to be kept within 30 km (Figure 1). Further constraint was to target the lidars collocation with the nighttime overpass, since this allows for the Raman detection and retrieval of the aerosol properties without assumptions of the so-called lidar ratio. Nighttime measurements enable additionally the detection of water vapor (both lidars) and fluorescence (solely EMORAL), which can be extremely useful in the interpretation of the **ATLID L2A (baseline AC)*** data products, especially in terms of the aerosol typing. The measurement taken in such demanding conditions and with such large and diverse detection possibilities serve as a great and rather unique dataset for comparison with ATLID.

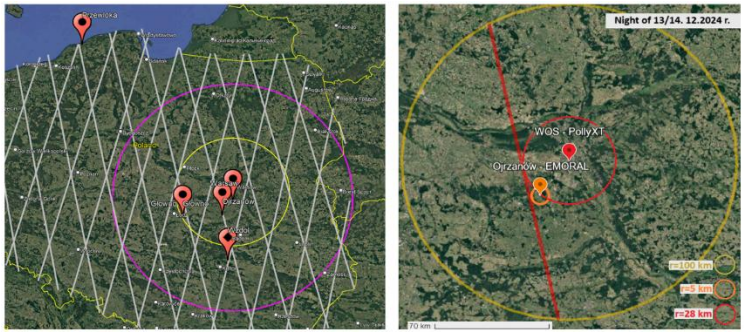

Figure 1. (left) Map of part of Poland territory with gray line as the predicted EarthCARE orbits, red pins are the location of measurement of ground-based lidars (EMORAL and PollyXT-UW), and magenta circle is the 200km radius from WOS; (right) Map with the WOS (red pin) and Ojrzanów (orange pin) measuring sites marked with the distance (circles) from the EarthCARE overpass (dark red line). The yellowish circle shows the distance of 100 km from WOS.

Aerosol optical properties profiles were retrieved using the Single Calculus Chain [5] for both lidars with the use of the Quality Assured configurations confirmed by ACTRIS CARS. ATLID L2 data products are downloaded from the ESA EarthCARE Database. The water vapor and fluorescence-related products are calculated using the in-house developed at UW tool – EMERALD. The target classification for EMORAL and PollyXT-UW was derived using the in-house developed at UW tool LiRaMi algorithm, Version: LiLi (only lidar data fed into the algorithm) [6]. For comparative analysis, we used the ground-based lidars optical properties derived from profiles averaged 30-60 minutes, covering at maximum ± 2 hours from overpass time with the least absolute difference with the corresponding ATLID products.

Results and Discussion

The quicklook plots from the three lidars (Figure 2) indicate the general atmospheric situation during the overpass. The atmosphere above ~1.5km was clear sky, with no aerosol and cloud layers. Hence, this analysis focuses on altitude range < 2 km. Note that the PollyXT-UW observations vary more over time.

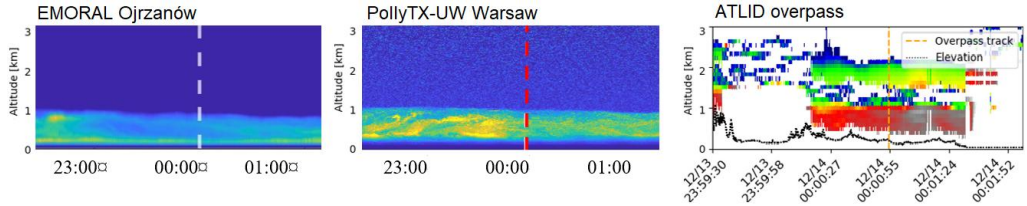

Figure 2. Lidar quicklook plots for data collected between 22:30 UTC on 13.12.2024 and 01:30 UTC on 14.12.2024 by EMORAL (a) and PollyXT-UW (b), and between 00:00:04-00:01:52 UTC by ATLID (c); Lidar plots are shown from surface up to 3km (no aerosol above)

Aerosol extinction (α) and backscatter (β) coefficients profiles (Figure 3) indicate more similarities in the latter. Comparison of β shows good agreement between the three lidars. As expected, EMORAL shows better agreement with ATLID because it is located much closer and measures in similar conditions (i.e., at the rural site, with no city effect). We can also observe structures in both EMORAL and ATLID, a layer at 0.7-1 km (similar signal strength in β), and a weaker layer at 1.5-1.8 km (ATLID slightly underestimated β). The comparison of α is more complicated as the ATLID error is quite large. We can still see the two layers, but ATLID underestimates the signal at lower layer and slightly overestimates at higher layer. In case of PollyXT-UW the backscattering profile can be affected by the urban heat island effect, which can demonstrate itself with slightly higher atmospheric boundary layer (ABL). The layer at 1.5-1.8 km is also visible in the PollyXT-UW profile but it is less pronounced than in the EMORAL or ATLID.

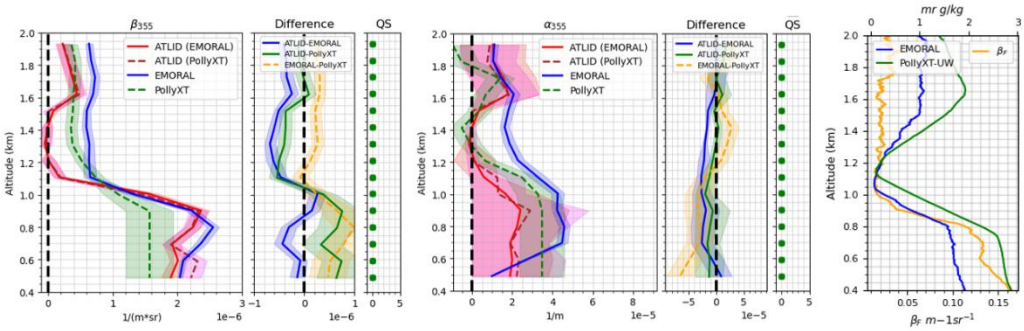

Figure 3. Comparison of backscatter (β) and extinction (α) coefficient at 355nm from ATLID (red), EMORAL (blue), and PollyXT-UW (green); the differences between ATLID vs EMORAL (blue) and ATLID vs PollyXT-UW (green) and EMORAL vs PollyXT-UW (orange) are also given along with the quality status (QS) of L2 products. Right plot depicts the Fluorescence backscatter (β_F) (EMORAL only) and water vapor mixing ratio (mr) (EMORAL in blue, PollyXT-UW in green). Please note that for extinction comparison, the EMORAL and PollyXT-UW are normalized to ATLID at the range identified as clear conditions.

In the case of α-profiles, PollyXT-UW demonstrates better agreement with ATLID than EMORAL, particularly in the free troposphere (FT) between 1.2 and 1.6 km. EMORAL shows notable discrepancies when compared to both ATLID and PollyXT-UW. These differences may, in part, be attributed to varying atmospheric conditions: Ojrzanów, located approximately 30 km from Warsaw, can be considered a background site. Given the meteorological situation, it is possible that the ABL over Ojrzanów was more polluted due to emissions from household heating systems. In the free troposphere (FT), all extinction profiles show good agreement, however, the uncertainty in the ATLID signal remains significant.

The β_F above 0.9km is quite low, $< 0.05\ m^{-1}sr^{-1}$, the signal increases up to $0.15\ m^{-1}sr^{-1}$ closer to the ground, with additional weak structure observed between 0.6-0,8km. The water vapor mixing ratio (mr) is relatively low, between 0.1 gr/kg up to 2.0 and 2.8 gr/kg for EMORAL and PollyXT-UW, respectively, indicating dry condition (with the drop between 0.9 – 1.5km). Within this range in β comparison, ATLID signal is transitioning from "well-fitting" to EMORAL to "underestimated", and then getting close to EMORAL value starting from 1.5km. This behavior is not clearly observed in α, although the difference between ATLID and EMORAL does get slightly larger at the altitude where the β_F and $wvmr$ are at the lowest. Classification target comparisons show only slight discrepancies in the lowermost atmosphere, < 1km (Figure 4), which can be explained with the highly variable fluorescence.

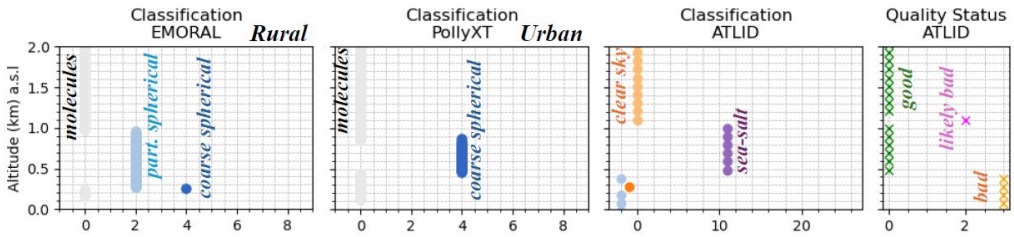

Figure 4. Comparison of Target Classification (TC) products retrieved from EMORAL and PollyXT-UW with ATLID (both closest in time to overpass results were the same). The color code for EMORAL and PollyXT-UW: grey: molecules, blue: partly non-spherical aerosol, and dark blue: coarse spherical aerosol. The color code for ATLID: light orange: clear condition, grey: surface, orange: noise, purple: sea salt. ATLID data quality status; green-cross: good, magenta-cross: likely bad, and orange-cross: bad

The resulting classification from the three lidars shows a good agreement for clear-sky condition, with small differences of the exact altitude where the clear-sky started (EMORAL 1.0 km; PollyXT-UW 0.9 km; ATLID 1.1 km). This can be explained by ATLID lower vertical resolution. Interestingly, the layer between 0.5-1.0km identified as partly non-spherical aerosol (EMORAL), coarse spherical aerosol (PollyXT-UW), and sea-salt (ATLID); data < 0.5 km is excluded, due to ATLID bad-data quality status. The type estimation by EMORAL and PollyXT-UW are realistic and the difference between the two can be accommodated by distance and city effect (Warsaw urban site). It is unlikely that ATLID detects sea-salt in this location during the overpass (closest sea ~300km to the north). However, sea-salt might not be fully excluded due to the winter road maintenance and sprinkling of the surface with mixture of salt and sand to reduce the slipperiness of the ground.

Conclusions

The analysis indicates good agreement between ATLID, EMORAL, and PollyXT-UW, with small variabilities observed below 2km. Comparison of β and α between EMORAL and ATLID have better agreement which can be associated with much closer collocation measurement as compared to PollyXT-UW, and PollyXT-UW location being much closer to the urban city of Warsaw. Further analysis is required to clarify aerosol type differences at 0.5-1km which is in general tricky for the satellite data. The use of water vapor and fluorescence signals from EMORAL are seen as additional input to understand and interpret these discrepancies.

Disclaimer

The present work includes preliminary data (not fully calibrated/validated and not yet publicly released) of the EarthCARE mission that is developed by the European Space Agency (ESA)and the Japan Aerospace Exploration Agency (JAXA). The analysis has been performed in the context of the EarthCARE Validation Team.

Acknowledgements

We thank the National Institute of R&D for Optoelectronics (INOE), Romania, for support and hosting of the EMORAL lidar during the EarthCARE Cal/Val Pilot Intercomparison Campaign in May 2024. The EarthCARE Cal/Val Pilot was realized as a part of the Trans-national Access program (TNA) within the EC-funded ATMO-ACCESS grant no.: 101008004. The ACTRIS National Facility in Warsaw is operationally supported since January 2024 by the Ministry of Science and Higher Education of Poland within ACTRIS-ERIC (grant no.: 2024/WK/04). The PollyXT-UW lidar was developed in a bilateral scientific collaboration of University of Warsaw (UW) and Leibniz Institute for Tropospheric Research (TROPOS) financed by the Polish Foundation of Science and Technology (FNTP-No. 519/FNITP/115/2010). We thank Opto-Electronics section (TEC-MME) at the European Space Research and Technology (ESTEC) of the European Space Agency (ESA) for providing the ESA Mobile Raman Lidar EMORAL developed in non-commercial scientific collaboration of University of Warsaw (UW), Ludwig Maximilian University of Munich (LMU), and Raymetrics S.A. within “Technical assistance for Polish Radar and Lidar Mobile Observation System (POLIMOS)” funded by ESA-ESTEC Contract no. 4000119961/16/NL/FF/mg. We thank R.Fortuna, L.Janicka, M.Karasewicz, W.Kumala, I.Okraska, P.Poczta, Z.Rykowska, A.Tomczak, and E.Ugboma for the operational running of PollyXT-UW and EMORAL lidars. We thank both ACTRIS Center for Aerosol Remote Sensing (CARS) for assessing the quality assurance of both lidars and ACTRIS Data Centre node for aerosol remote sensing profiling (ARES) for providing the data processing service.

References

[1] T. Wehr et al., The EarthCARE mission - science and system overview, Atmos Meas Tech, vol. 16, no. 15, pp. 3581–3608, Aug. 2023, doi: 10.5194/AMT-16-3581-2023.

[2] D. P. Donovan, G.-J. van Zadelhoff, and P. Wang, The EarthCARE lidar cloud and aerosol profile processor (A-PRO): the A-AER, A-EBD, A-TC, and A-ICE products, Atmos Meas Tech, vol. 17, no. 17, 5301–5340, Sep. 2024, doi.org/10.5194/AMT-17-5301-2024.

[3] V. Amiridis et al., Best Practice Protocol for the validation of Aerosol, Cloud, and Precipitation Profiles (ACPPV), doi.org/10.5281/ZENODO.15025627.

[4] I. S. Stachlewska et al., EMORAL—Mobile Mie-Raman Lidar with Fluorescence, Polarization and Water Vapor Observational Capabilities for Satellite Cal/Val Field Campaigns, Springer Aerospace Technology, vol. Part F2592, 239–251, 2024, doi.org/10.1007/978-3-031-53618-2_21.

[5] I. Mattis, G. D’Amico, H. Baars, A. Amodeo, F. Madonna, and M. Iarlori, EARLINET Single Calculus Chain - Technical - Part 2: Calculation of optical products, Atmos Meas Tech, vol. 9, no. 7, 3009–3029, Jul. 2016, doi.org/10.5194/AMT-9-3009-2016.

[6] D. Wang, I. S. Stachlewska, J. Delanoë, D. Ene, X. Song, and D. Schüttemeyer, Spatio-temporal discrimination of molecular, aerosol and cloud scattering and polarization using a combination of a Raman lidar, Doppler cloud radar and microwave radiometer, Opt Express, vol. 28, no. 14, 20117, 2020, doi.org/10.1364/oe.393625.

ATLID - one year after first light - performance, results and validation

G. Tzeremes[1], *J. v. Bismarck*[1],*F. Marnas*[1], *D . Bernaerts*[1], *B. Frommknecht*[2] , *K. Wallace*[1], *et al.*

(1) ESA, ESTEC, Noordwijk, Netherlands
(2) ESA, ESRIN, Frascati, Italy

Corresponding author: Georgios.tzeremes@esa.int

Introduction

EarthCARE was launched in 28th of May 2024 with a SpaceX Falcon 9. The ATLID instrument was first switched on a few days later on 10th of June, while we had first light coming out of the instrument on 25th of July. The schedule was primarily driven by the platform commissioning as well as the necessary decontamination phase (15 calendar days) essential for UV lasers operating from space. The instrument commissioning phase managed to reach hardware verification by 10th of August, allowing to take part in a series of Cal/Val activities at that time. The algorithm verification and validation continued throughout 2024 and early 2025. As of May 2025, ATLID EarthCARE Ground Processor ECGP is operating on version 5.1 with the data reprocessed in baseline BA from 11th of August till now.

Instrument Description

ATLID is a High Spectral Resolution Lidar, operating at 355 nm, with a depolarization channel. The lidar is bistatic with a transmitter that generates 26 ns pulses at a repetition rate of 51 Hz, with an average pulse energy around 31-35 mJ. The output beam is expanded so that the footprint at the ground is less than 15 m and pointed 3° backwards, to minimize potential specular reflection from ice clouds. There are two fully redundant pressurized transmitters.

The output beam from ATLID is linearly polarized. But the receiver optical train incorporates a polarization beam splitter that separates components cross and co-polar with respect to the emitted beam. The co-polar signal is further filtered by means of a high spectral resolution etalon filter, to separate the spectrally narrow signal at 355 nm from the part of the signal that has been spectrally broadened; this corresponds respectively to the scatter from aerosol particles (so called “Mie channel”) and the scatter from molecules (so called “Rayleigh channel”). Thus, there are three channels in the receiver, the cross-polar channel and the Rayleigh and Mie channels that are both co-polar to the emitted polarization. The channels are coupled via optical fibers to three Memory CCDs which collect signal response and time of flight, providing a vertical resolution of 103m from the ground up to 20km altitude and 500m in the range 20 to 40km altitude. Along-track the sampling distance is 140m, however two consecutive pixels are summed to increase the signal to noise ratio, resulting in a spatial resolution of 280m.

Preliminary Performance

Since its initial switch on last summer the instrument operates with an energy of about 31-35mJ without any measurable degradation. A decision was made during In Orbit Commissioning Review IOCR not to increase further the instrument energy (it is derated to ~20% of its total capabilities) since the SNR in space is about 25% better than anticipated on ground testing (due to less optimistic atmospheric attenuation modelling). In addition to the high energy stability, the instrument demonstrates an unparallel Frequency stability, with a drift of less than 50MHz over 1 year of operations.

The pressurization on both laser heads remains within nominal levels, ensuring operation above the corona effect region for a minimum of 10 more years.

All Performance indicators ensure us that the instrument can meet an extended operation lifetime exceeding the original mission requirements expectations.

ATLID Validation

The ground processor of ATLID ensures the provision of fully calibrated Level1 data. While some calibration coefficients have been fully characterized during ground testing and reported in the Calibration and Characterization Database (CCDB), some of the properties of ATLID are constantly monitored and updated in-flight.More precisely, the most sensitive part of the ECGP is the continuous evaluation of the various crosstalk coefficients for efficient inversion of the signals:

- The Rayleigh spectral crosstalk (Ɛ) is inferred from ground echoes or using a novel smoothness criteria on ratios of signals from dense clouds.
- The Mie spectral crosstalk (χ) is inferred from purely molecular signal in the high atmosphere and corrected from the vertical dependency in spectroscopic properties.
- The polarisation cross-talk values ($\psi^{\perp}$, $\psi^{//}$) are inferred from particle-free scenes.

Additionally, weekly dark-current maps (vertically resolved) are inferred for all channels and updated at processing level to ensure accurate radiometric calibration

The precise determination of these parameters will ensure the effective processing of the data.

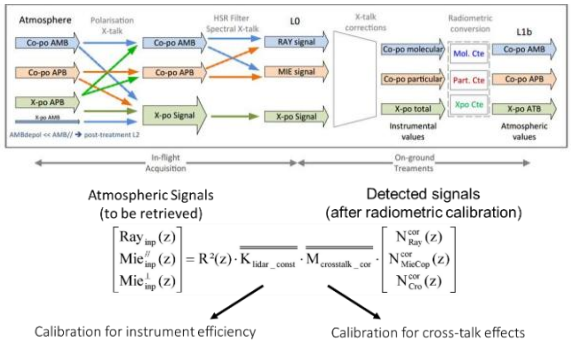

Figure 1: Schematic of the demultiplexing and of the cross-talk correction step

Conclusions

The ATLID history and performance is a demonstration of the dominance on Europe in the domain of Space lidar instrumentation, as well as the European Lidar scientific community to support the vision of a high power UV laser HSRL in space. This mission facilitates the road for Aeolus 2 mission as well as a pathfinder for a Copernicus Space Segment program.

References

[1] Wehr, T., Kubota, T., Tzeremes, G., Wallace, K., Nakatsuka, H., Ohno, Y., Koopman, R., Rusli, S., Kikuchi, M., Eisinger, M., Tanaka, T., Taga, M., Deghaye, P., Tomita, E., and Bernaerts, D.: The EarthCARE mission – science and system overview, Atmos. Meas. Tech., 16, 3581–3608, https://doi.org/10.5194/amt-16-3581-2023, 2023.

[2] do Carmo, J.P.; de Villele, G.; Wallace, K.; Lefebvre, A.; Ghose, K.; Kanitz, T.; Chassat, F.; Corselle, B.; Belhadj, T.; Bravetti, P. ATmospheric LIDar (ATLID): Pre-Launch Testing and Calibration of the European Space Agency Instrument That Will Measure Aerosols and Thin Clouds in the Atmosphere. *Atmosphere* **2021**, *12*, 76. https://doi.org/10.3390/atmos12010076.

[3] C. Haas, T. Belhadj, K.W. Kruse, G. de Villèle, M. Sauer, F. Chassat, B. Corselle, G. Tzeremes, J. Pereira do Carmo, K. Ghose, and K. Wallace "ATLID (ATmospheric LIDAR) integration and initial test results on EarthCARE satellite", Proc. SPIE 12777, International Conference on Space Optics — ICSO 2022, 127771I (12 July 2023); https://doi.org/10.1117/12.2689292

[4] Eisinger, M., Marnas, F., Wallace, K., Kubota, T., Tomiyama, N., Ohno, Y., Tanaka, T., Tomita, E., Wehr, T., and Bernaerts, D.: The EarthCARE mission: science data processing chain overview, Atmos. Meas. Tech., 17, 839–862, https://doi.org/10.5194/amt-17-839-2024, 2024.

Intercomparison of EarthCARE ATLID L2 Products with Ground-based Lidar Observations at El Arenosillo Station (Southwestern Iberian Peninsula): Preliminary Results on Selected Case Studies of Aerosol and Cloud Scenarios

C. Córdoba-Jabonero[1], *E. Leante-García*[2], *J. L. Guerrero-Rascado*[3,4]

(1) Instituto Nacional de Técnica Aeroespacial (INTA), Atmospheric Research and Instrumentation Branch, Ctra. Ajalvir km. 4, Torrejón de Ardoz, 28850, Madrid, Spain
(2) Universidad Complutense de Madrid (UCM), Ciudad Universitaria, Plaza Ciencias, 1, 28040, Madrid, Spain
(3) Andalusian Institute for Earth System Research (IISTA-CEAMA), 18006-Granada, Spain
(4) Department of Applied Physics, University of Granada (UGR), 18071-Granada, Spain

Corresponding author: cordobajc@inta.es

Introduction

The Earth Clouds, Aerosols and Radiation Explorer (EarthCARE) is a joint mission of the European Space Agency (ESA) and the Japan Aerospace Exploration Agency (JAXA) carrying four sensors: a cloud-profiling radar (CPR), a high-spectral-resolution cloud–aerosol lidar (ATLID), a cloud–aerosol multi-spectral imager (MSI), and a three-view broad-band radiometer (BBR). EarthCARE (EC) is devoted to investigating the aerosol-cloud-radiation interactions with the aim of enhancing the knowledge on the role of aerosols and clouds in the Earth-atmosphere energy balance, and hence their impact on the climate [1].

EC was launched at the end of May 2024, taking thus measurements for less than one year at the time of writing this abstract. Since then, diverse validation exercises are being currently performed. Within this framework, the purpose of this ongoing work is to introduce the first preliminary results obtained from the intercomparison of the ATLID L2 products with ground-based (G-B) lidar observations carried out at El Arenosillo station (ARN), one of the Spanish Institute for Aeroespace Technology (INTA) premises located at the southwest of the Iberian Peninsula. In particular, ATLID provides vertical profiles of particle extinction coefficient (σ_p), particle backscatter coefficient (β_p), lidar ratio (LR), and particle linear depolarization ratio (δ_p), among others, along the track of the satellite. Height-resolved polarized Micro-Pulse Lidar (P-MPL) measurements carried out at ARN were used for intercomparison purposes.

Methodology

Two case studies were selected, representing an aerosol and a cloud scenario, and being related to climate-relevant mineral dust particles and cirrus clouds. Moreover, the Aerosol Optical Depth (AOD) and the Cloud Optical Depth (COD) were also derived. Complementary, air mass backtrajectories were obtained using the HYbrid Single-Particle Lagrangian Integrated Trajectory (HYSPLIT) model from the National Oceanic and Atmospheric Administration (NOAA) web services (https://www.ready.noaa.gov/HYSPLIT.php) to likely assess EC target classification. Table 1 shows the selected cases with the day and closest time of the EC overpass, orbit/frame, minimum distance (d_{min}) between the EC ground-track and the G-B ARN station, and the aerosol/cloud scenario.

Table 1. Selected cases and information related to the EarthCARE overpasses.

Case	Day	Time (UTC)	d_{min} (km)	Orbit (frame)	Aerosol/cloud scenario
#1	30 August 2024	02:04	66.4	01449 (B)	Dusty mixture (likely dust+pollution)
#2	03 October 2024	14:48	5.5	01986 (D)	Cirrus

Satellite lidar methodology: EC L2 ATL-EBD (β_p, σ_p, δ_p, and LR) at 355 nm and ATL-TC (target classification, TC) products (baseline: AC; 103 m vertical resolution up to 20 km height, and 1 km horizontal resolution) [2] were downloaded for selected orbits (EC overpasses within a radius of 100 km around the station). In particular for case #1, ATLID profiles used in the comparison with P-MPL observations were those obtained at the minimum distance (d_{min}) due to the relatively long distance found for this case (see Table 1). For case #2, 17 ATLID (β_p, σ_p, δ_p, and LR) profiles within 10 km from the EC overpass to the

ARN station were averaged and used in this intercomparison study. A smoothing window (4 vertical points) is also applied along the ATLID β_p and σ_p profiles. The vertical errors for β_p and σ_p are obtained from the EC error data files in case #1, and the standard deviation is calculated for case #2 (averaged profile).

Ground-based lidar methodology: The ground-based lidar deployed at the ARN station (37.1ºN 6.7ºW; southwest of the Iberian Peninsula) is a polarized Micro-Pulse Lidar (P-MPL) in operation within NASA/MPLNET (Micro-Pulse Lidar Network, mplnet.gsfc.nasa.gov). MPLNET V3 L1.5 NRB (Normalized Relative Backscatter) products at 532 nm (75 m vertical resolution, and 1 min time integration) [3, 4], mainly containing the range-corrected signal and the volume depolarization ratio, were used. In particular for the selected cases (see Table 1), NRB profiles around ±5 minutes of the time of the closest EC overpass were averaged, and then β_p and δ_p profiles were retrieved and used in this intercomparison study. In the aerosol scenario (case 1), for comparison purposes, the ATLID LR is used for computing σ_p as obtained from the elastic P-MPL β_p, neglecting plausible differences associated with the retrieval methods. In the cloud scenario (case #2), the procedure described in [5, 6] is used to compute σ_p for cirrus clouds.

Results and Discussion

Case #1: 30 August 2024 at 02:04 UTC. This case corresponds to an aerosol scenario. Figure 1 shows β_p (km^{-1} sr^{-1}), LR (sr), and δ_p at 355 nm along the EC trajectory over the ARN station (a red dashed line indicates the overpass at the minimum distance from the station). Figure 2 shows the profile comparison of the optical properties between EC ATLID and G-B P-MPL retrievals, together with the EC target classification (TC) and data quality status (QS).

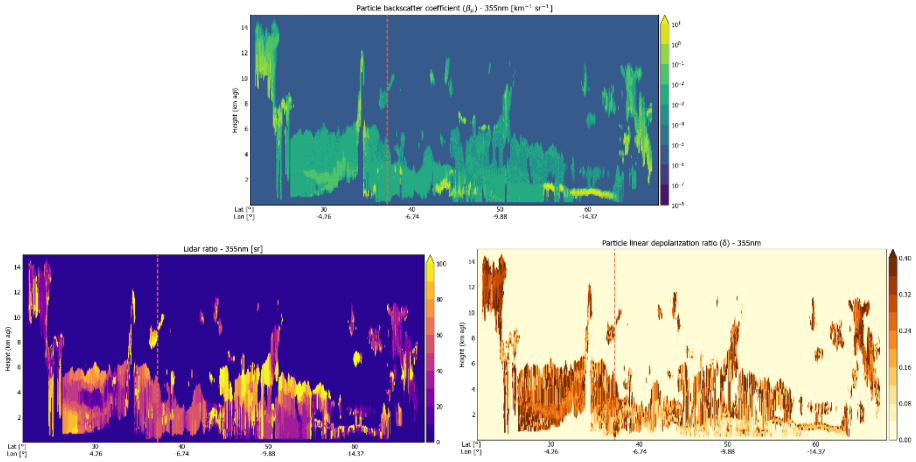

Figure 1. EC profiling of: (Top) particle backscatter coefficient (β_p, km^{-1} sr^{-1}), and (Bottom, left) lidar ratio (sr), and (Bottom, right) particle linear depolarization ratio (δ) at 355 nm along the satellite trajectory over the ARN station on 30 August 2024 at 02:04 UTC (case #1). The closest distance from the station is marked by the red dashed line.

The EC overpass is at 66 km minimum distance from the station (see Table 1). Discrepancies in the vertical structure can be associated to the relatively long distance. An EC mean LR of 51±3 sr is obtained. EC δ_p values range in a wide interval. The EC Target Classification scheme indicates 'Continental pollution' (TC=12, predominantly); however, HYSPLIT backtrajectories (not shown) indicated air masses coming from the Saharan region, likely carrying mineral dust (coarse) particles, but EC δ_p values are lower than those expected for Saharan dust. This could affect the target classification. The aerosol scenario could likely correspond to dusty mixtures (i.e. a mixture of dust and pollution). The EC and G-B AOD is 0.250 and 0.183 (LR^{EC}=51.3 sr at 532 nm), respectively. The ratio between them is 73%, reflecting the discrepancies due to the wavelength differences. Indeed, similar values are found for the AERONET AOD ratio

(AOD^{500}/AOD^{340}), which is ranging from 72% to 80% on 29-30 August 2024 (daytime measurements). Top aerosol boundaries are likely coincident (< 5 km height).

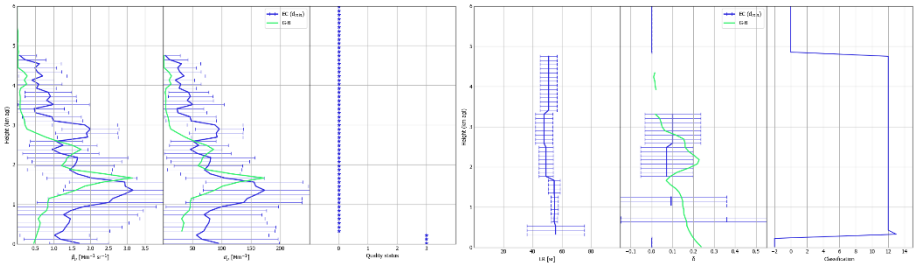

Figure 2. EC profiles at 355 nm of: (From Left to Right) particle backscatter coefficient (β_p, Mm^{-1} sr^{-1}), particle extinction coefficient (σ_p, Mm^{-1}), data quality status (QS), lidar ratio (LR, sr), particle linear depolarization ratio (δ_p), and target classification (TC) on 30 August 2024 at 02:04 UTC (case #1). Error bars correspond to the EC error data. G-B P-MPL β_p and σ_p (LR^{EC}=51.3 sr) profiles are also included (green lines).

Case #2: 3 October 2024 at 14:48 UTC. This case corresponds to a cloud scenario, particularly a cirrus case. Figure 3 shows the β_p (km^{-1} sr^{-1}), LR (sr), and δ_p at 355 nm along the EC trajectory over the ARN station (a red dashed line indicates the overpass at the minimum distance from the station). Figure 4 shows the profile comparison of the optical properties between ATLID and P-MPL retrievals, together with the EC target classification (TC) and data quality status (QS).

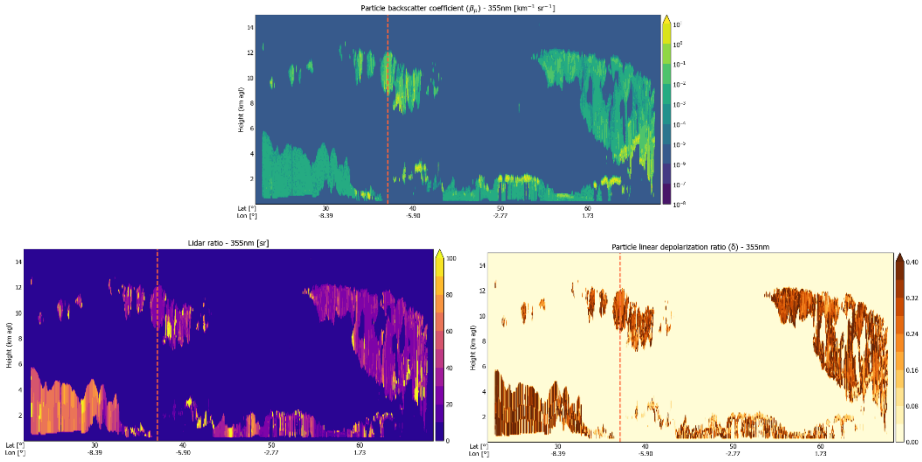

Figure 3. The same as Fig.1 but for the case #2 on 3 October 2024 at 14:48 UTC.

The EC overpass over the station is rather close (d_{min} = 5.5 km). Although EC and G-B cloud boundaries (base-top heights) are relatively similar, 8.6-12.0 and 8.4-11.8 km, respectively, COD values are rather different (2.15 and 0.38, respectively), being one order higher for EC. This could be expected due to the high cloud variability despite the close distance between the EC overpass and the ARN station. An EC mean LR of 21±2 sr is obtained. In addition, there are differences in the mean δ_p: EC values are lower (0.22±0.06) with respect to G-B (0.31±0.12). Nevertheless, the EC Target Classification scheme indicates 'Ice' (TC=3) corresponding to the cirrus cloud presence regarding the LR and δ_p values, with a good quality of the data (QS=0).

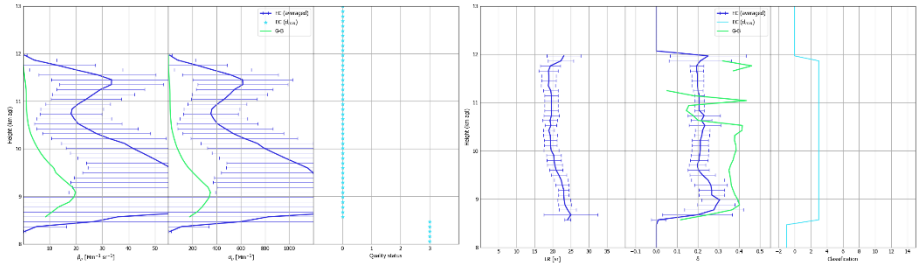

Figure 4. The same as Fig. 2 but on 3 October 2024 at 14:48 UTC (case #2). Error bars correspond to the standard deviation of the averaged EC profiles. G-B P-MPL β_p and σ_p (LR^{EC}=20.6 sr) profiles are also included (green lines).

Concluding remarks

(a) Depolarization ratio issues: The observed δ_p values tend to be lower, which affects the target classification. Indeed, the incorrect background correction observed in the EC L1 (AC baseline) products affects the calibration of the cross-polar channel in the L1 processor causing the cross-polar attenuated backscatter to be too low. In addition, according to the *EarthCARE Product Disclaimer – A-PRO* document, the A-PRO processor (v. 11.4) is generally performing well; however, futher improvements are needed in the classification procedures. *(b) Cloud Optical Depth (COD) discrepancies:* Significant differences have been observed, which may be expected given the high variability of cloud properties, even though the EC overpass is relatively close to the ARN station. Additional cirrus cloud cases need to be analyzed. *(c) Aerosol Optical Depth (AOD) variability:* While comparable AOD values are observed, discrepancies may arise due to the different wavelengths used by the lidar systems. *(d) The remaining EC overpasses* (30 cases in total, to be examined by the end of February 2025) should be analysed to enable a comprehensive statistical evaluation. The present work includes preliminary data (not fully calibrated/validated and not yet publicly released) of the EarthCARE ESA/JAXA mission. The analysis has been performed in the context of the EC ATLID Validation Team.

Acknowledgements

This work has received funding from the European Union's Horizon 2020 research and innovation programme through the ATMO-ACCESS Integrating Activity under GA Nº 101008004. It is also supported by the Spanish Agencia Estatal de Investigación (AEI)-Ministerio de Ciencia, Innovación y Universidades (MICIU) (grant PID2023-151666NB-I00). The MPLNET project is funded by the NASA Radiation Sciences Program and Earth Observing System.

References

[1] IPCC 2021: Climate Change 2021: The Physical Science Basis. Contribution of Working Group I to the Sixth Assessment Report of the Intergovernmental Panel on Climate Change [Masson-Delmotte, V., P. Zhai, A. Pirani, S.L. Connors, C. Péan, S. Berger, N. Caud, Y. Chen, L. Goldfarb, M.I. Gomis, M. Huang, K. Leitzell, E. Lonnoy, J.B.R. Matthews, T.K. Maycock, T. Waterfield, O. Yelekçi, R. Yu, and B. Zhou (eds.)]. Cambridge University Press, Cambridge, United Kingdom and New York, NY, USA, 2391 pp., https://doi.org/10.1017/9781009157896, 2023.

[2] Donovan, D. P. et al.: *The EarthCARE lidar cloud and aerosolprofile processor (A-PRO): the A-AER, A-EBD, A-TC, and A-ICE products*, Atmos. Meas. Tech., 17, 5301–5340, https://doi.org/10.5194/amt-17-5301-2024, 2024.

[3] Campbell, J.R. et al.: *Full-time, Eye-Safe Cloud and Aerosol Lidar Observation at Atmospheric Radiation Measurement Program Sites: Instrument and Data Processing*, J. Atmos. Oceanic Technol., 19, 431-442, https://doi.org/10.1175/JAMC-D-15-0217.1, 2002.

[4] Welton, E.J. and Campbell, J. R.: *Micro-pulse Lidar Signals: Uncertainty Analysis*, J. Atmos. Oceanic Technol., 19, 2089-2094, https://doi.org/10.1175/1520-0426(2002)019<2089:MLSUA>2.0.CO;2, 2002.

[5] Córdoba-Jabonero, C. et al.: *Diversity on subtropical and polar Cirrus clouds properties as derived from both ground-based lidars and CALIPSO/CALIOP measurements*, Atmos. Res., 183, 151-165, https://doi.org/10.1016/j.atmosres.2016.08.015, 2017.

[6] Córdoba-Jabonero, C. et al.: *Cirrus-induced shortwave radiative effects depending on their optical and physical properties: Case studies using simulations and measurements*, Atmos. Res., 246, 105095, https://doi.org/10.1016/j.atmosres.2020.105095, 2020.

Towards a Standardization of the Quality of Lidar Signals and Derived Optical Products at the LALINET stations in Medellín and La Paz.

J. L. Guerrero-Rascado[1,2], *R. Forno*[3], *E. Montilla-Rosero*[4], *J. V. Pallotta*[5], *S. A. Carvalho*[6], *K. S. Yoshihara-Gámez*[3], *S. Fernández-Carvelo*[1,2], *L. Cano*[3], *F. Ávila*[3], *M. Andrade*[3], *J. A. Bravo-Aranda*[1,2], *M J. Granados-Muñoz*[1,2], *I. Foyo-Moreno*[1,2], *F. Navas-Guzmán*[1,2], *L. Alados-Arboledas*[1,2]

(1) Andalusian Institute for Earth System Research (IISTA-CEAMA), 18006, Granada, Spain
(2) Department of Applied Physics, University of Granada (UGR), 18071, Granada, Spain
(3) Laboratory for Atmospheric Physics, Physics Research Institute, Universidad Mayor de San Andrés, casilla N 8635, La Paz, Bolivia
(4) School of Applied Sciences and Engineering, Natural Systems and Sustainability Area, SOPHIA Research Group, EAFIT University, 050022, Medellín, Colombia
(5) Research Center for Lasers and Applications, UNIDEF (CITEDEF-CONICET), Villa Martelli, B1603ALO, Argentina
(6) Fluminense Federal University, School of Industrial Metallurgical Engineering of Volta Redonda, Exact Sciences Department, Avenida dos trabalhadores 420, Vila Sta. Cecilia, Volta Redonda, 27255-125, Rio de Janeiro, Brazil

Corresponding author: rascado@ugr.es

Introduction

A comprehensive characterization of atmospheric aerosol particles is crucial to fully understanding their role in various atmospheric processes, which significantly influence both climate and human health. According to a 34-year study [1], a multi-regional analysis of aerosol loads revealed that aerosol optical depth (AOD) remained relatively stable across most regions prior to the 1990s. However, after that period, a positive trend in AOD was observed in several parts of the world, including South America [2]. Despite the importance of continuous global monitoring of aerosol particles, South America faces infrastructure limitations. South America lacks routine data on the vertical distribution of aerosols across the continent, which has led most studies to depend on short-term field campaigns. For instance, a three-month lidar campaign was coordinated with sun-photometer and air quality data in São Paulo (Brazil) [3]. Similarly, during the CHUVA project field campaigns [4], a portable Raman lidar measured cloud and aerosol extinction profiles. More extensive studies include a 1-year analysis of multiwavelength polarization Raman lidar observations in the Amazon Basin in 2008 [5] and Southern mid-latitudes in Punta Arenas in 2010 [6]. Hence, establishing a standardized, quality-assured ground-based lidar network would greatly benefit local and global scientific communities.

The Latin American Lidar Network (LALINET) [7, 8] originated from a series of technical meetings and gradually developed into a coordinated effort integrating lidar stations and complementary instrumentation. This process, spanning about 15 years, was marked by contributions and collaborations from scientists and institutions worldwide. A milestone was reached in 2013 when LALINET received recognition from the World Meteorological Organization (WMO) and was included as a contributor to the Global Atmosphere Watch (GAW) program through GALION (GAW Aerosol Lidar Observation Network), marking the beginning of a new chapter for the network. Notably, LALINET represents the first atmospheric observational regional network in Latin America established through the consensus of Latin American scientists. Looking forward, numerous opportunities exist to advance the understanding of climate dynamics in Central and South America. Achieving these goals will require extensive coordination and the pursuit of mechanisms to bolster the network. LALINET exemplifies the creation of a vibrant, young scientific community dedicated to atmospheric research. However, sustaining the network's momentum and excellence requires ongoing effort to ensure lasting progress.

The CAMOMILA project (Strengthening research and training in the atmospheric domain of the La Paz and Aburrá Valleys) addresses the limited availability of atmospheric data for public use and key sectors (e.g., health, environment, aviation) in these regions of Bolivia and Colombia. Through international collaboration, it promotes standardized monitoring protocols for detecting singular aerosol events, using lidar technologies. CAMOMILA adopts EARLINET protocols [9] within LALINET stations in both countries, enabling aerosol type discrimination in the troposphere. The project responds to the need

for improved lidar detection of critical aerosol events—such as air pollution episodes, biomass burning, volcanic eruptions, and dust intrusions—with significant implications for health, aviation safety, and environmental monitoring.

Methodology

The selected lidar stations are located in Medellín (6.1997º N, 75.5793º W, 1538 m asl, Colombia) and La Paz (16.5381º S, 68.0687º W, 3420 m asl, Bolivia). The lidar system in Medellín is equipped with a pulsed Nd:YAG laser emitting at 532 nm, with a repetition rate of 20 Hz and pulse energy of 200 mJ. As a collector it uses a 234.95 mm Schmidt-Cassegrain telescope. The detection channels are elastic parallel and cross-polarized ones with a spatial resolution of 3.75 m using a Licel TR40-16Bit-3. The system can take azimuth (up to 360 ± 0.35º) and zenith (up to 90 ± 0.82º) scans. The home-made polarization lidar system at La Paz is configured coaxially and supports scanning measurements with a maximum spatial resolution of 15 m. The transmitter consists of a Nd:YAG laser emitting 80 mJ pulses at 532 nm with a repetition rate of 20 Hz, coupled with a 5x beam expander. The receiver employs a Newtonian telescope (focal length: 700 mm; aperture: 250 mm) to collect the backscattered light. This light is then collimated and directed through a polarizing beam splitter cube, which separates the parallel and perpendicular polarization components. Each detection channel includes an interference filter with a 1-nm FWHM and focuses the light onto a PMT for signal detection. Data acquisition is handled by a Tektronix DPO3014 oscilloscope, which is operated via computer control.

Specifically, CAMOMILA proposes the implementation of standardization methods at two levels: (i) in the quality assurance (QA) protocols and (ii) in the development of signal inversion algorithms. Currently, the ATLAS software [**A**u**T**omated **L**idar quality **A**nalysis **S**oftware, https://github.com/nikolaos-siomos/ATLAS, last access on 09/04/2025], developed into ACTRIS, is being used for the assessment of the quality control of the lidar hardware and the LPP software (**L**idar **P**rocessing **P**ipeline) [10] as a standardized inversion algorithm in LALINET.

ATLAS is an open-source Python tool designed to support the quality assessment of lidar system, and it can be particularly valuable in the context of different lidar networks. Ensuring the consistency and accuracy of lidar measurements across different stations is essential, and ATLAS contributes to this goal by providing automatized assessments of lidar system analyzing telecover test, zero bin, bin-shift and Rayleigh fit [11]. It detects anomalies and offers visual diagnostics to evaluate lidar data quality. By streamlining these validation processes, ATLAS helped improve the reliability and harmonization of aerosol and atmospheric observations across the EARLINET network, and in this work is also applied at the LALINET stations of Medellín and La Paz.

Following the Single Calculus Chain (SCC) approach from EARLINET [12], the LPP is under collaborative development by LALINET lidar groups. It processes raw Licel-format files and generates NetCDF outputs containing Level 0, 1, and 2 data products. The processing chain comprises three independent C/C++ modules, executable on Linux, macOS, or Windows, all configured via a single settings file. Each module uses the output of the previous one, ensuring full traceability and reprocessability. Level 0 standardizes raw data by compiling metadata and unprocessed signals without converting to physical units. Level 1 applies key corrections (trigger delay, dark current, background subtraction), integrates user-supplied temperature and pressure profiles, and generates an aerosol/cloud layer mask via comparison with a molecular reference. Level 2 retrieves aerosol optical properties (backscatter and extinction coefficients) using the Klett-Fernald method with a user-defined constant lidar ratio (LR). More details can be found in [10].

Results and Discussion

Figure 1 shows an example of the application of the ATLAS software for the Medellín lidar station acquired on 13/04/2022. The plot shows the Rayleigh fit test for the 532nm lidar channel that checks the far range alignment of the system, detect far range signal issues and provides the reference range selection. To the left, we have the comparison between the range corrected signal normalized to a specific range and the molecular attenuated backscattered signal. Several masks are applied to the range close to 6-7 km (gray area) in order to analyse statistically the signal. Data from the Bogotá radiosonde, the nearest radiosounding station (located 400 km from Medellín), was applied for the molecular fit and the data analysis allowed to get preliminary information from the reference range, as illustrated in the gray part of the graphic. Future developments in LPP will include the use of models and/or reanalysis for the computation of molecular profiles. The right plot illustrates the relative difference signal that presents the measured and molecular signals subtraction. The ATLAS results can provide information that can be used to improve the system alignment for future measurements.

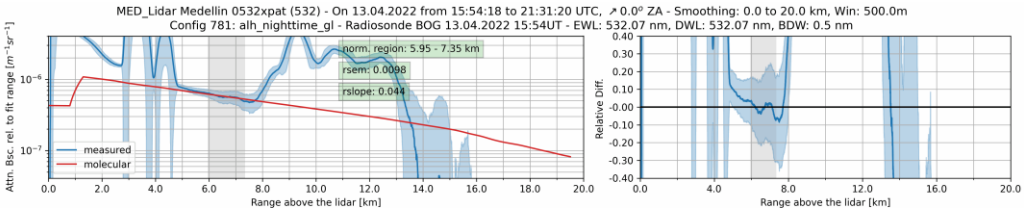

Figure 1. Rayleigh fit test for the 532 nm lidar channel as a function of the range above the lidar system for Medellin lidar station in Colombia: (left) range corrected signal and the molecular attenuated backscattered signal, (b) their relative difference. The best fit parameters are listed for the range 5.95 – 7.35 km.

CAMOMILA also helped to improve the home-made algorithm developed in La Paz. Across a series of online meetings, intercomparison results between LPP and La Paz home-made algorithms are being carried out, helping each other to improve the algorithms and results. These comparative analyses are currently ongoing, with preliminary results displayed in Figure 2, from 16:40 to 17:00 UTC on 26/08/2024. The observed discrepancies of less than 4% in the region with higher aerosol loads between both inversion methods demonstrate promising results and encourage both research groups to continue refining their algorithmic approaches.

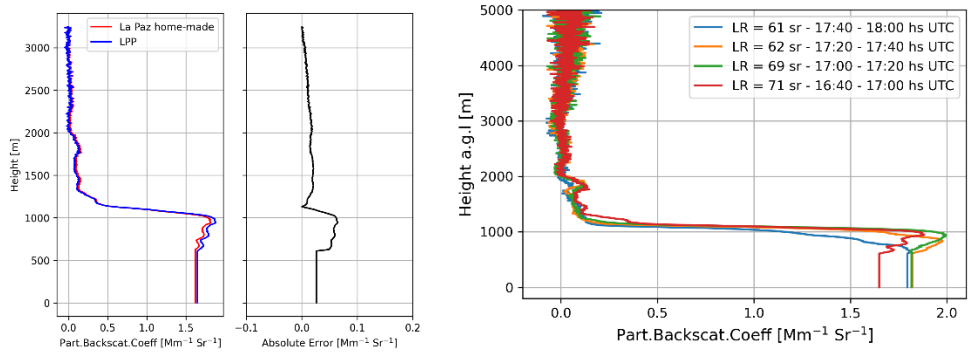

Figure 2: (Left) Particle backscatter coefficient comparison between LPP and La Paz home-made algorithm; (center) Absolute differences; (right) Particle backscatter coefficient profiles at 532 nm over La Paz on 26/08/2024 where each profile was retrieved using the lidar ratio obtained from AERONET synergy.

As an example, Figure 2 shows the analysis of lidar signals acquired by the La Paz lidar system on 26/08/2024 using the fully automated inversion pipeline implemented within the LPP software. This

approach enabled automatic synergy with AERONET data, while background and reference ranges were also determined automatically using LPP procedures. Figure 2 displays the 20-min particle backscatter coefficient profiles at 532 nm. Four lidar signals were successfully inverted against AERONET data, yielding lidar ratio (LR) values through this synergistic methodology. The calculated aerosol optical depth (AOD) values exhibit a maximum discrepancy of less than 1%. The lidar ratios obtained are characteristic of fine particles with high absorption, typically associated with biomass burning aerosols [13, 14]. These values correlate well with the expected aerosol types in the La Paz region.

Conclusions

CAMOMILA has made it possible, for the first time, to consolidate efforts within the LALINET community through a development cooperation project funded by the University of Granada. In the initial months of the project, both the Medellín and La Paz stations successfully launched quality assurance (QA) activities and began the implementation of the new standardized Lidar Processing Pipeline (LPP) software. QA testing has revealed deviations from optimal performance, prompting ongoing improvements to the hardware of the lidar systems. In terms of aerosol optical retrievals, upcoming efforts will focus on comparing results from the home-made software and the LPP under varying atmospheric conditions (e.g., high/low aerosol load, complex cloud scenarios), as well as on developing new LPP modules for the analysis of Raman and depolarization signals.

Acknowledgements

This work was financed by Center for Development Cooperation Initiatives (CICODE) of University of Granada (UGR) through the program 1.1 of the 2024 Sustainable Development Cooperation Plan of the University of Granada (project CAMOMILA). We want to thank Yoshitaka Jin from the National Institute for Environmental Studies in Tsukuba, Japan, for his valuable contributions to the development of the La Paz inversion code.

References

[1] Wang, K. et al.: *Clear sky visibility has decreased over land globally from 1973 to 2007*, Science, 323, 1468–1470. DOI: 10.1126/science.1167549, 2009.

[2] Hartmann, D. L. et al.: *Observations: atmosphere and surface. Climate Change 2013: The Physical Science Basis*. Contribution of Working Group I to the Fifth Assessment Report of the IPCC. Cambridge University Press, Cambridge, U. Kingdom and New York, NY, USA, 2013.

[3] Landulfo, E. et al.: *Study of the Properties of Aerosols and the Air Quality Index Using a Backscatter Lidar System and Aeronet Sunphotometer in the City of São Paulo, Brazil*, J. Air & Waste Manag. Assoc., 60, 386–392. http://dx.doi.org/10.3155/1047-3289.60.4.386, 2010.

[4] Machado, L. A. T. et al.: *The Chuva Project: How Does Convection Vary across Brazil?*, Bull. Am. Meteor. Soc., 95(9), 1365-1380. https://doi.org/10.1175/BAMS-D-13-00084.1, 2014.

[5] Baars, H. et al.: *Aerosol profiling with lidar in the Amazon Basin during the wet and dry season*, J. Geophys. Res., 117, D21201. http://dx.doi.org/10.1029/2012JD018338, 2012.

[6] Foth, A. et al.: *Vertical aerosol distribution in the southern hemispheric midlatitudes as observed with lidar in Punta Arenas, Chile (53.2 S and 70.9 W), during ALPACA*, Atmos. Chem. Phys., 19 (9), 6217-6233. https://doi.org/10.5194/acp-19-6217-2019, 2019.

[7] Guerrero-Rascado, JL. et al.: *Latin American Lidar Network (LALINET) for aerosol research: Diagnosis on network instrumentation*, J. Atmos. and Sol.-Terr. Phys., 138, 112-120. https://doi.org/10.1016/j.jastp.2016.01.001, 2016.

[8] Antuña-Marrero, J. A. et al.: *LALINET: The First Latin American–Born Regional Atmospheric Observational Network*, Bull. Am. Met. Soc., 98(6), 1255-1275. https://doi.org/10.1175/BAMS-D-15-00228.1, 2017.

[9] Pappalardo, G. et al.: *EARLINET: towards an advanced sustainable European aerosol lidar network*, Atmos. Meas. Tech., 7, 2389–2409, https://doi.org/10.5194/amt-7-2389-2014, 2014.

[10] Pallotta, JV. et al.: *Collaborative development of the Lidar Processing Pipeline (LPP) for retrievals of atmospheric aerosols and clouds*, Geosci. Instrum. Method. Data Syst., 12, 171–185, https://doi.org/10.5194/gi-12-171-2023, 2023.

[11] Freudenthaler, V. et al.: *EARLINET lidar quality assurance tools*, Atmos. Meas. Tech. Discuss, https://doi.org/10.5194/amt-2017-395, 2018.

[12] D'Amico, G. et al.: *EARLINET Single Calculus Chain – overview on methodology and strategy*, Atmos. Meas. Tech., 8, 4891–4916, https://doi.org/10.5194/amt-8-4891-2015, 2015.

[13] Wang, S. H. et al.; *Determination of Lidar Ratio for Major Aerosol Types over Western North Pacific Based on Long-Term MPLNET Data*. Remote Sens., 12, 2769. https://doi.org/10.3390/rs12172769, 2020.

[14] Midzak, N. et al.: *Constrained Retrievals of Aerosol Optical Properties Using Combined Lidar and Imager Measurements During the FIREX-AQ Campaign*. Frontiers in Remote Sensing, Volume 3, DOI:10.3389/frsen.2022.818605, 2022.

Climatology of aerosol vertical distribution over 4 Mediterranean sites based on Level 3 EARLINET data products

***C. Chatzizisis*[1]**, *K.A. Voudouri*[2,1], *A. Pantazi*[2], *L. Mona*[3], *A. Papayannis*[4,5], *C. Muñoz-Porcar*[6], *L. Alados Arboledas*[7], *D. Bortoli*[8], *K. Kotsias*[9], *D. Balis*[1]

(1) Laboratory of Atmospheric Physics, Physics Department, Aristotle University of Thessaloniki, Greece.
(2) Institute for Astronomy, Astrophysics, Space Applications and Remote Sensing, National Observatory of Athens, Greece.
(3) Consiglio Nazionale delle Ricerche – Istituto di Metodologie per l'Analisi Ambientale (CNR-IMAA), Italy.
(4) Laboratory of Atmospheric Processes and their Impacts (LAPI), School of Architecture, Civil & Environmental Engineering, Ecole Polytechnique Fédérale de Lausanne, Lausanne, Switzerland.
(5) Laser Remote Sensing Unit (LRSU), Physics Department, National Technical University of Athens, Greece.
(6) Universitat Politècnica de Catalunya, Barcelona.
(7) Andalusian Institute for Earth System Research, University of Granada (IISTA-CEAMA).
(8) Universidade de Evora, Center for sci-tech Research in EArth sysTem and Energy (CREATE), Evora, Portugal.
(9) University of Patra, Physics Department.

Corresponding author: kavoudou@noa.gr

Introduction

The aim of this work is to study the temporal variability of the geometric and optical properties of the aerosol particles using measurements from the European Aerosol Research Lidar Network (EARLINET, [1]; data.earlinet.org). The vertical distributions of the backscatter coefficient and the extinction coefficient, along with columnar products, such as the optical depth and the center of mass, are analyzed on a seasonal and yearly basis. The data used are Level 3 products and consist of climatological products derived from the fully quality-controlled Level 2 data. This quality-controlled data is utilized for trend analysis and the study of the long-term changes in particles at various EARLINET stations. The aerosol variability over four selected stations influenced by the Mediterranean climate (i.e., Evora, Barcelona, Granada and Athens), each characterized by distinct atmospheric conditions, are discussed herein.

Methodology

The EARLINET (European Aerosol Research Lidar NETwork) was established on a continental scale, with its primary interest being the long-term systematic monitoring of the vertically resolved aerosol distribution over Europe. To achieve this, systematic measurements were planned, and quality assurance strategies were designed for the maintenance and sustainability of lidar systems. Thus, long-term multiwavelength backscatter and extinction coefficient profiles are available through an easily accessible database, covering the European continent [1] . Since 2010, the EARLINET data are managed by ACTRIS (Aerosol Clouds Trace Gases Research InfraStructure), the pan-European research infrastructure producing high-quality data and information on short-lived atmospheric constituents and on the processes leading to the variability of these constituents in natural and controlled atmospheres [2].

The quality of the data in the database is assured by internal Q/A tests and intercomparisons at both instrument and algorithm level. Data included in the database are classified on the basis of the data quality as Level 1 and Level 2 through automatic procedures centrally executed by the ACTRIS ARES (Aerosol REmote Sensing) Data centre unit (https://earlinet.eu/wp-content/uploads/2025/03/EARLINET_QC_v4_0_20250225.pdf). Data are labelled as Level 1 if the files have passed Basic Quality Controls (BQC), which consist of checking for the presence of technical problems in the data files. Basic quality controls are applied to all products available in the database. Data are labelled as Level 2 if they have passed also the Advanced Quality Controls (AQC), which consist of checking the data from a physical point of view. Advanced Quality Controls are only applied to optical data.

The ACTRIS/EARLINET Level 3 standard products (https://earlinet.eu/level-3-data/) contain climatological datasets obtained as aggregated products from the fully quality controlled (QC) aerosol optical products (i.e. Level 2 products). In particular, these products provide high quality information on

the vertical distribution and optical properties of the aerosol over the European continent on a long-term scale. In order to avoid biases due to measurements performed during specific events (e.g., dust outbreaks), only a subset of data corresponding to the regular schedule and measurements made for satellite validation purposes are considered (i.e. climatological and CALIPSO category files according to the current EARLINET database organisation).

The Level 3 data are organised per station, allowing future updates of the climatological products also at station level. More specifically, both profile values and integrated quantities for each type of data, seasonal and annual temporal aggregations are provided.

For each extinction/backscatter vertical profile, an integrated quantity is calculated: aerosol optical depth (AOD) for extinction profiles, and aerosol integrated backscatter (IB) for backscatter profiles. AOD and IB are the integrals over the altitude of the aerosol extinction and backscatter profiles, respectively. These integrated products represent a proxy for the quantity of aerosol present in the considered portion of the atmospheric column. However, optical depth and integrated backscatter also depend on the type of particles because the extinction and the backscatter efficiencies depend on the size, shape, and refractive index of the particles. Another integrated reported quantity is the center of mass, which is a value associated to every backscatter vertical profile. The center of mass of the aerosol content in a certain portion of the atmospheric column is estimated as the backscatter weighted average altitude in the considered altitude range [3].

For each Level 2 file, geometrical information about layers is retrieved using an algorithm based on the algorithm shown in [4], applied to the backscatter vertical profile. These geometrical products (mainly, the altitude of the lower and upper bound of the layers) are then used to calculate the following optical products: mean extinction coefficient and mean backscatter coefficient, lidar ratio, particle depolarization, aerosol optical depth, integrated backscatter, center of mass.

The dataset includes 20 years (2000-2019) of aerosol observations from 33 European lidar stations. In this study we focus on the Southern European stations listed in Table 1 [5, 6, 7 and 8]. We examine the seasonal variability of the mean center of mass, as well as the seasonal variability of the mean aerosol backscatter coefficients.

Table 1. EARLINET stations that were considered in this study.

Station	Latitude	Longitude	Altitude (asl)
Athens, Greece	37.9600 N	23.7800 E	212 m
Barcelona, Spain	41.3930 N	2.1200 E	115 m
Granada, Spain	37.1640 N	3.6050 W	680 m
Evora, Portugal	38.5678 N	7.9115 W	293 m

Results and Discussion

The seasonal variability of the mean center of mass at 355 m, for the four stations is presented in Figure 1. Typically**,** the center of mass is observed at lower altitudes during winter, primarily due to the aerosols' presence associated with local pollution within the Planetary Boundary Layer (PBL). During spring and summer, it shifts to higher altitudes, indicating the influence of long-range dust transport. At the Granada and Évora stations, the center of mass is consistently found above 1500 meters during almost all seasons, whereas in Athens, it is generally lower**,** possibly due to the instrument's minimum altitude detection range.

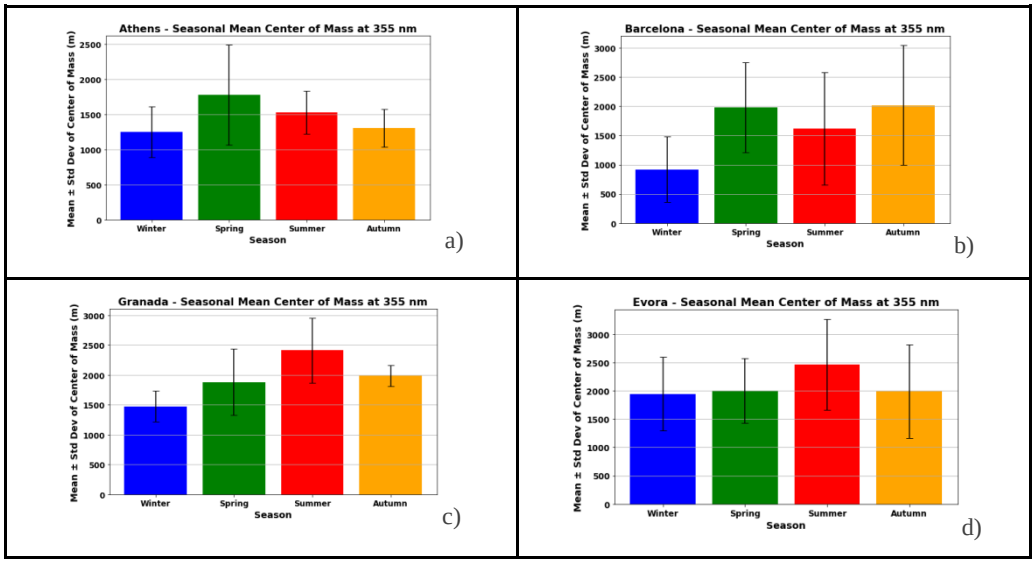

Figure 1. Seasonal variability of the mean center of mass at the EARLINET stations in Athens (a), Barcelona (b), Granada (c), and Évora (d).

Figure 2 presents the seasonal variation of mean backscatter coefficients at 1064 nm for the four stations. As expected, the mean backscatter decreases with altitude, as most particles are concentrated near the ground. The backscatter coefficient at 1064 nm exhibits elevated values during spring at altitudes above the atmospheric boundary layer. In Granada, a second aerosol layer is observed during spring at 4000 m, and in the summer, the highest backscatter coefficients are recorded compared to the other stations. Additionally, the Évora station has the least amount of available data. Data unavailability suggests either that no measurements were conducted or that they were not processed into Level 2 data. Winter exhibits the highest data scarcity, as many measurements are prevented by cloud cover.

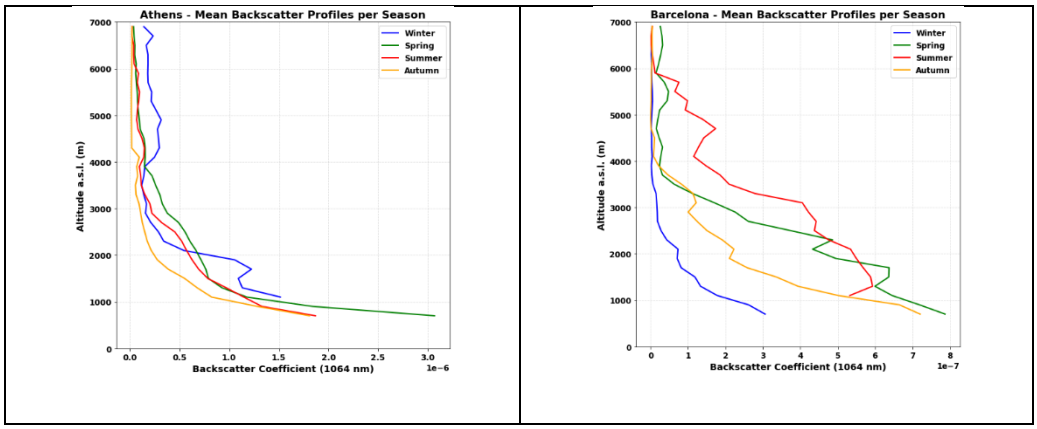

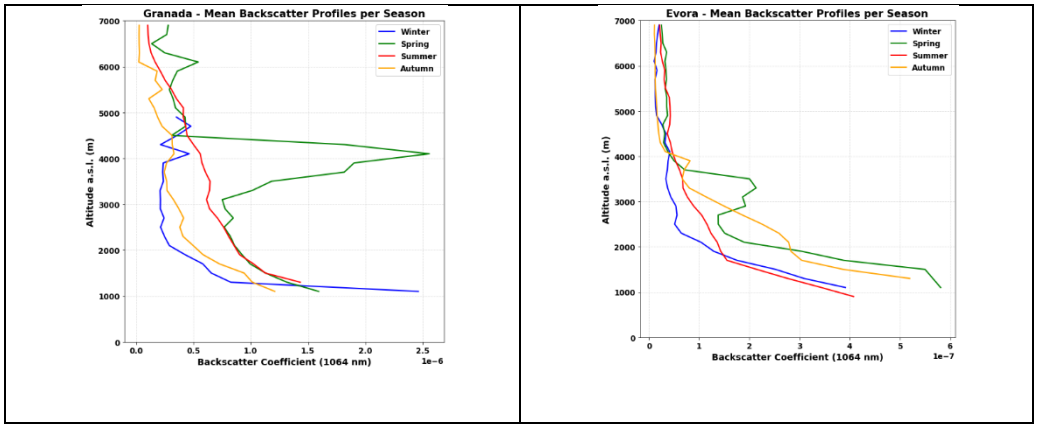

Figure 2. Seasonal time series of the mean of backscatter coefficients at 1064 nm at the EARLINET stations in Athens (upper left), Barcelona (upper right), Granada (down left), and Évora (down right).

Conclusions

Climatology of the aerosol properties based on the ACTRIS/EARLINET Level 3 products are analyzed herein. Four stations with different atmospheric conditions, along the Mediterranean are included in the study. The seasonal variability of the mean center of mass at 355 nm, along with the variation of mean backscatter coefficient at 1064 nm for Evora, Barcelona, Granada and Athens stations are presented and discussed. The four stations show differences in the aerosol properties detected, due to their different atmospheric and geographical conditions.

Acknowledgements

We acknowledge EARLINET and ACTRIS aerosol remote sensing teams for the provision of datasets, and for scientific support. KAV acknowledges the financial support of the PANGEA4CalVal project (Grant Agreement 101079201) funded by the European Union.

References

[1] Pappalardo, G., et al., (2014) : EARLINET: towards an advanced sustainable European aerosol lidar network. Atmospheric Measurement Techniques, 7(8), 2389–2409. https://doi.org/10.5194/amt-7-2389-2014.

[2] Laj, P., and Coauthors, (2024): Aerosol, Clouds and Trace Gases Research Infrastructure (ACTRIS): The European Research Infrastructure Supporting Atmospheric Science. Bull. Amer. Meteor. Soc., 105, E1098–E1136, https://doi.org/10.1175/BAMS-D-23-0064.1..

[3] Mona, L., Amodeo, A., Pandolfi, M., Pappalardo, G., (2006): Saharan dust intrusions in the Mediterranean area: Three years of Raman lidar measurements. J. Geophys. Res., vol. 111, D16203, doi:10.1029/2005JD006569.

[4] N. Siomos, et al., (2018): Are EARLINET and AERONET climatologies consistent? The case of Thessaloniki, Greece, Atmos. Chem. Phys., 18, 11885–11903, https://doi.org/10.5194/acp-18-11885-2018.

[5] Papayannis, A., et al., (2024). ACTRIS/EARLINET Level 3 2000-2019 climatological dataset over Athens, Greece (Version 1) [Data set]. National Research Council - Institute of Methodologies for Environmental Analysis. https://doi.org/10.57837/CNR-IMAA/ARES/ACTRIS-EARLINET/LEVEL3/CLIMATOLOGICAL/2000_2019/ATZ

[6] Comeron, A., et al., (2024). ACTRIS/EARLINET Level 3 2000-2019 climatological dataset over Barcelona, Spain (Version 1) [Data set]. National Research Council - Institute of Methodologies for Environmental Analysis. https://doi.org/10.57837/CNR-IMAA/ARES/ACTRIS-EARLINET/LEVEL3/CLIMATOLOGICAL/2000_2019/BRC

[7] Alados-Arboledas, L., et al., (2024). ACTRIS/EARLINET Level 3 2000-2019 climatological dataset over Granada, Spain (Version 1) [Data set]. National Research Council - Institute of Methodologies for Environmental Analysis. https://doi.org/10.57837/CNR-IMAA/ARES/ACTRIS-EARLINET/LEVEL3/CLIMATOLOGICAL/2000_2019/GRA

[8] Bortoli, D., et al., (2024). ACTRIS/EARLINET Level 3 2000-2019 climatological dataset over Evora, Portugal. (Version 1) [Data set]. National Research Council - Institute of Methodologies for Environmental Analysis. https://doi.org/10.57837/https://doi.org/10.57837/CNR-IMAA/ARES/ACTRIS-EARLINET/LEVEL3/CLIMATOLOGICAL/2000_2019/EVO

Automated Aerosol Classification via Neural Networks: Application of NATALi Software to Lidar Data in Cluj-Napoca

***H. Cămărășan*[1]**, *L. Deaconu*[1], *A. Mereuță*[1], *H. Ștefănie*[1], *A. Radovici*[1], *N. Ajtai*[1]

(1) Babeș-Bolyai University, Faculty of Environmental Sciences and Engineering, Fântânele no. 30, Cluj-Napoca, Romania

Corresponding author: horia.camarasan@ubbcluj,.ro

Introduction

Accurate atmospheric aerosol typing is vital for understanding climate impacts and air quality. Advanced tools within research infrastructures like ACTRIS aim to improve aerosol characterization. This study evaluates the NATALi (Neural network Aerosol Typing Algorithm based on LIdar data) Artificial Neural Network (ANN) software, using lidar data from the ACTRIS-UBB station in Cluj-Napoca, Romania. We assess NATALi's performance in classifying local aerosol types against established methods and discuss its potential utility.

Methodology

Lidar measurements from 2021 were acquired using a multiwavelength Raman depolarization lidar (Raymetrics LR231-D300) at the ACTRIS-UBB station in Cluj-Napoca.

Figure 1 – Map of the chosen ACTRIS site for the study (marked with the red pinpoint) in Cluj-Napoca, Romania (CALTOPO, 2023) (left), L231-D300 Multiwavelength Raman Lidar at FSIM and the acquisition unit

Processed data provided vertical profiles of backscatter coefficients (355, 532, 1064 nm), extinction coefficients (355, 532 nm), and depolarization ratio (532 nm). The NATALi ANN software [1] was applied to quality-controlled lidar profiles to classify aerosol layers based on these optical properties. Co-located AERONET sun photometer data (AOD, Angstrom Exponent) and EARLINET quicklooks were used for comparison and context. The analysis focused on 13 validated measurement datasets from 2021 exhibiting distinct aerosol layers.

Results and Discussion

NATALi successfully classified aerosol types over Cluj-Napoca, generally showing good agreement with EARLINET quicklooks and AERONET-derived properties for the 13 case studies analysed in 2021. The software effectively identified predominant aerosol layers, including continental, continental polluted, and smoke. Seasonal analysis revealed smoke prevalence in spring (33%), potentially linked to agricultural burning, and continental polluted aerosols dominance in summer (29%), likely due to traffic and photochemical activity. Dust intrusions were also identified.

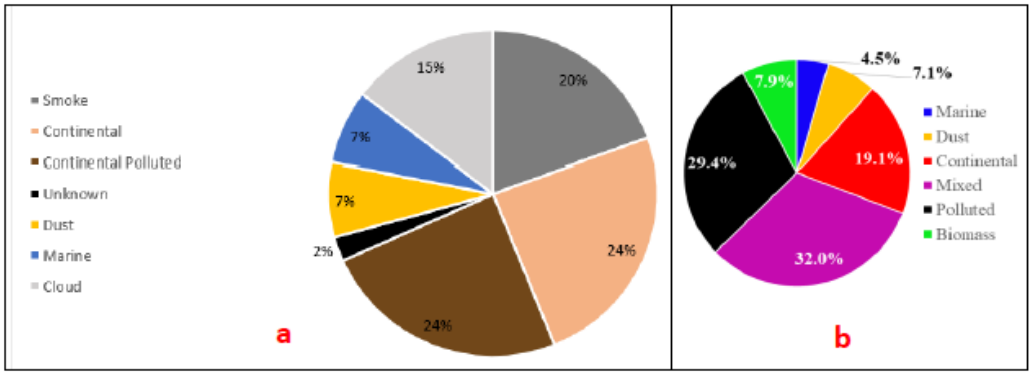

Figure 2. Comparison Between the NATALi Typed 1-year Aerosol Trend (a) and the Documented Aerosol 10-years Trend over Cluj-Napoca ((b), adapted from Ștefănie et. Al., 2023)

While generally reliable, NATALi faced challenges with complex scenarios like mixed layers or rapidly changing conditions, sometimes leading to inconsistent labelling. Potential misclassifications occurred for certain aerosol types (e.g., marine, unlikely for Cluj-Napoca) or when distinguishing between types with overlapping optical properties (e.g., certain smoke vs. coarse particles). Despite these limitations, the overall aerosol distribution derived from NATALi for 2021 (Continental 24%, Polluted 24%, Smoke 20%, Dust 7%, Marine 7%) aligned reasonably well with documented 10-year trends for the site [2], validating its general capability.

Conclusions

The NATALi ANN software proved to be a valuable tool for enhancing aerosol typing using ground-based lidar data in Cluj-Napoca. It provides classifications comparable to standard methods, contributing useful insights into local aerosol types and trends, despite limitations in complex situations. NATALi offers potential for improving atmospheric modelling and supporting air quality management policies. Further validation with extended datasets and diverse locations is recommended.

Acknowledgements

Data from the ACTRIS-UBB station (Cluj-Napoca), EARLINET, and AERONET were used. The work was financed by Smart Growth, Digitization and Financial Instruments Program (PoCIDIF) 2021-2027, Action 1.3 Integration of the national RDI ecosystem in the European and international Research Space, project "Supporting the operation of facilities in Romania within the ACTRIS ERIC research infrastructure", SMIS code 309113, ctr. no. G 2024-96579/17.12.2024/390010/19.12.2024.

References

[1] Nicolae, D. et al.: A Neural Network Aerosol-Typing Algorithm Based on Lidar Data, *Atmos. Chem. Phys.*, 18(19), 14511-14537, 2018.

[2] Ștefănie, H. et al.: Variation of Aerosol Optical Properties and Trends over Cluj-Napoca, Romania, Based on 10 Years of AERONET Data..., *Remote Sens.*, 15(x), [ID], 2023.

[3] EARLINET: https://www.earlinet.org/ [Accessed 5 May 2023].

[4] AERONET: https://aeronet.gsfc.nasa.gov/ [Accessed 10 May 2023].

Calibration of the water vapor vibro-rotational Raman channel using ground-based meteorological measurements

J.L. Gómez-Amo[1], *P.C. Valdelomar*[1], *C. Dameto de España*[1], *M.P. Utrillas*[1]

(1) Universitat of Valencia, Dpt. Física de la Terra i Termodinàmica, Solar Radiation Group, Dr. Moliner 50, 46100, Burjassot, Spain

Corresponding author: Jose.L.Gomez-Amo@uv.es

Introduction

An improved coverage of vertical profiles of atmospheric parameters is needed to better constrain the operative performance of the weather forecasting models [1]. It is is especially important for atmospheric components that significantly influence the Earth's energy balance and atmospheric thermodynamics, such as aerosols and water vapor. In the case of aerosols, the quality of their measurements and their spatial distribution have improved significantly in recent years, mainly due to the creation of high-quality observation networks such as ACTRIS-EARLINET. However, less attention has been paid to the measurement of the water vapor mixing ratio (WVMR), despite the fact that it can be measured with good precision with lidar systems and the technique has been well understood since the 1960s. The main factor affecting the quality of lidar-derived WVMR is the calibration against a reference profile. This is typically done using a neighboring radiosonde to correlate the lidar signal with the WVMR and determine the calibration constant. A collocated radiosonde is not always available to perform the WVMR calibration, and this substantially limits its usage. For this reason, various techniques have recently been developed for calibrating WVMR lidar measurements using much more common auxiliary measurements. In this regard, the comparison of lidar-derived WVMR with ground-based meteorological measurements can be a viable alternative, with results comparable to those obtained with a radiosonde [2].

The objective of this work is to use this alternative to calibrate the WVMR profile measured with the TONET lidar system (described in the Methodology section). The instrument is deployed at the Burjassot Atmospheric Measurements Station (BASS, 39.508° N, 0.418° W, 60 m a.s.l.), which is maintained by the Solar Radiation Group of the University of Valencia (GRSV). No reference measurements of WVMR profiles are available within a 350 km radius of BASS. For this study, we use lidar measurements taken during the Water Vapor Lidar Network Assimilation (WaLiNeAs) campaign, which results from an international collaborative effort between different research groups from France, Germany, Italy, and Spain ([1]. The campaign was carried out in the Western Mediterranean with the aim of studying whether WVMR profile measured by a lidar network can contribute to improving the prediction of extreme precipitation events in the Mediterranean basin. Nine lidars specifically designed for WVMR profiling were deployed along the Mediterranean coast of France and Spain, as well as in Corsica and Menorca islands, from September 2022 to January 2023 [3].

Methodology

TONET Lidar, which is 8-channel Raman depolarization Lidar (LR332-D300) manufactured by Raymetrics S.A:. The instrument is equipped with a Nd:YAG pulsed laser beam emitting 80 mJ at 355 nm, 532 nm, and 1064 nm pointed vertically upward. The receiver operates in three elastic channels and the UV and VIS channels are also sensitive to polarization. Moreover, there are three Raman detection channels corresponding to nitrogen (387 nm and 607 nm) and water vapor (408 nm). The system is based on a 300 mm Cassegrain optical telescope design. The backscattered signal is detected using photomultiplier tubes (PMTs) and then by a 16-bit analog-to-digital (A/D) converter. The sampling is either in analog and photon-counting modes with a rate of 20 and 800 MHz, respectively, providing 1-minute averaged profiles with vertical resolution of 7.5 m. The full overlap is reached around 250 m for all channels. Due to TONET's configuration, only night time measurements were taken during WaLiNeAs campaign. Thus we have 1-month of available data, around 12 hours per day (6 pm. – 6 am) from 20th October to 20th November. WVMR profiles were averaged with 15-min temporal resolution and 100 m vertical resolution; and sent to

Meteofrance in real time. The WVMR was calibrated at the factory before shipment and installation at BASS where ACTRIS-EARLINET QAQC tests were performed. During the campaign, a beam expander (BEX) was installed on 10th November, and new QAQC tests were performed.

The WVMR is proportional to the signal ratio between water vapor and nitrogen Raman channels at 408 nm and 387 nm, respectively (Eq.1).

$$WVMR(z) = K \cdot OR(z) \cdot \frac{S_{408}(z)}{S_{387}(z)} \cdot M(z) \cdot A(z) \quad (1)$$

where K is the calibration constant, in (g/kg), and S(z) is the lidar signal for each channel, already corrected from sky background, dark measurements and electronic background. $OR(z) = \frac{O_{387}(z)}{O_{408}(z)}$ is the ratio between the overlap function for the 387 nm and 408 nm channels. M(z) and A(z) are the molecular and aerosol corrections, respectively, due to the atmospheric transmittance at the Raman wavelengths used. Usually, the molecular correction is determined by a model while aerosol correction can be neglected for AOD < 0.2 or low spectral dependence (Angstrom exponents around 1) [2].

For calibration, we have used the comparison between the lidar derived $WVMR_{Lidar}$ at the first altitude above the full overlap for both lidar channels (250 m) with the $WVMR_{surface}$ derived using ground-based meteorological measurements. $WVMR_{Lidar}$ is obtained using the K provided by the manufacturer. In addition, the comparison has been performed in different conditions: using all the available data; and also only considering weak vertical gradient below 1 km, as an indicator of well-mixed lowermost atmosphere [2]. The vertical gradient has been evaluated using two criteria: a) the atmospheric transmission varies less than 0.02 and b) the $WVMR_{Lidar}$ changes less than 0.25 g/kg; in the first atmospheric kilometer.

The comparison is made using a linear regression and the new calibrated $WVMR_{Lidar}$‘ is obtained by applying (Eq. 2), where a and b are the slope and the intercept resulting from he fit.

$$\mathrm{WVMR}'_{\mathrm{Lidar}} = a \cdot \mathrm{WVMR}_{\mathrm{Lidar}} + b \quad (2)$$

Finally, the feasibility of our methodology is validated from the comparison of the recalibrated vertical profiles of $WVMR_{Lidar}$‘(z) and the $WVMR_{ERA5}$(z) derived from the vertical profiles provided by ERA-5 database that includes BASS coordinates. Hourly averaged Lidar measurements have been used for this validation, since it is the temporal resolution of the ERA-5 data.

Results and Discussion

Our ground-based meterological parameters are measured with a 1-minute temporal resolution and we have used 15-minutes averaging for the comparison with Lidar measurements.

Figure 1 shows the comparison between lidar and ground-based measurements for the WVMR. The different criteria indicating the vertical gradient in the first kilometer of atmosphere are shown in different colors. The results of the corresponding linear regression fits are shown in Table 1. Two separate branches are clearly observed, relating to measurements taken before and after 10th November (blue and red points in Figure 1). Both branches follow a linear trend with ground-based values, with substantially different slopes. These results indicate that the lidar overestimates the surface measurements before 10th November and underestimates them afterward. This indicates that the changes made to the system with the installation of the BEX had a significant impact on the WVMR measurements and that the calibration coefficient used is incorrect in both cases, as the slope is significantly different from 1. For this reason, different linear regression fits were performed for each of the branches. Furthermore, points that met the criteria for a weak vertical gradient in the first kilometer of atmosphere were selected and fitted separately for each of the branches. The results of the linear regression show no significant differences with any of the point selection criteria, neither in the slope nor in the intercept (Table 1). Furthermore, all regression fits show a correlation coefficient greater than 0.98. These results reinforce the need to calibrate the WVMR measurement in situ and after making significant changes to the lidar optical settings.

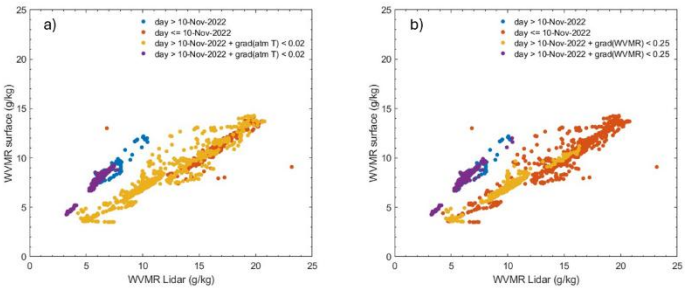

Figure 1. Comparison between Lidar derived WVMR at 250 m altitude with the WVMR derived from ground-based meteorological parameters. Colors indicate different criteria to select the weak vertical gradient based on. a) the atmospheric transmission and b) the $WVMR_{Lidar}$; changes thorugh in the first km.

Table 1. Results of the linear regression for the different cases in Figure 1.

	a	**b**	**R**	**RMSE**	**N**
>10-Nov	0.642 ± 0.008	0.54± 0.11	0.983	0.517	948
< 10- Nov	1.164 ± 0.016	0.54±0.11	0.991	0.206	334
>10-Nov + grad(atmT)	0.638 ± 0.012	0.66 ± 0.13	0.987	0.319	288
< 10- Nov + grad(atmT)	1.170 ± 0.014	0.50 ± 0.09	0.995	0.148	280
>10-Nov + grad(WVMR)	0.654 ± 0.010	0.49 ± 0.13	0.982	0.548	650
< 10- Nov + grad(WVMR)	1.177 ± 0.011	0.49 ± 0.13	0.998	0.097	216

We applied the new calibration to the entire lidar database, taking into account only the different trends observed before and after 10th November (i.e. applying the coefficients of the rows 1 and 2 in Table 1). The differences between $WVMR_{Lidar}$ and the WVMR derived from ERA5 are shown in Figure 2, before and after applying the new calibration, repectively. With the original calibration, provided by the manufacturer, the lidar overestimates the ERA5 before 10th November, while underestimating it afterward (Figure 2a). Furthermore, the average overestimation in the first period is especially evident at low altitudes, down to -4 g/kg, and decreases with altitude. This behavior could be related to the greater amount of WVMR in the lower atmosphere during this temporal period. However, after 10th November, no significant variation with altitude is observed and the average difference is around 2.5 g/kg.

After applying the new calibration, the WVMR differences between lidar and ERA-5 model are substantialy reduced and the values remain mostly constrained around zero for the entire campaign (Figure 2b). In addition, no significant differences are observed between the two different periods of the campaing (before and after 10th November). In average, the the lidar slightly underestimates by 1 g/kg the value provided by the ERA-5 model and show a reduced variation with altitude for the entire campaign (Figure 2d). Part of these differences may be due to the different temporal and vertical averaging between lidar and ERA-5 data. Furthermore, the $WVMR_{ERA}$ model at its lowest altitude (around 150 m) shows less correlation than the lidar with the ground-based measurements, with a correlation coefficient of 0.94 and a slope of 0.85 ± 0.02 for the entire campaign.

We obtain Lidar-ERA5 differences similar to those reported in the literature [1], where lidar-derived WVMR and the ERA5 model does not exceed ±1 g/kg. However, in [1], the $WVMR_{Lidar}$ calibration is performed for different heights, using collocated radiosonded or with meteorological probe measurements taken onboard

of an instrumented aircraft. These results demonstrate the feasibility of calibrating WVMR measurements using ground-based meteorological parameters.

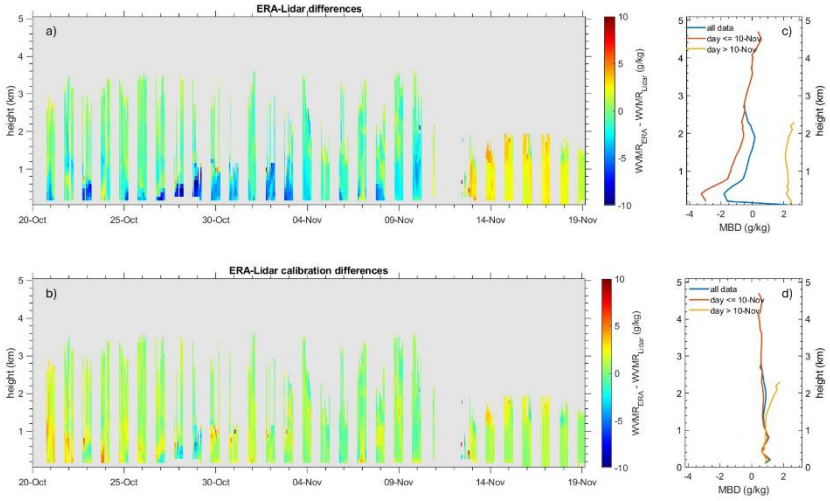

Figure 2. Hourly differences between $WVMR_{ERA5}$ and $WVMR_{Lidar}$ for the entire campaign using: a) manufacturer calibration coefficient and b) our ground-based calibration. The temporal averaged differences for the entire period; before and after 10th November using: c) manufacturer calibration coefficient and d) our ground-based calibration.

Conclusions

We have tested a method for calibrating the lidar-determined WVMR using ground-based meteorological measurements. Our calibration shows good agreement between lidar and ground-based measurements of WVMR, with correlation coefficients above 0.98 in all cases.

The feasibility of our calibration has been verified through comparison with WVMR profiles derived from ERA-5 reanalysis. The results of this validation are completely satisfactory, with a MBD of 1 g/kg, which is independent of altitude.

Acknowledgements

This work is supported by the Spanish Ministries of Economy and Competitiveness (MINECO) and Science, Innovation and Universities (MICIU) through the grants: PID2021-123881OB-I00, TED2021-129185BI00, RED2022-134824-E, RED2024-153756-E; and the Valencia Autonomous Government through CIAICO2023-088, and the CIAPOS/2023/211 grant for the participation of C. Dameto de España.

References

[1] Flamant et al.: *A network of water vapor Raman lidars for improving heavy precipitation forecasting in southern France: introducing the WaLiNeAs initiative*, Bull. Atmos. Sci. Technol., 2, doi.org/10.1007/s42865-021-00037-6, 2021.
[2] Chazette et al.: *Long-term evolution of the calibration constant on a mobile/field campaign water vapour Raman lidar*, Egusphere, doi.org/10.5194/egusphere-2024-3583.
[3] Laly et al.: *Water vapor Raman-lidar observations from multiple sites in the framework of WaLiNeAs*, Earth Syst. Sci. Data, doi.org/10.5194/essd-2024-73, 2024.

Validating ATLID Level 1B Nominal Track Products Against High-Resolution Ground-Based Lidar Data

G. Ciocan[1,2], *S. Nicolae*[3], *D. Nicolae*[1], *L. Belegante*[1], *A. M. Dandocsi*[1]

(1) National Institute of Research and Development for Optoelectronics INOE2000, Magurele,, Atomistilor 409, Romania
(2) Faculty of Physics, University of Bucharest, Magurele, Atomistilor 405, Romania
(3) National University of Science and Technology POLITEHNICA Bucharest, Splaiul Independentei 313, Bucharest, Romania

Corresponding author: gabriela.ciocan@inoe.ro

Introduction

Aerosols significantly influence the Earth's climate system by scattering and absorbing solar radiation, at all altitudes. As a consequence, their vertical distribution is critical for understanding the radiative effects [1]. Ground-based lidar systems offer high-resolution vertical profiles of aerosol backscatter and extinction, enabling detailed observations of aerosol layering, transport, and evolution [2]. However, these measurements are limited in spatial coverage and are often affected by local meteorological conditions [3].

On the other hand, satellite-based lidar systems offer a global perspective, extending aerosol profiling capabilities over remote and under-sampled regions. The ATLID (ATmospheric LIDar) instrument on board the EarthCARE satellite represents a new generation of spaceborne lidar, operating at 355 nm and designed to retrieve aerosol and cloud profiles based on high spectral resolution capabilities [4].

The synergy between satellite and ground-based observations is ideal for comprehensive aerosol characterization [5]. While ground-based systems deliver high temporal resolution and precision, satellite measurements provide spatial context and continuity. Validating and intercomparing these two sources of data builds up confidence in both platforms and supports the development of improved retrieval algorithms.

This study compares aerosol profiles from ATLID with those from two ground-based lidars at the RADO-Bucharest facility in Măgurele, România, with the purpose of understanding how sensitive the comparison is with regards to the distance of overpass. We focus on the scattering ratio (SR), which reflects aerosol presence, and evaluate the agreement between ATLID and ground-based SR profiles over coincident overpasses, including the effect of different temporal averaging windows.

Methodology

This study presents a quantitative comparison between aerosol scattering ratio (SR) profiles derived from ATLID and RALI (RAman LIdar) [6], at various distances of overpass. The comparison focuses on satellite overpasses with initial filtering within a 100km radius from the station.

The scattering ratio measured by the ground-based lidar was computed using data from the Single Calculus Chain (SCC) [7] products: ELIC 003 and ELIC 009, both for the wavelength 355 nm. The ELIC 003 files contain molecular extinction and atmospheric transmissivity profiles with a 30-minute resolution. The Rayleigh attenuated backscatter was obtained using:

$$\beta_{Rayleigh} = \left(\frac{\alpha_{mol}}{S_{mol}}\right) \cdot T_{em} \cdot T_{det} \tag{1}$$

where α_{mol} is the molecular extinction, $S_{mol} = 8.5034\ sr$ is the molecular lidar ratio, and T_{em} and T_{det} are the two-way transmissivities at the emission and detection wavelengths, respectively. As part of the files, these parameters are already altitude dependent, therefore, the term $\frac{\alpha_{mol}}{S_{mol}}$ was not divided by the square distance to avoid overcompensation.

The total attenuated backscatter β_{Total} was extracted from ELIC 009 files, recorded at a finer temporal resolution (one minute). These profiles were scaled using a dynamically selected aerosol-free layer, where Rayleigh scattering dominates with values larger than 80%, with a depth between 500 and 2000 m. A scale

factor was computed as the ratio of the mean Rayleigh to the mean total backscatter in this region and applied to the entire total attenuated backscatter profile [8].

The scattering ratio measured by RALI was then computed as:

$$SR_{RALI} = \frac{\beta_{Total}}{\beta_{Rayleigh}} \tag{2}$$

For each ATLID overpass, the ground-based SR profiles were averaged over a 30-minute window centered on the closest overpass time. These profiles were regridded using a weighted average method based on altitude bin overlap to match the vertical grid of ATLID to facilitate direct comparison.

The satellite data used in this study were pre-operational Level 1B nominal track products processed from the ATLID [9]. This product includes attenuated backscatter contributions from Mie (co-polarized), (Mie) Cross-polarized, and Rayleigh scattering.

The scattering ratio measured by ATLID was calculated as:

$$SR_{ATLID} = \frac{\beta_{MieCross} + \beta_{MieParallel} + \beta_{Rayleigh}}{\beta_{Rayleigh}}. \tag{3}$$

To reduce noise in ATLID scattering ratio (SR) profiles, averaging was applied over ±1 to ±10 minute windows centered on the satellite's closest point to the ground station. These intervals correspond to spatial spans of 450–4500 km along the orbit. While averaging enhances signal stability, only the shortest windows (±1 and ±2.5 min) maintain a reasonable spatial match for comparison with ground-based measurements.

Results and Discussion

To explore the consistency between ATLID and ground-based lidar observations, we analyzed seventeen available cases, out of which two are presented in this paper. These two cases are representative for nighttime overpasses: one at significant distance (78 km measured on 30th July 2024), and one very close to the location of the RALI system (11 km measured on 3rd February 2025). The analysis offers insights into how spatial proximity and temporal averaging influence the quality of comparison.

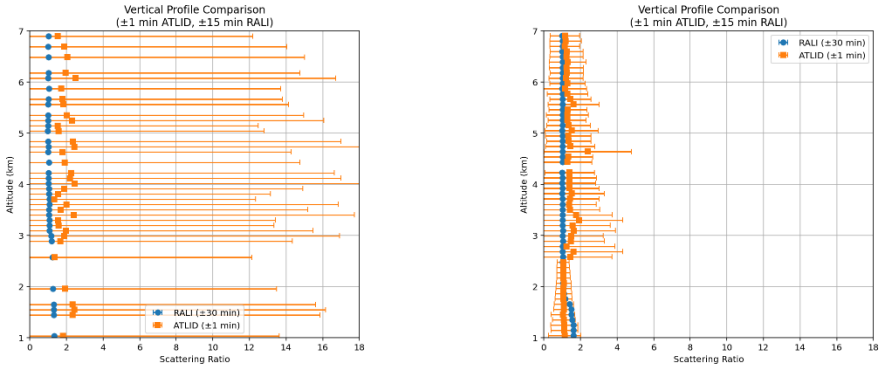

a. b.

Figure 1. Vertical profile comparison of scattering ratio (SR) between ATLID and ground-based (RALI) observations for the **nighttime overpass**. The closest point to the trajectory was located: **a. 78 km** from the measurement site; **b.11km** from the measurement site. ATLID profiles represent a ±1-minute averaging window, while RALI uses a 30-minute window centered around the closest point overpass time. The error bars represent the propagated measurement uncertainty

The first case (Fig. 1.a.) corresponds to a nighttime overpass that occurred approximately 78 km from the RADO-Bucharest Station. Due to the greater distance and nighttime conditions, this comparison is more sensitive to horizontal inhomogeneities and differences in atmospheric features sampled by each instrument. While the vertical profiles differ in magnitude, both ATLID and RALI indicate the presence of aerosol layers in the lower and upper altitudes. However, the degree of agreement is limited, especially in terms of SR variability.

When we examine the scatter plots, the correlation between ATLID and RALI remains weak across averaging windows, with Pearson r coefficients ranging from 0.06 to 0.27, in the case of all the averaging windows for the ATLID overpass presented in Fig. 2.a.

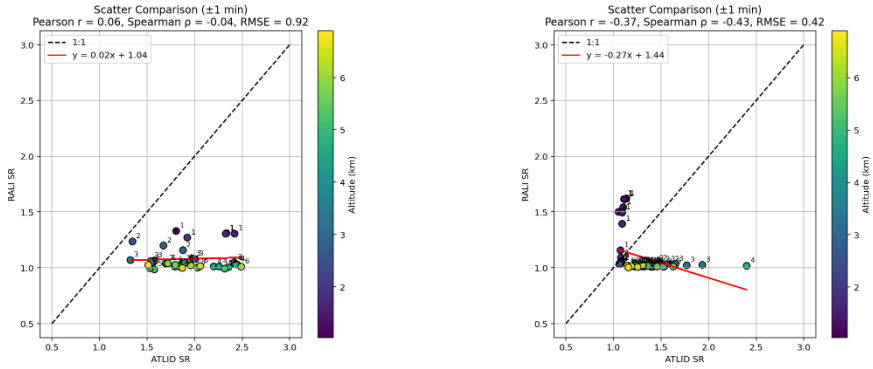

a. b.

Figure 2. Scatter plot comparison of scattering ratios between ATLID and ground-based (RALI) measurements for a night-time overpass. The closest point in the trajectory of the overall overpass was located: **a. 78 km** from the site; **b. 11 km** from the site. Each point represents an altitude-resolved value, with color providing a fine-scale visual cue of the altitude and the number next to each point indicating a coarser altitude bin.

The Pearson correlation coefficient quantifies the strength and direction of a linear relationship between two variables [10]—here, the scattering ratios from ATLID and RALI. A value near zero indicates little to no linear correlation, which is what we observe. The regression lines, which represent the best linear fit to the data, are relatively flat—this further reflects the weak relationship between the two datasets. Still, the majority of points are centered around a scattering ratio close to one, indicating that both instruments agree on the overall scattering regime. Despite the weak linear correlation, the ATLID SR values generally remain within expected physical bounds, suggesting that the instrument captures some aspects of the overall aerosol vertical distribution, though not with strong fidelity.

In contrast, the second overpass, which occurred only 11 km from the ground-based station, shows improved consistency between ATLID and RALI in terms of profile shape and spread (Fig. 1b). While the ATLID and RALI vertical profiles do not match point-for-point, the ATLID scattering ratio exhibits a more compact distribution with less variability compared to the distant overpass.

This reduced spread is reflected in the lower RMSE values (around 0.42), indicating better agreement in the magnitude of retrieved scattering ratios across the vertical column (Fig. 2.b.). RMSE, or Root Mean Square Error, quantifies the typical difference between the ATLID and RALI scattering ratios; lower RMSE implies better agreement overall [11]. Across the different ATLID averaging windows, the Pearson values vary between –0.37 and –0.41. The negative slope of the regression lines and the clustering of points within a narrow range of SR values suggest a systematic offset rather than random disagreement.

While correlation coefficients are not particularly high in none of the two cases presented here, the results remain meaningful and support the use of ATLID as a complementary observational tool. Linear

correlations capture one aspect of similarity, although they do not fully describe agreement in structure or physical consistency. The fact that ATLID retrievals tend to remain within realistic SR bounds (larger than 1), with propagated errors capturing the true variability, further supports the reliability of these observations.

These two case studies are part of a broader dataset comprising seventeen satellite overpasses. In the full analysis, we explore how the distance between ATLID overpasses and the ground-based site affects the agreement between measurements, as well as how different ATLID temporal averaging strategies influence the comparison.

Conclusions

This study explores the agreement between the scattering ratio profiles measured by ATLID and RALI ground-based lidar, respectively. Two nighttime overpasses are presented, corresponding to different distances from the station. The comparison reveals poor agreement between ATLID and ground-based RALI measurements in terms of correlation and SR magnitude. Nevertheless, ATLID profiles remain within physically plausible SR ranges, indicating potential for future consistency studies. Further work is needed with a larger dataset to better assess the factors affecting agreement.

In the full analysis of seventeen overpasses, we further explore how distance and temporal averaging affect ATLID–ground-based consistency. This work supports ATLID's role as a reliable complement to ground-based lidar observations in aerosol and cloud profiling.

Acknowledgements

The work was financed by Smart Growth, Digitization and Financial Instruments Program (POCIDIF) 2021-2027, Action 1.3 Integration of the national RDI ecosystem in the European and international Research Space, project "Supporting the operation of facilities in Romania within the ACTRIS ERIC research infrastructure", SMIS code 309113, the ATMO-ACCESS H2020 Grant Agreement no. 101008004, the CARGO-ACT HEU Grant Agreement no. 101132093, and through the ACTRIS ERIC and CARS Cooperation Agreement / 25 April 2023 and supported by the Core Program within the Romanian National Research Development and Innovation Plan 2022-2027, carried out with the support of MCID, project no. PN 23-05.

References

[1] J. Li, et al., 'Scattering and absorbing aerosols in the climate system', *Nat Rev Earth Environ*, vol. 3, no. 6, pp. 363–379, May 2022, doi: 10.1038/s43017-022-00296-7.

[2] V. Nicolae, et al., 'A multi-year analysis of aerosol properties using the calibrated multi-wavelength polarisation lidar in Măgurele', *Journal of Optoelectronics and Advanced Materials*, vol. 25, pp. 176–190, Apr. 2023.

[3] M. J. Granados-Muñoz, et al., 'A comparative study of aerosol microphysical properties retrieved from ground-based remote sensing and aircraft in situ measurements during a Saharan dust event', *Atmos. Meas. Tech.*, vol. 9, no. 3, pp. 1113–1133, Mar. 2016, doi: 10.5194/amt-9-1113-2016.

[4] T. Wehr, et al., 'The EarthCARE mission – science and system overview', *Atmos. Meas. Tech.*, vol. 16, no. 15, pp. 3581–3608, Aug. 2023, doi: 10.5194/amt-16-3581-2023.

[5] R. Solanki and N. Singh, 'LiDAR observations of the vertical distribution of aerosols in free troposphere: Comparison with CALIPSO level-2 data over the central Himalayas', *Atmospheric Environment*, vol. 99, pp. 227–238, Dec. 2014, doi: 10.1016/j.atmosenv.2014.09.083.

[6] A. Nemuc, et al., 'Assessment of aerosol's mass concentrations from measured linear particle depolarization ratio (vertically resolved) and simulations', *Atmos. Meas. Tech.*, vol. 6, no. 11, pp. 3243–3255, Nov. 2013, doi: 10.5194/amt-6-3243-2013.

[7] G. D'Amico, et al., 'EARLINET Single Calculus Chain – overview on methodology and strategy', *Atmos. Meas. Tech.*, vol. 8, no. 11, pp. 4891–4916, Nov. 2015, doi: 10.5194/amt-8-4891-2015.

[8] A. Ansmann, et al., 'Independent measurement of extinction and backscatter profiles in cirrus clouds by using a combined Raman elastic-backscatter lidar', *Appl. Opt.*, vol. 31, no. 33, p. 7113, Nov. 1992, doi: 10.1364/AO.31.007113.

[9] European Space Agency, 'EarthCARE ATLID NOM Level 1B'. European Space Agency. doi: 10.57780/ECA-224D95C.

[10] P. Schober, C. Boer, and L. A. Schwarte, 'Correlation Coefficients: Appropriate Use and Interpretation', *Anesthesia & Analgesia*, vol. 126, no. 5, pp. 1763–1768, May 2018, doi: 10.1213/ANE.0000000000002864.

[11] T. O. Hodson, 'Root-mean-square error (RMSE) or mean absolute error (MAE): when to use them or not', *Geosci. Model Dev.*, vol. 15, no. 14, pp. 5481–5487, Jul. 2022, doi: 10.5194/gmd-15-5481-2022.

ACTRIS/EARLINET Level 3 dataset: 20-years European aerosol vertical profile climatology

***Lucia Mona*[1]**, *S. Ciamprone*[1], *C. Dema*[1], *P. Guma Claramunt*[1], *G. D'Amico*[1], *E. Ripepi*[1], *N. Siomos*[11], *D. Balis*[2], *S. Romano*[3], *A. Papayannis* [4,12], *C. Muñoz-Porcar*[5], *L. Alados Arboledas*[6], *A. Amodeo*[1], *Z. Peshev*[7], *H. Baars*[8], *H. Vogelmann*[9], *D. Nicolae*[10], *Arnoud Apituley*[13], *Ronny Engelmann*[8], *Ove Gustafsson*[14], *Anatoli Chaikovsky*[16], *Matthias Wiegner*[17], *Iwona S. Stachlewska*[18], *Aleksander Pietruczuk*[19], *Holger Linne*[20], *A. A. Ruth*[31], *M. Fluegge*[21], *C. Pietras*[22], *S. Amoruso*[23], *D. Dionisi*[23], *I. Mattis*[24], *P. Goloub*[25], *P. Freville*[26], *J.P. Putaud*[27], *M. Alpers*[28], *D. Bortoli*[29], *Z. Peshev*[30], *G. Vaughan*[31], *D. Samulenkov*[32]

1 Consiglio Nazionale delle Ricerche - Istituto di Metodologie per Analisi Ambientali, Tito - Italy (CNR-IMAA) https://ror.org/024ye7w89
2 Laboratory of Atmospheric Physics, Physics Department, Aristotle University of Thessaloniki, Thessaloniki – Greece (AUTH) https://ror.org/02j61yw88
3 University of Salento, Mathematics and Physics Department, Lecce - Italy (UniSalento) https://ror.org/03fc1k060
4 National Technical University of Athens, Physics Department, Athens - Greece (NTUA) https://ror.org/03cx6bg69
5 Universitat Politecnica de Catalunya, Barcelona - Spain (UPC) https://ror.org/03mb6wj31
6 Andalusian Institute for Earth System Research, University of Granada, Granada - Spain (IISTA-CEAMA) https://ror.org/04njjy449
7 Institute of Electronics, Bulgarian Academy of Sciences, Sofia - Bulgaria (IE-BAS) https://ror.org/0299eyn73
8 Leibniz Institute for Tropospheric Research, Leipzig - Germany (TROPOS) https://ror.org/03a5xsc56
9 Karlsruher Institut für Technologie, Garmisch-Partenkirchen - Germany (KIT) https://ror.org/04t3en479
10 National Institute of R&D for Optoelectronics, Măgurele - Romania (INOE) https://ror.org/03epxcz56
11 Ludwig-Maximilians-Universität München Munich - Germany (LMU) https://ror.org/05591te55
12 Laboratory of Atmospheric Processes and their Impacts, School of Architecture, Civil & Environmental Engineering, École Polytechnique Fédérale de Lausanne, 1015 Lausanne, Switzerland
13 Royal Netherlands Meteorological Institute, Cabau – Netherlands (KNMI) https://ror.org/05dfgh554
14 Swedish Defence Research Agency, Linkoping – Sweden (FOI) https://ror.org/0470cgs30
16 B.I. Stepanov Institute of Physiscs, Minsk – Belarus
17 Meteorological Institute Munich (MIM), Munich – Germany
18 University of Warsaw, Faculty of Physics, Warsaw – Poland https://ror.org/039bjqg32
19 Institute of Geophysics, Polish Academy of Sciences, Belsk – Poland (IGF) https://ror.org/039bjqg32
20 Max-Planck-Institut für Meteorologie, Hamburg - Germany (MPI-M) https://ror.org/05esem239
21 ALOMAR/Andøya Space Center, Andøya – Norway https://ror.org/02q5gf687
22 Centre National de la Recherche Scientifique, Palaiseau - France (CNRS) https://ror.org/02feahw73
23 Consiglio Nazionale delle Ricerche - Istituto di Scienze Marine, Rome – Italy (CNR-ISAC) https://ror.org/02hdf6119
23Dipartimento di Fisica Ettore Pancini - Università degli studi di Napoli Federico II, Naples - Italy (UniNA) https://ror.org/05290cv24
24 DWD Meteorological Observatory Hohenpeissenberg – Germany (DWD) https://ror.org/02nrqs528
25 Lille University - Science and Technology, Lille – France https://ror.org/02feahw73
26 Observatoire de Physique du Globle, Clermont-Ferrand - France (OPGC-LaMP) https://ror.org/01a8ajp46
27 Joint Research Centre - Institute for Environment and Sustainability, Ispra – Italy https://ror.org/02qezmz13
28 Leibniz Institute of Atmospheric Physics, Kuehlungsborn – Germany (IAP) https://ror.org/04enhpe73
29 Institute for Earth Sciences, Evora – Portugal (ICT) https://ror.org/02gyps716
30 Institute of Electronics, Bulgarian Academy of Sciences, Sofia – Bulgaria https://ror.org/0299eyn73
31 Phys. Dep. and Env. Res. Institute, University College Cork, Cork – Ireland https://ror.org/03265fv13
32 University of Wales, Aberystwyth, Aberystwyth - United Kingdom (UWA) https://ror.org/015m2p889
33 Research Park of Saint-Petersburg State University - Observatory of environmental safety, St. Petersburg - Russia

Corresponding author: lucia.mona@cnr.it

Introduction

Aerosol particles into the atmosphere have a manyfold impacts on climate, air quality, atmospheric processes, but also on health, ecosystems, and society. To gain a better knowledge of the aerosol climatology for understanding the impact of the air quality regulations over the time and for providing inputs for climate modelling, the high-quality data provided by ACTRIS can be key. ACTRIS, built on the heritage of pre-existing networks like EARLINET, Cloudnet, EUSAAR and EUROCHAMP, is providing standardized, harmonized and traceable high-quality data for short-lived atmospheric quantities, i.e. aerosol, clouds and trace gases. Officially started as an ERIC in 2023, the ACTRIS activities started in 2010, but the pre-existing networks data are available through ACTRIS as data legacy. Aerosol profiles collected by the Raman lidar

stations aggregated first in the EARLINET network and then in the ACTRIS RI are curated and provided by ACTRIS ARES data centre through web interface and machine-to-machine REST-API. Currently the database stores 1234375 data files, covering 25 years of data and 55 stations. The NRT provision of data is implemented at about 15 stations distributed over Europe, and QC procedures run automatically and centrally on all the data during the submission phase.

Data and methodology

The Level 3 products are centrally and automatically produced by the ACTRIS Data Centre unit for the Aerosol REmote Sensing (ARES) at CNR, guarantying harmonized procedures on the datasets. This is compliant with the general structure of the EARLINET database, allowing for versioning, traceability, and harmonization of the processes. These Level 3 products are obtained as aggregated products from the fully quality controlled (Level 2) aerosol optical products, through an openly available R-code developed at CNR, handling Level 2 data and adopting specific aggregation methods for avoiding biases in aggregated ACTRIS/EARLINET files potentially due to the not continuous sampling and limitation of lidar measurements in bad weather conditions (low clouds-rain). To avoid biases due to measurements made on purpose specifically for capturing special events, it is considered only subset of data corresponding to regular schedule and measurements done for satellite validation purposes (i.e., climatological and calipso category files following the current database organization).

Data are organized for station. For each station, three types of data are released: profile values, integrated quantities, layer statistics. For each type of data, four different temporal aggregations are provided: seasonal, annual, normal seasonal, normal monthly.

ACTRIS/EARLINET Level 3 2000-2019 climatological products contains data for a total of 33 stations from 15 different countries. Full documentation is available on the at EARLINET website: www.earlinet.eu [1] and data are reachable at [7].

The following data are reported as integrated quantity: aerosol optical depth (AOD) and aerosol integrated backscatter (IB) for the total investigated atmospheric column and within the atmospheric boundary layer (identified from lidar profiles using the aerosol as a tracer). In the integrated products, are reported also the aerosol content center of mass (a proxy for the altitude where the most relevant part of the aerosol load is located) and the H63, the altitude below which stays 63% of the aerosol. These two quantities are calculated on the base of backscatter profiles at the different wavelength and from AOD and IB, respectively. Integrated products also include lidar ratio and particle depolarization averages in the considered atmospheric portion (total column and ABL).

Finally, for each Level 2 file, geometrical information about layers is retrieved using an algorithm based on the one shown in [2], applied to the backscatter vertical profile. These geometrical products (mainly, altitude of the lower and upper bound of the layers) are then used to calculate the following optical products: extinction, backscatter, lidar ratio, particle depolarization and AOD, IB and center of mass. In particular, pdf for all optical products inside the layers are reported in the level 3-layer products.

First Results

In the following, some examples of Level 3 data are reported. The reported examples are related, for the sake of simplicity in illustrative description to the same EARLINET station, namely Potenza – IT (POT). This station being located in the Southern part of Italy is often affected by desert dust intrusion from Northern Africa [3,4] and it also recorded some volcanic eruptions [5,6]. Potenza is located at about 800 m asl and it is far from big cities, so it could be considered as an almost clean site and reference for the background condition of a larger area in Italy.
Figure 2 reports the annual mean aerosol backscatter profile at 532 nm. At first glance, the plot clearly shows that most of the aerosol content is confined below 5 km of altitude with the largest part of it remaining below 2 km asl. The blue portion very close to the ground is a related to the vertical range where the lidar system is blind for overlap reason and therefore no data are available: this range changed in 2006 with a significant upgrade of the system which allowed among other aspects to reduce the overlap range.

Few data available (note that the number of samplings is one information reported in the Level 3 files) affected the mean profiles for 2005 and 2012-2014 producing blue-dominated stripe in the Fig 2.
Significant layers in the upper troposphere are evident in 2010 and 2017, respectively related to the Eyjafjallajökull eruption in 2010 and long range transported forest fires in 2017 [5].

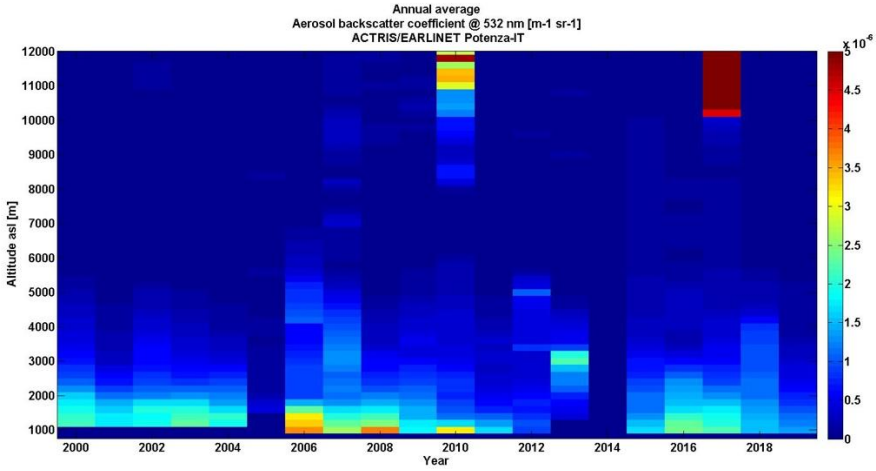

Figure 2. Annual mean aerosol backscatter profiles at 532 nm for the Potenza station. Data are reported with a fixed 200 m resolution from 100m up to 12100 m asl.

An example of Normal Season layer product is provided in Figure 3, which reports the pdf of mean lidar ratio values collected in the identified aerosol layers. The shape of the pdf is different season by season. During winter, when atmosphere is very clean few aerosol layers are identified and lidar ratio has a wide pdf covering 0-100 sr range. During Autumn, a more homogenous and flatter pdf is observed for lidar ratio with values equally distributed in the 20-50 sr range and with some occurrences for larger lidar ratio values. The larger number of mean values in Spring and Summer is the result of the many cases of free troposphere layers occurring in these seasons. During Spring the lidar ratio pdf is centered around 40 sr and has a tail toward values larger than 60 sr. In Summer the pdf has two modes: the first is centered around 40-50 sr and could be representative of layers dominated by desert dust content and the second one around 70 sr that could be instead related to biomass burning typically occurring in the Southern Europe in summer.

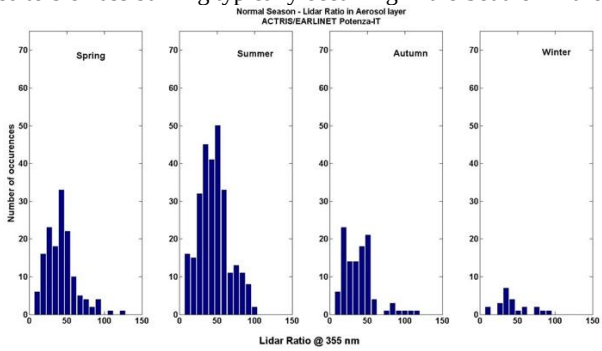

Figure 3. example of Normal Season lidar ratio pdf in the aerosol layers for Potenza-IT.

Summary and next steps

The advanced long-term dataset provided by the ACTRIS/EARLINET Level 3 2000-2019 collection [7] provides the possibility to investigate the differences between local and long range transported aerosol contribution, to investigate long term evolution of the aerosol content, the aerosol stratification in the vertical dimensions and the seasonal dependence of such characteristic everything at the different stations over

Europe. At the conference, the main characteristics will be discussed for the 10 stations collecting the highest number of data covering West Mediterranean (Granada and Barcelona), Central Mediterranean (Potenza and Lecce), Eastern Mediterranean (Athens and Thessaloniki), Central Europe (Leipzig and Garmisch), Eastern Europe (Bucharest and Sofia). The specific differences among the couple of stations for each "cluster" will provide additional information about representativeness and peculiarities of each site.

Acknowledgements

The precious work done by ACTRIS RI is essential for the presented work from managerial tasks at HO, to the QA/QC activities done at CARS and ARES, and at the stations side for collecting measurements and following the ACTRIS standards. The EARLINET activities are greatly acknowledged for pushing forward the standardization and quality of data since 2000.

This work was funded by MUR (Italian Ministry of University and Research) through PON "Ricerca e Innovazione 2014–2020" under the following projects: CIR PER-ACTRIS-IT (Potenziamento della componente italiana della Infrastruttura di Ricerca Aerosol, Clouds and Trace Gases Research Infrastructure—Rafforzamento del capitale umano)—Avviso MUR D.D. n. 2595 del 24.12.2019 Piano Stralcio "Ricerca e Innovazione 2015–2017", CIR01_00015, CUP B58I2000022000; by European Union under RI-Urbans (Research Infrastructures Services Reinforcing Air Quality Monitoring Capacities in European Urban & Industrial AreaS) project– Grant Agreement n. 871115 and by ECMWF/COPERNICUS under the contract C3S2_311: Collection and Processing of In Situ Observations; Lot.

References

[1] Mona L., S. Ciamprone, G. D'Amico, *EARLINET Level3 Data Product Catalogue*, available at https://www.earlinet.org/index.php?id=319 and https://github.com/actris-ares/actris-level3-aerosol-profiling-climatology, 2022.

[2] Siomos, N., Balis, D. S., Voudouri, K. A., Giannakaki, E., Filioglou, M., Amiridis, V., Papayannis, A., and Fragkos, K.: *Are EARLINET and AERONET climatologies consistent? The case of Thessaloniki, Greece*, Atmos. Chem. Phys., 18, 11885–11903, https://doi.org/10.5194/acp-18-11885-2018, 2018.

[3] Mona, L., A. Amodeo, M. Pandolfi, G. Pappalardo (2006): *Saharan dust intrusions in the Mediterranean area: Three years of Raman lidar measurements*. J. Geophys. Res., vol. 111, D16203, doi:10.1029/2005JD006569

[4] Mona, L., Papagiannopoulos, N., Basart, S., Baldasano, J., Binietoglou, I., Cornacchia, C., and Pappalardo, G.: *EARLINET dust observations vs. BSC-DREAM8b modeled profiles: 12-year-long systematic comparison at Potenza, Italy*, Atmos. Chem. Phys., 14, 8781–8793, https://doi.org/10.5194/acp-14-8781-2014, 2014.

[5] Mona, L., Amodeo, A., D'Amico, G., Giunta, A., Madonna, F., and Pappalardo, G.: *Multi-wavelength Raman lidar observations of the Eyjafjallajökull volcanic cloud over Potenza, southern Italy,* Atmos. Chem. Phys., 12, 2229–2244, https://doi.org/10.5194/acp-12-2229-2012, 2012.

[6] Pappalardo G., Amodeo, A., Mona, L., Pandolfi, M., Pergola, N., and Cuomo, V.: *Raman lidar observations of aerosol emitted during the 2002 Etna eruption*, Geophys. Res. Lett., 31, L05120, doi:10.1029/2003GL019073, 2004.

[7] ACTRIS ARES Data Centre, Mona, L., D'Amico, G., Ciamprone, S., Ripepi, E., Amato, F., Dema, C., & Guma-Claramunt, P. (2024). ACTRIS/EARLINET Level 3 2000-2019 climatological dataset (Version 2). National Research Council - Institute of Methodologies for Environmental Analysis. https://doi.org/10.57837/cnr-imaa/ares/actris-earlinet/level3/climatological/2000_2019/all

Near Real Time (NRT) provision of ACTRIS aerosol profiles

***Pilar Gumà-Claramunt*[1]**, *L. Mona*[1], *C. Dema*[1], *P. F. Amato*[1], *G. D'Amico*[1], *E. Ripepi*[1], *S. Lolli*[1], *N. Papagiannopoulos*[1], *S. Gagliardi*[1], *M. Proto*[1], *A. Amodeo*[1], *D. Balis*[2], *V. Amiridis*[3], *M. Komppula*[4], *C. Muñoz-Porcar*[5], *L. Alados Arboledas*[6], *I. Stachlewska*[7], *H. Baars*[8], *I. Mattis*[9], *D. Nicolae* [10], *R-E. Mamouri* [11], *L. Jone* [12], *J. Wilkinson*[12]

1 Consiglio Nazionale delle Ricerche - Istituto di Metodologie per Analisi Ambientali, Tito - Italy (CNR-IMAA) https://ror.org/024ye7w89
2 Laboratory of Atmospheric Physics, Physics Department, Aristotle University of Thessaloniki, Thessaloniki – Greece (AUTH) https://ror.org/02j61yw883
3 National Observatory of Athens, Athens - Greece (NOA) https://ror.org/03dtebk39
4 Finnish Meteorological Institute, Atmospheric Research Centre of Eastern Finland, Kuopio – Finland (FMI) https://ror.org/05hppb561
5 Universitat Politecnica de Catalunya, Barcelona - Spain (UPC) https://ror.org/03mb6wj31
6 Andalusian Institute for Earth System Research, University of Granada, Granada - Spain (IISTA-CEAMA) https://ror.org/04njjy449
7 University of Warsaw, Faculty of Physics, Warsaw - Poland (UW) https://ror.org/039bjqg32
8 Leibniz Institute for Tropospheric Research, Leipzig - Germany (TROPOS) https://ror.org/03a5xsc56
9 German Meteorological Service, Meteorological Observatory Hohenpeissenberg, Hohenpeissenberg – Germany (DWD) https://ror.org/02nrqs528
10 National Institute of R&D for Optoelectronics, Măgurele - Romania (INOE) https://ror.org/03epxcz56
11 ERATOSTHENES Centre of Excellence, Limassol – Cyprus (ECoE)
12 Copernicus Department, European Centre for Medium-Range Weather Forecasts, Reading - United Kingdom (ECMWF) https://ror.org/014w0fd65

Corresponding author: pilar.gumaclaramunt@cnr.it

Introduction

Atmospheric aerosols are considered one of the major uncertainties in climate forcing and a detailed aerosol characterization is needed to understand their role in the atmospheric processes as well as on human health and environment. The major cause of uncertainty is the large variability of aerosols in space and time. Due to their short lifetime and strong interactions, their global concentrations and properties are poorly known. For these reasons, information on the large scale 4-dimensional aerosol distribution in the atmosphere should be continuously monitored.

Since it is in particular the information on the vertical distribution that is lacking, advanced laser remote sensing is the most appropriate tool to close the observational gap. Lidar techniques represent the optimal tool to provide range-resolved aerosol data. Additionally, lidar observations can be even more beneficial, if used in coordinated networks. These arguments were the motivation for the establishment of EARLINET, the European Aerosol Research Lidar Network [1] in the 2000. Long term perspective and strategy for providing 4D aerosol observations with more and more increasing quality level are set up within ACTRIS (Aerosol Clouds and Trace Gases Research Infrastructure) [2]. ACTRIS integrates state-of-the-art European ground-based stations for long-term observations of aerosols, clouds and short-lived gases taking advantage of existing network with the aim of constructing of a user-oriented RI (Research Infrastructure) responding to needs expressed by a wide international atmospheric research community.

At the time being, the ACTRIS/EARLINET database is the largest ground-based database of aerosol optical property profiles. Based mainly on Raman observational capability, ACTRIS/EARLINET provides data of higher quality with respect to simple elastic backscatter lidars like ceilometer networks (low power backscatter lidars) widely distributed around the globe. These high-quality data can be essential for assimilation, near real time verification and off-line validation purposes.

This abstract shortly describes the steps done in ACTRIS for implementing the NRT aerosol profiles provision and some results about the first year of systematic NRT provision at 11 selected ACTRIS/EARLINET stations.

NRT data provision implementation

The NRT provision of ACTRIS/EARLINET data is currently tested at 11 stations involved in the CAMS21b_2 with ECMWF/Copernicus aiming to provide the ground-based high-quality profiles provided by ACTRIS for improving models. The 11 stations selected for such contract are reported in Figure 1: this group of stations covers different regions of Europe from deep north to Mediterranean from far end at West to Bucharest and Limassol at East.

Figure 1. ACTRIS/EARLINET stations involved in the CAMS21b2 provision.

To faster data provision from the station, automatic and machine to machine tools have been implemented: the submission from stations to ACTRIS ARES (Aerosol REmote Sensing) DC Unit has been typically automated at the station side; the automatic submission from the centralized processing suite of ARES to the ARES database has been made possible as choice for the stations. Finally, API has been developed on top of ACTRIS/EARLINET DB to guarantee CAMS access to all produced data through machine-to-machine connection. Finally, a priority has been associated to the processing of current measurements respect to the other stations and to the reprocessing of old measurements.

To provide the highest possible quality of data even in NRT, actions have been done also for improving the Quality Assurance (QA) and Quality Control (QC) procedures toward this direction. QA test performed at the stations are checked by the calibration center. The results are subsequently integrated into the SCC - Single Calculus Chain (the centralized lidar processing suite [3]) to fine-tune the "operational configurations" employed by ACTRIS stations for lidar data processing. Only data which are fully quality controlled (processed with a valid operational configuration and passing all quality checks along the processing chain) can reach the highest quality of data, namely the Level 2 [4].

To be labelled as Level 2 data should be compliant to all the QC procedures working on the data directly during the phase of submission of data to the ACTRIS database. Among these procedures, one requires the use of modelled profiles (or radiosounding) of atmospheric density, which is needed as input for the aerosol backscatter retrieval. A devoted system has been implemented within ACTRIS DC for accessing the model's data and made available profiles for the ACTRIS stations in a short time, so that the quality of provided data is not affected, neither in NRT, by error due to standard atmospheric profile in the retrieval.

Still to improve the quality even in NRT, multi-product quality controls (MPQC) are executed to assess the quality from a physical point of view of the products, by comparing different products from the same

measurement. This step can only be applied to the products that are being submitted automatically from the SCC.

Efficiency of NRT provision

In figure 2, the NRT provision from each one of the stations is reported. It is worth noticing that Palaiseau, France - SIR is not reported and analysed here because indeed they are not yet providing data on the database, after encountering internal problems at their side first in doing measurements and then in setting up the automatic data workflow. Overall good performances in NRT provision are observed at almost all the stations accounting for on average 90% of data uploaded in NRT. Only two stations namely Antikythera and Thessaloniki are currently not reaching the desired amount (80%) of data provided in NRT data: they currently uploading file in a manual mode and record around 35% and 83% of data uploaded not in NRT, respectively.

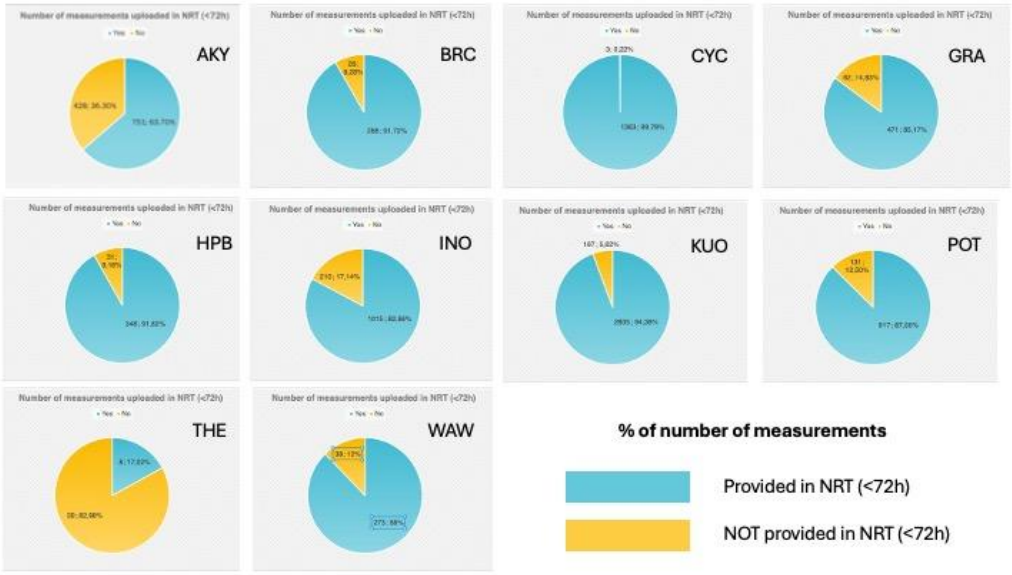

Figure 2. Pie chart about NRT provision for the 10 stations providing measurements in CAMS21b_2 project.

Summary and next steps

A first study case has been selected for starting the model's comparison/evaluation activity: the strong dust event occurred in February-April 2024 over Europe. Relevant observations of the events have been collected at Barcelona (ES), Potenza (IT), Leipzig (DE).

The arrival of dust is observed on March 29 over Barcelona at very low altitude and intruding into the boundary level and reaching the ground. The day after over Potenza (IT) a 4 km layer with high depolarization arrives and slowly reached the ground. The same day over Leipzig a lofted depolarizing layer arrives and part of it was deposited to the ground. Other days and other stations are involved in the dust intrusion in the beginning of Spring 2024, but these can be considered as the pivot case study for our aims.

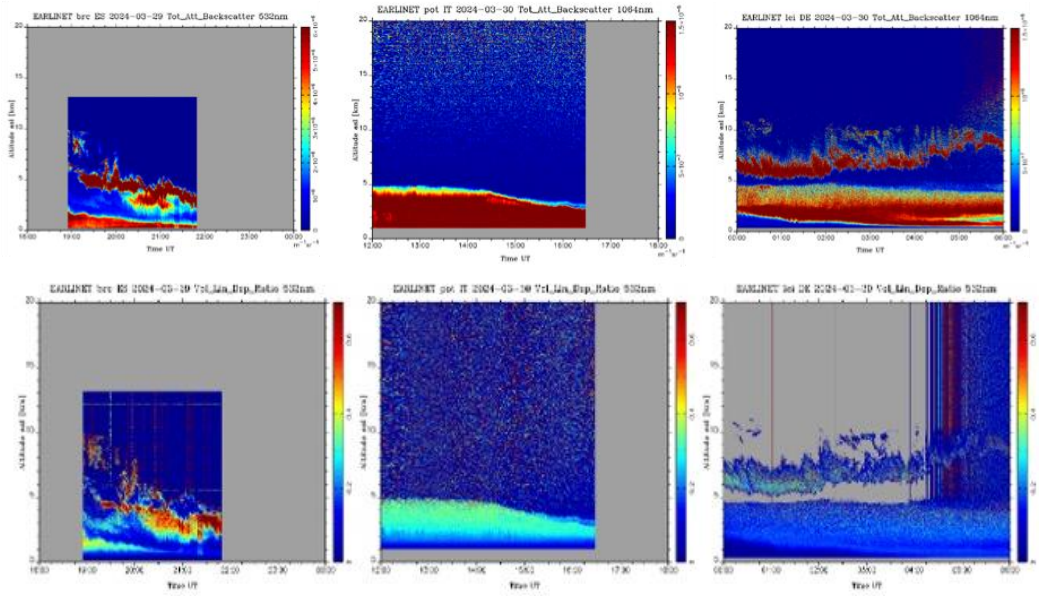

Figure 3. Dust intrusion over Europe. Examples of aerosol lidar observations at Barcelona (ES), Potenza (IT), Leipzig (DE) in 29-30 March 2024 period. In the top panel the total attenuated backscatter signals are reported (532 nm for BRC and POT, 1064 nm for LEI), while in the bottom panel the volume depolarization as tracer of dust (and clouds) presence is reported.

The comparison will be carried out in terms of models' capability to reproduce the mineral dust vertical structure and geographical distribution. Improvements eventually obtained through assimilation could be evaluated.

Finally, ACTRIS/EARLINET data back to 1999 are currently being ingested into ECMWF system to compare the ACTRIS/EARLINET data with the CAMS model predictions of backscatter and, where possible, with extinction. First results will be showed at the conference.

Acknowledgements

The precious work done by ACTRIS RI is essential for the presented work from managerial tasks at HO, to the QA/QC activities done at CARS and ARES, and at the stations side for collecting measurements and following the ACTRIS standards. The EARLINET activities are greatly acknowledged for pushing forward the standardization and quality of data since 2000.

This work was funded by MUR (Italian Ministry of University and Research) through ITINERIS (Italian Integrated Environmental Research Infrastructures System). PIANO NAZIONALE DI RIPRESA E RESILIENZA (PNRR) MISSIONE 4, COMPONENTE 2, INVESTIMENTO 3.1 "Fondo per la realizzazione di un sistema integrato di infrastrutture di ricerca e innovazione", Project code IR0000032 (1 November 2022 – 30 April 2025 + 6 months) and by ECMWF/COPERNICUS under the contract CAMS21b_2 ACTRIS- Aerosol Profile Provision (ACTRIS-APP).

References

[1] Pappalardo, G., and Coauthors: EARLINET: towards an advanced sustainable European aerosol lidar network, Atmos. Meas. Tech., 7, 2389–2409, https://doi.org/10.5194/amt-7-2389-2014, 2014.

[2] Laj, P., and Coauthors, 2024: Aerosol, Clouds and Trace Gases Research Infrastructure (ACTRIS): The European Research Infrastructure Supporting Atmospheric Science. Bull. Amer. Meteor. Soc., 105, E1098–E1136, https://doi.org/10.1175/BAMS-D-23-0064.1.

[3] D'Amico, G., and Coauthors.: EARLINET Single Calculus Chain – overview on methodology and strategy, Atmos. Meas. Tech., 8, 4891–4916, https://doi.org/10.5194/amt-8-4891-2015, 2015.

[4] EARLINET_QC_v4_0_20250225.pdf, available at https://www.earlinet.org/index.php?id=293.

Aerosol Typing Using Multiwavelength Lidar and Machine Learning Applied to EARLINET Stations

A. del Águila[1,2], P. Ortiz-Amezcua[1,2], S. Tabik[3], J. A. Bravo-Aranda[1,2], S. Fernández-Carvelo[1,2], A. Canella-Ortiz[1,2] and ***L. Alados-Arboledas[1,2]***

(1) Andalusian Institute for Earth System Research (IISTA-CEAMA), 18006 Granada, Spain
(2) Department of Applied Physics, University of Granada, 18071 Granada, Spain
(3) Department of Artificial Intelligence, University of Granada, 18071 Granada, Spain
Corresponding author: anadelaguila@ugr.es

Introduction

Aerosol typing from lidar observations is essential to assess aerosol properties, sources, and climatic effects. While classical methods rely on predefined optical property thresholds, recent advances suggest machine learning (ML) can improve classification robustness and consistency. Several automatic algorithms using European Aerosol Research Lidar Network (EARLINET) data have been proposed for aerosol typing in the recent years, including a supervised classification approach based on Mahalanobis distance [1] and neural network method [2], all demonstrating the potential of advanced techniques to enhance aerosol classification across the network [3]. In this work, we apply several ML algorithms to high-vertical-resolution multiwavelength lidar data from the University of Granada (UGR) station, part of EARLINET. Our approach allows automatic aerosol typing using both extensive and intensive optical properties, including depolarization, backscatter, extinction coefficients, lidar ratios and Ångström exponents. We test six ML models and validate the best-performing one, which is LightGBM, against a manually labeled dataset and an independent Saharan dust event [4]. The results of this work are extended to additional EARLINET stations and incorporate new capabilities from the latest multiwavelength lidar system in Granada, ALHAMBRA.

Methodology

Multiwavelength lidar profiles from the MULHACEN system (355, 532, 1064 nm) for 2012–2015 were obtained from the EARLINET database. Intensive parameters such as lidar ratio (LR), Ångström exponent (AE), color ratio (CR), and color index (CI) were derived and aggregated by aerosol layers, detected using the gradient method [5] applied to backscatter at 1064 nm. Layers were manually classified into five aerosol types: Continental polluted, Dust, Mixed, Smoke, and Unknown. Supervised ML algorithms were trained on the resulting labeled dataset (N=416 layers) for two configurations: with and without depolarization. The six ML models evaluated are: Decision Tree, Random Forest, Gradient Boosting, XGBoost, LightGBM, and a Neural Network, representing a mix of tree-based methods and a non-linear models.

The ML pipeline used GridSearchCV for hyperparameter tuning and GroupKFold to preserve the integrity of layer-based sampling. Feature importance was assessed using SHAP values to identify key contributors to classification performance. The final model was validated against an independent dataset corresponding to the July 2016 Saharan dust event in Granada.

Results and Discussion

Among the tested models, LightGBM consistently achieved the highest precision, recall, and F1-scores (>90% with depolarization; ~87% without). Depolarization emerged as a key feature, especially for distinguishing dust and smoke. Vertical resolution enhanced model performance, particularly for high-confidence cases, while the “Unknown” class enabled reliable treatment of noisy or non-physical meaning observations.

Figure 1 shows an example of the aerosol typing output for vertically resolved aerosol layers with LightGBM model over Granada during the period July–August 2013. The results demonstrate consistent classification of aerosol types, effectively capturing the temporal variability of distinct aerosol categories, including the Unknown class. The model also performed well in external validation, correctly identifying 82% of dust layers during the 2016 Saharan dust event.

Importantly, this methodology is foreseen to be scaled to other stations with similar instrumentation. As part of future work, we plan to apply the model to additional EARLINET locations and explore transfer learning techniques to account for local aerosol variability. Moreover, preliminary results are presented to incorporate measurements from ALHAMBRA, the newest multiwavelength lidar at UGR station, which enhances vertical resolution and polarization capabilities. This would allow assessing the generalizability of the classification model and exploring real-time applications with higher temporal/vertical resolution.

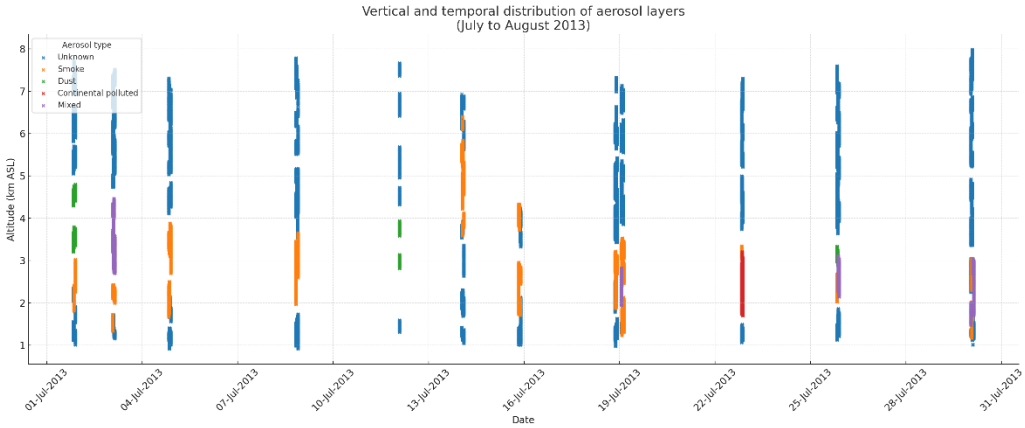

Figure 1. Results of the aerosol typing for UGR station from EARLINET for the period of July 2013. The different colors indicate the aerosol types for each profile.

Conclusions

This study demonstrates that ML methods, particularly LightGBM, can significantly enhance aerosol classification from lidar data. The inclusion of depolarization and vertically resolved features improves accuracy, while the flexible framework allows adaptation to new datasets and stations. Ongoing efforts aim to extend the methodology regionally, leveraging both historical datasets and new instruments like ALHAMBRA. Compared to existing ML approaches, the added value of this model lies in its ability to handle real, height-resolved lidar data efficiently while maintaining high accuracy.

Acknowledgements

This research is part of the Spanish national projects PID2023-151817OA-I00, PID2020-120015RB-I00 and PID2022-142708NA-I00, funded by MICIU/AEI/10.13039/501100011033 and by the "European Union NextGenerationEU/PRTR". It is also supported by ACTRIS-IMP grant agreement No 871115, ACTRIS-España (RED2022-134824-E), Scientific Unit of Excellence: Earth System (UCE-PP2017-02), and by University of Granada Plan Propio through Excellence Research Unit Earth Science and Singular Laboratory AGORA (LS2022-1) programs. P. Ortiz-Amezcua is funded by European project ATMO ACCESS - Solutions for Sustainable Access to Atmospheric Research Facilities (Ref. 101008004). S. Fernández-Carvelo received funding from the Spanish Ministry of Research and Innovation (Agencia Estatal de Investigación), grant PRE2021-098351 (co-funded by the European Social Fund Plus). A. del Águila is part of Juan de la Cierva programme through grant JDC2022-048231-I funded by MICIU/AEI/10.13039/501100011033 and by European Union "NextGenerationEU"/PRTR.

References

[1] Papagiannopoulos, N., et al.: An automatic observation-based aerosol typing method for EARLINET, *Atmos. Chem. Phys.*, 18, 15879–15901, doi:10.5194/acp-18-15879-2018, 2018.

[2] Nicolae, D., et al.: A neural network aerosol typing algorithm based on lidar data, *Atmos. Chem. Phys.*, 18, 14511–14537, doi:10.5194/acp-18-14511-2018, 2018.

[3] Voudouri, K.A., et al..: Comparison of two automated aerosol typing methods and their application to an EARLINET station, *Atmos. Chem. Phys.*, 19, 10961–10980, doi:10.5194/acp-19-10961-2019, 2019.

[4] del Águila, A., et al.: Aerosol type classification with machine learning techniques applied to multiwavelength lidar data from EARLINET, *EGUsphere [preprint]*, doi:10.5194/egusphere-2025-269, 2025.

[5] Belegante, L., et al.: Retrieval of the boundary layer height from active and passive remote sensors: Comparison with a NWP model, *Acta Geophys.*, 62, 276–289, https://doi.org/10.2478/s11600-013-0167-4, 2013.

Best Practice Protocol for the Validation of Aerosol, Cloud, and Precipitation Profiles (ACPPV) and its application for the validation of the EarthCARE lidar products

Amiridis, V.[1], *Marinou, E.[1], Hostetler, C.[2], Koopman, R.[3], Cecil, D., J.[4], Moisseev, D.[5], Tackett, J.[2], Gross, S.[6], Baars, H.[7], Redemann, J.[8], Marenco, F.[9], Baldini, L.[10], Tanelli, S.[11], Fielding, M.[12], Janisková, M.[12], Tanaka, T.[13], O'Connor, E.[14], Fjæraa, A., M.[15], P. Paschou[1], K.A. Voudouri[1], A. Karipis[1], M. Tsichla[1], K. Rizos[1], A. Tsekeri[1], I. Tsikoudi[1], G. Peletidou[16], D. Balis[16], K. Michailidis[16], and the ACPPV consortium [17]*

(1) Institute of Astronomy, Astrophysics, Space Applications & Remote Sensing (IAASARS), National Observatory of Athens (NOA), Athens, Greece
(2) NASA Langley Research Center, Hampton, United States
(3) European Space Research and Technology, European Space Agency (ESA/ESTEC, Noordwijk, The Netherlands
(4) NASA Marshall Space Flight Center, Earth Science Branch, Huntsville, United States
(5) Institute for Atmospheric and Earth System Research, Faculty of Science, University of Helsinki, Helsinki, Finland
(6) Institut für Physik der Atmosphäre, Deutsches Zentrum für Luft- und Raumfahrt (DLR), Weßling, Germany
(7) Leibniz Institute for Tropospheric Research (TROPOS), Leipzig, Germany
(8) School of Meteorology, University of Oklahoma, Norman, Oklahoma, United States
(9) The Cyprus Institute, Nicosia, Cyprus
(10) National Research Council, Insitute of Atmospheric Science and Climate (CNR-ISAC), Roma, Italy
(11) Jet Propulsion Laboratory, California Institute of Technology, Pasadena, California, United States
(12) European Centre for Medium-Range Weather Forecasts (ECMWF), Reading, United Kingdom
(13) Earth Observation Research Center, Japan Aerospace Exploration Agency (JAXA), Tsukuba, Japan
(14) Finnish Meteorological Institute, Climate Research Programme, Helsinki, Finland
(15) Climate and Research Institute NILU, Kjeller, Norway
(16) Aristotle University of Thessaloniki (AUTH), Thessaloniki, Greece
(17) 57 institutes, universities, and space agencies

Corresponding author: vamoir@noa.gr

Introduction

Aerosols, clouds, precipitation, and the processes governing their interactions are the grand challenges for current climate science, of the highest priority for the climate science-policy interface, and of great relevance for both Working Groups I and III of the 7th IPCC cycle. Satellite missions such as CALIPSO and CloudSat have demonstrated the value of aerosol and cloud profiling techniques in understanding the processes governing aerosol-cloud-radiation interactions. The ESA-JAXA EarthCARE satellite mission, launched in May 2024, will ensure the continuity of these efforts and further advance space-borne lidar and cloud radar profiling synergies, with the utilization of its state-of-the-art instrumental suite consisting of a high spectral resolution ATmospheric LIDar (ATLID), a Doppler Cloud Profiling Radar (CPR), a MultiSpectral Imager (MSI), and a BroadBand Radiometer (BBR). Following EarthCARE, the AOS, Aeolus2, LUCE, and WIVERN upcoming and anticipated missions will further contribute to our studies of the unknown links between aerosols, clouds, atmospheric convection, and precipitation.

Prior to their exploitation, Calibration and Validation (Cal/Val) of all the space-based products are needed. The geophysical validation of space-based high-resolution profilers for aerosols, clouds, and precipitation presents unique challenges. The need for a common practice, capturing lessons learned from earlier missions, was tracked under the CEOS Working Group Calibration and Validation action item CV-22-01. An international consortium of 97 scientists converged on the Best Practice Protocol for the Validation of Aerosol, Cloud, and Precipitation Profiles (ACPPV). To this end, suborbital collocated lidar measurements play a key role, and can be used to evaluate the spacebased lidar and aerosol products. Following the guidance provided from the ACPPV protocol, we are evaluating the EarthCARE lidar and aerosol products. Herein a brief summary of the protocol is presented, along with validation case studies from the first year of the EarthCARE mission.

Methodology

The ACPPV protocol [1] supports the community's efford for the optimization of Cal/Val techniques in terms of used instrumentation, sampling strategies and scenarios, and intercomparison methodologies. To this end, the scientific communities involved in satellite missions identified areas where convergence on

similar approaches is beneficial, and provide a detailed list of products from space profiles (i.e. CALIOP, CATS, CloudSat, GPM, EarthCARE Atlid & CPR, INCUS), including validation needs from the product developer's perspective (Chapter 2). The approaches and recommendations cover correlative measurements, site and instrument selection, data quality control, campaign criteria, configurations, scenarios, collocation criteria, suggestions on issues concerning scene spatiotemporal representativeness, and scene homogeneity (Chapter 3), and a thorough description of the available validation approaches for different lidar and aerosol products, including their limitations and poits of consideration (e.g. handling of wavelenght differences) (Chapter 5) and for different radar, cloud, and precipitation products (Chapter 6). In addition, for increased statistical relevance of the intercomparison with ground sites, guidance and recommendations for inter-calibration between networks are included, to achieve a "network of networks" to compensate for the profilers' sparse overpasses per site, and avoid biases (Chapter 4). Moreover, guidance on the statistical validation through the intercomparison between satellite-based remote sensing observations (Chapter 7) and the near-real-time validation through monitoring in an NWP data assimilation system (Chapter 8) is included. Finally, existing gaps in our Cal/Val knowledge are summarized (Chapter 9).

Given the complexity and diversity of geophysical scenarios and retrievals of aerosol, cloud, and precipitation regimes, the ACPPV document is aimed at knowledge exchange and conveying lessons learned, rather than definitions on single and strict protocols that have been agreed upon in some other domains with fewer degrees of freedom. We envision the ACPPV protocol as a first point of convergence, and we welcome any ideas for improvement and enlargement through e.g. the addition of new validation approaches, datasets, and methods. Table 1 lists the different ACPPV chapters and lead authors as main contact points for each chapter's future enrichment.

Table 1. ACPPV protocol chapters.

Ch.	Title	Leading Authors
1	Introduction	V. Amiridis, D. Cecil, R. Koopman
2	Validation needs for Space Profilers	L. Baldini, T. l'Ecuyer, H. Okamoto
3	Survey of validation measurements	S. Gross, J. Redemann, F. Marenco
4	Correlative metadata and data format	E. O'Connor, A. M. Fjæraa
5	Guidance for the validation of lidar & aerosol products	E. Marinou
6	Guidance for validation of radar, cloud, & precipitation products	D. Moisseev, S. Tannelli
7	Statistical validation	J. Tackett
8	Near-real time validation through data assimilation	M. Fielding, M. Janisková
9	Gaps and Challenges	H. Baars

The ACPPV best practices are used during the evaluation of the EarthCARE lidar and aerosol products. To this end, we are focusing on the Mediterranean basing, which provides a complex aerosol-cloud environment for the exploitation of EarthCARE's capabilities. Specifically, measurements from the ACROSS state-of-the-art ground-based lidar facilities in Greece are used, which include the PollyXT lidar in the PANGEA observatory (PANGEA-AKY) and the Thelisis lidar in the Thessaloniki station (THE). Correlative observations were performed during the EarthCARE overpasses over the two stations. While, from the beginning of the mission, we had 32 overpasses above PANGEA and 42 above the Thessaloniki site, only two golden nighttime cases & 3 daytime cases are found for the PANGEA-AKY site, and only three golden nighttime cases & thirteen daytime cases were found for the THE site, to date. The cases are used for the evaluation of the L1 and L2 lidar products.

Following the ACPPV guidelines, prior to the evaluation of the EarthCARE L1 lidar products, we are using the CARDINAL Campaign Tools (CCT) ATLID simulator [2] in order to account for the EarthCARE geometry, direction, and known instrument limitations. Furthermore, we are evaluating the atmospheric homogeneity and station representativeness during each EarthCARE overpass, to consider the most representative radius around the two sites for the intercomparisons. Finally, to convert the THE depolarization measurements from 532 nm (Dp_{532}) to 355 nm (Dp_{355}), we are using the conversion suggested in the ESA- EarthCARE-related DEDICATE study [3] (i.e., $Dp_{355}=Dp_{532}*0.89$). Results from the L1 and L2 intercomparisons are provided in the next session.

Results and Discussion

An example of the case of 6 March 2025, during EarthCARE overpass over the AKY site, is presented. EarthCARE time-height cross sections and the intercomparison of the L1 A-NOM products (AD baseline, low resolution) are presented in Figure 1. From the AKY lidar, we observe two dust layers at altitudes between 1-3 km and 3-7.5 km (below the system is affected by the overlap). The aerosol layer was also detected by ATLID (at a 50 km radius from the site). An excellent performance of the A-NOM retrieval algorithm is observed, as both the Mie and crosspolar signals are in great agreement with the AKY measurements.

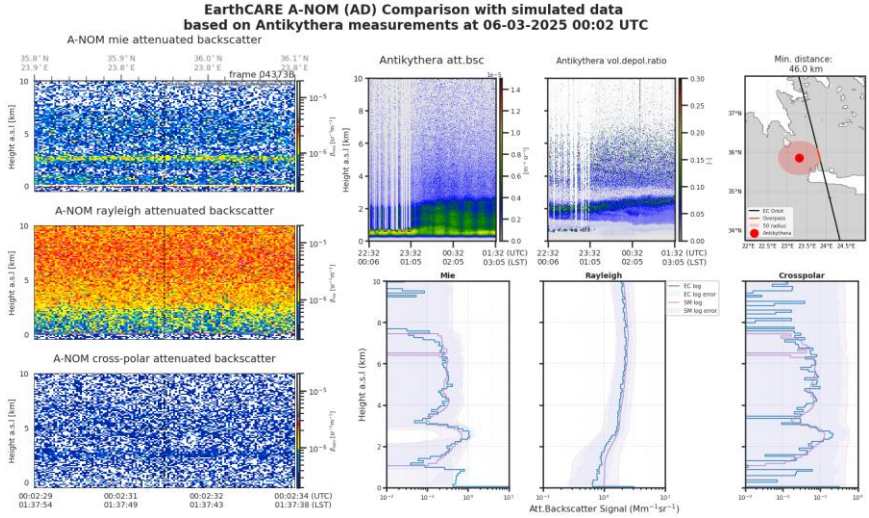

Figure 1. EarthCARE L2 A-EBD (baseline AD) case study intercomparison. Left column: EarthCARE products, three right top panels: Antikythera measurements and overpass from station, three right lower panels: Product intercomparisons (EC: EarthCARE, SM: AKY measurements using the CCT ATLID simulator).

The intercomparison of the EarthCARE L2 A-EBD and L2 A-TC products (AD baseline, low resolution) vs the AKY measurements are presented in Figure 2. The retrieval of the linear depolarization ratio products is in very good agreement with the AKY profiles. Similarly the lidar ratio (LR) retrieval is within the variability of the AKY LR, with an exception at altitudes between 3-4.5 km, where is lower. The ATLID Target Classification classify the dust layers using 3 different categories (polluted dust, dust, marine) indicating needed improvements on this EarthCARE classification algorithm.

Overall, after analyzing each orbital-suborbital collocation dataset separately, we conclude that in most cases at 50 km radius around the site, we had an excellent aerosol homogeneity (for cloud-free cases), while at 100 km, we were already observing homogeneity variations capable of altering the outputs of the EarthCARE performance. Hence, the L1 intercomparisons are performed using EarthCARE measurements in a radius of less than 50 km around the AKY and THE sites. An exception was observed during 7/10/2024

above AKY, when a thin pollution layer at 5-6.5km was detected from the AKY lidar, but was retrieved from EarthCARE only in the profiles at 50-100 km away from the site, and not in the closer profiles. This indicates the significance of investigating the scene homogeneity and representativeness of each case, prior to the derivation of mean performance intercomparison statistics. Although a case study is presented here, all the cases have been analyzed 1by1, and a short summary is provided in the conclusions.

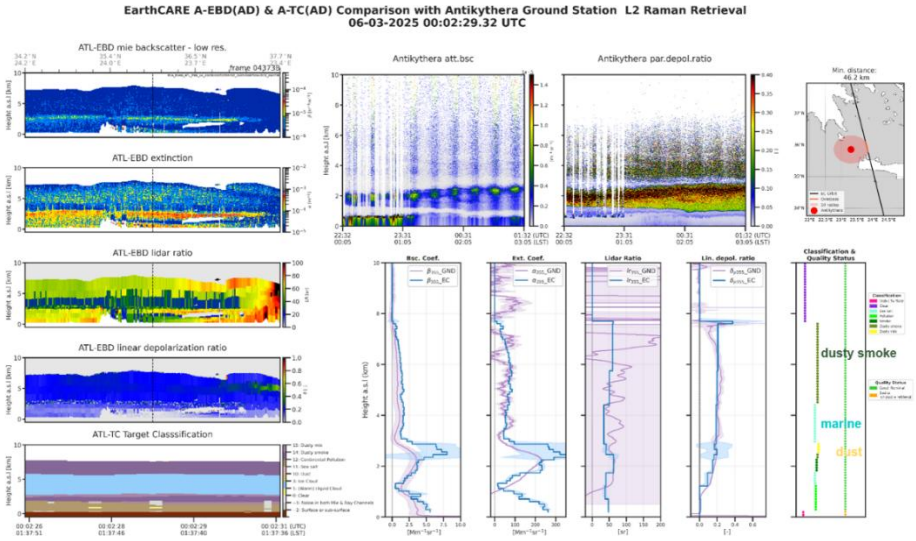

Figure 2. EarthCARE L2 A-EBD (AD baseline) case study intercomparison. Left column: EarthCARE products, three right top panels: Antikythera measurements and overpass from station, five right lower panels: Product intercomparisons (EC: EarthCARE, GND: AKY measurements).

Conclusions

The ACPPV protocol is available [1] and can support the evaluation of the EarthCARE mission, guiding the community towards a convergence to good practices and clear documentation of the assumptions used in the comparison methodology of each individual study. Following these guidance, we evaluate EarthCARE lidar and aerosol products using lidar measurements. We find very good layer detection, good agreement for Mie and Raileigh L1 A-NOM products, noisy crosspolar A-NOM products, and improved L2 liner depolarization ratio products in newer EarthCARE baselines. The A-TC, although accurate in a many cases, have miss-classifications and the algorithm can improve in upcoming releases. Statistics from the complete dataset will be derived once the complete EarthCARE dataset is reprocesses with the latest baseline (expected to be released soon by ESA).

Acknowledgements

Part of the work has been supported by the ESA ACPV project (Contract no. 4000140645/23/I-NS), and the PANGEA4CalVal project (Grant Agreement no. 101079201) funded by the European Union. Moreover, part of the work has been possible thanks to the knowhow available on EARLINET, the activities and resources provided by ACTRIS, and the support by the ATMO-ACCESS project (Grant Agreement no. 101008004), and the CERTAINTY project (Grant Agreement No.101137680).

References

[1] Amiridis, V., Marinou, E., Hostetler, C., Koopman, R., et al.: Best Practice Protocol for the validation of Aerosol, Cloud, and Precipitation Profiles (ACPPV) (Version 2), Zenodo, 2025, doi:https://doi.org/10.5281/zenodo.15025627.

[2] EarthCARE ESA-CARDINAL Campaign Tools (CCT) ATLID simulator. Available at: https://gitlab.com/KNMI-OSS/satellite-data-research-tools/cardinal-campaign-tools.

[3] DEDICAtE: Development of a dual-channel Depolarization lidar technique for the derivation of CALIPSO/ Aeolus/ EarthCARE-related conversion factors, Executive Summary, ESTEC Contract No. 4000112750/14/NL/MV/fk, Available at: https://nebula.esa.int/sites/default/files/neb_study/1219/C4000112750ExS.pdf.

PollyNET - A lidar Network

B. Heese[1], *R. Engelmann*[1], *H. Baars*[1], *M. Komppula*[2], *A. Klamt*[1], *D. Althausen*[1]

(1) Institute for Tropospheric Research (TROPOS), Permoserstraße 15, 04318 Leipzig, Germany
(2) Finnish Meteorological Institute (FMI), Yliopistonranta 8, 70210 Kuopio, Finland

Corresponding author: birgit.heese@tropos.de

Introduction

Lidar networks are part of the World Meteorological Organization (WMO), Global Atmospheric Watch Program (GAW), Aerosol Lidar Observation Network (GALION, https://galion.world/) as they contribute to the understanding of atmospheric constituents in an exclusive manner. Usually, these lidar networks base on regional, continental, or intercontinental communities. However, some of these networks or subnetworks are characterized by the fact that they use only one type of lidar system and thus may be called system networks. PollyNET is such a system network as it comprises only Polly lidar systems (**PO**rtab**L**e **L**idar s**Y**stems [1, 2, 4]. These lidars are manufactured by TROPOS and evolved during time with the overall technical progress: The number of detection channels increased, some lidars got new lasers, a new data acquisition system was implemented, and some adds-on for QA/QC were included into the systems. However, all Polly systems have the same basic structure of the emitter, the receiver, the measurement data structure, and they use the same retrieval algorithms. The next section refers to the embeddedness of PollyNET in EARLINET and ACTRIS. The following section will describe some features of PollyNET as the data-flow from the lidar systems to the server, the display of the data, and the last section will illustrate the successful deployment of PollyNET through European and worldwide measurements.

PollyNET as part of EARLINET and ACTRIS

Figure 1 shows the locations where Polly lidar systems were and are deployed worldwide. Most or the locations are operational sites of former projects (red dots), but there are also operational sites with permanent 24/7 measurements in Europe and even in Asia and Africa. All Polly systems were integrated in the European Aerosol Research Lidar Network EARLINET (https://earlinet.eu/), which was established in 2000. When the Polly systems were set up at their respective sites, e.g. Leipzig in 2007, all Polly systems fulfilled the required EARLINET criteria. By this, PollyNET can be considered as part of EARLINET. When the ACTRIS (Aerosol Cloud Trace Gases Research Infrastructure) was established, the EARLINET systems got part of ACTRIS and thus PollyNET can be understood as a sub-network of the aerosol remote sensing part of this European research infrastructure.

By the participation of PollyNET in EARLINET and ACTRIS, the PollyNET systems had to pass the acceptance of the networks and have to take part in the regular QA/QC checks, which is beneficial for the consistent long-term quality of the Polly measurements. On the other hand, the PollyNET systems and data retrieval software supported the activities within these networks as for instance the development of lidar systems (e.g. using the 5° zenith angle of measurements). In addition, the locations of the Polly systems helped to cover more regions of Europe or even outside of Europe for the vertically resolved measurements of the aerosol types and their transport within regional and intercontinental scales.

Data flow from the measurements to the retrieved data at polly.tropos.de

The development of the PollyNET database started in 2006. It was necessary for handling the worldwide automatic aerosol lidar measurements by the Polly systems. Easy access to measurement data, quick recognition of system faults, handling of huge data sets of the 24/7 measuring systems required automatic and unified data flow, data quality checks, system maintenances, and product provision. Figure 2 shows schematically the data flow from the measurements by the Polly systems until the products

Figure 1. Map of worldwide locations of Polly observations. Green dots mark currently operational sites and red dots mark previously operational sites. The red ships indicate the ship cruises with FS Polarstern and FS Meteor.

are published. First, all acquired data have to be stored at the local PC and transferred to the home server of TROPOS in Leipzig. Figure 2 (left) illustrates the data types that are stored. Of course, the measured data from the atmosphere are the main data. But also, the house keeping data get into special interest if system faults are recognized and the errors need to be fixed or even if some of the system or calibration constants for the data retrievals show deviations. The scheme of Fig. 2 (right) depicts the data flow at the Polly TROPOS server from the level 0 data level to data products displayed at the web page polly.tropos.de including the upload to the EARLINET data base which is handled by ACTRIS ARES (Aerosol REmote Sensing) DC unit. An example of the webpage polly.tropos.de is shown in Fig. 3.

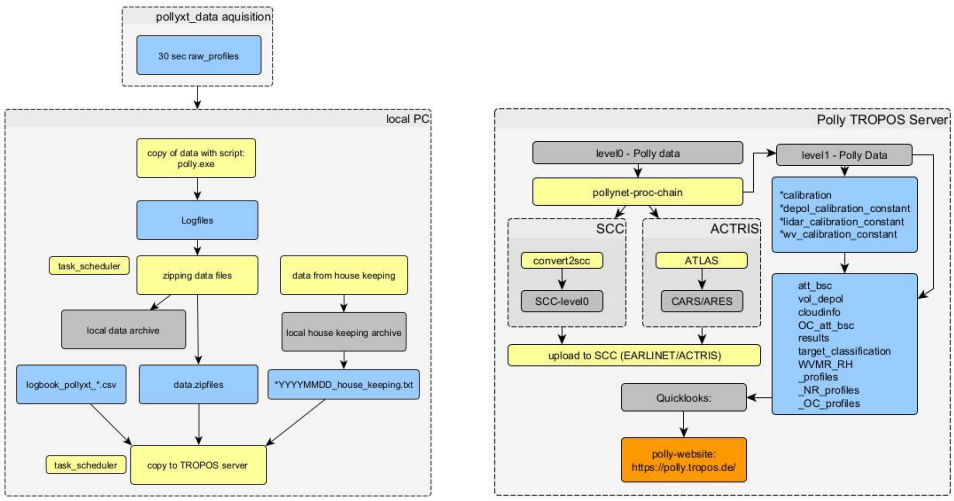

Figure **2**. Scheme of data flow from the Polly PC to the home server of TROPOS in Leipzig (left panel) and the scheme of data flow from level 0 data to the web page, including the upload to EARLINET and ACTRIS (right panel).

Table 1. List of Polly lidar systems developed at TROPOS from 2002 to present, their years of creation and number of detection channels and measurements sites

Name	Year of creation / update	Number of channels	Deployment sites (selection)
Polly 1st /1v2	2002/2017	2 / 5	Xinken, China Leipzig, Germany Are, Sweden Tirana, Albania
Polly IfT Polly TROPOS	2006/2014	6 / 12	Manaus, Brazil Shang dian zi, China Leipzig, Germany Guangzhou, China Haifa, Israel
Polly FMI	2007/2017	6 / 12	Dehli, India Stellenbosch, South Africa Helsinki and Kuopio, Finland
Polly NIER	2009	3	Baengnyeong, South Korea
Polly Évora	2009	6	Évora, Portugal
Polly Arielle	2012/2016/2018	8 / 12 / 13	Polarstern, Meteor Neumeyer, Antarctica
Polly LACROS	2012/2016/2018	8 / 12 / 13	Leipzig, Germany Punta Arenas, Chile Nicosia, Cyprus Eriswil, Swiss
Polly Warsaw	2013	12	Warsaw, Poland
Polly NOA	2014/2016	12	Athens, Antikythera, Greece
Polly DWD	2015	8	Lindenberg, Hohenpeißenberg, Germany
Polly Dushanbe	2019	13	Dushanbe, Tajikistan
Polly TAU	2019	12	Tel Aviv, Israel
Polly Cyprus	2020	13	Limassol, Cyprus
Polly CVAO	2021	15	Mindelo, Cabo Verde
Polly ACTRIS [5]	2025	18	Invercargill, New Zealand Melpitz, Germany

Using PollyNET at European and worldwide measurement sites

Baars et al. [3] showed in a detailed way, how PollyNET has been successfully used to perform 24/7 aerosol lidar measurements on four continents and two research vessels. Table 1 lists the 15 Polly systems that were manufactured between 2002 and 2025 and are deployed worldwide. Meanwhile, all systems are Raman lidars with polarization detection capabilities. The different aerosol types (mineral dust, smoke, dust-smoke and other dusty mixtures, urban haze, and volcanic ash) are identified by means of the determined products Ångström exponent, lidar ratio, and depolarization ratio. PollyNET ensures the automatic handling and processing in near-real time without manual intervention from the level 0 data level to the atmospheric products of aerosol profiles after the huge daily data record from the 24/7 measurements of the 15 systems has been transferred to the Polly server at TROPOS. Hence, PollyNET contributes essentially to the purpose of the Polly measurements.

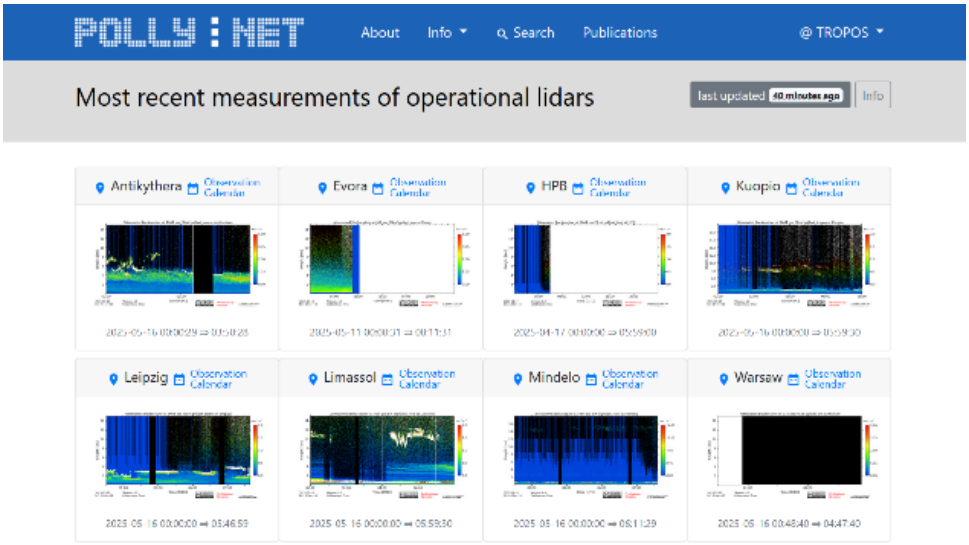

Figure 3. The PollyNET webpage displays the results of the automated data evaluation. It shows quick-looks of the attenuated backscatter coefficient at either 1064 nm or 532 nm of the currently operating Polly systems. The subpages show products as aerosol optical property profiles and housekeeping data.

These systems served and serve for aerosol detection from the Equator to the North Pole and Antarctica. Of course, the partly harsh environment for the measurements demanded intensive housing efforts, but the results show that the Polly systems were deployable at those environments. Although the housing efforts mean often hardware designs, the combined handling of the housing hardware and the measurements has to be managed as well and is realized by PollyNET. Hence, PollyNET is a prerequisite for the successful deployment of the Polly lidar systems worldwide.

Acknowledgements

The establishment of PollyNET was supported by:
- EUCAARI funded by the European Union (FP6, grant no. 036 833-2).
- ACTRIS under grant agreement no. 262254 of the European Union Seventh Framework Programme (FP7/2007-2013).
- EARLINET/ACTRIS-2 under grant agreement no. 654109 from the European Union's Horizon 2020 research and innovation programme.
- The German Federal Ministry of Education and Research (BMBF) under the FONA Strategy "Research for Sustainability" (ACTRIS-D, grant no. 01LK2001A).

In this work, we used data form PollyNET (polly.tropos.de).

References

[1] Althausen D. at al, *Portable Raman Lidar PollyXT for Automated Profiling of Aerosol Backscatter, Extinction, and Depolarization*, J. of Atmos. Ocean. Technology, 26, 2366–2378, https://doi.org/10.1175/2009JTECHA1304.1, 2009
[2] Engelmann, R. et al.: *The automated multi-wavelength Raman polarization and water-vapor lidar PollyXT: the neXT generation*, Atmos. Meas. Tech., 9, 1767–1784, https://doi.org/10.5194/amt-9-1767-2016, 2016.
[3] Baars, H. et al.: *An overview of the first decade of PollyNET: an emerging network of automated Raman polarization lidars for continuous aerosol profiling*, Atmos. Chem. Phys., 16, 5111–5137, https://doi.org/10.5194/acp-16-5111-2016, 2016.
[4] Jimenez, C. et al.: The dual-field-of-view polarization lidar technique: a new concept in monitoring aerosol effects in liquid-water clouds – case studies, Atmos. Chem. Phys., 20, 15265–15284, https://doi.org/10.5194/acp-20-15265-2020, 2020.
[5] Engelmann, R. et al.: Newest 18-channel PollyNET lidar with Rotational Raman, Fluorescence, and three- wavelength depolarization measurement capabilities, European Lidar Conference ELC 2025, 9.-12.Sept. 2025, Warsaw.

Airborne lidar measurements to validate EarthCARE's Atmospheric Lidar (ATLID)

S. Groß[1], *M. Wirth*[1], *K. Krüger*[1]

(1) German Aerospace Center (DLR), Institute of Atmospheric Physics, Münchener Str. 20, 82234 Wessling, Germany
Corresponding author: silke.gross@dlr.de

Introduction

In May 2024 the joint ESA (European Space Agency) and JAXA (Japan Aerospace Exploration Agency) satellite mission EarthCARE [1] [2] was launched. EarthCARE is the most complex mission within ESAs Earth Explorer program, combining for the first time a high spectral resolution lidar (HSRL) and a cloud radar with doppler capability as key instruments on one single platform. In addition, it is equipped with a multi spectral imager and a broadband radiometer. With this combination of new and advanced measurements in space, EarthCARE provides new horizons to study aerosol, clouds, precipitation, and radiation. But to fully make use of this unique data set for science applications and to gain confidence in the EarthCARE data products, a careful validation of the measurements is crucial. Together with partners from German research institutes and universities, we have implemented an EarthCARE-like payload onboard the German research aircraft HALO (High Altitude and LOng range) to prepare for the use of EarthCARE as well as for the validation of its data products. This instrumentation was flown during PERCUSION (Persistent EarthCARE underflight studies of the ITCZ and organized convection) mission. We will give an overview of the mission and how we use our measurements to validate EarthCARE's data products. The following study focuses on the validation of EarthCARE's Atmospheric Lidar (ATLID).

Methodology

From August to November 2024 PERCUSION took place as part of an overarching network of campaign activities ORCESTRA (Organized Convection and EarthCARE Studies over the Tropical Atlantic). PERCUSION is an airborne mission using the German research aircraft HALO. It is an initiative of German research institutes and universities (led by the Max-Planck-Institute for Meteorology and DLR) and had two main objectives:

(1) To test factors hypothesized to influence the organization of deep maritime convection in the tropics and the influence of organized convection on the large-scale environment.

(2) To establish confidence in EarthCARE by validating the EarthCARE measurements and data.

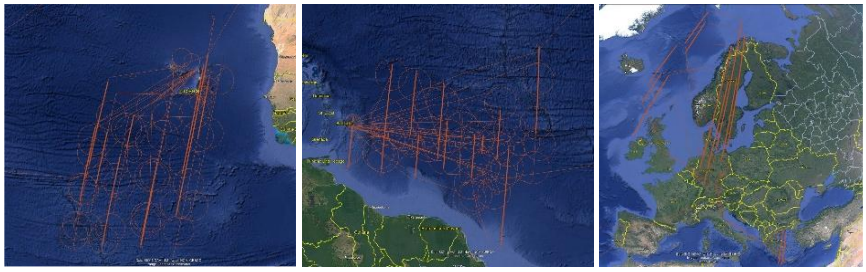

Figure 1. Flight tracks of the HALO research aircraft during the PERCUSION campaign out of Sal (left), Barbados (middle) and Oberpfaffenhofen (right). The straight thick lines indicate direct underpasses under the EarthCARE satellite. The plots have been performed using GoogleEarth (Google Earth).

To achieve these objectives, we planned our flights in a way, that they included at least one EarthCARE underpass in each research flight. HALO measurements were carriedout of three locations (Figure 1): In August 2024 we performed measurements out of Sal (Cape Verde) to target marine aerosol, Saharan dust and biomass burning aerosol as well as shallow to deep convective clouds and the ITCZ. In September 2024 measurement flights out of Barbados took place to address different kind of cloud and aerosol situations.

And in addition, measurement flights to target continental aerosol as well as frontal and high latitude clouds were conducted out of Oberpfaffenhofen (Germany) in November 2024.

During PERCUSION, HALO was equipped with an EarthCARE-like payload acting as airborne aerosol and cloud observatory [3]. One of the key instruments during the PERCUSION campaign is the WALES (demonstrator for a water vapor lidar system in space) lidar system allowing for ATLID-like observations. It is a combined airborne differential absorption lidar (DIAL) and HSRL system developed and built at the DLR Institute of Atmospheric Physic [4]. It measures profiles of backscatter ratio at 532 nm and 1064 nm, and depolarization ratio at 532 nm. In addition, it is equipped with an HSRL channel at 532 nm using an iodine filter. Additionally, WALES measures water vapor using the DIAL principle with four wavelengths in the 935 nm wavelength region.

Results and Discussion

During the PERCUSION campaign altogether, 33 EarthCARE underpasses could be carried out within 30 HALO research flights addressing different aerosol and cloud situations that have been identified as crucial for validation and identified in the EarthCARE Validation Implementation Plan. In the following we will focus on a research flight out of Sal targeting to compare ATLID products of Saharan dust on 13 August 2024.

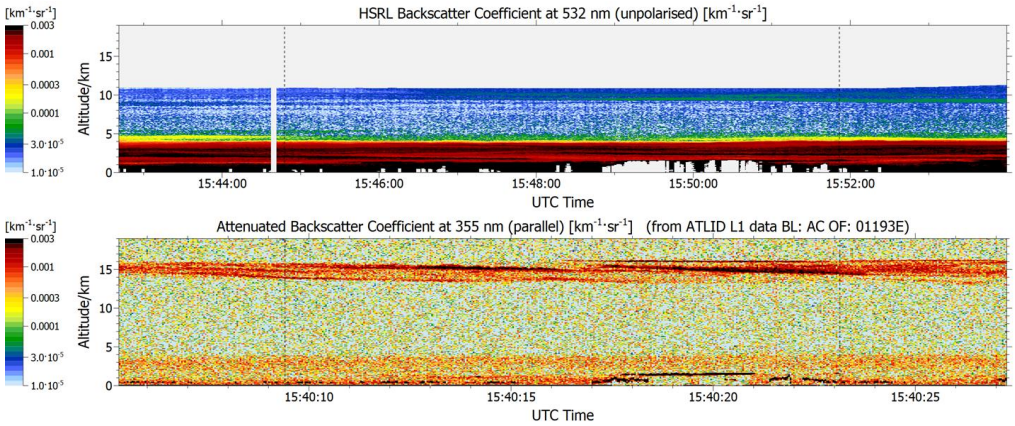

Figure 2. Comparison of the WALES HSRL Backscatter Coefficient at 532 nm (upper panel) and ATLID Attenuated Backscatter Coefficient at 355 nm (lower panel) for an underflight performed on 13 August 2024 out of Cape Verde. The dotted vertical lines show a distance of ±50 km around the direct overpass that is used for further comparisons.

Looking at the time-height cross section of the Backscatter coefficient of both lidar instruments (Figure 2) we can identify an aerosol layer up to about 4 to 5 km altitude. In the ATLID measurements we furthermore see enhanced backscattering at around 15 km altitude missed by the WALES measurements due to the lower flight altitude of the HALO aircraft of about 11 km. In addition, to the aerosol layer that is visible well in the measurements of both systems, we can identify signatures of low clouds up to about 0.5 km to about 2 km.

As a next step we directly compare the profiles of the measured Mie backscatter coefficient, Rayleigh backscatter coefficient and Cross-polar backscatter coefficient (not shown). In our comparison we have to take care of the fact that the measurements of WALES and ATLID are performed at different wavelength, i.e. 532 nm and 355 nm, respectively. For the current baseline version available of ATLID we can confirm a general good quality of the ATLID Mie and Rayleigh backscatter coefficient. Regarding the cross-polarized backscatter improvements are expected in the upcoming baseline.

After confirming the general good performance of the A-NOM (ATLID L1 measurements) data, we investigate the performance of the ATLID L2 products. These are the Target Classification (A-TC) and layer

properties (e.g. the ATLID cloud top height, A-CTH) and the optical properties (i.e. the extinction coefficient, backscatter ratio, lidar ratio and particle linear depolarization ratio). The optical properties are given as two products [5]: A-AER uses the conventional lidar analysis in very low resolution and mainly serves as a first guess for the optimal estimation approach used to derive A-EBD products, which are available for different resolutions. Therefor A-AER is not recommended to be used for scientific studies (D. Donovan personal communication) but still addressed in our validation efforts (not shown). Here, we focus on the comparisons of the A-EBD products. For the validation analysis we use the latest available baseline version AD (Figure 3). Again, we have to consider a possible wavelength dependence, but former studies (e.g. [6]) confirmed, that Saharan dust and marine aerosol layers do not show a wavelength dependence between 355 nm and 532 nm for the backscatter and extinction coefficient, and for the lidar ratio. For the particle linear depolarization ratio of Saharan dust, a wavelength dependence between 355 nm and 532 nm is expected, but we excluded this property from our comparisons, as there have already issues in the A-NOM data been identified. An improvement is expected for the upcoming baseline.

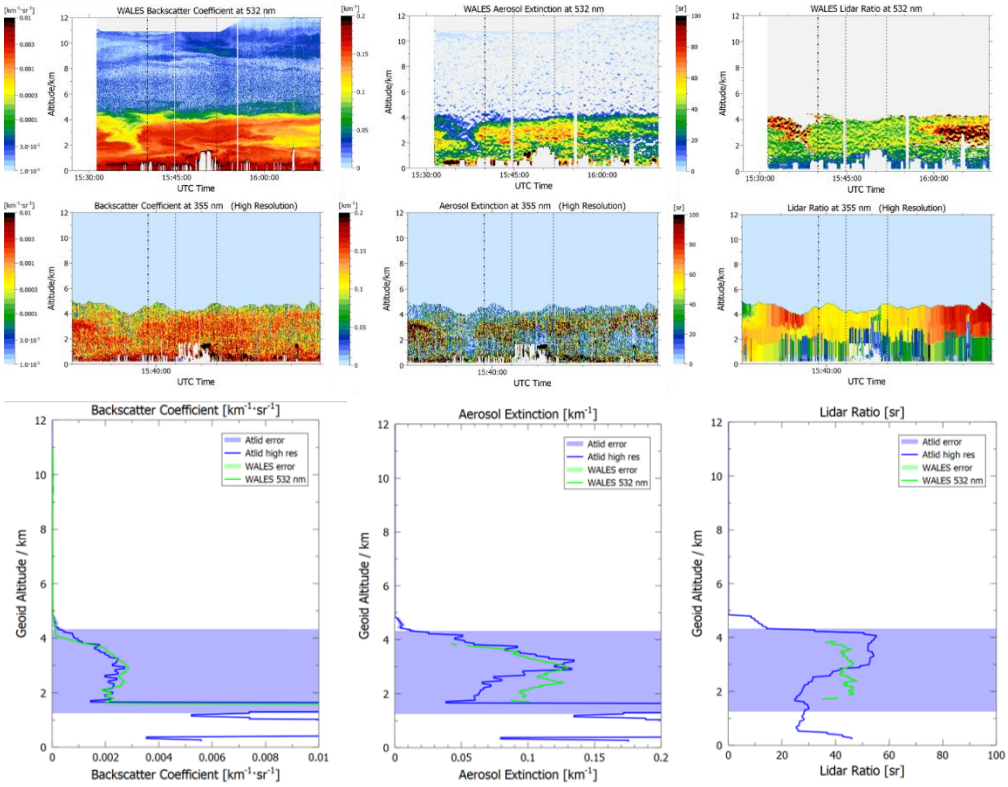

Figure 3. Time-height cross-section of the WALES optical properties (upper panel), and the ATLID optical properties (mid panel), as well as the profile comparisons (lower panel) of the backscatter coefficient (left), extinction coefficient (middle), and the lidar ratio (right) during the EarthCARE underpass on the 13 August 2013. The profiles are averaged within ±50 km around the EarthCARE overpass, indicated by the left and right vertical lines in the time-height cross-sections and in Figure 2.

We find a good agreement of the derived backscatter coefficient from ATLID and WALES, but significant differences for the extinction coefficient and the lidar ratio. Looking at the time-height cross-sections, one can further see unnatural features in the layering and boundaries of the A-EBD products. Those direct underpasses under EarthCARE provide a characterization of the whole measurement scene and are thus very helpful to investigate reasons for uncertainties. The comparisons shown above helped to identify

inadequacies in the layering of the A-EBD algorithms that will be solved in the new baseline version (personal communication D. Donovan).

Conclusions

Airborne measurements with EarthCARE-like payload have been carried out during the PERCUSION campaign. The flights were designed to plan for at least one EarthCARE underpass in each research flight. Those direct underpasses provide the possibility of direct comparisons over a distance of several ten to hundred kilometers. This is crucial to exclude mismatches of ATLID and WALES measurements due to temporal or spatial inhomogeneities. From our analysis we were able to identify issues in the early baseline version of the A-NOM data and in the optical properties of the A-AER and A-EBD data. To investigate the reasons for the deviations, a full scene characterization is of importance. Airborne measurements during direct underpasses provide a characterization of the full measurement scene seen by EarthCARE and are such a very useful tool for validation. Having a long-range and high-altitude aircraft furthermore gives the possibility for satellite validation in remote regions, e.g. over the ocean, where observational density is particularly sparse.

Acknowledgements

This work was financed by the ESA project GIVEair (EarthCARE: Give Airborne with Radar, Lidar – HALO EC-TOOC and Home-Base) under ESA Contract No. 4000145500/24/NL/SC, and has received funding from Horizon Europe programme under Grant Agreement No 101137680 via project CERTAINTY (Cloud-aERosol inTeractions & their impActs IN The earth sYstem). Furthermore, this work has been supported by the DLR internal funding within the MABAK project (Innovative Methoden zur Analyse und Bewertung von Veränderungen der Atmosphäre und des Klimasystems).

References

[1] Illingworth, A. J., Barker, H. W., Beljaars, A., Ceccaldi, M., Chepfer, H., Clerbaux, N., ... & Van Zadelhoff, G. J.: *The EarthCARE satellite: The next step forward in global measurements of clouds, aerosols, precipitation, and radiation*. Bulletin of the American Meteorological Society, 96(8), 1311-1332, 2015.

[2] Wehr, T., Kubota, T., Tzeremes, G., Wallace, K., Nakatsuka, H., Ohno, Y., ... & Bernaerts, D.: *The EarthCARE mission–science and system overview*. Atmospheric Measurement Techniques, 16(15), 3581-3608, 2023.

[3] Stevens, B., Ament, F., Bony, S., Crewell, S., Ewald, F., Gross, S., ... & Zinner, T. (2019). *A high-altitude long-range aircraft configured as a cloud observatory: The NARVAL expeditions*. Bulletin of the American Meteorological Society, 100(6), 1061-1077.

[4] Wirth, M., Fix, A., Mahnke, P., Schwarzer, H., Schrandt, F., & Ehret, G.: *The airborne multi-wavelength water vapor differential absorption lidar WALES: system design and performance*. Applied Physics B, 96, 201-213, 2009.

[5] Donovan, D. P., van Zadelhoff, G. J., & Wang, P.: *The EarthCARE lidar cloud and aerosol profile processor (a-PRO): The a-AER, a-EBD, a-TC, and a-ICE products*. Atmospheric Measurement Techniques, 17(17), 5301-5340, 2024.

[6] Groß, S., Tesche, M., Freudenthaler, V., Toledano, C., Wiegner, M., Ansmann, A., ... & Seefeldner, M.: *Characterization of Saharan dust, marine aerosols and mixtures of biomass-burning aerosols and dust by means of multi-wavelength depolarization and Raman lidar measurements during SAMUM 2*. Tellus B: Chemical and Physical Meteorology, 63(4), 706-724, 2011.

Lidar applications in atmospheric sciences

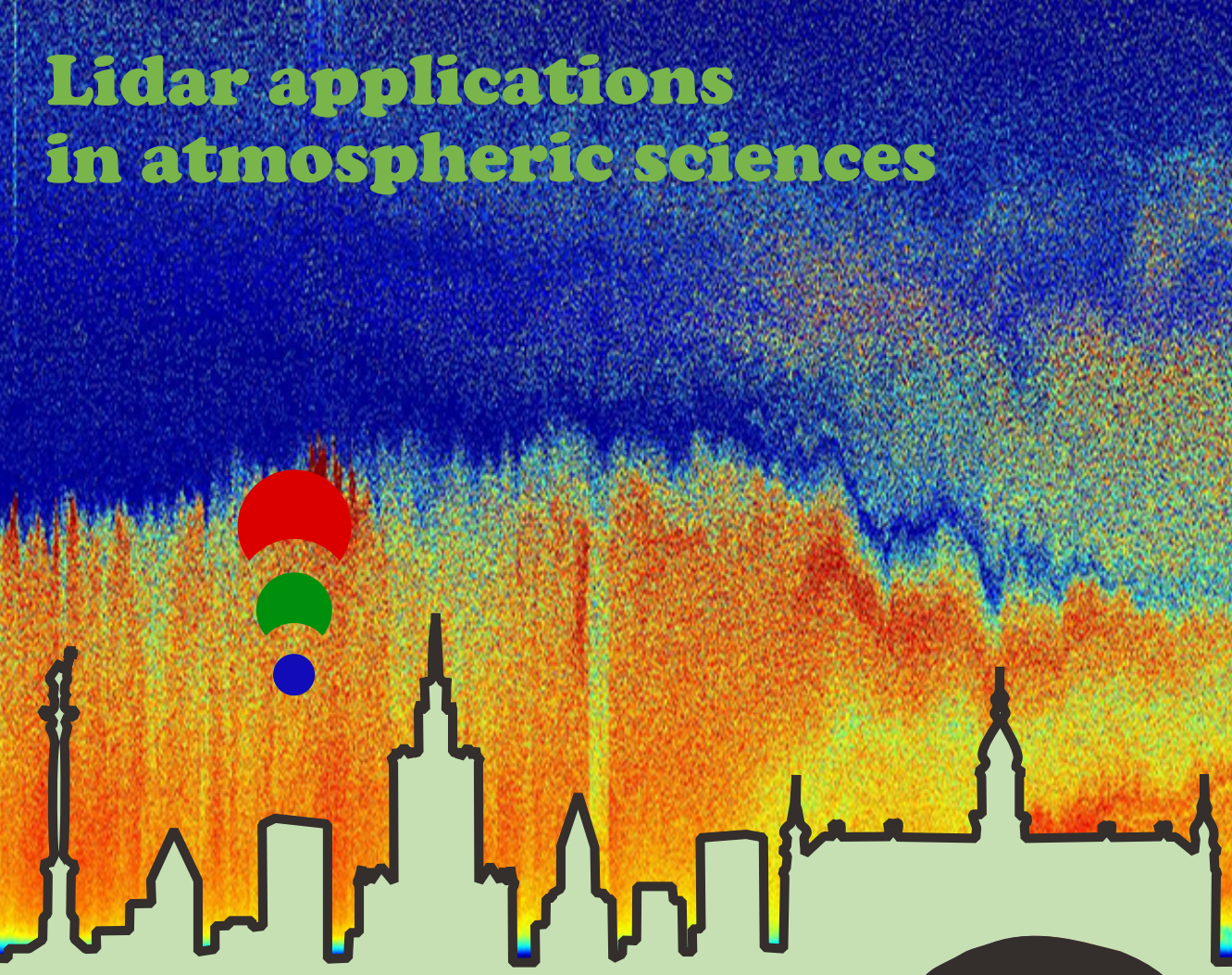

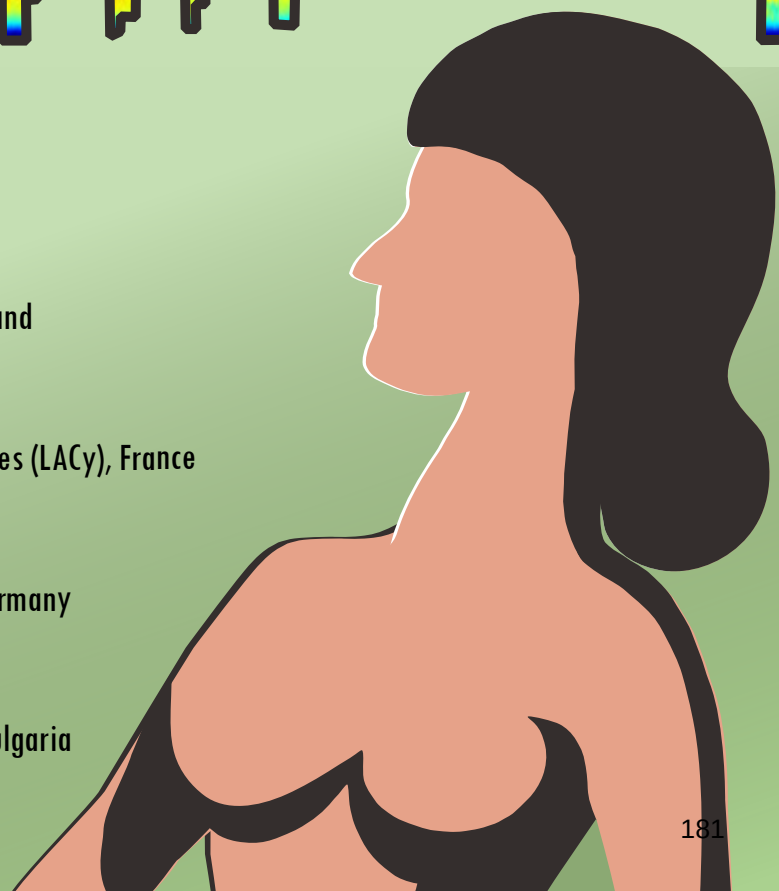

Session Chairs:

Mika Komppula

Finnish Meteorological Institute (FMI), Finland

Michael Sicard

Laboratoire de l'Atmosphère et des Cyclones (LACy), France

Hannes Vogelmann

Karlsruhe Institute of Technology (KIT), Germany

Tsvetina Evgenieva

Bulgarian Academy of Sciences (IE-BAS), Bulgaria

Experimental assessment of the CNRM-ALADIN64 model with lidar and passive measurements during the dust and heatwave event in the Iberian Peninsula in July 2019.

C. Gil-Díaz[1], Michael Sicard[1,2,3], P.Nabat[4], M. Mallet[4], C. Muñoz-Porcar[1], A. Comerón[1], ***A. Rodríguez-Gómez[1]****, D.C.F. dos Santos Oliveira[1]*

(1) CommSensLab, Dept of Signal Theory and Communications, Unversitat Politècnica de Catalunya (UPC), Barcelona 08034, Spain.
(2) Ciències i Tecnologies de l'Espai-Centre de Recerca de l'Aeronàutica i de l'Espai/Institut d'Estudis Espacials de Catalunya (CTE-CRAE/IEEC), Universitat Politècnica de Catalunya (UPC), Barcelona, 08034, Spain.
(3) Laboratoire de l'Atmosphère et des Cyclones, Université de La Réunion, Saint Denis, 97744, France.
(4) CNRM, Université de Toulouse, Météo-France, CNRS, Toulouse, France.

Corresponding author: alejandro.rodriguez.gomez@upc.edu

Introduction

An evaluation of the CNRM-ALADIN64 [1] model simulation with dust aerosols is carried out during the dust event and heatwave in the Iberian Peninsula in summer 2019. The model performance is assessed against a variety of observational datasets. In particular, the total aerosol AOD is evaluated across different AERONET stations using both VIIRS satellite data and AERONET measurements. Shortwave downward (SW DW) radiative flux is compared with SolRad-Net observations at the Barcelona lidar station, while longwave upward (LW UP) radiative flux is assessed using CERES data over the Iberian Peninsula. Additionally, the vertical distribution of dust extinction is also evaluated with the Barcelona MLPNET lidar.

Methodology

The ALADIN64 model makes use of a spectral nudging method [2], which enables to keep large scales from the boundary forcing and thus impose the measured natural climate variability that is essential to accurately represent dust events. In this study, three types of simulations are made with different spectral nudging: SN-All with a spectral nudging for temperature, humidity, surface pressure and wind; SN-Wind keeping only the spectral nudging for wind; and SN-Non, without spectral nudging. CNRM-ALADIN64 different outputs have been compared with measurements performed during the event by the following instruments:

AERONET Aerosol Optical Depth (AOD) products are used for the time period from 20th June to 5th July, 2019. To validate the hourly AOD at 550 nm obtained from the CNRM-ALADIN64 model, the AERONET Ängstrom exponent was applied to the AERONET AOD measurements at 675 nm [3]. Hourly averages were calculated to ensure temporal agreement.

The satellite-borne VIIRS instrument is a visible and infrared radiometer equipped with 22 spectral bands ranging from 0.412 to 12 μm. In this study, we use the NOAA20 VIIRS Deep Blue Level 3 daily aerosol dataset, with a horizontal resolution grid of 1º x 1º. This product provides satellite-derived measurements of AOD at 550 nm over both land and ocean with daily global coverage [4].

The lidar system used in this study is a Polarized Micro Pulse Lidar (P-MPLNET lidar) integrated within the NASA MPLNET Network [5]. The Barcelona MPLNET lidar is located on the roof of the CommSensLab building in the Campus Nord of the Universitat Politècnica de Catalunya (41.38ºN, 2.11ºE; 115 m a.s.l.). We used the aerosol extinction included in the AER product, Version 3 (released in 2021) and Level 1.5.

The Barcelona station hosts collocated SolRad-Net instruments. In this study, the Kipp and Zonen CM-21 pyranometer (0.305-2.8 μm) was used measuring the total solar downward short-wave flux, at Level 1.0, for the time period from 20th June to 5th July, 2019.

We also use the CERES instantaneous Single Scanner Foot-print (SSF) product at Level 2 dataset. We use the top-of-the-atmosphere upward fluxes in the longwave spectral range (5-35 μm), from 20th June to 5th July 2019. This variable is provided at a spatial resolution of 20 km at nadir [6].

Results and Discussion

The temporal evaluation of the total AOD at 550 nm obtained from the ALADIN64 simulations that consider the Saharan dust aerosols are first evaluated against AERONET and VIIRS observations in different locations over the Iberian Peninsula, as shown in Figure 1. The ALADIN64 model shows good agreement at locations like Badajoz, Valladolid, Murcia and other locations in the east of the peninsula, where the dust load was higher, while also performing reliably in regions with a flat orography, such as the center and western peninsula, independently of the dust load, as it has been previously highlighted [7], [8]. Regarding the temporal evolution, the largest discrepancies of AOD between the model and the observations are observed at the beginning and the end of the dust event.

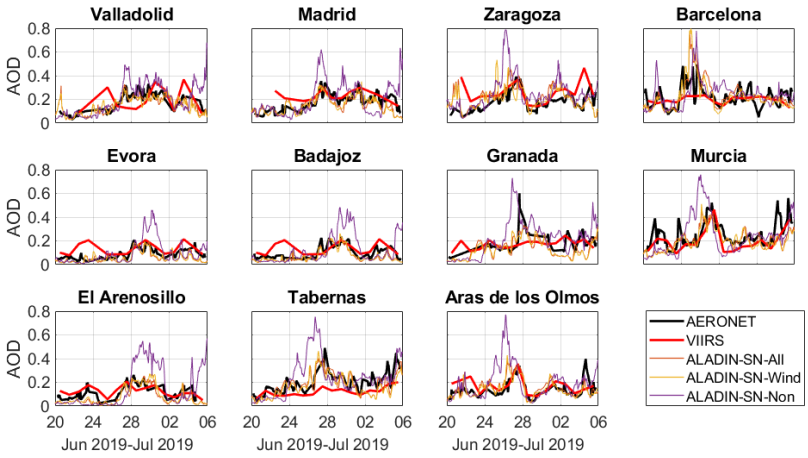

Figure 1. Temporal evolution of the total aerosol optical depth at 550 nm calculated with ALADIN64 model and measured with a photometer from AERONET photo-meter (black line) and with the VIIRS instrument (red line) in different stations over the Iberian Peninsula, during the period 20th June to 5th July, 2019.

Figure 2 shows the scatter plots of the total AOD at 550 nm simulated with ALADIN64 model vs the one measured by AERONET and VIIRS over the Iberian Peninsula. ALADIN simulations fit better with the AERONET measurements than with the VIIRS observations. The simulated AOD compared with AERONET observations shows a highest R^2 of 0.52 for the S-Dust-SN-All simulation, which is lower than 0.75 reported by [8]. The highest R^2 in the AOD evaluation using VIIRS observations is 0.24 for the S-Dust-SN-All simulation.

The average dust extinction from the simulation which includes Saharan dust aerosol is compared with MPLNET measurements at the Barcelona station in **Figure 3**. The best results are obtained with the simulation with the spectral nudging only for the wind (S-Dust-SN-Wind) with a bias = +7% and a R^2 = 0.78. According to these results, the slight relaxation of the spectral nudging in the ALADIN simulations favours the accurate representation of the vertical distribution of the dust particles. S-Dust-SN-All and S-Dust_SN-Non, yield slightly higher R2 values, but much higher biases (17.8% and 65.9% respectively).

Figure 4 shows the scatter plot of downward and upward radiative fluxes simulated with the ALADIN64 model vs. observations from a pyranometer belonging to the SolRad-Net network located at the Barcelona lidar station in a spectral range of SW (0.305-2.8 μm), at bottom-of- the-atmosphere (BOA), and vs. CERES measurements over the Iberian Peninsula in a spectral range of LW (5-35 μm) at top-of-the-atmosphere (TOA). The simulation with the most restrictive spectral nudging (S-Dust-SN-All) is the one that performs best, with a R^2 = 0.94 and bias < +1%. The other two simulations, on average, modestly underestimate the shortwave downward radiative flux at surface, with bias -6% for S-Dust-SN-Non. The evaluation of the longwave radiative flux at TOA is not as straightforward as the downward flux, resulting

in worse agreement between simulations and measurements by the CERES satellite. While many cases cluster along the unit-slope curve, others are more widely scattered. Nonetheless, they collectively exhibit a linear dependence, with mean and standard deviation 266±43 W/m^2. The most restrictive spectral nudging (S-Dust-SN-All) provides the best linear fit with a = 0.99 and R^2 = 0.63.

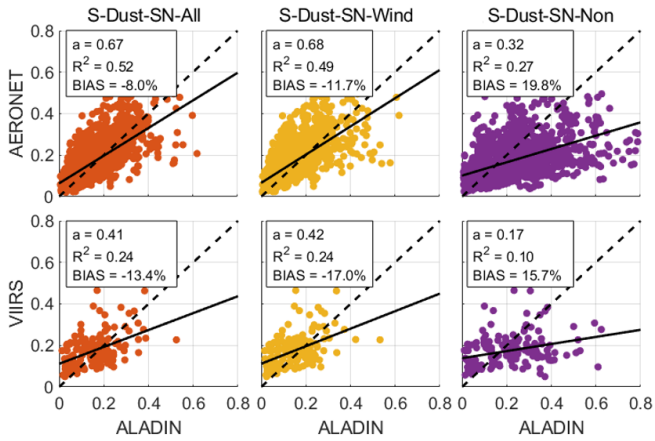

Figure 2. Scatter plots of the total aerosol optical depth at 550 nm measured by different AERONET and VIIRS observations (Y-axis) and simulated by the ALADIN model (X-axis) over the Iberian Peninsula, during the period 20th June to 5th July, 2019. The dashed line is the curve with the slope unity and the solid line corresponds to the linear regression of the points (y = ax + b), being a the slope and R^2 its coefficient of determination)

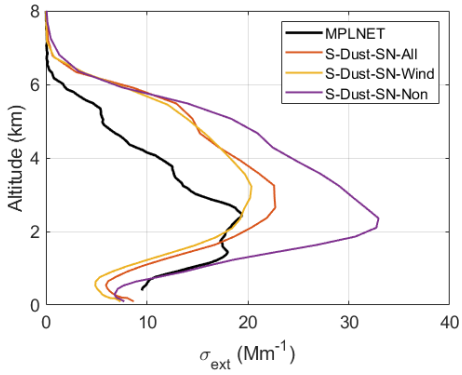

Figure 3. Plot of the mean dust extinction coefficient (σext) at 532 nm simulated by the ALADIN model and measured by MPLNET at Barcelona lidar station, during the period 20th June to 5th July, 2019.

Conclusions

The evaluation of ALADIN model simulations using different spectral nudging configurations against remote sensing observations is essential to validate the accuracy of the simulations. This step is key to analyse the event using the model's outputs. **Table 1** presents the assessment metrics for the different simulations. More metrics can be found in [9]. Overall, the best option for spectral nudging seems to be the one taking into account as many measured meteorological variables as possible, SN-All, although some parameters are replicated better by the SN-Wind option.

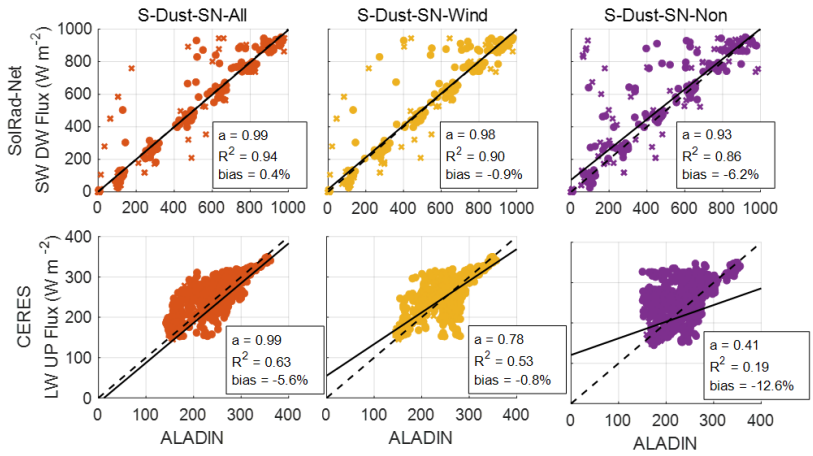

Figure 4. Scatter plots of (top) shortwave downward radiative fluxes at bottom-of-the-atmosphere at Barcelona lidar station and (bottom) longwave upward radiative fluxes at top-of-the-atmosphere, measured by SolRad-Net and CERES, respectively (Y-axis) and simulated by ALADIN64 model (X-axis). See footnote of **Figure 2** for details.

Table 1. Summary of the assessment of ALADIN64 simulations. The best metrics in bold print

Para meter	Instrument/ data-set	ALADIN64 simulations								
		S-Dust-SN-All			S-Dust-SN-Wind			S-Dust-SN-Non		
		a	R^2	Bias(%)	a	R^2	Bias(%)	a	R^2	Bias(%)
AOD	AERONET	0.67	**0.52**	**-8.0**	**0.68**	0.49	-11.7	0.32	0.27	+19.8
AOD	VIIRS	0.41	**0.24**	**-13.4**	**0.42**	0.24	-17.0	0.17	0.10	+15.7
σ_{ext}	MPLNET	0.78	0.83	+17.8	**0.83**	0.78	**+7.0**	0.57	**0.89**	+65.9
DFlux	SolRad-Net	**0.99**	**0.94**	**+0.4**	0.98	0.90	-0.9	0.93	0.86	-6.2
UFlux	CERES	**0.99**	**0.63**	-5.6	0.78	0.53	**-0.8**	0.41	0.19	-12.6

Acknowledgements
This work was funded by MICIU/AEI/ 10.13039/501100011033 grant PID2023-149747NB-I00 and H2020-INFRAIA-2020-1, ATMO-ACCESS, grant no. 10100800.
In this work we used data form CNRM-ALADIN64 (https://doi.org/10.5281/zenodo.15077499), AERONET, VIIRS, MPLNET, SolRadNet and CERES.

References
[1] Nabat P. *et al.*, doi: 10.5194/acp-20-8315-2020.
[2] Radu R., *et al*., doi: 10.1111/j.1600-0870.2008.00341.x.
[3] Wagner F. and Silva, A. M., doi: 10.5194/acp-8-481-2008.
[4] Sayer, A. M., *et al*., doi: 10.1002/2017JD027412.
[5] Welton, E. J., *et al*., doi: 10.1117/12.417040.
[6] Su, W., *et al.*, doi: 10.5194/amt-8-611-2015.
[7] Csima, G. and Horányi, A. https://api.semanticscholar.org/CorpusID:124779676.
[8] Nabat, P., *et al*., doi: 10.5194/acp-15-3303-2015.
[9] Gil-Díaz, C. *et al*, "Dust aerosol radiative effects during a dust event and heatwave in summer 2019 simulated with a regional climate atmospheric model over the Iberian Peninsula," Submitted *to Remote Sensing*, March 2025.

Seasonal Variability of Planetary Boundary Layer Height (PBLH) Over the Mediterranean Region (ACTRIS Potenza Station).

***Z. Ali*[1]**, *R. Damiano*[1], *A. Amodeo*[2], *B. De Rosa*[2], *M. Mytilinaios*[2], *S. Amoruso*[1], *A. Boselli*[2], *A. Sannino*[1]

(1) Department of Physics "Ettore Pancini", University of Naples Federico II, Naples, I-80126, Italy
(2) Institute of Methodologies for Environmental Analysis (IMAA), National Research Council of Italy (CNR), I-85050 Tito Scalo (PZ), Italy

Corresponding author email: zeeshan.ali@unina.it

Introduction

The planetary boundary layer (PBL) is the lowest part of the atmosphere that has direct interaction with Earth's surface, exchanging heat momentum and moisture. This layer spans from the surface up to a few hundred meters or even several kilometres, and plays a crucial role in shaping weather systems, influencing air quality, and driving climate behaviour. The height of the planetary boundary layer (PBLH) has a key role in atmospheric studies since it can help estimating the altitude up to which atmospheric mixing occurs, understanding the mechanisms related to pollutants spreading and clouds formation, as well as studying the energy transport between the Earth's surface and the atmosphere [1]. Therefore, an accurate assessment of the PBLH is useful for a range of atmospheric studies, from weather forecasting and climate modelling to air pollution and renewable energy systems [2]. However, a precise PBLH evaluation is challenging due to its high temporal variability (diurnal and seasonal scales), dependence on surface, and sensitivity to synoptic-scale atmospheric dynamics [3]. Remote sensing techniques have demonstrated significant potential to overpass these constraints and methodological challenges. More specifically, active remote sensing techniques, i.e. atmospheric lidar systems, provide high spatial resolution and near real-time atmospheric measurements [4, 5]. Validated approaches for pointing PBLH using lidar measurements include gradient-based methods (like using first- and second-order derivatives, logarithmic and cubic root gradients) [6], wavelet covariance transforms (WCT), and variance analysis. There is no universally optimal solution, and the selection of a specific model should be based on an assessment of key atmospheric factors, including stability, aerosol stratification, and potential interference from clouds or other atmospheric layers. In general, gradient methods are reliable during well-mixed conditions but less appropriate in stable or shifting situations. Meanwhile, wavelet approaches need a careful tuning to avoid getting misled by elevated aerosol layers. Seasonal shifts add even more complexity, as the different solar radiation rate, humidity, and broader weather patterns alter the behaviour of the boundary layer.
The Mediterranean region constitutes a particularly complex setting for studying the PBL behaviour, due to its geographical conformation as a combination of coastlines and mountains that can produce pronounced climate shifts [7, 8]. To improve understanding of the PBL dynamics and height variability in the Mediterranean regions, we are carrying out a study based on atmospheric lidar data from selected stations across the area. Here, we present preliminary findings based on lidar measurements from the ACTRIS (Aerosols, Clouds, and Trace Gases Research Infrastructure) station in Potenza.

Methodology

For this study data acquired from the Multi-wavelength System for Aerosol (MUSA) lidar has been used. MUSA is the main lidar system operated at Potenza station (760 m a.s.l.), the historical CNR hotspot for atmospheric studies located in south Italy (40.60°N, 15.72°E) and National Facility of ACTRIS. MUSA is an elastic-Raman lidar operated in the 3β+2α configuration, with possibility of depolarization ratio measurements [9], allowing state-of-art classification of atmospheric aerosol in terms of optical and microphysical properties. To ensure an analysis of the seasonal variation and a comparison of the different methods, eight days per season were selected in the years from 2020 to 2024 and corresponding data at 1064 nm were retrieved from the EARLINET (European Aerosol Research Lidar Network) database. The following sections detail the methodologies employed to derive the estimate of the PBLH from Range-Corrected Signal (RCS) profiles by means of gradient-based techniques and wavelet covariance transforms.

The Planetary Boundary Layer Height (PBLH) was estimated using five distinct algorithms applied to lidar RCS profiles, described by equation (Eq. 1)

$$RCS = [P(r)]\ r^2 \tag{1}$$

where *P(r)* is described by (Eq. 2)

$$P(r) = E_0 \frac{C}{r^2} O(r)\beta(r) \exp\left(-2\int_0^r \alpha\left(r'\right)dr'\right) \tag{2}$$

with *P(r)* the power of the lidar signal, *r* the altitude, *C* the system constant, O(*r*) the overlap function, and $\beta(r)$ and $\alpha(r)$ the backscatter and extinction coefficients, respectively. The overlap function O(*r*) characterizes the geometric coupling efficiency between the transmitted laser beam and the receiver field of view as a function of range, and for the MUSA system the full overlap is achieved at approximatively (250-300) meters above ground level (AGL) [5, 10]. The four gradient algorithms used to determine the PBLH are the First-Order Gradient Method (GM), the Second-Order Gradient Method (Inflection Point Method, IPM), the Logarithmic Gradient Method (LGM) and the Cubic Root Gradient Method (CRGM).The GM defines the PBLH as the altitude where minimum value occurs in the first derivative of the RCS profile and assumes an abrupt negative gradient near the top of the PBL characteristic of well-mixed convective conditions. The IPM locates PBLH as the altitude point corresponding to the minimum of second derivative (inflection point). This method decreases sensitivity to local noise by highlighting curvature variations in the RCS profile [11]. The LGM uses logarithmic transformation to enhance the detection of subtle gradients in stable or layered complex conditions. This approach is most effective in diffuse aerosol layer scenarios [12]. The CRGM aims to counteract the effect of gravity waves on the distribution of aerosols and calculates cubic root-transformed RCS gradients. This stabilization regularizes signal fluctuations, enhancing precision in the presence of mechanically induced turbulence [13]. Lastly, the Wavelet Covariance Transform (WCT) Method identifies the PBL top by matching the RCS profile to a Haar wavelet function that mimics the step-like topography at the top of the PBL. The wavelet covariance W(a,b) with dilation *a* and translation *b* is calculated by (Eq. 3)

$$W_f(\alpha,\zeta) = \frac{1}{\alpha}\int_{z_\zeta}^{z_\alpha} RCS(z)h\left(\frac{z-\zeta}{\alpha}\right)dz \tag{3}$$

where *h* is the Haar wavelet [6]. Gradient Methods, based on raw signal gradients, are particularly effective in identifying strong convective boundaries (afternoon summer), but tend to overestimate in multi-layered environments (spring and autumn) [14]. IPM, attuned to edge detection, performs better in stable winter conditions and identifies shallow stable boundary layers accurately; its high sensitivity to sharp transition, however, causes underestimation during transition (multilayered) regimes [11, 12]. CRGM and LGM preprocessing maximizes detection of thin elevated aerosol layers, making the highest PBLH estimations in all seasons but amplification brings about overestimation under stable or complicated aerosol regimes [7, 9]. Their performance supports the findings on the compromise between layer resolution and over detection in transformed gradient methods (e.g. LGM and CRGM) [13]. WCT optimizes noise reduction and sensitivity to gradients and provides intermediate values throughout seasons. It detects broad-layer changes under the convective summer and transitional spring/autumn regimes. Convective conditions (summer afternoons) reduce methodological differences since well-mixed convective boundary layer (CBL) yields clear gradients. Conversely, stable winter and transition seasons enhance biases and call for context-sensitive method selection. IPM and WCT are found to be robust in shallow stable boundary layers (SBLs) [6, 11], and in convective regimes, respectively, whereas LGM/CRGM need to be used with caution under layered atmospheres. All these features are consistent with global lidar literature and underscore the interconnection among algorithm physics, aerosol heterogeneity, and thermodynamic forcing.

The algorithms to retrieve the PBLH trend, with the different method illustrated above, were implemented with Python-based scripts. In an attempt to reduce false detections related to high-level aerosol layers or scattered clouds, results were capped at altitudes lower than 3 km, in agreement with Mediterranean PBL climatology [6].

Results and Discussion

The results of PBLH investigation over Potenza, Italy, with the application of the five retrieval algorithms based on gradient methods (GM, IPM, LGM, CRGM) and Wavelet Covariance Transform (WCT) are summarized in Figure 1 by displaying its daily variation for the four seasons obtained by averaging the corresponding data for each algorithm.

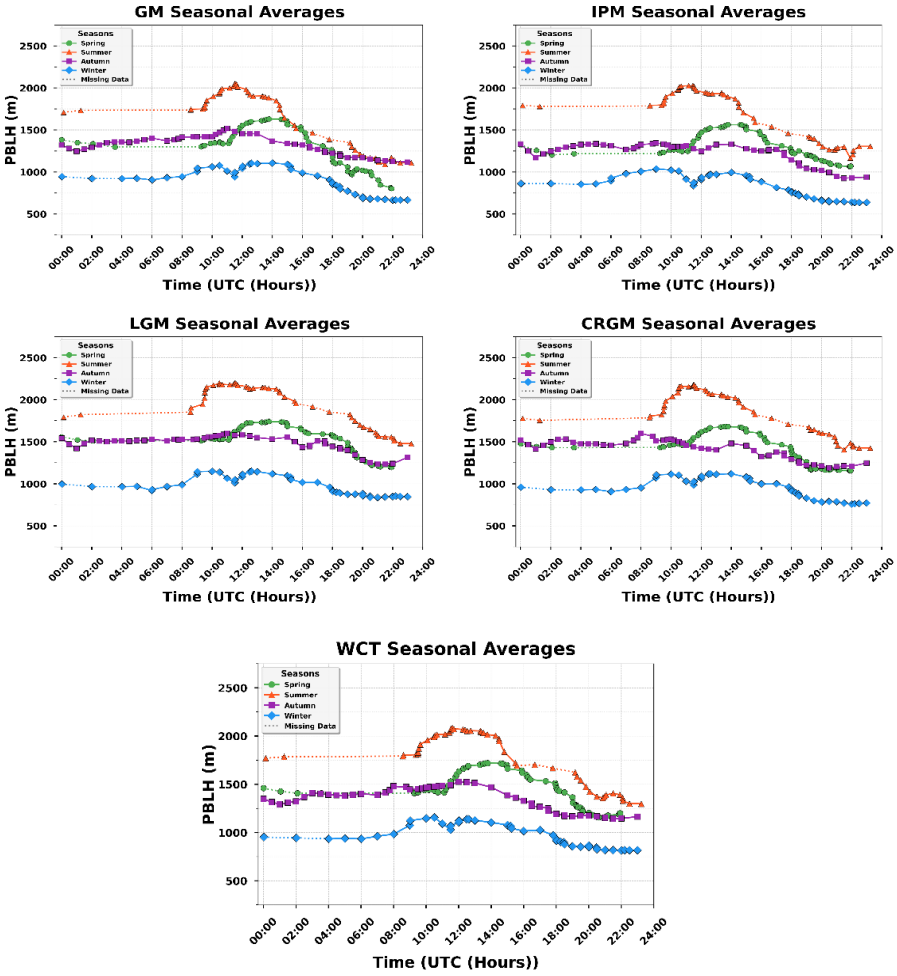

Fig 1. Seasonal averaged trends for Gradients methods and WCT method

Seasonal analysis (**Fig. 1**) shows systematic trends that clearly highlights the boundary layer dynamics. Summer records the deepest PBLH and all methods converge in peak daytime hours with well-developed CBL. This trend can be explained by owing to strong solar insolation and mixing by convection. After sunset, the plots show a divergence among methods particularly sensitive to fine-scale transients (e.g., IPM) and to amplification of lofted aerosol signals (e.g., LGM, CRGM). This behaviour might be caused by the

presence of multiple layers in the atmosphere during this period. Spring and Autumn are characterized by moderated growth in the PBLH. Even if the daily dynamics are different, the trend values are superimposable for both seasons except for the daily radiation peak. Winter has its shallowest PBLH, and minimal vertical gradients are problematic to all algorithms, with high-precision performance for IPM, as expected from theory [11], likely due to the presence of shallow layers providing the lowest estimate, while LGM and CRGM overestimation can be rationalized in relation to their sensitivity to remanent aerosol layers [13].

Conclusions

This study shows that identification of PBLH over the Mediterranean area needs adaptive and seasonally adjusted methods. Preliminary trends reveal systematic fluctuations attributed mainly to seasonal atmospheric processes and to algorithmic sensitivities. The results are consistent with fundamental concepts of boundary layer physics and highlight the interaction among algorithmic structure, aerosol stratification, and thermodynamics forcing. The increase in statistics and number of observational sites, as well as the identification of the main aerosol present in the atmosphere, in the prosecution of the present investigation will surely provide a better recognition of the PBLH and allow determining the best reconstruction method as climatic-atmospheric conditions vary.

Acknowledgements

This work is supported by the project IR0000032 – ITINERIS, Italian Integrated Environmental Research Infrastructures System. Funded by EU - Next Generation EU PNRR- Mission 4 "Education and Research" - Component 2.

References

[1] Seibert, P., et al. (2000). Review and intercomparison of operational methods for the determination of the mixing height. *Atmospheric Environment*, 34(7), 1001–1027. https://doi.org/10.1016/S1352-2310(99)00349-0.

[2] Baklanov, A., et al. (2011). The nature, theory, and modeling of atmospheric planetary boundary layers. *Bulletin of the American Meteorological Society*, 92(2), 123–128. https://doi.org/10.1175/2010BAMS2797.1.

[3] Wang, X., & Wang, K. (2016). Homogenized variability of radiosonde-derived atmospheric boundary layer height over the global land surface from 1973 to 2014. *Journal of Climate*, 29(19), 6893–6908. https://doi.org/10.1175/JCLI-D-15-0766.1

[4] Summa, D., et al. (2023). Atmospheric Boundary Layer Height: Inter-Comparison of Different Estimation Approaches Using the Raman Lidar as Benchmark. *Remote Sensing*, *15*(5), 1381. https://doi.org/10.3390/rs15051381

[5] Vivone, G., et al. (2021). Atmospheric boundary layer height estimation from aerosol lidar: a new approach based on morphological image processing techniques. *Atmospheric Chemistry and Physics*, *21*(6), 4249-4265. https://doi.org/10.5194/acp-21-4249-2021

[6] Brooks, I. M. (2003). Finding boundary layer top: Application of wavelet covariance transform to lidar backscatter profiles. *Journal of Atmospheric and Oceanic Technology*, 20(8), 1092–1105. https://doi.org/10.1175/1520-0426(2003)020<1092:FBLTAO>2.0.CO;2

[7] Melas, D., et al. (2000). Anatomy of the sea-breeze circulation in Athens area under weak large-scale ambient winds. *Atmospheric Environment*, 34(22), 3577–3591. https://doi.org/10.1016/S1352-2310(00)00130-2 .

[8] Papayannis, A., et al. (2005). Measurements of Saharan dust aerosols over the Eastern Mediterranean using elastic backscatter-Raman lidar, spectrophotometric and satellite observations in the frame of the EARLINET project. *Atmospheric Chemistry and Physics*, 5(8), 2065–2079. https://doi.org/10.5194/acp-5-2065-2005.

[9] Madonna, F., et al. (2020). ACTRIS aerosol profiling lidar observations of Saharan dust outbreaks at the Italian ACTRIS facilities: A multi-year study. *Atmospheric Measurement Techniques*, 13(8), 4521–4539. 10.5194/amt-13-4521-2020.

[10] Measures, R. M. (1984). Laser Remote Sensing: Fundamentals and Applications. Wiley.

[11] Sicard, M., et al. (2006). Mixed-layer depth determination in the Barcelona coastal area from regular lidar measurements: Methods, results and limitations. *Boundary-Layer Meteorology*, 119(1), 135–157.

[12] Dang, R., et al. (2019). Atmosphere boundary layer height (ABLH) determination under multiple-layer conditions using micro-pulse lidar. *Remote Sensing*, 11(3), 263. https://doi.org/10.3390/rs11030263.

[13] Li, J., et al. (2017). Characterization of planetary boundary layer height using ceilometer backscatter data in China. Atmospheric *Chemistry and Physics*, **17**(10), 6215–6225. https://doi.org/10.5194/acp-17-6215-2017.

[14] Menut, L., et al. (1999). Urban boundary-layer height determination from lidar measurements over the Paris area. *Applied Optics*, 38(6), 945–954.

Identification of Soil CO_2 and Rn Ventilation with Doppler-Lidar Derived Turbulence over Mediterranean Drylands

***J. Abril-Gago*[1,2]**, *I. Tovar*[3], *E. Echeverría-Martín*[4], *J. Andújar-Maqueda*[1,2], *P. Ortiz-Amezcua*[1,2], *P. Serrano-Ortiz*[1,3], *L. Alados-Arboledas*[1,2], *A. S. Kowalski*[1,2], *E. P. Sánchez-Cañete*[1,2], *J. L. Guerrero-Rascado*[1,2]**

(1) Andalusian Institute for Earth System Research (IISTA-CEAMA), Av. del Mediterraneo S/N, 18006, Granada, Spain

(2) University of Granada, Department of Applied Physics, Av. de Fuentenueva S/N, 18071, Granada, Spain

(3) Izaña Atmospheric Research Center, Agencia Estatal de Meteorología (AEMET), Santa Cruz de Tenerife, Spain

(4) Experimental Station of Arid Zones, Spanish National Research Council (EEZA-CSIC), Carr. Sacramento S/N, 04120 Almería, Spain

(5) University of Granada, Department of Ecology, Av. de Fuentenueva S/N, 18071, Granada, Spain

Corresponding author: jabrilgago@ugr.es

Introduction

In recent decades, rising CO_2 levels and climate change have highlighted the importance of understanding CO_2 fluxes, especially in terrestrial ecosystems, which act as major CO_2 sinks [1]. Drylands—including semiarid regions—cover nearly half the Earth's surface and are especially climate-sensitive [2, 3]. As aridity and desertification increase [4], studying CO_2 dynamics in these regions becomes critical. The CO_2 produced by microbial activity and root respiration can be directly emitted to the atmosphere via molecular diffusion [5] (commonly named “respiration process”) but also partially stored into the subsoil and released later via subterranean ventilation—a process driven by atmospheric pressure and airflow changes [6]. While “respiration process” dominate most CO_2 flux studies in drylands, subterranean ventilation is underrepresented and likely underestimated. Radon (Rn) is an inert gas generated by the radioactive decay of ^{226}Ra in the Earth's crust. As it is influenced solely by physical processes, its behavior during air exchanges makes it a reliable indicator of ventilation events [7]. Improving understanding of the subterranean ventilation is crucial for more accurate CO_2 flux modeling.

Lidar-based technologies offer new potential for profiling the atmospheric structure and dynamics at higher altitudes. Yet, their application to surface–atmosphere turbulent exchanges remain underdeveloped and lacks a proper standardization. In this study, we explore turbulence within the boundary layer—measured via a Doppler lidar—as a potential driver of subterranean CO_2 ventilation in Mediterranean drylands [8, 9]. We also assess the roles of atmospheric pressure and the friction velocity, previously identified as key factors.

This study is based on the SCARCE campaign (Synchronized Characterization of Aerosol, Radon and Carbon dioxide Exchanges in drylands), conducted from 18 July 2023 to 15 January 2024 at Balsa Blanca (36.94°N, 2.03°W, 205 m asl,), in southeastern Spain. The site, a Mediterranean semiarid shrubland 6 km from the coast, experiences a BSh (dry subtropical semiarid) climate [8]. Rainfall occurs in pulses, followed by prolonged dry periods, especially from June to October. At this site, soil CO_2 ventilation is well-documented, with pressure identified as the primary driver under dry conditions [8, 9]. However, turbulence has also shown relevance at nearby locations [8].

Instrumentation

A set of instruments was installed at the station, some permanently and some during SCARCE (Figure 1). A flux tower of around 3.5 m tall for eddy covariance (EC) provided 30-minute quality-flagged products of CO_2 flux (F_{CO2}) and concentration ($CO2_{air}$), horizontal wind speed (V_h), friction velocity (u^*) and atmospheric pressure (P_{air}), after processing of the data with EddyPro software (LI-COR, United States of America). A tipping-bucket rain gauge provided 30-minute precipitation data at 0.2 mm resolution. A soil profile included CO_2 concentration sensors at 15, 50 and 150 cm deep, and a Rn activity detector at 50 cm. An 18 m borehole included CO_2 and Rn concentration sensors at 1 m depth. Every variable is recorded in 30-minute intervals.

A HALO Photonics StreamLine XR Doppler lidar operated at the station during SCARCE. The system emits 1500 nm and 15 kHz radiation, and detects the Doppler-shifted backscatter with a heterodyne receiver.

Processing was carried out with the HALO lidar toolbox [10], yielding 3D wind fields and turbulence parameters. The system operated at 1 s pulse intervals with a vertical resolution of 30 m. The effective full-overlap height of the lidar is at 90 m above ground level (agl); thus, 105 m agl represents the middle altitude of the lowermost reliable bin. The upper measurement range depends on aerosol load and cloud cover but typically remains within the atmospheric boundary layer [11]. This study focuses on the turbulent kinetic energy (TKE) dissipation rate, ϵ [12]. Values of $\epsilon > 10^{-4}$ m^2 s^{-3} indicate strong turbulence often linked to surface convection [13]. ϵ profiles were filtered based on the signal-to-noise ratio (SNR), discarding layers with SNR < 0.006 (−22.2 dB) [13]. The 3-minute ϵ data were averaged into 30-minute intervals.

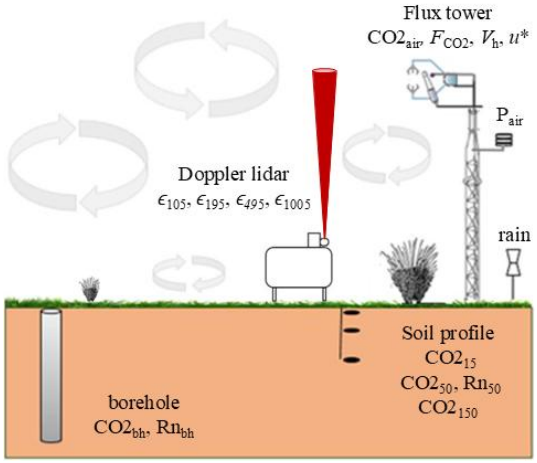

Figure 1. Scheme of the instrumentation setup at Balsa Blanca. Numerical lower scripts indicate the altitude (Doppler lidar) or depth (soil profile) at which the variables are sampled.

Methodology

The 30-minute products from the flux tower, soil profile, borehole and Doppler lidar are processed prior to the statistical analysis. These datasets typically exhibit strong daily cycles driven by solar heating and atmospheric tides which can mask the variability of interest. To remove these fluctuations, the 24-hour trend (daily variations) is removed from the series, except for P_{air}, which shows pronounced 12-hour (semi-daily) tidal variations. A simple 24-hour or 12-hour rolling average, previously proven to be effective, is applied to the respective series. Once detrended, the normality of the data is rejected based on the Shapiro-Wilk and Anderson-Darling normality tests. Additionally, an augmented Dickey-Fuller test confirms the stationarity of the detrended 30-minute series.

Our analysis focuses on specific ventilation events, which are identified precisely. To be considered, each case must exhibit a marked increase in soil CO_2 and Rn concentrations (recharge), coinciding with a decrease in P_{air}, followed by a sharp drop in concentrations (ventilation) when the pressure rebounds. This behavior is consistent with previously reported ventilation events [7, 8, 9]. Significant turbulence, as indicated by Doppler lidar ϵ values, is also a prerequisite for the considered events. Finally, rain is excluded to avoid biological influences on the CO_2 concentration and to allow ventilation of air-filled pores. Figure 2 displayed an example of two events classified according to the mentioned methodology.

Finally, each variable is normalized by its absolute average for each event, and the Spearman correlation coefficients, non-parametric measures of association suitable for non-normally distributed variables, are calculated for selected variable combinations. In the resulting matrix, the correlations between CO_2 and Rn concentrations at different depths ($CO2_{air}$, $CO2_{15}$, $CO2_{50}$, $CO2_{150}$, $CO2_{bh}$, Rn_{50}, Rn_{bh}) against the atmospheric variables (P_{air}, u^*, V_h, ϵ_{105}, ϵ_{195}, ϵ_{495} and ϵ_{1005},) are presented.

Results and Discussion

A total of 10 ventilation events were identified across the observation period. The Spearman correlation coefficients between the most relevant variables are shown in Figure 3. In general, most variable combinations exhibit consistent patterns across the recharge and ventilation phases. However, correlations involving gas concentrations and variables such as V_h, as well as ϵ_{105} and ϵ_{195}, either change in magnitude or lose significance during specific periods.

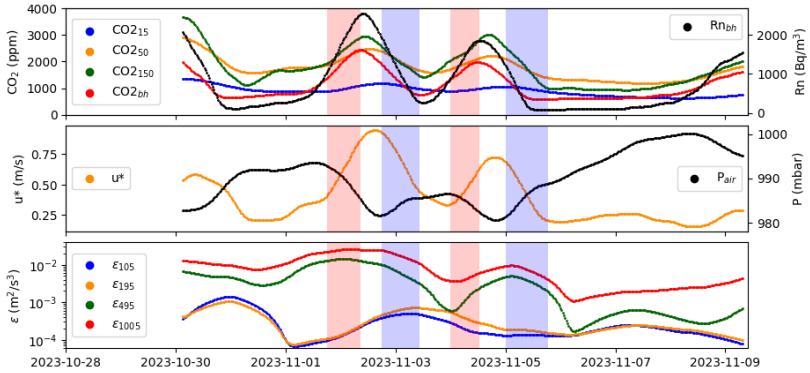

Figure 2. Time series of CO_2 and Rn concentrations, u^*, P_{air} and ϵ values during two ventilation events observed between 1 and 5 November 2023. Red and blue shading indicate recharge and ventilation periods respectively

Rn concentrations show strong positive correlations with the other concentrations, confirming that both gases respond similarly to subsurface dynamics during recharge and ventilation phases. In contrast, correlations between Rn and CO_2 with F_{CO2} are negative and generally less significant, suggesting that F_{CO2} is influenced by different processes or timescales.

P_{air} displays strong, negative correlations with the concentrations, which aligns with previous findings [9, 11]. When P_{air} increases, CO_2- and Rn-poor atmospheric air is drawn into the soil through pores and fissures, diluting the concentrations. Conversely, when P_{air} decreases, CO_2- and Rn-rich air from deeper soil layers expands to occupy near-surface layers, increasing observed concentrations.

u^*, ϵ_{495} and ϵ_{1005} show strong positive correlations with gas concentrations, indicating that elevated turbulence within the boundary layer—driven by processes such as daytime convection and wind shear—enhances upward transport of CO_2 and Rn from depth.

Interestingly, ϵ_{105} correlates significantly and negatively with gas concentrations during ventilation periods. This may point to a localized effect of near-surface turbulence, where higher ϵ_{105} values promote the intrusion of CO_2- and Rn-poor atmospheric air into the soil, thereby triggering ventilation.

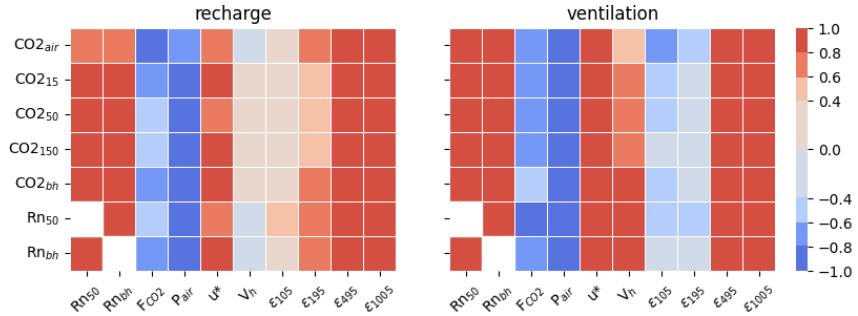

Figure 3. Spearman correlation coefficients between the most significant variables of the study and for the two different periods of the events.

Conclusions

This study confirms that atmospheric pressure is the primary driver controlling the vertical transport of CO_2 and Rn within the vadose zone at Balsa Blanca, a semiarid grassland in SE Spain. However, our results also highlight the significant role of turbulence, as indicated by Doppler lidar measurements, in influencing CO_2 and Rn dynamics. High turbulence within the boundary layer, particularly due to daytime convection or wind shear, facilitates the upward movement of CO_2- and Rn-rich air from deeper soil layers. This process increases the concentration of these gases at the sampling levels. The study findings suggest that both atmospheric pressure and turbulence regulate CO_2 and Rn concentrations within the vadose zone, impacting their fluxes. This emphasizes the need to consider abiotic processes, such as ventilation, in CO_2 flux models, at least for these ecosystems.

While this study primarily focuses on identifying ventilation and recharge events and calculating covariances between measurements, further integrative analyses are underway to better understand how the main drivers influence and modify CO_2 and Rn vertical transport within the vadose zone. Understanding these interactions is crucial for improving the accuracy of carbon cycle predictions in dryland regions, especially as climate change intensifies aridity and impacts the behavior of these ecosystems.

Acknowledgements

This work was supported by the project INTEGRATYON[3] (PID2020-117825GB-C21 and PID2020-117825GB-C22) funded by MICIU/AEI/10.13039/501100011033, and by University of Granada *Plan Propio* through Excellence Research Unit Earth Science and Singular Laboratory AGORA (LS2022-1) program and Project for Early-Career Researchers EMITE-EC (PPJIB-2024-12), and the strategic network ACTRIS-*España* (RED2022-134824-E). This study is part of a project that is supported by the European Commission under the Horizon 2020 – Research and Innovation Framework Programme, H2020-INFRAIA-2020-1, Grant Agreement number: 101008004. Jesús Abril-Gago received funding through the grants FPU21/01436 and EST24/00285 funded by MICIU/AEI/10.13039/501100011033.

References

[1] Friedlingstein, P. et al.: *Global Carbon Budget 2023*, Earth Syst. Sci. Data, 15, 5301–5369, doi.org/10.5194/essd-15-5301-2023, 2023.

[2] Mirzabaev, A. et al.: *Cross-Chapter Paper 3: Deserts, Semiarid Areas and Desertification. In: Climate Change 2022: Impacts, Adaptation and Vulnerability. Contribution of Working Group II to the Sixth Assessment Report of the Intergovernmental Panel on Climate Change*,Cambridge University Press, Cambridge, UK and New York, NY, USA, pp. 2195–2231, https://www.ipcc.ch/report/ar6/wg2/downloads/report/IPCC_AR6_WGII_CCP3.pdf, 2022.

[3] Ali, E. et al.: *Cross-Chapter Paper 4: Mediterranean Region. In: Climate Change 2022: Impacts, Adaptation and Vulnerability. Contribution of Working Group II to the Sixth Assessment Report of the Intergovernmental Panel on Climate Change*, Cambridge University Press, Cambridge, UK and New York, NY, USA, pp. 2233–2272, https://www.ipcc.ch/report/ar6/wg2/downloads/report/IPCC_AR6_WGII_CCP4.pdf, 2022.

[4] Abel, C. et al.: *Contrasting ecosystem vegetation response in global drylands under drying and wetting conditions*, Global Change Biol., 29, 3954–3969, doi.org/10.1111/gcb.16745, 2023.

[5] Kowalski, A.S., and Serrano-Ortiz, P.: *On the relationship between the eddy covariance, the turbulent flux, and surface exchange for a trace gas such as CO_2*, Boundary-Layer Meteorol, 124, 129–141, doi.org/10.1007/s10546-007-9171-z, 2007.

[6] Moya, M. R. et al.: *Ecosystem CO2 release driven by wind occurs in drylands at global scale*, Global Change Biol., 28, 5320–5333, doi.org/10.1111/gcb.16277, 2022.

[7] Sanchez-Cañete, E. P. et al.: *Subterranean CO2 ventilation and its role in the net ecosystem carbon balance of a karstic shrubland, Geophys*, Res. Lett., 38, L09802, doi.org/10.1029/2011GL047077, 2011.

[8] López-Ballesteros, A. et al.: *Subterranean ventilation of allochthonous CO2 governs net CO2 exchange in a semiarid Mediterranean grassland*, Agric. For. Meteorol., 234, 115-126, doi.org/10.1016/j.agrformet.2016.12.021, 2017.

[9] Moya, M. R. et al.: *CO2 dynamics are strongly influenced by low frequency atmospheric pressure changes in semiarid grasslands*, Journal of Geophysical Research: Biogeosciences, 124, 902–917, doi.org/10.1029/2018JG004961, 2019.

[10] Manninen, A. J.: *Halo Lidar Toolbox*, Github, https://github.com/manninenaj/HALO_lidar_toolbox, 2019.

[11] Ortiz-Amezcua, P. et al.: *Dynamics of the Atmospheric Boundary Layer over two middle-latitude rural sites with Doppler lidar*, Atmos. Res., 280, 106434, https://doi.org/10.1016/j.atmosres.2022.106434, 2022.

[12] O'Connor, E. J. et al.: *A Method for Estimating the Turbulent Kinetic Energy Dissipation Rate from a Vertically Pointing Doppler Lidar, and Independent Evaluation from Balloon-Borne In Situ Measurements*, J. Atmos. Oceanic Technol., 27, 1652–1664, doi.org/10.1175/2010JTECHA1455.1, 2010.

[13] Manninen, A. J. et al.: *Atmospheric boundary layer classification with Doppler lidar*, Journal of Geophysical Research: Atmospheres, 123, 8172–8189, doi.org/10.1029/2017JD028169, 2018.

First considerations about APINA (Aerosol Properties by Integrated measurements in Naples Area) multi-parametric measurement campaign

M. Manzo[1], *S. Amoruso* [1], *M.R. Calvello* [2], *R. Damiano*[1], *F. Esposito*[3], *A. Giunta*[2], *G. Pavese*[2], *A. Sannino.*[1], *S. Spinosa*[1] *and A.Boselli*[2]

(1) University of Naples "Federico II", Department of Physics "Ettore Pancini", Via Cintia, I-80126, Naples, Italy
(2) Consiglio Nazionale delle Ricerche Istituto di Metodologie per l'Analisi Ambientale, I-85050, Tito Scalo, Italy
(3) University of Basilicata, ctr.da Macchia Romana, I-85100, Potenza, Italy

Corresponding author: matteo.manzo@unina.it

Introduction

Systematic environmental observation and monitoring are essential to improve quality of life on our planet. Since each territory faces unique challenges, tailored efforts are required to address local emergencies. In this context, cities can be considered valuable case studies, providing insights and data that enhance regional monitoring capabilities. Atmospheric aerosols in urban areas play a significant role, as they are among the primary contributors to health issues and have a considerable impact on the Earth's radiative balance. In recent years, several studies have focused on the influence of anthropogenic emissions at the local scale, examining both their surface-level and vertical distribution. Among the different aerosol types, black carbon particles are of particular concern due to their health implications and associated mortality risks [1]. These particles, largely produced by local sources, are mainly confined within the Planetary Boundary Layer (PBL), the lowest part of the atmosphere characterized by intense convective and turbulent activity. Due to the complex nature of aerosol properties within the PBL, effective environmental policies in the metropolitan area of Naples must be grounded in a thorough assessment of emission impacts, the identification of pollution sources and long-term monitoring of aerosol optical and microphysical characteristics, as well as their variability.

To support this objective, the APINA (Aerosol Properties by Integrated measurements in Naples Area) multi-parametric measurement campaign was carried out through in the frame of a scientific collaboration between the National Research Council (CNR), the University of Naples Federico II, and the University of Basilicata. The campaign focuses on characterizing aerosol properties in the urban district of San Giovanni a Teduccio, located in the eastern part of the city. Given its proximity to the port area, the study aims to monitor and distinguish various emission sources, evaluate their impact on urban air quality and investigate their seasonal variations.

Methodology

To achieve this multi-parametric characterization, a combination of near-surface and remote sensing instruments was employed (see Figure 1).

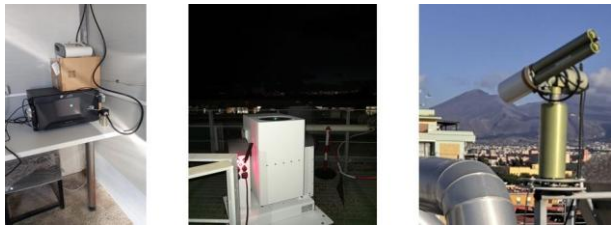

Figure 1. Photos of some of the instrumentation used during the APINA campaign. Aethalometer (left), lidar (center) and Sun-sky-lunar photometer (right).

The near-surface setup included an aethalometer for the measurement of equivalent Black Carbon Concentrations (eBC) and the estimate of Ångström Absorption exponent (AAE). This instrument allows the investigation of carbonaceous particles and their transformation processes in the atmosphere. Complementing this, an Optical Particle Counter (OPC) was installed at ground level to provide real-time measurements of particle number size distributions in the 0.3 μm to 10 μm range to monitor the temporal variability of local pollution events. These observations were further supported by remote sensing instruments from the CARS (Centre for Aerosol Remote Sensing) section within ACTRIS [2]. Systematic lidar measurements were performed to retrieve optical properties of atmospheric aerosols and additionally, a CIMEL Sun–Sky–Lunar photometer, part of the AERONET network [3], was used to assess the variability of column-integrated aerosol optical and microphysical properties. These measurements were also linked to long-term records during specific events such as wildfires, volcanic eruptions, Saharan dust outbreaks and other long-range transport episodes.

Results and Discussion

The first noteworthy outcome of this measurement campaign was the possibility to observe the evolution of the PBL over different days. This was made possible thanks to the availability of continuous lidar measurements collected over several days, which provide a vertically resolved characterization of atmospheric aerosol.

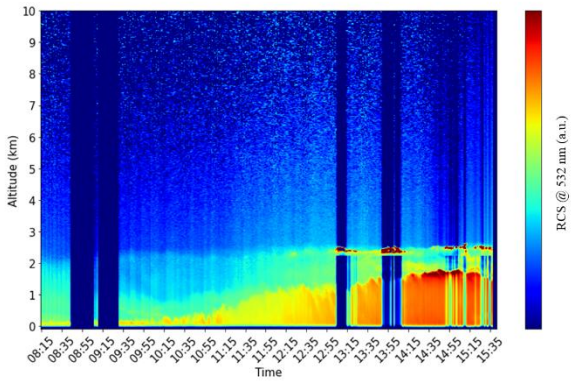

Figure 2. False colour map for 2nd December 2024. Warmer colours depict stronger presence of aerosol.

Figure 2 shows a false colour map of the Range Corrected Lidar signal (RCS). It is possible to observe an increasing layer in the low troposphere that can be associated with the PBL height evolution, in agreement with the expected behavior [4].

Within this seasonal characterization, aerosol transport phenomena following specific events were observed. This is the case for the week from December 2nd to 8th, 2024, during which two significant variations in the trend were observed. In fact, the Aerosol Optical Depth (AOD) of the total, fine, and coarse fractions at 500 nm, computed using the algorithm provided by [5], show an anomalous behavior on December 4th (Figure 3) with the coarse fraction becoming predominant over the fine one. The same information can be assessed when looking at the Angstrom exponent at 440/870 nm ($\alpha_{440/870}$) for the same day, which evidences a decrease in the retrieved value, suggesting the presence of larger particles over the column.

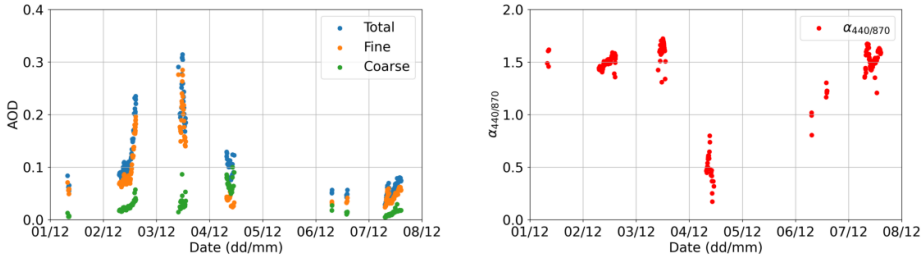

Figure 3. AOD at 500 nm (left) and $\alpha_{440/870}$ (right) computed for the week 2-8 December 2024. The AOD at 500 nm is expressed in total, fine and coarse fractions.

This situation agrees with the results of the near-surface measurements in Figure 4, where the right panel depicts the comparison between NC1 (number concentration of particles with diameter lower than 1 µm) and NC1-10 (number concentration of particles with diameter between 1 and 10 µm). It is evident that on December 4th the coarse component observed at ground level dominates over the fine, indicating that the predominant coarse contribution observed along the column is the one reaching the surface.

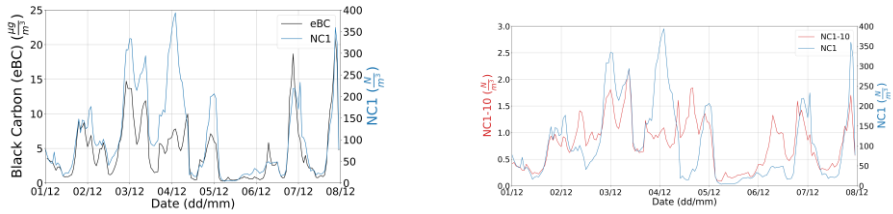

Figure 4. Weekly trends for NC1 vs equivalent Black carbon (left) and for NC1-10 vs NC1 (right) for the period 2-8 December 2024.

Another deviation from the trend is observed in the early hours of December 4th, as shown in the left panel of Figure 4. Differently of the other days, with a strong agreement between eBC and NC1, the peak in NC1 concentration is not followed by a corresponding eBC increase. This could be related to the presence of fine particles such as those emitted during a volcanic eruption and subsequently transported over long distances. Identifying the source of these variations requires further optical and chemical analyses, which will be presented as part of this contribution.

Conclusions

The APINA measurement campaign aims to derive information and data that can provide added value to territorial monitoring capabilities through the multi-parametric characterization of urban atmospheric aerosol in the Naples area. During these continuous measurements, long-range aerosol transport events were observed, allowing for their comprehensive characterization thanks to the combined use of near-surface instruments and remote sensing techniques. The following step of this campaign will be to complement these preliminary analyses completing the characterization of the transport events described earlier.

In this communication, a thorough analysis of optical and microphysical parameters provided by the various techniques used in the APINA measurement campaign will be illustrated and discussed.

Acknowledgements
This work was supported by CIR01_00015 “PER-ACTRIS-IT” – Volto al rafforzamento del capitale umano nell’ambito della compagine di progetto di PER-ACTRIS-IT and by EU - Next Generation EU Mission 4, Component 2 - CUP B53C22002150006 - Project IR0000032 – ITINERIS - Italian Integrated Environmental Research Infrastructures System.

References
[1] Yang, J. et al.: *Long-term exposure to black carbon and mortality: A 28-year follow-up of the GAZEL cohort*, Environment International, 157, 10685, https://doi.org/10.1016/j.envint.2021.106805, 2021.
[2] Pappalardo G.: *ACTRIS Aerosol, Clouds and Trace Gases Research Infrastructure*, EPJ Web of Conferences, 176, https://doi.org/10.1051/epjconf/201817609004, 2018.
[3] Holben, B.N. et al.: *AERONET—A Federated Instrument Network and Data Archive for Aerosol Characterization*, Remote Sensing of Environment, 66, Issue 1, 1-16, https://doi.org/10.1016/S0034-4257(98)00031-5, 1998.
[4] Boselli, A. et al: *Atmospheric Aerosol Characterization Over Naples During 2000–2003 EARLINET Project: Planetary Boundary-Layer Evolution and Layering*, Boundary-Layer Meteorol. 132, 151,2009

Water Vapor Mixing Ratio Lidar Profiles Related to Atmospheric Conditions During an Intensive Measurements WaLiNeAs Period in Burjassot Site.

C. Dameto de España1, *J.L. Gómez-Amo[1], P.C. Valdelomar[1], M.P. Utrillas[1]*

(1) Universitat of Valencia, Dpt. Física de la Terra i Termodinàmica, Solar Radiation Group, Dr. Moliner 50, 46100, Burjassot, Spain

Corresponding author: Maria.C.Dameto@uv.es

Introduction

Climate models have identified the Mediterranean Basin as a hotspot of climate change, with significant implications for global warming. As a result, heavy precipitation events (HPEs) have become more frequent during the autumn season, often leading to floodings and overflowings. Water vapor mixing ratio (WVMR) is a relevant parameter in the evaluation of HPEs. Moreover, WVMR as well as the CAPE play a significant role in the atmospheric energy balance [1].

WVMR is highly variable in space and time and together with aerosol particles contribute to cloud formation processes [2]. Aerosols and clouds are involved in the direct and indirect effect, respectively. These effects represent one of the largest piece of uncertainty in the calculation of the radiation budget and in the calculation of cooling/warming effect. Therefore, a more accurate characterization of atmospheric WVMR is essential for improving and enhancing the performance of climate models [3].

In order to assess the WVMR and its influence on HPEs, the Water Vapor Lidar Network Assimilation (WaLiNeAs) campaign was carried out to measure WVMR profiles across the Western Mediterranean region [4]. During this campaign, eight lidars specifically designed for WVMR profiling were deployed along the western Mediterranean coast [5]. Lidar technology is a well-established method for measuring atmospheric WVMR with high spatial and temporal resolution. In particular, Raman lidars may include a water vapor channel. The Raman Lidar used in this campaign provides accurate retrievals of WVMR . This instrument is also capable of simultaneously measuring optical properties.

The principal objective of this study is to evaluate retrievals of WVMR profiles associated with atmospheric conditions obtained during the WaliNeAs campaign. Results of WVMR retrievals measured with the depolarization Raman Lidar in the Burjassot Atmospheric measurements Station (BASS), maintained by the Solar Radiation Group of the University of Valencia will be presented. Influences of atmospheric conditions on WVMR variations observed during the campaign will also be outlined.

Methodology

Measurements were conducted at BASS (39.508º N, 0.418º W, 60 m a.s.l), situated on the Burjassot campus of the University of Valencia. This station is located near the city of Valencia, a major urban center with a population of approximately 1.4 million inhabitants. It is directly influenced by urban and industrial pollution, which contributes significantly to the presence of anthropogenic aerosols. Moreover, its proximity to the western Mediterranean coast modulates the amount of water vapor levels in the atmosphere.

WVMR profiles were measured with TONET Lidar, which is 8-channel depolarization Raman Lidar (LR332-D300) manufactured by Raymetrics S.A:. The emitting system of this LIDAR consists of a frequency tripled Nd: YAG laser emitting pulsed laser beam of 355 nm, 532 nm, and 1064 nm wavelength pointed vertically. The receiving system is equipped with three channels for the elastic-backscattered signals at 355 nm, 532 nm, and 1064 nm. The 355 nm and 532 nm channels are also sensible to polarization. Moreover, there are three Raman channels centered at 387 nm, 408 nm, and 607 nm, corresponding to nitrogen (387 nm and 607 nm) and water vapor (408 nm), respectively. The system is based on a 500 mm Cassegrain optical telescope design.

The backscattered signal is detected using photomultiplier tubes (PMTs) and subsequently digitized by an analog-to-digital (A/D) converter. The system samples the signal at a rate of 20 MHz, providing a vertical resolution of 7.5 meters, which is suitable for detecting lidar returns from distances up to 8–10 km. For higher altitudes, typically above 8 km, a photon-counting mode is employed, using PMTs with a sampling rate of 800 MHz to detect low-intensity signals.

The LIDAR data during WaLiNeAs campaign were collected from the 20th of October to the 20th of November 2022. Only night time data were sampled, comprising 12 hours (6 p. m. – 6 a.m.). WVMR profiles were obtained and averaged in 1 minute with a vertical resolution of 100 m and 15 minutes of time resolution. Averaged data were sent in near-real time to the Météo-France server. The WVMR after a calibration can be calculated in g/kg against altitude z and without correction of the atmospheric transmission as following (Eq. 1) [5] and [6]:

$$WVMR(z) = K \cdot OR(z) \cdot \frac{S_{408}(z)}{S_{387}(z)} \cdot M(z) \cdot A(z) \quad (1)$$

where WVMR is proportional to the signal ratio between water vapor and nitrogen Raman channels at 408 nm and 387 nm, respectively. K is the calibration constant, in (g/kg), and S(z) is the lidar signal for each channel, already corrected for sky background, dark measurements and electronic background.

$OR(z) = \frac{O_{387}(z)}{O_{408}(z)}$ is the ratio between the overlap functions for the 387 nm and 408 nm channels.

M(z) and A(z) are the molecular and aerosol corrections, respectively, due to the atmospheric transmittance at the Raman wavelengths used. M(z) and A(z) are the molecular and aerosol corrections, respectively, due to the atmospheric transmittance at the Raman wavelengths used.

In our case, the calibration of WVMR has been calibrated using ground-based meteorological measurements and validated against ERA-5 profiles. Very good agreement is obtained between our calibrated WVMR profiles and ERA-5 reanalysis profiles with Mean Bias Deviation (MBD) of 1 g/kg.

Results and Discussion

This section presents the results of Lidar - derived WVMR profiles retrieved with a vertical resolution of 100 meters and a temporal resolution of 15 minutes. Figure 1 displays a time series of vertical profiles of WVMR extending up to 4 km in altitude. Elevated concentrations of WVMR are observed between the 20th of October and the 3rd of November, with values ranging from 10 to 15 g/kg. After 3rd of November, a noticeable shift in the WVMR trend occurs. Between the 3rd of November and the 17th of November, the WVMR concentrations decrease significantly, with consistently low values recorded throughout this period. The lidar-derived WVMR profiles shown in (Fig. 1) were calibrated with surface WVMR measurements

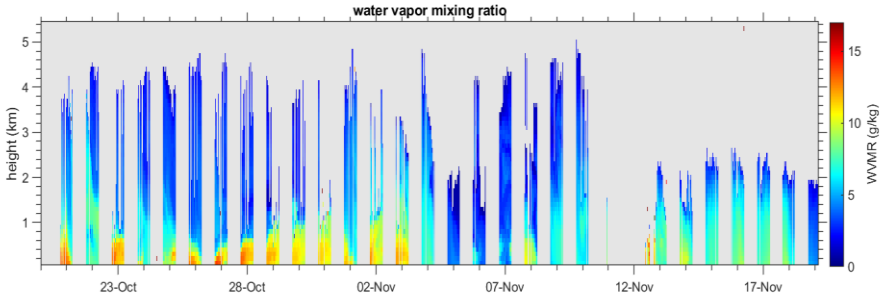

Figure 1. Time series of Lidar-derived WVMR during the WaLiNeAs campaign

Based on the observations presented in Figure 1, two distinct periods can be identified in terms of water vapor content: a wet period and a dry period. The abrupt change in the water vapor mixing ratio (WVMR), observed in both the lidar-derived profiles and the surface measurements, is likely attributable to meteorological variability. Given the proximity of the BASS station to the coastline, the WVMR values may be influenced by changes in wind direction.

Figures 2a and 2b present wind rose diagrams corresponding to the wet and dry periods, respectively. These plots depict the Water Vapor Mixing Ratio (WVMR) as a function of wind direction, with WVMR values represented using a color scale. In Figure 2a, associated with the wet period, WVMR values range between 8 and 12 g/kg, indicating generally higher atmospheric vapour. In contrast, Figure 2b, corresponding to the dry period, shows a broader WVMR range from 4 to 12 g/kg, suggesting greater variability and generally drier conditions. A clear shift in prevailing wind direction is also observed between the two periods. During the wet period, winds predominantly originate from the northwest, whereas in the dry period, the dominant wind direction shifts to the southwest. This change in wind patterns may influence the observed variations in atmospheric vapour content.

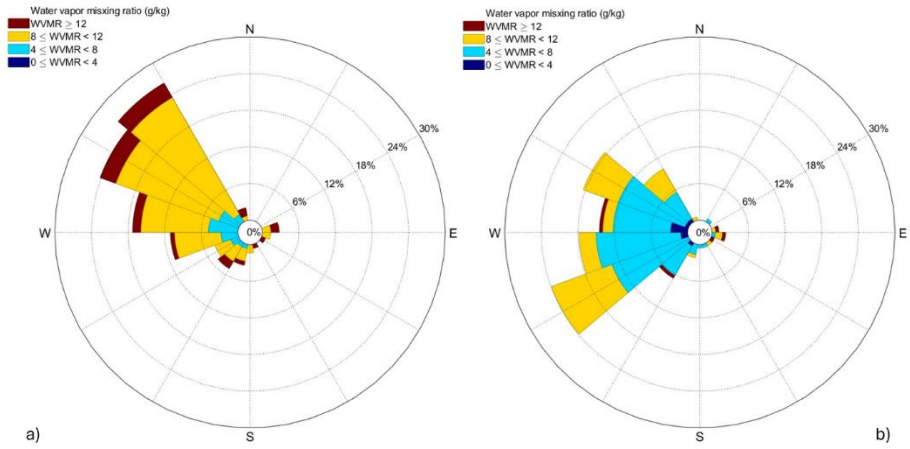

Figure 2 . WVMR profile measured at the surface during the WaLiNeAs campaign

Conclusions

The Raman lidar system has proven to be a highly effective instrument for profiling water vapor and aerosols with vertical resolution, ranging between 15 and 50 meters. During the WaLiNeAs campaign, the system operated continuously, providing nighttime measurements of WVMR.

The lidar-derived WVMR profiles obtained during the campaign were classified into two distinct periods, wet and dry. This differentiation appears to be associated with variations in wind direction. Specifically, the analysis of WVMR as a function of wind direction revealed that during the wet period, prevailing winds predominantly originated from the northwest, whereas during the dry period, they mainly came from the southwest.

These findings demonstrate the capability of Raman lidar to deliver high-resolution vertical and temporal data, which are essential for enhancing meteorological forecasting and supporting the development of early warning systems through accurate WVMR monitoring.

Acknowledgements

This work is supported by the Spanish Ministries of Economy and Competitiveness (MINECO) and Science, Innovation and Universities (MICIU) through the grants: PID2021-123881OB-I00, TED2021-129185BI00, RED2022-134824-E, RED2024-153756-E; and the Valencia Autonomous Government through CIAICO2023-088, and the CIAPOS/2023/211 grant for the participation of C. Dameto de España

References

[1] Held, I. M. and Soden, B. J.: *Water vapor feedback and global warming,* Annu. Rev. Energ. Environ., 25, 441–475, https://doi.org/10.1146/annurev.energy.25.1.441, 2000

[2] IPCC: Climate Change 2022: *Impacts, Adaptation, and Vulnerability.Contribution of Working Group II to the Sixth Assessment Report of the Intergovernmental Panel on Climate Change*,edited by: Pörtner, H.-O., Roberts, D. C., Tignor, M., Poloczanska,E. S., Mintenbeck, K., Alegría, A., Craig, M., Langsdorf,S., Löschke, S., Möller, V., Okem, A., and Rama, B., Cambridge University Press, Cambridge, UK and New York, NY, USA, 3056pp., https://doi.org/10.1017/9781009325844, 2022.

[3] J.T. Houghton, Y. Ding, D.J. Griggs, M. Noguer, P.J. van der Linden, D. Xiaosu
Climate Change 2001: The Scientific Basis: Cambridge University Press, Cambridge (2001)

[4] Flamant, C., Chazette, P., Caumont, O., Di Girolamo, P., Behrendt,A., Sicard, M., Totems, J., Lange, D., Fourrié, N., Brousseau, P., Augros, C., Baron, A., Cacciani, M., Comerón, A., De Rosa, B., Ducrocq, V., Genau, P., Labatut, L., Muñoz-Porcar, C., Rodríguez-Gómez, A., Summa, D., Thundathil, R., and Wulfmeyer, V.: *A network of water vapor Raman lidars for improvingheavy precipitation forecasting in southern France: introducing the WaLiNeAs initiative*, B. Atmos. Sci. Technol., 2,10, https://doi.org/10.1007/s42865-021-00037-6, 2021

[5] Chazette et al.: *Long-term evolution of the calibration constant on a mobile/field campaign water vapour Raman lidar*, Egusphere, doi.org/10.5194/egusphere-2024-3583.

[6] Laly et al.: *Water vapor Raman-lidar observations from multiple sites in the framework of WaLiNeAs*, Earth Syst. Sci. Data, doi.org/10.5194/essd-2024-73, 2024.

Comparison of PSC measurements with the ALV and RAMSES lidars of the Lindenberg Meteorological Observatory and ATLID onboard the EarthCARE satellite

J. Reichardt[1], *F. Lauermann*[1], *O. Behrendt*[1]

(1) Deutscher Wetterdienst (DWD), Meteorologisches Observatorium Lindenberg, Am Observatorium 12, 15848, Tauche OT Lindenberg, Germany

Corresponding author: jens.reichardt@dwd.de

Introduction

The Lindenberg Meteorological Observatory participates in the German Initiative for the Validation of EarthCARE (GIVE). As a contribution to this project, measurements with the new ATLID Validator (ALV) lidar are performed during satellite overflights, which corresponds to the Atmospheric Lidar (ATLID) on EarthCARE in terms of measurement parameter set and observation geometry (3° tilt). It supplements the routine measurements with the spectrometric fluorescence and Raman lidar RAMSES, which is even more powerful but, unlike ATLID, measures vertically [1, and references therein].

In early March 2025, the rather rare meteorological situation developed in which the Arctic polar vortex extended to northern mid-latitudes. Lindenberg came under its influence, and the stratospheric temperatures were so cold that stratospheric clouds (PSCs) could be measured with RAMSES and ALV on 4 March and especially on 5 March 2025. Only a few hours later, around 00:00 UTC on 6 March, the PSC system was observed by ATLID during the EarthCARE overpass over Eastern Europe. In this contribution, the PSC measurements with the two ground-based lidars and with ATLID are presented and compared.

Methodology

ALV measurements presented in this paper have been analyzed using standard Raman and polarization lidar techniques. RAMSES data were processed differently. To preserve the ultra-fine wavy stratification of the PSCs visible in the raw data as well as possible, the Raman signals were not used and only the attenuated particle backscatter coefficient was calculated. The height range used for the Rayleigh calibration varied between 17–19 and 18–20 km depending on the optical thickness of the cirrus underneath. Nominal Level 1b ATLID data were used (baseline AD, orbit 4373, frame B) [2]. ATLID altitude bin size is about 500 and 100 m above and below 20 km, respectively. ECMWF Reanalysis v5 (ERA5) data helped to visualize the meteorological conditions in the lower stratosphere [3].

Results and Discussion

For the EarthCARE overpass over Lindenberg at 13:38 UTC on 5 March 2025, ALV started operation around noon and measured until the next morning. Thick cirrus clouds prevented measurements in the stratosphere before 17:00 UTC, but then the cirrus layer gradually opened up and allowed the detection of a PSC system around 22 km height. Figure 1 presents the ALV measurement for the 5-hour period between 17:00 and 22:00 UTC which covers the peak of PSC activity. Below 14 km height the cirrus layer can be seen, slowly dissipating over time. Above a PSC is observed between 20.5 and 24 km. It is optically thin, particle backscatter coefficient reaches values of up to 0.5 $Mm^{-1}sr^{-1}$. More interesting is the volume depolarization ratio (Fig. 1b), as it reveals the inner structure of the stratospheric cloud. Embedded in a field of liquid PSC particles (PSC Ib) as manifested by the depressed values, a filament with volume depolarization ratios of up to 6.5 % emerges slightly below 22 km between 19:00 and 20:00 UTC. This maximum value corresponds with a particle depolarization ratio of about 11 %. The polarizing layer appears even more pronounced in the high-resolution RAMSES data (Fig. 2b). Here, the implied particle depolarization ratio reaches 20 %. In summary, the lidar observations suggest that a short-lived ice PSC formed. The radiosonde launch on site at 17:36 UTC of 5 March 2025 corroborates this interpretation as it confirmed stratospheric temperature dropping to about -85 °C. So it is possible that intermittently temperatures fell below the frost point and indeed a transient ice PSC II occurred.

Figure 2a nicely illustrates the delicate structure of the PSC field. Thin layers with enhanced droplet backscattering are stacked and exhibit wavy patterns, often the filaments are only a few hundred meters

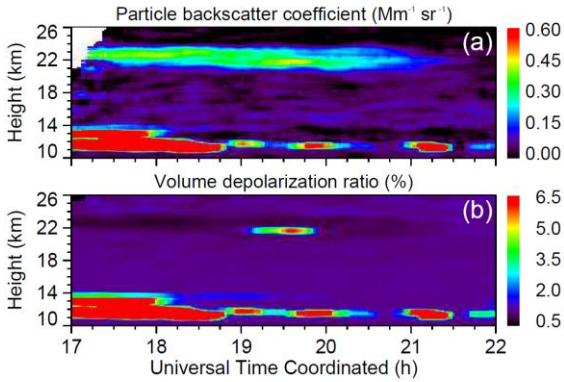

Figure 1. ALV measurement on 5–6 March 2025, only the main PSC event between 17:00 and 22:00 UTC is shown. Temporal evolution of (a) particle backscatter coefficient, and (b) volume depolarization ratio. For each profile, 1200 s of lidar data are integrated, the calculation step width is 120 s. The resolution of the raw data is 60 m, signal profiles are smoothed with a sliding-average length of 780 m. White areas indicate where data were rejected by the automated quality control process.

thick. Not surprisingly, this information is lost when the height bin width of the observation is deliberately reduced to 510 m, a value which is close to the ATLID profile resolution in the stratosphere of about 500 m. Consequently, it cannot be expected that ATLID would resolve such structural features.

As already mentioned, EarthCARE crossed Eastern Europe and Scandinavia just a few hours after the main PSC event over Lindenberg at around midnight. ATLID also detected PSCs during the overpass, as can be seen from the ground track of ATLID in Fig. 3b which visualizes the maximum of the attenuated total particle backscatter coefficient between 20.5 and 25.0 km. This provides the opportunity to compare the

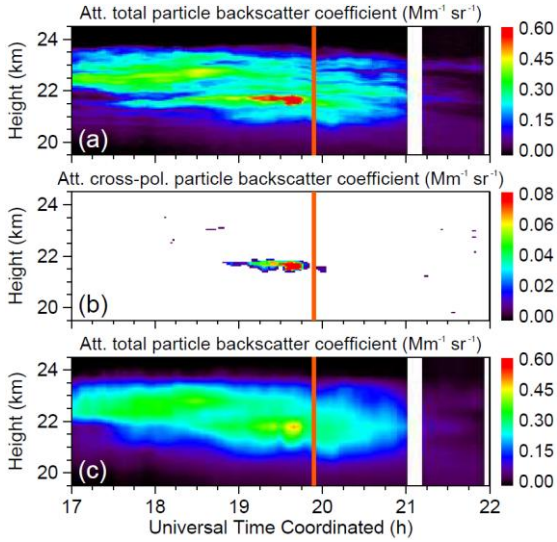

Figure 2. RAMSES measurement on 5–6 March 2025, only the main PSC event between 17:00 and 22:00 UTC is shown. Temporal evolution of (a) attenuated total particle backscatter coefficient (60 m vertical resolution), (b) attenuated cross-polarized particle backscatter coefficient (60 m vertical resolution), and (c) attenuated total particle backscatter coefficient with the vertical resolution reduced to 510 m. For each profile, 240 s of lidar data are integrated, the calculation step width is 120 s. The measurement at 19:54 UTC (time marked by vertical orange line) exhibits the highest cross correlation with an ATLID profile measured during the EarthCARE overpass over Eastern Europe and Scandinavia around 00:00 UTC on 6 March 2025 (see Figs. 3–5).

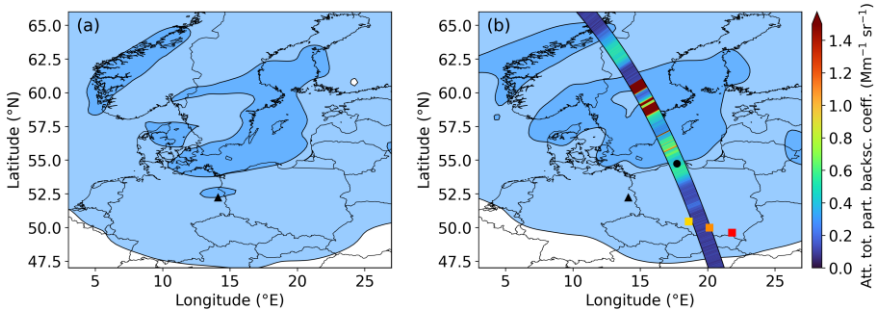

Figure 3. ERA5 reanalysis of the atmospheric temperature at the 30 hPa level [3] for (a) 5 March 2025 20:00 UTC, and (b) 6 March 2025 00:00 UTC; light and dark blue coloring is used for temperatures below -78 °C and -85 °C, respectively. The EarthCARE overpass over Eastern Europe and Scandinavia around 00:00 UTC on 6 March 2025 is visualized by the maximum of the attenuated total particle backscatter coefficient between 20.5 and 25.0 km as measured with ATLID (line width not to scale). Symbols indicate the coordinates of the ALV and RAMSES site (black triangle), of the ATLID profile with the highest cross correlation (black disk), and of the air parcels at midnight measured over Lindenberg at 19:00, 20:00, and 21:00 UTC (HYSPLIT trajectories [4,5]; red, orange, and yellow square, respectively).

RAMSES and ATLID PSC measurements. A lidar match, i.e., two lidars probing the same air parcel at different times, cannot be expected because the trajectory of the PSC observed over Lindenberg headed to southern Poland where, by the time it crossed the ground track of ATLID, temperatures have apparently gotten too warm to sustain a PSC (Fig. 3b). A cross-correlation analysis was carried out to investigate where and when the similarity between the ground- and satellite-based lidar PSC observations was greatest. For each statistically independent RAMSES measurement between 17:00 and 21:00 UTC (Fig. 2c) the cross correlation with the ATLID profiles measured consecutively between approximately 00:03:50 and 00:10:07 UTC (averages over 4 s, or 800 laser pulses) were calculated; a possible vertical displacement of the PSC was considered. Figure 4 presents the results of the correlation analysis. It shows the maximum cross correlation along the ATLID flight track (Fig. 4a) as a function of RAMSES observation time, and for which ATLID profile number and offset (lag) it was obtained (Fig. 4b). The agreement improves significantly shortly before 19:00 UTC when the vertical offset between the PSC profiles vanishes. This means that the PSC center height as measured with ATLID is not compatible with those of the RAMSES observations prior to this point in time but lower. The best match is found for the RAMSES measurement at 19:56 UTC and the ATLID profile 55 (cross correlation > 0.98), which has a mean observation time of approximately

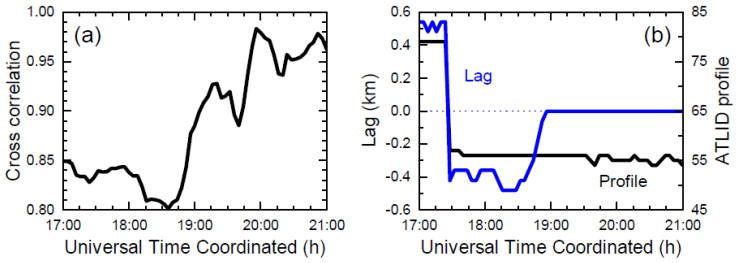

Figure 4. Similarity analysis between RAMSES and ATLID profiles of attenuated total particle backscatter coefficient. (a) Maximum cross correlation, and (b) optimum vertical profile offset (lag) and ATLID profile number along the midnight EarthCARE overpass as a function of RAMSES measurement time. The lidar profiles were compared between 19.4 and 23.5 km. Low-resolution RAMSES data (Fig. 2c) are used; ATLID profiles are averages over 800 consecutive laser pulses. All lidar data were interpolated to the standard RAMSES height vector with a bin width of 60 m. Profile 55 was obtained at 54.852367 °N, 17.668459 °E around 00:07:27.887170 UTC on 6 March 2025.

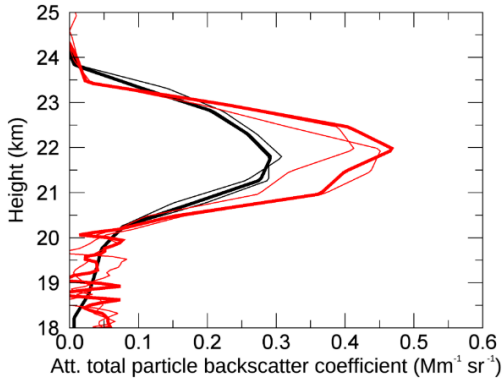

Figure 5. Comparison of the lidar profiles with the highest cross correlation. Attenuated total particle backscatter coefficient as measured by RAMSES at 19:56 UTC on 5 March 2025 (black curve) and by ATLID shortly after 00:07 UTC on 6 March 2025 (red curve). Statistically independent neighboring profiles are also shown to illustrate measurement variability (thin curves). For data resolution, see caption of Fig. 4.

00:07:28 UTC on 6 March 2025 (location is indicated by a black disk in Fig. 3b). These RAMSES and ATLID profiles are compared in Fig. 5. Vertical extent and shape of the PSCs agree well, but the peak attenuated total particle backscatter coefficients differ, with the RAMSES value being about 38 % smaller. It should be noted that similar results are obtained if the aerosol scattering ratio is considered. The difference may be related to the higher integration time (240 s vs. 4 s), but other factors might play a role, too. For example, the ambient temperature or partial pressures of the constituents of the liquid particles might have been slightly different at the two locations, and since local thermodynamic equilibrium between the vapor and the liquid phase is assumed instantaneously, the amount of condensed matter and thus of light scattering would respond directly. According to the ERA5 analysis, temperatures at the 30 hPa level were near the -85 °C isotherm over Lindenberg at 20:00 UTC and in the same range at 00:00 UTC when ATLID performed the measurements at 54.9 °N, 17.7° (Fig. 3), therefore it is conceivable that the atmospheric conditions were comparable, thus explaining the apparent similarity, but not quite the same.

Conclusions

The case study presented in this paper shows that ground-based Raman lidars can be useful to evaluate even stratospheric cloud measurements with ATLID onboard the EarthCARE satellite. Although the northern mid-latitudes are obviously not ideal for such comparisons, we hope that more opportunities will arise in the coming winters.

Acknowledgements

GIVE is partly funded by Bundesministerium für Wirtschaft und Klimaschutz (grant number 50EE2403D). The authors acknowledge the NOAA Air Resources Laboratory (ARL) for the provision of the HYSPLIT transport and dispersion model and READY website (https://www.ready.noaa.gov).

References

[1] Reichardt, J., Lauermann, F., and Behrendt, O.: *Fluorescence spectra of atmospheric aerosols*, EGUsphere [preprint], https://doi.org/10.5194/egusphere-2024-3928, 2024.

[2] European Space Agency, 2025, "EarthCARE ATLID NOM Level 1B", (version AD), https://doi.org/10.57780/eca-91a8dad

[3] Hersbach, H., et al.: ERA5 hourly data on pressure levels from 1940 to present. Copernicus Climate Change Service (C3S) Climate Data Store (CDS), DOI: 10.24381/cds.bd0915c6, 2023 (Accessed on 10-04-2025).

[4] Stein, A.F., et al.: *NOAA's HYSPLIT atmospheric transport and dispersion modeling system*, Bull. Amer. Meteor. Soc., 96, 2059-2077, http://dx.doi.org/10.1175/BAMS-D-14-00110.1, 2015.

[5] Rolph, G., Stein, A., and Stunder, B.: *Real-time Environmental Applications and Display sYstem: READY*, Environmental Modelling & Software, 95, 210-228, https://doi.org/10.1016/j.envsoft.2017.06.025, 2017.

Aerosol-optical and fluorescence properties of stratospheric volcanic sulfate over Leipzig

B. Gast[1], *C. Jimenez*[1], *A. Ansmann*[1]

(1) Leibniz Institute for Tropospheric Research, (TROPOS), Permoserstraße 15, 04318, Leipzig, Germany

Corresponding author: bgast@tropos.de

Introduction

Aerosol particles are a key aspect in atmospheric research given the variety of their interaction paths with radiation and clouds. Remote sensing with lidar is a well-suitable method to characterize the vertical distribution of aerosol particles in the atmosphere. Most of the lidar-based aerosol studies focus on the (lower) troposphere, as the major fraction of aerosol load is found there. The upper troposphere and lower stratosphere (UTLS) are somewhat disregarded. This is partly because an accurate aerosol detection and typing with lidar can be challenging in the UTLS region, especially in the case of low aerosol loads. While mineral dust can be clearly identified by its characteristically high depolarization ratio, the extinction-related properties needed for the distinction between wildfire smoke and volcanic sulfate are more difficult to be obtained properly at cirrus level and low aerosol optical depth. One option to tackle this problem is the usage of high-power lasers and large telescopes to increase the signal-to-noise ratio.

Furthermore, the recently evolving fluorescence lidar technique adds an additional intensive quantity for the characterization of aerosol particles – the fluorescence capacity, which is defined as the ratio of the fluorescence backscatter coefficient to an elastic particle backscatter coefficient [1,2]. In combination with the particle depolarization ratio, the fluorescence capacity has proven itself as promising to distinguish among smoke, mineral dust, pollen and urban pollution in the (lower) troposphere [3,4]. Also in the UTLS, smoke aerosol could be clearly identified by its strong fluorescence emission with (spectral) fluorescence capacities (444–488 nm) in the range of 2 x 10^{-4} to 7 x 10^{-4} (2 × 10^{-6} to 9 × 10^{-6} nm^{-1}) [5].

In this contribution, we demonstrate the feasibility to unambiguously identify wildfire smoke and volcanic sulfate at the troposphere-stratosphere interface by presenting observations of stratospheric volcanic sulfate with a high-power Raman and fluorescence lidar system.

Methodology

The lidar measurements were performed with the lab-based Multiwavelength Atmospheric Raman Lidar for Temperature, Humidity, and Aerosol profiling (MARTHA) system located at the Leibniz Institute for Tropospheric Research (TROPOS) in Leipzig, Germany. A diode-pumped high-power laser emits an overall pulse energy of about 900 mJ at a repetition rate of 100 Hz. As a result, the MARTHA system provides an overall laser power of 90 W, a prerequisite for studying UTLS aerosol. A broadband fluorescence channel detects the laser-induced aerosol fluorescence in a wavelength range from 444–488 nm [5].

Results and Discussion

Volcanic sulfate is expected to show no or very low fluorescence. However, up to now, the observational evidence for that is rare and, to our knowledge, has only been reported for the troposphere [6]. In this contribution, we show first preliminary results of fluorescence observations of volcanic sulfate in the stratos-

Table 1. Aerosol-optical properties (lidar ratios at 355 and 532 nm and extinction-related Ångström exponent) of stratospheric aerosol layers for three measurement cases in March and April 2025.

Time UTC	Altitude range [km]	Lidar ratio 355 nm [sr]	Lidar ratio 532 nm [sr]	Extinction-related Ångström exponent
07.03.2025 01:00-04:15	11–16	33	68	-0.2
18.–19.03.2025 23:35-04:35	15–20.25	30	65	-0.1
03.–04.04.2025 20:08-00:30	12–16	33	63	-0.1

sphere. Table 1 shows aerosol-optical properties for three measurement cases in March and April 2025. The lidar ratio values were in the range of 30–33 sr and 63–68 sr at 355 nm and 532 nm, respectively. This is similar to values that have been expected for long-range transported volcanic sulfate in the stratosphere from Lorenz-Mie computations [7]. The extinction-related Ångström exponent was around zero. Furthermore, the linear particle depolarization ratio was low, indicating spherical, or small, aerosol particles. Considering all these optical properties we can conclude, that this stratospheric aerosol layer consisted of volcanic sulfate.

Figure 1 displays the vertical profiles of the aerosol-optical properties for one exemplary measurement case on 18–19 March 2025. While the elastic backscatter coefficients are enhanced compared to the background, clearly indicating the presence of aerosol particles, the fluorescence backscatter coefficient is very low (~10^{-7} Mm^{-1} sr^{-1}; values which are typical for background aerosol). The fluorescence capacity is also very low with values of <10^{-5}. As a result, volcanic sulfate seems to show no laser-induced fluorescence.

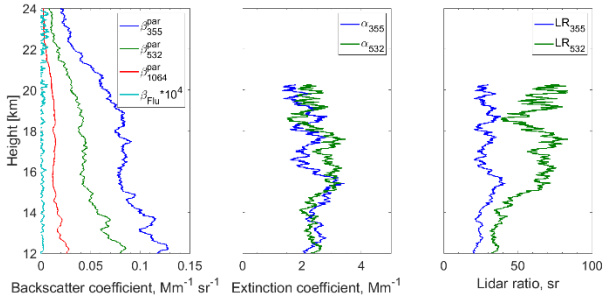

Figure 1. Vertical profiles of the aerosol-optical properties from 23:35–04:35 UTC on 18–19 March 2025. Left: elastic and fluorescence backscatter coefficients, center: extinction coefficients, right: lidar ratios.

Conclusions

In this contribution, we present Raman and fluorescence lidar measurements of volcanic sulfate in the lower stratosphere over Leipzig in March and April 2025. Our preliminary results suggest sulfate aerosol lidar ratios in the range of 30–33 sr and 63–68 sr at 355 and 532 nm, respectively. The extinction-related Ångström exponent was around zero. The volcanic sulfate showed no fluorescence. This finding demonstrates that the fluorescence lidar technique should enable the unambiguous discrimination between smoke and volcanic sulfate in the UTLS. However, to prove that, observations of the simultaneous occurrence of wildfire smoke and volcanic sulfate in the UTLS will be needed.

Acknowledgements

This research was supported by tax revenues on the basis of the budget adopted by the Saxon State Parliament (Sächsische Aufbaubank: grant no. 100669383).

References

[1] Reichardt, J.: *Cloud and Aerosol Spectroscopy with Raman Lidar*, J. Atmo. Ocean. Tech., 31, 1946–1963, /doi.org/10.1175/JTECH-D-13-00188.1, 2014.

[2] Reichardt, J., Leinweber, R., and Schwebe, A.: *Fluorescing aerosols and clouds: investigations of co-existence*, EPJ Web Conferences, 176, 05010, doi.org/10.1051/epjconf/201817605010, 2018.

[3] Veselovskii, I. et al.: *Combined use of Mie–Raman and fluorescence lidar observations for improving aerosol characterization: feasibility experiment*, Atmos. Meas. Tech., 13, 6691–6701, doi.org/10.5194/amt-13-6691-2020, 2020.

[4] Veselovskii, I. et al.: *Combining Mie–Raman and fluorescence observations: a step forward in aerosol classification with lidar technology*, Atmos. Meas. Tech., 15, 4881–4900, doi.org/10.5194/amt-15-4881-2022, 2022.

[5] Gast, B. et al.: *Invisible aerosol layers: improved lidar detection capabilities by means of laser-induced aerosol fluorescence*, Atmos. Chem. Phys., 25, 3995–4011, doi.org/10.5194/acp-25-3995-2025, 2025.

[6] Hedelt, P. et al.: *Analysis of the long-range transport of the volcanic plume from the 2021 Tajogaite/Cumbre Vieja eruption to Europe using TROPOMI and ground-based measurements*, Atmos. Chem. Phys., 25, 1253–1272, doi.org/10.5194/acp-25-1253-2025, 2025.

[7] Ansmann, A. et al.: *Comment on "Stratospheric Aerosol Composition Observed by the Atmospheric Chemistry Experiment Following the 2019 Raikoke Eruption" by Boone et al.*, Journal of Geophysical Research: Atmospheres, 129, doi.org/10.1029/2022JD038080, 2024.

Pollen Observations with Multiwavelength Mie-Raman Lidar over Warsaw: What we learned from a decade of measurements?

A. Tomczak[1], *Ł. Janicka*[1], *K. Misiura*[2], *J. Vasilescu*[3], *B.Heese*[4], *I.S. Stachlewska*[1]

(1) University of Warsaw, Faculty of Physics, Institute of Geophysics, (UW), Warsaw, Poland
(2) Institute of Geodesy and Cartography (IGIK), Warsaw, Poland
(3) National Institute of Research and Development for Optoelectronics (INOE), Măgurele, Romania
(4) Leibniz Institute for Tropospheric Research (TROPOS), Leipzig, Germany

Corresponding author:Iwona.Stachlewska@fuw.edu.pl

Introduction

Over the last decades an increase in the number of individuals experiencing respiratory illnesses has been observed [1]. Bioaerosols, such as pollen grains and fungal spores released into the atmosphere during the pollination process can cause, during the respiration process, an allergic reaction and result a.o. in asthma [2,3]. Monitoring and early alerting of the near-surface airborne pollen levels allows to reduce negative impact of allergies on people [4]. Pollination episodes can affect clouds properties in areas of high pollen and strong convection, especially due to the ruptured pollen [5], and even precipitation [6]. Thus determining of both surface and vertical extent of pollen particles is important to be measured.

We analyzed the Mie-Raman polarization lidar observations at the Warsaw ACTRIS site for a nearly decade (2013-2021) to assess effectiveness of its ability to observe pollen grains and fungal spores pollination events. Daytime episodes characterized by a bell-like increase of the lidar-derived volume depolarization ratio (VDR), both in absolute value and vertical span were selected with the aim to derive the characteristic of pollination event in terms of VDR, relative humidity, wind speed and direction, temperature, pollination time, and maximum of the boundary layer top. Such information together with in situ pollen measurements shall be valuable for future machine learning to discern pollen types.

Methodology

A new methodology has been developed for pollination episodes identification. Daily lidar signal plots were classified into strictly specified categories. Image analysis (e.g. Fig. 1) was done to retrieve data characteristics and verify whether pollination event can be differentiated from the background. In addition to that, to specify best case pollination events, the meteorological conditions and the likeliness of availability of different aerosol types (e.g. desert dust) were done with use of publicly available data of the Institute of Meteorology and Water Management (IMGW), in combination with Hybrid Single-Particle Lagrangian Integrated Trajectory (HYLSPLIT), and Navy Aerosol Analysis and Prediction System (NAAPS).

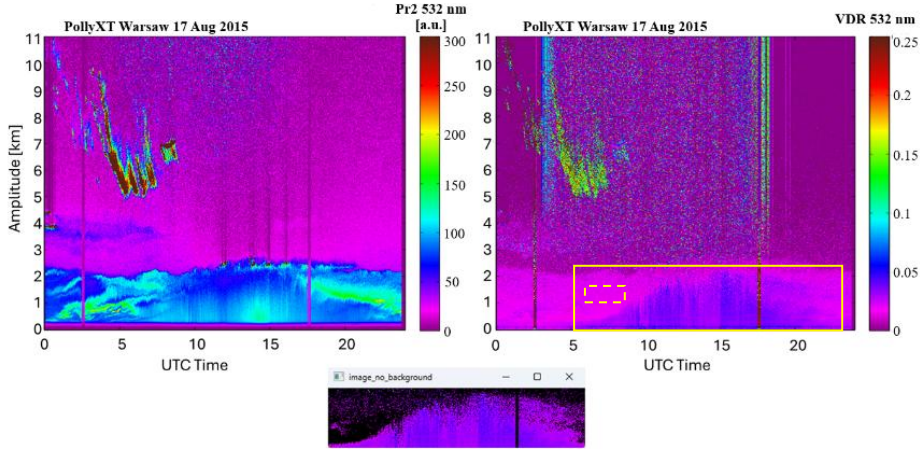

Figure 1. Characteristic lidar image for pollen event, 17th August 2015, Warsaw. The range and background corrected signal at 532 nm (Pr2, left) and the volume depolarization ratio at 532 nm (VDR, right) (source: www.polandaod.pl, last access 01-04-2025). Identified bell-like shape (solid line) and sample of surrounding background (dashed line).

Results and Discussion

The characteristic values of pollen-related average VDR, the maximum level of boundary layer top (BL), and the pollination times are shown in Fig. 2. The average VDR at 532 nm over all data points within the bell-like shape was 3.4% with standard deviation σ of 1.3% and 95th percentile values of VDR reached 4.48%, with σ of 2.15%. The average maximum BL top was 1832 +/- 441 m. The pollination times ranged between 7 and 19.5 h with an average of 13.6 h with σ of 3.28 h.

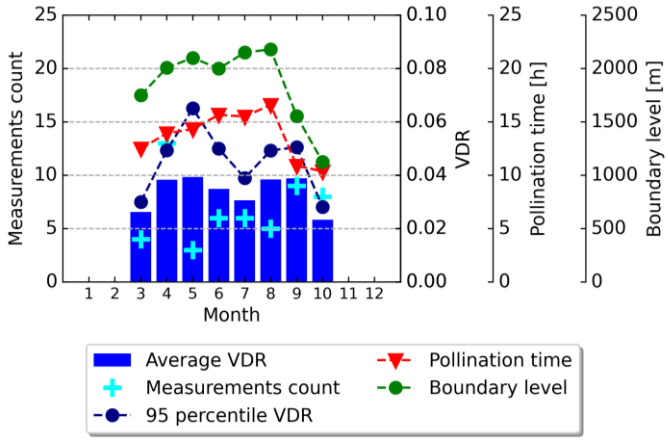

Figure 2. Monthly averaged volume depolarization ratio (VDR; σ=1.3%), maximum of the boundary layer top (σ=441 m), and pollination time (σ=3.28 h) extracted from quick looks for pollination events 2013-2021 in Warsaw.

Two pollination occurrence peaks are evident. Based on the Allergen Research Centre (OBAS) surface in situ pollen data, the Polish Chief Inspectorate of Environmental Protection (CIEP/GIOS) air-quality data, and the IMGW meteorological data, those two peaks were related as due to the plant pollination (April peak) and fungi pollination (September-November peak).

To verify lidar-identified pollination cases in terms of particle distribution over the city we used the particulate matter (PM) data from CIEP, whereby the fine to coarse mass ratio (Eq. 1) was used to determine particle size predomination. CIEP monitoring sites within the city had similar fine to coarse mass ratio (FCR). The meteo-data of IMGW indicated large (~10 km) footprint of pollination during the episodes.

$$\mathrm{FCR} = \frac{PM2.5}{PM10-PM\,2.5} \qquad (1)$$

Based on the HYSPLIT model 48h-backward directories retrieved for every of the pollination case, and with use of 25% threshold (defined as maximum time of a trajectory in more than one azimuth) the "best" pollination events were classified in terms of the prevailing winds (see Table 1). We found that winds from South and West prevail for all trajectory levels during pollination events.

Table 1. Share of HYSPLIT trajectories in total number (54) of pollination events (applying the threshold 25%).

Level / Direction (azimuth)	500 m	1000 m	2000 m
North (315.0°-45.0°)	13.51%	12.21%	19.05%
East (45.0°-135.0°)	21.62%	21.21%	11.90%
South (135.0°-225.0°)	35.14%	36.36%	26.19%
West (225.0°-315.0°)	29.73%	30.30%	42.86%
Trajectories excluded due to threshold [count]	17	21	12

Despite meteorological factors affecting the pollination of plants and fungi, the analyzed area of Warsaw (in North, South and West of the city), can be considered as an area with homogeneous pollen emission conditions. The process of plant homogenization in the city certainly adds to this [7].

The pollen of various species differs in the particle diameter size and have characteristic shapes and grooves, furrows, ornamentations [8]. Fungi and plant pollen were characterized in terms of depolarization ability. *Cladosporium* and *Alternaria* fungal spores and *Artemisia, Pinus, Chenopodium, Ambrosia* pollen grains shall cause depolarization of the lidar beam due to their shape. The pollen grains of several other plants (*Urtica, Poaceae, Rumex, Betula*) can be regarded as spherical particles with negligible depolarization. In areas of high pollen and strong convection as well as very high relative humidity, the ruptured pollen contributes to increased depolarization.

An extensive review in situ OBAS data collected between 2013-2021 in Warsaw was conducted to confirm bioaerosol origin. Results indicate that *Cladosporium, Alternaria* are dominant fungal spores, and *Betula* (birch), *Urtica* (nettle), and *Alnus* (alder) pollen grains. For each dominant specie pollination periods were distinguished. A characteristic feature observed for fungal spores was an almost uninterrupted period of pollination lasting almost the entire growing season.

For 15 different pollen taxa and 2 types of fungi spores, the daily mean threshold concentrations causing allergy symptoms were aggregated together with the maximum observed value during the entire investigated period. Based on this *Betula, Poacae,* and *Alternaria* were identified as species that can cause the highest allergenic reactions.

Conclusions & Outlook

A large dataset of over 1000 lidar 24h-observations (2013-2021), from which more than a 100 was characterized by bell-like shape, allowed to i) identify the pollination events, ii) assess the relations between the physical parameters of the atmosphere and pollen episodes, and iii) draw conclusions on aerosol particles present in the air as due to the airborne pollen emission of fungal spores and plant pollen over Warsaw, Poland.

We obtained pollination characteristic in terms of volume depolarization ratio ($\bar{x}$VDR=3.4%, σVDR=1.3%), relative humidity ($\bar{x}$RH=55.9%, σRH=21.6%), temperature ($\bar{x}$T=18.7 °C, σT=7.2 °C), wind speed ($\bar{x}$V=3.9 m/s, σV=1.9 m/s) and direction (South and West), maximal of boundary layer top ($\bar{x}$BL=1832m, σBL=441m), and pollination time ($\bar{x}$pt=13.6h, σpt=3.28h) starting from 6:30 UTC (σ=1.5h) and ending at 19:56UTC (σ=2.2h); dataset published [9]. The remaining challenge is to assess to what extent this information can be used as an input for the machine learning algorithms applications in pollen typing, which will be applied in the next future.

Pollen measurements in the cities, in general, are considered as representative for relatively large areas, otherwise they cannot serve the allergy alert. Thus, a very local pollination episodes (a few meters footprint) are ignored in that case. The implication of this on measurement sample is not sufficiently investigated. Therefore, currently we are working on addressing this topic.

During unfavorable meteorological conditions (e.g. low clouds) observation of pollination events with lidar can be limited. This effect so far has not been quantified and we are working on addressing this.

The advantage of using the Mie-Raman lidar is its high potential to derive wavelength-dependent particle optical properties and microphysical parameters. Bear in mind that those quantities derived during pollination episodes may suffer from a detection limit due to huge sizes of pollen grains and fungi spores.

For the near-surface pollen observations in situ measurements are obviously a better choice. Although lidar provides important information on pollination, it seems not realistic, for the moment, to use only lidar data for pollen monitoring. Still, increasing health issues related to pollen urge the need to co-locate both instruments, especially in the urban environment.

Knowledge on the distribution of the vertical pollen particles in the atmosphere is highly interesting from the point of view of the model simulations of the transport and rupture of pollen in the atmosphere. Lidar is able to provide information on the abundance of the ruptured pollen particles at different height is the atmosphere, thus as next step we will also try to tackle this fundamental research topic.

Acknowledgements

We acknowledge the open-access use of the existing data form the webportals and databases of the Aerosol Research Network (PolandAOD) of UW, the PollyXT Lidar Network (PollyNET) of TROPOS, the European Lidar Network (EARLINET), the Aerosol Clouds and Trace gases Research Infrastructure (ACTRIS), the Allergen Research Centre (OBAS), the Polish Chief Inspectorate of Environmental Protection (CIEP/GIOS), the Institute of Meteorology and Water Management (IMGW), the Hybrid Single-Particle Lagrangian Integrated Trajectory (HYLSPLIT) of the Air Resources Laboratory of National Oceanic and Atmospheric Administration (NOAA) of U.S. Department of Commerce, and the Navy Aerosol Analysis and Prediction System (NAAPS) of U.S. Naval Research Laboratory (NRL).

Funding

Artur Tomczak and Iwona Stachlewska acknowledge that the review of the existing databases (PolandAOD, POLLYNET, EARLINET-ACTRIS, OBAS) and literature (mainly OBAS), and the proposed data analysis scheme to identify cases of pollination captured by lidar data was done within the National Research Council of Poland funding (Preludium-BIS UMO-2020/39/O/ST10/03586).

Artur Tomczak acknowledges support of the EC Horizon 2020 – Research and Innovation Framework Programme: ATMO-ACCESS Integrating Activity (GA no. 101008004) for financing TNA: POLLENAT realized at UPC, Spain.

Jeni Vasilescu acknowledges support form the Core Program of Romanian National Research Development and Innovation Plan 2022-2027, carried out with support of MCID, project no. PN 2305 and through the European Regional Development Fund through the Competitiveness Operational Programme 2014–2020, Action1.1.3 Creating synergies with H2020 Programme, project Strengthen the participation of ACTRIS-RO consortium in the pan-European research infrastructure ACTRIS, ACTRIS-ROC, MYSMIS code107596 (CTR.no.337/2021)

Regular measurements at the Warsaw site of UW have been long-term supported within the Aerosol Clouds and Trace gases Research Infrastructure (ACTRIS) with several projects financed within the EC Horizon 2020 GAs no. 654109 (ACTRIS-2), 759530 (ACTRIS-PPP), 871115 (ACTRIS-IMP), and the EC 7th Framework Programme FP7/2007–2013 GA no. 262254 (ACTRIS) and ACTRIS-ERIC.

References

[1] Asher, M.I., & Ellwood, P. (2014). The global asthma report 2014

[2] Strzelczyk, Z., Roszkowski, M., Feleszko, W., & Krauze, A. (2020). Avoidance of allergens as an environmental method in the prevention of inhaled allergy symptoms. Allergologia et Immunopathologia, 48(6), 745–752. doi.org/10.1016/J.ALLER.2019.06.011

[3] Rapiejko, P., Jurkiewicz, D., Pietruszewska, W., Zielnik-Jurkiewicz, B., Woroń, J., & Lipiec, A. (2018). Treatment strategy of allergic rhinitis in the face of modern world threats. Otolaryngologia Polska, 72(2), 1–12, doi.org/10.5604/01.3001.0011.8057

[4] Cariñanos, P., & Casares-Porcel, M. (2011). Urban green zones and related pollen allergy: A review. Some guidelines for designing spaces with low allergy impact. Landscape and Urban Planning, 101(3), 205–214. doi.org/10.1016/J.LANDURBPLAN.2011.03.006

[5] Subba, T., Zhang, Y., & Steiner, A. L. (2023). Simulating the transport and rupture of pollen in the atmosphere. Journal of Advances in Modeling Earth Systems, 15, e2022MS003329. https://doi.org/10.1029/2022MS003329

[6]Wozniak, M. C., Solmon, F., & Steiner, A. L.(2018). Pollen rupture and its impact onprecipitation in clean continentalconditions. Geophysical Research Letters,45, 7156–7164. https://doi.org/10.1029/2018GL077692

[7] Singh, A. K., Singh, H., & Singh, J. S. (2018). Plant diversity in cities: call for assessment and conservation. CURRENT SCIENCE, 115(3)

[8] Kolpakova, A., Hovorka, J., & Klán, M. (2017). Pollen Characterization in Size Segregated Atmospheric Aerosol. IOP Conference Series: Earth and Environmental Science, 95(6), 062001, doi.org/10.1088/1755-1315/95/6/062001

[9] Tomczak, A., & Stachlewska, I.S. (2023). Pollen lidar observations in Warsaw (2013-2021), RepOD, V1, doi.org/10.18150/OAYSAO

Models, In situ, and Remote sensing of Aerosols (MIRA) — An International Working Group

***E. Marinou*[1]**, *V. Amiridis*[1], *C.R. Trepte*[2], *M. Saito*[3], *O. Dubovik*[4], *M.O. J. Redemann*[5], *Cambaliza*[6], *M. Chin*[7], *S.-W. Kim*[8], *E. Andrews*[9], *T. Toth*[2], *L. Ziemba*[2], *P. Yang*[10], *C. Di Biagio*[11], *K. Rizos*[1], *K.-A., Voudouri*[1], *A. Gialitaki*[1], *A. Tsekeri*[1], *E. Proestakis*[1], *G.L. Schuster*[12]

(1) National Observatory of Athens (NOA), IAASARS, Athens, 15236, Greece
(2) NASA Langley Research Center, Hampton, 23681, USA
(3) University of Wyoming, Laramie, 82071, USA
(4) CNRS/University of Lille, Lille, F-59000, France
(5) Ateneo de Manila University and Manila Observatory, Quezon City, Metro Manila,1108, Philippines
(6) University of Oklahoma, Oklahoma, USA
(7) NASA Goddard Space Flight Center, Greenbelt, Maryland, 20771, USA
(8) Seoul National University, Seoul, 08826, Korea
(9) CIRES, University of Colorado and NOAA Global Monitoring Laboratory, Boulder, 80305, USA
(10) Texas A&M University, College Station, 77843, Texas, USA
(11) LISA, CNRS, U. Paris Est Créteil, U. Paris Cité, IPSL, France
(2) NASA Langley Research Center, Hampton, 23681, USA; retired

Corresponding author: elmarinou@noa.gr

Introduction

Aerosol-related research spans three key areas: numerical modeling, remote sensing, and in situ measurements. The community sees enhanced measurement and modeling capabilities through interactions among these groups, and this strengthens the overall scientific impact on climate and air quality research. The Models, In situ, and Remote sensing of Aerosols (MIRA) working group [1] is an international forum that fosters collaboration across these fields of aerosol research at an international level. MIRA collaborations advance scientific knowledge about aerosol properties and improve our understanding of air quality, weather, and climate through the pursuit of specific goals under community working groups. Here, the five inter-disciplinary MIRA topics and relevant working groups are presented, along with a short description of their activities. All of the MIRA projects seek additional input from others (observationalists and modelers), and we are also open to ideas for new aerosol-related collaborative topics.

Methodology

MIRA focuses on aerosol-related interdisciplinary efforts where the fields of numerical modeling, remote sensing, and in situ measurements intersect. MIRA currently supports five initiatives which are presented herein.

1. Satellite-Assisted Particulate Matter (SAPM): SAPM aims to provide intercomparisons of various methods and techniques for retrieving surface PM2.5 assisted by satellite remote sensors, global aerosol models, and in situ aerosol measurements. These comprehensive $PM_{2.5}$ estimates can be useful for current and future efforts in air quality research, modeling, forecasting, and applications. We seek international in situ datasets (e.g., mass scattering/absorption coefficients and aerosol hygroscopic properties) for various aerosol species to develop more robust $PM_{2.5}$ estimates. We also seek international ground-based in situ $PM_{2.5}$ datasets to validate the $PM_{2.5}$ concentration estimates.

2. Maps of Aerosol lidar ratios for CALIPSO (MAC): Elastic-backscatter lidars depends upon a priori knowledge of aerosol properties to convert lidar backscager measurements into aerosol extinction profiles. We investigate relationships between aerosol type and lidar ratios using collocated CALIPSO-MODIS/SODA products, collocated CALPSO-GOCART/AeroCom datasets lidar ration measurements, and long-term in-situ measurements collocated with lidar ratio measurements. More specifically, with the collocated CALPSO-GOCART/AeroCom dataset, we are using forward model analysis to compute the relative proportion of each aerosol type at the lidar measurement location/period. This is an empirical

approach that assumes a linear relationship between multiple hydrated aerosol species and the lidar ratio, but it does not require the use of Mie Theory or any other optical calculations. On the synergy between the long-term in-situ measurements collocated with lidar ratio measurements, we are interested in quantifying the dry mass of five aerosol types: fine solubles, fine insoluble carbonaceous, fine mineral dust, coarse mineral dust, and coarse marine. We choose this classification scheme because (a) we expect this scheme to provide different lidar ratios for each aerosol type, since lidar ratio is determined by size, shape, and complex refractive index, and (b) this scheme is easy to map with transport models. MIRA desire worldwide lidar ratio measurements to support this activity.

3. Tables of Aerosol Optics (TAO): The Table of Aerosol Optics (TAO) is a community repository of optics computations (extinction, absorption, single-scatter albedo, lidar ratio, etc) that are useful for global models and remote sensing applications. TAO expands upon historical efforts by building an open database that uses new measurements and computational techniques for non-spherical particles. Some groups are advancing new techniques that can accommodate complex fractal aggregates of black carbon, while other groups are working on realistic irregular shapes for mineral dust. The TAO database gives these scientists a place to distribute their products. As TAO grows, modelers and remote sensing specialists will look to TAO as a place to find a wide variety of choices for testing. At the present time, TAO is a highly fluid and loosely organized collection of optical tables that are available at the MIRA online database [2].

4. Tables of Cloud Optics (TaCO): The Table of Cloud Optics (TaCO) initiative is developing a community-accessible cloud optics table. TaCO includes a suite of bulk optical properties for liquid clouds, ice clouds, and other hydrometeors across the entire spectral domain using state-of-the-art ice crystal models and light-scattering computational capabilities.

5. Harmonization of aerosol Assimilation Models and Retrievals (HAMR): There are some differences in the representation of aerosol properties by climate models and remote sensing. Satellites in low Earth orbits provide daily ‘snapshots’ (at best) at any given location, while climate models can provide the spatial and temporal variability of aerosol components (or species) between the snapshots. The HAMR objective is to harmonize aerosol representations, connecting climate models and remote sensing.

Results and Discussion

In the framework of the MIRA collaborations, the community provides publicly available codes and datasets, which are available in the MIRA databases [2]. The publicly available codes include, among others, the Multi-Sphere T-Matrix (MSTM) Code of Dan Mackowski et al. [4, 5, 6]; the Community radiative transfer model (CRTM); and the SCIATRAN radiative transfer model and retrieval algorithms [7, 8]. We also provide a common repository of aerosol refractive index databases that include atmospheric aerosol species and journal articles with supplementary refractive indices (not part of MIRA) to support its exploitation from the community. Similarly, a global multiyear 3D dataset of cloud condensation nuclei derived from spaceborne lidar measurements (PANGAEA) by Choudhury and Tesche [9] is included.

An example of the latest advancements on the Maps of Aerosol lidar ratios for CALIPSO (MAC) working group is shown in Figure 1. In this figure, a global distribution of dust lidar ratio based on the ESA-Aeolus measurements is provided, using three-year averaged measurements from the mission in dusty cases. This product is based on a refined dust product from Aeolus developed in the framework of the ESA L2A+ project. The enhanced aerosol product is derived through a series of intermediate processing steps that integrate spaceborne retrievals/products from multiple sensors, reanalysis numerical outputs, and reference ground-based measurements. More information about the refined Aeolus dust product is available in [10].

Here, an enhanced dust lidar ratio product is products by exploiting the synergy between Aeolus ALADIN’s HSRL capability, which retrieves aerosol optical properties without requiring assumptions

about the lidar ratio; and CALIPSO CALIOP's ability to measure the particle depolarization ratio, which supports dust aerosol classification. Specifically, by analyzing collocated Aeolus and CALIPSO profiles from June 2019 to October 2022, we used CALIPSO's 532 nm depolarization ratio measurements to identify atmospheric layers with a strong dust presence along Aeolus overpasses. For these dust layers, the Aeolus total backscatter coefficient was computed after correcting for the missing cross-polarization component. This correction enabled the derivation of a new lidar ratio product from Aeolus, which can be used to refine CALIOP's extinction retrievals, resulting in an improved, synergistic dust aerosol product. The new lidar ratio product is evaluated using ACTRIS lidar measurements from the ASKOS campaign in Cabo Verde [11].

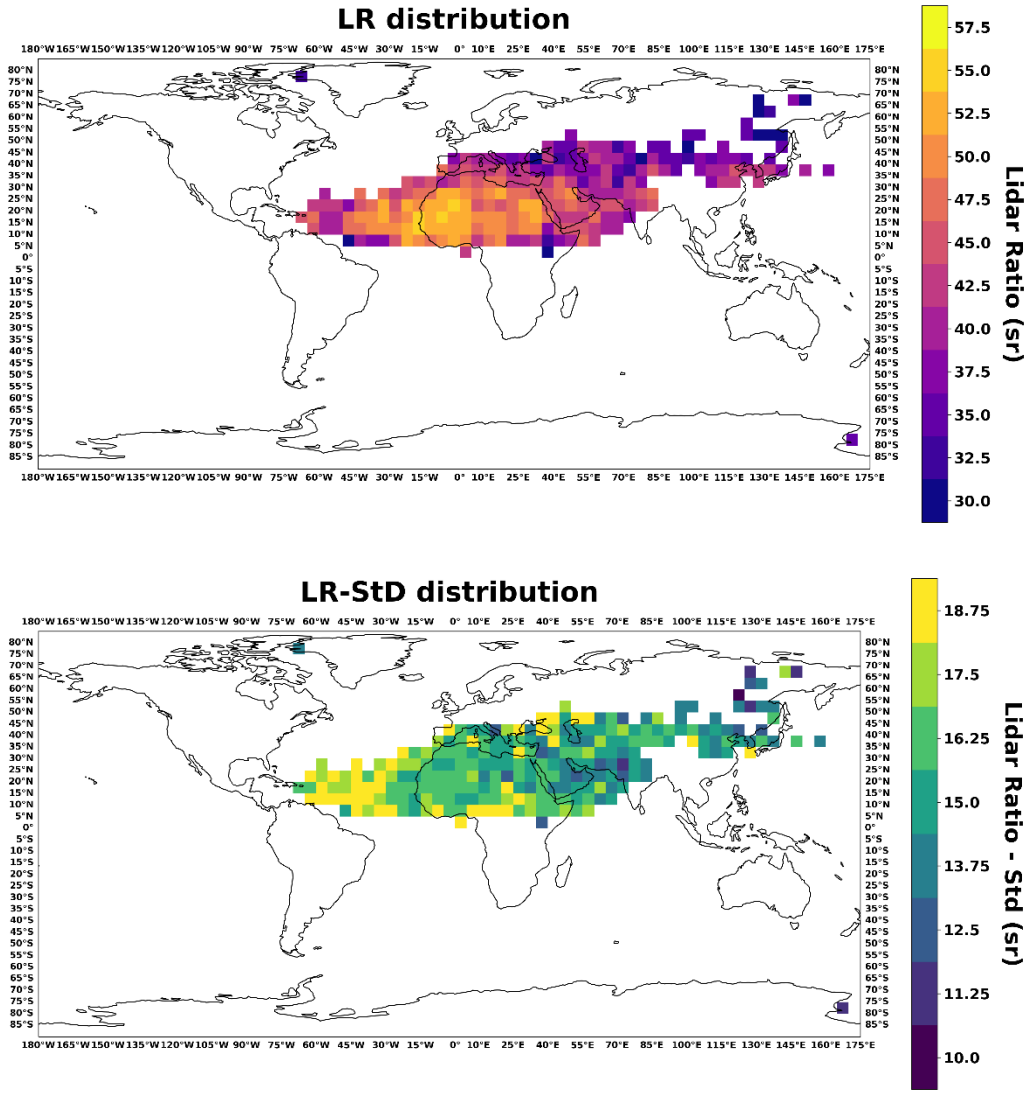

Figure 1. Dust lidar ratio distribution (up) and standard deviation (down), based on collocated Aeolus and CALIPSO measurements, in the period June 2019 - October 2022.

Conclusions

MIRA international forum supports the aerosol-related research, enhancing scientific synergies. All of the MIRA projects seek additional input from others (observational and modeled), and we are also open to ideas for new collaborative topics. The information provided here and more are available at the MIRA website [1]. Join our email distribution [3] to receive our newsletters and other information about MIRA.

Acknowledgements

MIRA working group is supported by NASA. The new Aeolus/CALIPSO product were funded by the European Space Agency under the L2A+ project (contract no.9054000139424/22/I-NS), and the AIRSENSE project (contract no. 4000142902/23/I-NS). The evaluation of the new products is supported by the PANGEA4CalVal project (Grant Agreement 101079201) funded by the European Union, and the CERTAINTY project (Grant Agreement 101137680) funded under the Horizon Europe program. We are grateful to ESA for making available the AEOLUS products used in this study, to NASA for making available the CALIPSO products, and to ACTRIS and EARLINET for providing access in lidar-related services and expertise.

References

[1] MIRA working group website. https://science.larc.nasa.gov/mira-wg/
[2] MIRA online databases. https://science.larc.nasa.gov/mira-wg/databases/
[3] MIRA news list. https://espo.nasa.gov/lists/listinfo/mira
[4] Mackowski, D.W. and Mishchenko, M.I.: A multiple sphere T-matrix Fortran code for use on parallel computer clusters, J. of Quantitative Spectroscopy and Rad. Transfer, 112, 13, 2011, doi:10.1016/j.jqsrt.2011.02.019.
[5] Mackowski, D.W.: The extension of the Multiple Sphere T Matrix code to include multiple plane boundaries and 2-D periodic systems, J. of Quantitative Spectroscopy and Rad. Transfer, 290, 2022, doi: 10.1016/j.jqsrt.2022.108292.
[6] Mackowski, D.W. and Kolokolova, L.: Application of the multiple sphere superposition solution to large–scale systems of spheres via an accelerated algorithm, J. of Quantitative Spectroscopy and Rad. Transfer, 287, 2022, doi:10.1016/j.jqsrt.2022.108221.
[7] Rozanov, V.V., Rozanov, A.V., Kokhanovsky, A.A., and Burrows, J.P.: Radiative transfer through terrestrial atmosphere and ocean: Software package SCIATRAN, J. of Quantitative Spectroscopy and Rad. Transfer, 133, 13-71, 2014, doi:10.1016/j.jqsrt.2013.07.004.
[8] Mei, L., Rozanov, V., Rozanov, A., and Burrows, J. P.: SCIATRAN software package (V4.6): update and further development of aerosol, clouds, surface reflectance databases and models, Geosci. Model Dev., 16, 1511–1536, 2023, doi:10.5194/gmd-16-1511-2023.
[9] Choudhury, G., and Tesche, M.: Global multiyear 3D dataset of cloud condensation nuclei derived from spaceborne lidar measurements [dataset]. PANGAEA, 2023, doi:10.1594/PANGAEA.956215.
[10] Rizos, K., Proestakis, E., Georgiou, T., Gkikas, A., Marinou, E., Paschou, P., Voudouri, K. A., Tsikerdekis, A., Donovan, D., van Zadelhoff, G.-J., Benedetti, A., Baars, H., Floutsi, A. A., Benas, N., Stengel, M., Retscher, C., Malina, E., and Amiridis, V.: Derivation and validation of a refined dust product from Aeolus (L2A+), EGUsphere [preprint], https://doi.org/10.5194/egusphere-2025-1175, 2025.
[11] Marinou, E., Paschou, P., Tsikoudi, I., Tsekeri, A., Daskalopoulou, V., Kouklaki, D., Siomos, N., Spanakis-Misirlis, V., Voudouri, K.A., Georgiou, T., Drakaki E., Kampouri A., Mallios S., Proestakis E., Gkikas. A., Koutsoupi I., Papakonstantinou E., Raptis P., Kazadzis S., Baars H., Floutsi A., Pirloaga, R., Nemuc, A., Marenco, F., Kezoudi M., Papetta, A., Grisa, M.m Yus Diez, J., Ryder., A., Ratcliffe, N., Kandler, K., Sudharaj, A., and Amiridis, V.: An Overview of the ASKOS Campaign in Cabo Verde. Environ. Sci. Proc., 26, 200, 2023, doi: https://doi.org/10.3390/environsciproc2023026200.

Lidar-Based Characterization of Desert Dust and Biomass Burning Aerosol Mixtures over Warsaw (PollyXT) and Wrocław (EMORAL) in August 2024

L. Janicka[1], *D.M. Szczepanik*[1], *P. Poczta*[1,2], *J. Vasilescu*[3], *A. Drzeniecka-Osiadacz*[4], *M. Jabłońska*[5], *I.S. Stachlewska* [1]

(1) University of Warsaw, Faculty of Physics, Institute of Geophysics, (IGFUW), Pasteura 5, 02-093, Warsaw, Poland
(2) Poznan University of Life Sciences, Faculty of Environmental and Mechanical Engineering, (PULS), Piatkowska 94, 60-649 Poznan, Poland
(3) National Institute of Research and Development for Optoelectronics, (INOE2000), Magurele, 077125, Romania
(4) Department of Climatology and Atmosphere Protection, Faculty of Earth Science and Environmental Management, University of Wrocław, Kosiby 8 Str, 521-621 Wrocław, Poland
(5) University of Silesia in Katowice, University Laboratories of Atmosphere Control, (ULAC), ul. Bankowa 12, 40-007 Katowice

Corresponding author: lucja.janicka@fuw.edu.pl

Introduction

Biomass burning is one of the most commonly observed aerosol types in the free troposphere over Central Europe, originating from various regions, even as far as Canada [1,2]. The transport of such aerosols over long distances can alter the local energy balance by absorbing and scattering solar radiation and by influencing cloud formation, thereby affecting the regional climate.

At the same time, within the boundary layer, pollen—observed due to natural plant pollination processes—plays a significant role for human health, particularly for individuals with allergies. The *In situ and remote sensing assessment of bio-aerosols (SARA)* project, part of the Trans-national Access (TNA) program, aimed to enhance understanding of bio-aerosol dynamics through comprehensive observational campaigns.

As part of the SARA project, an intensive measurement campaign was conducted at the WOPAS site in Wrocław (51°06′N, 17°02′E, 120 m a.s.l.). During this campaign, an intriguing, prolonged case of long-range aerosol transport was observed, especially between days 22-24.08.2024 at altitudes of approximately 2.0–4.0 km. Similar aerosol layers were detected at the WOS station in Warsaw (52°13′N, 21°01′E, 112 m a.s.l.). These observations suggest a widespread atmospheric phenomenon affecting multiple regions.

This study presents preliminary results from a multifaceted analysis of data collected at both stations, aiming to examine the characteristics and implications of the observed aerosol layers.

Methodology

A full description of the EMORAL mobile lidar is provided in Stachlewska et al. (2024) [3], while PollyXT is described in Engelmann et al. (2016) [4]. Lidar data were analyzed using the Single Calculus Chain (SCC), the EARLINET-ACTRIS approved tool [5], following an approach similar to that detailed in Szczepanik et al. (2023) [6].

To identify potential aerosol sources, the HYSPLIT model [7] was employed to compute backward air mass trajectories. Additionally, inversion data products from AERONET were analyzed to assess the aerosol size distribution observed during the event [8].

Results and Discussion

The first thin aerosol layers were detected starting at 19:00 UTC on 22/08/2024, initially appearing as two separate layers at 2.5 and 4.0 km over WOPAS, and three layers at 1.8, 3.0, and 4.0 km over WOS, which subsequently merged into a single thick layer (Figure 1). The main part of the aerosol inflow began at approximately 07:00 UTC on 23/08/2024 and was observed over the following 24 hours at WOPAS, while at WOS it persisted slightly longer (Figure 1). Although the stations are separated by approximately 355 km (Figure 2, left panel), the aerosol layers were observed at similar altitudes, forming dense plumes. The event lasted longer over Warsaw, likely due to changes in airmass movements.

To investigate the possible aerosol origins, backward trajectories were calculated at 2.0, 2.5, and 3.0 km for several ending times during the inflow, simultaneously for both WOS and WOPAS stations. An example of the obtained results is shown in the right panel of Figure 2. The simulations indicate a relatively uniform inflow of air masses originating from Canada, most likely carrying biomass-burning aerosols from wildfires. Initially, the air masses were transported rapidly over the Atlantic Ocean, then slowed down slightly and descended over western Europe (France and Germany).

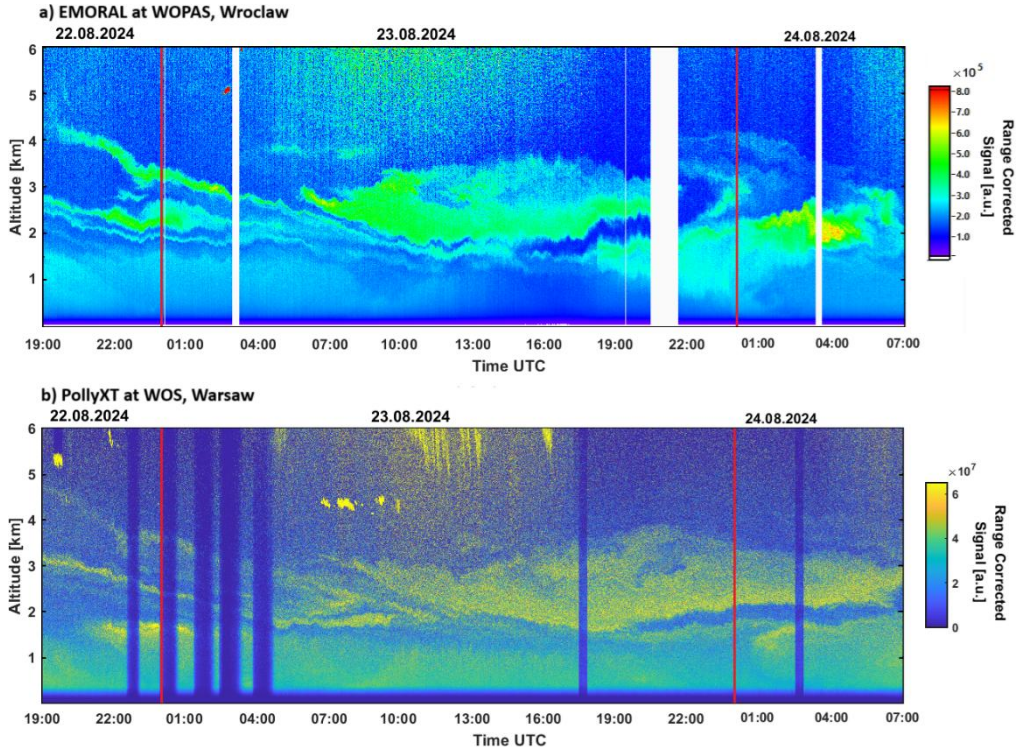

Figure 1. Quicklook plots from EMORAL at WOPAS (Wrocław, panel a) and PollyXT at WOS (Warsaw, panel b) showing the range-corrected signal at 1064 nm between 19:00 UTC on 22/08/2024 and 07:00 UTC on 24/08/2024. The red vertical line indicates the date change.

For the optical data analysis, the SCC was used, allowing successful retrieval of daytime profiles using the Klett method and nighttime profiles using the Raman method. Thanks to 1-hour averaged vertical profiling, it was possible to select the so-called core of the layer, defined as the part of the profile with the highest backscattering values. Mean values of the three particle backscattering coefficients (3β) and two particle linear depolarization ratios (2δp) for this selected core of the layer are provided in Table 1.

The analysis showed that at both stations, aerosols were observed at almost the same altitudes; however, WOS exhibited higher backscattering values than WOPAS. Interestingly, at WOPAS, aerosols also displayed relatively high particle linear depolarization ratios, ranging from 13.61–26.59 at 355 nm and 5.73–24.66 at 532 nm, suggesting the possible presence of irregularly shaped particles, such as desert dust.

Analysis of aerosol extinction profiles obtained from the Raman observations revealed elevated values of α=115±27 Mm^{-1} and α=85±12 Mm^{-1} at WOPAS and α=191±11 Mm^{-1} and α156±16 Mm^{-1} at WOS, at 355 and 532 nm, respectively. The lower extinction values observed at WOPAS might be explained by the admixture of less absorbing aerosol within the observed layer.

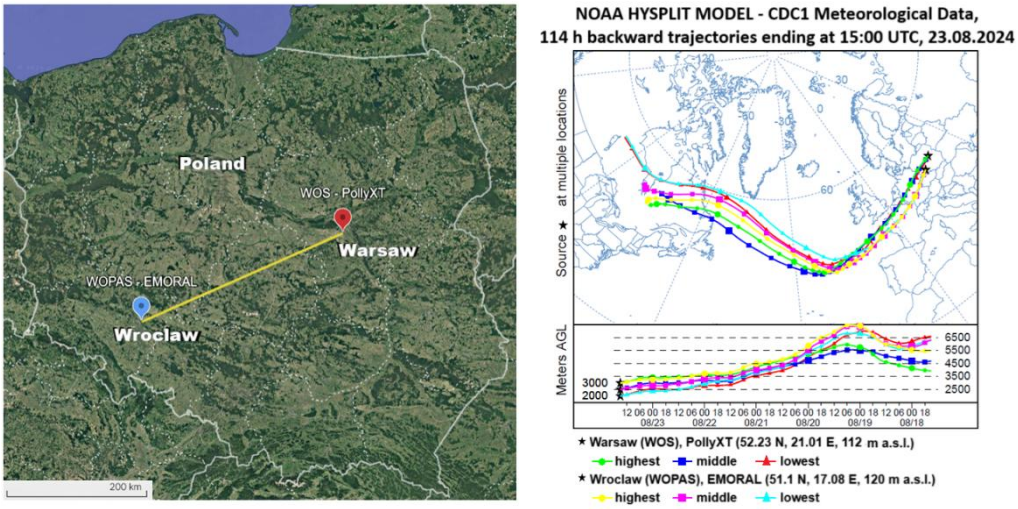

Figure 2. Left panel: map of Poland showing the measurement locations in Warsaw (WOS, PollyXT, red pin) and Wrocław (WOPAS, EMORAL, blue pin). Right panel: HYSPLIT backward trajectories simulated over 114 hours, ending at 15:00 UTC on 23/08/2024, at 2.0, 2.5, and 3 km altitude for both measuring sites.

Table 1. Mean values of aerosol backscatter β and particle linear depolarization ratio δ_p for the core layer observed over Warsaw (WOS) and Wrocław (WOPAS) on 23 August 2024. Profiles were obtained with the SCC using the Klett and Raman methods (boldface row).

Lidar	Time [UTC]	Altitude [km]	β 355 nm [Mm^{-1} sr^{-1}]	β 532 nm [Mm^{-1} sr^{-1}]	β 1064 nm [Mm^{-1} sr^{-1}]	δ_p 355 nm [$x10^{-2}$]	δ_p 532 nm [$x10^{-2}$]
WOPAS	15:00	2.5 ± 3.0	4.00 ± 0.66	1.90 ± 0.34	0.37 ± 0.01	13.61 ± 1.95	7.54 ± 1.41
WOS		2.2 - 2.7	4.27 ± 0.39	2.87 ± 0.23	1.31 ± 0.12	0.99 ± 0.14	3.15 ± 0.25
WOPAS		2.2 ± 3.6	3.89 ± 0.77	2.69 ± 0.32	0.43 ± 0.02	26.59 ± 4.78	24.66 ± 5.57
WOS		2.2 ± 3.0	5.87 ± 0.85	2.71 ± 0.56	1.05 ± 0.12	1.71 ± 0.11	2.07 ± 0.21
WOPAS	**23:00**	**2.7 ± 3.5**	**5.71 ± 0.94**	**2.41 ± 0.39**	**0.53 ± 0.09**	**15.02 ± 1.55**	**5.73 ± 0.39**
WOS		**2.2 ± 3.1**	**7.25 ± 0.35**	**3.15 ± 0.23**	**1.19 ± 0.08**	**2.43 ± 0.08**	**2.48 ± 0.07**

To provide an overview of the possible sizes of the observed aerosol, the size distribution inverted from the sun photometer measurements was analyzed. Unfortunately, during the main part of the inflow, high-level clouds were present, which strongly affected the sun photometer measurements. The only available data are from 24/08/2024, but they still provide information about the final stage of the event.

At both sites, the aerosol size distribution was bimodal, with a more pronounced fine mode. The maximum value of dV(r)/dln(r) for the fine mode was 0.026 $\mu m^3/\mu m^2$ and 0.047 $\mu m^3/\mu m^2$ at r=0.25 μm for WOPAS and WOS, respectively. The coarse mode maximum for both stations was observed at r=5.06 μm, with dV(r)/dln(r)= 0.014 $\mu m^3/\mu m^2$ at WOPAS and 0.015 $\mu m^3/\mu m^2$ at WOS.

The lower amount of fine aerosol over WOPAS compared to WOS may be explained by the reduced transport intensity at WOPAS on 24.08.2024, which marked the end of the inflow as mentioned above.

Conclusions

The multi-instrument observations at WOPAS and WOS during 22–24.08.2024 provided a comprehensive view of a long-range transported aerosol event. The main inflow, observed as a thick aerosol layer at 2.0–4.0 km, was detected at both stations despite their ~355 km separation, indicating the widespread nature of the transport. Backward trajectory simulations suggested that the aerosol originated from biomass burning in Canada, with air masses transported over the Atlantic Ocean and western Europe.

Optical data analysis showed higher backscattering at WOS, while WOPAS displayed elevated particle depolarization ratios, suggesting the presence of irregularly shaped particles, possibly desert dust. Aerosol extinction profiles confirmed these findings, with lower extinction at WOPAS likely due to the admixture of less absorbing particles. Sun-photometer measurements during the final stage of the event revealed a bimodal size distribution with a pronounced fine mode, consistent with transported biomass-burning aerosols and supporting the possible presence of desert dust.

These results demonstrate the value of coordinated ground-based lidar, sun-photometer, and model analyses in characterizing long-range aerosol transport. Nevertheless, further studies are required to better understand aerosol composition, microphysical properties, and vertical structure. Future work should incorporate satellite observations and predictive aerosol models to improve assessment of transport pathways, aerosol types, and potential impacts on air quality and climate.

Acknowledgements

We acknowledge the European Space Agency (ESA) for funding the AIRSENSE project under contract 4000142902/23/I-NS within the ESA Atmosphere Science Cluster – Research Opportunities 5 – European Coordinated Study on Aerosols and Aerosol/Cloud Interactions. We thank the Opto-Electronics Section (TEC-MME) at ESA's European Space Research and Technology Centre (ESTEC) for providing the Mobile Raman Lidar EMORAL, developed in collaboration with the University of Warsaw (UW), Ludwig Maximilian University of Munich (LMU), and Raymetrics S.A., as part of the *Technical Assistance for Polish Radar and Lidar Mobile Observation System (POLIMOS)* funded by ESA-ESTEC contract no. 4000119961/16/NL/FF/mg.

Measurements and analysis at the WOPAS site were conducted during the *In situ and remote sensing assessment of bio-aerosols (SARA)* project, as part of the Trans-national Access (TNA) program within the EC-funded ATMO-ACCESS grant no. 101008004.

The Warsaw lidar station is supported by the Ministry of Science and Higher Education through ACTRIS-ERIC (no. 2024/WK/04).

We also acknowledge the NOAA Air Resources Laboratory (ARL) for providing HYSPLIT model data via the READY website (https://www.ready.noaa.gov).

References

[1] Janicka, L. et al.: *Long term observations of biomass burning aerosol over Warsaw by means of multiwavelength lidar*, Opt. Express, 31, 33150-33174, doi.org/10.1364/OE.496794, 2023.

[2] Janicka L.et al.: *Temporal variations in optical and microphysical properties of mineral dust and biomass burning aerosol derived from daytime Raman lidar observations over Warsaw,* Poland, Atm. Envir., 169, 162-174, 10.1016/j.atmosenv.2017.09.022, 2017

[3] Stachlewska I.S. et al.: *EMORAL—Mobile Mie-Raman Lidar with Fluorescence, Polarization and Water Vapor Observational Capabilities for Satellite Cal/Val Field Campaigns,* Springer Aerospace Technology, vol. Volume Part F2592, 239-251, 10.1007/978-3-031-53618-2_21, 2024

[4] Engelmann, R. et al.: *The automated multiwavelength Raman polarization and water-vapor lidar PollyXT: The neXT generation*., Atmospheric Measurement Techniques, 9. 1767-1784, doi:10.5194/amt-9-1767-2016, 2016.

[5] Mattis, I. et al.: *EARLINET Single Calculus Chain – technical – Part 2: Calculation of optical products*. Atmospheric Measurement Techniques, 9(7), 3009–3029. https://doi.org/10.5194/amt-9-3009-2016, 2016

[6] Szczepanik D. et al.: *Spatio-temporal evolution of long-range transported mineral desert dust properties over rural and urban sites in Central Europe*, Science of The Total Environment, Volume 903, https://doi.org/10.1016/j.scitotenv.2023.166173, 2023

[7] Stein, A. et al.: *NOAA's HYSPLIT atmospheric transport and dispersion modelling system*, Bulletin of American Meteorological Society, 96, 2059–2077. http://dx.doi.org/10.1175/BAMS-D-14-00110.1, 2015.

[8] Sinyuk, A. et al.: *The AERONET Version 3 aerosol retrieval algorithm, associated uncertainties and comparisons to Version 2*. Atmos. Meas. Tech. 13, 3375–3411, https://doi.org/10.5194/amt-13-3375-2020, 2020.

Extreme Saharan Dust Event over Europe of the Spring 2024 as Observed above Sofia, Bulgaria

***Ts. Evgenieva**, Z. Peshev, S. Dosev, L. Gurdev, L. Vulkova, E. Toncheva, T. Dreischuh*

Institute of Electronics, Bulgarian Academy of Sciences, 72 Tsarigradsko Chaussee Blvd, 1784 Sofia, Bulgaria

Corresponding author: tsevgenieva@ie.bas.bg

Introduction

Saharan dust (SD) emissions, releasing colossal amounts of mineral particulate matter into the atmosphere spreading over vast areas, significantly affect important components of the regional and global climate, as well as the state of Earth's biosphere. In the spring-summer period of recent years, extremely strong in intensity and dust quantity episodes of Saharan dust outbursts have been increasingly observed, in particular over the Mediterranean basin and Europe [1]. These abnormal events have much stronger than usual impacts on the thermal and radiative budget of the atmosphere, air quality, and possibly human health. Such an extreme Saharan dust intrusion was observed over Europe in the late March and early April 2024 [2,3]. In Bulgaria, and particularly above Sofia, this SD event was registered in the period from 27 March to 2 April 2024.

In this work we present a thorough study and characterization of the specific layered structure of the atmosphere and the aerosol optical and microphysical properties during this exceptionally intensive SD transport to Sofia by using remote sensing and model data.

Measurement Site, Instrumentation and Data

The city of Sofia is located in a heavily urbanized mountain valley. The experimental measurements were performed in the southeastern part of the city, at the Sofia aerosol remote sensing station (42.653733N, 23.387372E, 610 m ASL), located in the Institute of Electronics at the Bulgarian Academy of Sciences (IE – BAS). The station is included in EARLINET, E-Profile, AERONET and ACTRIS (as an observational National Facility).

The data presented were obtained by: a model LR332 – D3008 eight-channel depolarization and Raman lidar (Raymetrics S.A.); a CHM15k "NIMBUS" ceilometer (Lufft, a part of OTT HydroMet); and a sun/sky/lunar photometer CE318 – TS9 (Cimel Electronique). Validation data are also employed on the backward trajectories of the air masses ending over Sofia and the spread of SD plume by the models HYSPLIT and MONARCH, respectively.

Results and Discussion

The quicklook obtained by the ceilometer at wavelength λ = 1064 nm (Figure 1a) describes the evolution of the total attenuated-backscatter above Sofia in the period 31 March – 2 April 2024. It shows the beginning of an intense prolonged SD intrusion on 31 March after midnight with dust layer centered at about 2 km. This layer further expands and descends, covering the city from heights of about 2 – 4 km down to the ground.

The dust layers in the period considered were also observed with the depolarization Raman lidar of the Sofia IE-BAS station. Figure 1b shows a quicklook of the aerosol distribution and dynamics in the first hours of 2 April. Desert aerosols are localized in the altitude range 1.5 – 4.5 km, varying in height and density and entering the local planetary boundary layer (PBL). Figure 2 presents retrieved and/or calculated vertical profiles of optical (backscatter coefficient - BSC, extinction, BSC-related Ångström exponents - BAE and lidar ratio) and depolarization (volume linear depolarization ratio - VLDR, particle linear depolarization ratio - PLDR) parameters of the detected general aerosols and desert dust. Although the time interval considered is after the maximum of the dust event (31 March – 1 April), the BSC and extinction values, up to 3 $Mm^{-1}sr^{-1}$ and up to 90 Mm^{-1}, respectively, are high and indicate significant aerosol/dust densities. The BAE of both pairs of lidar wavelengths exhibits values in the range of 0.2 – 0.5 up to heights of 4 km, indicating the dominance of rather coarse dust size fractions. The lidar ratios at 355 nm and 532 nm

vary with close values in the range of 35 – 40 sr, being among the ones reported for Saharan dust [4]. The weakly changing values of the VLDR around 0.2 – 0.25, as well as those of the PLDR around 0.48 indicate dust particles with a high degree of non-sphericity.

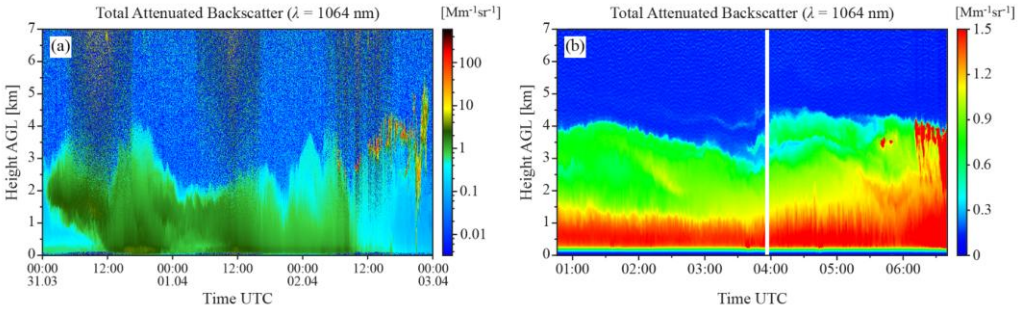

Figure 1. Ceilometer (a) and lidar (b) quicklooks at λ = 1064 nm visualizing the evolution of the total attenuated backscatter above the Sofia IE-BAS station in the period 31 March – 2 April 2024 and on 2 April 2024, respectively.

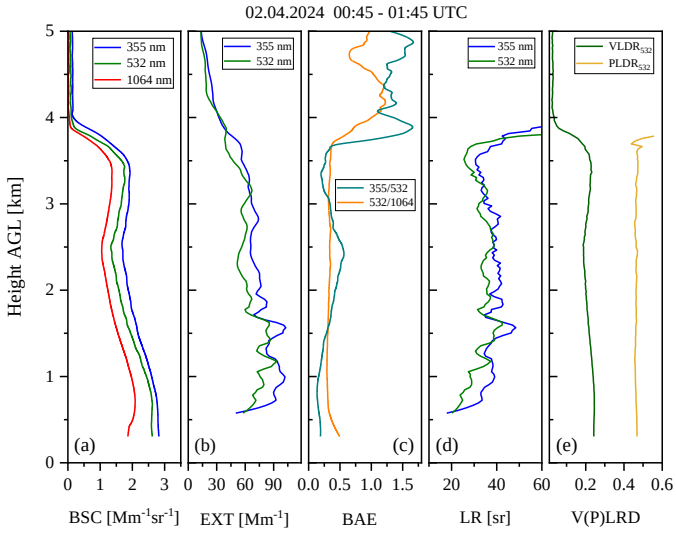

Figure 2. Vertical profiles of the aerosol backscatter coefficient at λ = 355, 532 and 1064 nm (a), extinction at λ = 355 and 532 nm (b), backscatter-related Ångström exponent at the wavelength pairs 355/532 nm and 532/1064 nm (c), lidar ratio at λ = 355 and 532 nm (d), and volume and particle linear depolarization ratios at at λ = 532 nm (e) obtained within the time interval 00:45 – 01:45 UTC on 2 April 2024.

The MONARCH forecast of the dust load spreading over Africa, Europe, and Asia on 31 March is shown in Figure 3a. The most intensive SD transport passed via the Mediterranean Sea and Eastern Europe and reached the Baltic Sea and Scandinavia. Figure 3b presents the MONARCH forecast of the evolution of the dust load over Sofia from 30 March to 2 April. The dust load over Sofia reached the unusually high peak value of 1.16 gm^{-2} on 31 March and declined afterwards. A secondary peak in the dust load is seen at the end of 1 April.

The backward trajectories provided by HYSPLIT of the air masses arriving over Sofia on 31 March and 2 April after midnight at heights below 4 km are shown in Figure 4. As one can see, the backward trajectories have long sections over Northwest Africa, at heights below 5 km, which provides the opportunity for entrainment of large amount of Saharan dust before reaching Sofia.

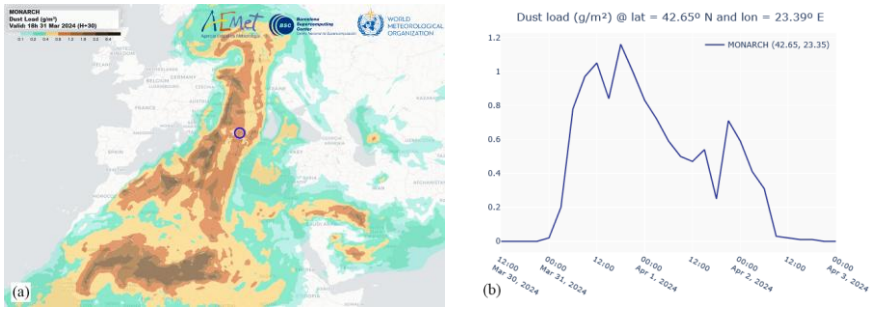

Figure 3. MONARCH forecast of the dust load distribution on 31 March 2024 (a) and forecast of the dust load evolution over Sofia in the period 30 March – 2 April 2024 (b). The location of Sofia is marked by a blue circle.

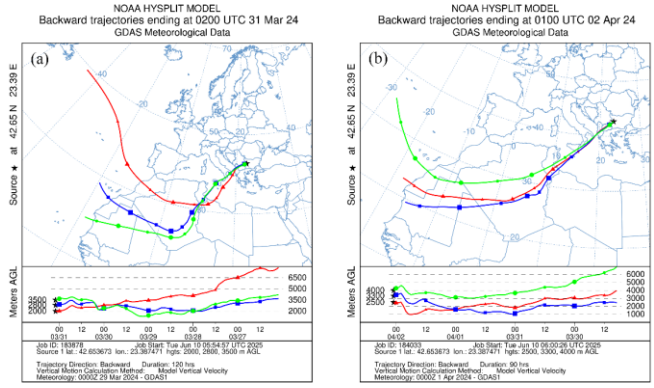

Figure 4. HYSPLIT model 120-hrs backward trajectories of the air masses ending over Sofia at 02:00UTC at heights of 2000 m, 2800 m and 3500 m AGL on 31 March 2024 (a) and 90-hrs backward trajectories of the air masses ending over Sofia at 01:00 UTC at heights of 2500 m, 3300 m and 4000 m AGL on 2 April 2024 (b).

The AERONET sun photometer data (ver. 3, level 1.5) outline a set of typical optical and microphysical aerosol characteristics intrinsic to Saharan dust [5]. Thus, the aerosol optical depth (AOD) at wavelength $\lambda = 440$ nm is unusually high and reaches a maximum value of 1.25, having a daily mean value of 0.86 ± 0.32 on 31 March. The minimum Ångström exponent value for the wavelength pair 440/870 nm is 0.04, and the daily mean is 0.10 ± 0.03 on the same day, indicating the presence of coarse-mode-dominated aerosol in the atmosphere.

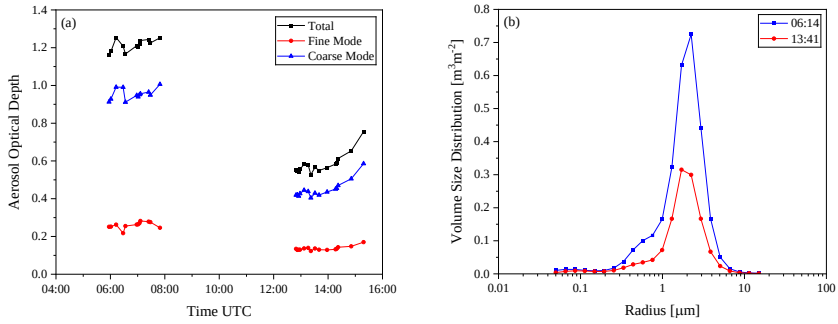

Figure 5. Daily variations of the total, fine mode and coarse mode AOD at $\lambda = 500$ nm (a) and of the volume size distribution (b) of the aerosol ensembles over Sofia obtained from AERONET sun photometer data on 31 March 2024.

The daily variation of the total AOD and AOD of the fine and coarse modes at λ = 500 nm obtained on 31 March are presented in Figure 5a. It is seen that the fine mode AOD has much smaller values (mean value of 0.19 ± 0.06) compared to those of the coarse mode AOD (mean value of 0.67 ± 0.26), i.e., the fine mode aerosol has a very small contribution to the optical depth compared to the contribution of the coarse mode. The fine mode in the volume size distribution is practically absent (Figure 5b), while the coarse one displays a strong peak at radii of about 2-3 μm. The AERONET-derived particle single-scattering albedo increases with λ in a way typical for the Saharan dust [5]. The particle sphericity factor is as low as 0.10 – 0.30%, showing that the aerosols are rather non-spherical. The particle linear depolarization ratio at λ = 440 nm is high and varies between 0.28 and 0.31.

Conclusions

The results obtained in this work show that the Saharan dust episode taking place in late March and early April 2024 is an extraordinary event of an extremely intense large-scale direct transport of desert aerosols over the Mediterranean and Europe, reaching the northern parts of the continent with unabated power. Accordingly, the values of dust load over Central and Eastern Europe at the height of the event approach several grams per square meter. Ceilometer and lidar dynamic maps of aerosol stratification over Sofia show that desert aerosols are localized in an approximately compact layer at altitudes below 4 km, entering the local PBL down to the surface. Moreover, the estimated ground-level dust concentrations in the measurement area reach nearly 400 μg m^{-3}, creating a high potential risk for local ecosystems and human health. Expectedly, according to the data from the sun photometer of the Sofia AERONET station, the columnar values of the AOD at λ = 440 nm on March 31 reached record values of up to 1.25. The aerosol composition of the atmosphere over Sofia during the dust event has been totally dominated by desert dust, as evidenced by the sun-photometer volume size distributions of aerosol particles, exhibiting nearly mono-modal shape in which the fine component is practically absent.

Based on the lidar height profiling of optical, microphysical, and depolarization aerosol parameters, the dust density (in terms of backscattering and extinction) remained high early on 2 April, when a dust load of about 0.6 gm^{-2} was revealed. The values of the BSC-related Ångström exponent for the 532/1064 nm pair below 0.5, the particle linear depolarization ratio at 532 nm close to 0.5, as well as the lidar ratios at 355 and 532 nm in the range of 35 – 40 sr, unambiguously indicate the dominance of coarse Saharan dust fractions with a high degree of non-sphericity. In summary, the studied dust event had a significant influence on the aerosol composition and the thermal and radiative state of the local troposphere over Sofia, with strong potential impacts on air quality and human health.

Acknowledgements

This work is financially supported by the Ministry of Education and Science of Bulgaria (support for ACTRIS BG, part of the National Roadmap for Research Infrastructure).

In this work we used data form HYSPLIT model obtained via NOAA Air Resources Laboratory (ARL) through the READY website (https://www.ready.noaa.gov) and MONARCH dust forecast model provided by the WMO Barcelona Dust Regional Center (https://dust.aemet.es/products/daily-dust-products).

References

[1] Peshev, Z. et al.: *Large-scale Saharan dust episode in April 2019: Study of desert aerosol loads over Sofia, Bulgaria, using remote sensing, in situ, and modeling resources*, Atmosphere, 13, 981, https://doi.org/10.3390/atmos13060981, 2022.

[2] Loskot, J. et al.: *Impact of Saharan dust on particulate matter characteristics in an urban and a natural locality in Central Europe*, Sci. Rep., 14, 32002, https://doi.org/10.1038/s41598-024-83603-0, 2024.

[3] EUMETSAT: Dust transport from Sahara to Mediterranean and beyond, URL: https://user.eumetsat.int/resources/case-studies/dust-transport-from-sahara-to-mediterranean-and-beyond

[4] Mona, L. et al.: *Saharan dust intrusions in the Mediterranean area: Three years of Raman lidar measurements*, J. Geophys. Res., 111, D16203, https://doi.org/10.1029/2005JD006569, 2006.

[5] Dubovik, O. et al.: *Variability of absorption and optical properties of key aerosol types observed in worldwide locations*, J. Atmos. Sci., 59, 590-608, https://doi.org/10.1175/1520-0469(2002)059<0590:VOAAOP>2.0.CO;2, 2002.

Forecasting and analysing wildfire plumes in the European atmosphere, demonstrated by the case of Canadian wildfire plumes in June 2025

S. Eckhardt[1], *N. Evangeliou*[1], *E. Sollum*[1], *K. Stebel*[1], *J. Kaiser*[1], *C. Lund Myhre*[1], *L.E. Murberg*[1], *L. Janicka*[2], *I. S. Stachlewska*[2]

(1) NILU, Department of atmosphere and climate, Kjeller, Norway
(2) University of Warsaw, Faculty of Physics, Institute of Geophysics, (IGFUW), Pasteura 5, 02-093, Warsaw, Poland
Corresponding author: sabine.eckhardt@nilu.no

Introduction

Aerosols are important not only for human health but also for their impact on climate. For climate-related effects, the vertical distribution of aerosols is particularly important, as it influences the radiative balance. In order to properly evaluate models and interpret observational data more effectively, atmospheric modelling is essential. It provides a critical tool for understanding transport patterns and transformations of aerosols. Models can also be used to forecast the transport of aerosol plumes, which is highly valuable for targeting observational methods and campaigns.

Wildfires are becoming more frequent and intense with a warming climate, especially at higher latitudes. These fires are episodic in nature, with locations and magnitudes that vary greatly from year to year. Additionally, the transport patterns of wildfire emissions are highly variable. Large areas can burn over the course of several weeks, releasing significant amounts of gases and aerosols into the atmosphere. Among these, black carbon is especially relevant due to its considerable warming effect in the atmosphere and its potential to alter surface albedo when deposited on snow, accelerating snow and ice melt.

The exact amounts of emissions from wildfires and the atmospheric scavenging processes they undergo are both highly uncertain. Since these factors are crucial for determining atmospheric concentrations of aerosols and their impacts, it is important to study actual atmospheric concentrations to improve our understanding. In this analysis, we focus on the European atmosphere, which is particularly well covered by a network of lidar stations operated within the Aerosol, Cloud and Trace-gases Research Infrastructure (ACTRIS). These stations are capable of identifying biomass burning plumes that often remain in elevated layers of the atmosphere and do rarely reach the surface, after crossing the Atlantic.

Methodology

We apply the Lagrangian particle dispersion model FLEXPART [1]. We perform forward simulations covering the years 2015 to 2025 to investigate the transport of biomass burning black carbon. Emissions are derived from the Global Fire Assimilation System (GFAS) [2], using a spatial resolution of 0.5° × 0.5°. The model simulates, based on 0.5 degree hourly ERA-5 data key atmospheric processes including advection, turbulent diffusion, moist convection, and gravitational settling. The output provides three-hourly concentrations of black carbon throughout the atmosphere. Monthly climatologies of black carbon concentrations over Europe have been established to characterise typical transport patterns and seasonal variability. In addition, two detailed case studies are conducted for the summers of 2023 and 2025, both of which experienced severe wildfire activity in Canada with significant transatlantic smoke transport.

As part of the IRISCC EU project, we also provide operational seven-day forecasts of wildfire smoke transport. These forecasts have a temporal resolution of three hours and a spatial resolution of 0.5° × 0.5°, with 20 vertical levels covering the troposphere and lower stratosphere. The forecasted transport of black carbon emissions, based on GFAS and CAMS data, is distributed using the FLEXPART model driven by meteorological data from the Global Forecast System (GFS). The GFS meteorological data used in this work are provided by the National Centers for Environmental Prediction (NCEP) through the National Oceanic and Atmospheric Administration (NOAA).

The hemispheric transport of the wildfire smoke aerosol and trace gases is further analysed using e.g., ultraviolet (UV) Absorbing Aerosol Index (AAI), aerosol optical depth (AOD), and carbon monoxide (CO) from TROPOspheric Monitoring Instrument (TROPOMI) onboard Sentinel-5P. The vertical curtains

of smoke over Canada can be identified and the particle extinction can be quantified by data from Atmospheric Lidar on the Earth Clouds, Aerosols and Radiation Explorer (EarthCARE).

Results and Discussion

In 2023, approximately 100 Mt carbon have been released by mid-June from forest burned in Canada, with many fires classified as out of control. The resulting smoke plumes were transported eastward over the Northern Atlantic, reaching Europe after about six days. In 2025, the fire season also began abruptly in June, once again leading to large-scale emissions and transatlantic smoke transport. By June 10th, the same amounts of emissions are released as in 2023 by this day of the year. The GFAS-FLEXPART climatology shows, that in 2023 Canada was the prominent source for wildfire emissions (Fig 1). Wildfires in Siberia, which are also dominating during some years, e.g in 2019, were not significantly important.

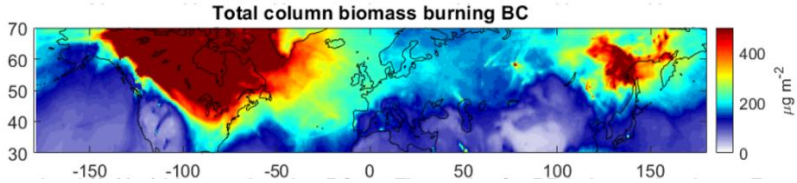

Figure 1. Total column of biomass burning BC in the wild fire season May to October 2023, based on FLEXPART simulations an GFAS/CAMS wildfire emissions.

In June 2025 several transatlantic transport events have been observed. While in the beginning of the months (Fig. 2.) the wildfire emissions were transported to UK and the Northern Sea, later the aerosols have been mixed downwards and were captured by an inversion layer over the Alpine region.

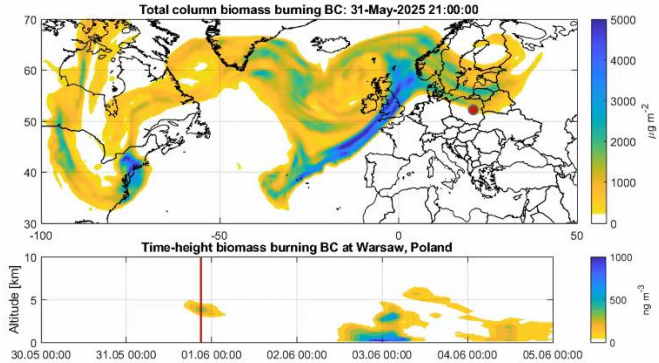

Figure 2. Total column of BC from Canadian wildfires for 1 June 2025 12:00, lower panel: curtain plot of modelled wildfire black carbon height versus time for the 30 May to the 5 June over Warsaw (red dot in the upper panel).

This plume could be observed very clearly by a ground-based stations, as well as satellite observations. The PollyXT lidar observations in the beginning of June at ACTRIS-PL station in Warsaw captured varying cloud systems above 6 km and two aerosol layers below (Fig. 3). The lower layer is due to urban emissions, while the middle layer corresponds well to the altitudes range that can be attributed to the Canadian wildfire emissions (compare Fig. 2). Long-term lidar observations of aerosol properties over this continental urban site show dominance of city-generated aerosols within boundary layer [4]. While lidar observations of biomass burning aerosol in Warsaw over a decadal scale (2013-2018) show clear domination of the wildfire aerosol transport from North America (39%) over transport pathways (Eastern European (35%), Western European (21%), and Iberian Peninsula wildfires (5%) [5].

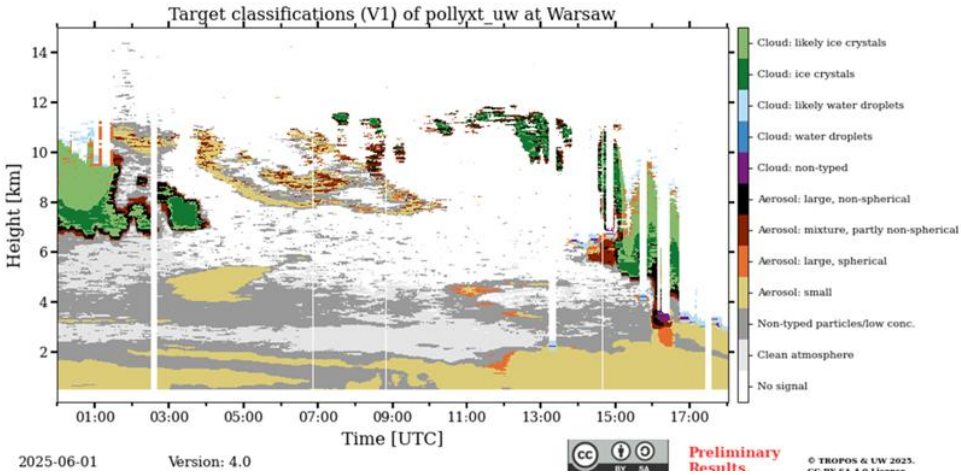

Figure 3. ACTRIS site of University of Warsaw – PollyXT lidar observation on 1 June 2025, aerosol and cloud layers are indicated in different colours (https://polly.tropos.de, last access 12 June 2025).

Conclusions

The Canadian wildfire plume of 2025 represents one of the strongest transatlantic aerosol events observed in the recent years.

1) The plume was clearly detectable in satellite imagery and, even in visible wavelengths.

2) Cloud cover often complicated the identification of aerosol layers in optical satellite data.

3) Ground-based lidar networks are essential for confirming the vertical structure and transport of smoke.

4) For the first time in recent years, air quality in central Europe, particularly over the Alps, was severely impacted, as aerosol layers mixed down into the boundary layer.

Our analysis underscores the importance of integrated observational and modelling approaches for monitoring wildfire smoke transport. FLEXPART simulations provide valuable guidance for both satellite-based and ground-based observation strategies. Lidar observations of tropospheric aerosol layers within and above the atmospheric boundary layer are essential to validate the model outputs. Given the projected increase in wildfire frequency and intensity under a warming climate, sustained model–observation synergy will be critical for improving both air quality forecasts and climate impact assessments.

Acknowledgements

This work was financed by IRISCC funded by the European Union - Grant Agreement Number 101131261 and Healthriskadapt funded by the European Union - Grant Agreement Number 101157458.
ACTRIS-PL station in Warsaw is operationally supported by the Ministry of Science and Higher Education of Poland under grant agreement 2024/WK/04.

References

[1] Pisso, I., Kristiansen, N.I., et al.: The Lagrangian particle dispersion model FLEXPART version 10.4, *Geoscientific Model Development*, **12**, 4955–4997, doi:10.5194/gmd-12-4955-2019, 2019.
[2] Kaiser, J.W., Heil, A., and Schultz, M.G.: Global Fire Assimilation System (GFASv1.0) – Description and evaluation, *Geoscientific Model Development*, **5**, 309–339, doi:10.5194/gmd-5-309-2012, 2012.
[3] Hersbach, H., Bell, B., and Berrisford, P.: The ERA5 global reanalysis, *Quarterly Journal of the Royal Meteorological Society*, **146**, 1999–2049, doi:10.1002/qj.3803, 2020.
[4] Wang, D., Szczepanik, D., and Stachlewska, I. S.: Interrelations between surface, boundary layer, and columnar aerosol properties derived in summer and early autumn over a continental urban site in Warsaw, Poland, Atmos. Chem. Phys., 19, 13097–13128, https://doi.org/10.5194/acp-19-13097-2019, 2019.
[5] Lucja Janicka, Lina Davuliene, Steigvile Bycenkiene, and Iwona S. Stachlewska, "Long term observations of biomass burning aerosol over Warsaw by means of multiwavelength lidar," Opt. Express 31, 33150-33174 (2023)

Identifying Source Regions for Arctic Smoke Layers and Characterizing Their Optical Properties using CALIPSO observations.

***M. Filioglou*[1]**, *X. Shang*[1], *A. Lipponen*[1], *A. M. Sundström*[2], *L. Sogacheva*[1], *T. Mielonen*[1]

(1) Finnish Meteorological Institute, Atmospheric Research Centre of Eastern Finland, Yliopistonranta 8, 70211, Kuopio, Finland

(2) Finnish Meteorological Institute, Erik Palménin aukio 1, 00560 Helsinki, Finland

Corresponding author: maria.filioglou@fmi.fi

Introduction

Wildfires are becoming more frequent and larger across various regions, driven by a combination of climate change and human activities with adverse effects in ecosystems and climate [1]. Of particular interest are emissions from boreal fires located in the vicinity of the Arctic as they can be transported in this sensitive to climate change region contributing further to Arctic amplification [2]. Depending on the fuel available, meteorological and burning conditions, their emission and aerosol characteristics may differ. Wildfires emit vast amounts of carbonaceous aerosols such as organic carbon and black carbon (BC) into the atmosphere. Currently, BC emissions, the second largest contributor to global warming after CO2 [3], rely heavily on model estimations due to lack of global-scale observations. Consequently, models significantly underestimate surface BC concentrations in the Arctic by one to two orders of magnitude [4].

Constraining the properties and amount of the smoke aerosols and attributing a source region for smoke transported over long distances to pristine regions is challenging due to the vastness of the boreal region since ground-based observations or/and flight campaigns are scarce. Space-borne remote sensing has the potential to provide useful information with a reasonable temporal resolution. In this study, we focus on identifying the source regions and optical characteristics of smoke layers in the Arctic utilizing a synergy of CALIPSO satellite observations, trajectory analysis from MERRA-2 and injection heights from CAMS Global Fire Assimilation System (GFAS) model.

Methodology

CALIPSO observations: The Cloud-Aerosol Lidar and Infrared Pathfinder Satellite Observation (CALIPSO) satellite has been providing observations on aerosols and clouds since June 2006. The Cloud-Aerosol Lidar with Orthogonal Polarization (CALIOP) instrument on board CALIPSO provides the vertical structure of aerosol and cloud properties. In this study, the CALIOP level 2 Version 4.51 5-km Aerosol Layer (ALay) data were used. Layers flagged as ‘elevated smoke’ in the aerosol classification mask after quality control were considered only [5]. Aerosol layers with horizontal averaging of 5, 20 and 80 km were analysed independently, and each layer was considered only once utilizing the unique detection method described in [6]. For simplicity, we present here the 5 km horizontal averaging smoke layer.

Trajectory analysis: We computed air parcel trajectories using a custom Lagrangian trajectory model following MERRA-2 wind fields [7]. We linearly interpolated the MERRA- 2 wind field information to get the wind components for the exact location and time of the air parcel. A 5-minute time step and simple forward Euler method were used for the trajectory computations.

Injection height of smoke: Daily estimated injection heights (mean altitude of maximum injection, MAMI) were provided by the Plume Rise Model and IS4FIRES which are incorporated in CAMS Global Fire Assimilation System (GFAS) fire radiative power (FRP) [8]. The dataset combines satellite-based FRP observations with meteorological information from the ECMWF operational weather forecast to produce daily estimates of biomass burning emissions.

Smoke layer source identification: For each detected elevated smoke layer, a 10-day backward trajectory was considered. A source area for each smoke layer was appointed when the altitude of the trajectory point was lower than the daily MAMI.

Results and Discussion

Five years of CALIPSO overpasses over the Arctic between 2018 and 2022 were used to depict elevated smoke layers above 59º N latitude and further attribute their source region and optical properties. The majority of the elevated smoke layers were observed during the months of July and August with an annual periodicity which is related to the fire activity. Of particular interest is August 2021 which exhibited an exceptionally high occurrence of elevated smoke layers compared to other years (Figure 1). The majority of these elevated smoke layers are located 2 to 3 km in the atmosphere and have a mean geometrical depth of ~1 km.

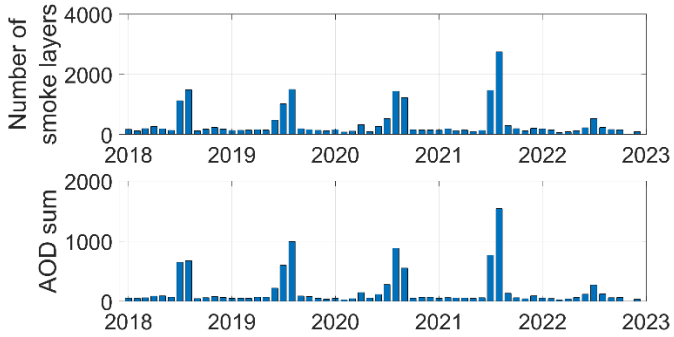

Figure 1. Top: Monthly accumulated number of elevated smoke layers above 59º N using the 5 km horizontal resolution. Bottom: Equivalent monthly accumulated Aerosol Optical Depth (AOD).

A total of 21240 quality assured elevated smoke layers have been detected out of which 51% have been attributed to a source region (5 km horizontal resolution). The source identification method resulted in distinct areal clustering of the smoke layers in Eurasia and North America (Figure 2). Five fire source regions were defined, and the majority of the smoke layers originate from Siberia, Central Asia, Europe, Canada, and USA in descending order.

We have further estimated the accumulated mass concentration of the smoke layers assuming a smoke mass density of 1.3 g cm^{-3} and a smoke volume-to-extinction conversion factor of $0.13x10^{-12}$ Mm [9]. The majority of the smoke layers above 59º N are located in Eurasia resulting to an accumulation of mass concentration over the Northern parts of Central Asia and Siberia. The optical properties corresponding to these distinct source regions were grouped further considering the time of travel to the Arctic and the type of burned area. It was found that smoke layers originating from regions in Central and East Russia had the highest Aerosol Optical Depth (AOD) compared to those originating from Europe in which the travel time of smoke layers was longer implying possible dilution of the smoke layer on the way to the Arctic region.

Conclusions

Five years of CALIPSO observations were used to locate elevated smoke layers in latitudes above 59º N. We found that most of the fire activity is during the months of July and August. Specifically, the highest smoke layer numbers were observed in August (2018, 2019, 2021), September (2020), or July (2020). The majority of the smoke layers are located in the northern part of Russia resulting to higher cumulative mass concentrations compared to Canada. This was in line with the fire sources of these smoke layers which were also attributed to boreal forests in the Central Asia and Siberia regions. The mean injection heights of these fire sources were lower in North Europe compared to South Europe implying a lower fire density with the mean injection heights in the rest of the regions to be comparable.

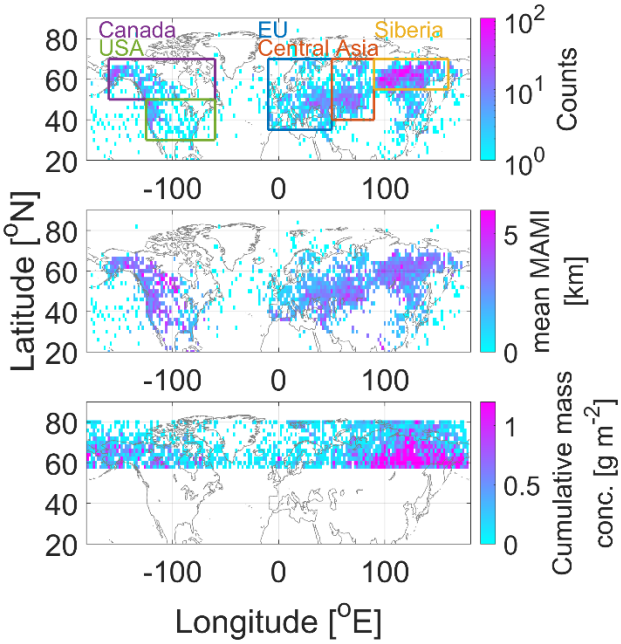

Figure 2. Top: Fire source areas for the elevated smoke layers above 59º N using the 5 km horizontal resolution. The counts have resulted using a 2ºx2º box. Middle: Mean MAMI height. Bottom: Accumulated mass concentration for the detected smoke layers.

Acknowledgements

The authors gratefully acknowledge the support from the Research Council of Finland and the Atmosphere and Climate Competence Center (ACCC) Flagship.

References

[1] Cunningham, C.X., Williamson, G.J. and Bowman, D.M.J.S.: Increasing frequency and intensity of the most extreme wildfires on Earth. *Nat Ecol Evol* 8, 1420–1425, 2024.

[2] Rantanen, M., Karpechko, A.Y., Lipponen, A. *et al.* The Arctic has warmed nearly four times faster than the globe since 1979. *Commun Earth Environ* 3, 168, 2022.

[3] Bond, T.C., S.J. Doherty, D.W. Fahey, P.M. Forster, T. Berntsen, B.J. DeAngelo, M.G. Flanner, S. Ghan, B. Kärcher, D. Koch, S. Kinne, Y. Kondo, P.K. Quinn, M.C. Sarofim, M.G. Schultz, M. Schulz, C. Venkataraman, H. Zhang, S. Zhang, N. Bellouin, S.K. Guttikunda, P.K. Hopke, M.Z. Jacobson, J.W. Kaiser, Z. Klimont, U. Lohmann, J.P. Schwarz, D. Shindell, T. Storelvmo, S.G. Warren, and C.S. Zender: Bounding the role of black carbon in the climate system: A scientific assessment. *J. Geophys. Res. Atmos.*, 118, no. 11, 5380-5552, 2013.

[4] Matsui, H., Mori, T., Ohata, S., Moteki, N., Oshima, N., Goto-Azuma, K., Koike, M., and Kondo, Y.: Contrasting source contributions of Arctic black carbon to atmospheric concentrations, deposition flux, and atmospheric and snow radiative effects, Atmos. Chem. Phys., 22, 8989–9009, 2022.

[5] Kim, M.-H., Omar, A. H., Tackett, J. L., Vaughan, M. A., Winker, D. M., Trepte, C. R., Hu, Y., Liu, Z., Poole, L. R., Pitts, M. C., Kar, J., and Magill, B. E.: The CALIPSO version 4 automated aerosol classification and lidar ratio selection algorithm, Atmos. Meas. Tech., 11, 6107–6135, 2018.

[6] Shang, X., Lipponen, A., Filioglou, M., Sundström, A.-M., Parrington, M., Buchard, V., Darmenov, A. S., Welton, E. J., Marinou, E., Amiridis, V., Sicard, M., Rodríguez-Gómez, A., Komppula, M., and Mielonen, T.: Monitoring biomass burning aerosol transport using CALIOP observations and reanalysis models: a Canadian wildfire event in 2019, Atmos. Chem. Phys., 24, 1329–1344, 2024.

[7] Gelaro, R., McCarty, W., Suárez, M. J., Todling, R., Molod, A., Takacs, L., Randles, C. A., Darmenov, A., Bosilovich, M. G., Reichle, R., Wargan, K., Coy, L., Cullather, R., Draper, C., Akella, S., Buchard, V., Conaty, A., da Silva, A. M., Gu, W., Kim, G., Koster, R., Lucchesi, R., Merkova, D., Nielsen, J. E., Partyka, G., Pawson, S., Putman, W., Rienecker, M., Schubert, S. D., Sienkiewicz, M., & Zhao, B.: The Modern-Era Retrospective Analysis for Research and Applications, Version 2 (MERRA-2). *Journal of Climate*, *30*(14), 5419-5454, 2017.

[8] Rémy, S., Veira, A., Paugam, R., Sofiev, M., Kaiser, J. W., Marenco, F., Burton, S. P., Benedetti, A., Engelen, R. J., Ferrare, R., and Hair, J. W.: Two global data sets of daily fire emission injection heights since 2003, Atmos. Chem. Phys., 17, 2921–2942, 2017.
[9] Ansmann, A., Ohneiser, K., Mamouri, R.-E., Knopf, D. A., Veselovskii, I., Baars, H., Engelmann, R., Foth, A., Jimenez, C., Seifert, P., and Barja, B.: Tropospheric and stratospheric wildfire smoke profiling with lidar: mass, surface area, CCN, and INP retrieval, Atmos. Chem. Phys., 21, 9779–9807, 2021.

A 15-year climatology of solar background calibrated temperature profiles measured by the RAman Lidar for Meteorological Observations.

*V. Jayaweera[1], **G. Martucci[2]**, R. J. Sica[1], and A. Haefele[2,1]*

(1) Department of Physics and Astronomy, The University of Western Ontario, London, N6A 3K7, Canada
(2) Federal Office of Meteorology and Climatology, MeteoSwiss, 1530 Payerne, Switzerland

Corresponding author: giovanni.martucci@meteoswiss.ch

Introduction

The contribution of operational Raman lidars to the study of dynamics and long-term trends of water vapour and temperature in the troposphere and lower stratosphere is exceptionally important, and is made possible by autonomous Raman lidars capable of measuring uninterruptedly for extended periods of time, namely for many years. This is the case of the RAman Lidar for Meteorological Observations (RALMO) installed at the MeteoSwiss station of Payerne since 2008 [1]. This study presents a climatology of nighttime temperature profiles calibrated automatically using the solar background for the last 15 years. The nighttime temperature climatology obtained by RALMO is compared to the one measured by the collocated operational radiosonde of MeteoSwiss at 23h00 UTC. An application of real-time retrieval of temperature profiles using both the solar background method and by the "traditional" radiosonde-calibrated method will also be presented at the conference, applicable to both the traditional temperature analysis as well as to temperatures retrieved using the optimal estimation method [2].

Methodology

The methodology used for this study is based on the recent publication by Jayaweera and colleagues [3]. The method uses the returned signals from the pure-rotational Raman spectra (Stokes and anti-Stokes) emitted by the diatomic molecules N_2 and O_2 present in the atmosphere after excitation by the 355-nm RALMO laser. The raw pure-rotational Raman (PRR) signals are then calibrated automatically every morning when cloudless conditions occur using the signal coming from the sun when it reaches an altitude of 19.80° elevation angle. The solar background signal allows for an independent measurement and correction of the instrumental drift of the acquisition modules of the N_2 and O_2 signals (for the water vapour retrieval) and of the PRR signals (for the temperature retrieval). Along with the solar background calibration, an optimal estimation method (OEM) has been used to retrieve the temperature profiles [2,4] from the raw PRR high (JH) and low (JL) quantum-shifted signals. Following [3], the signal coming from the solar background extracted from the PRR JH and JL profiles for altitudes above 55 km along with an initial radiosonde calibration (used as anchor calibration point) can be combined in a single calibration coefficient and used to calibrate the temperature profiles at any time *t*,

$$C_t^* = \frac{C_0^*}{r_0^{solar}} r_t^{solar} \quad (1)$$

r_t^{solar} is the relative calibration at time *t* and corresponds to the ratio of the JH to the JL solar background contributions, C_0^* is the external calibration obtained by the collocated radiosonde at the initial time (or an average over a time interval) and the corresponding relative calibration r_0^{solar} also at the initial time (or an average over a time interval).

Using the calibration factor C_t^*, the OEM retrieval can provide calibrated temperature profiles at any time *t* between 2010 and 2025. The obtained temperature profiles are then combined in a monthly climatology and averaged. We chose to use an OEM-based method for the many advantages of using an inverse model, but we could have also calibrated the same time series analyzed using the traditional temperature retrieval.

Results and Discussion

The solar background-calibrated temperature profiles, T_{PRR}, retrieved from RALMO PRR JH and JL raw signals have been obtained by the OEM method for the period 2010-2025. Amongst the available T_{PRR} profiles, only those between 23h00 and 00h00 UTC have been selected to match the collocated radiosounding launched every night at 23h00 UTC. The selected T_{PRR} profiles have been filtered using their signal-to-noise (SNR) ratio to prevent noisy profiles and cloudy conditions as done in [3]. The SNR-filtered T_{PRR} profiles have then been combined into monthly means and shown as time-height cross sections as shown in the left panel of Figure 1. The same climatology has been generated using the nighttime radiosonde profiles and is shown in the right panel of Figure 1. The sonde models used for the climatology for the analyzed period are the SRS-C34 (2011-2017), SRS-C50 (2017-2018) and the Vaisala RS41 (2018-2025).

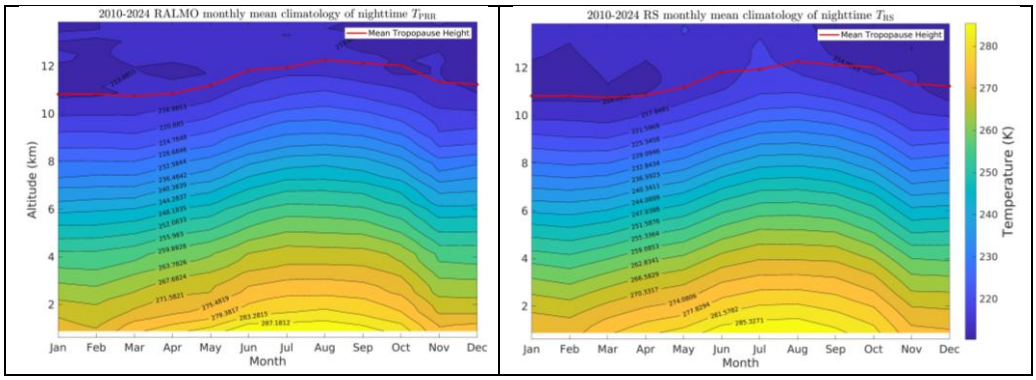

Figure 1. Climatology of the nighttime T_{PRR} (left) and T_{RS} profiles averaged into monthly values. The RALMO profiles are retrieved during 1h from 23h00 to 00h00 UTC to match the collocated night radiosonde flight at 23h UTC.

Table 1 and 2 show the mean monthly biases and standard deviations of the differences between the RALMO T_{PRR} and the radiosonde T_{RS} at four atmospheric layers in the climatology. The mean monthly biases show that the deviation of RALMO with respect to the radiosonde never exceeds 1.2 K in the first 10 km for all months. The T_{PRR} -T_{RS} values are mainly positive in the lower troposphere (warm bias) and become more negative (cold bias) reaching the tropopause region (shown by the red curve in figure 1).

Table 1. Mean bias of the T_{PRR} -T_{RS} at 4 atmospheric layers.

Mean bias [K]												
Altitude range [km]	**Jan**	**Feb**	**Mar**	**Apr**	**May**	**Jun**	**Jul**	**Aug**	**Sep**	**Oct**	**Nov**	**Dec**
0-2	-0.12	-0.77	0.17	0.02	0.33	1.04	0.39	0.80	1.19	1.22	0.16	1.07
2-5	-0.47	0.31	-0.01	0.06	-0.07	0.01	-0.05	-0.09	0.08	0.49	-0.18	-0.27
5-10	-0.73	0.25	-0.36	-0.32	-0.39	-0.23	-0.56	-0.63	-0.48	0.03	-0.26	-0.33
10-12	-1.14	-0.52	-0.32	-0.40	-0.74	-0.92	-1.64	-0.94	-0.88	-0.26	-0.66	-0.40

The mean monthly standard deviations of the T_{PRR} -T_{RS} differences shown in Table 2 highlight the fact that in the lower troposphere, mainly within the boundary layer, the standard deviations are smaller during winter

than during summer when the convection is stronger. This difference between summer and winter is somehow attenuated above the boundary layer in the region 2-10 km. The standard deviation is also larger during the warmer months in the tropopause region. The largest mean monthly standard deviations never exceed 1.5 K.

Table 2. Mean standard deviation of the T_{PRR} -T_{RS} at 4 atmospheric layers.

Standard deviation [K]												
Altitude range [km]	**Jan**	**Feb**	**Mar**	**Apr**	**May**	**Jun**	**Jul**	**Aug**	**Sep**	**Oct**	**Nov**	**Dec**
0-2	0.58	0.45	0.90	1.00	1.09	1.49	1.08	0.90	1.10	1.08	0.72	1.43
2-5	0.30	0.57	0.28	0.32	0.38	0.33	0.38	0.28	0.25	0.36	0.52	0.38
5-10	0.43	0.43	0.35	0.43	0.32	0.37	0.56	0.40	0.41	0.38	0.64	0.56
10-12	0.90	0.60	1.01	0.67	0.82	1.06	0.74	0.57	0.35	0.68	0.65	0.83

The RALMO temperature data T_{PRR} and radiosonde data T_{RS} that have been used to calculate the climatology are shown in timeseries in Figure 2 at three atmospheric levels. As explained above, the RALMO temperature profiles have been filtered based on their SNR, so that only the clear sky T_{PRR} data contributed to the climatology. This explains why there are gaps in the timeseries (in addition to the gaps due to the instrument's failure). The gap occurring from July 2020 till July 2021 is due to a failure of the laser unit that could not be repaired by the manufacturer due to the COVID-19 travel ban. As also shown by the T_{PRR} -T_{RS} values in Table 1 and 2, the agreement at different levels in the atmosphere is satisfactory and the spread of the T_{PRR} data with respect to the T_{RS} data is relatively small (< 1.5 K). This is well seen in the overlaying of the T_{PRR} and T_{RS} data points.

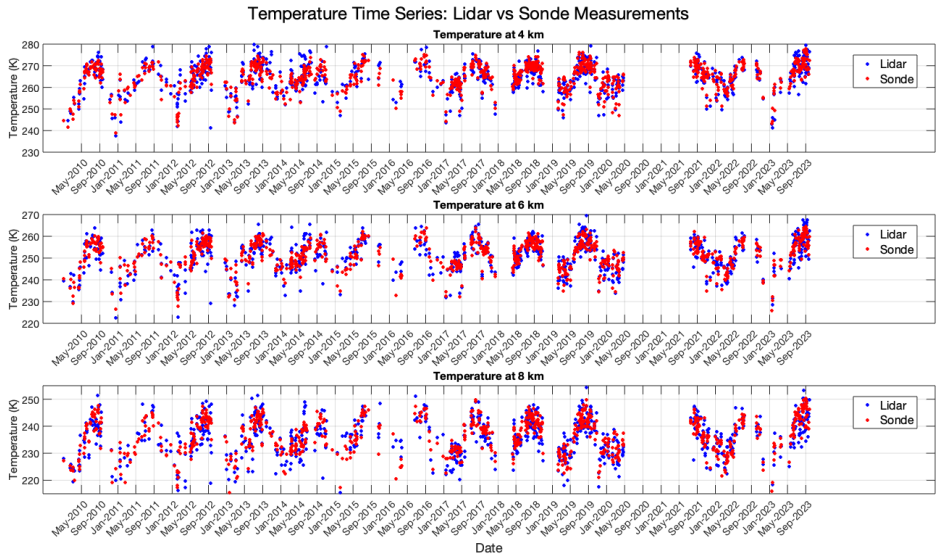

Figure 2. Timeseries of T_{PRR} (blue) and T_{RS} (red) data points since 2010 at three atmospheric levels.

Real-time solar background method vs traditional temporal retrieval

Currently, the operational retrieval scheme of the temperature from the RALMO PRR data is the one described in [5]. We refer here to the currently operational retrieval scheme as "traditional", as this hinges on the automatic calibration by collocated radiosonde data. The traditional retrieval method has been validated against the collocated operational radiosonde for a period of 18 months proving very good agreement. The next step in the validation of the solar background calibrated temperature product is to implement it in the operational retrieval chain of RALMO. This will be implemented in the next months in parallel with the traditional retrieval scheme, allowing for a direct comparison.

Conclusions

The solar background calibration method ensures good quality temperature data as shown by the study [3] and allows to construct a climatology that can be used also for the trend analysis. Compared to the traditional radiosonde-calibrated method, the solar-background method is independent from the external radiosounding reference and can compensate for the instrumental drift in a very efficient way. This method is especially beneficial for remote sites or for any site where the radiosounding is not available. In the forthcoming months an application of real-time retrieval of both the solar-background and traditional method will be implemented to the operational retrieval scheme of RALMO and presented at the conference.

Acknowledgements

This research has been supported by the Natural Sciences and Engineering Research Council of Canada (grant no. RGPIN-2018-04999). This project has also been funded in part by the National Science and Engineering Research Council of Canada and the CASSAVA PEARL (Canadian Anchor Sites for SATellite Validation – Polar Environment Atmospheric Research Laboratory) project, supported by the Canadian Space Agency (grant no. 19FATORA07)..

References

[1] Brocard, E., Philipona, R., Haefele, A., Romanens, G., Mueller, A., Ruffieux, D., Simeonov, V., and Calpini, B.: *Raman Lidar for Meteorological Observations, RALMO – Part 2: Validation of water vapor measurements*, Atmos. Meas. Tech., 6, 1347–1358, https://doi.org/10.5194/amt-6-1347-2013, 2013b.

[2] Mahagammulla Gamage, S., Sica, R. J., Martucci, G., and Haefele, A.: *Retrieval of temperature from a multiple channel pure rotational Raman backscatter lidar using an optimal estimation method*, Atmos. Meas. Tech., 12, 5801–5816, https://doi.org/10.5194/amt-12-5801-2019, 2019.

[3] Jayaweera, V., Sica, R. J., Martucci, G., and Haefele, A.: *Solar Background Radiation Temperature Calibration of a Pure Rotational Raman Lidar*, EGUsphere [preprint], https://doi.org/10.5194/egusphere-2024-1081, 2024.

[4] Gamage, S. M., Sica, R., Martucci, G., and Haefele, A.: *A 1D Var retrieval of relative humidity using the ERA5 dataset for the assimilation of Raman lidar measurements*, J. Atmos. Ocean. Tech., 37, 2051–2064, 2020.

[5] Martucci, G., Navas-Guzmán, F., Renaud, L., Romanens, G., Gamage, S. M., Hervo, M., Jeannet, P., and Haefele, A.: *Validation of pure rotational Raman temperature data from the Raman Lidar for Meteorological Observations (RALMO) at Payerne*, Atmos. Meas. Tech., 14, 1333–1353, https://doi.org/10.5194/amt-14-1333-2021, 2021.

Annual aerosol and dust cycle observed by lidar in Central Asia, Dushanbe, Tajikistan

***G. H. Müller*[1,2]**, *A. A. Floutsi*[1], *H. Baars*[1], *J. Hofer*[1], *R. Engelmann*[1], *D. Althausen*[1], *S. F. Abdullaev*[3] *and S. Khalifaeva*[3]

(1) Leibniz Institute for Tropospheric Research (TROPOS), Permoserstraße 15, Leipzig, Germany
(2) University of Leipzig, Faculty of Physics and Earth System Science, Leipzig Institute for Meteorology (LIM), Stephanstraße 3, Leipzig, Germany
(3) Physical Technical Institute of the National Academy of Sciences of Tajikistan, Dushanbe, Tajikistan

Corresponding author: G. H. Müller (gmueller@tropos.de)

Introduction

After the scientifically successful Central Asian Dust Experiment (CADEX) [1], [2], [3], [4] in 2015/16, a containerized Polly^{XT} lidar system [5] was deployed in Dushanbe, Tajikistan, in June 2019 for continuous and automated operation. The Polly^{XT} system deployed is a multiwavelength-Raman-polarization lidar operating at 355, 532, and 1064 nm and equipped with near-range capabilities. Based on lidar observations collected between June 2019 and May 2024, and in combination with the Polarization Lidar and Photometer Networking (POLIPHON) method [6], [7], [8], the dust and non-dust backscatter coefficients were determined from the measured particle backscatter coefficient and the particle linear depolarization ratio. This allowed the investigation of the annual cycle of dust aerosol particles above Dushanbe. The seasonal analysis of dust and non-dust aerosol particles above Dushanbe performed in this study provides a first insight into a growing dataset of long-term lidar observations. Being the only ground-based station of the Aerosol, Clouds and Trace Gases Research Infrastructure (ACTRIS) in the Central Asian region, the retrieved data is especially valuable. Since Dushanbe is surrounded by various deserts and lies within the global dust belt [1], [2], it is affected by local dust emissions as well as from long-range transport of dust from other source regions and is therefore a key region to study atmospheric dust.

Methodology

The seasonal analysis is based on the measurements of a polarization Raman lidar Polly^{XT}, located at the premises of the National Academy of Sciences of Tajikistan (NAST) at the outskirts of Dushanbe (38°33'34" N, 68°51'22" E, 864 m a.s.l.). The data retrieved by the lidar has been automatically analyzed in a first step by the Polly^{NET} Processing Chain (PPC) [9], deriving among others vertical profiles of the aerosol backscatter coefficient β_{par}, the aerosol extinction coefficient α_{par}, the aerosol lidar ratio S_{par} and the particle linear depolarization ratio δ_{par}. For the analysis, only the data derived with the Raman method has been used (mainly nighttime measurements). Although the dataset is continuous between June 2016 and May 2024, two large data-gaps occurred between February 2020 and November 2021 as well as June 2023 and November 2024, due to technical issues with the device that could not be easily fixed.

Two very important tasks that are especially relevant for this study are also performed by the PPC: Firstly, the automated target classification and cloud screening ensures that the derived particle-related profiles are not contaminated by clouds. Secondly, the first step of the POLIPHON method is performed, separating the measured particle backscatter coefficient into a dust and non-dust related part. The two steps will be described in more detail below.

Since the aim of this study is to use all available data without manual sorting, the first step is crucial, since even a few cloud-contaminated profiles can already have a strong effect on the results. The cloud screening of the PPC proved to be insufficient in several cases, leaving cloud-contaminated profiles in the screened data and creating the need of a further quality control. An approach using the automated target classification of the PPC that distinguishes the measurements in aerosol particles and clouds of different types was therefore developed to identify cloud-free periods. Unfortunately, this approach was also not completely solving the issue due to misclassifications within the target classification of the PPC, especially between highly depolarizing dust and ice clouds. Therefore, a robust solution chosen by introducing threshold-based criteria on several optical parameters, below which, the data was used within

the monthly or seasonal averaging of the data. For the presented data, β_{par} = 6 Mm^{-1} sr^{-1}, α_{par} = 300 Mm^{-1}, S_{par} = 150 sr and δ_{par} = 0.6 were used. Furthermore, for all temporal averages, the median values have been investigated to furthermore reduce the influence of outliers and to give a general idea of the dominating value of the backscatter coefficient.

The second important analysis step within the PPC is the separation of the derived particle backscatter coefficient into a dust and a non-dust part. This is performed according to [6] with a threshold for the particle lineal depolarization ratio of $\delta_{par} \geq 0.31$ for pure dust and $\delta_{par} \leq 0.05$ for pure non-dust conditions. This represents the first step within the POLIPHON method [7], [8], which aims to derive aerosol microphysical properties from polarization lidar and photometer measurements. The result of this separation can be used to assess the fraction of dust and non-dust aerosol particles contributing to the total measured backscatter signal on an annual basis, which has been done in this study.

Results and Discussion

Figure 1 shows the seasonal median of the particle backscatter coefficient β_{par} exemplarily for 2022, as well as its separation into the dust and non-dust particle backscatter coefficient along with the 25 to 75 % percentile range (shaded area). The winter season (Fig. 1a) is characterized by low values of β_{par} and generally a strong decrease of β_{par} with increasing height. The backscatter coefficient is dominated by the non-dust fraction, most likely attributed to local pollution from heating and other urban sources. Only a very low amount of dust can be found in the atmosphere in the winter season, indicating not only fewer local emissions, but also less transport to the measurement site. The spring season (Fig. 1b) shows an increase in the dust backscatter coefficient compared to the winter season. The dust fraction of the backscatter coefficient is strongly increased in 2022. Apart from the increased backscatter coefficient close to the planetary boundary layer (PBL), the backscatter coefficient is also increased in the troposphere above. Even compared to summer and autumn, the values above 4.5 km are higher in spring, indicating lofted aerosol layers that are advected to the measurement site. In the summer season (Fig. 1c), the backscatter coefficient is strongly increased and dominated by the dust fraction with a nearly constant non-dust fraction. The high values of the backscatter coefficient also range higher into the troposphere up to 4.5 to 5 km. Therefore, the main dust season can be seen in the summer season, still continuing into autumn (Fig. 1d). The total and dust backscatter coefficient are still high within and close to the PBL, with a strong decrease with height up until 4 km. The high spread between the 25 and 75 % percentile indicates the sharp transition of the dust season to the season with low atmospheric dust.

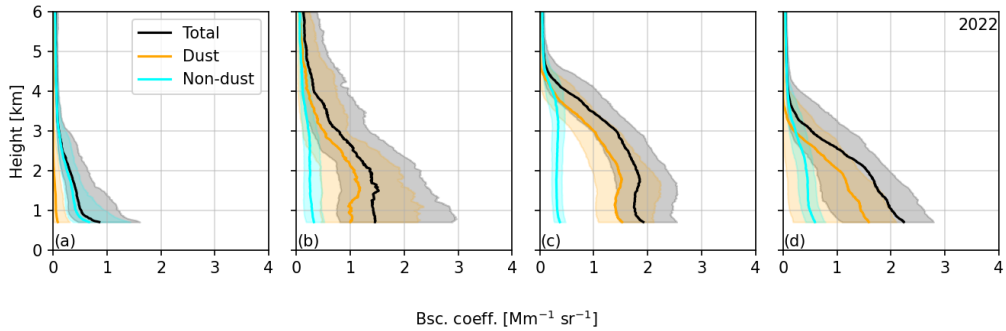

Figure 1. Seasonal median of the particle backscatter coefficient for 2022 with the total backscatter coefficient (black), the dust backscatter coefficient (orange) and the non-dust backscatter coefficient (cyan). The 25 to 75% percentile range is given through the shaded areas. Panels a, b, c and d correspond to winter, spring, summer and autumn, respectively

The investigation on a seasonal basis grants a first, height-resolved insight into the annual cycle of atmospheric dust. Yet, this investigation has also be performed on a monthly basis, especially to investigate the inter-annual variability. Figure 2 shows the vertical mean of the backscatter coefficient with the standard deviation of the monthly median profiles. Two height-ranges have been chosen for the in-depth investigation: between 700 and 2000 m (lower panel) and between 2000 and 5000 m (upper panel). Both height-ranges show the same pattern of the annual dust cycle. The general findings from the seasonal analysis can also be seen in Fig. 2. As already discussed, the non-dust fraction of the backscatter coefficient tends to vary only slightly, whereas the dust fraction of the backscatter coefficient shows stronger variations over the course of the year. Very low values with almost no dust in the atmosphere have been seen from November to February, with the peak of the dust season occurring around August and September. The increase of dust within the atmosphere happens within the spring season over the course of several months. Although the annual dust cycle is similar for the investigated years, its characteristics also varied partially. For example, in 2024, the buildup of dust happened slower than in 2022. The end of the dust season is, contrastingly, usually marked by a sharp decrease of the dust backscatter coefficient within one or two months, usually September and October. For the higher atmospheric range chosen between 2000 and 5000 m, the annual dust cycle follows the same general characteristics as in the lower height range.

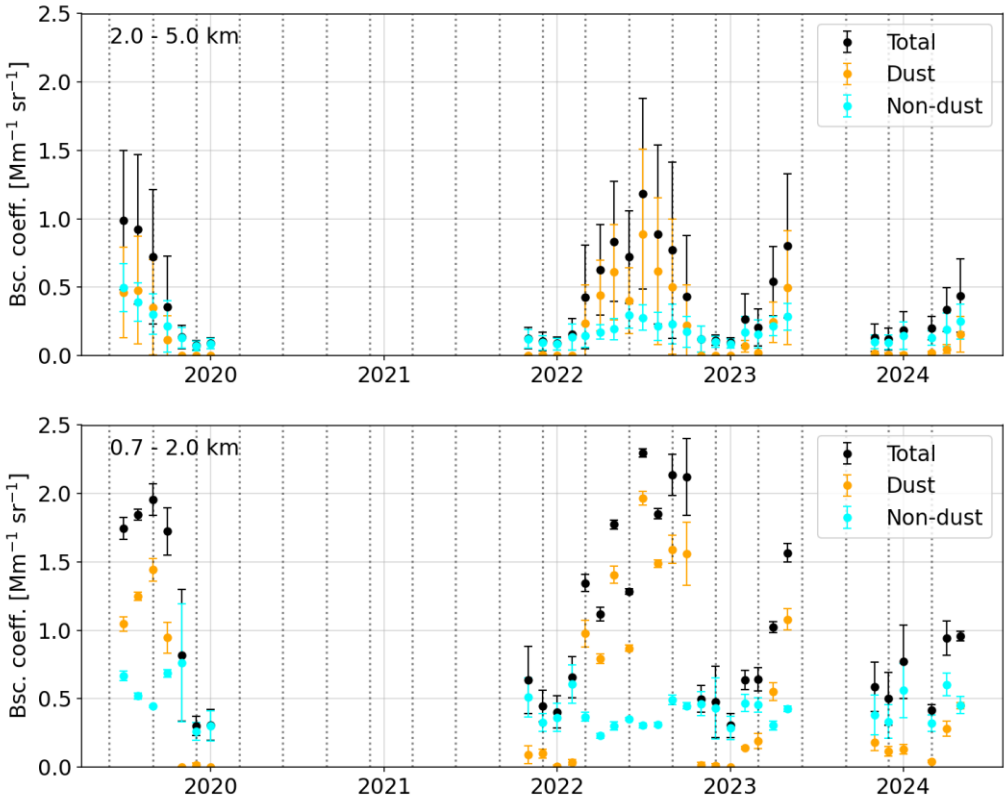

Figure 2. Vertical mean of the monthly median of the particle backscatter coefficient with the standard deviation. The beginning of each year (January) is indicated by the years given on the horizontal axis, the beginning month of each new season is indicated by the dotted lines. The lower panel shows the vertical mean taken for a low atmospheric layer between 700 and 2000 m, the upper panel shows an upper height range from 2000 to 5000 m.

The main differences lie in the maximum of the layer-mean backscatter coefficient being reached around a month earlier and an earlier decline of the atmospheric dust towards the winter season. Since the non-dust fraction of the backscatter coefficient also follows the general annual dust cycle in the upper height range, the uplift of locally emitted aerosol particles, including dust and pollution, seems to be one major driver of the increased aerosol load above the PBL.

Conclusions

The annual cycle of dust and non-dust aerosol properties above Dushanbe, Tajikistan, was examined based on Polly^{XT} lidar measurements. In comparison with the CADEX-campaign, the found seasonality of atmospheric dust shows a good agreement regarding the general shape of the annual dust-cycle, allowing the conclusion on the main dust season in Dushanbe, Tajikistan, spanning from July to September with not only strongly increased atmospheric dust within the PBL, but also in the troposphere above. The non-dust aerosol fraction is more constant over the course of the year, with an increased uplift of non-dust aerosol particles during the summer months above the PBL. The study performed highlights the applicability of the POLIPHON method on single cases but also larger datasets. The study also highlights the need for automated, high-quality data processing, especially with respect to cloud screening lidar data. Appropriately cloud-screened data would allow for more, perhaps automated, statistical investigations at different sites and therefore make the comparison of different regions possible.

Acknowledgements

In this study we used data from the CADEX field campaign as well as data from the succussing permanent lidar in Dushanbe. The CADEX project was funded by the German Federal Ministry of Education and Research (BMBF) in the context of "Partnerships for sustainable problem solving in emerging and developing countries" (grant no. 01DK14014). The construction of a new lidar for permanent observations in Tajikistan is funded by the BMBF (grant no. 01LK1603A). This project has also received funding from the European Union's Horizon 2020 research and innovation program ACTRIS-2 Integrating Activities (H2020-INFRAIA-2014-2015,60 grant no. 654109) and from the European FP7 project by the European Union's Seventh Framework Program (FP7/2007–2013) collaborative project BACCHUS (grant no. 603445). This activity has received funding from the European Union's Horizon 2020 research and innovation program through the ATMO-ACCESS Integrating Activity under grant agreement No 101008004. This research has been supported by the German Federal Ministry of Education and Research (BMBF) under the FONA Strategy "Research for Sustainability" (grant65 no. 01LK2001A). We gratefully acknowledge the European Space Agency (ESA) for AIRSENSE (Aerosol and aerosol-cloud Interaction from Remote SENSing Enhancement) project through the contract 4000142902/23/I-NS in the framework of the ESA Atmosphere Science Cluster – Research Opportunities 5 – European Coordinated Study on Aerosols and Aerosol/Cloud Interactions.

References

[1] Hofer, J. et al.: *Central Asian Dust Experiment (CADEX): Multiwavelength Polarization Raman Lidar Observations in Tajikistan*, EPJ Web of Conferences 119 18006, doi.org/10.1051/epjconf/201611918006, 2016

[2] Hofer J. et al.: *Long-term profiling of mineral dust and pollution aerosol with multiwavelength polarization Raman lidar at the Central Asian site of Dushanbe, Tajikistan: case studies*, Atmos. Chem. Phys., 17, 14559–14577, doi.org/10.5194/acp-17-14559-2017, 2017

[3] Hofer, J. et al.: *Long-term profiling of aerosol light extinction, particle mass, cloud condensation nuclei, and ice-nucleating particle concentration over Dushanbe, Tajikistan, in Central Asia*, Atmos. Chem. Phys., 20, 4695–4711, doi.org/10.5194/acp-20-4695-2020, 2020

[4] Hofer, J. et al.: *Optical properties of Central Asian aerosol relevant for spaceborne lidar applications and aerosol typing at 355 and 532 nm*, Atmos. Chem. Phys., 20, 9265–9280, doi.org/10.5194/acp-20-9265-2020, 2020

[5] Engelmann, R. et al.: *The automated multiwavelength Raman polarization and water-vapor lidar PollyXT: the neXT generation*, Atmos. Meas. Tech., 9, 1767-1784, doi.org/10.5194/amt-9-1767-2016

[6] Tesche, M. et al.: *Vertically resolved separation of dust and smoke over Cape Verde using multiwavelength Raman and polarization lidars during Saharan Mineral Dust Experiment 2008*, J. Geophys. Res., 114, D13202, doi.org/10.1029/2009JD011862, 2009

[7] Mamouri, R.E. and Ansmann, A.: *Fine and coarse dust separation with polarization lidar*, Atmos. Meas. Tech., 7, 3717–3735, doi.org/10.5194/amt-7-3717-2014, 2014

[8] Mamouri, R.E. and Ansmann, A.: *Potential of polarization lidar to provide profiles of CCN- and INP-relevant aerosol parameters*, Atmos. Chem. Phys., 16, 5905–5931, doi:10.5194/acp-16-5905-2016, 2016

[9] Yin, Z. and Baars, H.: *PollyNET/Pollynet Processing Chain: Version 3.0 (Version v3.0)*, Zenodo., doi.org/10.5281/zenodo.5571289, 2021

Investigating smoke optical properties in Eastern Mediterranean: Lidar observations in Cyprus.

M. Poutli[1,2], *R. E. Mamouri*[1,2], *A. Nisantzi*[1,2], *K. Michailidis*[3], *M. Prodromou*[1, 2], *and D. Hadjimitsis*[1,2]

(1) Eratosthenes Centre of Excellence, Franklin Roosevelt 82, 3012, Limassol, Cyprus
(2) Cyprus University of Technology, Department of Civil Engineering and Geomatics, Archiepiskopou Kyprianou 30, 3036, Limassol, Cyprus
(3) Laboratory of Atmospheric Physics, Physics Department, Aristotle University of Thessaloniki, Thessaloniki, Greece
Corresponding author: maria.poutli@eratosthenes.org.cy

Introduction

Wildfires are large, uncontrolled fires that often occur in rural or sparsely populated areas. The main causes of wildfires can be attributed to either human activity or natural factors. When key conditions such as heat, drought, and fuel availability reach critical thresholds, wildfires can ignite or become more intense. Climate change affects these parameters by lowering the critical values required for fire activity to occur [1]. The IPCC (AR6) states with medium confidence that weather conditions favoring wildfires have become more probable in southern Europe, northern Eurasia, the USA, and Australia over the last century [2]. Smoke particles play a significant role in the climate system, affecting it directly by absorbing solar radiation and indirectly by influencing cloud formation as cloud condensation nuclei (CCN) and ice-nucleating particles (INPs) [3]. They also impact air quality, visibility, and pose health risks. Studying their optical properties is essential for understanding their role in the climate system and improving weather and climate models.

The Mediterranean region is a key area for atmospheric studies due to the diverse aerosol types it experiences. Cyprus, the third-largest island in the Mediterranean, provides a strategic location for investigating the vertical distribution of aerosols, including marine particles, desert dust, smoke, and anthropogenic particles. Hence, this is a great opportunity to study the behavior of smoke in such aerosol mixtures. This study emphasizes on the intense activity of wildfires in Turkey's Mediterranean Region in July and August 2021, and the corresponding smoke layers that were observed above Limassol site.

Methodology

Observations were performed using the multiwavelength polarization Ramam lidar, PollyXT (POrtabLe Lidar sYstem) [4], operated in Limassol (34.677° N, 33.0375° E) as part of the Cyprus Atmospheric Remote Sensing Observatory National Facility (CARO NF) of the Eratosthenes Centre of Excellence (ECoE). This lidar system operates continuously, 24/7, with a diode-pumped laser that emits the first (1064nm), second (532 nm) and third (355 nm) harmonic frequency with a pulse repetition rate of 100 Hz. In the present configuration the lidar can measure the backscatter coefficient profiles at three wavelengths (355, 532 and 1064 nm), and the extinction coefficient profiles and the depolarization ratio at two wavelengths (355 and 532 nm). Four near-field channels (355, 387, 532, and 607 nm) extend the vertical range of the lidar towards lower altitudes and a water-vapor Raman channel at 407 nm is also included.

To identify atmospheric particle layers, we relied on the temporal evolution of the calibrated attenuated backscatter coefficient at 1064 nm and the volume depolarization ratio at 532 nm. Relatively high backscatter coefficient values, indicating considerable aerosol loading, along with low depolarization ratio values, which are typical signatures of smoke at tropospheric levels [5-8], suggested the presence of smoke particles. To confirm the origin of the particles, we examined the backward trajectories from HYSPLIT (Hybrid Single-Particle Lagrangian Integrated Trajectory model) simulations [9] together with VIIRS (Visible Infrared Imaging Radiometer Suite) fire and thermal anomalies data [10], available from the joint NASA/NOAA Suomi National Polar orbiting Partnership satellite. For the statistical analysis of the particles' optical properties we used nighttime measurements to which the Raman method could be applied [11]. In the cases presented here, vertical profiles of the optical properties were retrieved from nighttime observations, with a temporal averaging window of 60–70 minutes, typically between 18:00 and

00:00 UTC, and a vertical smoothing of 500 m. For each case, the mean depolarization and lidar ratios within the detected aerosol layers were calculated.

To assess the impact of fires along Turkey's south coast, we estimated the fire radiative power (FRP) at three key clusters where wildfire hotspots were identified. These areas were selected based on fire activity during the period under study. FRP values were calculated using the VIIRS 375 m active fire product from the Suomi NPP satellite, which offers improved nighttime performance and a better response over small fire areas. Only FRP values with high or nominal detection confidence level were used. To characterize the vegetation burned, we referred to the CORINE Land Cover (CLC) product [12], which provides land cover and land use data across Europe.

Results

A series of wildfires affected a large part of Turkey's Mediterranean region in July and August 2021. The fires began in July 2021 and continued until August 12, 2021. To study the fire radiative power, we divided the southern coast of Turkey into three major clusters based on the temporal evolution of the hotspots observed with FIRMS data. Some fire pixels in these regions displayed high values reaching 300 MW but most of them ranged between 50-100 MW. Based on the CORINE product, the burned areas were primarily characterized by coniferous vegetation (51%) and transitional woodland-shrub (23%). Studies showed that the 2021 wildfires resulted in the largest area loss in the history of forest fires in Turkey [13].

The daily distribution of FRP values for July and August 2020 and 2021 was also estimated, across all three clusters. These two years were used for comparison to assess the intensity of wildfire events in 2021. It was observed that during the period 28 July-12 August 2021, FRP values were considerably higher compared to the corresponding period in 2020. Elevated FRP values were also recorded on 15 July 2021, coinciding with another wildfire event along the southern coast of Turkey. Throughout the study period, the wide range of boxplot values indicated significant variability, with maximum FRP values approaching 100 MW. Continuous vertically resolved aerosol measurements performed by the PollyXT instrument in CARO station, combined with HYSPLIT trajectory analysis, confirmed the transport of smoke plumes from intense wildfires to the Limassol region within 12 hours. This rapid northward transport was driven by the Etesian winds, a persistent and well-known regional wind system in the eastern Mediterranean [14].

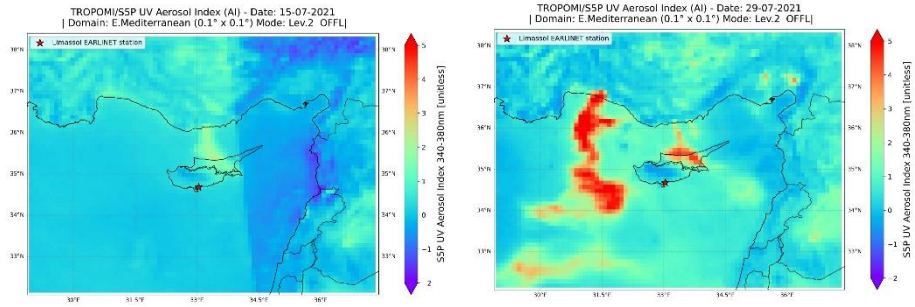

Figure 1. Spatial distribution of gridded UV Aerosol Index measurements obtained by the TROPOMI/Sentinel-5p on 15.07.2021 (left) and 29.07.2021 (right). The location of CARO station is marked by red stars.

In this study we present two case studies - 15.07.2021 and 29.07.2021 – during which FRP values reached their highest levels, according to the daily distribution estimations. The spatial dispersion of emitted smoke particles from southern Turkey towards Cyprus during this period is highlighted by the UV Aerosol Index (UVAI), captured by the TROPOMI (Tropospheric Monitoring Instrument) onboard the Sentinel-5P satellite [15]. The data were gridded to a 0.1˚x 0.1˚ (latitude x longitude) grid covering an extended area of E. Mediterranean, from 29˚E to 37˚E and from 32˚N to 38˚N. As shown in Figure 1, the high positive values reveal the significant load of absorbing aerosols, for both case studies, clearly illustrating that the smoke emitted from the occurred fires was transported southward to Cyprus.

Figure 2 (left) presents the temporal evolution of the attenuated volume backscatter signal at 1064nm, obtained by the PollyXT system on 15 July 2021 between 18:10-19:20 UTC. The vertical profiles of the optical properties for the same time interval, are also presented (Fig. 2, right). An intense smoke layer was detected between 1.8 and 2.8 km. Lidar signals averaged over 1 hour to retrieve the lidar and particle depolarization ratios vertical profiles. The mean lidar ratios were 72.31 ± 9.42 sr at 355 nm and 44.45 ± 3.51 sr at 532 nm, within the observed layer height, values typical of fresh smoke [5-8, 16]. The retrieved values are also in agreement with the typical behavior of fresh smoke, where the lidar ratio at 355 nm is generally higher than that at 532 nm. Mean particle depolarization ratios of 4 ± 0.6 % at 355 nm and 5 ± 1.3 % at 532 nm align with typical values observed for tropospheric smoke [5-8]. The Ångström exponents indicated the presence of fine-mode particles [17].

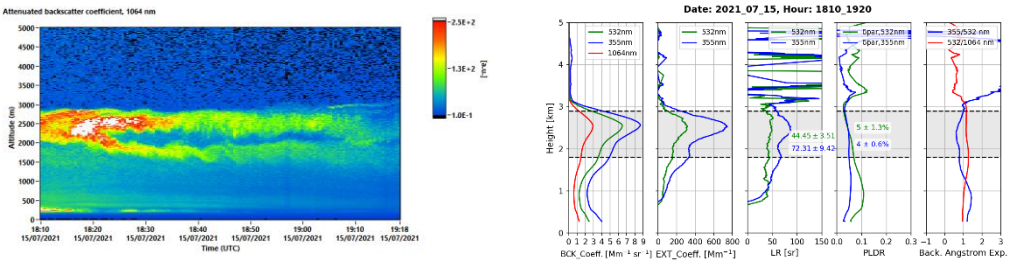

Figure 2. (left) Time–height display of the attenuated backscatter signal at 1064nm on 15.07.2021, 18:10-19:20 UTC, and (right) vertical profiles of intensive and extensive optical properties.

In late July 2021, the PollyXT lidar detected an intense smoke layer at 2.6–3.5 km altitude. The smoke, classified as fresh, reached Limassol in less than 12 hours. Figure 3 shows the time evolution of the attenuated backscatter coefficient at 1064 nm (23:00–23:59 UTC) and corresponding vertical profiles of the optical parameters. The backscatter and extinction coefficients at the detected layer were similar to those observed on 15.07.2021, though the aerosol index was notably higher on 29.07.2021 (Fig. 1). This may be attributed to meteorological factors and plume dispersion. Mean lidar ratios were 97.50 ± 14.54 sr (355 nm) and 66.38 ± 7.30 sr (532 nm), higher than in the previous fresh smoke case but still within typical values referred in the literature. The $LR_{532}/LR_{355} < 1$ pattern, characteristic of fresh smoke, was again observed. Mean particle depolarization ratios were 12 ± 1.0 % (355 nm) and 7 ± 0.5 % (532 nm), with values near 0.1 indicating possible influence of soil dust and dust injected during the fire into the aerosol mixture [18].

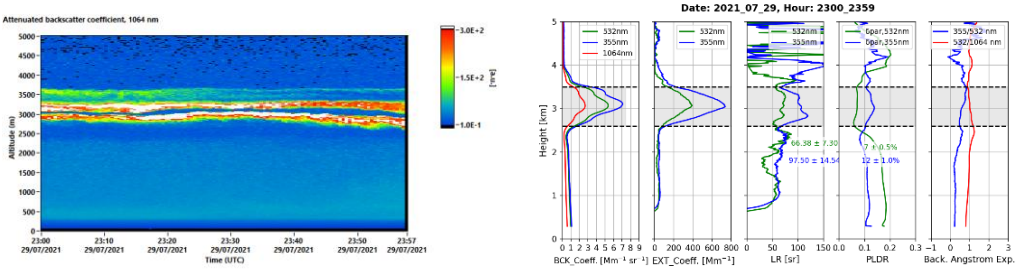

Figure 3. Same as Figure 2 but for 29.07.2021 and for 1-h average lidar signal between 23:00-23:59 UTC.

Conclusions

During July and August 2021, Turkey's Mediterranean Region experienced a series of wildfires that affected a large area, burning various types of vegetation. FRP values indicated intense wildfire activity in the clusters under study, compared to the previous year, making this wildfire season the worst on record in the country's history. Backward trajectories and satellite imagery indicated that smoke particles reached the Limassol site within 12 hours. The PollyXT lidar system detected these fresh smoke layers, and the analysis of the optical properties confirmed the presence of fresh smoke above Limassol. It also suggested the presence of soil dust and dust injected during the fire into the aerosol mixture. Further study will focus on comparing the optical properties of fresh smoke cases with those of background smoke observed in the subsequent days. Additionally, the hygroscopic growth of aerosol particles and the influence of humidity on the depolarization of smoke particles will be examined.

Acknowledgements

This work has been supported by the EXCELSIOR project under GA No 857510, funding from the EU Horizon 2020, the Government of the Republic of Cyprus and the Cyprus University of Technology. The authors also acknowledge the support received by ATARRI Horizon Europe Widespread Twinning Project under the GA No 101160258.

References

[1] Pausas, J.G. et al.: *Are wildfires a disaster in the Mediterranean basin?–A review,* International journal of wildland fire, 17, 713-723, doi.org/10.1071/WF07151, 2008.

[2] Arias, P.A. et al.: *Technical Summary. In Climate Change 2021: The Physical Science Basis. Contribution of Working Group I to the Sixth Assessment Report of the Intergovernmental Panel on Climate Change*, 33-144, doi:10.1017/9781009157896.002, 2021.

[3] Knopf, D.A., Alpert, P.A., and Wang, B.: *The Role of Organic Aerosol in Atmospheric Ice Nucleation: A Review*, ACS Earth and Space Chem., 2, 168-202, doi.org/10.1021/acsearthspacechem.7b00120, 2018.

[4] Engelmann, R. et al.: *The automated multiwavelength Raman polarization and water-vapor lidar PollyXT: The neXT generation*, ACP, 9, 1767–1784, doi.org/10.5194/amt-9-1767-2016, 2016.

[5] Haarig, M. et al.: *Depolarization and lidar ratios at 355, 532, and 1064 nm and microphysical properties of aged tropospheric and stratospheric Canadian wildfire smoke*, ACP, 18, 11847–11861, doi.org/10.5194/acp-18-11847-2018, 2018.

[6] Floutsi, A. A. et al.: *DeLiAn - a growing collection of depolarization ratio, lidar ratio and Ångström exponent for different aerosol types and mixtures from ground-based lidar observations*, Atmos. Meas. Tech., 16, 2353-2379, doi.org/10.5194/amt-16-2353-2023, 2023.

[7] Janicka, L. et al.: *Long term observations of biomass burning aerosol over Warsaw by means of multiwavelength lidar, Opt. Express*, 31, 33150-33174, doi.org/10.1364/oe.496794, 2023.

[8] Janicka, L. and Stachlewska, I. S.: *Properties of biomass burning aerosol mixtures derived at fine temporal and spatial scales from Raman lidar measurements: Part I optical properties*, ACP Discussions, (March), 1–46, 2019.

[9] HYbrid Single-Particle Lagrangian Integrated Trajectory model, backward trajectory calculation tool, National Oceanic and Atmospheric Administration (NOAA), https://www.ready.noaa.gov/HYSPLIT.php

[10] FIRMS (Fire Information for Resource Management System): https://firms.modaps.eosdis.nasa.gov/

[11] Ansmann, A. et al.: *Independent measurement of extinction and backscatter profiles in cirrus clouds by using a combined Raman elastic–backscatter lidar*, App. Opt., 31, 7113–7131, 1992.

[12] CORINE (Coordination of Information on the Environment) Land Cover: https://land.copernicus.eu/en/products/corine-land-cover.

[13] Acar, Z. and Gonencgil, B.: Forest fires in southern Turkey July-August 2021, Revista de Climatología, 23, 46–57, doi.org/10.59427/rcli/2023/v23.46-57, 2023.

[14] Anagnostopoulou, C. et al.: *Recent past and future patterns of the Etesian winds based on regional scale climate model simulations*, Clim. Dyn., 42, 1819–1836, doi.org/10.1007/s00382-013-1936-0, 2014.

[15] Veefkind, J. P. et al.: *TROPOMI on the ESASentinel-5 Precursor: A GMES mission for global observations of the atmospheric composition for climate, air quality and ozone layer applications*, Remote Sens. Environ., 120, 70–83, doi.org/10.1016/j.rse.2011.09.027, 2012.

[16] Nicolae, D. et al..: *Characterization of fresh and aged biomass burning events using multiwavelength Raman lidar and mass spectrometry*, JGR Atmospheres, 118, 2956–2965, https://doi.org/10.1002/jgrd.50324, 2013.

[17] Mamouri, R.E. et al.: *Wildfire smoke triggers cirrus formation: lidar observations over the eastern Mediterranean*, Atmos. Chem. Phys., 23, 14097–14114, doi.org/10.5194/acp-23-14097-2023, 2023.

[18] Nisantzi, A. et al.: *Injection of mineral dust into the free troposphere during fire events observed with polarization lidar at Limassol, Cyprus*, Atmos. Chem. Phys., 14, 12155-12165, doi.org/10.5194/acp-14-12155-2014, 2014.

Characteristics of the smoke aerosol layers as observed by the EARLINET lidar stations in 2015-2023

D.N. Nicolae[1], *J. Vasilescu*[1], *C. Talianu*[1,2], *V. Nicolae*[1], *G. Ciocan*[1,3], *L. Belegante*, *Florica Toanca*[1], *Alexandru Dandocsi*[1]

(1) National Institute of Research and Development for Optoelectronics INOE 2000, Măgurele, Romania
(2) BOKU University, Institute of Meteorology and Climatology, Vienna, Austria
(3) University of Bucharest, Măgurele, Romania

Corresponding author: jeni@inoe.ro

Introduction

Beginning in 2000, EARLINET (European Aerosol Lidar NETwork) conducted aerosol lidar observations throughout Europe. However, with the creation of ACTRIS (Aerosol, Clouds and Trace Gases Research InfraStructure), the methods and instruments for quality certification have recently advanced. The quality and physical substance of lidar data products have been standardized in this context, making it possible to more confidently analyze the aerosol properties in the troposphere. Biomass burning represents one of the major sources of atmospheric particles (aerosols). The sources of smoke particles are both natural (wildfires) and anthropogenic (controlled fires). They contribute significantly to direct radiative forcing, have strong impact on cloud properties, and influence human health. The direct effect on radiative transfer can be both negative and positive as a consequence of the opposite effects of the two main components, black carbon (absorption, positive effect) and organic carbon (scattering, negative effect).

The optical characteristics of smoke aerosol particles measured in Europe are examined in this paper, as determined by EARLINET-ACTRIS lidars between 2015 and 2023 and obtained using the NATALI (Neural network Aerosol Typing Algorithm based on LIdar data) software.

The NATALI method, developed by [1], uses Artificial Neural Networks (ANN) to determine the most probable aerosol type from multispectral data. This technique is executed in Python and modified for use with EARLINET profiles, which include three backscatters, two extinctions, and one linear particle depolarization ratio. ANNs are employed to address the overlapping values of intense optical parameters computed for each recognized layer in the multiwavelength Raman lidar profiles. The aerosol optical characteristics derived from the model [2][3] were compared to existing literature and found to be compatible with observations. Variability in optical characteristics was achieved by examining various mixing ratios and relative humidity levels. The uncertainty of the observations was used to align with actual noisy lidar data.

NATALI employs two parallel typing methodologies to accommodate data sets with or without the measured linear particle depolarization ratio at 532 nm: high-resolution typing for the identification of 14 aerosol mixtures when the linear particle depolarization ratio at 532 nm is present in the input data files, and low-resolution typing for the identification of 5 predominant aerosol types in the absence of the depolarization value. Three artificial neural networks are executed concurrently for each strategy, and a vote mechanism determines the most likely response. NATALI analyzes lidar files in EARLINET NetCDF format, verifies the presence of all necessary parameters, determines the geometrical boundaries of layers, computes intensive optical parameters within each layer, their mean values, and corresponding uncertainties. Only layers exceeding a thickness of 300 m are considered pertinent due to their substantial signal-to-noise ratio. The intensive optical parameters and their corresponding uncertainties are calculated for the central region of each layer, where the signal-to-noise ratio is maximized.

Methodology

In this work we used NATALI to analyse the characteristics of smoke aerosol layers in Europe, by making advanatge of a large lidar dataset that was gathered by EARLINET stations from 2015 to 2023. Level 2 EARLINET-ACTRIS data packages with complete quality assurance were used in our research [4][5]. In total, 23785 aerosol layers were identified based on the 1064 backscatter coefficient profiles.

However, NATALI incorporates many filters, ensuring that only layers meeting the specified requirements are eligible for typing. a) Availability of all requisite intensive optical parameters; b) Values of the intensive optical parameters fall within acceptable limits (Angstrom coefficients between -1 and 3; lidar ratios between 20 and 150 sr); c) The relative error of each intensive optical parameter (Angstrom exponent (AE), color ratios, color indexes (CI), lidar ratios (LR), and linear particle depolarization ratio) is below 50%.

For each layer and for each intensive optical parameter, the module generates a number of values (N, adjustable) between [average – uncertainty] and [average + uncertainty]. Data are then scrambled, considering that any combination has a similar probability to describe the reality. The cluster of possible combinations of intensive optical parameters is prepared for the ANN input. The typing module runs in parallel the ANNs for each data set representing a layer, and applies the voting procedure to identify the most probable aerosol type. A voting procedure selects the most probable answer out of the three (possibly different) individual returns. Selection is done based on the confidence level of the ANN outputs, and the stability over the uncertainty range (percentage of agreement for values between error limits). The analysis focuses on local influences and long-range transport in the low and in the free troposphere. Low troposphere refers to the first layer closest to the ground with a bottom above the minimum product height, potentially carrying particles generated locally. Free troposphere includes all other layers higher than the first layer, potentially transporting particles from large distances. The minimum product height represents the altitude from which optical products are valid, while the maximum first layer bottom is calculated based on climatological values of the Planetary Boundary Layer (PBL) height at each station.

NATALI in low resolution mode was used to identify smoke aerosol layers. Additionally, we used the ratio of the lidar ratios (LR532/355) to account for the age of the smoke particles [6] and the Angstrom exponent values to distinguish between layers with a predominance of pure smoke particles, and layers with mixtures of smoke. Layers with LR532/355 below 1 were considered "fresh", and layers with LR532/355 above 1 were considered "aged". Also, layers with an Angstrom exponent between 1 and 2 were considered "pure", all other being considered "mixtures" (with marine, mineral dust, industrial or continental polluted aerosol).

Results and Discussion

Out of the 23785 aerosol layers identified in the available dataset, only 3778 datasets were complete and satisfying the criteria for typing. In 122 of the cases the ANNs failed to retrieve the predominant aerosol type. For 20129 of the layers, either the set of parameters was incomplete, or the uncertainty of the parameters was too high (Table 1).

Table 1. Number of aerosol layers failing the typing; reasons for each input parameter

Reason of failure	**LR532**	**LR355**	**AE355/532**	**CI355/532**	**CI532/1064**
Missing value of one parameter at the layer altitude	7954	9735	10428	6947	3095
Uncertainties too high	0	0	1726	1358	562
Total	**7954**	**9735**	**12154**	**8305**	**3657**

Distribution of the Angstrom exponent and of the LR532/355 values for all valid smoke datasets measured between 2015 and 2023 by the EARLINET stations are presented in Figure 1. Figure 2 shows the correlation between AE355/532 and the lidar ratio at 355 nm (LR355). Pure and fresh smoke is characterized by almost monomodal distribution for both LR532/355 and the AE355/532, with mean values of the Angstrom exponent around 1.4 and LR355 ranging from 60 to 140 sr. Fresh mixtures show a three-modal distribution for the AE355/532, with medians at -0.5 (mixtures with marine), 0.5 (mixtures with mineral dust) and 2.2 (mixtures with industrial) respectively, while the LR355 values are similar as in the case of fresh and pure smoke. Aged pure smoke is characterized by mono-modal distributions but with lower median

for the AE355/532 around 1.1, and wider spread of the LR532/355 values. The values of the LR355 are lower than in the case of pure and fresh smoke, ranging from 40 to 120 sr. Aged smoke mixtures show a wide spread of all intensive optical parameters, with LR355 values as low as 20 sr, and AE355/532 values as low as -1.

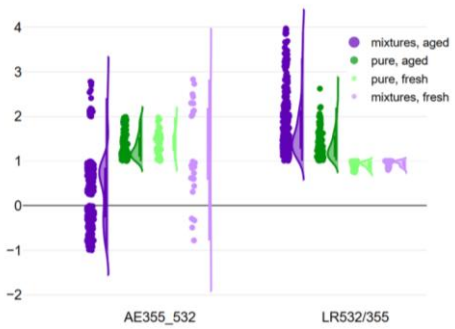

Fig. 1 Distribution of the Angstrom exponent and of the ratio of lidar ratios (532/355) values for pure, fresh, mixed and aged smoke particles

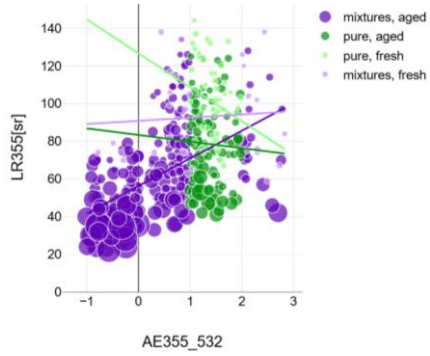

Fig. 2 Correlation of the lidar ratio @ 355 nm and the Angstrom exponent for pure, fresh, mixed and aged smoke particles. Ratio of the lidar ratios (532/355) as the bubble size

The geographical distribution of frequency of apperance of the smoke layers is presented in Figure 3. Smoke is detected in the atmospheric column at almost all lidar stations, with several regions more often affected in Central and East Europe, and in Central and East Mediterranean. In the southern part of Central Europe, smoke seems to be more frequently measured in the free troposphere, while in the northern part is more frequently measured at low levels. Smoke is measured frequently at all levels in East Mediterranean region, more frequently at low altitudes in Central Mediterranean, and more frequently in the free troposphere in Eastern Europe.

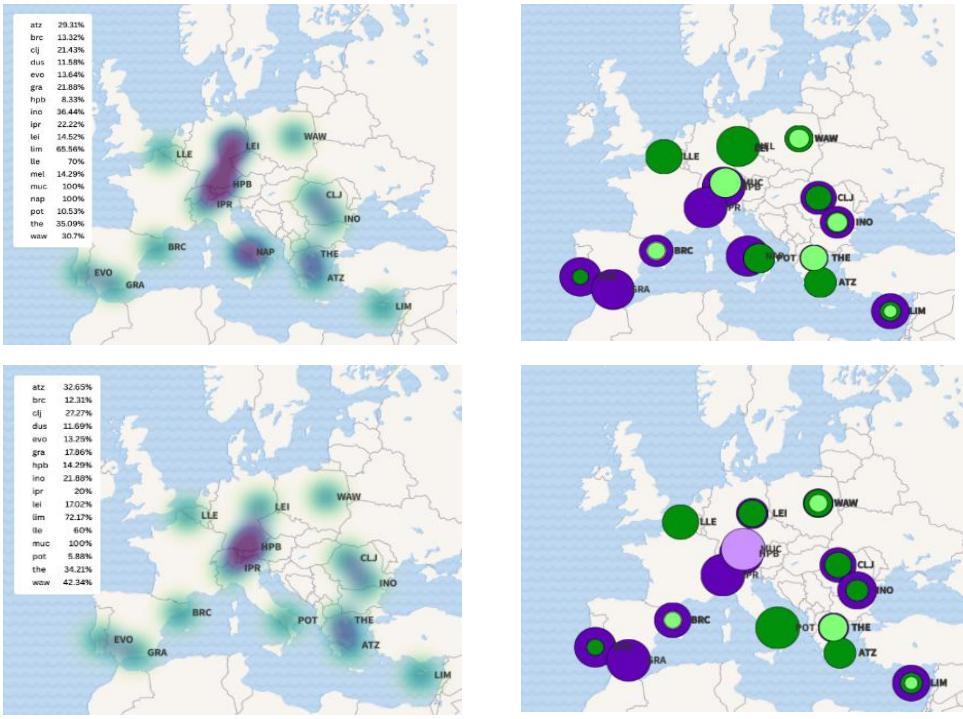

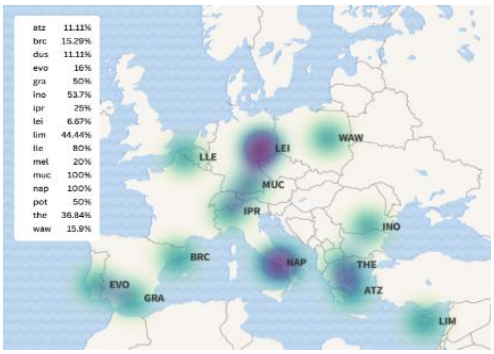

Fig. 3 Frequency of smoke layers, out of total aerosol layers. Increasing frequency from light yellow to green to violet: total column (top), free troposphere (middle) and boundary layer (bottom)

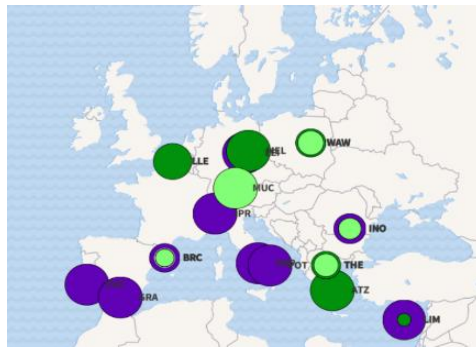

Fig. 4 Preponderance of pure, fresh, mixed and aged smoke particles. Mixtures aged (dark violet), mixtures fresh (light violet), pure aged (dark green), pure fresh (light green): total column (top), free troposphere (middle) and boundary layer (bottom)

The geographical distribution of preponderance of pure, fresh, mixed and aged smoke particles is shown in Figure 4. Within the atmospheric column, mixed smoke (violet colours) is measured at almost all lidar stations, with the exception of the East Mediterranean and the northern part of Central Europe where pure smoke (green colours) is also present. Particles are usually aged (darker shades), although fresh smoke aerosol layers (light shades) are sometime detected at MUC, WAW, INO, THE, LIM and BRC, especially at low altitudes.

Conclusions

The EARLINET database contains important information about the characteristics of aerosols, spanning 2015 to 2023, with an increasing quality in the last years. However, additional filtering is necessary in order to perform aerosol typing or to investigate the specifics of a certain aerosol type. With the available datasets, we managed to characterize pure, fresh, mixed and aged smoke particles in terms of spectral properties and geographical distribution, at low levels and in the free troposphere, for the period 2015-2023.

Acknowledgements

This work is supported by the Core Program within the Romanian National Research Development and Innovation Plan 2022-2027, carried out with the support of MCID, project no. PN 23-05, the ATMO-ACCESS H2020 Grant Agreement no. 101008004, the CARGO-ACT HEU Grant Agreement no. 101132093, and through the ACTRIS ERIC and CARS Cooperation Agreement / 25 April 2023.

References

[1] Nicolae, D. et al.: *A neural network aerosol-typing algorithm based on lidar data*, Atmos. Chem. Phys., 18, 14511–14537, https://doi.org/10.5194/acp-18-14511-2018, 2018

[2] Hess, M., Koepke, P., and Schult, I.: *Optical properties of aerosols and clouds: The software package OPAC*, B. Am. Meteorol. Soc., 79, 831–844, https://doi.org/10.1175/1520-0477(1998)0792.0.CO;2, 1998.

[3] Koepke, P. et al.: *Global Aerosol Data Set, Report No. 243*, Max-Planck-Institut für Meteorologie, Hamburg, ISSN 0937-1060, 1997

[4] D'Amico, G. et al.: *EARLINET Single Calculus Chain – technical – Part 1: Pre-processing of raw lidar data*, Atmos. Meas. Tech., 9, 491–507, https://doi.org/10.5194/amt-9-491-2016, 2016

[5] Mattis, I. et al.: *EARLINET Single Calculus Chain – technical – Part 2: Calculation of optical products*, Atmos. Meas. Tech., 9, 3009–3029, https://doi.org/10.5194/amt-9-3009-2016, 2016.

[6] Nicolae, D. et al.: Characterization of fresh and aged biomass burning events using multiwavelength Raman lidar and mass spectrometry, J. Geophys. Res. Atmos., 118, 2956–2965, doi:10.1002/jgrd.50324, 2013.

Long range transport complexity of mixed biomass burning aerosols over the southwest Indian Ocean: a case study in September 2017.

D. Gantois[1], *A. Baron*[1,2], *M. Sicard*[1], *V. Duflot*[1,3], *N. Bègue*[1], *N. Evangeliou*[3], *G. Payen*[4], *P. Chazette*[5], *C. Flamant*[6]

(1) Laboratoire de l'Atmosphère et des Cyclones, UMR 8105 Université de La Réunion – CNRS – Météo-France, Saint Denis de La Réunion, France
(2) Now at: Cooperative Institute for Research in Environmental Sciences (CIRES), University of Colorado, Boulder, CO, USA and NOAA Chemical Sciences Laboratory
(3) Now at: Department for Atmospheric and Climate Research, NILU – Norwegian Institute for Air Research, Kjeller, Norway
(4) Observatoire des Sciences de l'Univers de La Réunion (OSU-Réunion), UAR3365, Université de La Réunion, CNRS, IRD, Météo-France, 97490 Saint-Denis de La Réunion, France
(5) Laboratoire des Sciences du Climat et de l'Environnement (LSCE)/IPSL, UMR CNRS 1572, CEA, UVSQ, Gif-sur-Yvette, France
(6) Laboratoire Atmosphère Milieux Observations Spatiales (LATMOS)/IPSL, UMR CNRS 8190, Sorbonne Université, UVSQ, Paris, France

Corresponding author: dominique.gantois@univ-reunion.fr

Introduction

The biomass burning (BB) season in the southern hemisphere occurs during the dry season (April - November) [1]. During this period, many fires occur in South America (SA), Austral Africa (AA) and Madagascar (M). Smoke plumes emitted by these fires can influence atmospheric composition over the Indian Ocean after following long-distance routes throughout the troposphere and sometimes recirculate over their emission sites [2, 4].

During September 19th and 25th, 2017, high total column Aerosol Optical Depth (AOD) values were observed over Reunion Island (21.1°S, 55.3°E). Measurements from multi-wavelength ground-based lidars at Maïdo observatory (2160 m asl) were used to confirm the tropospheric origin of the aerosols, derive the vertical structure of the plumes, and assess the vertical distribution of aerosol optical properties and water vapor content. A Lagrangian model was then used to identify the aerosols origins and follow their transport.

Methodology

All ground-based instruments used in this study belong to the Observatory of Atmospheric Physics of La Réunion (OPAR) [5].

The AOD values over Reunion Island were measured by an AERONET CIMEL sun-photometer located in Saint-Denis [4]. Vertical profiles of aerosol extinction and backscatter coefficients were derived from a 532-nm (LiO3T) and 355-nm (Li1200) lidar. Technical specifications for both instruments can be found in a dedicated data paper [6]. A Raman inversion was performed with the 387-nm channel of the Li1200 and allowed us to obtain an LR vertical profile for the highest plume [7]. The high overlap of our instruments made it impossible to perform a correct Raman inversion under 5 km. Klett inversion was then used with the average lidar ratio (LR) deduced from Raman inversion for both lidars [8]. Water vapor content (Water Vapor Mixing Ratio: WVMR) of the aerosol layers was derived from the 407-nm channel of the Li1200 [9]. Depolarization characteristics were determined using polarization channels at 532 nm from the LiO3T [10]. An Ångström exponent (ÅE) was deduced for each plume identified.

The Lagrangian model FLEXPART was used to determine the source and preferred pathways for every plume identified during this event [11]. Black Carbon (BC) was used as the air mass tracer.

Results and Discussion

On September 19th, 2017, the total AOD values at 340 and 500 nm measured by sun-photometer were respectively 0.35 and 0.23. The ground based lidars captured an aerosol plume in the low troposphere between 2.5 and 4.7 km. The specific AOD values at 355 and 532 nm of this plume derived from the lidar measurements were respectively 0.19 and 0.14 (Table 1), lower than total AOD values. This suggests the

presence of aerosols from the ground up to 2.5 km, in a blind zone inherent to the optical geometry of our instruments.

Table 1. Parameters representing the characteristics of the different aerosol plumes previously identified.

Date	Layer height [km]	AOD_{355} [UA]	AOD_{532} [UA]	Ångström [UA]	WVMR [$g.kg^{-1}$]	LR [sr]	PLDR 532 nm [%]
19/09/2017	2.5 → 4.7	0.19	0.14	1.32 ± 0.23	2.10 ± 1.37	75	0.23 ± 0.09
25/09/2017	3.3 → 5	0.12	0.08	1.02 ± 0.12	1.29 ± 0.69	75	0.30 ± 0.02
25/09/2017	5 → 9	0.17	0.10	1.33 ± 0.05	0.09 ± 0.05	75 ± 9	0.15 ± 0.02

Moreover, the sun-photometer used in this study is located above the city of Saint-Denis (80 m asl), which suggests the presence of urban pollution under 2 km affecting the total AOD. This plume was characterized by a WVMR of 2.10 ± 1.37 $g.kg^{-1}$, an ÅE of 1.32 ± 0.23, and a small particle lidar depolarization ratio (PLDR) of 0.23 ± 0.09 %, suggesting the presence of rather small and spherical particles and a strong water content. FLEXPART simulations showed that the plume essentially originated from Austral African fires and recirculated over Austral Africa before travelling over Reunion Island.

On September 25th, 2017, the total AOD values at 340 and 500 nm measured by sun-photometer were respectively 0.39 and 0.25. Ground based lidars captured two aerosol plumes in the low troposphere between 3.3 and 5 km, and in the middle troposphere between 5 and 9 km (Figure 1).

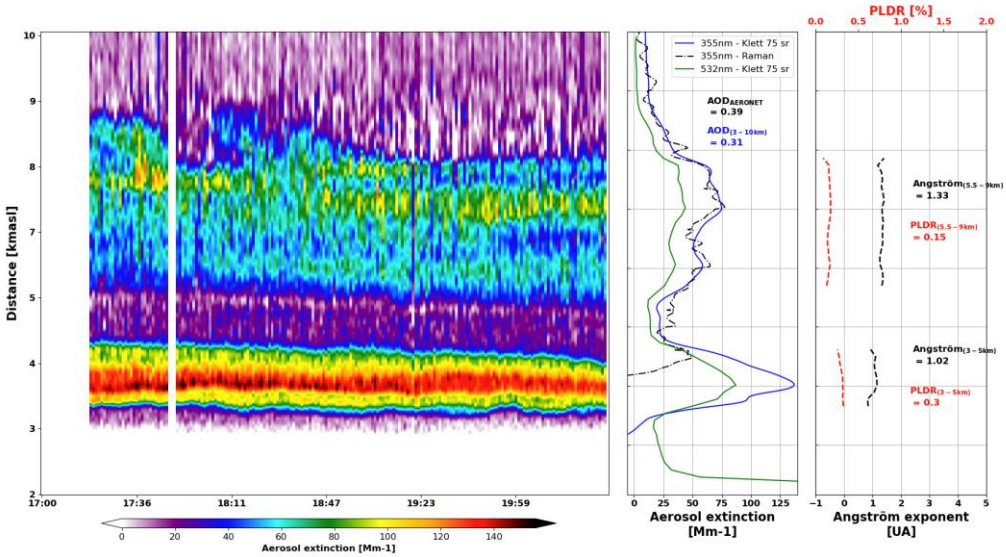

Figure 1. **[left]** Aerosol extinction time-height cross-section over Maïdo facility (Reunion Island) on September 25th, 2017. **[center]** Mean vertical profile of aerosol extinction from Klett inversion at 355 nm (blue curve: Li1200, LR = 50 sr), 532nm (green curve: LiO3T, LR = 50 sr), and from Raman inversion at 387 nm (black dotted curve: Li1200). AOD between 3 and 10 km (blue) is obtained from the Li1200 retrieval, and total AOD (black) from AERONET sun-photometer. **[right]** Ångström exponent (black dotted line) and Particle Linear Depolarization Ratio (red dotted line) vertical profiles from the LiO3T 532nm channels. Corresponding mean values are given for each aerosol layer.

The specific AOD values at 355 and 532 nm for both plumes derived from lidar measurements were respectively 0.12 and 0.08 for the lowest, and 0.17 and 0.10 for the highest (Table 1). Again, the sum of these AODs (0.29 and 0.18) is lower than the total AOD measured by AERONET, probably due to the high overlap of our instruments and the effect of urban pollution on the sun-photometer's measurements. A mean

LR of 75 ± 9 sr was determined from Raman inversion for the highest plume, consistent with biomass burning aerosols. The comparison between extinction and WVMR values (Figure 2) showed two different aerosol layers among the lowest plume with equivalent high values of WVMR but different extinction values.

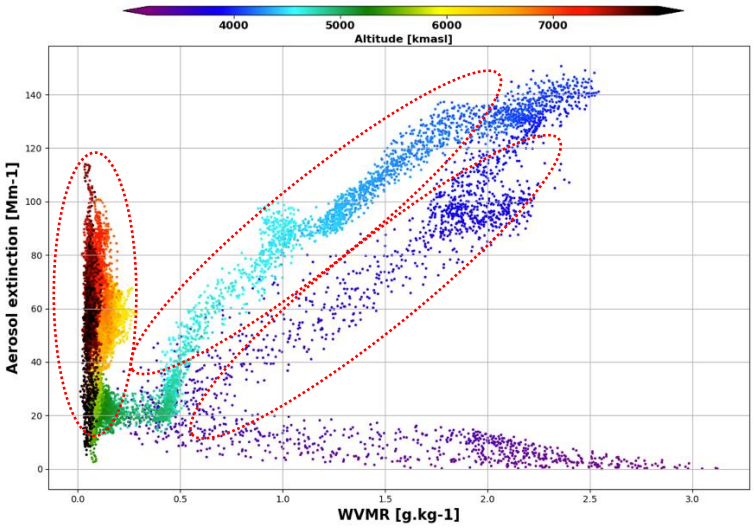

Figure 2. Scatter plot between height-dependent aerosol extinction and water vapor mixing ratio on September 25th, 2017. The three circles with a red dotted line represent different aerosol layers.

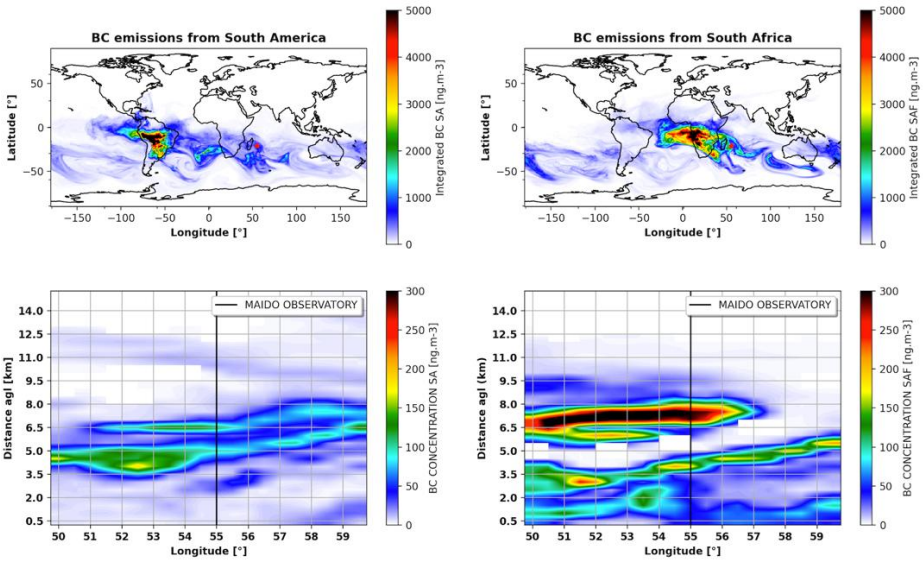

Figure 3. BC total column (0.5 → 15km) from South American (SA) Total Particulate Matter (TPM) emissions (upper-left) and Austral African (AAF) TPM emissions (upper-right) and corresponding vertical profiles of BC concentration over Reunion Island (black line) on September 25th, 2017, using FLEXPART model.

The highest plume was dryer than the lowest plume (WVMR = 0.09 ± 0.056 g.kg^{-1} vs 1.29 ± 0.69 g.kg^{-1}, respectively), with higher values of ÅE (1.33 ± 0.05 vs 1.02 ± 0.12, respectively), and smaller depolarization values (0.15 ± 0.02 % vs 0.30 ± 0.02 %, respectively). This suggests the presence of older and smaller particles in the highest plume. FLEXPART simulations showed that the highest plume essentially originated from Austral African fires and recirculated over Austral Africa before travelling over Reunion Island, whereas the lowest plume was made of mixed aerosols from Austral African fires, and South American fires, following an inter-hemispheric transport (Figure 3).

Conclusions

In this work, multiwavelength ground-based lidars and a Lagrangian model enabled us to analyze two episodes of Biomass Burning plumes responsible for high AOD values over Reunion Island. Lower plumes were made of larger aerosols with higher water content levels and higher depolarization values than those from higher plumes. Aerosols from South African fires are the main contributors of BB plumes over Reunion Island, and follow specific circulatory patterns, explaining their presence at different altitude ranges. Aerosols from South American fires also affect the atmosphere composition, but with a weaker influence.

Acknowledgements

This work was financed by the Horizon Europe European Research Council (project REALISTIC, grant no. 101086690), the Agence Nationale de la Recherche (project OBS4CLIM, grant no. ANR-21-ESRE-0013) and CNES through the projects EECLAT, AOS, and EXTRA-SAT. The authors acknowledge the CNRS (INSU), Météo France, and Université de la Réunion for funding the infrastructure Observatoire de Physique de l'Atmosphère à la Réunion (OPAR) and acknowledge the Observatoires des Sciences de l'Univers à la Réunion, UAR 3365 (OSU-R), for managing it. Finally, Eric Golubic, Patrick Hernandez, and Yann Hello are greatly thanked for the routine lidar measurements obtained at OPAR.

In this work we used L2b lidar data from the Li1200 lidar instrument (https://doi.org/10.25326/714) and from the LiO3T system (https://doi.org/10.25326/712).

References

[1] Edwards, DP. et al.: *Satellite-observed pollution from Southern Hemisphere biomass burning*, J Geophys Res., 111(D14): D14312, 2006.

[2] Bencherif H. et al.: *Investigating the Long-Range Transport of Aerosol Plumes Following the Amazon Fires (August 2019): A Multi-Instrumental Approach from Ground-Based and Satellite Observations.* Remote Sens., 12(22):3846, 2020.

[3] Duflot V. et al.: *Aerosols on the Tropical Island of La Reunion (21°S, 55°E): Assessment of Climatology, Origin of Variability and Trend.* Remote Sens, 14(19):4945, 2022

[4] Ranaivombola M. et al.: *Aerosol Optical Properties and Types over Southern Africa and Reunion Island Determined from Ground-Based and Satellite Observations over a 13-Year Period (2008–2021).* Remote Sens., 15 (6), pp.1581, 2023.

[5] Baray J.-L et al.: *Maïdo observatory: a new high-altitude station facility at Reunion Island (21° S, 55° E) for long-term atmospheric remote sensing and in situ measurements.* Atmospheric Meas. Tech., 6, 2865–2877, https://doi.org/10.5194/amt-6-2865-2013, 2013.

[6] Gantois D. et al.: *Multiwavelength aerosol lidars at the Maïdo supersite, Réunion Island, France: instrument description, data processing chain, and quality assessment.* Earth System Science Data, 16 (9), pp.4137-4159. ⟨10.5194/essd-16-4137-2024⟩. ⟨insu-04595142v2⟩, 2024.

[7] Ansmann A. et al.: *Independent measurement of extinction and backscatter profiles in cirrus clouds by using a combined Raman elastic-backscatter lidar*. Appl. Opt., 31, 7113, https://doi.org/10.1364/AO.31.007113, 1992.

[8] Klett, J. D.: *Stable analytical inversion solution for processing lidar returns.* Appl. Opt., 20, 211, https://doi.org/10.1364/AO.20.000211, 1981.

[9] Vérèmes H. et al.: *Validation of the Water Vapor Profiles of the Raman Lidar at the Maïdo Observatory (Reunion Island) Calibrated with Global Navigation Satellite System Integrated Water Vapor*. Atmosphere, 10, 713, https://doi.org/10.3390/atmos10110713, 2019.

[10] Behrendt A. and Nakamura T.: *Calculation of the calibration constant of polarization lidar and its dependency on atmospheric temperature*. Opt. Express, 10, 805, https://doi.org/10.1364/OE.10.000805, 2002.

[11] Pisso I. et al.: *The Lagrangian particle dispersion model FLEXPART version 10.4*. Geosci. Model Dev., 12, 4955–4997, https://doi.org/10.5194/gmd-12-4955-2019, 2019.

Exceptionally intensive Saharan dust transport over Warsaw, Poland in April 2024

D. M. Szczepanik[1], *W. Kumala*[1], *R. Engelmann*[2], *L. Belegante*[3], *I.S. Stachlewska*[1]

(1) University of Warsaw, Faculty of Physics, Institute of Geophysics, (IGFUW), Pasteura 5, 02-093, Warsaw, Poland
(2) Leibniz Institute for Tropospheric Research (TROPOS), Permoserstraße 15, 04318 Leipzig, Germany
(3) National Institute of Research and Development for Optoelectronics-INOE 2000, Str. Atomistilor 409, Măgurele, 077125, Ilfov, Romania

Corresponding author: dominika.szczepanik@fuw.edu.pl

Introduction

Mineral dust aerosol which is formed over the desert areas, is not only one of the most common aerosol types in the atmosphere but also plays a significant role in the climate system (dust-climate feedback) and is weather-relevant due to its interactions with clouds and precipitation formation.

Due to the increasing frequency of desert dust events over Central and Eastern Europe, it is essential to investigate their properties in order to better assess its impact on the climate. Moreover, such studies contribute to the improvement of aerosol forecast models, which currently tend to underestimate the amount of desert dust observed in this region.

In this work we are presenting the analysis of a wide-spread and exceptionally intensive Saharan dust inflow over Warsaw (52.21 N, 20.98 E, 112 m a.s.l.). It was observed thanks to the 24/7 lidar measurements taken with the next-generation PollyXT lidar [1] on the Remote Sensing Laboratory (RS-Lab), which is a part of European Aerosol Research LIdar NETwork (EARLINET) research infrastructure.

Methodology

For the data evaluation and the interpretation of the results, we followed the methodology described in details in Szczepanik et al. 2021 [2].

To analyze the lidar measurements and derive atmospheric optical property profiles, the Raman method was employed [2]. The POLIPHON separation algorithm [3] was applied to estimate the contribution of desert dust to the particle backscatter coefficient profile at 532 nm.

To identify potential aerosol sources, the HYSPLIT model [4] was used to compute backward air mass trajectories. The interpretation of these results was further supported by multi model desert dust forecast product available at available at the WMO Barcelona Dust Regional Center site [5].

Last but not least the inversion data products provided by the AERONET were analyzed to discuss the aerosol size distribution observed during the event [6].

Results and Discussion

The event started approximately at 07:00 UTC on 07.04.2019 and lasted for 93 hours, which is the most intensive dust inflow captured in Warsaw. The strongly depolarizing aerosol was observed with the evolving layer between 2-7 km in the vertical direction. After more than 2 days of dust presence in almost clear sky conditions (Figure 1), clouds started to form at the aerosol layer strongly affecting the measurements.

During this airmasses inflow Warsaw citizens experienced extremely hot air temperatures, reaching the maximum values of 27.8°C, which is approx. 18°C higher than the climatological mean temperature of April in Poland. Such raised temperatures can also suggest the transport from the desert areas.

To verify the hypothesis of desert dust presence within the free troposphere backward trajectories were calculated and superimposed on the desert dust prediction model outputs. One of the obtained results is depicted in Figure 2. Thanks to this approach one can see the good agreement between model outputs. The air masses associated with this aerosol inflow followed the predicted path of mineral dust over Western Europe. Notably, the trajectories passed through Eastern France and Germany, while bypassing Spain, which is quite unusual for Saharan dust transport to Poland. Additionally, the airflow was very rapid in the last 24 hours, suggesting that the observed Saharan dust was relatively fresh.

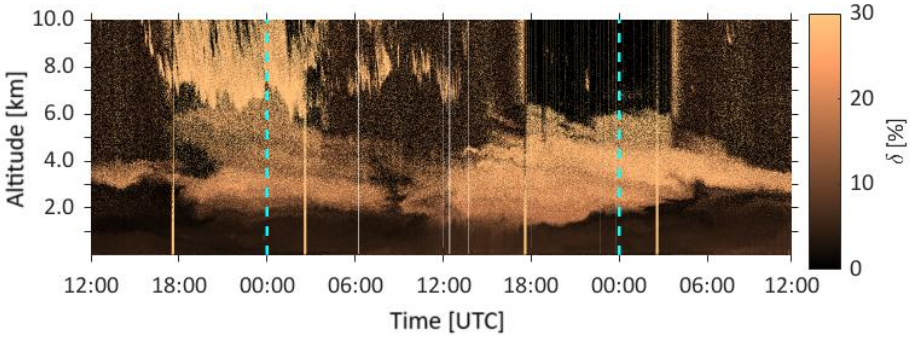

Figure 1. Lidar signal polarization δ quick look at 532 nm for the period 7–9.04.2024. Here, we present the most interesting (cloud-free) part of the intense dust inflow from the Sahara, observed between 7–11.04.2024.

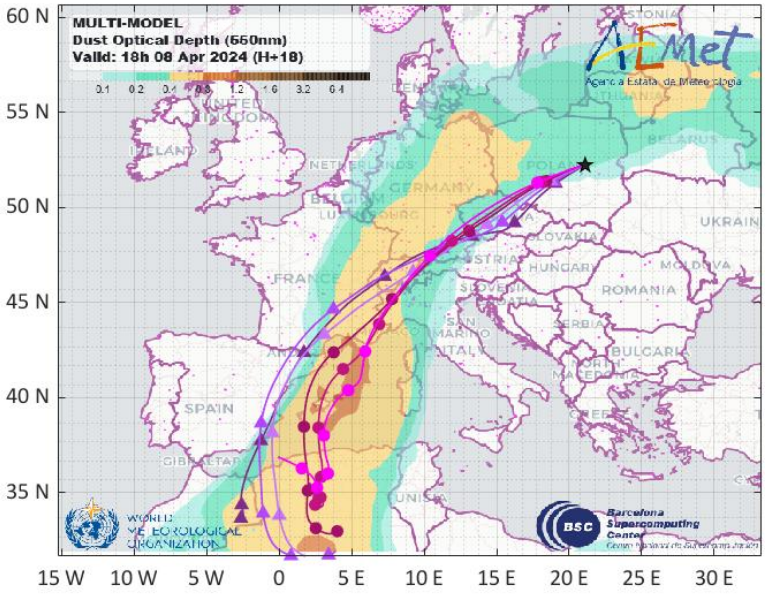

Figure 2. Aerosol optical depth at 550 nm (color bar) of mineral dust forecast, with superimposed backward trajectories for 08.04.2024. Multi-model desert dust optical depth forecast at 12:00 UTC, valid for 18:00 UTC. HYSPLIT model calculations for 96 hours, starting at 18:00 UTC, were conducted within the aerosol plume. The forecast indicates that the air masses originating from North Africa likely contained mineral dust, as the trajectories followed a similar path. Source: https://ready.arl.noaa.gov/index.php & https://dust.aemet.es/products/daily-dust-products?tab=forecast&var=aod&model=median&date=20240408&view=light&step=12

For the optical data analysis, we obtained more than 70 full sets of profiles which are considered to be the set of three particle backscattering ($3\beta_p$), two particle extinction ($2\alpha_p$), and two particle linear depolarization ratios ($2\delta_p$), which allows the calculation of the lidar ratio (LR) and Ångström exponents (AE_α and AE_β), an example of such full set of profiles is given in Figure 3a. Observed Saharan dust was strongly depolarizing light resulting in δ_p of 24±2% and 30±2% at 355 and 532 nm respectively. Obtained lidar ratios varying between 55±10 sr for 355 nm and 50±10 sr for 532 nm are in agreement with the literature values for the Saharan dust over Warsaw [2, 7]. Low values of Ångström exponents (AE_α and AE_β oscillating

around 0) suggest the presence of large particles. This effect is also seen in the values of the particle backscattering coefficient, which is the highest at 532 nm, while comparable for 355 and 1064 nm.

POLIPHON separation results show that 66±8% of the backscattering profile was caused by coarse dust particles (Figure 3b, brown line), while 23±10% by the fine dust particles (Figure 3b, yellow line). This suggests the freshness of the observed aerosol, which was not affected by the gravitational sedimentation and did not undergo interactions with water vapor.

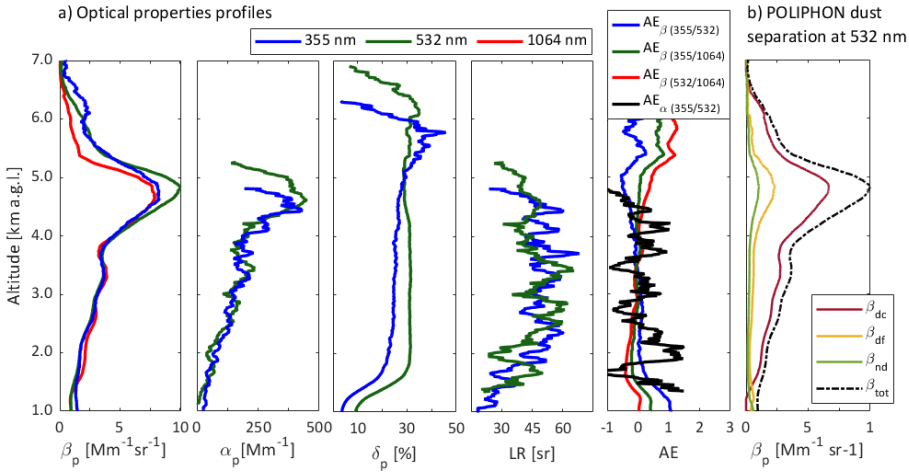

Figure 3. a) Mean of manually evaluated profiles of aerosol optical properties from 18:00-18:30 and 19:00-19:30 on 08.04.2024 (from left-hand-side): aerosol backscattering β_p, extinction α_p, particle linear depolarization δ_p coefficients, lidar ratio LR and Ångström exponents AE_α and AE_β; **b)** Saharan dust-related backscattering coefficient at 532 nm divided into coarse dust fraction β_{dc} and fine dust fraction β_{df}. The contribution from other aerosol types β_{nd} is marked with green and the total backscattering coefficient for the 532 nm channel - β_{tot} - marked in black [3].

To have an overview of the possible sizes of the observed aerosol we analysed the size distribution inverted from the sun photometer measurements (Figure 4, [6]). It revealed that the distribution was changing with the inflow evolution, which suggest the high dynamics of the inflow, but on every stage was dominated by the particles of the radius larger than 1μm. During the full evolution of the event it was even bi-modal (Figure 4, brown line).

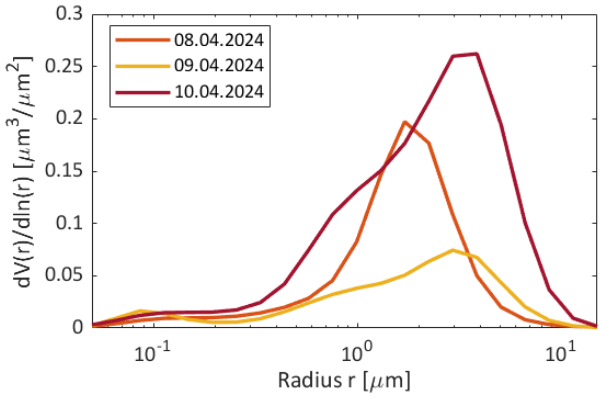

Figure 4. Aerosol size distribution in the vertical column of the atmosphere inverted from the sun photometer data. Modified after AERONET, https://aeronet.gsfc.nasa.gov

Conclusions

Between 07-11.04.2024, Warsaw experienced a very intensive Saharan dust inflow which was also causing exceptionally high air temperatures. This long-lasting aerosol transport (longer than 90 hours) led to cloud formation and significantly changed the optical properties of the atmosphere.

This rapid inflow of an unexpected pathway carried a massive amount of Saharan dust, which did not undergo the aging and gravitational sedimentation processes, which is rare for Central and Eastern Europe.

The increasing intensity of the dust transport can lead to the conclusion of the intensification of the desertification processes and for sure one can expect the stronger effect of the climate-dust feedback. Such observations can be treated as another piece of evidence of the ongoing climate changes and the shift of the climate zones.

Acknowledgements

This work was financed by NCN Preludium 19 „ProDust" (no. 2020/37/N/ST10/02682), ACTRIS-ERIC (no. 2024/WK/04), and NCN Wave-UNISONO AEROPAN (no. 2021/03/Y/ST10/00206) project.

In this work we used data from HYSPLIT model obtained via NOAA Air Resources Laboratory (ARL) through the READY website (https://www.ready.noaa.gov) and dust data images provided by the WMO Barcelona Dust Regional Center and the partners of the Sand and Dust Storm Warning Advisory and Assessment System (SDS-WAS) for Northern Africa, the Middle East and Europe (https://dust.aemet.es/products/daily-dust-products).

References

[1] Engelmann, R. et al.: The automated multiwavelength Raman polarization and water-vapor lidar PollyXT: The neXT generation., Atmospheric Measurement Techniques, 9. 1767-1784, doi:10.5194/amt-9-1767-2016, 2016.

[2] Szczepanik D., Stachlewska I.S., Tetoni E., and Althausen D.: Properties of Saharan dust versus local urban dust—A case study. Earth and Space Science, 8, e2021EA001816. https://doi.org/10.1029/2021EA001816, 2021

[3] Mamouri, R. E., and Ansmann, A.: Fine and coarse dust separation with polarization lidar, Atmospheric Measurement Techniques, 7, 3717-3735, https://doi.org/10.5194/amt-7-3717-2014, 2014.

[4] Stein, A. et al.: NOAA's HYSPLIT atmospheric transport and dispersion modelling system, Bulletin of American Meteorological Society, 96, 2059–2077. http://dx.doi.org/10.1175/BAMS-D-14-00110.1, 2015.

[5] Basart S. et al.: The WMO SDS-WAS Regional Center for Northern Africa, Middle East and Europe, E3S Web Conf. Volume 99 Central Asian DUst Conference (CADUC 2019), https://doi.org/10.1051/e3sconf/20199904008, 2019
Atmospheric Chemistry and Physics, 12, 2933–2958, doi:10.5194/acp-12-2933-2012, 2012.

[6] Sinyuk, A. et al.: The AERONET Version 3 aerosol retrieval algorithm, associated uncertainties and comparisons to Version 2. Atmos. Meas. Tech. 13, 3375–3411, https://doi.org/10.5194/amt-13-3375-2020, 2020.

[7] Szczepanik D. et al.: Spatio-temporal evolution of long-range transported mineral desert dust properties over rural and urban sites in Central Europe, Science of The Total Environment, Volume 903, https://doi.org/10.1016/j.scitotenv.2023.166173, 2023

The Change of the lidar ratio with hygroscopic growth – A lidar study at 355, 532 and 1064 nm for continental aerosol

M. Haarig[1], *H. Baars*[1], *R. Engelmann*[1], *J. Hofer*[1], *B. Gast*[1], *D. Althausen*[1], *A. Ansmann*[1]

(1) Leibniz Institute for Tropospheric Research (TROPOS), Permoserstr. 15, 04318 Leipzig, Germany

Corresponding author: haarig@tropos.de

Introduction

The extinction-to-backscatter ratio (lidar ratio) is an important quantity in aerosol typing (e.g., [1]). It requires independent observations of the backscatter and extinction coefficients which can be achieved by high spectral resolution lidars (HSRL) or Raman lidars. The much simpler backscatter lidars, like ceilometers or the spaceborne lidar CALIPSO, have to assume a lidar ratio to retrieve the extinction coefficient. The lidar ratio depends on aerosol type (e.g., [2]). For a given aerosol type, the lidar ratio might vary with source region (e.g., for mineral dust [3]) with age (e.g., for smoke [4]) or relative humidity as in the case of continental aerosol. An increase of the lidar ratio with RH for continental aerosol was predicted by [5], and retrieved from in situ observations by [6] in central Germany.

Here, we present a case study of the hygroscopic growth of the lidar ratio of continental aerosol observed at Leipzig, Germany. Extinction observations are available at 1064 nm as well [7] and so we can present the hygroscopic growth parameters at 355, 532 and 1064 nm for the backscatter coefficient, extinction coefficient and lidar ratio.

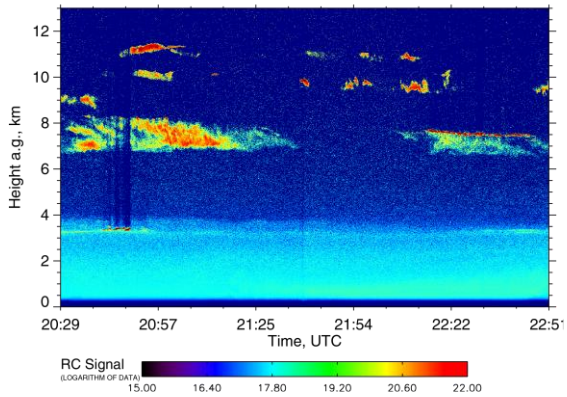

Figure 1. Time-height display of the range-corrected signal at 532 nm (cross-polarized channel) observed by BERTHA at Leipzig on 7 August 2018. The figure is adapted from Haarig et al., 2025 [8].

Lidar observations

Figure 1 presents the time-height section of the observations with the Backscatter Extinction lidar-Ratio Temperature Humidity profiling Apparatus (BERTHA, [9]) obtained on 7 August 2018. The scene is characterized by an extended planetary boundary layer reaching up to 4 km height. The profiles of the optical properties shown in Fig. 2 reveal a strong increase of the backscatter and extinction coefficient between 2.9 and 3.3 km height. This increase is characterized by a strong increase in relative humidity (RH). The relative humidity was derived from the water vapor mixing ratio from Polly^{XT}, which was calibrated by a microwave radiometer and the temperature profile from ECMWF.

The hygroscopic growth can be studied in the layer between 2 and 3.3 km height. In this height range, the potential temperature and water vapor mixing ratio stayed constant [8]. These are important parameters to check that the increase of the optical properties is due hygroscopic growth and not due to different particle concentrations. Backward trajectories indicated that the airmasses travelled during the 72 h prior to its arrival from northern France to Leipzig. The intensive optical properties fit the expectations of continental aerosol (e.g., [1,2]).

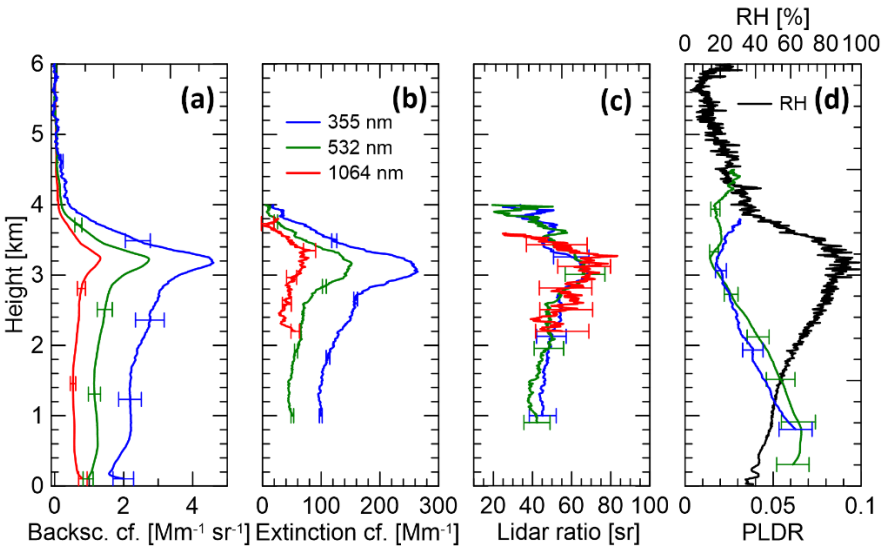

Figure 2. Profiles of the (a) backscatter coefficient, (b) extinction coefficient, (c) lidar ratio and (d) particle linear depolarization ratio (PLDR) and the relative humidity (RH). The lidar measurements were performed on 7 August 2018 between 20:55 and 22:51 UTC at Leipzig, Germany. Data at 355 (blue) and 532 nm (green) were obtained from Polly^{XT} observations, whereas the profiles at 1064 nm (red) were obtained from BERTHA. The figure is adapted from [8].

Hygroscopic growth parameterization

Enhancement factors *f* of the optical properties *x* are calculated

$$f_x(\mathrm{RH},\lambda) = \frac{x(\mathrm{RH},\lambda)}{x(\mathrm{RH_{ref}},\lambda)}$$

From these enhancement factors, the hygroscopic growth parameters $\gamma_x(\lambda)$ [10] can be derived by fitting the points shown in Fig. 3:

$$f_x(\mathrm{RH},\lambda) = \left(\frac{1-RH/100}{1-\mathrm{RH_{ref}}/100}\right)^{-\gamma_x(\lambda)}$$

In total, it results in 9 hygroscopic growth parameters, for the backscatter coefficient, the extinction coefficient and the lidar ratio at 355, 532 and 1064 nm, respectively.

Results and Discussion

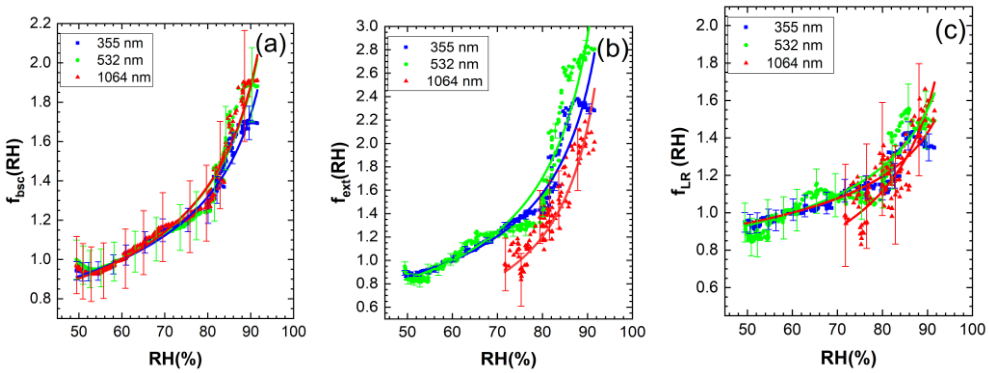

Figure 3. Hygroscopic growth parameterization for the (a) backscatter coefficient, (b) extinction coefficient and (c) lidar ratio at 355 nm (blue), 532 nm (green) and 1064 nm (red). The figure is adapted from Haarig et al., 2025 [8].

In the abstract, we focus on the most important findings, a detailed discussion is provided in [8].

1. The extinction enhancement is stronger than the backscatter enhancement, which results in an enhancement of the lidar ratio as can be clearly seen in Fig. 3.
2. The lidar ratio enhancement increases with wavelength. The strongest enhancement was found at 1064 nm (γ_{LR}(1064 nm) = 0.45 ±0.07), compared to γ_{LR}(532 nm) = 0.32 ±0.01 and γ_{LR}(355 nm) = 0.26 ±0.01.

Let's briefly compare the values to previous literature (Tab. 1). Backscatter enhancement factors for continental aerosol were reported in lidar literature [11-13] and are in the same range as our observations. The extinction enhancement factors are in the upper range of the values reported by [14] from 4 years of measurements at Leipzig with a spectral aerosol extinction monitoring system (γ_{ext}(550 nm) 0.46 ± 0.30). Continental aerosol is a mixture of different sources (anthropogenic, biological, soil, etc.) and may vary with location and season. Therefore, its optical properties can vary considerably which makes it hard to compare between different studies, e.g., [15] measured at Barcelona, which is more affected by marine aerosol than Leipzig which is located 400 km away from the coast.

The focus will be given to the comparison to the lidar ratio enhancement factors. [5] modeled the lidar ratio enhancement for continental aerosol and found that the lidar ratios vary between 40 and 80 sr. However, his modeled spectral behavior is not consistent with our observations. [16] derived the hygroscopic growth parameter (γ_r = 0.3 ± 0.05) from the in-situ measurements to describe the changes in particle radius r. In these observations, they found an increase in the lidar ratio of f_{LR} (351 nm) = 1.26 when increasing RH from 60 to 90-95%. For the same RH range, the lidar ratio enhancement factor in our observations was 1.34 at 355 nm. From a combination of in situ instrumentation on an airborne platform and Mie calculations, [6] derived lidar ratio hygroscopic growth parameters of γ_{LR}(355 nm) = 0.29 ±0.01, γ_{LR}(532 nm) = 0.48 ±0.01 and γ_{LR}(1064 nm) = 0.31 ±0.01 for the rural site of Melpitz, Germany. These calculations are now confronted with Raman lidar measurements and agreement was found only at 355 nm. During their campaign, [6] could not reach closure with the collocated lidar observations for the longer wavelengths.

Table 1. Hygroscopic growth parameters for the extinction coefficient, backscatter coefficient and lidar ratio.

Location	γ_{ext}**(355 nm)**	γ_{ext}**(532 nm)**	γ_{ext}**(1064 nm)**	**Reference**
Leipzig, Germany	0.65 ±0.01	0.77 ±0.03	0.83 ±0.16	This study [8]
	γ_{bsc}**(355 nm)**	γ_{bsc}**(532 nm)**	γ_{bsc}**(1064 nm)**	
Leipzig, Germany	0.40 ±0.01	0.45 ±0.02	0.46 ±0.03	This study [8]
Sierra Nevada, Spain	0.40 ±0.01	0.45 ±0.01	--	[11]
Payerne, Switzerland	0.48 ±0.08	--	0.29 ±0.08	[12]
Barcelona, Spain (>2km)	0.71 ±0.32	0.70 ±0.30	0.73 ±0.30	[15]
	γ_{LR}**(355 nm)**	γ_{LR}**(532 nm)**	γ_{LR}**(1064 nm)**	
Leipzig, Germany	0.26 ±0.01	0.32 ±0.01	0.45 ±0.07	This study [8]
Melpitz, Germany	0.29 ±0.01	0.48 ±0.01	0.31 ±0.01	[6]

Conclusions

With our study, we could show with direct measurements that the lidar ratio of continental aerosol depends on RH and we could derive hygroscopic growth parameters for each wavelength for the backscatter coefficient, extinction coefficient and lidar ratio. The main uncertainty in the practical application of our findings lies in the variability of the composition of continental aerosol.

References

[1] Groß, S.; Esselborn, M.; Weinzierl, B.; Wirth, M.; Fix, A. & Petzold, A.: *Aerosol classification by airborne high spectral resolution lidar observations*, Atmospheric Chemistry and Physics, 13, 2487–2505, https://doi.org/10.5194/acp-13-2487-2013, 2013.

[2] Floutsi, A.A. et al.: *DeLiAn – a growing collection of depolarization ratio, lidar ratio and Ångström exponent for different aerosol types and mixtures from ground-based lidar observations*, Atmospheric Measurement Techniques, 16, 2353–2379, https://doi.org/10.5194/amt-16-2353-2023, 2023.

[3] Hofer, J.; Ansmann, A.; Althausen, D.; Engelmann, R.; Baars, H.; Fomba, K.W.; Wandinger, U.; Abdullaev, S.F. & Makhmudov, A.N.: *Optical properties of Central Asian aerosol relevant for spaceborne lidar applications and aerosol typing at 355 and 532 nm*, Atmospheric Chemistry and Physics, 20, 9265–9280, https://doi.org/10.5194/acp-20-9265-2020, 2020.

[4] Janicka, L. et al.: *Long term observations of biomass burning aerosol over Warsaw by means of multiwavelength lidar*, Optics Express, 31, 33150–33174, https://doi.org/10.1364/OE.496794, 2023.

[5] Ackermann, J.: *The Extinction-to-Backscatter Ratio of Tropospheric Aerosol: A Numerical Study*, Journal of Atmospheric and Oceanic Technology, 15, 1043–1050, https://doi.org/10.1175/1520-0426(1998)015<1043:TETBRO>2.0.CO;2, 1998.

[6] Düsing, S.; Ansmann, A.; Baars, H.; Corbin, J. C.; Denjean, C.; Gysel-Beer, M.; Müller, T.; Poulain, L.; Siebert, H.; Spindler, G.; Tuch, T.; Wehner, B. & Wiedensohler, A.: *Measurement report: Comparison of airborne, in situ measured, lidar-based, and modeled aerosol optical properties in the central European background – identifying sources of deviations*, Atmospheric Chemistry and Physics, 21, 16745–16773, https://doi.org/10.5194/acp-21-16745-2021, 2021.

[7] Haarig, M.; Engelmann, R.; Ansmann, A.; Veselovskii, I.; Whiteman, D.N. & Althausen, D.: *1064 nm rotational Raman lidar for particle extinction and lidar-ratio profiling: cirrus case study*, Atmospheric Measurement Techniques, 9, 4269–4278, https://doi.org/10.5194/amt-9-4269-2016, 2016.

[8] Haarig, M.; Engelmann, R.; Baars, H.; Gast, B.; Althausen, D. & Ansmann, A.: *Discussion of the spectral slope of the lidar ratio between 355 nm and 1064 nm from multiwavelength Raman lidar observations*, EGUsphere[preprint], 2025, 1–35, https://doi.org/10.5194/egusphere-2025-449, 2025.

[9] Haarig, M.; Ansmann, A.; Althausen, D.; Klepel, A.; Groß, S.; Freudenthaler, V.; Toledano, C.; Mamouri, R.-E.; Farrell, D.A.; Prescod, D.A.; Marinou, E.; Burton, S.P.; Gasteiger, J.; Engelmann, R. & Baars, H.: *Triple-wavelength depolarization-ratio profiling of Saharan dust over Barbados during SALTRACE in 2013 and 2014*, Atmospheric Chemistry and Physics, 17, 10767–10794, https://doi.org/10.5194/acp-17-10767-2017, 2017.

[10] Hänel, G.,: *Parameterization of the influence of relative humidity on optical aerosol properties*, in Gerber H.E. & Deepak, A. (Eds.): Aerosols and their Climatic Effects, Deepak Publishing Hampton VA, 117–122, ISBN 0937194069, 1984.

[11] Bedoya-Velásquez, A.E.; Navas-Guzmán, F.; Granados-Muñoz, M.J.; Titos, G.; Román, R.; Casquero-Vera, J. A.; Ortiz-Amezcua, P.; Benavent-Oltra, J.A.; de Arruda Moreira, G.; Montilla-Rosero, E.; Hoyos, C.D.; Artiñano, B.; Coz, E.; Olmo-Reyes, F.J.; Alados-Arboledas, L. & Guerrero-Rascado, J.L.: *Hygroscopic growth study in the framework of EARLINET during the SLOPE I campaign: synergy of remote sensing and in situ instrumentation*, Atmospheric Chemistry and Physics, 18, 7001–7017, https://doi.org/10.5194/acp-18-7001-2018, 2018.

[12] Navas-Guzmán, F.; Martucci, G.; Collaud Coen, M.; Granados-Muñoz, M. J.; Hervo, M.; Sicard, M. & Haefele, A.: *Characterization of aerosol hygroscopicity using Raman lidar measurements at the EARLINET station of Payerne*, Atmospheric Chemistry and Physics, 19, 11651–11668, https://doi.org/10.5194/acp-19-11651-2019, 2019.

[13] Miri, R.; Pujol, O.; Hu, Q.; Goloub, P.; Veselovskii, I.; Podvin, T. & Ducos, F.: *Innovative aerosol hygroscopic growth study from Mie–Raman–fluorescence lidar and microwave radiometer synergy*, Atmospheric Measurement Techniques, 17, 3367–3375, https://doi.org/10.5194/amt-17-3367-2024, 2024.

[14] Skupin, A.; Ansmann, A.; Engelmann, R.; Seifert, P. & Müller, T.: *Four-year long-path monitoring of ambient aerosol extinction at a central European urban site: dependence on relative humidity*, Atmospheric Chemistry and Physics, 16, 1863–1876, https://doi.org/10.5194/acp-16-1863-2016, 2016.

[15] Sicard, M.; Fortunato dos Santos Oliveira, D. C.; Muñoz-Porcar, C.; Gil-Díaz, C.; Comerón, A.; Rodríguez-Gómez, A. & Dios Otín, F.: *Measurement report: Spectral and statistical analysis of aerosol hygroscopic growth from multi-wavelength lidar measurements in Barcelona, Spain*, Atmospheric Chemistry and Physics, 22, 7681–7697, https://doi.org/10.5194/acp-22-7681-2022, 2022.

[16] Ferrare, R.A.; Melfi, S.H.; Whiteman, D.N.; Evans, K.D.; Poellot, M. & Kaufman, Y.J.: *Raman lidar measurements of aerosol extinction and backscattering: 2. Derivation of aerosol real refractive index, single-scattering albedo, and humidification factor using Raman lidar and aircraft size distribution measurements*, Journal of Geophysical Research: Atmospheres, 103, 19673–19689, https://doi.org/10.1029/98JD01647. 1998.

Observation of a mixed dust and BBA layer with RAMSES, ALV, and ATLID over the Lindenberg Meteorological Observatory on 4–5 April 2025

J. Reichardt[1], *F. Lauermann*[1], *O. Behrendt*[1]

(1) Deutscher Wetterdienst (DWD), Meteorologisches Observatorium Lindenberg, Am Observatorium 12, 15848, Tauche OT Lindenberg, Germany

Corresponding author: jens.reichardt@dwd.de

Introduction

The Lindenberg Meteorological Observatory operates, among its comprehensive suite of instruments, the spectrometric fluorescence and Raman lidar RAMSES for investigations into cloud microphysics, aerosol fluorescence, and aerosol-cloud interaction. Since 2024, the observatory participates in the German Initiative for the Validation of EarthCARE (GIVE). As a contribution to this project, the new ATLID Validator (ALV) lidar was developed to perform measurements during the satellite's overflights. ALV duplicates the Atmospheric Lidar (ATLID) onboard EarthCARE in terms of measurement parameter set and observation geometry (3° tilt) while RAMSES measures vertically [1, and references therein].

During the night of 4–5 April 2025, RAMSES and ALV made measurements of a cirrus system with an embedded elevated aerosol layer that can be considered unique in several respects. First, the aerosols exhibited clearly the elastic scattering properties of dust while the fluorescence spectra indicated the presence of biomass burning aerosol (BBA), a combination that had not been observed over Lindenberg before. Second, EarthCARE had an overpass very near to the observatory during a gap in the cirrus cover shortly after midnight, which permits evaluation of the ATLID data products obtained for the mixed aerosol layer. In this contribution, the aerosol measurements with the two ground-based lidars and with ATLID are presented and compared.

Methodology

Standard Raman, polarization, and spectrometric lidar techniques were applied to analyze the RAMSES and ALV measurements. Data integration time is 1200 s. The resolution of the raw data is 60 m, signal profiles are smoothed with a sliding-average length increasing with height. The Level 2a ATLID aerosol (A-AER) and target classification (A-TC) products were used (baseline AE, orbit 4840, frame B) [2,3]. HYSPLIT trajectory analyses [4,5] were carried out following the approach described in [1], but augmented by an assessment of northern-hemisphere ATLID transects in the period between the emission of the aerosols and their observation.

Results and Discussion

Figure 1 displays the RAMSES measurement in the night of 4–5 April 2025 between 20:00 and 03:00 UTC. The key parameters for spectrometric aerosol fluorescence studies are presented. The aerosol field covers almost the entire free troposphere, but its most striking feature is the strongly fluorescence layer at 8–11 km. In fact, fluorescence was so pronounced that even with the correction scheme demonstrated in [6] relative humidity could not reliably be obtained in this height range. An interplay between the surrounding ice clouds and the aerosol is obvious, especially intriguing is the intermittent ice particle formation at 23:20 and 00:00 UTC, but it is not further discussed here for reasons of limited space. Instead we focus on its elastic and inelastic particle properties. As can be seen from Fig. 1, these are largely stable between 22:30 and 01:30 UTC. A particularly good example is the measurement at 00:48 UTC, which is shown in Fig. 2. The maximum of the particle backscatter coefficient is only about 1 $Mm^{-1}sr^{-1}$ (Fig. 2a), but still the intensive parameters are measured with low statistical errors. Both particle depolarization ratio and lidar ratio are fairly height-constant, and their respective values of 20 % and ~50 sr indicate the presence of dust particles. This is in stark contrast to the fluorescence properties, which suggest a different interpretation. Above 7.5 km, the mean spectral fluorescence backscatter coefficients (Fig. 2b) follow nicely the particle backscatter coefficient, which results in nearly height-independent mean spectral fluorescence capacities (Fig. 2d).

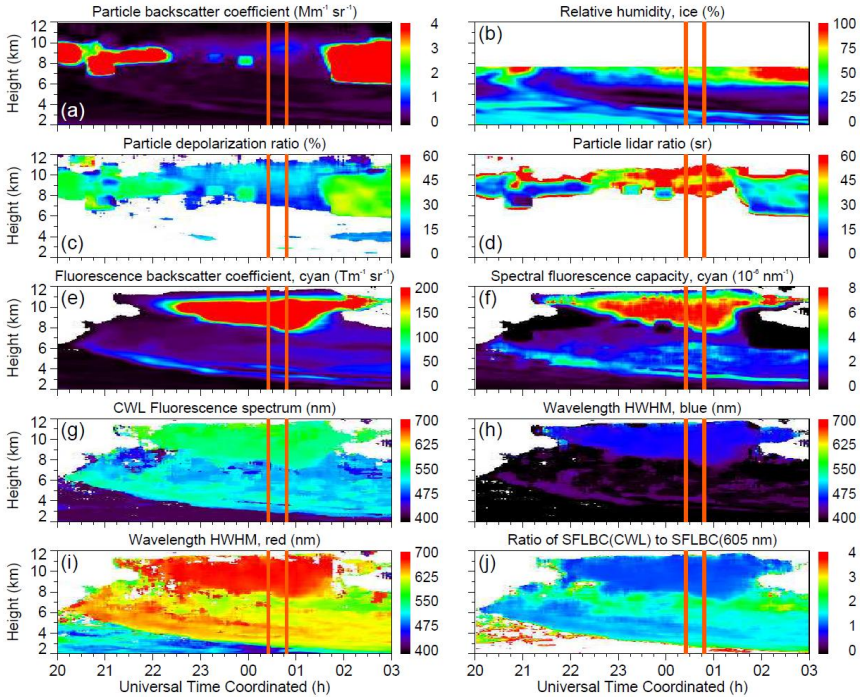

Figure 1. RAMSES measurement in the night of 4–5 April 2025 between 20:00 and 03:00 UTC. Temporal evolution of (a) particle backscatter coefficient, (b) relative humidity (with respect to ice), (c) particle depolarization ratio, (d) particle lidar ratio (not corrected for multiple scattering), (e) fluorescence backscatter coefficient (cyan false color: spectrum integrated from 455 to 535 nm), (f) spectral fluorescence capacity (mean value, 455–535 nm), (g) wavelength of the maximum of the fluorescence spectrum (CWL), (h) wavelength of the spectrum half width (HWHM) on the blue shoulder, (i) wavelength of the spectrum half width on the red shoulder, and (j) ratio of CWL to 605-nm spectral fluorescence backscatter coefficients (SFLBC). The aerosol measurement at 00:48 UTC is analyzed in Figs. 2 and 3, the comparison of RAMSES, ALV, and ATLID profiles measured during the EarthCARE overpass at 00:25 UTC is presented in Fig. 4 (times marked by vertical orange lines). White areas indicate where data were rejected by the automated quality control process.

The characteristic wavelengths of the fluorescence spectrum (Fig. 2c) as well as its skewness (R_{605}^{CWL}, Fig. 2d) exhibit a similar insensitivity. Thus the inelastic properties of the aerosol do not show a red shift with height, which is rather the exception than the rule [1]. The long characteristic wavelengths together with the high spectral fluorescence capacities leave no doubt that the observed fluorescence originated from BBA. If there were contributions by other aerosol types such as dust, these would not be detected against this background. The BBA hypothesis is corroborated by the fluorescence capacity spectra shown in Fig. 3 for selected heights. The shapes of the spectra are nearly Gaussian with center wavelengths around 552 nm (Fig. 3a). The curves are slightly wavy, but it remains to be seen whether these features are statistically significant. The essentially spectrally flat capacity ratios showcase the height invariance of fluorescence over the aerosol layer (Fig. 3b). Only a slight decrease in spectral fluorescence capacity is found at its edges. In conclusion, our analysis suggests that the aerosol layer consisted of a mixture of dust particles and BBA, whereby the former must have provided the bulk of the aerosol mass as it dominated elastic scattering while the latter overwhelmed the weak mineral fluorescence signal. Our preliminary back-trajectory analysis indeed supports this notion. Accordingly, the air masses which were measured over Lindenberg originated from the Gobi Desert, carrying significant amounts of dust. On their eastward journey, they then crossed an intense wild fire in South Korea, where probably the BBA got mixed in.

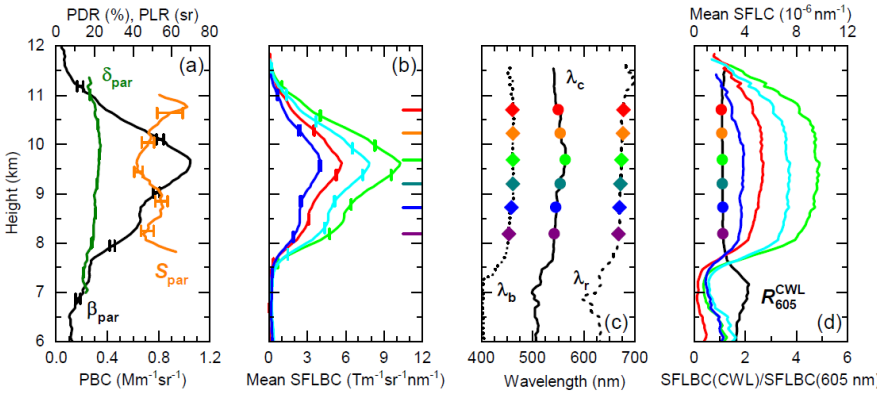

Figure 2. RAMSES measurement of the BBA/dust layer at 00:48 UTC on 5 April 2025. Profiles of (a) particle backscatter coefficient (PBC, β_{par}), particle depolarization ratio (PDR, δ_{par}) and particle lidar ratio (PLR, S_{par}), (b) mean spectral fluorescence backscatter coefficients (SFLBC) for the spectral bands ranging from 430–450 nm (blue), 455–535 nm (cyan), 545–625 nm (green), and 630–710 nm (red), (c) wavelength of the maximum of the fluorescence spectrum (CWL, λ_c), wavelength of the spectrum half width on the blue shoulder (λ_b) and wavelength of the spectrum half width on the red shoulder (λ_r), and (d) ratio of CWL to 605-nm spectral fluorescence backscatter coefficients (R_{605}^{CWL}) and mean spectral fluorescence capacities (SFLC) for the blue, cyan, green, and red spectral bands (colored curves). Colored symbols and horizontal lines indicate altitudes for which the fluorescence spectra are presented in Fig. 3. Bars in panels a and b indicate statistical errors of the lidar measurement (omitted in panels c and d for the sake of conciseness).

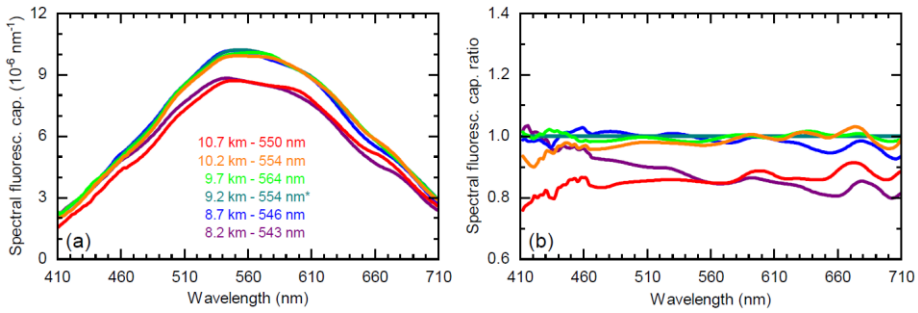

Figure 3. Spectral measurements of the BBA/dust layer at 00:48 UTC on 5 April 2025: (a) spectral fluorescence capacity, and (b) spectral fluorescence capacity relative to reference spectral fluorescence capacity. Spectra are presented for the heights selected in Fig. 2 (altitude and wavelength of the maximum of the fluorescence spectrum are indicated in panel a, reference height is marked with an asterisk).

Shortly before the RAMSES measurement discussed in Figs. 2–3, the EarthCARE satellite flew over Lindenberg at 00:25 UTC. It can be regarded as a fortunate coincidence that ATLID measured the aerosol layer without any cloud interference. Furthermore, the ground track of ATLID passed the surface lidars at a distance of only 1.4 km. This permits a direct comparison between all three instruments on a spatially and temporally stable aerosol layer with significant depolarization, thus fulfilling all requirements for a meaningful validation. Figure 4 compares the measured profiles of particle backscatter coefficient, particle depolarization ratio, particle extinction coefficient, and lidar ratio. Generally, the agreement is excellent. In particular, ATLID particle depolarization ratio compares well with the RAMSES and ALV results (Fig. 4b). A bit surprising, however, is the observation that both ATLID particle backscatter and extinction coefficient profiles appear more rounded than those of the Lindenberg instruments (Figs. 4a, 4c), even though the latter have a much longer integration time (1200 s) and are vertically smoothed. Finally, it should be noted that the ATLID target classification product [3, classification_low] attributes to the aerosol layer the aerosol

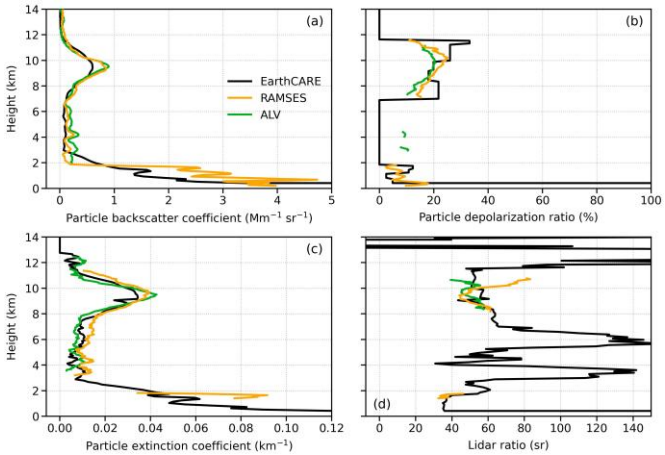

Figure 4. Comparison between the Lindenberg Meteorological Observatory Raman lidars RAMSES and ALV and ATLID onboard the EarthCARE satellite during its overpass at approximately 00:24:56 UTC on 5 April 2025. Profiles of (a) particle backscatter coefficient, (b) particle depolarization ratio, (c) particle extinction coefficient, and (d) lidar ratio. For the ground-based lidars, data integration time is 1200 s centered at 00:24 UTC, for ATLID [2] it is 0.14 s. To avoid an unrealistic peak in the ATLID particle depolarization ratio at the aerosol layer upper edge, not the profile measured at the time of the closest satellite approach is selected but the one 1.1 s earlier.

types Dusty_smoke, Dusty_mix, and Dust for the heights below 9.1 km, between 9.1 and 10 km, and above 10 km, respectively, which is in qualitative agreement with the analysis of the elastic and inelastic scattering properties.

Conclusions

The night of 4–5 April 2025 proved to be an exceptional observation period for both aerosol studies and ATLID validation at the Lindenberg Meteorological Observatory, Germany. For the first time, an upper-troposphere aerosol layer could be confirmed as being composed of a mixture of dust particles and BBA transported from central and eastern Asia to the lidar site. The measurements taken simultaneously with the ground-based lidars RAMSES and ALV as well as ATLID on the EarthCARE satellite showed very good agreement in all measurement parameters for this aerosol layer. Furthermore, the EarthCARE target classification agreed very well with the results of the analysis of the fluorescence and elastic scattering properties.

Acknowledgements

GIVE is partly funded by Bundesministerium für Wirtschaft und Klimaschutz (grant number 50EE2403D). The authors acknowledge the NOAA Air Resources Laboratory (ARL) for the provision of the HYSPLIT transport and dispersion model and READY website (https://www.ready.noaa.gov).

References

[1] Reichardt, J., Lauermann, F., and Behrendt, O.: *Fluorescence spectra of atmospheric aerosols*, EGUsphere [preprint], https://doi.org/10.5194/egusphere-2024-3928, 2024.

[2] European Space Agency, 2025, "EarthCARE ATLID AER Level 2A", (version AE), https://doi.org/10.57780/eca-bd87949

[3] European Space Agency, 2025, "EarthCARE ATLID TC Level 2A", (version AE), https://doi.org/10.57780/eca-5828141

[4] Stein, A.F., et al.: *NOAA's HYSPLIT atmospheric transport and dispersion modeling system*, Bull. Amer. Meteor. Soc., 96, 2059-2077, http://dx.doi.org/10.1175/BAMS-D-14-00110.1, 2015.

[5] Rolph, G., Stein, A., and Stunder, B.: *Real-time Environmental Applications and Display sYstem: READY*, Environmental Modelling & Software, 95, 210-228, https://doi.org/10.1016/j.envsoft.2017.06.025, 2017.

[6] Reichardt, J., Behrendt, O., and Lauermann, F.: *Spectrometric fluorescence and Raman lidar: absolute calibration of aerosol fluorescence spectra and fluorescence correction of humidity measurements*, Atmos. Meas. Tech., 16, 1–13, https://doi.org/10.5194/amt-16-1-2023, 2023.

Lidar-derived Vertical Aerosol Fluxes in the Boundary Layer

M. Karasewicz[1], *L.Janicka*[1], *P. Ortiz-Amezcua*[1], *I.S. Stachlewska*[1]

(1) Faculty of Physics, University of Warsaw, Pasteura 5, Warsaw, Poland

Corresponding author: Iwona.Stachlewska@fuw.edu.pl

Introduction

Aerosol sedimentation and resuspension, associated with vertical aerosol fluxes, can be studied using the Eddy Covariance (EC) technique with use of in-situ instruments. The vertical aerosol fluxes are then defined as a covariance of aerosol mass concentration and vertical velocity of the air mass movement close to the Earth surface [1]. The use of Doppler lidar measurements in combination of EC technique can provide information in larger extent of altitudes. The lidar-based EC method utilizes the lidar backscatter coefficient as an equivalent to aerosol mass concentration and lidar vertical velocity of the air mass movement at different altitudes [2]. Thus, remote measurements of vertical aerosol fluxes and their characterization across full height of Atmospheric Boundary Layer (ABL) are possible. However, obtained results are not so trivial to interpret and depend on the meteorological conditions within and optical properties of the ABL, then appropriate data curation and filtration is required [3]. Various types of precipitation or vertical movement within the cloud may be mistakenly interpreted as an aerosol vertical flux during analysis of the long-term data, affecting the final results. Thus appropriate filtration, e.g. precipitation flagging using disdrometer data and/or cloud flagging based on the Doppler Lidar attenuated backscatter threshold can be applied. Additional misinterpretations can be related to the fluctuations of the backscatter coefficient caused by an inflow of different aerosol type and or aerosol hygroscopic growth. Then additional data analysis regarding an aerosol typing, using multiwavelength depolarization lidar measurements and relative humidity profiles from the microwave radiometer may be justified.

Methodology

For the calculations of an aerosol flux the quasi-particle backscatter coefficient ${}^{quasi}\beta_p$ and vertical wind velocity w from Doppler lidar system (StreamLine, HaLoPhotonics) have been used. The ${}^{quasi}\beta_p$ is an atmospheric parameter which estimates the value of the particle backscatter coefficient β_p and can be obtained in high temporal resolution from the Doppler lidar-derived attenuated backscatter coefficient β_{att} [4][5]. Instrumentation systems were operating with 1s and 30 m of, respectively, temporal and spatial resolution. The aerosol vertical fluxes were calculated as a 30 minute means of the covariances between ${}^{quasi}\beta_p$ and w. The detrending process to isolate the fluctuating component was performed using a linear method. Aerosol fluxes intensification was represented as resuspension/sedimentation velocity (sometimes referred to emission/deposition velocities which we consider as an imprecise nomenclature as these two processes are strictly connected with a surface and an air particles exchange, while our results apply to the entire height extent of an atmospheric boundary layer), i.e. the ratio of the mean values of the covariances and ${}^{quasi}\beta_p$. The data curation of signal to noise ratio SNR has been applied, filtering all values of SNR < 1.006 [6]. Moreover in the current study the additional data curation using precipitation flags from the disdrometer OTT Parsivel^2 and clouds flags for $\beta_{att} > 10^{-5}$ sr^{-1}m^{-1} threshold [7] have been applied. However, no filtering based on the ABLH regime was applied. The algorithm was used not only within the boundary layer, but also for the upper parts up to 1995 m a.g.l. All of the instrumentation was installed in close proximity to each other at the measurement roof platform of the Warsaw Observatory Station (WOS) at Institute of Geophysics, Faculty of Physics, University of Warsaw.

Results and Discussion

We analyzed two years (2022-2023) of the Doppler lidar (StreamLine, Halo Photonics) and disdrometer (OTT Parsivel^2) observations. The aerosol fluxes within the boundary layer were derived with a resolution of 30 m and 30 min. The example representation of the obtained results for one day of observations is

presented on Fig. 1. The blank region represents the data filtered using the SNR threshold, which will be in a following analysis referred to as a no-signal. Further data analysis consisted of grouping all obtained results depending on height and diurnal time.

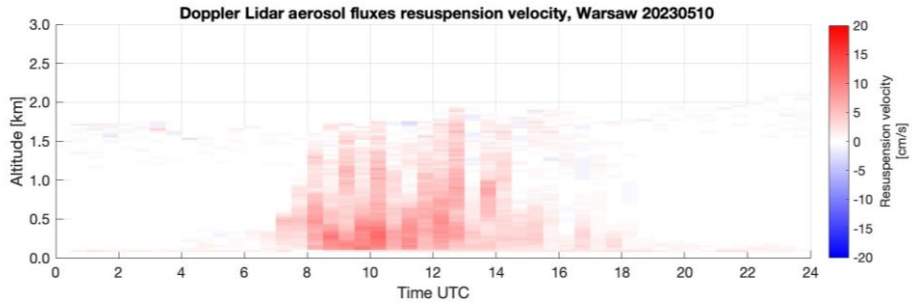

Figure 1. Example of a flux resuspension velocity profiles from the 10th of May 2023 measured in Warsaw..

Fig. 2 presents the observed combined frequencies of occurrence for different flux velocities and precipitation, and cloud presence for two years of the observations within a spatial interval between 105 and 1995 m a.g.l. during a diurnal cycle. The data marked as a no-signal refers to the data filtered out using the SNR threshold.

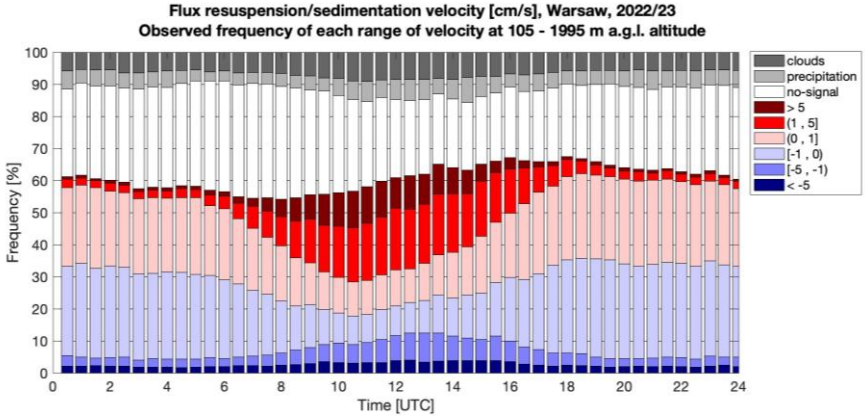

Figure 2. Observed occurence frequencies of each resuspension and sedimentation flux velocity ranges, precipitation episodes, clouds and no-signal presence at altitudes between 105 and 1995 m a.g.l. for 2 years (2022/23) of observations in Warsaw.

Observed frequencies of occurrence are analyzed based on a different velocitiy thresholds and classified as a significant ($v > 1$ or $v < -1$ [cm/s]) or non-significant ($-1 \leq v \leq 1$ [cm/s]) resuspension/sedimentation velocities, what was shown in Fig. 3. One can observe relation between aerosol fluxes and diurnal cycle indicating resuspension as a dominant type of an aerosol fluxes, especially during midday. This phenomenon was observed for all of the seasons. During spring, summer and autumn seasons (MAM, JJA, SON) differences in the resuspension and sedimentation velocities within ABL occurred with non-significant velocities prevailing at night and significant during daytime. However during winter season (DJF)

practically no such differences (except at the lowest altitudes) were observed; the resuspension and sedimentation velocities were mostly classified as significant.

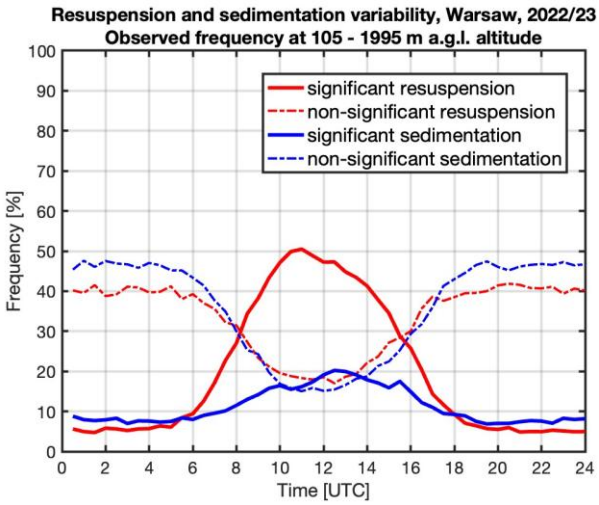

Figure 3. Significant and non-significant flux velocity variability at altitudes between 105 and 1995 m a.g.l. for 2 years (2022/23) of observations in Warsaw.

The summary of the seasonal analysis for all seasons is presented in Tab.1. Data analysis showed that the urban ecosystem of Warsaw can be characterized as a one with a higher rate of atmospheric aerosol resuspension, especially during a spring season, compared to sedimentation processes.

Table 1. The percentage of a presence of each of the classified aerosol fluxes .

	MAM	**JJA**	**SON**	**DJF**
Sedimentation	44,30%	47,87%	48,83%	49,16%
Resuspension	55,70%	52,13%	51,17%	50,84%

Conclusions

Differences in seasonal and diurnal cycles at various altitude ranges were obtained in terms of the velocity changes of aerosol resuspension and sedimentation, thus providing the first-ever characterization of vertical aerosol fluxes in an urban environment based on WOS long-term measurements. However, data analysis from the other remote sensing instruments should be applied to minimize potential sources of errors. For the future plans the sensitive study will be performed of how depending on the data curation the final characterisation differs from each other and which additional instrumentation, in terms of providing unbiased characterization, is required to be involved.

Acknowledgements

The Doppler Lidar measurement performed in Warsaw in 2022/23 was supported by the European Commission under the Horizon 2020- Research and Innovation Framework Programme with the ACTRIS-IMP project (G.A. no 871115)

and ATMO-ACCESS (G.A. no. No 101008004). The algorithm to obtain the aerosol fluxes from the Doppler Lidar measurements was developed with support from the National Science Centre, Poland (NCN) through project 2021/40/C/ST10/00023 of programme SONATINA 5. This work contributes to the activities within the Aerosol Cloud and Trace gases Research Infrastructure (ACTRIS-ERIC) and ACTRIS-PL, funded by the Ministry of Science and Higher Education of Poland under grant agreement 2024/WK/04.

References

[1] Järvi, L., Rannik, Ü., Mammarella, I., Sogachev, A., Aalto, P. P., Keronen, P., Siivola, E., Kulmala, M., and Vesala, T.: Annual particle flux observations over a heterogeneous urban area, Atmos. Chem. Phys., 9, 7847– 7856, doi.org/10.5194/acp-9-7847-2009, 2009.

[2] Engelmann, R., Wandinger, U., Ansmann, A., Müller, D., Žeromskis, E., Althausen, D., Wehner, B.: Lidar observations of the vertical aerosol flux in the planetary boundary layer, J. Atmos. Ocean Tech., 25, 1296–1306, doi.org/10.1175/2007JTECHA967.1, 2008.

[3] Ortiz-Amezcua, P., Janicka, Ł., Abril-Gago, J., Karasewicz, M., Poczta, P., Guerrero-Rascado, J. L., Alados-Arboledas, L., and Stachlewska, I. S. (2023). Particle fluxes over rural and urban ABL in Poland using remote sensing. Book of Abstracts European Lidar Conference, 2023 - Cluj-Napoca, Romania.

[4] Baars, H., Seifert, P., Engelmann, R., Wandinger, U.: Target categorization of aerosol and clouds by continuous multiwavelength-polarization lidar measurements, Atmos. Meas. Tech., 10, 3175–3201, doi.org/10.5194/amt-10- 3175-2017, 2017.

[5] Wang, D., Stachlewska, I. S., Delanoë, J., Ene, D., Song, X., and Schüttemeyer D., (2020). Spatio-temporal discrimination of molecular, aerosol and cloud scattering and polarization using a combination of a Raman lidar, Doppler cloud radar and microwave radiometer, Opt. Express 28, 20117-20134 (2020).

[6] Manninen, A. J., O'Connor, E. J., Vakkari, V. and PetÅNajÅNa, T. (2016). A generalised background correction algorithm for a halo doppler lidar and its application to data from finland Atmos. Meas. Tech. 9. https://doi.org/10.5194/amt-9-817-2016

[7] Manninen, A. J., Marke, T., Tuononen, M. and O'Connor, E. J. (2017). Atmospheric boundary layer classification with doppler lidar Journal of Geophysical Research: Atmospheres 122(10), 10,897–10,910.

Aircraft wake vortex measurements using a Doppler wind lidar at Amsterdam Airport

T.Mathijssen[1]

(1) Royal Netherlands Meteorological Institute (KNMI), Utrechtseweg 297, 3731CA, De Bilt, The Netherlands

Corresponding author: Tiemo.Mathijssen@knmi.nl

Introduction

Runway usage of airports are strictly regulated, depending on the meteorological conditions. It is well known that airborn aircraft generate wake vortices that can linger for long time, which can cause hazardous wind conditions to following aircraft. The minimum separation of aircraft and maximum runway use is based on experience of the time such vortices tend to remain before advecting or dissipating. Better knowledge on such wake vortices could result in a higher capacity of runways [1].

ICAO [2] prescribes that measurements should be representative of the conditions at touchdown or along the runway. The Royal Netherlands Meteorological Institute (KNMI) operates several cup anemometer and wind vane of own design, positioned at a mast of 10m altitude to provide wind measurements at Amsterdam Schiphol Airport. These instruments occasionally record impinging wake vortices of aircraft, shortly increasing wind speed. These measurements affect not only the instantaneously recorded wind, but also the 10-minute average, which is typically used to report the wind speed. Since the effect of wake vortices tend to be shorter lived than this 10 minute average wind, an algorithm has been developed by Van der Meulen [3] to identify the occurrence of a wake vortex on the cup anemometer measurements and to correct for them. Investigations indicate that this algorithm indeed is selective for wake vortices, but validation that these identifications are caused by wake vortices is still lacking due to the absence of appropiate measurement techniques.

Advances in lidar technology has recently opened new possibilities for wind measurements at airports [4][5]. The recent placement of a long range scanning Doppler wind lidar at Amsterdam Schiphol Airport [6] has created the possibility to validate the wake vortex algorithm by correlating wake vortex identifications with lidar measurements of wake vortex impingement. Fast repetition of the wind lidar scan allows tracking and evolution of aircraft wake vortices [7], and correlate them with the identification in the in-situ cup anemometer measurements. This manuscript describes the process and initial results of such correlation and provides a validation case for simulated research [8]

Methodology

The Royal Netherlands Meteorological Institute (KNMI) has acquired a Leonardo Skiron3D long-range scanning Doppler wind lidar and placed it at Amsterdam Schiphol Airport. It is foreseen to place the instrument at several locations at the airport to investigate the entire extent of the airport. The instrument has been placed on a trailer to facilitate transport, see **Figure 1.1**. The current location allows it to scan several runways, depending on which ones are in use, see figure 2. Since wake vortices only show variations in wind speed perpendicular to the aircraft flight direction, it is only possible to visualize aircraft wake vortices if the lidar scan is done perpendicular to the runway. Moreover, to assess wake vortex impingement on a cup anemometer, a combination must be present of detectability of wake vortices and visibility of the cup anemometer from the lidar location. From the current location, this is possible only for Aalsmeerbaan, Zwanenburgbaan and Polderbaan. On the other hand, wake vortices can be detected at close range on the Buitenveldertbaan and Oostbaan, but without the possibility to correlate them to cup anemometer measurements.

The lidar is configured to rapidly execute Range Height Indicator (RHI) scans, i.e. keeping azimuth constant and scan quickly up and down in elevation. Two different scan directions have been selected, see figure 2. The first scan direction is selected to visualise wake vortices from aircraft at close range to maximize resolution, while the second scan direction is aimed at correlating wake vortices with measurements of the cup anemometer. In the first scan, the pulse width is set to approximately 200 ns. The range was set to 1 km with a range resolution of 24 m. By applying an overlap factor of 8, a display

resolution of 3m is achieved. The elevation angle resolution is set to 0.2 degrees. At a capturing distance of 200 m from the lidar, the vertical resolution is as small as 0.7 m. In order to ensure capturing the wake vortices for departing aircraft, a relatively high elevation range is chosen between 0 degrees and 70 degrees. To achieve a sufficient signal-to-noise ratio, a scan speed of 12 °/s is set. Because the scan is alternated between bottom to top and reversed, a new image is produced every 11 seconds.

The second scan captures wake vortices much further away, emerging from the Zwanenburgbaan at 4.5 km distance. The azimuth direction is selected to pass exactly above one of the cup anemometers next to this runway at a distance of 4.6 km. The pulse width was kept the same as the first scan at 200 ns. The range was set to a maximum of 7 km in order to track any vortices moving in westerly direction. For this scan, a maximum elevation of 10 degrees was sufficient. The resolution in elevation angle was kept at 0.2 degrees, leading to a vertical resolution of approximately 24 m at the runway location. In order to keep sufficient signal-to-noise ratio, it was necessary to reduce the scan speed to 2.1 °/s, leading generation of an image every 7 seconds.

The cup anemometers take measurements at a 4 Hz rate, but report averages of 50 measurements every 12 s. Moreover, the maximum and minimum, 1-minute average and 10-minute average are reported in each 12 s interval.

Figure 1.1 The Skiron3D Doppler wind lidar

Figure 2. Schiphol airport runways

Results and Discussion

An example of the capture of a wake vortex in the first scan direction emerging from the Buitenveldertbaan is displayed by visualisation of the radial velocity in figure 3. At a distance of 160m, the laser is passing through the structure of the ILS system, partly obscuring the visibility up to approximately 5m altitude. The background radial wind was between 0 and 2 m/s. A clear pattern for a wake vortex emerges at 10:19:04 UTC, which is recognizable with 4 regions of alternating positive and negative radial velocity organised in a square form, indicating two counter rotating pockets of the air. The measured radial velocity varies between -6 m/s and 7 m/s. The wake vortex moves in northern direction and eventually dissipates.

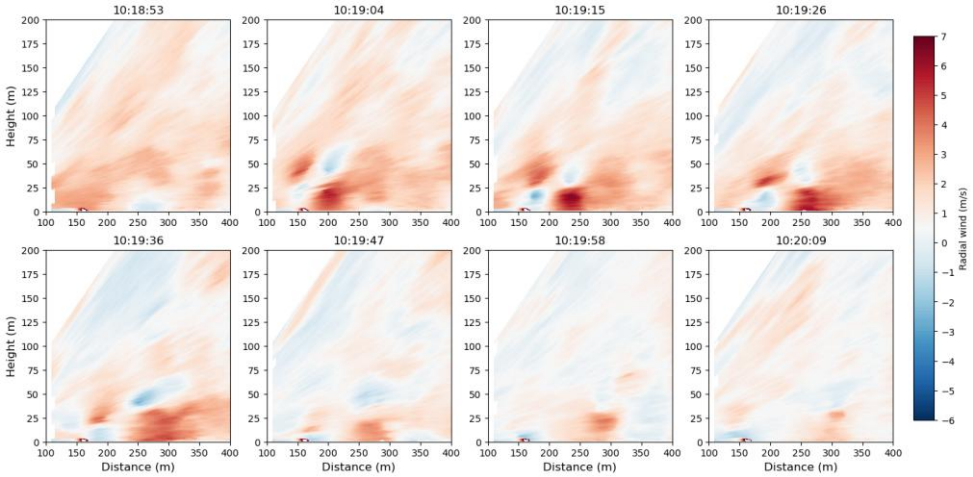

Figure 2. Wake vortex measurement emerging from a landing aircraft at the Buitenveldertbaan

In the scan of the second direction, see figure 2, it is possible to capture wake vortices directly above the cup anemometer of the Zwanenburgbaan to correlate the two measurements. The cup anemometer is located at 4600 m from the lidar on a mast of 10m altitude. Unfortunately some objects in the horizontal path to the cup anemometer obstruct the path, but measurements above 0.2 degrees above the horizon were feasible. The algorithm on the cup anemometer data detected the occurrence of a wake vortex at 13:48:53h UTC. Figure 4 shows the lidar images just prior to this detection. The lidar measruements show the appearrance of a wake vortex at 13:48:07 UTC, which then advects in westerly direction, impinging on the cup anemometer at 13:48:49 UTC. The vortex slowly advected in westerly direction, away from the lidar. The lidar measurements of the wake vortex passing over the cup anemometer correlates within a 12s sampling interval to the detection of a wake vortex by the cup anemometer algorithm. Velocities ranging from -2 m/s to 5 m/s were detected.

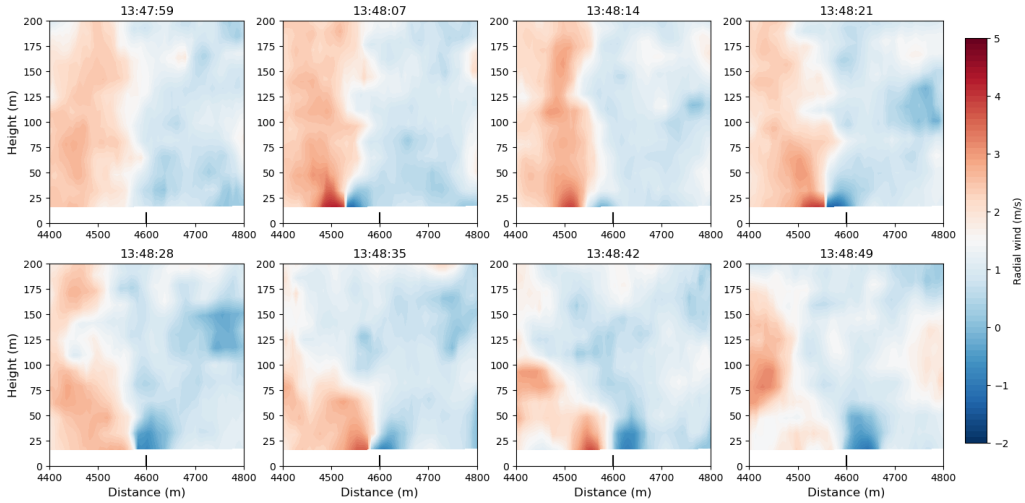

Figure 3. Impingement of a wake vortex on a cup anemometer at the Zwanenburgbaan

Conclusions

A Skiron3D scanning Doppler wind lidar has successfully been deployed at Schiphol airport. Measurements of the radial velocity in RHI scans were conducted in two directions. In the first direction, aircraft wake vortices were measured using the lidar at a display range resolution 3 m and vertical resolution of 0.7 m at a distance of 200 meters. The measurements show a clear square pattern indicative of the presence of a vortex pair and dissipation of the wake vortex pair.

The second scan is done right above a cup anemometer 4600m away from the lidar, during a period in which it was expected that wake vortices of aircraft taking off from the adjacent runway would impinge on the cup anemometer. The algorithm on the cup anemometer data identified a wake vortex. Measurements of the Doppler wind lidar indicate that a wake vortex pair was generated approximately 35 seconds prior to the trigger of the algorithm. Due to the lower height resolution of 24 m, and the low altitude of the wake vortex, only the top of the wake vortex was visible. The time at which the algorithm identified a wake vortex at the cup anemometer correlates very well with the time the Doppler wind lidar measured the wake vortex impinging on the cup anemometer.

References

[1] Hallock, J.N., Holzäpfel, F., *A review of recent wake vortex research for increasing airport capacity*, Progress in Aerospace Sciences, Volume 98, 2018, pp. 27-36, ISSN 0376-0421, https://doi.org/10.1016/j.paerosci.2018.03.003.

[2] ICAO: Manual of Aeronautical Meteorological Practice, Doc 8896 AN/893, 9th edition, International Civil Aviation Organization, Montréal, Canada, 2011.

[3] Meulen, van der, J.P.: *Wake Vortex Induced Wind measurements at Airfields: A simple Algorithm to Reduce the Vortex Impact*, Instruments and Observing Methods Reports No. 70, WMO/TD No. 877, 1998.

[4] Thobois, L., Cariou, J.P. & Gultepe, I.: *Review of Lidar-Based Applications for Aviation Weather*, Pure Appl. Geophys. 176, 1959–1976 (2019). https://doi.org/10.1007/s00024-018-2058-8.

[5] Chan, P. W., & Shao, A. M., *Depiction of complex airflow near Hong Kong International Airport using a Doppler LIDAR with a two-dimensional wind retrieval technique*. Meteorologische Zeitschrift, *16*, 491–504, 2007.

[6] Mathijssen, T., Knoop, S.: *Comparison of wind profiles of Skiron3D and Windcube 200s Doppler lidars*, 22nd Coherent Laser Radar Conference, 2024.

[7] Köpp, F., Rahm, S., Smalikho, I, Dolfi, A., Cariou, J-P, Harris, M., Young, R.I., *Comparison of Wake-Vortex Parameters Measured by Pulsed and Continuous-Wave Lidars*, Journal of Aircraft, Volume 4, Number 4, 2005, pp. 916-923, https://doi.org/10.2514/1.8177.

[8] Wartha, N., Stephan A., Holzäpfel F., *Assessment of a Wake Vortex Retrieval Method Using Large-Eddy Simulations and a Lidar Simulator*, Journal of Atmospheric and Oceanic Technology, Volume 43, Issue 3, 2025, pp. 233–251, https://doi.org/10.1175/JTECH-D-24-0093.1.

Lidar applications in ocean sciences

Session Chairs:

Davide Dionisi, Italian National Research Council (CNR-ISMAR), Italy

Cedric Jamet, Laboratoire d'Océanologie et de Géosciences (LOG), France

Consistency Analysis of Diffuse Attenuation Coefficients from ICESat-2 and MODIS in Marginal Seas: Implications for Ocean Optical Observations

Z. Zhang[1], *P. Chen*[1,2], *S. Zhang*[1,2]

(1) Southern Marine Science and Engineering Guangdong Laboratory (Guangzhou), No. 1119, Haibin Rd., Nansha District, Guangzhou 511458, China

(2) State Key Laboratory of Satellite Ocean Environment Dynamics, Second Institute of Oceanography, Ministry of Natural Resources, 36 Bochubeilu, Hangzhou 310012, China

Corresponding author: chenp@sio.org.cn

Introduction

The diffuse attenuation coefficient (Kd) plays a vital role in oceanographic studies as it quantifies the attenuation of light in the water column, essential for understanding the interactions between light and water, such as heat exchange, photosynthesis, and primary productivity [1]. Accurate measurements of Kd are crucial for assessing marine environments, yet traditional methods such as the Secchi disk offer limited spatial and temporal coverage. Recent advancements in satellite technology have provided alternative methods for Kd measurements, such as MODIS (Moderate Resolution Imaging Spectroradiometer), which offers global coverage but is limited by cloud cover and lack of nighttime data [2]. Lidar-based systems, particularly ICESat-2, offer a promising solution, as they provide continuous data unaffected by cloud cover and time of day, making them ideal for accurate and consistent ocean optical observations [3, 4]. However, the consistency between Kd measurements obtained from ICESat-2 and MODIS, especially in the complex and variable environments of marginal seas, remains uncertain. This study aims to fill this gap by comparing and analyzing the Kd data from both sources, evaluating the potential of lidar technology to improve the reliability and accuracy of ocean optical data in these challenging conditions.

Methodology

ICESat-2, launched by NASA in 2018, is a satellite designed primarily to measure the elevation of Earth's ice sheets, clouds, and land surfaces using its Advanced Topographic Laser Altimeter System (ATLAS). ATLAS is an advanced lidar system that utilizes single-photon counting technology, emitting laser pulses at a wavelength of 532 nm with a pulse repetition frequency of up to 10 kHz. This high-frequency emission allows for continuous measurements along the satellite's track, providing an exceptional horizontal resolution of nearly 0.7 meters. The laser beam, upon reaching the Earth's surface, has a spot diameter of about 11 meters, and it splits into six beams. These beams are reflected back from the surface and detected by a highly sensitive photon-counting receiver, enabling precise elevation measurements. ICESat-2's data collection spans from 88°N to 88°S with a repeat period of 91 days, ensuring near-global coverage [5]. For this study, we used the geolocation L2A data from ICESat-2 [6], which was obtained from the National Snow and Ice Data Center (NSIDC) for the period between October 2018 and August 2023. The data processing starts with a filtering step where only nighttime data is used, along with photons from sea surface returns within a specified range of 1-12 photons per laser pulse, ensuring the signal quality. Cases with fewer than 1 count per pulse are removed due to low signal-to-noise ratio (SNR), while those exceeding 12 counts per pulse are excluded to prevent potential signal saturation caused by specular reflection [4]. To minimize atmospheric effects on the ocean-returned lidar profiles, measurements are restricted to conditions where the atmospheric column optical depth is less than 0.2, thereby avoiding interference from atmospheric forward scattering. After identifying the sea surface position, a refraction correction is applied to underwater photons, adjusting for the mean sea level and multiplying by 0.75 to account for refraction effects. These corrected photons are accumulated along the track, considering both sliding and cumulative distances of 4 km and 20 km, respectively, to generate pseudo-waveforms of the water column. This horizontal binning of photons over a specified distance is crucial for improving the signal-to-noise ratio in photon-counting lidar data [7]. The 20 km bin size, in particular, ensures that a sufficient number of photons are collected to enhance the SNR for an accurate measurement [3]. The 4 km step length enables the alignment of lidar-derived profiles with MODIS data

at corresponding resolutions. Once background noise is removed, the profile waveforms undergo deconvolution to eliminate the influence of afterpulses from the detector. Subsequently, the lidar system attenuation coefficient (K_{lidar}) is computed based on the exponential decay of the lidar return signal, following the formula [4]:

$$K_{lidar} = -0.5 \frac{d \ln (S(z))}{dz} \quad (1)$$

where S(z) is the lidar pseudo-waveform signal at depth z after transient response correction. A linear fit on the logarithmic return signal within the first 14 meters of the water column provides the value for K_{lidar}.

To compare the K_{lidar} with the MODIS-derived K_d, the study uses the MODIS $K_d(490)$ product from the Aqua and Terra satellites, covering data from October 2018 to August 2023. While the original MODIS $K_d(490)$ product measures the diffuse attenuation coefficient at 490 nm, for a more accurate comparison with the ICESat-2 lidar data (which operates at 532 nm), the MODIS $K_d(490)$ values are converted to $K_d(532)$ as follows [8] :

$$K_d(532) = 0.68(K_d(490) - 0.022) + 0.054 \quad (2)$$

To assess the performance and consistency of K_d estimates from ICESat-2, several statistical parameters are employed: the Pearson Correlation Coefficient (R), the bias, the Root Mean Square Difference (RMSD), and the Mean Absolute Percentage Difference (MAPD):

$$R = \frac{\sum_{i=1}^{n}(x_i-\bar{x})(y_i-\bar{y})}{\sqrt{\sum_{i=1}^{n}(x_i-\bar{x})^2 \sum_{i=1}^{n}(y_i-\bar{y})^2}} \quad (3)$$

$$bias = \frac{\sum_{i=1}^{n}(x_i-y_i)}{n} \quad (4)$$

$$RMSD = \sqrt{\frac{\sum_{i=1}^{n}(x_i-y_i)^2}{n-1}} \quad (5)$$

$$MAPD = \frac{\sum_{i=1}^{n}\left|\frac{x_i-y_i}{y_i}\times 100\%\right|}{n} \quad (6)$$

where, x represents the ICESat-2 inversion results, and y represents the reference data.

Then, a multiple scattering correction model is developed to address the issue of multiple scattering, which distorts lidar-derived attenuation measurements, especially in turbid waters. To improve the accuracy of K_d estimates from ICESat-2, a correction model was developed. The model utilize simulated lidar echo signals [9] under different water conditions and incorporate lidar system parameters to correct the impact of multiple scattering. The models were trained using a matched dataset of ICESat-2 and MODIS $K_d(532)$ data, and machine learning techniques, specifically XGBoost [10], were employed to identify patterns and optimize the correction process. The result is a refined model that reduces discrepancies between lidar-derived and MODIS-derived K_d values, significantly improving the consistency and accuracy of K_d estimates, particularly in challenging, turbid environments.

The BGC-Argo [11] data was used to validate the MSCM developed for ICESat-2-derived K_d estimates. BGC-Argo float measurements of downwelling irradiance at 490 nm served as in-situ reference data for comparing the corrected K_d values from ICESat-2. The validation process involved matching Argo data with ICESat-2 and MODIS data, ensuring spatial and temporal consistency. The matching process considers both spatial proximity (within 25 km²) and temporal consistency (within 24 hours) between the Argo data and satellite-derived K_d values. The Argo measurements serve as a reference to evaluate the accuracy of the lidar-derived K_d values, particularly after applying the multiple scattering correction models. This approach helps assess the effectiveness of the corrections in reducing discrepancies between remote sensing data and in-situ observations.

Results and Discussion

The comparsion between K_{lidar} and MODIS $K_d(532)$ reveals a significant discrepancy between the two datasets (Figure 1a). The Bias is -0.007, indicating a small underestimation of Klidar values compared to MODIS Kd532, and the R is 0.53, demonstrating a weak linear relationship between the two data sources. The RMSD of 0.035 andMAPD of 23.4% further confirm the differences between the datasets, highlighting that raw K_{lidar} values do not closely match MODIS $K_d(532)$. The a MSCM is developed to eliminate the discrepancy. Figure 1c presents the results of the MSCM for the training dataset, where the comparison between K_{lidar} and MODIS $K_d(532)$ shows an exceptionally high R value of 0.97, with a Bias of 0, RMSD of 0.007, and MAPD of 7.3%, indicating a nearly perfect fit and minimal error. Figure 1d shows the results for the test dataset, which also demonstrate strong performance with a R of 0.93, Bias of 0, RMSD of 0.009, and MAPD of 9.4%. Although the performance on the test data is slightly less optimal than on the training data, the model still provides a highly accurate and consistent fit, demonstrating its robustness and ability to generalize well to new, unseen data. Figure 1(b) shows the comparison after applying the MSCM correction model, which significantly improves the consistency between the datasets. After correction, the Bias becomes 0, indicating no systematic under- or over-estimation, and the R value increases to 0.94, reflecting a much stronger linear correlation. Additionally, the RMSD reduces to 0.01 and the MAPD decreases to 5.7%, showing that the correction model successfully reduces the discrepancies and aligns the Klidar estimates much more closely with MODIS Kd532. Overall, the results confirm that the MSCM significantly improves the accuracy and consistency of Klidar estimates, reducing biases and discrepancies when compared to MODIS Kd532, and that the model performs well across both training and test datasets. The successful application of this correction model enhances the reliability of ICESat-2 lidar data for ocean optical measurements, particularly in complex marine environments.

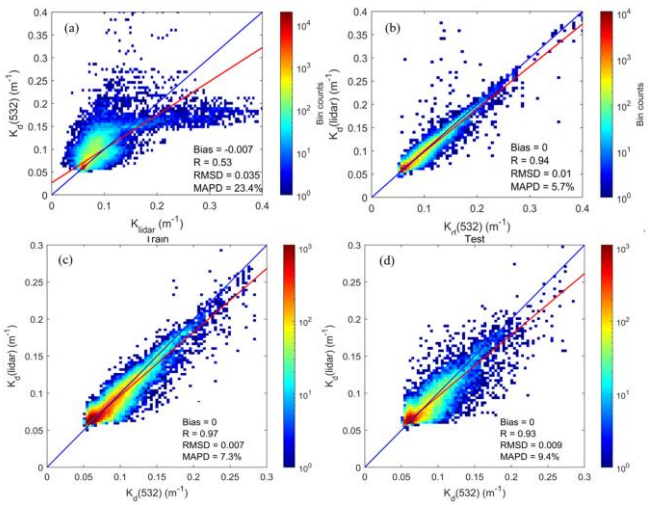

Figure 1. Comparison of K_{lidar} and MODIS $K_d(532)$ before and after applying the MSCM: the raw comparison (a); the comparison after MSCM correction (b); the MSCM model results for the training (c) and test (d) datasets.

The corresponding Argo float data that was successfully matched is depicted in the map, showing 80 valid match-ups across diverse global sea areas (Figure 2a). When comparing the raw K_{lidar} values with the Argo measurements of K_d, the results reveal a moderate correlation, with a Bias of -0.01, a R of 0.39, RMSD of 0.036, and MAPD of 26%, indicating noticeable discrepancies between the two datasets (Figure 2b). After applying the correction model, the comparison between the corrected Klidar values and Argo

Kd measurements shows a significant improvement. The correlation strengthens with a Bias of -0.01, R of 0.71, RMSD of 0.022, and MAPD of 15.7%, reflecting better consistency and accuracy (Figure 2c).

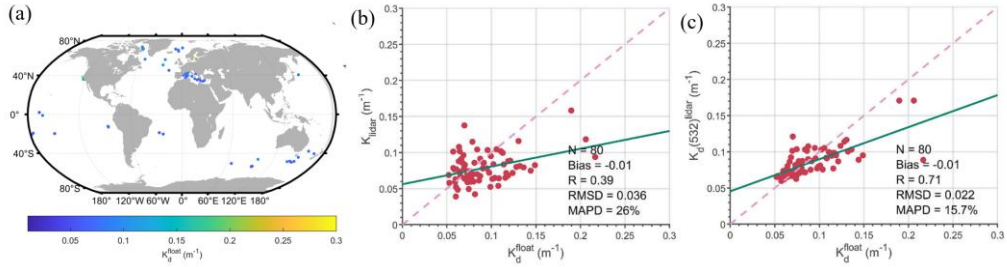

Figure 2. Comparison of K_{lidar} and Argo float K_d before and after applying the MSCM: (a) Distribution of matched data; (b) The raw comparison; (c) The comparison after applying the correction model.

A comprehensive analysis of the uncertainty budget for the diffuse attenuation coefficient (Kd) derived from our Multiple Scattering Correction Model (MSCM) is crucial for understanding the reliability of the final data product. The total uncertainty (E) for the $K_d$values derived from the Multiple Scattering Correction Model (MSCM) is estimated by combining three primary error sources: measurement (M), representation (R), and prediction (P), according to the formula $E = \sqrt{M^2 + R^2 + P^2}$ [12]. The largest component is the measurement error (M), estimated at ~21.63%, which is dominated by the inherent uncertainty of the reference MODIS K_d product [13] used for model training. The prediction error (P), which is intrinsic to the machine learning model, is approximately 10% as determined through validation with Argo float data. The representation error (R) arises from spatial and temporal mismatches between the different datasets. By integrating these sources, the total estimated uncertainty for the MSCM is approximately 23.8%.

Conclusions

This study explores the potential of ICESat-2 for detecting the diffuse attenuation coefficient in marginal seas. ICESat-2 demonstrates strong capabilities in retrieving the diffuse attenuation coefficient across various aquatic environments, although discrepancies between the lidar system's attenuation coefficient and MODIS-derived values arise due to factors like multiple scattering. These discrepancies can be effectively reduced using a multiple scattering correction model, which performs well across different cumulative distances. Validation with BGC-Argo data shows that the correction model significantly enhances the accuracy of the lidar-derived coefficient. The corrected lidar data improves understanding of light availability in marine ecosystems, aiding environmental studies and management. However, the study relies on MODIS data for correction, and future research should focus on gathering more in-situ data to further refine the model and improve accuracy.

Acknowledgements

This work was financed by China Postdoctoral Science Foundation (2023M740809) and National Natural Science Foundation (42322606; 42276180; 61991453). In this work we used data from NASA National Snow and Ice Data Center (NSIDC) and International Argo Program.

References

[1] Loiselle, S.A., et al., *Variability in photobleaching yields and their related impacts on optical conditions in subtropical lakes.* Journal of Photochemistry and Photobiology B: Biology, 2009. **95**(2): p. 129-137.

[2] Jamet, C., et al., *Going Beyond Standard Ocean Color Observations: Lidar and Polarimetry.* Frontiers in Marine Science, 2019. **6**.

[3] Yang, J., et al., *Examining the Consistency of Lidar Attenuation Coefficient Klidar From ICESat-2 and Diffuse Attenuation Coefficient Kd From MODIS.* IEEE Geoscience and Remote Sensing Letters, 2023. **20**: p. 1-5.

[4] Lu, X., et al., *Lidar attenuation coefficient in the global oceans: insights from ICESat-2 mission.* Optics Express, 2023. **31**(18): p. 29107-29118.

[5] Magruder, L.A., K.M. Brunt, and M. Alonzo, *Early ICESat-2 on-orbit Geolocation Validation Using Ground-Based Corner Cube Retro-Reflectors.* Remote Sensing, 2020. **12**(21): p. 3653.
[6] Neumann, T., et al., *ATLAS/ICESat-2 L2A global geolocated photon data, version 6.* Boulder, CO: NASA National Snow and Ice Data Center Distributed Active Archive Center., 2023.
[7] Zheng, H., et al., *Deriving vertical profiles of chlorophyll-a concentration in the upper layer of seawaters using ICESat-2 photon-counting lidar.* Optics Express, 2022. **30**(18): p. 33320-33336.
[8] Lu, X., et al., *Retrieval of ocean subsurface particulate backscattering coefficient from space-borne CALIOP lidar measurements.* Optics Express, 2016. **24**(25): p. 29001-29008.
[9] Wu, D., et al., *A Novel Semi-Analytical Method for Modeling Polarized Oceanic Profiling LiDAR Multiple Scattering Signals.* IEEE Transactions on Geoscience and Remote Sensing, 2024. **62**: p. 1-17.
[10] Chen, T. and C. Guestrin, *XGBoost: A Scalable Tree Boosting System*, in *Proceedings of the 22nd ACM SIGKDD International Conference on Knowledge Discovery and Data Mining*. 2016, Association for Computing Machinery: San Francisco, California, USA. p. 785–794.
[11] Begouen Demeaux, C. and E. Boss, *Validation of Remote-Sensing Algorithms for Diffuse Attenuation of Downward Irradiance Using BGC-Argo Floats.* Remote Sensing, 2022. **14**(18): p. 4500.
[12] Gregor, L. and N. Gruber, *OceanSODA-ETHZ: a global gridded data set of the surface ocean carbonate system for seasonal to decadal studies of ocean acidification.* Earth Syst. Sci. Data, 2021. **13**(2): p. 777-808.
[13] Zhao, W., et al., *Comparison of diffuse attenuation coefficient of downwelling irradiance products derived from MODIS-Aqua in the South China Sea.* Optics and Precision Engineering, 2018. **26**(1): p. 14-24.

Simulating oceanic lidar observational capabilities: PROTEO project in the Luce mission.

L. Masi[1,2], *P. Di Girolamo*[3], *M. Di Paolantonio*[1], *G. Giuliano*[1], *G. L. Liberti*[1], *G. Volpe* [1], *A. Andrisani*[4], *S. Venafra*[4], *S. Zoffoli*[4], *D. Dionisi*[1]

(1) National Research Council, Institute of Marine Science (CNR-ISMAR), Roma, Italia
(2) Università "Parthenope", Napoli, Italy
(3) Scuola di Ingegneria, Università della Basilicata, Potenza, Italy
(4) Agenzia Spaziale Italiana, Roma, Italy

Corresponding author: lorenzamasi@cnr.it

Introduction

Luce (formerly CALIGOLA) is a space-based lidar mission led by the Italian Space Agency (ASI) in partnership with the National Aeronautics and Space Administration (NASA). The mission objective is of significantly advancing the understanding of the coupled atmosphere-ocean-land system. The payload of Luce will be the first ever spaceborne multi-wavelength elastic-Raman-fluorescence backscatter lidar system for Earth observations. [1]

CNR-ISMAR is in charge of defining Luce observational capabilities in providing information about bio-optical and bio-geochemical properties of the ocean. This will be done in the frame of PROTEO (PeRfOrmance simulaTor for ocEan Observations) ASI funded project that is aimed at contributing to the development of the mission end-to-end simulator for what concern the sea-surface, the ocean and the bottom surface

This study reports some preliminary results of the development of the forward model component relevant to the marine environment.

Methodology

The lidar forward simulator should estimate the whole signal acquired by the instrument. This includes the laser simulated backscattered signal ($S_{lidar}(z)$), the background signal (BKG) as well as the detector noise (Dark Count Rate - DCR).

$$S_{tot}(z) = S_{lidar}(z) + BKG + DCR$$

The development of the background [2] and the proper lidar signal [2] is implemented taking advantage of existing and consolidated radiative transfer model (RTM) SCIATRAN [3] that implements several features of interest for the project: full vectorial coupling of Atmosphere and Ocean, including inelastic processes such as vibrational and rotational Raman and fluorescence.

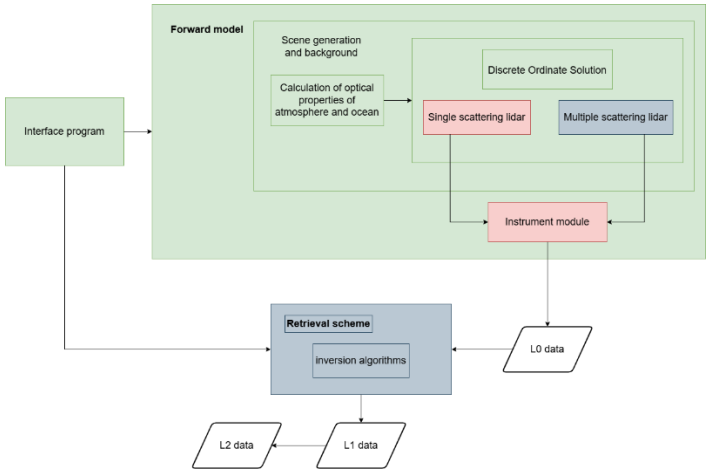

Figure 1. Structure of SCIATRAN (green), added modules (red) and future features to be implemented

The forward module includes 3 submodules:

- Radiative transfer for the background – already present in SCIATRAN
- Radiative transfer for the lidar signal. Currently implemented assuming single scattering for atmosphere and ocean and includes a dedicate routine for RTM through rough ocean surface
- Instrument module (spatio-temporal sampling, spectral response, radiometric behavior) simulating the overall instrument response to the optical signal.

Results and Discussion

Here, the simulation capabilities of the lidar module, and the observational performance of the Luce mission are presented.

Based on the current characteristics of the mission [2], the results shown in the following refer to a satellite with a sun synchronous orbit at 450 km altitude and 97° inclination, a lidar transmission/receiving geometry of 12.86° off-nadir zenith angle and the simulating 4 spectral windows, as reported in Table 1.

SW #	Start λ (nm)	End λ (nm)	Δλ (nm)	CWL (nm)
1	354.5	355.5	0.5	354.7
2	402.0	408.0	0.5	405.0, 407.5
3	531.5	532.5	0.5	532.1
4	675.0	695.0	0.5	685.0

Table 1. Simulated spectral windows and corresponding Luce channels dedicated to ocean

Firstly, we report some example of background simulations based on different illumination geometries/wind speed/chlorophyll concentration values (Table 2). Relative azimuth value of respectively 165.5°, 133.0° and 123.0° were assumed based on the illumination geometry at nominal overpass time (13.30 LST).

The simulations were run in coupled atmosphere-ocean mode, with polarization on (total signal displayed).

SW#	Mean Radiance mW/m²/nm/sr									ϑ_s
1	22.5	22.0	20.8	21.3	20.8	19.6	25.6	25.1	24.1	20°
2	33.5	31.4	28.1	31.1	29.1	25.6	35.2	33.3	30.2	
3	51.0	48.6	43.9	38.3	35.8	31.1	31.8	29.5	25.0	
4	20.7	20.6	20.5	16.6	16.5	16.3	13.8	13.7	13.6	
1	15.6	15.3	14.4	15.2	14.8	14.0	17.2	16.9	16.1	40°
2	22.8	21.2	18.7	22.0	20.4	17.9	25.5	24.1	21.9	
3	24.6	22.7	19.2	22.3	20.4	16.9	26.9	25.5	22.8	
4	11.1	11.0	10.9	10.0	10.0	9.8	16.2	16.2	16.1	
1	8.4	8.2	7.8	8.2	8.0	7.6	7.6	7.4	6.9	60°
2	12.5	11.7	10.3	12.2	11.4	10.1	11.5	10.7	9.3	
3	12.6	11.7	9.8	12.3	11.3	9.4	11.8	10.9	9.1	
4	6.1	6.1	6.0	5.8	5.8	5.7	5.3	5.3	5.2	

Chl-a conc mg/m³		
0.1	1	10

Wind speed m/s		
0.1	5	10

Table 2. Background radiance values for each spectral window for different values of Chl-a concentration, surface wind speed and solar illumination. Color legend on the right.

At this stage the lidar signal through atmosphere and ocean is simulated in single scattering approximation. The sea surface is modeled according to Nakajima and Tanaka BRDF [4] and the ocean bottom is considered as a lambertian surface. Morel description of seawater bio-optical properties is used [4], and some atmospheric features like aerosol and a thin cirrus have been added in order to verify the

sensitivity in the signal response. An example of a full (atmosphere+ocean) noise free lidar profile and corresponding background for 3 solar zenith angles values is reported in Figure 2.

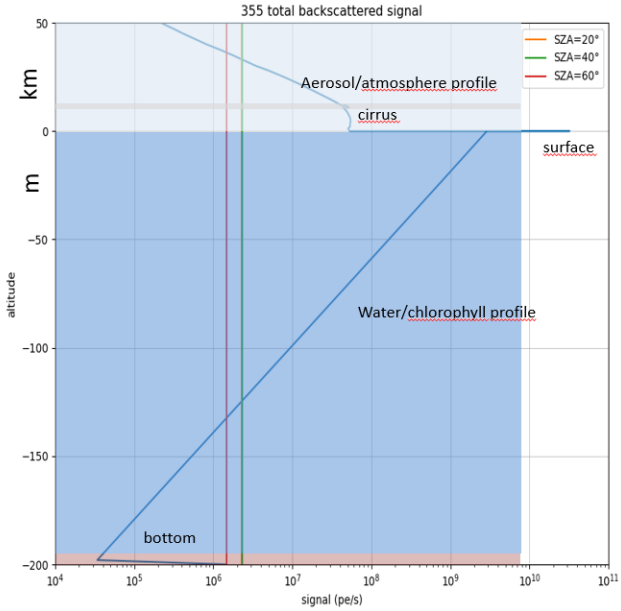

Figure 2. Example of a full (atmosphere+ocean) lidar profile and corresponding background for 3 solar zenith angles values

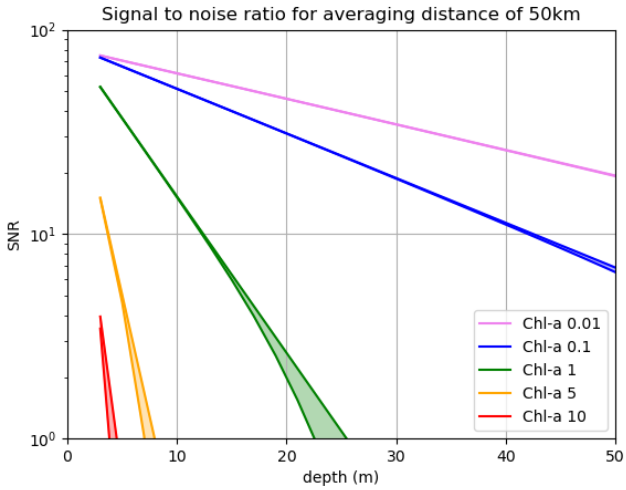

Figure 3. Signal-to-noise-ratio for 355nm signal at varying chlorophyll concentration [mg m-3] (color) and SZAs (shaded area, with the maximum value corresponding to night and the minimum to SZA=20°)

The current instrument model assumes ideal box-car like as single channel spectral response and introduce a signal induced noise. The detector noise is modeled as a detector DCR and the corresponding signal-to-noise ratio is calculated as follows:

$$SNR_{tot}(z) = \frac{S_{lidar}(z)}{\sqrt{ENF \cdot S_{tot}(z)}} \cdot \sqrt{n_s}$$

Where ENF ist he excess noise factor, assumed as 1.5, accounting for variations in the detector gain and n_s is the number of shots which one takes into account.

Examples of SNR profiles, as a function of Chl-a concentration, are shown in Figure 3.

Conclusions

With this preliminary demonstration, the capabilities of the single scattering lidar simulator have been proved. The next steps for the forward model consist in:

- adding the possibility of performing multiple scattering for atmosphere and ocean, either with a parametric approximation of multiple scattering contribution to the diffuse attenuation coefficient based on Monte-Carlo calculations [5] or by using a semi-analytic Montecarlo [6]
- taking into account polarization as well as inelastic processes
- further detail the illumination/reception geometry

In parallel, to fully assess the potential of the mission which aims to observe Raman scattering and fluorescence, and to exploit depolarization ratio to measure oceanic particulate, inversion models (L0->L2) will be developed (as anticipated in Figure 1).

Acknowledgements

This work was financed by ASI (DTA.AD004.583 RM_ASI Proteo) and University of Naples "Parthenope" (40th PhD Cycle funded in accordance with DM 630).

A kind acknowledgment goes to Alexei Rozanov (Uni Bremen) for his valuable advice on SCIATRAN.

References

[1] Behrenfeld, M. J., Lorenzoni, L., Hu, Y., Bisson, K. M., Hostetler, C. A., Di Girolamo, P., Dionisi, D., Longo, F., Zoffoli, S.: *Satellite Lidar Measurements as a Critical New Global Ocean*, Remote Sensing, 15, 5567, doi.org/10.3390/rs15235567, 2023.

[2] Di Girolamo, P. et al.: *CALIGOLA Mission Requirement Document Rev. 8.0*, Agenzia Spaziale Italiana, https://www.asi.it/wp-content/uploads/2024/07/CALIGOLA-fase-A-B1-bando-All.-1.b_MRD_CALIGOLA_DC-UIC-2024-061-8.0.pdf (last visited on 14/04/2025), 2024.

[3] Rozanov, V., Rozanov, A.V., Kokhanovsky, A. and Burrows, J..: *Radiative transfer through terrestrial atmosphere and ocean: Software package SCIATRAN*, Journal of Quantitative Spectroscopy and Radiative Transfer, 133, 13-71, doi: 10.1016/j.jqsrt.2013.07.004, 2014.

[4] Nakajima, T. and Tanaka, M.: *Effect of wind-generated waves on the transfer of solar radiation in the atmosphere-ocean system*, Journal of Quantitative Spectroscopy and Radiative Transfer, 29(6), 521-537, doi:10.1016/0022-4073(83)90129-2, 1983.

[5] Morel, A. and Maritorena, S.: Bio-optical properties of oceanic waters: A reappraisal, Journal of Geophysical Research, 106(C4), 7163-7180, doi/ 10.1029/2000JC000319, 2001.

[6] Churnside, J. H.: Review of profiling oceanographic lidar, Opt. Eng., 53(5), 051405, doi:10.1117/1.OE.53.5.051405, 2017.

[7] D'Alimonte, D., Liberti, G. L., Di Paolantonio, M., Kajiama, T., Franco, N., Di Girolamo, P. and Dionisi, D.: *In-water lidar simulations: the ALADIN ADM-Aeolus backscattered signal at 355 nm*, Opt. Exp., 32(13), 22781-22803, doi.org/10.1364/OE.510919, 2024.

Sea Surface pCO_2 and CO2 Flux in the Arctic Ocean Using Spaceborne LiDAR

S. Zhang[1], *P. Chen*[2], *Z. Zhang*[3]

(1) Second Institute of Oceanography, State Key Laboratory of Satellite Ocean Environment Dynamics (SOED), Baochubei Road 36, Hangzhou, Zhejiang, China

Corresponding author: chenp@sio.org.cn

Introduction

The Arctic Ocean plays a critical role in the global carbon cycle, acting as both a dynamic carbon sink and a region highly sensitive to climate change. Since the industrial revolution, anthropogenic activities have led to a significant increase in atmospheric carbon dioxide (CO_2), with the ocean absorbing nearly 30% of these emissions and thereby buffering the effects of global warming. However, regional uncertainties remain substantial, particularly in high-latitude oceans where observational coverage is limited [1, 2]. The Arctic is among the most rapidly changing oceanic environments, experiencing record sea ice loss, freshening surface waters, altered surface circulation, and enhanced primary production. These changes have strong implications for oceanic CO_2 uptake and acidification, especially as lower alkalinity and higher solubility at cold temperatures make the Arctic more vulnerable to anthropogenic CO_2 [3].

Despite its importance, estimating Arctic air–sea CO_2 fluxes remains challenging due to sparse in situ data, particularly in winter, when harsh conditions limit ship-based observations. Additionally, passive satellite sensors, which rely on solar radiation, are ineffective during polar night, leading to extensive seasonal data gaps in chlorophyll-a (Chl-a) and derived partial pressure of CO_2 (pCO_2) products. To address these challenges, we leverage spaceborne LiDAR from the CALIPSO mission, which provides diurnal and nighttime measurements independent of solar illumination. Previous studies demonstrated its ability to retrieve global ocean Chl-a and particulate backscatter [4, 5]. Building on this capability, we developed a novel LiDAR-based feedforward neural network (FNN-LID) to reconstruct long-term, diurnally-resolved pCO_2 fields in the Arctic.

This study aims to (1) reconstruct Arctic sea surface pCO_2 and air–sea CO_2 fluxes from 2007 to 2020, and (2) analyze diurnal, seasonal, and long-term variations in carbon dynamics. By exploiting the synergy between active remote sensing and machine learning, we offer new insights into the Arctic carbon system under changing climate conditions.

Methodology

This study integrated multi-source datasets to investigate marine carbon dynamics. Spaceborne lidar observations (2007-2020) from NASA's CALIPSO mission provided ocean optical profiles through dual-polarization measurements at 532 nm and 1064 nm via the Cloud-Aerosol Lidar with Orthogonal Polarization (CALIOP). These data underwent rigorous quality control, including outlier removal and sensor error correction. Global seawater Chl-a concentrations were derived using the neural network algorithm of Zhang et al. (2022) [6], which establishes nonlinear relationships between CALIPSO lidar signals and in situ Chl-a. Independent validation utilized BGC-Argo float measurements (0–25 m depth). Ancillary parameters included wind speed at 532/1064 nm wavelengths, corrected for polarization crosstalk and atmospheric attenuation. Surface ocean CO_2 fugacity (fCO_2) data were obtained from the Surface Ocean CO_2 Atlas (SOCATv2022) spanning 1957–2022 [7]. Environmental variables—sea surface temperature (SST), salinity (SSS), height (SSH), mixed layer depth (MLD), and atmospheric xCO_2—were acquired from CMEMS and CarbonTracker2019B. All datasets underwent unified gridding and quality screening for model compatibility.

A two-step FNN-LID was developed to reconstruct seawater pCO_2. Step 1 addressed spatial resolution limitations by training a 5-layer FNN to generate high-resolution (1°×1°) pCO_2 climatology (pCO_2_clim) using monthly climatological data from Takahashi et al. (2009) as reference. Input variables included SST, SSS, SSH, Chl-a, MLD, and geographic coordinates. Step 2 calculated pCO_2 anomalies (pCO_2_anom) as deviations between SOCAT observations and pCO_2_clim. Normalized anomalies were modeled against

normalized environmental predictors (SST, SSS, SSH, Chl-a, MLD, xCO_2, coordinates). Final pCO_2 estimates combined pCO_2_clim and pCO_2_anom. Model development employed the Keras neural network library with strict anti-overfitting protocols. Training followed a 10:1 data-to-connection ratio, with dataset partitioning into training (50%), evaluation (25%), and validation (25%) subsets. Monthly models underwent 4-fold cross-validation, with five iterations per fold to optimize accuracy and stability. This architecture enabled robust reconstruction of spatiotemporal pCO_2 patterns while maintaining physical interpretability of marine carbon cycle drivers.

Results and Discussion

1 Spatial and Seasonal pCO_2 Patterns

Spatial and seasonal analysis of pCO_2 revealed significant meridional gradients and seasonal amplitudes exceeding 80 µatm across the Arctic Ocean. The reconstructed monthly maps and time series (Fig. 1A–J) highlighted distinct regional patterns: the Chukchi and East Siberian Seas exhibited elevated pCO_2 in winter, while the central Arctic remained a CO_2 sink year-round. The seasonal variation from June to December reached ~81.1 µatm in the Greenland and Barents Seas. These patterns are influenced by both physical and biological mechanisms. For example, higher pCO_2 in winter is attributed to weak biological drawdown and sustained respiration, while summer lows correspond to enhanced primary production. Additionally, winter measurements derived from LiDAR data filled observational gaps left by passive sensors, enabling full seasonal coverage. This allowed quantification of regions with the most pronounced seasonal fluxes, such as the Bering Strait and the shelf edge of the White Sea. The FNN-LID model proved essential for characterizing the full seasonal amplitude, especially where satellite data are otherwise missing due to sea ice or polar night conditions.

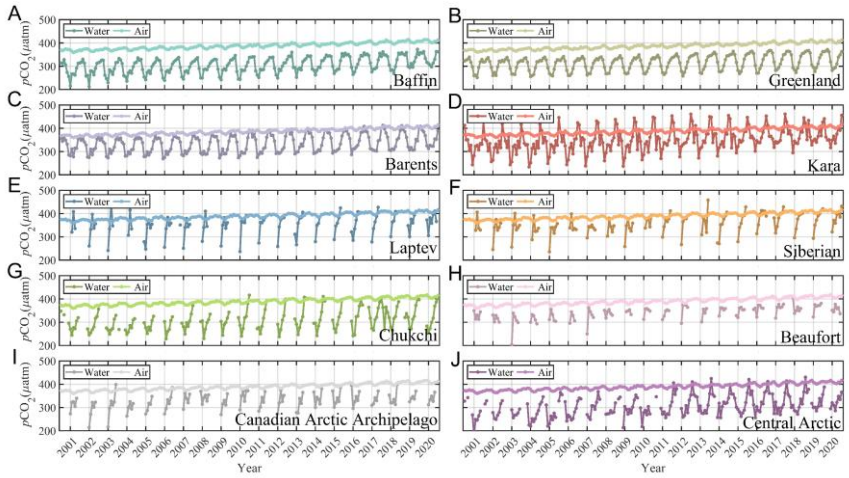

Figure 1. The long-time-series monthly pCO_2 values in 10 sectors in the Arctic Ocean: (A) Baffin Bay, (B) Greenland Sea, (C) Barents Sea, (D) Kara Sea, (E) Laptev Sea, (F) East Siberian Sea, (G) Chukchi Sea, (H) Beaufort Sea, (I) Canadian Arctic Archipelago and (J) central Arctic Ocean. The light color represents atmospheric pCO_2 and the dark color represents seawater pCO_2.

2 Diurnal Air–Sea CO_2 Flux Patterns

The diurnal variability in air–sea CO_2 fluxes showed sector-dependent patterns. In the Atlantic Arctic (e.g., Baffin Bay, Barents Sea), daytime carbon uptake was greater due to higher wind speeds (mean diurnal ratio ~101.1%), despite weaker pCO_2 gradients. Conversely, the Pacific Arctic (e.g., Chukchi, East Siberian Seas) showed stronger CO_2 uptake at night, driven by both higher pCO_2 gradients and stronger nocturnal winds (mean diurnal ratio ~93.9%) (Fig. 2C,F). This contrast arises from spatial asymmetries in

wind regimes and sea–air CO_2 disequilibria (ΔpCO_2). Notably, these patterns remain consistent across seasons (Fig. 2A–F), suggesting that the controlling processes are not purely seasonal but structurally driven by geography and atmospheric circulation. The study is among the first to document such diurnal differences in polar carbon exchange using satellite-based active sensing. These findings highlight the importance of capturing diurnal cycles in flux estimation models, as conventional monthly-averaged climatologies may mask such variability, especially under changing wind and pressure dynamics in the polar boundary layer.

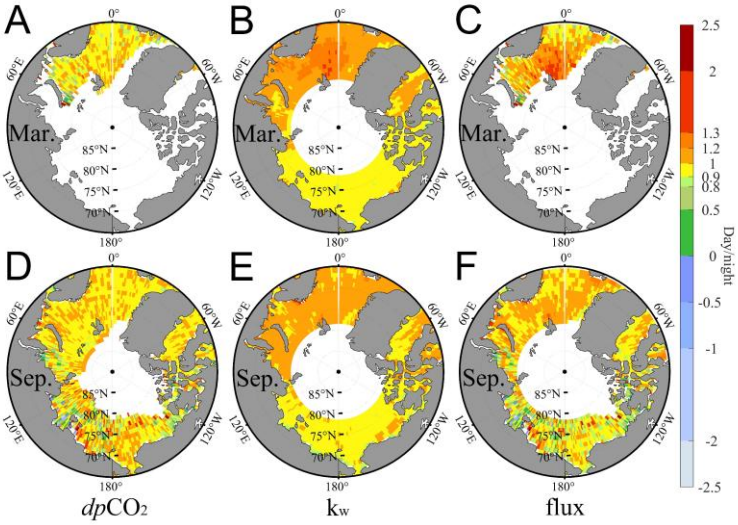

Figure 2. Ratios of daytime to nighttime (A) dpCO_2, (B) kw and (C) air–sea carbon fluxes in March and of daytime to nighttime (D) dpCO_2, (E) kw and (F) air–sea carbon fluxes in September.

3 Long-Term pCO_2 Trends and Sea Ice Retreat

Long-term trends (2001–2020) indicate a consistent increase in Arctic surface pCO_2 at a rate of 1.41 µatm yr^{-1} (2001–2010) and accelerating to 2.16 µatm yr^{-1} (2011–2020), approaching the atmospheric CO_2 growth rate (2.17 ± 0.21 µatm yr^{-1}). This suggests the Arctic Ocean remains a CO_2 sink, but the buffer capacity is weakening. Spatial trend analysis (Fig. 3A) showed that regions with rapid sea ice retreat, notably the East Siberian and Kara Seas, experienced the steepest pCO_2 increases. This is attributed to meltwater dilution, which lowers alkalinity and reduces buffering capacity, allowing atmospheric CO_2 to acidify the upper ocean more rapidly. Concurrent SIC trends (Fig. 3B) confirm strong sea ice decline in these areas. These findings emphasize the growing vulnerability of Arctic shelf seas to ocean acidification and their dynamic response to climate forcing. The results call for high-resolution carbon cycle monitoring in the Arctic, especially in transition zones where sea ice loss exposes low-buffered waters to atmospheric CO_2, intensifying air–sea exchange and ecological impacts.

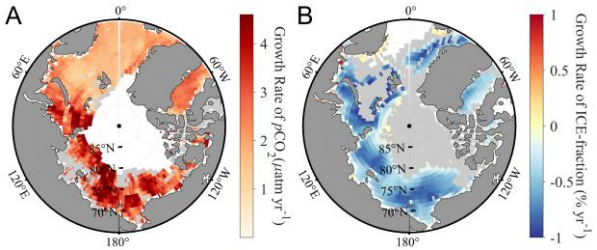

Figure 3. The annual growth rates of (A) pCO_2 (µatm yr^{-1}) and (B) SIC (% yr^{-1}) from 2001 to 2020. Gray indicates a nonsignificant trend.

Conclusions

In this study, we developed a long-term diurnal dataset of sea surface pCO_2 and air–sea CO_2 fluxes in the Arctic Ocean by integrating active spaceborne LiDAR measurements with feedforward neural network modeling (FNN-LID). Leveraging CALIPSO's diurnal LiDAR data, we reconstructed daily variations of Chl-a and wind speed, and filled crucial observational gaps during polar night, which have been inaccessible to traditional passive remote sensing approaches due to low solar angles and sea ice coverage. The FNN-LID method demonstrated strong agreement with both passive remote sensing data and in situ observations, particularly in marginal seas heavily influenced by terrestrial inputs. The high-resolution LiDAR-derived products exhibit clear seasonal and spatial variability in Arctic pCO_2, with meridional patterns and seasonal amplitudes exceeding 80 µatm. Notably, Arctic surface water pCO_2 is generally higher in winter than in summer, revealing a previously underrepresented dynamic due to wintertime data scarcity. Our results confirm that the Arctic Ocean has consistently functioned as a net sink of atmospheric CO_2 over the past two decades. However, in regions experiencing significant sea ice retreat, such as the East Siberian and Kara Seas, the rate of pCO_2 increase is accelerating. We also highlight substantial diurnal variability in air–sea CO_2 fluxes: the Atlantic Arctic Ocean exhibits a stronger carbon sink during the day than at night, while the Pacific Arctic Ocean shows the opposite trend, reflecting regional differences in sea surface pressure and wind patterns. This study demonstrates the feasibility and advantages of combining active satellite remote sensing and machine learning to monitor polar carbon dynamics. It underscores the importance of diurnal observations in polar biogeochemistry and offers a valuable data resource for future climate studies and carbon budget assessments in the rapidly changing Arctic environment.

Acknowledgements

This research was supported by the National Natural Science Foundation of China (Grants No. 42322606, 42276180, 61991453, 2022YFC3104200). We acknowledge the Surface Ocean CO_2 Atlas (SOCAT) and the Global Ocean Data Analysis Project (GLODAP) for providing essential in situ pCO_2 data used in this study. We are also grateful to NASA for access to the CALIPSO satellite data and the Copernicus Marine Environment Monitoring Service (CMEMS) for providing oceanographic reanalysis datasets.

References

[1] T. Takahashi et al., *Climatological mean and decadal change in surface ocean pCO2, and net sea–air CO2 flux over the global oceans*. Deep Sea Research Part II: Topical Studies in Oceanography 56, 554-577 (2009).

[2] C. Rödenbeck et al., *Data-based estimates of the ocean carbon sink variability–first results of the Surface Ocean pCO 2 Mapping intercomparison (SOCOM)*. Biogeosciences 12, 7251-7278 (2015).

[3] M. Yamamoto‐Kawai et al., *Surface freshening of the Canada Basin, 2003‐2007: River runoff versus sea ice meltwater*. Journal of Geophysical Research: Oceans 114 (2009).

[4] X. Lu et al., *New attenuated backscatter profile by removing the CALIOP receiver's transient response*. Journal of Quantitative Spectroscopy and Radiative Transfer 255, 107244 (2020).

[5] M. J. Behrenfeld et al., *Space‐based lidar measurements of global ocean carbon stocks*. Geophysical Research Letters 40, 4355-4360 (2013).

[6] Z. Zhang et al., *Retrieving bbp and POC from CALIOP: A deep neural network approach*. Remote Sensing of Environment 287, 113482 (2023).

[7] B. Pfeil et al., *A uniform, quality controlled Surface Ocean CO 2 Atlas (SOCAT)*. Earth System Science Data 5, 125-143 (2013).

15 years of experience in remote measurement of suspended particulate matter in water using laser-induced fluorescence shipborne LiDAR

A.A. Molkov[1], *V.V. Pelevin*[1], *E.S. Koltsova*[1]

(1) LIfeLiDAR SAS, 1 Place Sophie Laffitte, 06560, Sophia Antipolis, France

Corresponding author: alex.molkov@lifelidar.com

Introduction

Measuring suspended particulate matter (SPM) concentration in water is essential for hydro-optical studies, environmental monitoring, and the assessment of aquatic ecosystems. Gravimetric analysis, based on filtration and direct mass measurement, remains the reference method due to its high accuracy and independence from calibration. Submersible turbidimeters offer a faster alternative by measuring light scattering at specific angles. When installed on drifting platforms such as Argo floats or ferry systems, they provide continuous observations for spatial analysis. Remote sensing methods offer valuable synoptic information and are widely used in combination with in situ techniques. For example, the Nechad [1] and Novoa [2] algorithms estimate SPM from reflectance in red and near-infrared bands, showing acceptable errors in coastal and turbid waters. Their performance, however, decreases in optically complex conditions where dissolved substances and phytoplankton overlap with mineral signals.

Similar methodological challenges are observed in lidar-based sensing of aquatic environments. Numerous studies in the literature have focused on retrieving the backscattering coefficient of water and establishing its correlation with suspended particulate concentrations (for example, [3]), as well as on utilizing polarization effects to differentiate between various types of suspended particles [4]. Several works have also addressed the estimation of chlorophyll *a* concentration by measuring its natural fluorescence in the upper water layer [5], which can be conditionally related to the organic fraction of suspended matter. However, direct quantitative assessments of suspended particulate matter concentrations in water using lidar techniques are virtually absent in the published literature, with the notable exception of a series of studies conducted by Pelevin with its laser-induced fluorescence (LIF) shipborne LiDARs (Fig.1 and Table 1). The present paper offers a theoretical framework for the proposed method, an outline of the measurement procedures, and, most importantly, a summary of its practical application based on the results of more than a dozen field campaigns conducted over the past 15 years in diverse aquatic environments around the globe.

Methodology

In the 2000s, the fluorescence shipborne UFL-7,8,9 LiDAR was developed and subsequently employed for the estimation of colored dissolved organic matter (CDOM), chlorophyll *a*, and total suspended matter (TSM) [6]. This LiDAR emits excitation pulses on 355 nm from a Nd:YAG laser operating at a repetition rate of 2 Hz, and detects returning signals across 11 spectral bands at stationary measurement sites, where concurrent water sampling was performed for instrument calibration. In transect mode, when operating from a moving vessel, the system records signals in 4 bands. The LiDAR captures the integrated echo signal from the upper layer without vertical resolution. Fluorescence intensities at 440 and 685 nm, along with

Figure 1. The laser-induced fluorescence shipborne LiDAR UFL-9 in different expeditions

Table 1. Technical description of ULF-9

Excitation laser wavelengths	355, 532 nm
Spectral channels	355, 385, 404, 424, 440, 460, 499, 532, 620, 651, 685 nm
Bandwidth	10-15 nm FWHM
Optical configuration	Monostatic (coaxial geometry)
Laser pulse repetition rate	2 Hz
Laser pulse duration	6 ns
Laser pulse energy	1.5 mJ (355 nm pulse), 3 mJ (532 nm pulse)
Telescope	Kepler; adjustable length to target range 1.5–25 m
Laser beam divergence	6 mrad
FOV	1 degree
Power supply	220 V, 50 Hz, 120 W
Dimensions; weight	800 × 550 × 250 mm; 35 kg netto
Receivers	Photomultipliers
Telescope clear aperture	140 mm
ADC frequency	50 MHz
ADC resolution	10 bit

backscattering at 355 nm, are normalized to the Raman scattering signal at 404 nm, and subsequently calibrated against a set of laboratory-analyzed reference samples to derive quantitative estimates of CDOM, chlorophyll *a*, and TSM concentrations, respectively. Detected signals of fluorescence and backscattering in Raman units depend on many factors: for chlorophyll a - species composition of phytoplankton, its phase of succession and physiological state, abiotic factors of the aquatic environment; for CDOM - its molecular composition; for mineral suspended matter - its particle size distribution, shape, and refractive index. Therefore, the LiDAR calibration should be performed for each water body and each season to obtain maps of the spatial distribution of water quality parameters in absolute weight units with the highest precision. As experience has shown, this is achieved by collecting water samples as close as possible to the lidar footprint, with strict synchronization of the sampling time.

Below, we provide a brief overview of the theoretical background of the lidar-based method for estimating suspended matter in water. A more detailed description is presented in [7]. Let's assume that the laser pulse of energy N_0 (λ=355 nm) is sounding the sea surface in the direction close to a vertical line. To the depth z it is coming energy equals to

$$N = N_0 \exp\{-K_{d,355} z\}, \quad (1)$$

where $K_{d,355}$ is the vertical attenuation coefficient.

Although the sensing is performed using a narrow laser beam, the vertical diffuse attenuation coefficient K_d traditionally defined for a broad beam of sunlight should be applied in this context. This is justified by the fact that the energy pulse is considered to have reached a given depth z, irrespective of any lateral broadening of the beam during its propagation. The angular aperture of our LiDAR receiver system substantially exceeds the angular divergence of the laser beam, even when accounting for its lateral spread. As a result, all photons that reach a depth z contribute to the formation of the backscattered signal, fluorescence signal, and other optical returns. Consequently, to properly account for light attenuation in the vertical direction, it is appropriate to use the vertical attenuation coefficient K_d, which was originally introduced for the downward flux of solar radiation.

A layer of water with dz thickness scatters back radiation of energy that equals to

$$dN_{355} = N_0 \exp\{-K_{d,355} z\} \beta_{355} dz, \quad (2)$$

where β_{355} is the backward scattering coefficient by elementary volume of water at λ =355 nm.

Backscattered (BS) by elementary layer and reached to the surface energy and full energy scattered by semi-infinite sea medium into the photo detector are calculated as

$$dN_{355} = N_0 \exp\{-2K_{d,355}z\}\beta_{355}dz, \quad (3)$$

$$N_{BS} = N_0 G\beta_{355}/(2K_{d,355}), \quad (4)$$

where G is the «geometrical» factor that depends on the LiDAR height, its inclination, hade of beam on the border "water-air" and etc.

By analogy, we can write that the energy of the Raman scattering signal reached the receiver (i.e. N_{RS}) is following:

$$N_{RS} = N_0 G\gamma_{404}/(K_{d,355} + K_{d,404}), \quad (5)$$

where γ_{404} is the constant that defines by Raman scattering of water medium.

After division (4) on (5) and taking into account that $2K_{d,355} \approx K_{d,355} + K_{d,404}$, the concentration of total suspended matter can be made using the following equation:

$$\beta_{355} = kN_{BS}/N_{RS}, \quad (6)$$

where k is the calibrating coefficient. Here we suppose that TSM concentration is proportionate to β_{355}, i.e., backward scattering coefficient of the medium at this wavelength, with the deduction of backward scattering being created by the "absolutely pure" sea water.

Results and Discussion

Figure 2 presents the results of a comparison between the lidar Raman-normalized backscatter signal at a wavelength of 355 nm and water samples collected synchronously in space and time, with subsequent laboratory analysis. The measurements were conducted for different waters from oligotrophic to hypertrophic, and from fresh and brackish to hyperhaline waters, including Lake Issyk-Kul (Kyrgyzstan) and Lake Balaton (Hungary), the Black, Baltic, Caspian, Norwegian, and North Seas, several marginal seas of the Arctic Ocean (Kara, East Siberian, and Laptev Seas), as well as the coastal waters of the Atlantic Ocean near Patos Lagoon. A robust linear relationship is established between suspended particulate matter (SPM) concentration and Raman-normalized lidar backscatter at 355 nm across global aquatic systems. The dataset containing 393 samples spans SPM concentrations from ~0.1–100+ mg/l and backscatter values spanning three orders of magnitude.

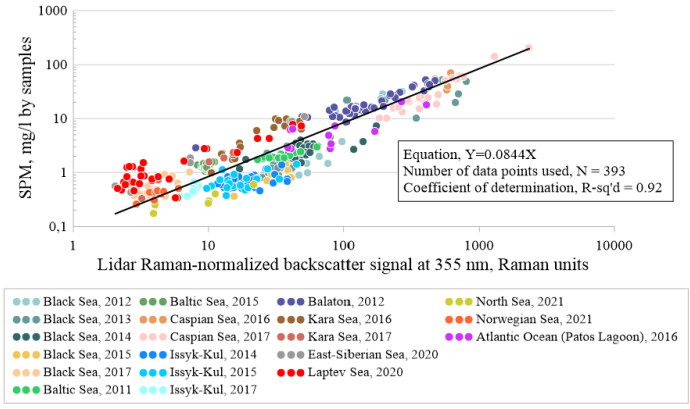

Figure 2. Results of suspended particulate matter measurements in the surface layer of lakes, seas, and oceans using the UFL-9 fluorescence lidar obtained during 20 field campaigns conducted over 15 years

Fits and corresponding error metrics for each case are not shown in Fig.2 for clarity, only the average ones across all samples. The coefficient of determination R^2, calculated on 20 or more water samples per

each case (expedition), ranged from 0.7 to 0.98. The largest scatterings of points were observed in cases of temporal desynchronization between water sampling and LiDAR sensing, or during operations from small vessels under conditions of strong wind-driven surface waves, which affected the stability of laser beam focusing on the highly dynamic sea surface.

However, while the obtained linear relationship is strong and broadly applicable, we have observed that the slope of the regression, represented by the coefficient k, can vary (from 0.028 to 1.15). Our current understanding suggests that the primary source of this variability is the geometry of the lidar sensing, especially its height above water, inclination, and focus settings. Recognizing the impact of these geometric factors, we are now focusing on quantifying and correcting for them. Our goal is to refine this coefficient into a more universal constant, reducing the need for site-specific calibrations and improving the reliability of SPM retrievals from lidar data. Ultimately, these efforts will enhance the accuracy and comparability of lidar-based SPM monitoring across different aquatic environments.

Conclusions

This study presents the results of suspended particulate matter measurements in the waters of lakes, seas, and oceans, obtained during 20 field campaigns conducted over 15 years. The core of these measurements is based on collecting the integral energy of elastic backscattering and Raman scattering from the upper water layer, the thickness of which depends on the inherent optical properties (IOPs). The ratio of these two signals is then used to estimate the concentration of suspended particulate matter. This approach effectively compensates for the variability in lidar sounding conditions, such as distance to the target, incidence angle, and the thickness of the sounded layer, making the method applicable across a wide range of water types and deployment platforms.

It should be noted that the method does not provide vertical resolution; instead, it yields the average concentration within the surface layer, whose thickness is governed by water turbidity and typically ranges from 0.5 to 5 meters. This layer is usually well mixed by wind-driven turbulence.

The proposed method enables the acquisition of in situ data on suspended particulate matter concentration in the upper water column with high spatial resolution. These data can be used for rapid assessment of water quality within a given aquatic area, as well as for the calibration and validation of satellite-derived products, supported by a large statistical dataset covering regions with widely varying hydro-optical characteristics.

References

[1] Nechad, B., Ruddick, K.G., Park, Y. *Calibration and validation of a generic multisensor algorithm for mapping of total suspended matter in turbid waters*. Remote Sensing of Environment, 2010, 114(4), 854–866.

[2] Novoa, S., Neukermans, G., Ruddick, K., Park, Y., Gohin, F. *Remote sensing of suspended particulate matter in coastal waters: An uncertainty and sensitivity analysis approach applied to the MW algorithm*. Remote Sensing, 2017, 9(9), 943.

[3] Zhao, X., Zhao, J., Zhang, H., Zhou, F. *Remote Sensing of Suspended Sediment Concentrations Based on the Waveform Decomposition of Airborne LiDAR Bathymetry*. Remote Sensing, 2018, 10, 247.

[4] Churnside, J. H., *Polarization effects on oceanographic lidar*, Opt. Express, 2008, 16(2), 1196–1207

[5] Fiorani, L., Angelini, F., Colao, F., Nuvoli, M., Palucci, A., *Laser radars for marine monitoring*, Proc. SPIE 11042, XXII International Symposium on High Power Laser Systems and Applications, 2018, 1104212

[6] Palmer, S.C.J., Pelevin, V.V., Goncharenko, I., Kovács, A.W., Zlinszky, A., Présing, M., Horváth, H., Nicolás-Perea, V., Balzter, H., Tóth, V.R. *Ultraviolet Fluorescence LiDAR (UFL) as a Measurement Tool for Water Quality Parameters in Turbid Lake Conditions*. Remote Sensing, 2013, 5, 4405-4422.

[7] Pelevin, V., Zavialov, P., Konovalov, B., Zlinszky, A., Palmer, S., Toth, V., Goncharenko, I., Khymchenko, L., Osokina, V. *Measurements with high spatial resolution of chlorophyll-a, CDOM and total suspended matter in coastal zones and inland water bodies by the portable UFL lidar.* Proceedings of the 35th EARSEL Symposium 2015, Stockholm, Sweden, 15-19.

New LIFL-11 portable fluorescence LiDAR for multi-parameter measurements of water column bio-optical properties

V. Pelevin[1], *A. Molkov*[1], *E. Koltsova*[1]

(1) LIFeLiDAR SAS, 1 Place Sophie Laffitte, 06560 Sophia Antipolis, France

Corresponding author: vadim.pelevin@lifelidar.com

Introduction

Operational, non-invasive surveying of aquatic areas through remote sensing — particularly using active optical methods based on laser-induced fluorescence (LIF) technology — has become an essential and, in many cases, irreplaceable tool in modern oceanography. This approach enables real-time, in situ measurements of key water quality parameters, including phytoplankton chlorophyll a, colored dissolved organic matter (CDOM), total suspended matter (TSM), and various organic contaminants, the most important of which are oil and petroleum products, as well as sewage.

By employing high-frequency laser excitation, LIF LiDAR technology provides fine-scale spatial resolution and enables both the detection and quantitative assessment of optically active substances at the surface as well as within the upper water column. When operated with ultraviolet laser excitation, which is particularly effective for inducing the fluorescence of organic compounds, the effective penetration depth of the integrated upper layer extends to approximately 10 meters. This capability allows for real-time and accurate assessments of spatial variability, thereby supporting investigations of submesoscale structures and dynamic processes in surface waters. Moreover, when a time-resolved approach is combined with green laser excitation, the sensing depth can reach 50 meters or more, enabling the retrieval of vertical profiles of the inherent optical properties of the water column.

The UFL-series LIF LiDARs have played a pivotal role in advancing this technology, demonstrating high efficiency of the method while being deployed in over 50 scientific expeditions worldwide during 20+ years. They were applied during routine oceanographic campaigns without any special preparations and in limited timeframes, in various remote and challenging regions, such as the Arctic and Antarctic seas as well as inland water bodies (a field campaign example is presented Figure 1).

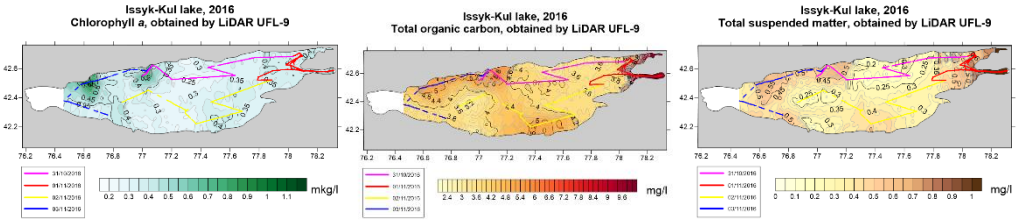

Figure 1. Examples of key water quality parameters mapping (Chl *a*, TOC, TSM) based on LiDAR data on Lake Issyk-Kul, Kyrgyzstan.

Shipborne LIF LiDAR systems have proven highly effective for studying the spatial and temporal variability of key water quality parameters, including phytoplankton, colored dissolved organic matter (CDOM), and suspended particulate matter. By combining fluorescence measurements of chlorophyll a and CDOM with elastic backscatter signals, these systems enable detailed investigations of small- and submesoscale variability in the ocean's surface layer. Compared to satellite observations, lidar provides higher sensitivity, finer spatial resolution, and independence from weather conditions, allowing detection of localized blooms, pollution events, and particulate patchiness. UFL systems thus remain essential tools for advancing the understanding of marine ecosystem dynamics.

Based on the results of many years of field experiments and operations under diverse environmental conditions, we have undertaken the development of a new, improved lidar system. This next-generation

instrument is designed to be more compact, robust, and versatile, featuring enhanced capabilities for vertical profiling of the ocean's upper layers using a green laser pulse.

Methodology

Below is a brief summary of the basic method for integral sensing of the upper ocean layer without vertical profiling, aimed at estimating total suspended matter.

Laser pulse of energy N_0 is sounding the sea surface in the direction, closely to vertical line. To the depth z it is coming energy equals to

$$N = N_0 \exp\{-K_{d,355} z\}, \quad (1)$$

where $K_{d,355}$ is the vertical attenuation coefficient.

A layer of water with depth dz scatters back radiation of energy that equals to

$$dN_{355} = N_0 \exp\{-K_{d,355} z\} \beta_{355} dz, \quad (2)$$

where β_{355} – backward scattering coefficient by elementary volume of water at λ = 355 nm.

Scattered back (BS) by elementary layer and reached to the surface energy equals to

$$dN_{BS} = N_0 \exp\{-2K_{d,355} z\} \beta_{355} dz, \quad (3)$$

Full energy scattered by semi-infinite sea medium in the direction back to the laser beam follows (after integration by z), and a portion of energy having hit into the photo detector considered by introduction of multiplier G:

$$N_{BS} = \frac{N_0 G \beta_{355}}{2K_{d,355}}, \quad (4)$$

Here G – «geometrical» factor, it is dependent on the altitude of the lidar above the sea surface, the slope angle of laser axle to the horizon and to the border "water-air" plane and etc.

The energy of the pulse of Raman scattering that reached the receiver (i.e. N_{RS}) equals:

$$N_{RS} = \frac{N_0 G \gamma_{RS}}{K_{d,405} + K_{d,355}}, \quad (5)$$

where γ_{RS} is a constant, which is defined by Raman scattering of water medium.

The concentration of TSM estimation can be made on a basis of lidar measurements by the following way. As follows from the formulas shown above for N_{BS} and N_{RS}, quotient after their division one on another equals to β_{354}/γ_{RS} (taking into account that $2\alpha_{355} \cong (\alpha_{355} + \alpha_{405})$).

$$\beta_{355} = k N_{BS} / N_{RS}, \quad (6)$$

where k – a calibrating coefficient. The concentration of suspended matter is proportional to β_{354} — the backscattering coefficient of the medium at this wavelength — after subtracting the contribution of backscattering from optically pure seawater.

Results and Discussion

Drawing on extensive fieldwork and analysis of numerous potential applications of LIF technology and UFL lidars, a new lidar system was developed in 2024 (Figure 2). The main goal was to preserve the unique features of the UFL series, which include discrete optical signal detection using highly sensitive PMTs across four simultaneous optical channels. Each of the 4 channels supports 12 interchangeable optical filters, enabling flexible combinations to study the spatial variability of key parameters at up to 20 measurements per second (Table 1).

For example, when mounted on a patrol vessel cruising at 50 km/h, the system provides spatial resolution of under 1 meter, allowing for rapid aquatic surveys — ideal for pollution monitoring or coordination with satellite overpasses. Even on faster airborne platforms, the resolution remains well-

suited for environmental monitoring, detection of harmful algal blooms, disaster response in both marine and terrestrial environments, etc.

A key development focus was also adapting the lidar for vertical profiling with a green laser. The test version supports 10 cm vertical resolution, with future versions targeting resolution in the centimeter range.

Additional improvements include:

- Optimized optics for stable measurements under variable distances, wave motion, and bright sunlight, with adjustable field of view and range targeting.
- A tri-wavelength laser (355 + 532 + 1064 nm), with a planned upgrade to a quad-wavelength system (266 + 355 + 532 + 1064 nm), expanding experimental capabilities.
- Extended applicability to land and atmospheric studies.
- Enhanced spatial orientation tracking (roll, pitch, acceleration, and tilt).
- Integrated video camera, including infrared, for enriched surface data collection.

Figure 2. LIFL-11. Left – the prototype at OceanOptics XXVI Conference, Gran Canaria, Spain (https://2024.oceanopticsconference.org/our-exhibitors/); right – system layout on a boat.

The LIFL-11's multispectral optical receiving system, with a spectral resolution of less than 10 nm over the range of 380–750 nm, allows for highly detailed environmental assessments (Figure 3). This capability is particularly valuable in waters with varying turbidity levels, supporting the detection of pollution and other ecological phenomena with high sensitivity.

Table 1. Table of LIFL-11 measured parameters.

CDOM/FDOM	Marine litter	Oil	Phytoplankton	TSM
Colored Dissolved Organic Matter	Plastics	Fuels	Chlorophyll *a*	Total Suspended Matter
Sewage waters	Polyethylene	Diesel	Pigment index	Mineral matter
Fulvic & Humic acids	Polypropylene	Crude oil	Phycoerythrin	Suspended sediment
Yellow substance	Wood, Leafs, Seagrass and Foam exception	Oil-in-water emulsion	Phycocyanin	Inorganic matter
			Vegetation index	Seston

The system integrates a range of advanced technical features designed to optimize environmental sensing in diverse aquatic conditions. It supports multi-wavelength laser excitation, receiver with up to 48

selectable spectral bands (4 channels × 12 filters each), allowing the user to configure four active bands in monitoring mode at a pulse repetition rate of 20 Hz. Data acquisition is performed independently for each laser pulse, ensuring high temporal and spectral resolution. The system includes an integrated IR camera, GNSS module with 10 Hz geo-tagging, and an inertial measurement unit (IMU) providing pitch, roll, yaw, gyroscopic, and angular data. Remote operation is supported via WiFi, 4G, and 5G networks, with real-time control, smartphone-based visualization, and cloud-based data storage and processing.

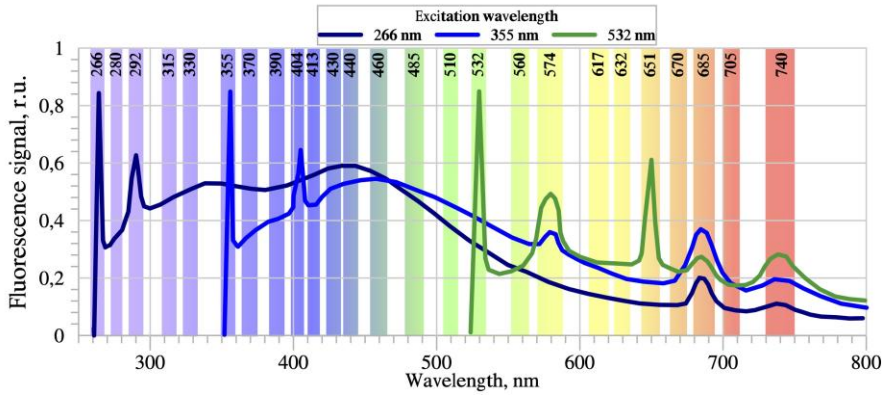

Figure 3. Spectral range of the LIFL-11 receiving system

The LIFL-11 enables integral sensing of the upper water layer with a thickness of 0.5 to 5 meters using a 355 nm excitation source. Optional vertical profiling to depths of up to 50+ meters is available with a 532 nm source, along with polarization-sensitive analysis and a ±30° scanning system for azimuthal coverage. A multispectral optical detector (MOD) with spectral resolution less than 10 nm can also be integrated. The compact design (44×33×28 cm, 26 kg) and standalone operation using an external battery make it suitable for deployment on a wide range of vessels, including in remote or logistically challenging environments.

Key advantages of the LIFL-11 include highly reliable registration of both elastic and laser-induced fluorescence signals, support for distinct or combined multi-wavelength excitation, and exceptional sensitivity. The system is well-suited for investigating the sea surface microlayer (SML) and the upper ocean structure in waters of any type and trophic state.

Conclusions

The LIFL-11 LiDAR represents a significant advancement in environmental monitoring technologies, enabling high-resolution detection and analysis of both aquatic and terrestrial phenomena. Its advanced four-channel architecture, featuring precise spectral band selection, combined with outstanding spatial and temporal resolution, facilitates the detailed assessment of environmental hazards such as oil slicks, algal blooms, and suspended particulate matter. Designed for versatile operation across aquatic and terrestrial environments, the LIFL-11 provides a robust, real-time solution for high-precision monitoring in diverse ecological settings.

References

[1] V. Pelevin, P. Zavialov, B. Konovalov, et al., “Measurements with high spatial resolution of chlorophyll-a, CDOM and total suspended matter in coastal zones and inland water bodies by the portable UFL lidar,” 35th EARSeL Symposium “European Remote Sensing: Progress, Challenges and Opportunities” (Stockholm, 2015).

[2] Palmer, Stephanie CJ, Vadim V. Pelevin, Igor Goncharenko, Attila W. Kovács, András Zlinszky, Mátyás Présing, Hajnalka Horváth, Virginia Nicolás-Perea, Heiko Balzter, and Viktor R. Tóth. "Ultraviolet fluorescence LiDAR(UFL) as a measurement tool for water quality parameters in turbid lake conditions." *Remote Sensing 5*, no. 9 (**2013**): 4405-4422

Investigating Decay of Underwater Laser Signal as Measure of Water Properties for Ocean Lidar – Experimental Study

N. Wierzbicka-Mróz[1], *A. Abramowicz*[2,3], *T. Kossowski-Kołodziej*[1,4], *A. Rubin*[2,3], *M. Szczyrba*[1,2,3], *G. Georgoussis*[5], *G. Giuliano*[6], *D. Dionisi*[6], *M. Jabłońska*[2,3], *I.S.Stachlewska*[1]

(1) *University of Warsaw, Faculty of Physics, Institute of Geophysics, (UW), Pasteura 5, 02-093, Warsaw, Poland*
(2) *University of Silesia in Katowice, University Laboratories for Atmosphere Survey (ULAS), Sosnowiec, Poland*
(3) *University of Silesia in Katowice, Institute of Earth Sciences, Będzińska 60, 41-200 Sosnowiec, Poland*
(4) *AGH University of Science and Technology, Adama Mickiewicza 30, 30-059 Kraków, Poland*
(5) *Raymetrics S.A., 32 Spartis, Metamorfosis 14452, Athens, Greece*
(6) *Consiglio Nazionale delle Ricerche, Istituto di Scienze Marine (CNR-ISMAR), 00185 Roma, Italy*

Corresponding author: iwona.stachlewska@fuw.edu.pl, mariola.jablonska@us.edu.pl

Introduction

This study investigates the application of the multi-channel scanning lidar system for assessing the optical properties of water, with particular emphasis on the decay of underwater laser signals as a function of depth and instrument settings. Measurements were carried out at Żywiec Lake, a retention reservoir near the Tresna Dam in southern Poland. The main objective was to identify optimal lidar configurations that enhance the accuracy of underwater optical profiling, particularly regarding incidence angle of the laser beam into the water and the voltage settings applied to the photomultipliers of the detection channels. The findings provide valuable insights for the development of future water lidar applications, especially in terms of minimizing measurement uncertainties and improving signal clarity. The present research contributes to a broader understanding of lidar capabilities in aquatic environments.

Methodology

A dedicated field campaign was done in 8-20 October 2024 within the project entitled *Feasibility study of using Atmospheric LIdar for Ocean applications* (ALIO) as a part of the Trans-national Access program (TNA) within funding of the European Commission Horizon 2020 Programme project *Solutions for Sustainable Access to Atmospheric Research Facilities* (ATMO- ACCESS).

The core measurements were done with the ACTRIS-Poland Mobile Platform (AMP) of University Laboratories for Atmosphere Survey (ULAS) at University of Silesia in Katowice. Measurements were performed from an 18m high scissor-lift platform using the eye-safe scanning lidar capable of both analog and photon-counting detection at four independent channels (Fig.1, photo). Signal types recorded backscattered light at polarized and depolarized Mie components (355nm), as well as Raman at N_2 (387nm) and H_2O (408nm). The scanning lidar was manufactured by Raymetrics S.A. as a custom-designed lidar system and it was serving as one of the core instruments during the ALIO TNA.

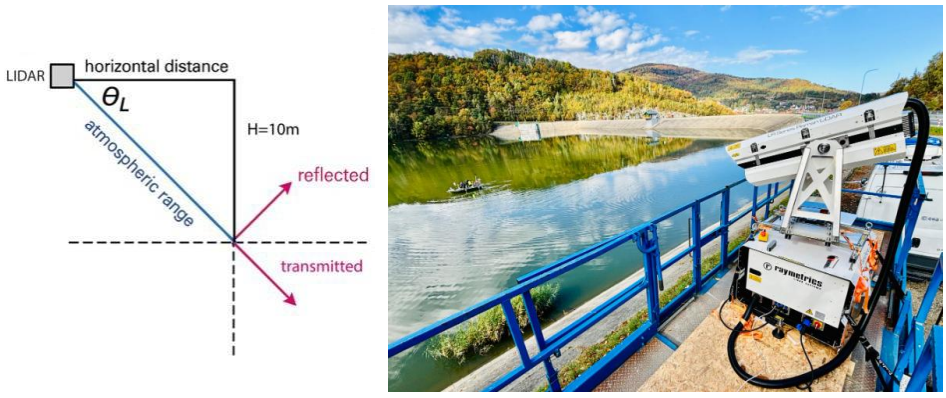

Figure 1 Schematic of scanning lidar measurements (left) done with the ACTRIS-Poland Mobile Platform of ULAS (right) during the Atmo-Acces ALIO TNA in October 2024 field campaign at Żywiec Lake. In-situ water samples from the boat (middle of the photo) were taken to validate the lidar-derived water optical properties. (*photo A.Abramowicz*)

Deployment of the scanning lidar mounted on the scissor lift provided flexibility in measuring at different heights and different angles. Although initially designed for atmospheric research, the scanning lidar system was adapted during this filed campaign for use in studying how light interacts with water surfaces, especially under varying angles (see Fig.1, schematics). Operating the lidar in this way posed a significant challenge, particularly given the logistical factors involved, such as selecting an optimal location for the measurement campaign (deep lake, secure place close to the lake shore, etc.). Measurements were taken for about a week at Żywiec Lake, both during the day and at night, enabling the ALIO TNA teams to assess the lake's diurnal optical properties and improve lidar techniques for diverse environments (Fig.2). In addition to this lidar data, the boat-based measurements were taken to validate the optical readings. Water and sediment samples were collected for analysis, allowing the team to measure inherent optical properties like turbidity and particle composition, which helped ensure that the lidar data accurately reflected the physical conditions of the lake. A hot-air balloon of ULAS equipped with gas analyzers and a particle counter as well as the mobile Mie-Raman multiwavelength lidar (EMORAL) provided also atmospheric data, contributing essential information on aerosol and gas concentrations, which are important for interpreting lidar measurements above the water.

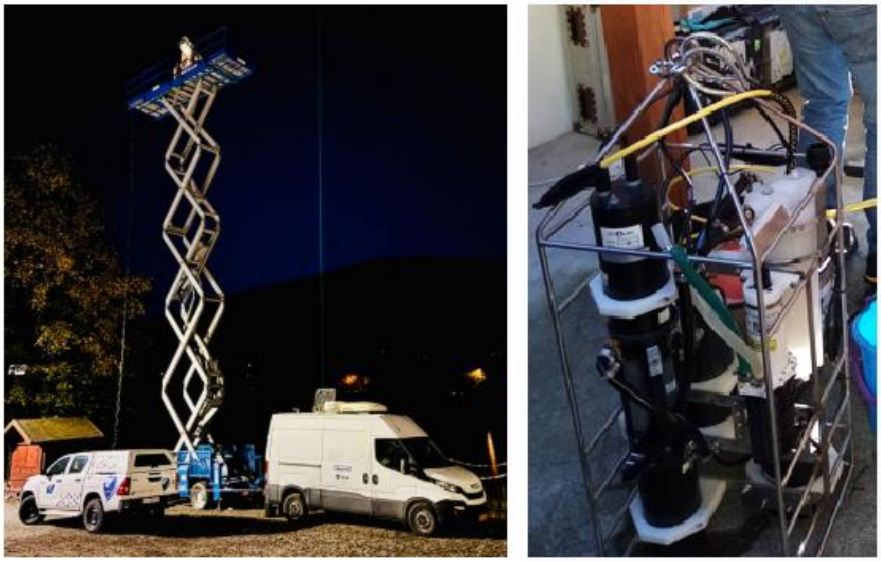

Figure 2 Scanning ULAS lidar measurements done from 18m high scissor lift and EMORAL lidar measutements done from the van (left, *photo A.Abramowicz*) and equipment used for CNR-ISMAR in-situ water samples from the boat (right, *photo I.Stachlewska*) during the Atmo-Access ALIO TNA in October 2024 field campaign at Żywiec Lake.

One of the major aims of the ALIO TNA study was to investigate measurements from different incidence angles; thus, the lidar laser beam was directed at the water surface at several specific angles: 13°, 17°, 21°, 25°, and 29° (θ_L measured from the horizon; Fig.1). An important aspect of the analysis was the variation of the PMT voltage settings, which ranged from 800 to 950 V and could be adjusted independently for each lidar detection channel. Two main configurations were tested: one with identical voltage values across all channels, and another with each channel set to a different value. The signals at each channel were analyzed. Later on, the mixing ratio (signals at 378/408) and the depolarization ratio (signals 355s/355p) were also calculated.

In-situ water samples collected by the CNR-ISMAR ocean color experts were done directly in the water form a rubber-boat in a regular net of sampling points covering the area in vicinity of the lidar operation in the water. The water optical depth was measured and water chemical analysis was also done, serving as a validation for the optical measurements (not in scope of this paper). Additional observations taken with the non-scanning, zenith-pointing, multiwavelength EMORAL Lidar by the University of Warsaw team. These vertical lidar measurements served as providing information on the atmospheric conditions and aerosol load over the Żywiec Lake.

Results and Discussion

The scanning-lidar results indicate that voltage configuration plays a critical role in the quality of lidar signals. Measurements with identical voltage settings across all four channels, particularly set to around 820 – 830 V (Fig.3), yield the most stable and noise-free signals, both in analog and photon-counting detection modes. These settings enabled consistent detection of the air–water interface and a clearly visible decay of the laser pulse, which may be related to the optical depth of the water. This aligns with earlier findings highlighting the importance of detector balance for accurate signal interpretation [1].

Incidence angle also influenced signal quality, although its impact was surprisingly less significant. Voltage configuration (closely linked to detector sensitivity) proved to be the dominant factor. Greater angles (e.g. 29°) provided clearer signals (Fig. 3), including less noise in the atmospheric part near water surface and smoother underwater signal transitions, likely due to reduced surface scattering and better beam penetration [2]. At low angles, increased noise in the atmospheric part near waterline was observed.

The mixing ratio at analogue signals was especially effective in identifying the laser entry point into the water and the subsequent signal decay, possibly allowing for the estimation of attenuation coefficients. The mixing ratio is less affected by atmospheric noise, making it potentially more suitable for representing water-specific properties, in contrary to depolarization ratio, which also indicates strong noise in the atmosphere, near to the detector.

Although photon-counting data offered high sensitivity, it was more susceptible to noise, particularly below the waterline. Therefore, the analog signals shown were prioritized for analysis. Interestingly, pre-peaks observed just above the water surface in the depolarized channels may indicate microdroplet presence or water evaporation effects (Fig.3).

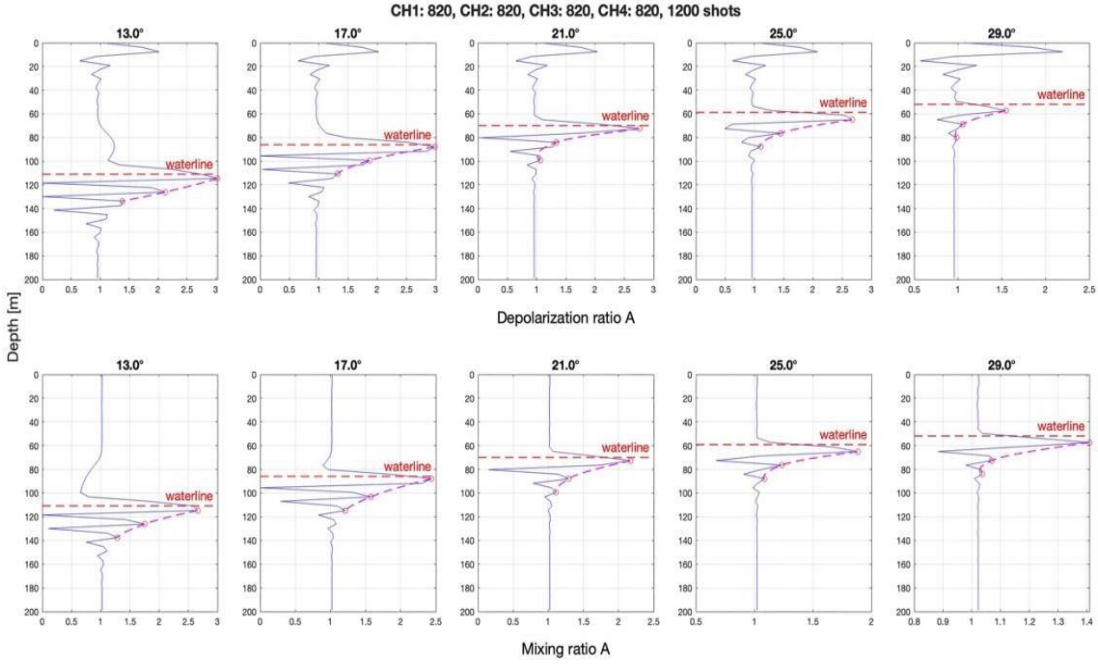

Figure 3 Attenuation of laser pulse with depth when entering water (red dashed line) with different incidence angles (13°, 17°, 21°, 25°, 29°) for depolarization ratio (upper row) and mixing ratio (bottom row) analogue signals. Blue line indicates the signal itself, pink line indicates the decay of the signal, assuming that minima are the artefacts, and maxima indicate true information about the signal. Scanning lidar measurements done with ACTRIS-Poland Mobile Platform of ULAS of University of Silesia taken in Żywiec Lake in October 2024 during the Atmo-Access ALIO TNA.

Conclusions

Optimal lidar configuration for underwater optical measurements includes the uniform PMT voltage settings across all of the lidar channels along with the greater incidence angles applied. These conditions help to reduce noise and enhance signal clarity, allowing for a more accurate profiling of water optical properties. The results indicate that PMT voltage settings have a stronger impact on the signal quality than the variations in angle within the tested angle range. Among all signal types, the analog mixing ratio provided the most reliable information about the beam entry into the water and the signal decay, making it especially valuable for identifying the waterline and, moreover, for estimating the attenuation. These findings offer a practical guidance for improving the design and deployment of lidar systems in the aquatic environments, both in controlled settings and in future field applications.

An important demonstration from this study was also to assess the possibility of using a lidar that has been designed solely for the atmospheric observations to its applications for the water/ocean studies. Obviously, the used wavelengths of the lidar (355p, 355s, 387, and 407 nm) are not optimal, however the results obtained are promising. We explore currently the possibility of using the data measured with all four lidar channels to obtain the optical properties under water surface from the information that is hidden in the slope of the signal decay due to the laser light attenuation in water. The wide range of the tested angles shall allow us to derive different ratios of the decay and translate them into the optical depths.

During the ALIO TNA field campaign vast amount of other instruments was deployed. The aforementioned in-situ water-sampling that was done from the boat into the water in a direct vicinity of the laser spot/footprint will be used in the future as a validation measure of the lidar-derived optical properties of water. The measurements of the AMP/ULAS scanning lidar will be combined with the vertical observations of the ground-based EMORAL lidar. It will be also linked to satellite observations (e.g. Sentinel overpass directly over the Żywiec Lake; EarthCARE overpass in vicinity of the EMORAL lidar location) to provide a closure picture of the activity.

This field work is interesting for its interdisciplinary approach, integrating both atmospheric and aquatic observations to deepen our understanding of interconnected Earth systems, such as the carbon cycle between oceans and the atmosphere. The findings could have important implications for future oceanic lidar missions.

Looking ahead, the ALIO TNA team plans to continue research with further tests aimed at assessing lidar's capabilities for studying water and atmospheric conditions. These tests, scheduled for the next years, will extend to different bodies of water, allowing the researchers to examine the differences in aquatic environments. This ongoing work will be critical for refining hybrid lidar methods and broadening the scope of geophysical insights, ultimately advancing the application of lidar technology in environmental science and Earth monitoring.

Acknowledgements

The measurements of the ACTRIS-Poland Mobile Platform of University Laboratories for Atmosphere Survey (ULAS) at University of Silesia in Katowice were done within the project *Feasibility study of using Atmospheric LIdar for Ocean applications* (ALIO) as a part of the Trans-national Access program (TNA) within funding of the European Commission Horizon2020 Programme, project *Solutions for Sustainable Access to Atmospheric Research Facilities* (ATMO-ACCESS); grant agreement no.101008004. ACTRIS-PL is funded by the Ministry of Science and Higher Education of Poland under grant agreement 2024/WK/04.

References

[1] Zhou, Y. et al. (2022). *Shipborne oceanic high-spectral-resolution lidar for accurate estimation of seawater depth-resolved optical properties.* Light: Science & Applications, 11, 261.

[2] Churnside, J.H., & Shaw, J.A. (2020). *Lidar remote sensing of the aquatic environment: invited.* Applied Optics, 59(10), C92–C102.

Evaluation of CALIOP derived backscattering coefficient (bbp(532)) product over contrasted oceanic waters

*S. Vadakke-Chanat[1], **C. Jamet[1]**, X. Lu[2], Y. Hu[2]*

(1) Université du Littoral Côte d'Opale, Université de Lille, CNRS, IRD, UMR 8187-LOG-Laboratoire d'Océanologie et de Géosciences, Wimereux, France
(2) Lidar Science Branch, Science Directorate, NASA Langley Research Center, Hampton, VA 23681, USA
Corresponding author: cedric.jamet@univ-littoral.fr

Introduction

Satellite ocean color observations have revolutionized our understanding of marine ecosystems and facilitated the monitoring of temporal changes induced by both natural processes and anthropogenic activities [1]. However, global coverage is limited by clouds, absorbing aerosols, and low Sun angles, particularly in polar regions. Additionally, no nighttime data is available [2, 3]. Lidar, has proven to be a valuable tool that addresses these limitations of traditional passive remote sensing methods [2, 3]. Several studies have utilized data from the Cloud-Aerosol-lidar Orthogonal Polarization (CALIOP) sensor aboard Cloud-Aerosol lidar and Infrared Pathfinder Satellite Observations mission (CALIPSO) satellite, and the Advanced Topographic Laser Altimeter System (ATLAS) sensor aboard Ice, Cloud, and Land Elevation Satellite-2 (ICESat-2), both of which were not originally designed for ocean applications [4, 5, 6].

In this work, validation of CALIOP between 2006 and 2021 is proposed using several sets of in-situ measurements. The in-situ $b_{bp}(532)$ data sets were obtained from multiple sources, including publicly available compilation of ocean datasets which provides a comprehensive and diverse range of measurements across various aquatic environments, enabling a rigorous evaluation of the accuracy and reliability of CALIOP $b_{bp}(532)$ estimates. Additionally, to enhance the number of matchups in the evaluation data sets, in-situ remote sensing reflectances (R_{rs}) were used to derive $b_{bp}(532)$ values, if the later was not available. In the rest of the manuscript, b_{bp} corresponds to $b_{bp}(532)$.

Methodology

CALIOP, a nadir-pointing lidar system, measured the backscatter lidar signal at 532 nm and 1064 nm wavelengths, operating from June 2006 till July 2023 [7]. The measurements obtained by CALIOP consist of the vertically integrated backscatter, including the co-polarized and cross-polarized components or with a vertical resolution of 22.5 when not vertically integrated in ocean waters [8]. For this study, we utilized the day- and night-time lidar-derived b_{bp} products published by Behrenfeld et al., 2019 [9] for the period 2008 – April 2017. The data from May 2017- October 2021 were similarly processed. Similar to Bisson et al. [10], a modification was applied to these datasets by changing the key conversion factor ($\beta(\pi)/b_{bp}$) to 0.32 instead of 0.16, effectively scaling it by a factor of 0.5.

The standardized match-up protocol from Vadakke-Chanat and Jamet [11] was used to compare CALIOP b_{bp} product to in-situ b_{bp}. A match-up is obtained by choosing a distance window of 15 km and a time window of 24 hours between the in-situ measurements and the CALIOP estimates.

The in-situ datasets from LOG, CCI [12] and Casey [13] were used for the validation process.

Results and Discussion

The validation of CALIOP backscattering coefficient (b_{bp}) product using in-situ datasets resulted in a limited number of matchups despite utilizing the global datasets spanning over a decade. Figure 1 displays the scatterplot of in-situ direct measured bbp data against the CALIOP-derived and MODIS-Aqua b_{bp} products. The pink circle markers denote MODIS-Aqua derived b_{bp} vs in-situ bbp, while the green circle markers represent CALIOP derived bbp with in-situ b_{bp}. Similarly, the pink star markers denote MODIS-

Aqua derived b_{bp} vs in-situ derived bbp, while the green star markers represent CALIOP derived b_{bp} with in-situ derived b_{bp}.

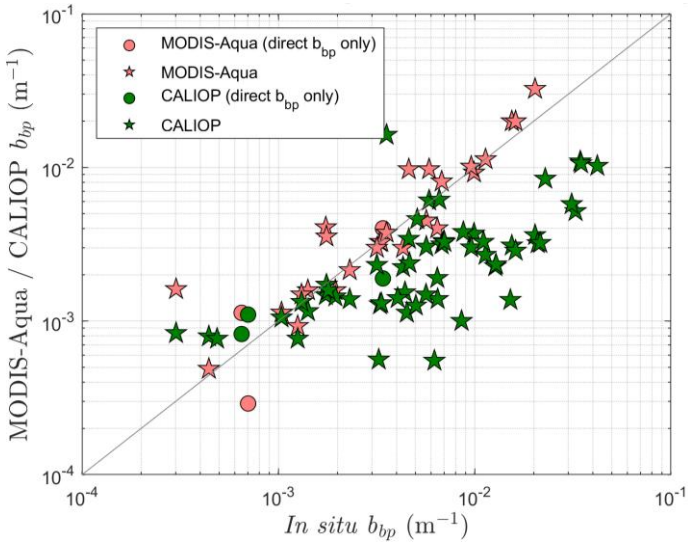

Fig. 3. The in-situ measured as well as estimated bbp data compared against the CALIOP derived data sets, and the MODIS-Aqua bbp products. The circle markers represent the stations with the directly measured in-situ bbp and the star makers represent the estimated bbp from in-situ Rrs.

Subsequently, a total of 58 matchup points were identified between CALIOP b_{bp} estimates and corresponding in-situ measurements. The validation outcomes as displayed in the Fig. 1, revealed a reasonable correlation between CALIOP b_{bp} and in-situ data, as evidenced by a coefficient of determination (R^2) valued at 0.37 and RMSE of 0.01 m^{-1}. The observed bias of –36.88% indicative of low systematic deviation of the CALIOP derived b_{bp} product from the data used for the evaluation. The MRE between the CALIOP b_{bp} estimates and the in-situ measurements were observed to be 63.2%. However, an underestimation of b_{bp} is observed for in-situ b_{bp} higher than 0.05 m^{-1}, and an overestimation is observed for values of b_{bp} lower than 0.001 m^{-1} by CALIOP sensor as evident in Fig. 1. In contrast, the MODIS derived bbp, when considering daytime data only (based on CALIOP product daytime flags), has maintained a strong correlation with the same set of in-situ data with R^2 being 0.97, the RMSE equal to 0.003 m^{-1}, but with a bias of 47.76%, and MRE of 56.4% for 15 data match-ups. These results are also summarized in Table 1.

Table 1. Statistics for the in-situ validation for CALIOP and comparison with that of MODIS

Sensor	Data Group	N	R^2	RMSE (m^{-1})	Bias (%)	MRE (%)	Scores
CALIOP	Day & Night	58	0.37	0.010	-36.88	63.17	1.35
	Direct b_{bp} only	3	0.94	0.001	13.09	42.73	4.79
	Daytime only	31	0.24	0.010	-19.45	62.99	1.73
MODIS	Day & Night	29	0.91	0.003	31.42	46.26	3.85
	Direct b_{bp} only	3	0.95	0.001	11.07	50.13	4.91
	Daytime only	15	0.97	0.003	47.76	56.42	2.45

Conclusions

A rigorous evaluation of the CALIOP backscattering coefficient (b_{bp}) product, using high-quality in-situ datasets over contrasted oceanic waters, has been performed. The results demonstrate a robust correlation between CALIOP b_{bp} estimates and in-situ measurements, with low levels of error and a slight underestimation at higher values and over estimation at lower values of b_{bp} by CALIOP when evaluated with the shipborne and fixed in-situ data sets. However, when evaluated against BGC-Argo data sets for the period 2017-2021, intended to complement previous studies, the errors in the CALIOP product increased. This study contributes to the multiple efforts to objectively assess the CALIOP oceanic product despite the scarcity of field data. These findings highlight the potential of using CALIOP for oceanographic research and marine ecosystem monitoring. More studies need to investigate the potential decrease of the quality of the CALIOP lidar from 2018.

While the results are promising, the scarcity of field data with sufficient matchups with CALIOP remains a challenge. Future efforts should focus on collecting more field data from ships of opportunity or by developing a network of autonomous oceanic profiling lidar on fixed platforms to better document the accuracy and reliability of lidar technology for ocean color studies. The potential launch of new lidar satellites, such as LUCE, in the near future could pave the way for the gradual development of dedicated sites to measure time series for the calibration, validation and characterization of lidar data retrieval. In the meantime, validation efforts like the current one, following the standardized scheme, remain of utmost importance.

Acknowledgements

We would like to thank the Ocean Productivity Group at the Oregon State University for providing the CALIOP dataset. This research was supported by the International Space Science Institute (ISSI) in Bern and Beijing, through ISSI/ISSI-BJ International Team project #530; ISSI-BJ Team project #50. We would like to thank Kelsey Bisson from the Oregon State University and NASA for help in getting the CALIOP data and in understanding the processing. This work and SV-C position were supported by CNES through the TOSCA program.

References

[1] Groom, S. B., Sathyendranath, S.,.Ban, Y. Bernard, S. Brewin, B. Brotas, V. Brockmann, C. Chauhan, P et al..: Satellite ocean colour: Current status and future perspective, Frontiers Marine Science, 6, 485, 2019.
[2] Hostetler, C.A., Behrenfeld, M.J., Hu, Y., Hair, J.W. and Schulien, J.A.: Spaceborne Lidar in the Study of Marine Systems," https://doi.org/10.1146/annurev-marine-121916-063335 10, 121–147, 2018.
[3] Jamet, C., Ibrahim, A., et al.: Going Beyond Standard Ocean Color Observations: Lidar and Polarimetry, Frontiers in Marine Science, 0, 251, 2019.
[4] Behrenfeld, M.J., Hu, Y., Hostetler, C.A. et al.: Space-based lidar measurements of global ocean carbon stocks, Geophysical Research Letter. 40, 4355–4360, 2013.
[5] Lu, X., Hu, Y.. Pelon, J. et al.: Retrieval of ocean subsurface particulate backscattering coefficient from space-borne CALIOP lidar measurements, Optics Express 24, 29001, 2016.
[6] Lu, X., Hu, Y., Zeng, Z. et al.: Deriving snow depth from ICESat-2 Lidar multiple scattering measurements: uncertainty analyses, Frontier in Remote Sensing, 3, 36, 2022.
[7] Winker, D.M. Pelon, J. Coakley, J.A., et al.: The CALIPSO Mission, Bulletin of the American Meteorological Society, 91, 1211–1230, 2010.
[8] Behrenfeld, M.J.,. Hu, Y., Bisson, K.M. et al.: Retrieval of ocean optical and plankton properties with the satellite Cloud-Aerosol Lidar with Orthogonal Polarization (CALIOP) sensor: Background, data processing, and validation status, Remote Sensing of Environment. 281, 113235, 2022.
[9] Behrenfield M.J., "Ocean Productivity Site, " Oregon State University (2024), http://orca.science.oregonstate.edu/lidar_public_v2.php.
[10] Bisson, K.M. Boss, E. Werdell, P.J. et al.: Particulate backscattering in the global ocean: a comparison of independent assessments," Geophysical Research Letter, 48, e2020GL090909, 2021.

[11] Vadakke-Chanat, S. and C. Jamet: Validation protocol for the evaluation of space-borne lidar particulate backscattering coefficient bbp, Frontiers in Remote Sensing, 4, 1194580, 2023.
[12] Valente, A. Sathyendranath, S. Brotas, V. et al.: A compilation of global bio-optical in situ data for ocean colour satellite applications – version three, Earth System Science Data ,14, 5737–5770, 2022.
[13] Casey, K. A. Rousseaux, C.S. Gregg, W.W. et al.: A global compilation of in situ aquatic high spectral resolution inherent and apparent optical property data for remote sensing applications, Earth System Science Data, 12, 1123–1139, 2020.

Synergy of LIF LiDAR, radiometric, and Sentinel-2/MSI, -3/OLCI Data for Regional Bio-Optical Modeling: Case Study on Lake Issyk-Kul

E. Koltsova[1], *S. Zhai*[2], *V. Pelevin*[1], *A. Molkov*[1], *O. Dubovik*[2], *S. Alymkulov*[3]

(1) LIFeLiDAR SAS, 1 Place Sophie Laffitte, Sophia Antipolis, France
(2) GRASP SAS, 3 avenue Louis Neel, Lezennes, France
(3) Razzakov Kyrgyz State Technical University, Str. Aitmatova 66, Bishkek, Kyrgyzstan
Corresponding author: katie.koltsova@lifelidar.com

Introduction

Satellite ocean color sensors play a crucial role in the long-term monitoring of water quality parameters, such as chlorophyll *a* (Chl *a*), colored dissolved organic matter (CDOM) and total suspended sediments (TSS), especially in large inland waters. However, accurate regional bio-optical models remain a challenge, particularly in optically complex and oligotrophic environments. We present a synergistic approach to regional bio-optical model development by integrating LIF LiDAR, *in situ* radiometric measurements, and satellite data. This combined method addresses limitations of existing models by enhancing spatial representativeness and temporal coherence, and offers a robust basis for routine water quality monitoring, especially in oligotrophic lake systems. This study focuses on Issyk-Kul Lake in Kyrgyzstan, a large alpine brackish lake with strong spatial and seasonal variability in optical properties.

Methodology

The primary method involved LIF LiDAR sensing using the UFL-9 system [1], which emitted UV pulses (355 nm) at 2 Hz and recorded backscattered signals at eight wavelengths. For this study, only signals at 355 nm and 685 nm were analyzed, normalized by Raman scattering at 404 nm. Mounted on the bow of a moving boat, the LiDAR provided continuous measurements of chlorophyll *a* (Chl *a*) and total suspended solids (TSS) with a 2 m spatial resolution. Calibration was performed by comparing LiDAR signals with lab-analyzed water samples taken at 40 locations along the track, filtered through 0.7 µm GF/F filters and analyzed spectrophotometrically [2, 3]. As a result, the following calibration matches were obtained (eq. 1, 2; Figure 1):

$$Chl\ a = 0.2083\ x_{685} - 0.0012,\ R^2 = 0.95, \quad (1)$$

$$TSS = 0.056\ x_{355} + 0.396,\ R^2 = 0.98 \quad (2)$$

where x_{685} and x_{355} are the LiDAR signals at 685 nm and 355 nm in Raman units, respectively, and R^2 is the determination coefficient.

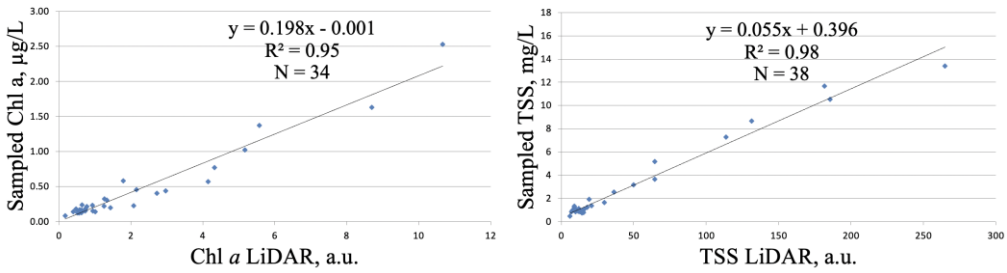

(a) **(b)**

Figure 1. Results of comparison of LiDAR signals at stations and water samples analyzed in the laboratory according to concentrations of **(a)** Chl *a* and **(b)** TSS. Black lines correspond to the best calibration matches (1) and (2), respectively.

Simultaneous radiometric measurements were collected using Ocean Optics STS spectrometers (400–750 nm, 1 Hz), following NASA protocols [4]. Remote sensing reflectance (R_{rs}) (or water-leaving reflectance ρ_w) was calculated after median filtering and time-averaging, using the Mobley method [5].

Field measurements were conducted on July 16, 17 and July 19, 2022, in the eastern and northern parts of Issyk-Kul Lake, influenced by runoff from major tributaries such as the Tyup and Jergalan Rivers. The study focused on deeper regions (up to 90 m) where bottom effects are negligible due to high turbidity (Secchi depth < 5 m), allowing reliable use of satellite and shipborne data [6]. On July 16, due to the long route, the vessel track was divided into seven zones based on hydrological and optical conditions, such as river inflows, bottom influence, and water depth. This zoning was taken into account when developing algorithms for Chl *a* and TSS retrieval [7].

For July 16th, Sentinel-2/MSI Level-2A imagery (10 m, 05:36 UTC) [https://scihub.copernicus.eu] was used to match satellite and *in situ* data. Over 47,000 LiDAR and 28,000 radiometric points were filtered based on time (±3 h from overpass [https://seabass.gsfc.nasa.gov/wiki/validation_description]), depth (to avoid bottom influence using B3 band), and statistical outliers. Final datasets included 4,111 matchups for Chl *a* and 1,071 for TSS, spatially averaged per satellite pixel and used for regional model development.

As of July 19th, a total of 11,902 LiDAR and 5,951 radiometric measurements were collected. Sentinel-3/OLCI Level-1 Top-of-Atmosphere (TOA) imagery was processed using the multi-pixel GRASP algorithm (https://www.grasp-open.com). The results were compared with several well-known atmospheric correction (AC) algorithms (Figure 2), emphasizing GRASP, whose 600×600 m resolution output showed the highest consistency with *in situ* spectra. While most algorithms performed adequately beyond 665 nm (within 10–12%), notable overestimations of water-leaving reflectance (ρ_w) by a factor of 2–3 were observed in the 412–510 nm range, likely due to incomplete Rayleigh scattering correction and inaccuracies in aerosol profiles. A subset of GRASP-averaged pixels was used to test various Sentinel-3A/OLCI band combinations for bio-optical modeling of Chl *a* and TSS.

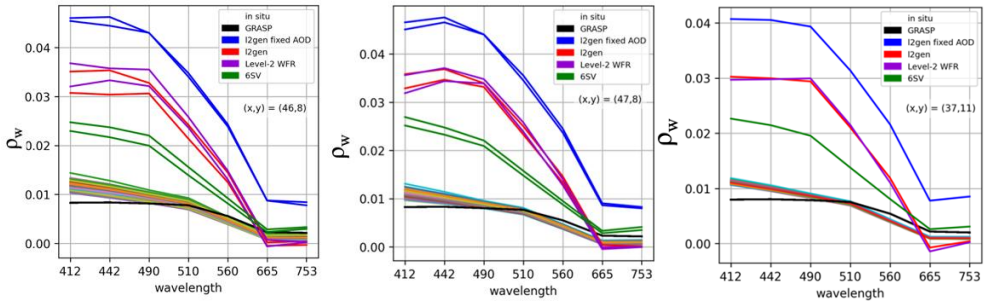

Figure 2. Comparison of atmospheric correction (AC) algorithms. The legend on each figure displays the names of the AC algorithms. The multiple colored lines represent *in situ* ρ_w measurements; the black curves represent GRASP ρ_w.

Results and Discussion

Examples of high-resolution spatial maps of LiDAR Chl *a* and TSS, are illustrated in Figure 3. The central basin of Lake Issyk-Kul showed low concentrations of both parameters (≤1 µg/L for Chl *a* and 1.2 mg/L for TSS), while significantly higher values were recorded near river mouths, with maxima of 2 µg/L for Chl *a* and 10 mg/L for TSS. These maps demonstrate the utility of LIF LiDAR in capturing spatial gradients and localized variability of optically active water constituents, especially in transitional coastal areas.

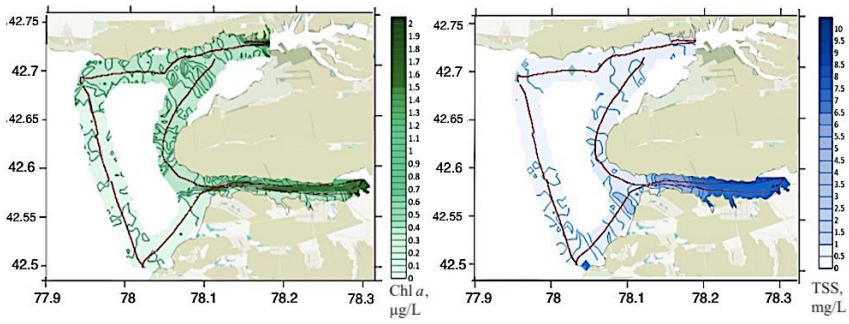

(a) **(b)**

Figure 3. Spatial distribution of **(a)** Chl *a* and **(b)** TSS in Issyk-Kul Lake on July 16, 2022 obtained by LiDAR.

Based on Sentinel-2 data, the Chl *a* model was developed using 2,057 calibration and 2,054 validation spectra, showing strong agreement with the OC2 band-ratio algorithm (B2/B3) [8], which was recalibrated using collected data. The model demonstrated high performance with $R^2 = 0.94$ and MAPE = 32.46%. Elevated errors were linked to ultra-oligotrophic zones with Chl *a* < 0.2 µg/L, where Sentinel-2 showed limited sensitivity, in contrast to LiDAR's higher detection capability (Figure 3a).

For TSS, 536 calibration and 535 validation points were used to develop a linear model based on the 560 nm band (B3), yielding excellent results ($R^2 = 0.96$, RMSE = 0.07 mg/L, MAPE = 6.07%) (Figure 3b). The model outperformed the widely used Nechad algorithm [9] applied to 665 nm, which significantly overestimated TSS. Likewise, the standard OC2 algorithm overestimated *in situ* Chl *a* concentration by over threefold.

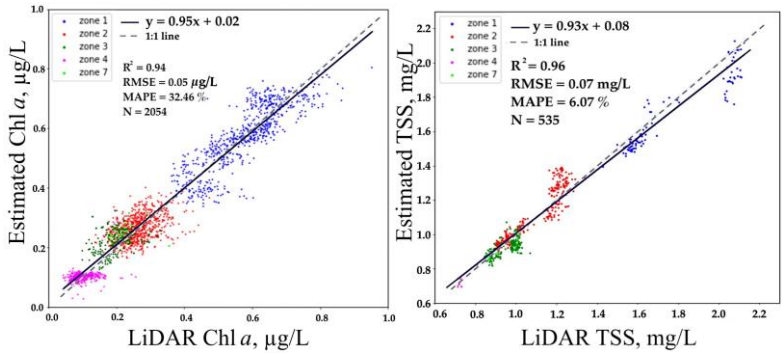

(a) **(b)**

Figure 3. Results of validation of (**a**) NASA OC2 standard algorithm for Chl *a* and (**b**) Nechad algorithm for TSS in Issyk-Kul Lake. The colors of the dots correspond to the zones described in [7].

The developed regional models for Chl *a* and TSS were applied to assess their seasonal dynamics in Issyk-Kul Lake and its tributaries in 2022, using 46 Sentinel-2 images. Results revealed characteristic patterns of variability, crucial for understanding lake dynamics and planning future fieldwork. Elevated Chl *a* and TSS concentrations were observed in spring during snowmelt-driven river inflows, especially from the Tyup and Jergalan rivers, and during strong autumn winds causing shoreline erosion. Summer months showed peak values (Chl *a* > 6 µg/L, TSS > 3 mg/L), with visible algal blooms, particularly near the Jergalan River. To ensure accuracy, shallow zones were excluded based on optical depth analysis. This highlights the value of satellite data in capturing spatial-temporal changes in bio-optical parameters across seasons. Several of the most illustrative satellite images and corresponding concentration maps are presented in the Figure 4 below.

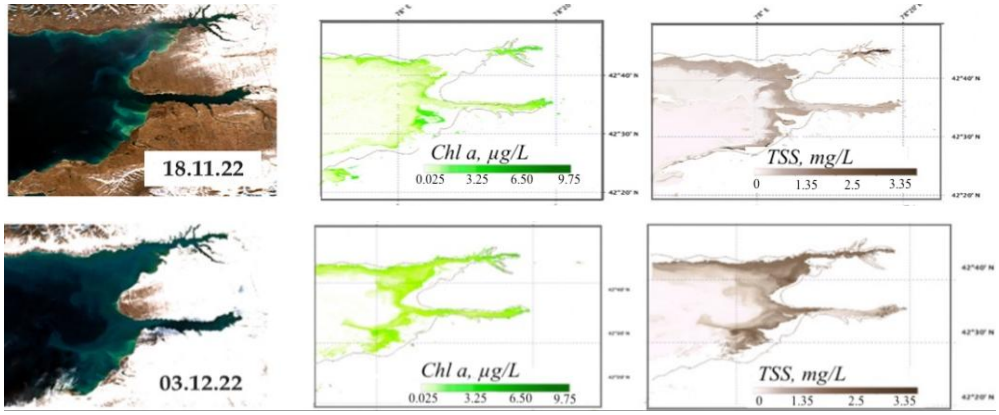

Figure 4. Some examples of RGB-compositions of the Sentinel-2/MSI images (left column) and spatial distribution of Chl *a* (center column) and TSS (right column) in Issyk-Kul Lake, obtained using the proposed bio-optical models.

Conclusions

This case study demonstrates the effectiveness of the proposed methodology for developing regional bio-optical models, integrating LIF LiDAR, in situ radiometric measurements, Sentinel-2/MSI, -3/OLCI data, and the GRASP atmospheric correction algorithm. Applied to Issyk-Kul Lake, an oligotrophic system, the approach overcomes traditional method limitations, enhancing spatial representativeness and temporal coherence. LiDAR from a moving vessel allows for the collection of a dense dataset (~15,000 data points) close to satellite overpasses, enabling accurate calibration and validation of bio-optical models with a single satellite image. GRASP further improves model accuracy, particularly in challenging conditions. While the methodology does not account for temporal variability, it provides a reliable framework for monitoring water quality in oligotrophic lakes. For all-season models, additional subsatellite measurements are needed across diverse conditions. This case study offers a solid foundation for advancing regional bio-optical models and their operational use in satellite-based monitoring.

Acknowledgements
This research received no external funding.

References

[1] Palmer, S. C. J., Pelevin, V. V., Goncharenko, I., Kovács, A. W., Zlinszky, A., Présing, M., Horváth, H., Nicolás-Perea, V., Balzter, H., & Tóth, V. R. (2013). Ultraviolet fluorescence LiDAR (UFL) as a measurement tool for water quality parameters in turbid lake conditions. *Remote Sensing, 5*(9), 4405–4422.
[2] SCOR-UNESCO. (1966). *Report of SCOR-UNESCO working group 17 on determination of photosynthetic pigments in sea water*. Monographs on Oceanographic Methodology, Vol. 1. UNESCO, Paris, 9–18.
[3] Konovalov, V. B., Kravchishina, M. D., Belyaev, N. A., et al. (2014). Determination of the concentration of mineral particles and suspended organic substance based on their spectral absorption. *Oceanology, 54*, 660–667.
[4] Mueller, J. L., Bidigare, R. R., Trees, C., Balch, W. M., Dore, J., Drapeau, D. T., Karl, D., Van Heukelem, L., & Perl, J. (2003). *Ocean Optics Protocols for Satellite Ocean Color Sensor Validation, Revision 5, Volume 5: Biogeochemical and Bio-Optical Measurements and Data Analysis Protocols* (pp. 5–24). Greenbelt, MD: Goddard Space Flight Center.
[5] Mobley, C. D. (1999). Estimation of the remote sensing reflectance from above–water methods. *Applied Optics*, *38*, 7442–7455.
[6] Zavialov, P. O., Pelevin, V. V., Belyaev, N. A., Izhitskiy, A. S., Konovalov, B. V., Krementskiy, V. V., Goncharenko, I. V., et al. (2018). High resolution LiDAR measurements reveal fine internal structure and variability of sediment-carrying coastal plume. *Estuarine, Coastal and Shelf Science, 205*, 40–45.
[7] Pelevin, V., Koltsova, E., Molkov, A., Fedorov, S., Alymkulov, S., Konovalov, B., Alymkulova, M., & Jumaliev, K. (2023). Regional models for Sentinel-2/MSI imagery of chlorophyll a and TSS, obtained for oligotrophic Issyk-Kul Lake using high-resolution LIF LiDAR data. *Remote Sensing, 15*, 4443.
[8] NASA Ocean Color *Chlorophyll-a Algorithm*. Retrieved from https://oceancolor.gsfc.nasa.gov/atbd/chlor_a/
[9] Nechad, B., Ruddick, K. G., & Park, Y. (2010). Calibration and validation of a generic multisensor algorithm for mapping of total suspended matter in turbid waters. *Remote Sensing of Environment, 114*, 854–866.

Lidar synergy with other instruments

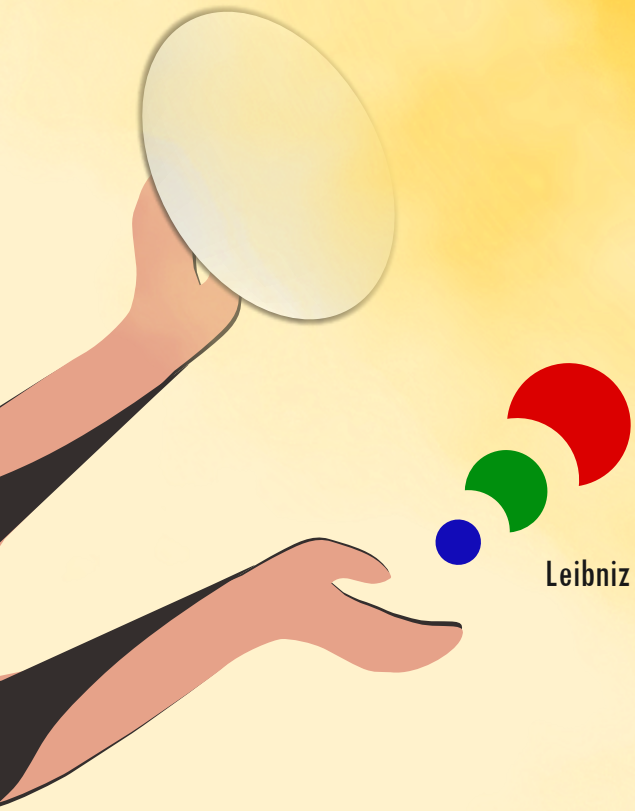

Session Chairs:

Holger Baars

Leibniz Institute for Tropospheric Research (TROPOS), Germany

Rodanthi Elisavet Mamouri

ERATOSTHENES Centre of Excellence (ECoE), Cyprus

Iwona Stachlewska

University of Warsaw (UW), Poland

Alexander Geiß

Ludwig Maximilian University of Munich (LMU), Germany

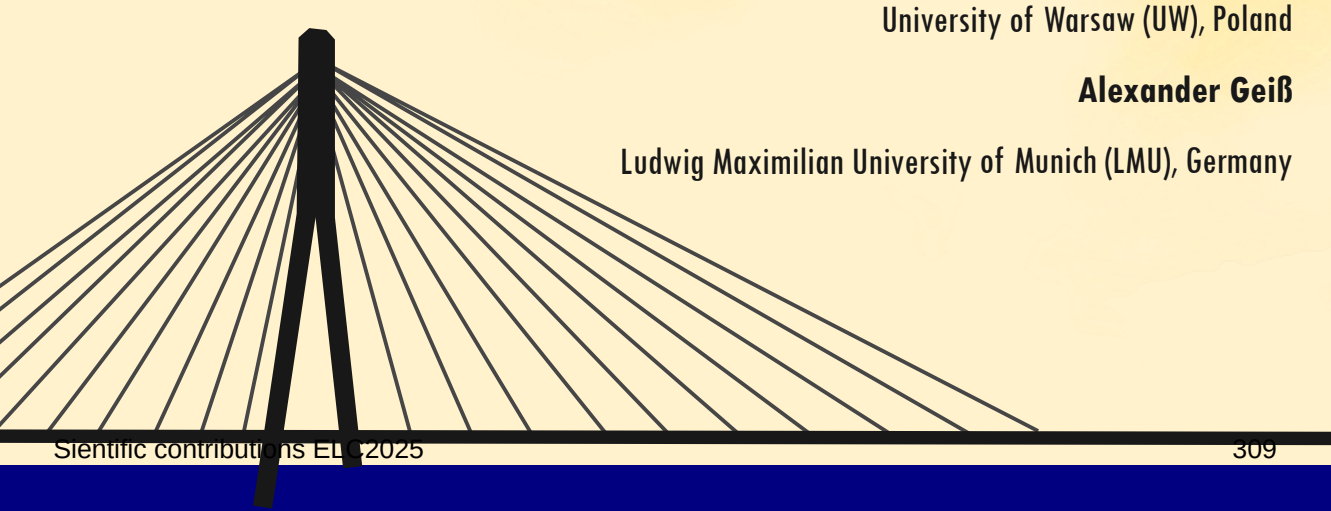

A UAV-based and Lidar Synergistic Approach for Estimating Dust Volume-to-Extinction Ratios

A. Papetta [1], *M. Kezoudi* [1], *A. Tsekeri* [2], *H. Baars* [3], *E. Drakaki* [2], *K. Kandler* [4], *E. Luca* [1], *T. Christoudias*[1], *E. Marinou* [2], *C. Stopford* [5], *T. Thornberry* [6], *V. Amiridis* [2], *J. Sciare* [1] *and F. Marenco* [1]

(1) Climate and Atmosphere Research Centre (CARE-C), The Cyprus Institute, Nicosia 2121, Cyprus
(2) Institute for Astronomy, Astrophysics, Space Applications and Remote Sensing, National Observatory of Athens, Athens, 15236, Greece
(3) Leibniz Institute for Tropospheric Research (TROPOS), 04318 Leipzig, Germany
(4) Institute of Applied Geosciences, Technical University of Darmstadt, Darmstadt 64287, Germany
(5) University of Hertfordshire, Hatfield, United Kingdom
(6) National Oceanic Atmospheric Administration (NOAA), Boulder, CO 80305, USA

Corresponding author: a.papetta@cyi.ac.cy

Introduction

Aerosol loading in the atmosphere is often expressed in terms of mass concentration (for example, in units of μg/m3) or extinction coefficient (e.g. in units of Mm−1). Remote sensing technologies such as spaceborne imagers, lidars and sun photometers, provide valuable optical measurements of extinction and aerosol optical depth (AOD) . These quantities must be converted into physical quantities like mass concentration for directly comparing with surface gravimetric measurements and for many applications (e.g. air quality assessment, aircraft safety, etc.). On the other hand, gravimetric quantifications of dust can be converted into optical properties to express how much the aerosols affect the radiative field and their direct impact on climate.

The volume-to-extinction ratio is an important aerosol property, allowing (in combination with knowledge of the density) to relay gravimetric and optical quantifications: it is often used in remote sensing and in climate models. The main microphysical and optical properties affecting this parameter are the effective radius, the degree of particle sphericity, and for fine particles the extinction efficiency. Existing methods [1] utilize column average AOD and volume concentrations taken from AERONET [2], which often underestimate or entirely miss giant-particles of dust [3].

This study presents a novel, synergistic approach combining ground-based lidar and airborne in-situ particle size distributions to study the volume-to-extinction ratio of mineral dust, during dust events originating in the Middle East, Central, and West Saharan regions and examine its variability and general estimation uncertainty. During the Fall Campaign 2021 in Cyprus and the ASKOS Campaign 2022 in Cape Verde, synergistic measurements were conducted using lidar, UAV-mounted in-situ sensors, and sun photometers during dust episodes. These observations provide a unique dataset for deriving volume-to-extinction ratios across different dust conditions. The retrieved ratios are compared with MOPSMAP (Modeled Optical Properties of Ensembles of Aerosol Particles) [4] optical model calculations and WRF-Chem model estimates to assess their accuracy and applicability.

Methodology

The volume-to-extinction ratio (ζ) quantifies how the volume of aerosol particles relates to their extinction properties. It is influenced by particle size, with larger particles increasing the ratio due to their volume (r^3) growing faster than their extinction efficiency (r^2). To establish the conversion between volume concentration (V) and extinction coefficient (α), the present study makes use of the following formulation:

$$\zeta = \frac{V}{\alpha} = \frac{4}{3}\frac{\Psi \cdot r_{eff}}{\overline{q_{ext}}} \quad (1)$$

where r_{eff} is the effective radius of the particle size-distribution, $\overline{q_{ext}}$ the mean extinction efficiency over the size-distribution, weighted by surface area and Ψ is a sphericity parameter defined as $\Psi = \frac{3\sqrt{\pi}}{4} V_p A_p^{-\frac{3}{2}}$ where V_p and A_p are the particle volume and particle projected area (with $\Psi = 1$ for spheres and decreases with increasing non-sphericity, [4],[5]). To relate this parameter with aspect ratio, for spheroids

$\Psi \sim \frac{1}{\sqrt{AR}}$, with values between ~0.6-0.9. Whilst remote sensing observations via lidar, sunphotometers, and passive satellite imagers provide extinction and AOD measurements, in-situ airborne optical particle counters provide observations of the volume concentration from the particle size distribution (PSD).

The study is focused on observations during two measurement campaigns; The Cyprus Fall Campaign 2021 (Oct–Nov 2021) investigated mineral dust transport over Cyprus using UAV-based in situ measurements and ground-based lidar and sun-photometers to study aerosol microphysics and vertical distribution. ASKOS (2021-2022) in Cabo Verde supported Aeolus satellite validation, examining Saharan dust transport, cloud interactions, and radiation effects using advanced ground-based instruments. We calculate the volume-to-extinction ratio for cases where data were available from co-located UAV-based Optical Particle Counters (OPCs) and lidar observations. Additional selection criteria include cloud-free conditions, AOD > 0.2, and dominance of dust over other aerosols. Back trajectory analysis via the HYSPLIT model helped us identify the dust sources for the events considered, revealing Middle Eastern, Central, and Western Saharan and mixed origins.

To assess the difference in the columnar average PSDs from AERONET and the UAV-based vertically resolved PSDs, we scale them to comparable units by vertically integrating the airborne observations, and we fit them to a bimodal lognormal distribution to smooth out artifacts typical of OPC measurements. Fig. 1 compares the AERONET and OPC PSDs during two cases: 15th November 2021 (a dust event from the Middle East, affecting Cyprus) and 24th June 2022 (a Western Saharan dust outbreak observed above Cape Verde). In the first case there is a relatively good agreement between the two methods, although AERONET shows a stronger contribution from particles <0.2 μm. For the second case, both method show a strong contribution of coarse particles, but the UAV-based observations reveal a larger abundance of particles even exceeding 1 μm, compared to AERONET. This can be attributed to AERONET's 15 μm cut-off and inversion constraints.

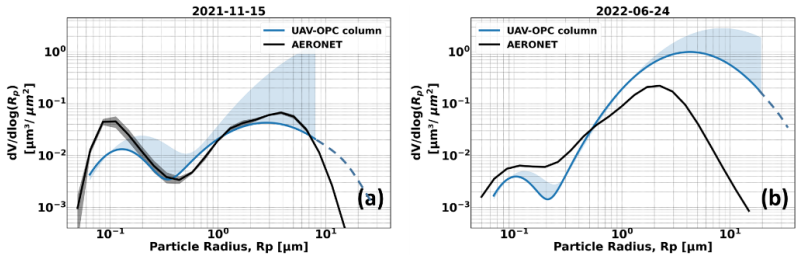

Figure 1. Column integrated UAV-based volume size distributions compared to AERONET for 15th November 2021 (a) and 24th June 2022 (b). The shaded area indicates the uncertainty of the fitted log-normal. The dashed line corresponds to the extrapolated log-normal curve beyond the maximum observed size bin.

Taking the ratio of extinction (observed by lidar) and volume concentration (measured with UAV-based OPCs), we calculate ζ for the selected cases (Eq. 1). The ζ parameter is also computed from the airborne observations alone, using the MOPSMAP model and incorporating OPC-based PSDs with refractive indices and aspect ratios derived from scanning electron microscope analysis (SEM) on samples collected onboard the UAVs. Moreover, the observations are compared to the ζ utilized in the Weather Research and Forecasting regional atmospheric model coupled with chemistry (WRF-Chem) using the GOCART dust emission scheme (model setups used described in [6,7]).

Results and Discussion

The vertically resolved observations of ζ are compared to the MOPSMAP calculations for different aspect ratios, the values used by WRF-Chem, the literature-reported values as summarized by [8,9] and

column-averaged derivations based on AERONET. The results are shown in Fig. 2. In the first dust event, the observed ζ (0.56 ± 0.26 μm) between 1.5–3 km a.s.l, was 7% lower than the minimum literature value, whereas in the second case, the observed ζ (2.05 ± 0.03 μm) 1.5–3.5 km a.s.l., exceeded the literature range by 37% and was 69% higher than values computed from AERONET observations. At the upper boundary of dust layers, observed ζ values were consistently lower than literature values. AERONET-derived ζ values showed better alignment with observed data on November 15th 2021. However, on June 24th 2022, AERONET underestimated ζ by nearly 60%, reflecting thus the observed difference in the PSD (Fig. 1). MOPSMAP calculations generally followed the profiles derived from the combination of lidar and OPCs, but showed some discrepancies. For the 15th November 2021 the calculations with spheroidal particles of low aspect ratios (AR = 1; red spheres, Kandler distribution; green triangles, SEM analysis of impactor samples; orange hexagons) provide the best match for most of the observed profile. For June 24, 2022, the observations at the lower altitude ranges (closer to the marine boundary layer) align better with spheres of AR = 1 (red circles) than with spheroids with higher AR (except in the 2.5–3 a.s.l km layer). In the upper layers (above 3.5 km a.s.l.) spheroids with an aspect ratio of 5 show the closest agreement with observations. The findings emphasize the need to consider the variability of dust properties and not averaged values of ζ.

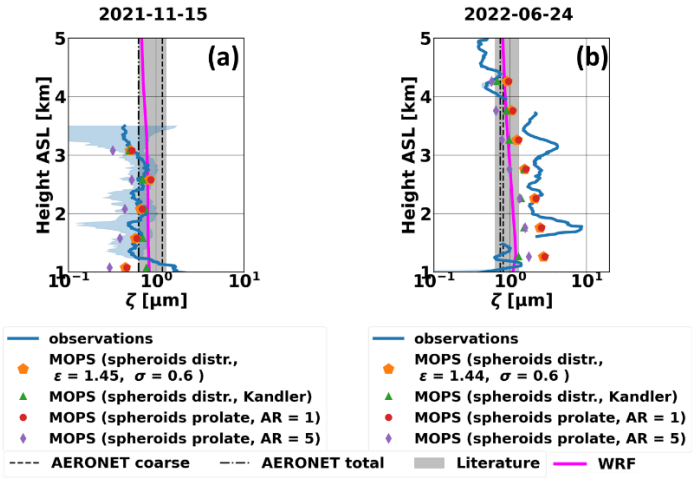

Figure 2. Observed ζ parameter (blue line) compared to MOPSMAP-derived quantities for different spheroidal aspect ratios (markers) for 15th November 2021 (a) and 24th June 2022 (b). The blue shaded area corresponds to the statistical variability of ζ calculated by the lidar and UAV observations. The shaded gray area indicates the literature range. The dashed and dotted lines are the AERONET corresponding parameters for total and coarse aerosols, respectively. Magenta line corresponds to the WRF simualted ζ values.

The comparison with WRF-Chem demonstrates a good agreement with the observations for the Middle Eastern dust case, capturing also ζ values at the lower limit of the literature range. However, in the Saharan dust case, the WRF-Chem-derived values aligned well with literature values but significantly underestimated the observed ζ.

Conclusions

The findings of this study contribute to improved aerosol characterization and enhance the reliability of remote sensing-based aerosol mass retrievals through a synergistic approach combining UAV-based OPC and lidar observations during dust events. The analysis highlights the ability of the UAV-based observations, to capture localized variations in PSDs and the contribution of coarse particles larger than 20 μm (often neglected). The observed ζ exhibits some agreement, but also discrepancies, in relation to previously recorded literature and AERONET values. These results suggest that current aerosol retrieval techniques,

particularly those relying on column-integrated measurements, may require adjustments to account for the observed variability in ζ.

MOPSMAP calculation on the demonstrated cases followed well the observed profiles, whilst remaining discrepancies point to the need for further refinement of refractive index and particle shape assumptions (e.g. spheroids). The discrepancies of the WRF model for cases with the presence of giant-particles is attributed to the model's representation of particles up to 10 μm in radius, whereas observations revealed the presence of particles exceeding 20 μm highlighting the importance on refining dust size bin representations in WRF-Chem to better account for the presence of giant particles to improve forecasting accuracies.

The study highlights the need for region-specific studies to enrich available conversion volume-to-extinction tables mainly focused on Saharan dust events. In addition, these tables should be updated to include the contribution of larger particles, as currently they are based on methods—such as AERONET—that do not account for giant particles. Location-specific calculated extinction-to-volume parameters can be used to refine retrieval algorithms and dust parameterizations in climate models and will directly boost the accuracy of aerosol radiative forcing estimates, climate predictions and eventually lead to more actionable environmental strategies. The proposed methodology will also be applied to the dataset collected during the #CHOPIN (CleanCloud Helmos Orographic Site Experiment) campaign, conducted from October 11 to November 1, 2024, at Mt. Helmos, Greece.

Acknowledgements

The EMME-CARE project partially supported this work under the European Union's Horizon 2020 Research and Innovation Programme (Grant Agreement No. 856612). The ESA project (Contract No. 4000131861/20/NL/IA) funded the ASKOS campaign. Part of this work was supported by the COST Action Harmonia (CA21119) supported by COST (European Cooperation in Science and Technology and the European Union's Horizon Europe project "CleanCloud" (Grant agreement No. 101137639). We extend our gratitude to the AERONET network and to the principal investigators of the Mindelo and Agia Marina Xyliatou stations, for maintaining the instrument operation and providing valuable data. We acknowledge AERONET-Europe (part of ACTRIS Research Infrastructure) for providing the calibration service. Also the authors. Finally, we sincerely thank the USRL team for their support in advancing the scientific vision through the provision and operation of their UAV fleet.

References

[1] Ansmann, A. et al.: Ash and fine-mode particle mass profiles from EARLINET-AERONET observations over central Europe after the eruptions of the Eyjafjallajökull volcano in 2010, J. Geophys. Res., 116, D00U02, https://doi.org/10.1029/2010JD015567 , 2011

[2] Holben, B., et al.: AERONET: A Federated Instrument Network and Data Archive for Aerosol Characterization, Remote Sensing of Environment, 66, 1–16, https://doi.org/https://doi.org/10.1016/S0034-4257(98)00031-5 , 1998.

[3] Ryder, C. L., et al.: Coarse-mode mineral dust size distributions, composition and optical properties from AER-D aircraft measurements over the tropical eastern Atlantic, Atmospheric Chemistry and Physics, https://api.semanticscholar.org/CorpusID:54789216 , 2018.

[4] Gasteiger, J et al: Volcanic ash from Iceland over Munich: mass concentration retrieved from ground-based remote sensing measurements, Atmospheric Chemistry and Physics, 11, 2209–2223, https://doi.org/10.5194/acp-11-2209-2011 , 2011.

[5] Schumann, U., B. Mayer, K. Gierens, S. Unterstrasser, P. Jessberger, A. Petzold, C. Voigt, and J. Gayet, 2011: Effective Radius of Ice Particles in Cirrus and Contrails. J. Atmos. Sci., 68, 300–321, https://doi.org/10.1175/2010JAS3562.1.

[6] Georgiou, G. K. et al.: Air quality modelling in the summer over the eastern Mediterranean using WRF-Chem: chemistry and aerosol mechanism intercomparison, Atmos. Chem. Phys., 18, 1555–1571, https://doi.org/10.5194/acp-18-1555-2018 , 2018.

[7] Drakaki, E. et al.: Modeling coarse and giant desert dust particles, Atmos. Chem. Phys., 22, 12727–12748, https://doi.org/10.5194/acp-22-12727-2022 , 2022.

[8] Ansmann, A. et al.: Profiling of fine and coarse particle mass: Case studies of Saharan dust and Eyjafjallajökull/Grimsvötn volcanic plumes, Atmospheric Chemistry and Physics, 12, 9399–9415, https://doi.org/10.5194/acp-12-9399-2012 , 2012.

[9] Ansmann, A. et al.: Dust mass, cloud condensation nuclei, and ice-nucleating particle profiling with polarization lidar: updated POLIPHON conversion factors from global AERONET analysis, Atmospheric Measurement Techniques, 12, 4849–4865, https://doi.org/10.5194/amt-12-4849-2019 , 2019.

Observation and evaluation of a huge smoke transport event in September 2020 using Aeolus Baseline16 data and multi-platform data.

K. Sun[1,2], G. Dai[2], S. Wu[2,3,4], H. Baars[1], D. Trapon[1], A. Ansmann[1]

(1) Leibniz Institute for Tropospheric Research (TROPOS), Leipzig, Germany
(2) Ocean University of China (OUC), Faculty of Information Science and Engineering, College of Marine Technology, Qingdao, China
(3) Laoshan Laboratory, Qingdao, China
(4) OUC, Institute for Advanced Ocean Study, Qingdao, China

Corresponding author: ksun@tropos.de

Introduction

Developed by European Space Agency (ESA), Aeolus is the worldwide first lidar satellite for global wind profile observation, launched in August 2018 and ended in April 2023. During its lifetime of more than 4 years, Aeolus had been demonstrating its capability to accurately measure atmospheric wind profiles from the ground to the lower stratosphere on a global scale deploying the first ever spaceborne wind lidar system Atmospheric Laser Doppler Instrument (ALADIN).

Due to the design principle of high spectral resolution lidar, Aeolus had the capability to measure wind profiles and aerosol optical properties profiles synchronously, which provides the possibility for studying the wind-driven evolution of aerosol. Combining the measurements of ALADIN and the data from other spaceborne sensors, together with NWP models, wind-driven dust aerosol transport and marine aerosol production have been analyzed [1,2].

In this study, we focus on the transport of smoke aerosol. Based on the observation of ALADIN, combined with the data of CALIOP (Cloud-Aerosol Lidar with Orthogonal Polarization), MODIS (Moderate Resolution Imaging Spectroradiometer), MERRA-2 (HYbrid Single-Particle Lagrangian Integrated Trajectory) and HYSPLIT (Modern-Era Retrospective analysis for Research and Applications, Version 2), a long-term smoke aerosol transport event which occurred during 11 to 21 September 2020 from western America to northern Europe is observed. The smoke layers of different transport phases are identified and analyzed. We propose a new strategy for ALADIN to estimate smoke mass concentration based on extinction coefficients at 355 nm and column mass concentrations from MERRA-2.

Data

Table 1 Data and models used in this study

Instruments/Models	Products
ALADIN/Aeolus	**L2A Baseline16 product** Particle optical properties: Extinction coefficient at 355 nm NWP: Relative Humidity (RH), Molecular backscatter coefficient at 355 nm
CALIOP/CALIPSO	**L2 VFM product** Aerosol subtypes
VIIRS/Soumi NPP	True color
MODIS/Aqua&Terra	AOD@550 nm (daily)
MERRA-2	Column mass density (organic carbon&black carbon&dust, kg/m2, hourly)
The Hybrid Single-Particle Lagrangian Integrated Trajectory (HYSPLIT) model	

In this study, we use multi-platform data from satellite observations, reanalysis and model, including ALADIN onboard Aeolus, CALIOP onboard CALIPSO, MODIS onboard Aqua and Terra, MERRA-2 reanalysis model, and HYSPILT model. Designed as a direct detection high-spectral-resolution lidar, apart from wind profile observation, ALADIN can also provide global aerosol optical properties (e.g., extinction coefficient (α) and backscatter coefficient (β)) profiles at 355 nm (Level 2A product) [3,4]. CALIOP can

provide global vertical feature mask (VFM) products [5]. In this study, we use aerosol subtype information from the VFM products [6]. The passive remote sensing spaceborne instruments involved in this study include Visible Infrared Imaging Radiometer Suite (VIIRS) on board the Suomi National Polar-orbiting Partnership (NPP) satellite and MODIS onboard Aqua and Terra [7,8]. The models used in this study are MERRA-2 and HYSPLIT [9,10]. All the data and models used are listed in Table 1.

Methodology

1) Spatial and temporal identification of the smoke transport event using true color and AOD products.

2) Aerosol type analysis to illustrate the dominant of smoke aerosol.

3) Processing Aeolus data to capture and describe the smoke layers. (1) Quality control using QC flag from Aeolus: profile flag, extinction flag, backscatter flag. (2) outlier elimination: eliminate backscatter coefficient with the range of > 100 $Mm^{-1}sr^{-1}$ or < 0.1 $Mm^{-1}sr^{-1}$; eliminate extinction coefficient with the range of > 1000 Mm^{-1}; eliminate isolated single or double bins in one profile. (3) cloud screening: eliminate data bins with RH > 94% or backscatter ratio > 2.5 [11]. (4) smoke data selection: retain Aeolus data bins with smoke column mass density > 10mg/m^2 and smoke column mass density proportion > 60% (aerosol column mass density information provided by MERRA-2). (5) depolarization ratio correction (due to that only co-polar backscatter coefficient was provided by Aeolus): correct backscatter coefficient with depolarization ratio of 0.027 [12, 13]. (6) extension of smoke extinction and backscatter using original extinction and backscatter and the averaged lidar ratio of a smoke layer.

4) Smoke mass concentration (MC) calculation using Aeolus extinction and MERRA-2 column mass concentration. Assuming the directly proportional relationship between smoke MC and its extinction of an individual layer, the smoke MC of each cross sections are calculated with extinctions and column MC.

Results

According to Fig. 1, the temporal range (11st to 21st September 2020) and the horizontal study region (30°N to 70°N, 140°W to -40°E) are selected as at this period the distinct high AOD values at 550 nm appeared from California to Northern European.

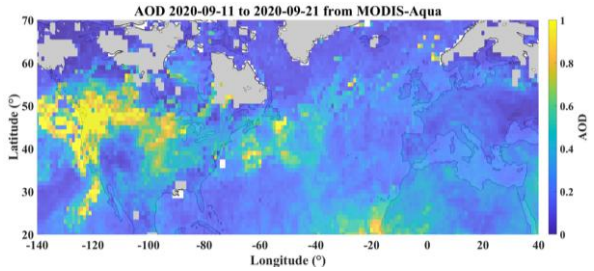

Fig. 1 Accumulated AOD at 550 nm from 11 to 21 September 2020 provided by MODIS/Aqua

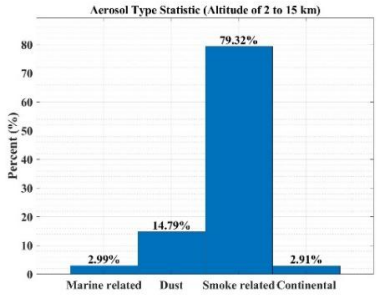

Fig. 2. Aerosol type analysis using CALIOP VFM product

Then, with the use of the aerosol classification data from CALIOP, the selected study region is found dominated by smoke-related aerosol, which verifies the smoke transport event, as Fig. 2 shows.

After Aeolus data processing and smoke MC calculation, six Aeolus smoke MC cross-sections on 14st, 15th, 16th, 18th, 19th, 20th and 21st September (called CS14 to CS21), located from western America over the Atlantic Ocean to Northern Europe capturing smoke aerosol layers are discovered, as Fig. 3 indicates. These six MC cross-sections are considered describe the whole smoke aerosol transport.

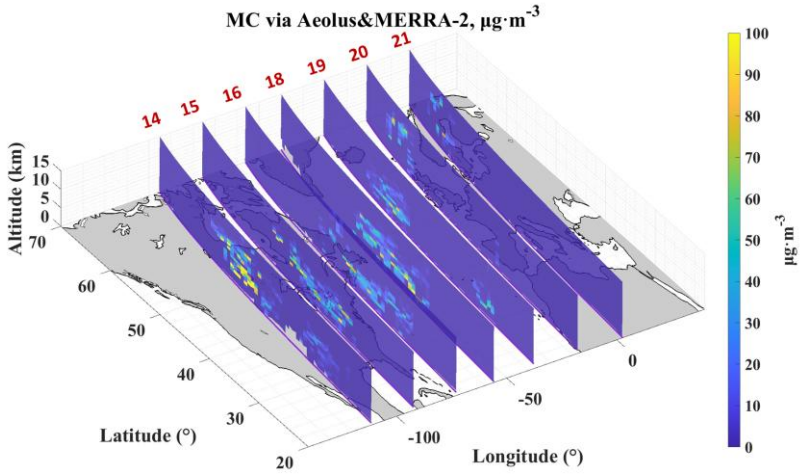

Fig. 3. Smoke mass concentration of six cross-sections calculated using Aeolus extinction coefficient and MERRA-2 smoke column mass density

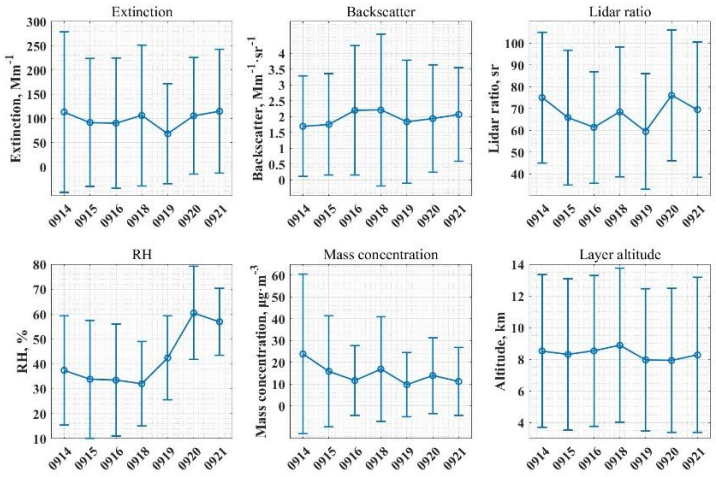

Fig. 4. Statistical results of extinction coefficient, backscatter coefficient, lidar ratio, RH, mass concentration, layer altitude during the smoke transport

From the statistical results of each cross-sections, shown in Fig. 4, it can be found that the averaged extinction coefficients from CS14 to CS19 decreased from 113 Mm^{-1} to 68 Mm^{-1}, and then increased to above 100 Mm^{-1} in CS19 and CS21. The averaged lidar ratios decreased from 75 sr (CS14) to 60 sr (CS19), with a high value of 69 sr deviating from the downward trend in CS 18, and increased back to 76 sr and 70 sr on 20th and 21st. This may be related to the relatively high relative humidity in CS20 and CS21. The

maximum averaged MC in CS14 was up to around 24 μg/m^3. At northern Europe, the averaged MC was 11 μg/m^3 in the end phase of the transport.

Acknowledgements

In this work we used data from Aeolus, CALIPSO, Soumi NPP, Aqua, Terra, MERRA-2 and HYSPLIT. We thank the production teams of these data sources.

References

[1] Dai, G., Sun, K., Wang, X., Wu, S., E, X., Liu, Q., and Liu, B.: Dust transport and advection measurement with spaceborne lidars ALADIN and CALIOP and model reanalysis data, Atmos. Chem. Phys., 22, 7975–7993, https://doi.org/10.5194/acp-22-7975-2022, 2022.

[2] Sun, K., Dai, G., Wu, S., Reitebuch, O., Baars, H., Liu, J., and Zhang, S.: Effect of wind speed on marine aerosol optical properties over remote oceans with use of spaceborne lidar observations, Atmos. Chem. Phys., 24, 4389–4409, https://doi.org/10.5194/acp-24-4389-2024, 2024.

[3] Reitebuch, O.: The Spaceborne Wind Lidar Mission ADM-Aeolus, in: Atmospheric Physics, Research Topics in Aerospace, edited by: Schumann, U., ISBN 978-3-642-30182-7, Springer-Verlag Berlin Heidelberg, 815–827, https://doi.org/10.1007/978-3-642-30183-4_49, 2012.

[4] Flament, T., Trapon, D., Lacour, A., Dabas, A., Ehlers, F., and Huber, D.: Aeolus L2A aerosol optical properties product: standard correct algorithm and Mie correct algorithm, Atmos. Meas. Tech., 14, 7851–7871, https://doi.org/10.5194/amt-14-7851-2021, 2021.

[5] Winker, D. M., Vaughan, M. A., Omar, A., Hu, Y., Powell, K. A., Liu, Z., Hunt, W. H., and Young, S. A.: Overview of the CALIPSO mission and CALIOP data processing algorithms, J. Atmos. Ocean. Tech., 26, 2310–2323, https://doi.org/10.1175/2009JTECHA1281.1, 2009.

[6] Kim, M.-H., Omar, A. H., Tackett, J. L., Vaughan, M. A., Winker, D. M., Trepte, C. R., Hu, Y., Liu, Z., Poole, L. R., Pitts, M. C., Kar, J., and Magill, B. E.: The CALIPSO version 4 automated aerosol classification and lidar ratio selection algorithm, Atmos. Meas. Tech., 11, 6107–6135, https://doi.org/10.5194/amt-11-6107-2018, 2018.

[7] Jackson, J. M., H. Liu, I. Laszlo, S. Kondragunta, L. A. Remer, J. Huang, and H.-C. Huang (2013), Suomi-NPP VIIRS aerosol algorithms and data products, J. Geophys. Res. Atmos., 118, 12,673–12,689, doi:10.1002/2013JD020449.

[8] Remer, L. A., and Coauthors, 2005: The MODIS Aerosol Algorithm, Products, and Validation. J. Atmos. Sci., 62, 947–973, https://doi.org/10.1175/JAS3385.1.

[9] Gelaro, R., and Coauthors, 2017: The Modern-Era Retrospective Analysis for Research and Applications, Version 2 (MERRA-2). J. Climate, 30, 5419–5454, https://doi.org/10.1175/JCLI-D-16-0758.1.

[10] Stein, A. F., R. R. Draxler, G. D. Rolph, B. J. B. Stunder, M. D. Cohen, and F. Ngan, 2015: NOAA's HYSPLIT Atmospheric Transport and Dispersion Modeling System. Bull. Amer. Meteor. Soc., 96, 2059–2077, https://doi.org/10.1175/BAMS-D-14-00110.1.

[11] Flamant, P. H., Lever, V., Martinet, P., Flament, T., Cuesta, J., Dabas, A., Olivier, M., Huber, D., Trapon, D., and Lacour, A.: Aeolus Level-2A Algorithm Theoretical Basis Document, version 5.7, https://earth.esa.int/eogateway/documents/20142/37627/Aeolus-L2A-Algorithm-Theoretical-Baseline-Document, 2020.

[12] Haarig, M., Ansmann, A., Baars, H., Jimenez, C., Veselovskii, I., Engelmann, R., and Althausen, D.: Depolarization and lidar ratios at 355, 532, and 1064 nm and microphysical properties of aged tropospheric and stratospheric Canadian wildfire smoke, Atmos. Chem. Phys., 18, 11847–11861, https://doi.org/10.5194/acp-18-11847-2018, 2018.

[13] Floutsi, A. A., Baars, H., Engelmann, R., et al.: DeLiAn – a growing collection of depolarization ratio, lidar ratio and Ångström exponent for different aerosol types and mixtures from ground-based lidar observations, Atmos. Meas. Tech., 16, 2353–2379, https://doi.org/10.5194/amt-16-2353-2023, 2023.

[14] Ansmann, A., Ohneiser, K., Mamouri, R.-E., Knopf, D. A., Veselovskii, I., Baars, H., Engelmann, R., Foth, A., Jimenez, C., Seifert, P., and Barja, B.: Tropospheric and stratospheric wildfire smoke profiling with lidar: mass, surface area, CCN, and INP retrieval, Atmos. Chem. Phys., 21, 9779–9807, https://doi.org/10.5194/acp-21-9779-2021, 2021.

Synergistic Exploitation of Aerosol Products from Active and Passive Polar-Orbiting Satellites for Wildfire Monitoring: The Los Angeles Case, January 2025

***K. Michailidis*[1]**, *A. Pseftogkas*[1], *M-E. Koukouli*[1], *C. Biskas*[1] *and D. Balis*[1]

(1) Aristotle University of Thessaloniki, Physics Department, Laboratory of Atmospheric Physics, 54124, Thessaloniki, Greece

Corresponding author: komichai@physics.auth.gr

Introduction

In January 2025, a series of wildfires erupted across the Los Angeles (LA) region of California, driven by unusually dry conditions and strong Santa Ana winds. These fires resulted in loss of life, extensive damage to residential areas, large-scale evacuations, and a marked deterioration in air quality across Southern California. Figure 1 (left) illustrates the affected areas. Beyond their immediate destruction, the wildfires released vast amounts of smoke, aerosols, and trace gases into the atmosphere, significantly degrading air quality both locally and in downwind regions due to long-range atmospheric transport. In this study, we analyze satellite-based observations from two advanced instruments: The Tropospheric Monitoring Instrument (TROPOMI) aboard ESA's Sentinel-5P satellite, and the ATLID (ATmospheric LIDar) instrument onboard EarthCARE (Earth Cloud Aerosol and Radiation Explorer), a joint ESA–JAXA mission launched in May 2024. Passive and active remote sensing systems provide complementary insights into the distribution and evolution of wildfire smoke plumes, aerosol properties, and gas-phase pollutants such as carbon monoxide and formaldehyde. ATLID, is a high-spectral-resolution lidar (HSRL) technology, offering detailed vertical profiles of aerosol and cloud layers, enabling a 3D understanding of atmospheric structure. By combining the wide horizontal coverage of TROPOMI with the high-resolution vertical profiling capabilities of ATLID, this study aims to deliver a comprehensive assessment of the wildfires dynamic processes and atmospheric impacts of smoke.

Data and Methodology

In this study we employ a multi-sensor satellite and ground-based observational approach to analyze the atmospheric impacts of the January 2025 Los Angeles wildfires. Key datasets include TROPOMI (Sentinel-5P [1]), providing Ultraviolet Aerosol Index (UVAI) and Aerosol Layer Height (ALH) products, which were used to evaluate the horizontal dispersion and vertical distribution of UV-absorbing aerosols such as smoke. Daily Level-2 data with high spatial resolution allowed detailed tracking of plume evolution across Southern California. Complementing this, EarthCARE's ATLID [2] high-spectral-resolution lidar offered vertical profiles of specific products such as backscatter, extinction, lidar ratio and depolarization, enabling precise characterization of smoke layer altitude, structure, and optical properties. ATLID proved particularly valuable in detecting lofted aerosol layers and assessing their interaction with meteorological conditions. Moreover, the Fire Radiative Power (FRP [3]) data from Sentinel-3 SLSTR were used to locate active fire sources and quantify fire intensity during peak activity, supporting temporal correlation with aerosol loading and transport. Ground-based AERONET [4] observations from selected stations in affected areas were also used, providing independent and high quality aerosol optical properties, with aerosol optical depth (AOD) and Ångström exponent data offering insights into aerosol type and load. Together, these multi-sensor datasets provide a robust, multidimensional perspective on the wildfire event, capturing its temporal evolution, spatial extent, and vertical structure of smoke dispersion. Most of the damage has been done by the two largest fires: i) the Palisades Fire (Pacific Palisades) and ii) the Eaton Fire (Altadena). Figure 1 (right) displays the spatial distribution and intensity of wildfires in the Los Angeles region on January 9, 2025, captured by the Sentinel-3 OLCI true-color image overlaid with Fire Radiative Power (FRP) data from the Sea and Land Surface Temperature Radiometer (SLSTR) instrument aboard Sentinel-3A and 3B. Two prominent fire-affected zones, labeled Cluster 1 and Cluster 2, correspond to the Palisades and Eaton Canyon areas, respectively. These regions are outlined in red, with color-coded pixels indicating varying levels of FRP, a direct proxy for fire intensity. The FRP values range from as low as ~12 MW to peaks of 1180.99 MW in

Cluster 1 and 1422.02 MW in Cluster 2. Cluster 1 contains 23 active fire pixels with an average FRP of 246.3 ± 358.66 MW, while Cluster 2 comprises 15 pixels with a higher average FRP of 385.85 ± 432.32 MW, signifying more intense combustion activity. The dense smoke plumes emanating from both clusters are clearly visible in the OLCI imagery, dispersing southwestward over the Pacific Ocean.

Figure 1. (Left) A map of the major wildfires that burned in Los Angeles County in January 2025 (Source: New York Post). (Right) Sentinel-3 OLCI true-color image of the Los Angeles wildfires on 9 January 2025, overlaid with SLSTR-derived fire radiative power (FRP). Clusters 1 (Palisades) and 2 (Eaton) indicate areas of intense fire activity.

Results

On January 8 and 9, dense smoke is observed drifting southwestward, indicating active fire emissions and prevailing wind-driven transport. By January 11, the plume becomes more dispersed, suggesting a reduction in fire activity or altered meteorological conditions. The upper panels display the TROPOMI-derived Ultraviolet Aerosol Index (UVAI), which quantifies the presence of UV-absorbing aerosols such as smoke.

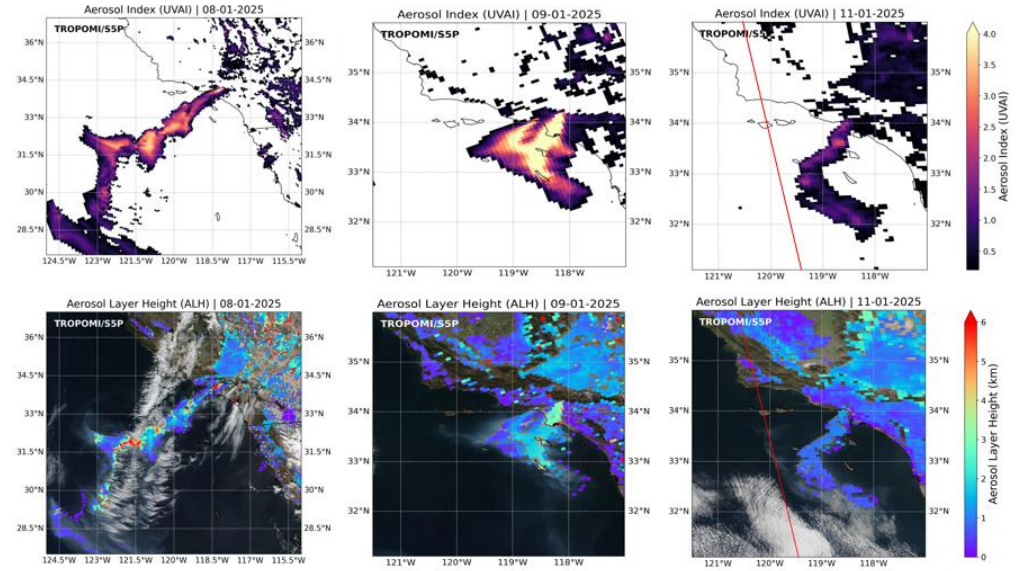

Figure 2. TROPOMI/S5P observations during the Los Angeles wildfires in January 2025. (Upper panels) UV Aerosol Index on 8, 9 and 11 January highlights the spatial extent and intensity of absorbing aerosols). (Bottom panels) Aerosol Layer Height retrievals for the same days are overlaid on VIIRS/Suomi-NPP true-color imagery indicate the vertical distribution of the aerosol plumes, showing elevated smoke layers transported over Southern California and the Pacific Ocean. The red line denotes EarthCare's orbit track.

A pronounced increase in UVAI is observed on January 9, with peak values centered over the Los Angeles region and extending offshore, consistent with elevated aerosol concentrations and intense fire activity. The bottom row shows TROPOMI-retrieved Aerosol Layer Height (ALH), highlighting the vertical distribution of the smoke plumes. The ALH retrievals superimposed with true-color imagery from VIIRS aboard Suomi-NPP, offering a visual representation of smoke plume development across Southern California and the adjacent Pacific Ocean. Elevated aerosol layers, reaching up to approximately 6 km, are evident on January 8 and 9, indicating strong vertical lofting of smoke particles. By January 11, both UVAI and ALH values decrease, aligning with the visual reduction in smoke and pointing to diminished emissions or changing atmospheric dynamics.

Figure 3 provides a detailed assessment of the smoke plume generated by the Los Angeles wildfires on 11 January 2025, utilizing observations from the ATLID (ATmospheric LIDar) instrument aboard the EarthCARE satellite. The top-left panel displays a MODIS/Aqua true-color image with the EarthCARE orbital ground track superimposed, illustrating the satellite's close spatial coincidence with the smoke-laden region. The upper-left panel shows ATLID's target classification product, which distinctly identifies elevated aerosol layers attributed to smoke (indicated in deep green), reaching altitudes of up to ~3 km. The bottom row presents vertical profiles of key aerosol optical properties retrieved by ATLID: i) backscatter coefficient, ii) extinction coefficient, iii) lidar ratio, and iv) depolarization ratio at 355nm. The backscatter profile indicates enhanced aerosol loading primarily between 1–2 km altitude, with maxima corresponding closely to the ALH derived from TROPOMI (including only pixels over sea [5]), as marked by horizontal reference lines. The extinction profile corroborates the presence of optically active particles in the same vertical range. The lidar signals measured at 355 nm revealed elevated lidar ratio values ranging from 65 to 80 sr, indicative of aged, optically dense smoke aerosols with enhanced light absorption and scattering properties. Simultaneously, the depolarization ratio profile showed values below 0.1 within the detected smoke layer, suggesting the presence of moderately aspherical particles resulting from aerosol aging and coagulation [6].

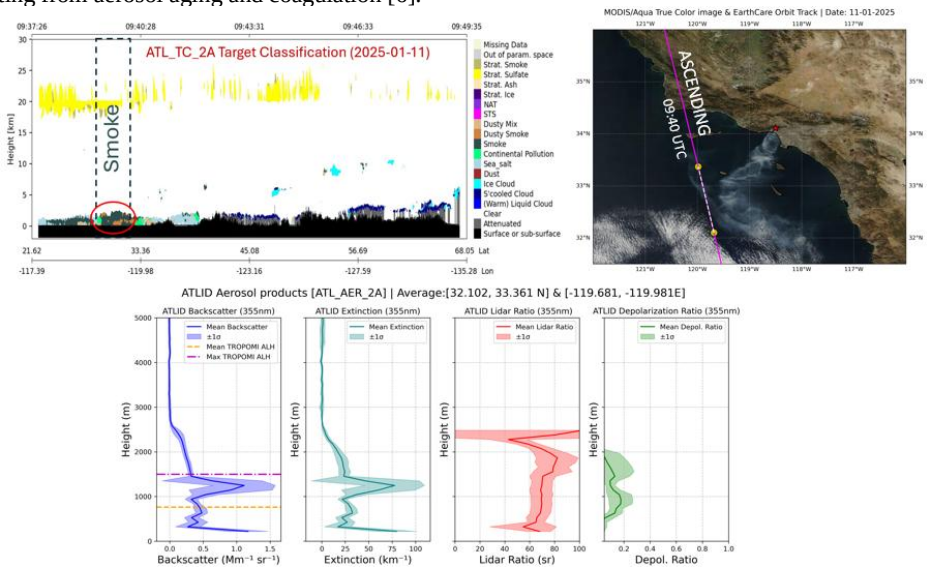

Figure 3. (Upper Left) Vertical distribution of Low-Resolution Target Classification from EarthCare overpass on January 11, 2025. (Upper Right) Map showing the relevant EarthCare orbit track in ascending mode. (Bottom) Vertical distribution of ATLID aerosol products (particle backscatter and extinction coefficients, lidar ratio and linear particle depolarization ratio at 355nm) at the same location as spotted in overpass.

To complement satellite-based observations and better understand the local-scale impact of wildfire smoke, ground-based measurements from AERONET stations, near the affected areas, were utilized. The Eaton fire, at the northern part of Los Angeles, was profoundly captured by two AERONET stations at Pasadena, MISR-JPL and CalTech, at 11km apart. MISR-JPL (34.2°N, 118.2°E, 367m) is located at the rooftop at the NASA/ Jet Propulsion Laboratory (JPL) campus. The CalTech station

(34.1ºN, 118.1ºE, 260m) is on top of the Milliken Library at CalTech campus. Being south from the main fire zone, it also captured the smoke plumes, providing valuable data. Aerosol optical depth time-series at various wavelengths (340, 380, 440, 500, 675, 870 and 1020nm) are presented at ***Fig. 4*** for Caltech (left) and MISR-JPL (Left). Until January 8th, AOD at both stations presents a small temporal variation, ranging from 0 to 0.5. At January 9th, less than two days after the beginning of Eaton fire, AOD values reached up to 3.83 for MISR-JPL and 3.22 for CalTech, indicating the detection of the smoke plumes by both stations.

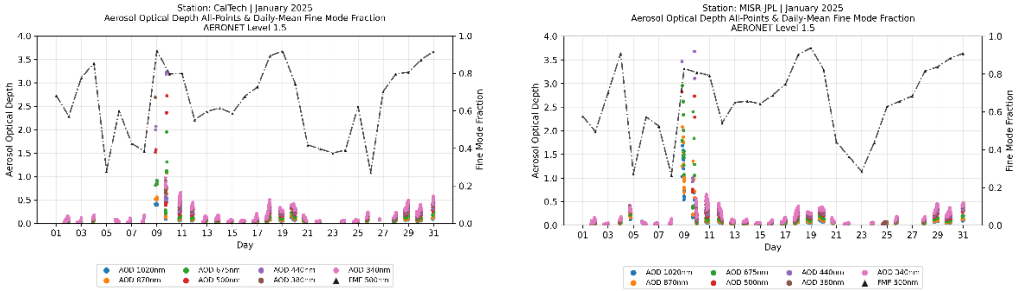

Figure 4. Time series during January 2025 of Cimel spectral AOD and measured by Cimel sun-photometer at MISR-JPL (Left) and CalTtech (Right) AERONET sites, respectively.

Conclusions

The synergistic use of aerosol products from TROPOMI and EarthCARE has demonstrated strong potential for enhancing the characterization and monitoring of wildfire events, as exemplified by the January 2025 Los Angeles wildfires. By integrating high-resolution observations from TROPOMI with the vertical profiling capabilities of ATLID lidar, this study effectively captured both the horizontal dispersion and vertical structure of wildfire-related aerosols. The methodology adopted highlights the value of combining passive/active satellite observations for detailed atmospheric analysis. It also reinforces the importance of such synergistic strategies for supporting near-real-time response to extreme fire events. Looking forward, the upcoming Sentinel-4, 5 missions offer promising capabilities to extend this approach, with improved spatial and temporal resolution for monitoring trace gases and aerosols.

Acknowledgements

Results presented in this work have been produced using the Aristotle University of Thessaloniki (AUTh) High Performance Computing Infrastructure and Resources. The authors would like to acknowledge the support provided by the IT Center of the Aristotle University of Thessaloniki (AUTh) throughout the progress of this research work. We gratefully acknowledge the TPOΠOMI data provided by Copernicus Data Space Ecosystem (https://dataspace.copernicus.eu/). EarthCARE ESA L2 collection is available only to the EarthCARE Commissioning Team and to Principal and Co-Investigators of accepted proposals to the ESA Announcement of Opportunity for the Validation of EarthCARE (https://ec-pdgs-dissemination2.eo.esa.int/oads/access/). The AERONET sun-photometer version 3 data are publicly available and can be accessed via https://aeronet.gsfc.nasa.gov.

References

[1] Veefkind, J. P., et al.: TROPOMI on the ESA Sentinel-5 Precursor: A GMES mission for global observations of the atmospheric composition for climate, air quality and ozone layer applications. Remote Sensing of Environment, 120 (2012), 70–83. https://doi.org/10.1016/j.rse.2011.09.027, 2012

[2] Donovan, D. P. et al.: The EarthCARE lidar cloud and aerosol profile processor (A-PRO): the A-AER, A-EBD, A-TC, and A-ICE products, Atmos. Meas. Tech., 17, 5301–5340, https://doi.org/10.5194/amt-17-5301-2024, 2024.

[3] Xu Weidong, et al.: First study of Sentinel-3 SLSTR active fire detection and FRP retrieval: Night-time algorithm enhancements and global intercomparison to MODIS and VIIRS AF products, Remote Sensing of Environment, Volume 248, 111947, ISSN 0034-4257, https://doi.org/10.1016/j.rse.2020.111947, 2020.

[4] Holben, B., et al.: AERONET – A Federated Instrument Network and Data Archive for Aerosol Characterization, Remote Sens. Environ., 66, 1–16, https://doi.org/10.1016/S0034-4257(98)00031-5, 1998.

[5] Michailidis, K., et al.: Validation of the TROPOMI/S5P aerosol layer height using EARLINET lidars, Atmos. Chem. Phys., 23, 1919–1940, https://doi.org/10.5194/acp-23-1919-2023, 2023.

[6] Haarig, M., et al.: Depolarization and lidar ratios at 355, 532, and 1064 nm and microphysical properties of aged tropospheric and stratospheric Canadian wildfire smoke, Atmos. Chem. Phys., 18, 11847–11861, https://doi.org/10.5194/acp-18-11847-2018, 2018.

Assessing the influence of anthropogenic aerosols on climate by combining remote sensing data with atmospheric models

C. Talianu[1,2], *D.N. Nicolae*[1], *A.M. Dandocsi*[1], *V.A. Nicolae*[1], *A.V. Dandocsi*[1,3]

(1) National Institute of Research and Development for Optoelectronics INOE 2000, Măgurele, Romania
(2) BOKU University, Institute of Meteorology and Climatology, Vienna, Austria
(3) UNST Politehnica of Bucharest, Bulevardul Iuliu Maniu 1-3, Bucharest, 061071, Bucharest, Romania
Corresponding author: camelia@inoe.ro; camelia.talianu@boku.ac.at

Introduction

The State of the Climate reports from the National Oceanic and Atmospheric Administration (NOAA) over the past decade and the Copernicus Climate Change Service (C3S) shows that Europe has warmed much faster than the global average, with large-scale variability over time periods. This climate variability have often been accompanied by anomalies in atmospheric circulation and precipitations. Recent studies have shown that anthropogenic aerosols can affect atmospheric circulation through aerosol radiative forcing and/or cloud-aerosol interactions, see [1], [2], and [3]. The re-analysis data from satellite shows that the main change in aerosol emissions is a decrease in sulfate aerosols (shortwave reflectors) and an increase in downward surface solar radiation, see [4] and [5]. Also, the studies in the last decade shows that spatial changes in shortwave radiation are larger and modify the annual mean Hadley circulation [6], weakening the northward energy transport [7].They induce different surface temperature trends over the Pacific and Atlantic oceans, see [6], [8], and [9], or over Europe [10]. However, it is still unclear how changes in aerosol properties influence regional circulation in the Northern Hemisphere, especially during the warm season, and what the underlying mechanisms are. It is also not yet known to what extent the rapid soil-atmosphere response to the reduction of anthropogenic emissions of aerosol precursors (reduction required by European air quality legislation), can influence climate in Europe. No previous studies have estimated the changes in temperature and precipitations due to changes in the composition of the anthropogenic aerosol in different climate states.

In this study, the relationship between changes in the composition of the anthropogenic aerosol and climate was investigated using the synergy between measurements from lidar and PANDORA systems combined with Copernicus Atmosphere Monitoring Service (CAMS) [11] and NATALI aerosol-typing model [12].

Methodology

The study was conducted for the period 2020–2024, covering five years of remote sensing measurements at the Magurele Centre for Atmosphere and Radiation Studies (MARS). MARS is part of RADO-Bucharest facility, one of the few ACTRIS site with collocated lidar and PANDORA measurements. For the analysis, all available lidar and PANDORA datasets were considered. A total of 1291 high-quality lidar datasets were used, covering 159 days with aerosol transport events recorded at the RADO-Bucharest station during the period selected for analysis. Only days with nighttime lidar measurements were considered, as the nighttime measurements provide the five profiles of the aerosol optical properties (three backscatter profiles and two extinction profiles) required as input data to NATALI. To identify the presence of anthropogenic aerosol in the atmosphere, the backscatter and extinction profiles from lidar data were retrieved with the last version of EARLINET's Single Calculus Chain, see [13] and [14]. These profiles were further used as input data to the NATALI model to retrieve the types of aerosols present in the atmosphere. To identify the dominant species of each aerosol type, NATALI outputs were coupled with the CAMS aerosol module, which predicts the mass mixing ratios of major aerosol components: sulfate, black carbon, organic matter, dust, and sea salt. From all the aerosol types identified by the NATALI model, only the "continental" and "continental polluted" types and their associated components from CAMS were selected, as only they originate from anthropogenic sources. In this study, the two types of continental aerosols were added together, constituting the "anthropogenic aerosol". From the data provided by PANDORA, only quality-data anthropogenic emission amounts of sulfur dioxide (SO_2), a precursor of sulfate aerosol, were considered. The following

time series were considered for the analysis: frequency of anthropogenic aerosol polluted events, SO_2 total-column concentration, average daily temperature and total daily precipitation. Daily average temperature and daily total precipitation were retrieved from C3S ERA5-Land hourly data. All the time series involved in this study were decomposed into three components (trend, seasonality and residual) weighted-averaged over a quarterly time period using the Python statistical modules. The trend was calculated using a centered moving average of the time series, with a window length of 91 days.

Results and Discussion

The number of aerosol transport events observed during the lidar nighttime measurements from period 2020–2024, distributed on aerosol type and years, is given in Table 1. Aerosol transport events identified by NATALI as: "Marine/CC", "Unknown" or "Mineral Mixtures/Volcanic" are quantified in the aerosol type called "Other". As can be seen from Table 1, a lower number of anthropogenic aerosol transport events was recorded in 2020. The number of anthropogenic aerosol transport events in 2020 is due to the lock-downs period caused by the COVID-19 pandemic. During this period, most human activities were reduced or even closed. Also, the number of lidar measurements are reduced, compared to the years 2021 - 2024.

Table 1. Annual distribution of numbers of aerosol transport events recorded at RADO-Bucharest station, during the nighttime lidar measurements.

Aerosol type	2020	2021	2022	2023	2024
Anthropogenic	9	28	17	21	68
Dust	3	15	10	6	29
Smoke	4	18	10	5	38
Other	6	17	5	1	6

Figure 1 shows the trend components of the selected time series data, as seasonal patterns observed over the period 2020–2024. From the analysis of meteorological data and air mass circulation, it was observed that most cases of anthropogenic aerosols with high sulfate content were recorded during periods of air mass stagnation, characterized by weak winds and lack or very low precipitations. We can also observe in Fig. 1 the seasonal variability of the ratio of sulfate and organic matter species in the composition of anthropogenic aerosol obtained from lidar data, correlated with SO_2 concentrations obtained from PANDORA. Concerning the meteorological parameters, Fig. 1 shows a general increase in near-surface air temperature (red line) and a decrease in total precipitation (blue line) throughout the study period. Furthermore, in Fig. 1, it can be seen that:

- Sulfate is the dominant species in anthropogenic aerosols observed in the atmosphere in 2022. This may be due to the higher concentrations of SO_2 recorded in 2022. The secondary sulfate found in anthropogenic aerosol is produced mainly from the conversion of SO_2 by gas-phase oxidation in gaseous environments, aqueous-phase oxidation in liquid environments and heterogeneous oxidation on aerosol surfaces.
- In 2024 we observe a significant increase in anthropogenic aerosol with a much higher content of organic matter (55%) than sulfate (35%). According to the meteorological parameters, 2024 recorded the largest increase in near-surface air temperature, being the warmest year in the history of meteorological measurements in Romania, as stated by the Romanian National Meteorological Administration. Also, C3S confirms 2024 as the warmest year recorded globally.

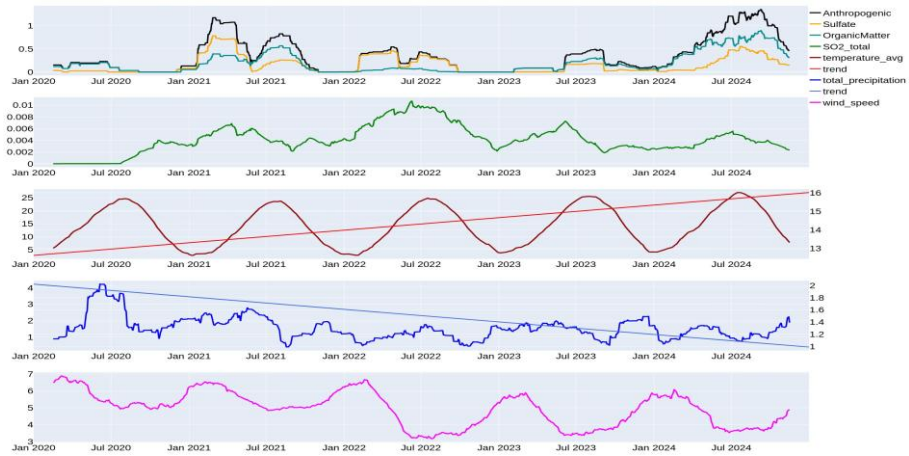

Figure 1. Time series data patterns observed over time period 2020–2024 for: anthropogenic aerosols, SO_2 total column (mol/m^2), daily averege temperature (°C), daily total precipitation (mm) and daily averege wind speed (km/h).

To identify possible correlations between changes in dominant species in the composition of anthropogenic aerosol and meteorological parameters (temperature, total precipitation, snow depth and wind speed), the Pearson correlation coefficients were calculated. The results are shown in Table 2.

Table 2. Correlation between anthropogenic aerosol and meteorological parameters from 2020–2024, expressed in Pearson coefficients

	2020	**2021**	**2022**	**2023**	**2024**
Temperature [°C]	-0.03	0.10	0.13	0.34	0.65
Total precipitation [mm]	-0.03	-0.09	-0.05	-0.02	-0.25
Snow depth [mm]	-0.10	0.22	-0.03	-0.14	-0.25
Wind speed [km/h]	0.09	0.12	0.13	-0.21	-0.41

Overall, Table 2 highlights the annual differences in the impact of anthropogenic aerosol on temperature, total precipitation and snow depth. From Table 2 it can be seen that the trend of increased concentration of organic matter in the composition of anthropogenic aerosol against the background of decreasing SO_2 concentrations, reflected in the correlation coefficient between anthropogenic aerosol and temperature, is consistent with the trend of increased temperature observed in the time series from period 2020–2024. It can also be observed that anthropogenic aerosol is anti-correlated with total precipitation recorded during the period 2020–2024, with a weak anti-correlation for 2020–2023 and a higher anti-correlation for 2024. This means that, with the decrease in SO_2 emissions and implicitly the reduction in the sulfate component of anthropogenic aerosol, the trend of decreasing precipitation is much slower in 2024 compared to 2022. Also, from Table 2, a variation in the correlation coefficient between anthropogenic aerosol and snow depth can be observed. This variation is strongly dependent on the distribution of organic matter and sulfate in the composition of anthropogenic aerosol. As seen in Fig. 1, sulfate (50%) and organic matter (30%) are the dominant species in the composition of the anthropogenic aerosol in 2021 during the cold season. In 2020, 2023 and 2024, the organic matter is the dominant species, while in 2022 the sulfate is the dominated species. The snow depth is correlated with anthropogenic aerosols observed in 2021 and anti-correlated with anthropogenic aerosols observed in other years.

Conclusions

This study presents the relationship between changes in anthropogenic aerosol composition and climate factors related to temperature and total precipitation for five years (2020–2024) using the synergy between measurements from lidar and PANDORA systems from RADO-Bucharest station combined with CAMS products and the NATALI aerosol model. The results showed that:

- changes in the composition of anthropogenic aerosols show seasonal variability;
- meteorological conditions, such as air stagnation (lack of atmospheric movement), contribute to increased concentrations of anthropogenic aerosols in the atmosphere;
- the reduction of SO_2 emissions produces an increase in the organic matter content of anthropogenic aerosols;
- the changes in the composition of anthropogenic aerosols are correlated with the changes in the surface air temperature and total precipitation.

Acknowledgements

This work is supported by the CARGO-ACT (www.cargo-act.eu) project supported by the European Commission under the Horizon Europe (HORIZON) – Strengthening the international dimension of ESFRI and/or ERIC research infrastructures, HORIZON-INFRA-2023-DEV-01-07, Grant Agreement no. 101132093, by the Core Program within the Romanian National Research Development and Innovation Plan 2022-2027, carried out with the support of MCID, project no. PN 23 05 and through ATMO-ACCESS Grant Agreement no. 101008004.

References

[1] Dong, B., & Sutton, R. T.: *Recent trends in summer atmospheric circulation in the North Atlantic/European region: Is there a role for anthropogenic aerosols?* Journal of Climate, 34(16), 6777–6795, 2021.

[2] Dong, B., Sutton, R. T., Shaffrey, L., & Harvey, B.: *Recent decadal weakening of the summer Eurasian westerly jet attributable to anthropogenic aerosol emissions*. Nature Communications, 13(1), 1–10. https://doi.org/10.1038/s41467-022-28816-5, 2022.

[3] Dow, W. J., Maycock, A. C., Lofverstrom, M., & Smith, C. J.: *The effect of anthropogenic aerosols on the Aleutian low*. Journal of Climate, 34(5), 1725–1741. https://doi.org/10.1175/jcli-d-20-0423.1, 2021

[4] Hodnebrog, Ø., et al.: *Recent reductions in aerosol emissions have increased Earth's energy imbalance*. Communications Earth & Environment, 5(1), 166. https://doi.org/10.1038/s43247-024-01324-8, 2024.

[5] Quaas, J., et al.: *Robust evidence for reversal of the trend in aerosol effective climate forcing*. Atmospheric Chemistry and Physics, 22(18), 12221–12239. https://doi.org/10.5194/acp-22-12221-2022, 2022

[6] Diao, C., Xu, Y., & Xie, S.-P.: *Anthropogenic aerosol effects on tropospheric circulation and sea surface temperature (1980–2020): Separating the role of zonally asymmetric forcings*. Atmospheric Chemistry and Physics, 21(24), 18499–18518. https://doi.org/10.5194/acp-21-18499-2021, 2021

[7] Needham, M. R., & Randall, D. A.: *Anomalous northward energy transport due to anthropogenic aerosols during the twentieth century*. Journal of Climate, 36(19), 6713–6728. https://doi.org/10.1175/jcli-d-22-0798.1, 2023

[8] Kang, S. M., et al:. *Zonal mean and shift modes of historical climate response to evolving aerosol distribution*. Science Bulletin, 66(23), 2405–2411. https://doi.org/10.1016/j.scib.2021.07.013, 2021

[9] Kang, J. M., Shaw, T. A., & Sun, L.: *Anthropogenic aerosols have significantly weakened the regional summertime circulation in the Northern Hemisphere during the satellite era*. AGU Advances, 5, e2024AV001318. https://doi.org/10.1029/2024AV001318, 2024

[10] Dong, B., Sutton, R.T.: Drivers and mechanisms contributing to excess warming in Europe during recent decades. npj Clim Atmos Sci 8, 41. https://doi.org/10.1038/s41612-025-00930-3, 2025

[11] https://ads.atmosphere.copernicus.eu; last access, 20/03/2025

[12] Nicolae, D., Vasilescu, J., Talianu, C., Binietoglou, I., Nicolae, V., Andrei, S., and Antonescu, B.: A neural network aerosol-typing algorithm based on lidar data, Atmos. Chem. Phys., 18, 14511–14537, https://doi.org/10.5194/acp-18-14511-2018, 2018

[13] D'Amico, G., Amodeo, A., Mattis, I., Freudenthaler, V., and Pappalardo, G.: EARLINET Single Calculus Chain – technical – Part 1: Pre-processing of raw lidar data, Atmos. Meas. Tech., 9, 491–507, https://doi.org/10.5194/amt-9-491-2016, 2016

[14] Mattis, I., D'Amico, G., Baars, H., Amodeo, A., Madonna, F., and Iarlori, M.: EARLINET Single Calculus Chain – technical – Part 2: Calculation of optical products, Atmos. Meas. Tech., 9, 3009–3029, https://doi.org/10.5194/amt-9-3009-2016, 2016.

Towards Accurate Aerosol Characterisation: Integrative Analysis Using Remote and In-situ Techniques

*J. Vasilescu[1], **A. Nemuc[1]**, L.Belegante[1], R. Pirloaga[1], V. Nicolae[1], D. Nicolae[1], A. V. Dandocsi[1,2]*

[(1)]National Institute of Research and Development for Optoelectronics INOE 2000, Atomistilor Street 409, Magurele, Ilfov Romania
[(2)]National University of Science and Technology POLITEHNICA Bucharest, Splaiul Independentei 313, Bucharest, Romania

Corresponding author: anca@inoe.ro

Introduction

Understanding the vertical distribution and chemical composition of aerosols is essential for evaluating their impacts on air quality, climate, and health. Ground-based in situ instruments like the Aerosol Chemical Speciation Monitor (**ACSM**) provide detailed chemical data at the surface but lack vertical resolution, whereas lidar remote sensing offers vertical profiles but no chemical specificity. This study integrates source apportionment from ACSM chemical analyses and multiwavelength Raman lidar (**RALI**) aerosol classifications, complemented by **Doppler wind lidar** measurements of boundary-layer dynamics. This combined approach allows assessment of elevated aerosol layer entrainment into the planetary boundary layer, particularly relevant in peri-urban settings like Măgurele, Romania affected by both local and transported pollutants. Such integrated characterization supports improved air quality forecasting, climate modeling, and policy development within frameworks like the Aerosol, Clouds and Trace Gases Research Infrastructure (**ACTRIS**) initiative.

Methodology

This research makes use of precise, high-resolution data collected from the three components of the ACTRIS national facility **RADO_Bucharest**—aerosol in situ observations, aerosol remote sensing, and cloud remote sensing—to thoroughly evaluate the ability to detect the influence of elevated aerosol layers at the surface level.

The observations took place in 2021 and 2022, during two intensive measurement campaigns held between June 1 – July 30, 2021, and March 1 – July 30, 2022, at the Măgurele Centre for Atmosphere and Radiation Studies (**MARS**), situated in a peri-urban area southwest of Bucharest, Romania (44.34°N, 26.01°E, 93 m above sea level)[1]. The Măgurele_INO site is also a WMO-GAW station.

The multiwavelength Raman polarization lidar (**RALI**), operational since 2008 in Măgurele, Romania, is a high-power, low-repetition atmospheric lidar system that combines Raman scattering and polarization techniques to characterize aerosols at 355,532 and 1064 nm. Its multiwavelength capability enables retrieval of aerosol size, shape, composition, and microphysical properties [2]. RALI provides vertical profiling of aerosol and cloud layers with a spatial resolution of 3.75 m and a temporal resolution of 1 minute. The system operates following a predetermined schedule and during focused intensive measurement campaigns, complying with the quality assurance standards set by EARLINET-ACTRIS.

The **NATALI** software [3] was employed to determine the dominant aerosol types using data from **RALI**. Based on an Artificial Neural Network algorithm, the NATALI package enables fast and accurate classification of aerosols in lofted layers by utilizing optical parameters from ACTRIS standard lidar products, including lidar ratios at 355 and 532 nm, Ångström exponent (355/532), linear particle depolarization at 532 nm, and color ratios and indexes (532/1064 and 1064/532).

The source apportionment of organic aerosols using **ACSM** data was carried out through Positive Matrix Factorization **(PMF**), employing the ME-2 solver within the Source Finder tool in IGOR Pro software[4][5] . The optimal factor solutions were determined by analyzing mass spectral profiles within the m/z range of 13 to 120, applying several criteria including the identification of specific marker ions and correlation with external datasets. The PMF analysis followed the methodology outlined by [5] and [6] incorporating

bootstrapping and performing up to 100 iterations per factor. For the MARS site during the summer of 2021, a four-factor solution was found to best represent the data. This solution included two primary organic aerosol types—hydrocarbon-like organic aerosol (**HOA**) and biomass burning organic aerosol (**BBOA**)—as well as two secondary oxygenated organic aerosols, namely less oxidized (**LO-OOA**) and more oxidized (**MO-OOA**) components. The contribution of primary organic aerosols was estimated by constraining the model with average HOA spectra specific to the site and reference BBOA spectra from [7].

An optical particle counter (Environmental Dust Monitoring – EDM180, manufactured by GRIMM), capable of detecting particles in the 0.25–32 μm size range across 31 channels, is measuring continuously the mass concentration for 3 particle matter sizes (PM10, PM2.5, PM1) of ground-level aerosol particles with a temporal resolution of one minute since 2020.

PBL downdrafts were investigated using a **Doppler wind lidar system** [1]. Vertical wind profiles with a 30 meters spatial and a 6 seconds temporal resolution were collected continuosly at MARS site since December 2019 and are available real time on **Cloudnet data portal** [8]. The maximum range achieved is 2–3 km depending on the atmospheric aerosol load. This study focuses exclusively on downward vertical velocities during selected case study periods to capture descending atmospheric motions and assess the potential influence of elevated aerosol layers at ground-level.

Results and Discussion

Over 200 aerosol layers were detected by lidar between June and August 2021, and clasified by NATALI software as 69% Continental, Continental Polluted, or Smoke. These three dominant aerosol types, are suitable for comparison with ACSM ground-based observations due to their comparable chemical and physical characteristics.

An analysis of the downdrafts using the wind lidar data in the mixing layer have been performed. The elevated layers up to 3km exhibit the greatest potential to impact aerosol concentration and properties at ground level. Downdrafts were found to be more frequent during morning hours and noon, on average, but narrow downdraft are present sometimes up to 4pm with mean velocity ranges from 0.8–2.0 m/s. Peak velocity values in the downdrafts frequently exceed 2 m/s.

For 94 out of the 200 identified lofted layers we could find increased values of organic aerosol at ground level.

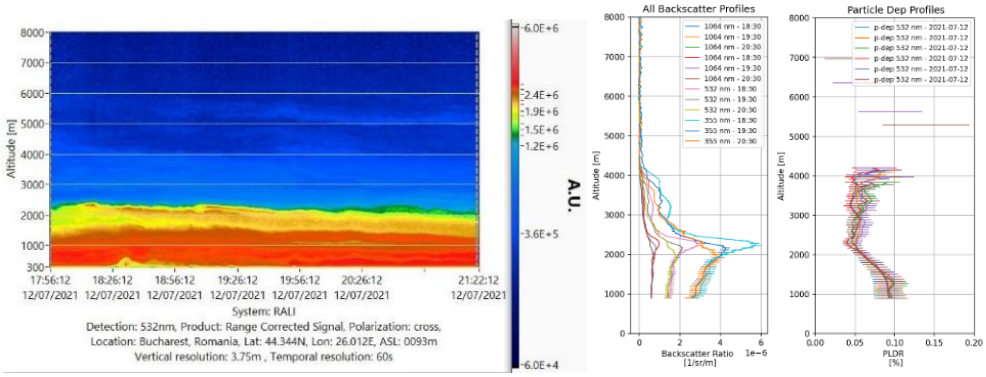

Figure 1. RCS, Backscatter (355/532/1064) and particle depolarisation profiles from multiwavelength lidar data measured between 18:30 and 20:30 UTC on 12.07.2021

In here we have selected to present a study case, measurements on 12-13.07.2021. Time series of Range Corrected Signals (RCS) and profiles of aerosol properties as derived from Lidar measurements are represented in Figure 1, indicating a persistent aerosol layer at 2 km. In Figure 2 time series of **BBOA** LO-OOA and MO-OOA types from ACSM data are presented as a snapshot for their temporal variability

for few days in June 2021. Increased loadings of BBOA time series from organic aerosols ACSM data (grey shaded area in Figure 2) correlates to a previous period with the persistent lofted smoke layer at 2 km, visible in Figure 1 and also classified as smoke by NATALI during the night 12-13.07.2021.

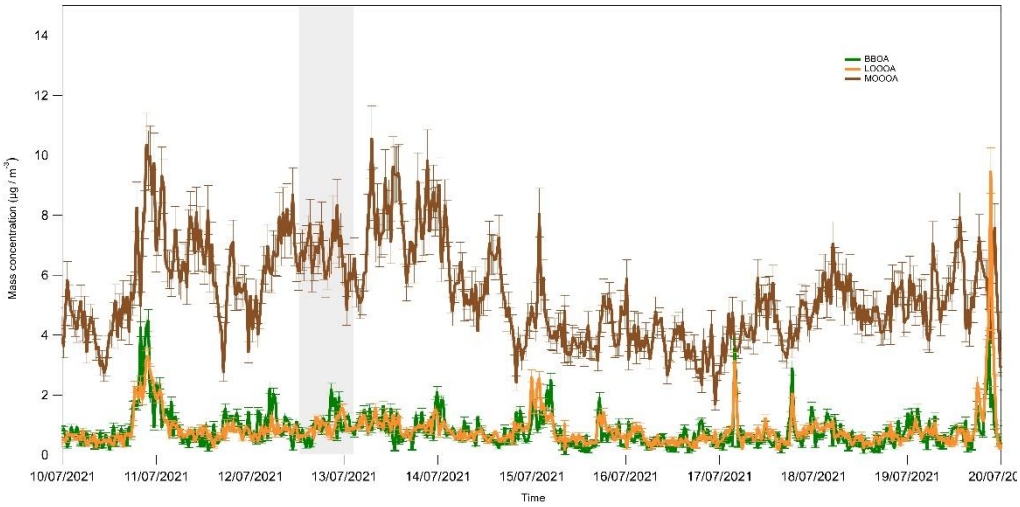

Figure 2. LO-OOA (yellow), BBOA (green) and MO-OOA (brown) timeseries from ACSM data retrieved using PMF method during 10 to 20 of July 2021

During March-July 2022, 14 layers were classified by NATALI as pure dust. We have chosen to highlight in here measurements on 12.05.2022 (grey shaded area in Figure 3) since pure dust layers were depicted by lidar during several night hours below 2km (Figure 4). After all events with pure dust in the elevated layers the ratios PM2.5/PM10 measured by GRIMM at ground level are close to 0.5 or less, indicative of the predominance of particles in the coarse mode (Figure 3 -PM2.5/PM10 timeseries at ground level as retrieved from GRIMM measurements versus dust layers altitude as retrieved by NATALI from lidar data).

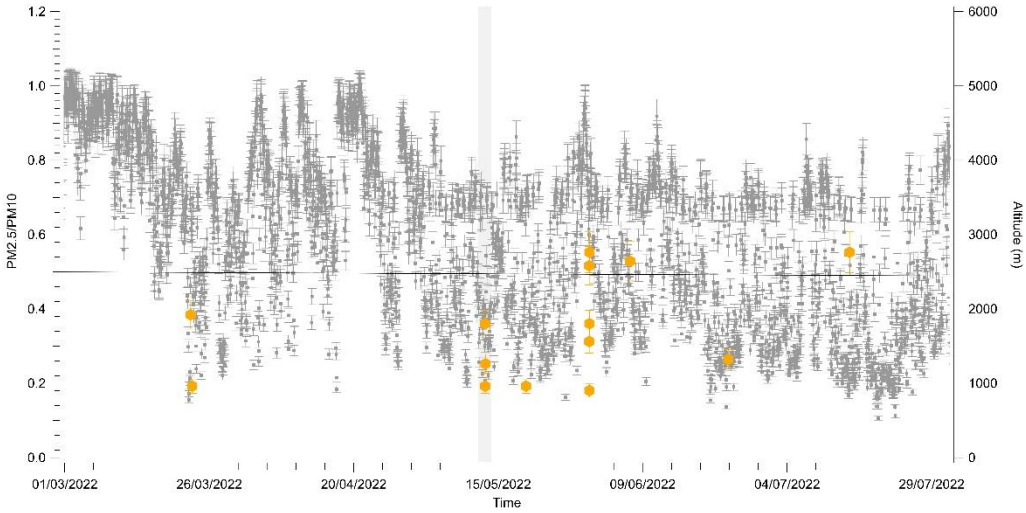

Figure 3. Dust cases retrieved using NATALI software on multiwavelength Raman lidar data (in yellow versus altitude-right vertical axis) and PM2.5/PM10 timeseries at ground level as retrieved from GRIMM measurements

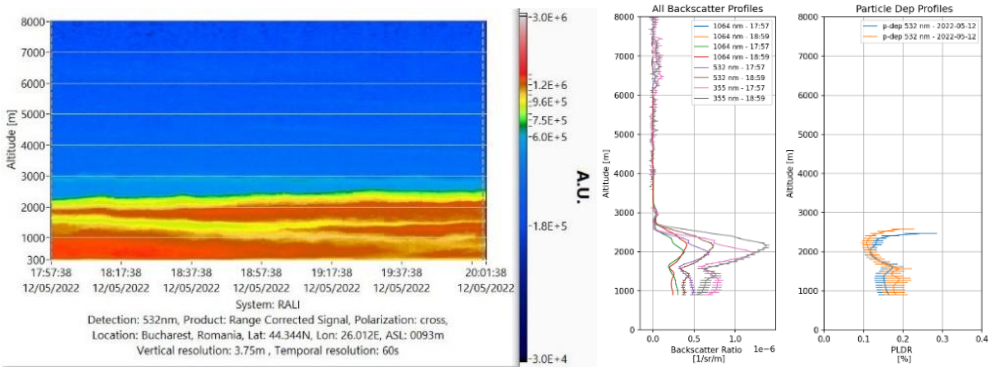

Figure 4. RCS (left panel), Backscatter (355/532/1064) (middle panel) and particle depolarisation profiles (right panel) from multiwavelength lidar data on 12.05.2022 from 6pm to 8pm UTC.

Conclusions

This study integrates remote sensing and in-situ measurements to comprehensively characterize aerosols, emphasizing instances where elevated aerosol layers influence ground-level concentrations. Elevated aerosol layers (continental and smoke), up to 3 km altitude and associated with downdraft winds (average velocities of 0.8–2.0 m/s and peaks exceeding 2 m/s), corresponded with increased surface-level organic aerosol concentrations in 94 out of 200 observed cases during the summer of 2021. Additionally, between March and July 2022, episodes characterized by elevated dust layers consistently resulted in a predominance of course-mode particles at ground level.

Acknowledgements

This work was financed by the European Commission under the Horizon 2020 – Research and Innovation Framework Programme, H2020-INFRAIA-2020-1, ATMO-ACCESS Grant Agreement no. 101008004, CARGO-ACT HEU Grant Agreement no. 101132093 by the Core Program within the National Research Development and Innovation Plan 2022-2027, with the support of MCID, project no. PN23 05/ 3.01.2023. and by Smart Growth, Digitization and Financial Instruments Program (PoCIDIF) 2021-2027, Action 1.3 Integration of the national RDI ecosystem in the European and international Research Space, project "Supporting the operation of facilities in Romania within the ACTRIS ERIC research infrastructure", SMIS code 309113.

References

[1] Pîrloagă, R., et al.: *Ground-based measurements of wind and turbulence at Bucharest–Măgurele: First results. Remote Sensing*, 15(6):1514, 2023.

[2] Nicolae, V. et al.: *A multi-year analysis of aerosol properties using the calibrated multi-wavelength polarisation lidar in Magurele*, Journal of Optoelectronics and Advanced Materials, volume 25, issue 3-4, page 176-190, ISSN 1454-4164, eISSN 1841-7132, 2023.

[3] Nicolae, D. et al. (2018). A neural network aerosol-typing algorithm based on lidar data, Atmos. Chem. Phys. 18, 14511–14537, https://doi.org/10.5194/acp-18-14511-2018

[4] Paatero, P. and Tapper, U.: *Positive matrix factorization: A non-negative factor model with optimal utilization of error estimates of data values*. Environmetrics 5, 111–126, 1994.

[5] Canonaco, F. et al. :*A new method for long-term source apportionment with time-dependent factor profiles and uncertainty assessment using SoFi Pro: application to 1 year of organic aerosol data*, Atmos. Meas. Tech.14, 923–943, https://doi.org/10.5194/amt-14-923-2021, 2021.

[6] Chen, G. et al.: *European Aerosol Phenomenology - 8 : Harmonised Source Apportionment of Organic Aerosol using 22 Year-long ACSM / AMS Datasets*, Environment International, https://doi.org/10.1016/j.envint.2022.107325, 2022.

[7] Ng, N. L. et al.: *An Aerosol Chemical Speciation Monitor (ACSM) for Routine Monitoring of the Composition and Mass Concentrations of Ambient Aerosol*, Aerosol Sci. Tech. 45, 780–794, https://doi.org/10.1080/02786826.2011.560211, 2011.

[8] https://cloudnet.fmi.fi/search/visualizations?site=bucharest&dateFrom=2025-02-01&dateTo=2025-02-01&experimental=true&product=doppler-lidar

Synergistic Retrieval of Aerosol Properties Using GRASP/GARRLiC: Case Studies of Long-Range Transported Dust and Smoke

C. Gînscă[1], *L.T. Deaconu*[1], *C. Botezan*[1], *H. Cămărășan*[1], *N. Ajtai*[1],

(1) University of Babeș-Bolyai, Faculty of Environmental Science and Engineering, Fântânele 30, 400294, Cluj-Napoca, Romania

Corresponding author: lucia.deaconu@ubbcluj.ro

Introduction

Atmospheric aerosols play a crucial role in the Earth's climate system by modulating radiative forcing and influencing cloud microphysics. Accurate characterisation of aerosol properties is essential to assess their climatic and air quality impacts. While established networks such as AERONET and EARLINET provide valuable data, they have inherent limitations when used independently [1]. The GRASP/GARRLiC algorithm [2] addresses these by combining passive radiometer observations, sensitive to aerosol optical depth (AOD), size, and morphology, with vertically resolved lidar backscatter profiles. This integrated retrieval enables a more complete characterisation of aerosol properties [3].

Methodology

This study improves aerosol characterisation by overcoming the limitations of individual remote sensing instruments through a synergistic retrieval framework. We combined AERONET sun-photometer data (direct sun AOD and almucantar sky radiance, sensitive to aerosol size, refractive index, and SSA) with elastic lidar backscatter profiles from the EARLINET network, which offer high-resolution vertical information. These complementary datasets served as input for the GRASP algorithm, enabling a joint inversion that simultaneously minimises the difference between observed and simulated signals from both measurement types. Specifically, the algorithm adjusts a common set of aerosol parameters (such as size distribution, complex refractive index, and vertical profile of aerosol concentration) until it achieves the best possible match to both the measured sky radiances and sun photometry from AERONET and the lidar backscatter profiles. This integrated fitting process ensures consistency across the different datasets and leads to a more robust and accurate retrieval of vertically resolved aerosol properties, including extinction profiles, fine and coarse mode separation, complex refractive index, and single scattering albedo (SSA).

Results and Discussion

The reliability and versatility of the GRASP/GARRLiC retrievals were assessed through comparison with AERONET and EARLINET products, alongside detailed analysis of long-range transported aerosol types such as desert dust, biomass-burning smoke, and mixed layers, and their spatiotemporal evolution We demonstrated the algorithm's versatility and broad applicability by analyzing real-world aerosol events that featured complex mixtures and long-range transport dynamics.

The first case study was measured on 16 April 2025 in Cluj-Napoca, Romania, during a significant Saharan dust intrusion. AERONET measurements recorded an AOD of 0.24 at 500 nm. The standard AERONET inversion provides additional information on the aerosol properties, specifically the particle size distribution is mostly characterised by coarse mode particles, with an SSA of 0.95 at 675 nm, specific for dust particles. The GRASP/GARRLiC algorithm successfully retrieved detailed information on the dust plume's vertical structure and optical properties, including size distribution, single scattering albedo (SSA), and complex refractive index, which have been compared to the AERONET inversion retrievals.

The second aerosol episode, on 12 July 2023 in Bucharest, Romania, corresponds to a multilayer aerosol event captured by EARLINET lidar. The total attenuated backscatter profiles revealed the presence of distinct aerosol layers. GRASP retrievals indicated a fine-mode aerosol layer overlaying a coarse-mode layer. Figure 1a) shows the range-corrected signal (RCS) measured at the Bucharest EARLINET site alongside the modelled RCS from GRASP, demonstrating good agreement across all three wavelengths (335, 532 and 1064 nm). Figure 1b) presents the aerosol extinction coefficient retrieved separately by the

GRASP algorithm for the fine and coarse modes, revealing a fine-mode-dominated upper layer consistent with transported biomass-burning smoke, and a coarse-mode-dominated lower layer (within the boundary layer) likely related to local pollution sources.

The third case study examined a long-range transported Canadian biomass burning event measured at several AERONET/ EARLINET stations across Europe in 2023 (1. Évora, Portugal, the 27th of June; 2. Potenza, Italy, the 29th of June; 3. Cluj-Napoca, Romania, the 30th of June). Analysis of GRASP retrievals revealed significant temporal and spatial variations in fine-mode size distribution and absorption features, underscoring the algorithm's ability to capture aerosol ageing processes and long-range transport dynamics.

We employed HYSPLIT backward trajectory analyses for all these events to identify the origin and transport pathways of the observed aerosol plumes.

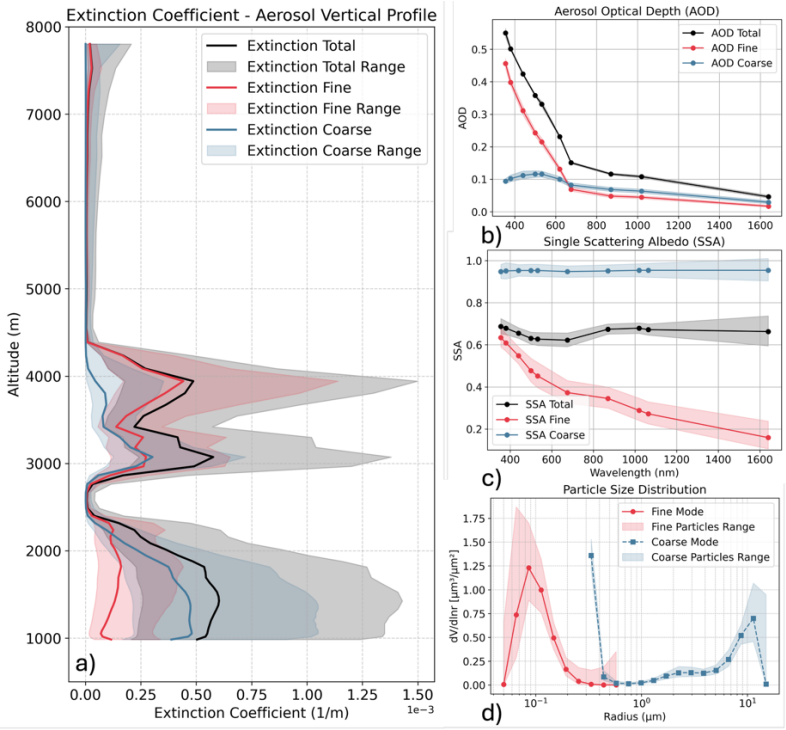

Figure 1. Characterisation of atmospheric aerosol properties for the case study of 12th of July 2023, at Bucharest, Romania. **(a)** Vertical profile of the aerosol extinction coefficient (1/m), showing total (black line), fine (red line), and coarse mode (blue line) contributions with their respective ranges. **(b)** Aerosol Optical Depth (AOD) as a function of wavelength for total, fine, and coarse aerosols. **(c)** Single Scattering Albedo (SSA) as a function of wavelength for total, fine, and coarse aerosols. **(d)** Particle size distribution (dV/dlnR) for fine and coarse mode particles. The ranges for all parameters are indicated by the shaded areas in black (for total), red (for fine) and blue (for coarse) modes.

Conclusions

The GRASP/GARRLiC algorithm effectively retrieves vertically resolved and column-integrated aerosol properties, offering clear advantages over traditional inversion methods. The synergy of passive and active ground-based sensors enables robust monitoring of diverse aerosol events, including dust, smoke, and mixed layers. These capabilities are vital for advancing our understanding of aerosol-climate interactions and informing air quality and climate monitoring frameworks.

Acknowledgements

The work was financed by Smart Growth, Digitization and Financial Instruments Program (PoCIDIF) 2021-2027, Action 1.3 Integration of the national RDI ecosystem in the European and international Research Space, project “Supporting the operation of facilities in Romania within the ACTRIS ERIC research infrastructure”, SMIS code 309113, ctr. no. G 2024-96579/17.12.2024/390010/19.12.2024.
The authors gratefully acknowledge the AERONET and EARLINET facilities for maintaining and providing the aerosol measurements. The authors also thank the NOAA Air Resource Laboratory (ARL) for providing the HYSPLIT transport and dispersion model used in this publication.

References

[1] Torres, B., Dubovik, O., Toledano, C., Berjon, A., Cachorro, V. E., Lapyonok, T., Litvinov, P., and Goloub, P.: Sensitivity of aerosol retrieval to geometrical configuration of ground-based sun/sky radiometer observations, Atmos. Chem. Phys., 14, 847–875, https://doi.org/10.5194/acp-14-847-2014, 2014.
[2] Dubovik, O., T. Lapyonok, P. Litvinov, et al.: GRASP: a versatile algorithm for characterizing the atmosphere, SPIE: Newsroom, Published Online: September 19, 2014. doi:10.1117/2.1201408.005558
[3] Lopatin, A., Dubovik, O., Fuertes, D., et al.: Synergy processing of diverse ground-based remote sensing and in situ data using the GRASP algorithm: applications to radiometer, lidar and radiosonde observations, Atmos. Meas. Tech., 14, 2575–2614, 2021. doi:10.5194/amt-14-2575-2021

Quantifying dust concentration and internal mineralogical mixture, by combining remote sensing and airborne in-situ observations, during ASKOS.

M. Tsichla[1,2], *A. Tsekeri*[1], *K. Kandler*[3], *H. Baars*[4], *M. Haarig*[4], *A. Gialitaki*[1,5], *M. Kezoudi*[6], *A. Floutsi*[4], *A. Papetta*[6], *F. Marenco*[6], *E. Marinou*[1], *K. A. Voudouri*[1,7], *N. Mihalopoulos*[1,2], *V. Amiridis*[1]

(1) National Observatory of Athens, IAASARS, Greece
(2) Environmental Chemical Processes Laboratory, Department of Chemistry, University of Crete, Greece
(3) Institute of Applied Geosciences, Technical University of Darmstadt, Darmstadt, Germany
(4) Leibniz Institute for Tropospheric Research (TROPOS), Leipzig, Germany
(5) School of Physics and Astronomy, Earth Observation Science Group, University of Leicester, UK
(6) Climate and Atmosphere Research Centre, The Cyprus Institute, Nicosia, Cyprus
(7) Laboratory of Atmospheric Physics, Physics Department, Aristotle University of Thessaloniki, Greece

Corresponding author: mtsichla@noa.gr

Introduction

Airborne dust plays an important role in the Earth's system, affecting weather patterns, climate dynamics, atmospheric chemistry, radiation balance, and human health ([1]-[3]). Improving the quantification of dust concentration, its vertical distribution, along with improving the monitoring of size and chemical composition, along with optical properties, can contribute to the development of more accurate quantification of its effects.

Lidar instruments (especially the ones that operate continuously and offer high temporal resolution data), can provide valuable information on dust concentration vertical distribution [4]. Integrating their results with in situ-based methods would not only enhance their validity but also provide complementary insights that neither remote sensing nor in situ observations alone can fully capture.

Over the years, multiple field campaigns have been conducted to investigate dust properties and interactions in the atmosphere. One of the latest was the ASKOS campaign [5], which formed the ground-based segment of the ESA/NASA JATAC campaign (2021–2022) in Cabo Verde, an ideal location for monitoring dust outbreaks.

A combination of aircraft, UAV, and ground-based measurements was deployed in this work in order to derive a combination of dust properties in the Saharan Air Layer, concerning dust concentration profiles and dust mineral components.

Methodology

In this work the dust concentration is calculated using (a) remote sensing and (b) in situ observations. The dust volume concentration profile from remote sensing (Vd_{lidar}) is calculated using ground-based 24/7 Polly$^{\text{XT}}$ lidar [6] measurements and the POLIPHON method [7] (Eq. 1)

$$Vd_{\text{lidar}} = c_d \beta_d S_d \tag{1}$$

where c_d is the extinction to volume conversion factor with value of 0.64 [8], β_d the backscatter coefficient of dust assuming dust depolarization ratio of 0.31 and non-dust depolarization ratio of 0.05 [7] and S_d the lidar ratio of dust which was calculated from the closest nighttime observations.

The dust volume concentration profile from the in situ observations ($Vd_{\text{in situ}}$) is calculated using the total volume of particles per volume air, measured with OPCs at different heights [9], and the dust percentage acquired from impactor samples [10] onboard UAVs (Eq. 2), using single particle electron microscopy and energy-dispersive X-ray fluorescence (SEM / EDX) analysis.

$$Vd_{\text{in situ}} = V_{\text{OPC}} \frac{\sum_{j=1}^{M}(V_j)}{\sum_{i=1}^{N} V_i} \tag{2}$$

where V_{OPC} is the total volume of particles per m^3 of air at different heights from OPC, and $\frac{\sum_{j=1}^{M}(V_j)}{\sum_{i=1}^{N} V_i}$ is the dust percentage as it is calculated from the impactor analysis, for the height range of the impactor sampling. j corresponds to all the particles sampled by the impactor characterized as "dust", which contain dust

minerals for at least 5% of their volume. This percentage is low, in order to ensure that we do not exclude particles containing even a small amount of dust. i corresponds to all the particles sampled by the impactor.

SEM / EDX analysis allowed the assessment of the internal dust fraction within the particles. Specifically, to calculate the size of a dust inclusion and the according volume fraction for an internally mixed particle from the derived chemical composition, the different elemental contributions have to be attributed to the dust or non-dust components. Al, Si, P, Ti and Fe are assigned to the dust component and S and Cl to the non-dust component. However, Na, Mg, K and Ca are ambiguous and can be presented in fractions [10]. Therefore, two model pathways are applied: an upper limit estimate (f_up), where the ambiguous elements surpassing the ion equilibrium with S and Cl are attributed to the dust component, and a lower limit estimate (f_low), where all ambiguous elements are attributed to the non-dust component.

So two dust volume concentration estimates—corresponding to upper ($V_{\text{int\_mix\_up}}$) and lower ($V_{\text{int\_mix\_low}}$) limits—provide the volume concentration of the internal dust fraction within the particles (Eq. 3-4)

$$V_{\text{int\_mix\_up}} = V_{\text{OPC}} \frac{\sum_{j=1}^{M} (f_{\text{up}_j} * V_j)}{\sum_{i=1}^{N} V_i} \tag{3}$$

$$V_{\text{int\_mix\_low}} = V_{\text{OPC}} \frac{\sum_{j=1}^{M} (f_{\text{low}_j} * V_j)}{\sum_{i=1}^{N} V_i} \tag{4}$$

where f_{up_j} and f_{low_j} are the upper and lower values estimations for the volume percentage of dust minerals in particle j, sampled by the impactor.

Finally, a categorization in terms of mineral compounds was derived for the observed dust cases based on the element index and additional
elemental ratios of the sampled particles [11].

Based on the above methodology, the analysis relies on the following datasets/products: a) the backscatter coefficient and particle depolarization ratio retrieved from lidar measurements, b) the total volume of particles per m^3 of air from OPC measurements at multiple heights, and c) the dust percentage measured by the impactor along the height range of its operation. The selected lidar measurements for our analysis were acquired from the nearest interval to the UAV flight and with optimal signal-to-noise characteristics for robust retrievals.

Results and Discussion

In this section, we present the results from a representative case study, selected to illustrate the application of the proposed methodology. Figure 1 presents the case study from 26 June. The OPC measurements were acquired at 4:00-5:00 UTC and the impactor sampled at 04:27-04:33 UTC. The Raman lidar signals were averaged over the period 00:00–05:00 UTC to improve the signal-to-noise ratio, as the presence of low, broken clouds affected the later part of the night. Additionally, atmospheric conditions remained homogeneous throughout the averaging period. The impactor sampled between 3-5 km, as shown by the gray area in the plot, so we restricted our analysis to that height range. The volume concentration of dust derived using the POLIPHON method (Vd_{lidar}, Eq. 1) is shown with the blue line (the shaded area provides the associated uncertainties). The volume concentration of dust particles derived from in situ observations, $Vd_{\text{in situ}}$ (Eq. 2) is shown with the asterisk symbol, whereas considering the internal mixture of dust we derive $V_{\text{int\_mix\_up}}$ and $V_{\text{int\_mix\_low}}$ (Eq. 3 and 4, respectively), which are shown with the bars. Overall, there is an agreement between the methods inside the impactor sampling height range.

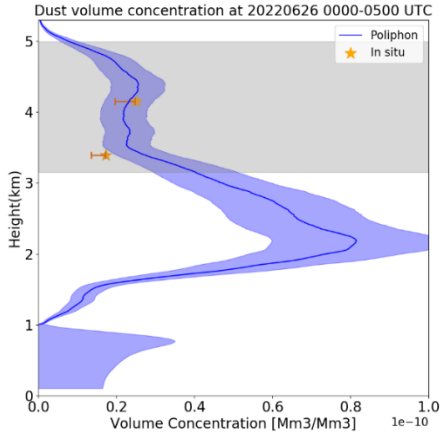

Figure 1. Comparison of volume concentration of dust derived using POLIPHON (Vd_{lidar}; blue line and shaded area to illustrate the uncertainties) and the volume concentration calculated from in situ measurments ($Vd_{\mathrm{in\ situ}}$, $V_{\mathrm{int\_mix\_up}}$, $V_{\mathrm{int\_mix\_low}}$; yellow stars and bars, respectively) for the case of 26th June 2022 over Mindelo, Cabo Verde.

The chemical composition of the particles in terms of approximated mineralogy, for all cases acquired during the UAV flights during the ASKOS campaign, is shown in Figure 2. The cloud-free cases (shown with the green circles) have a similar composition with an average of 48% silicates (probably aggregates of different silicates), 42% clay minerals, 4% feldspar, 2% (phyllo-)silicate/clay minerals, 2% calcium-rich compounds and 2% other compounds.

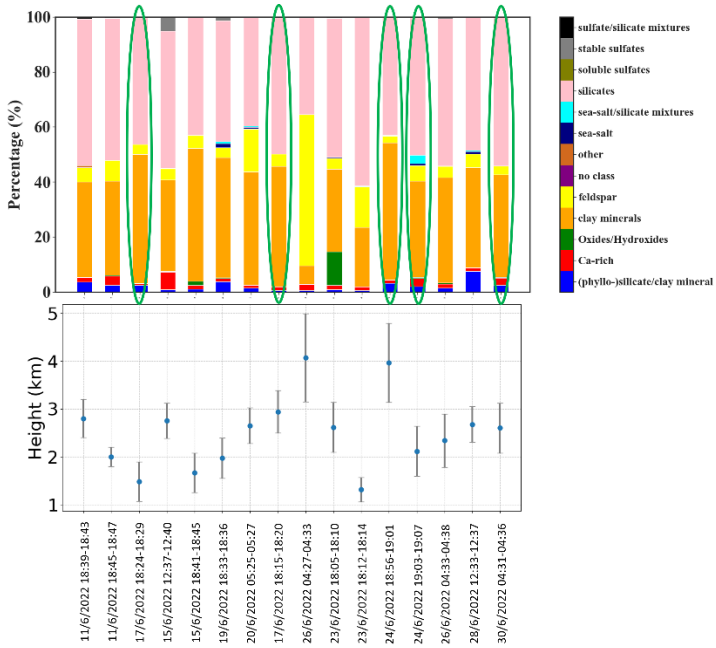

Figure 2. Top figure: Approximated mineralogical composition inside the dust layer during the ASKOS campaign. The circled cases are cloud-free. Bottom figure: Height range where each impactor sampled. Note that the "silicates" class refers to particles with a silicate composition which are not clay minerals or feldspars. These particles might be aggregates of different minerals.

Two cases present a percentage of <10% of oxides/hydroxides (15th and 23th June). These are mainly Fe-oxide/Fe-hydroxide-like compounds which originated from the same region from Southeast of Mindelo, above Cote D'Ivoire, according to HYSPLIT trajectory analysis. Moreover, the HYSPLIT analysis shows that they remained for 4 days near the surface.

The 26th of June is the day with the highest relative abundance of feldspar compounds (sampled by the impactor at 3-5 km). HYSPLIT analysis assesses the origin of the corresponding air masses to be from the East coast of Africa.

Conclusions

The vertical distribution of dust concentration derived from remote sensing techniques and in situ observations shows good agreement. This complementarity highlights that lidar instruments, which operate continuously and offer high spatial and temporal resolution, can provide valuable insights for improving dust forecasts.

The composition of Saharan dust mainly included silicates, of which a major fraction were probably aggregates with significant contributions of clay minerals and feldspars. Minor compounds were quartz and non-silicates like calcite and dolomite. In some cases, fractions of externally mixed iron-rich materials were observed. These results agree with the results shown in [12], [13] and [14].

Acknowledgements

This work was financed by the REVEAL project (GA 7222) funded by the Hellenic Foundation for Research & Innovation, the PANGEA4CalVal project (GA 101079201) funded by the European Union, the European Union's Horizon 2020 research and innovation programme under grant agreement No. 856612 and the Cyprus Government. Additional support was provided through the ATMO-ACCESS Integrating Activity under grant agreement No 101008004.

In this work we used data from the ASKOS campaign which was funded by the ASKOS ESA project (contract nr. 4000131861/20/NL/IA), the D-TECT ERC Consolidator Grant (ERC-CoG grant agreement 725698) and by the German Federal Ministry for Economic Affairs and Energy (BMWi) (grant no. 50EE1721C).

References

[1] Seifert, A. et al.: Atmos. Chem. Phys., 23, 6409–6430, https://doi.org/10.5194/acp-23-6409-2023, 2023.
[2] Flamant, C. et al.: Bull. of the Amer. Meteor. Soc., 99(1), 83–104. https://doi.org/10.1175/BAMS-D-16-0256.1, 2018.
[3] World Health Organization. *Ambient air pollution: A global assessment of exposure and burden of disease*, 2016.
[4] Escribano, J. et al.: Atmos. Chem. Phys., 22, 535–560, https://doi.org/10.5194/acp-22-535-2022, 2022.
[5] Marinou, E. et al.: Environ. Sci. Proceed., 26(1), 200. https://doi.org/10.3390/environsciproc2023026200, 2023.
[6] Engelmann, R. et al.: Atmos. Meas. Tech., 9, 1767–1784, https://doi.org/10.5194/amt-9-1767-2016, 2016.
[7] Mamouri, R. E. and Ansmann, A: Atmos. Meas. Tech., 7, 3717–3735, https://doi.org/10.5194/amt-7-3717-2014, 2014.
[8] Ansmann, A. et al.: Atmos. Meas. Tech., 12, 4849–4865, https://doi.org/10.5194/amt-12-4849-2019, 2019.
[9] Kezoudi, M. et al.: EGU23-17090, https://doi.org/10.5194/egusphere-egu23-17090, 2023.
[10] Kandler, K. et al.: Atmos. Chem. Phys., 18, 13429–13455, https://doi.org/10.5194/acp-18-13429-2018, 2018.
[11] Kandler, K., et al.: Tellus, 63B, 475–496, https://doi.org/10.1111/j.1600-0889.2011.00550.x, 2011a.
[12] Kandler, K. et al.: Atmos. Environ., 41, 37, 8058-8074, https://doi.org/10.1016/j.atmosenv.2007.06.047, 2007.
[13] Jeong, G. Y.: Atmos. Chem. Phys., 16, 12397–12410, https://doi.org/10.5194/acp-16-12397-2016, 2016.
[14] Chou, C. et al.: J. of Geophys. Res.: Atmos., 113(D00C10). https://doi.org/10.1029/2008JD009897, 2008.

High-Resolution Monitoring of Particulate Pollution in Urban Environments Using Doppler Lidar

P. Ortiz-Amezcua[1,2], *J. Andújar-Maqueda*[1,2], *J.A. Bravo-Aranda*[1,2], *A. del Águila*[1,2], *S. Castillo*[1,2], *J. Abril-Gago*[1,2], *J. L. Guerrero-Rascado*[1,2], *L. Alados-Arboledas*[1,2]

(1) Andalusian Institute for Earth System Research (IISTA-CEAMA), Av. del Mediterraneo S/N, 18006, Granada, Spain
(2) University of Granada, Department of Applied Physics, Av. de Fuentenueva S/N, 18071, Granada, Spain

Corresponding author: portizamezcua@ugr.es

Introduction

Urban air pollutants such as particulate matter (PM) are highly variable in space and time, and their concentration is strongly influenced by the urban boundary layer behaviour. Understanding such interaction is not straightforward due to the heterogeneity of the urban surface, and for this reason, high-resolution observations are needed. Because of the high cost and complexity that having a permanent network of high-resolution stations would imply, local air quality is frequently monitored using few representative stations. However, the location of those areas may not capture full variability, especially in the case of background stations, which can be influenced by horizontal transport of pollution and dispersion.

The recent advances in ground-based remote sensing techniques such as Lidar allow the routine measurements of profiles of many atmospheric parameters with high temporal and spatial resolution. In particular, elastic and Raman lidar techniques are widely used to retrieve optical and microphysical properties of atmospheric aerosol particles (e.g. [1, 2]), the latter being directly related to PM concentration. However, these methods are restricted to highly specific measuring and atmospheric conditions and their application in pollution studies under heterogeneous areas is not straightforward. For this reason, some studies have searched for empirical factors to obtain PM concentrations from lidar-retrieved aerosol optical properties [3-5].

Doppler lidars, those measuring the Doppler shift due to the movement of aerosol particles, have been developed in the last decades to measure wind field with high resolution and usually present scanning capabilities allowing to measure profiles even with horizontal elevation. Moreover, recent efforts have been made to calibrate the Doppler lidar signal intensity not only to retrieve wind but also aerosol attenuated backscatter (β_{att}) [6-8]. This opens great potential for these systems on aerosol observations and pollutant dispersion studies [9].

In this context, this work applies these techniques to obtain calibrated high resolution PM maps over a medium-size city by the combination of Doppler lidar quasi-horizontal scans and in-situ PM measurements at a certain location in the city. The objective of this approach is to study the spatial and temporal variability of particulate pollution across the city in order to assess the appropriateness of the locations of the regular pollution monitoring stations.

Methodology

The study has been performed in Granada (Spain), a medium-size city located in a basin delimited by Sierra Nevada Mountain range (3478 m above sea level, a.s.l.). The city is characterized for large temperature differences, low relative humidity, scarce precipitation and light winds influenced by local mountain-valley flow, facilitating pollution levels to exceed EU threshold limits.

The remote sensing scans were performed with the Doppler lidar StreamLine XR+ system, a pulsed laser device operating at a wavelength of 1565 nm, equipped with a heterodyne detector and optical-fiber technology. It emits pulses with an energy of 100 μJ and a high repetition rate of 10 Khz. For this study, the system was configured with a spatial resolution of 30 m, an effective range spanning from 90 m to 12000 m, and the focal length of the optical system was set to 500 m. Quasi-horizontal scans were systematically conducted at an elevation of less than 10º, with an azimuth resolution of less than 0.1º and a sweep velocity

of 1º/s (thus performing every full scan in 6 minutes). The system was located on the roof terrace of the UGR station (13 meters above ground level), at Andalusian Institute for Earth System Research (IISTA, 37.16° N, 3.61° W, 680 m a.s.l.). This station belongs the experimental observatory AGORA (Andalusian Global Observatory of the Atmosphere), which is included in Aerosol remote sensing, Cloud remote sensing and Aerosol in situ components of ACTRIS (*https://www.actris.eu/, last access, 14/04/2025*).

PM concentration data were collected at air quality monitoring stations located in the metropolitan area of Granada, belonging to the Automatic Air Quality Network (*https://www.juntadeandalucia.es/medioambiente/portal/areas-tematicas/atmosfera/la-calidad-del-aire/red-de-vigilancia-y-control-de-la-calidad-del-aire-de-andalucia, last access, 14/04/2025*). Specifically, data from the 'Palacio de Congresos' station have been used for this study, an urban background station (located approximately 50 meters away from most surrounding roads, and thus not influenced by traffic) which is located 500 m from UGR station.

The methodology followed from the raw data to the final calibration and its application included several steps in order to ensure data quality and homogeneity (Fig. 1). Firstly, β_{att} data were obtained from Doppler lidar scans by correcting and calibrating the measured signal [6-8]. After filtering data with enough signal-to-noise ratio, the attenuation of the calibrated signal was corrected using an iterative procedure [10] to obtain particle backscatter coefficient (β_{part}). Those data coinciding in space and time with the air quality monitoring station measurements were used to find an empirical conversion factor from β_{part} to PM10, which was then applied to the rest of β_{part} values to generate PM10 for the whole lidar scans. It is important to notice that given the fact that the actual relationship between β_{part} and PM10 depends on aerosol microphysical properties (strongly influenced by aerosol type), this empirical calibration was conducted for each measurement day.

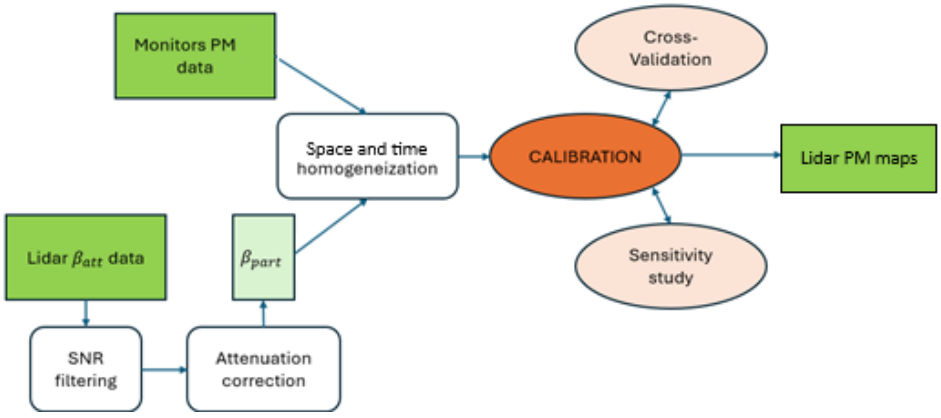

Figure 1. Flow chart of the methodology followed to perform the data processing and calibration to generate PM maps from Doppler lidar scans.

Results and Discussion

The results showed, firstly, that a generally accurate empirical calibration was possible with the proposed measurement configuration. Moreover, areas were the PM pollution is frequently higher could be successfully identified.

Figure 2 shows an example of the calibration for the scan performed on 01/04/2023 at 08:40 h UTC. For that day, the calculated empirical conversion factor was $9.0 \cdot 10^6\ (\mu g \cdot m^{-3})/(m^{-1} \cdot sr^{-1})$. The comparison between the attenuated backscatter signal (β_{att}) in Figure 2a and the calibrated PM10

concentration map in Figure 2b illustrates the precision of the approach. While β_{att} initially revealed areas of elevated aerosol presence, the attenuation correction and the subsequent calibration accurately delimited areas with high PM10.

Notably, the western section of the scan, which displayed PM concentrations exceeding 80 $\mu g \cdot m^{-3}$, corresponds to a high-traffic highway surrounding the city. This direct correlation between pollution levels and traffic emissions underscores the importance of integrating remote sensing techniques with urban planning strategies to mitigate pollution in critical zones.

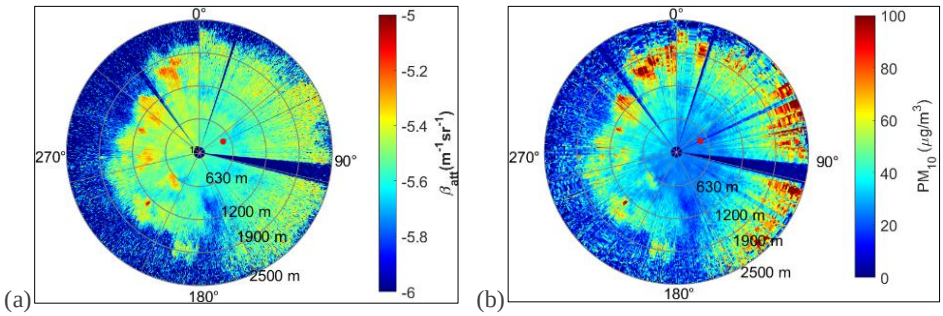

Figure 2. (a) example Doppler lidar β_{att} measurements; (b) PM10 map created after applying the calibration. Red dot indicates the location of the air quality monitoring station.

Furthermore, the study emphasizes the limitations of regular air quality monitoring stations, which may fail to capture the full extent of spatial variability in PM concentrations. By comparing lidar-generated maps with station-based measurements, it becomes evident that many pollution hotspots remain undetected by conventional monitoring approaches, particularly in areas influenced by horizontal transport and dispersion mechanisms.

Conclusions

This study demonstrated the feasibility of combining Doppler lidar quasi-horizontal scans with in-situ PM measurements to create high-resolution particulate matter (PM) concentration maps in urban areas. The proposed methodology successfully captured the spatial and temporal variability of PM pollution, enabling the identification of high-pollution hotspots, such as those influenced by traffic emissions. Moreover, the study highlighted the importance of evaluating the appropriateness of regular air quality monitoring station locations to ensure comprehensive urban pollution coverage.

Future work will focus on conducting a statistical analysis of the most polluted areas identified in these maps, along with validating the proposed technique using independent measurements. These steps will further enhance the accuracy and applicability of this approach for urban air quality monitoring.

Acknowledgements

This work is funded by University of Granada through project PPJIA2024-50 and through Excellence Research Unit Earth Science and Singular Laboratory AGORA (LS2022-1). It is also part of the Spanish national projects PID2023-151668OB-I00, PID2020-120015RB-100, PID2022-142708NA-I00, PID2023-151817OA-I00 funded by MICIU/AEI/10.13039/501100011033, strategic network RED2022-134824-E, ATMO-ACCESS grant agreement No 101008004, Scientific Unit of Excellence: Earth System (UCE-PP2017-02). A. del Águila is part of Juan de la Cierva programme through grant no. JDC2022-048231-I and funded by MCIN/AEI/10.13039/501100011033 and by European Union "NextGenerationEU"/PRTR". Jesús Abril-Gago received funding through the grants FPU21/01436 and EST24/00285 funded by MICIU/AEI/10.13039/501100011033.

References

[1] Mattis, I.., et al: *EARLINET Single Calculus Chain – technical – Part 2: Calculation of optical products*, Atmos. Meas. Tech., 9, 3009–3029, 2016.
[2] Böckmann, C.: *Hybrid regularization method for the ill-posed inversion of multiwavelength lidar data in the retrieval of aerosol size distributions*, Appl. Opt., 40, 1329-1342, 2001.
[3] Parracino, S., et al.: *Real-time vehicle emissions monitoring using a compact LiDAR system and conventional instruments: first results of an experimental campaign in a suburban area in southern Italy*, Opt. Eng., 55(10), 103107, 2016.
[4] Lyu, L., et al.: *Vertical Distribution Characteristics of PM2.5 Observed by a Mobile Vehicle Lidar in Tianjin, China in 2016*, Journal of Meteorological Research, 32, 60-68, 2018.
[5] Shin, J., et al.: *Multi-section reference value for the analysis of horizontally scanning aerosol lidar observations*, Atmos. Meas. Tech., 17, 397-406, 2024.
[6] Manninen, A. J., et al: *A novel post-processing algorithm for Halo Doppler lidars*, Atmos. Meas. Tech., 9, 817–827, 2016.
[7] Vakkari, V., et al: *A generalised background correction algorithm for a Halo Doppler lidar and its application to data from Finland*, Atmos. Meas. Tech., 12, 839–852, 2019.
[8] Pentikäinen, P., et al: *Methodology for deriving the telescope focus function and its uncertainty for a heterodyne pulsed Doppler lidar*, 13, 2849–2863, 2020.
[9] Dieudonné, E., et al.: *Can commercial Doppler lidars serve air quality applications? Results from a field comparison with PM10, PM2.5, and granulometric observations in a multi-influenced harbor city*, Aerosol Science and Technology, 59(5), 608-622, 2024.
[10] Di Girolamo, P., et al: *Aerosol observations by lidar in the nocturnal boundary layer*, Appl. Opt., 38(21), 4585–4595, 1999.

Recent advances in lidar studies of airborne birch pollen in Finland

M. Filioglou[1], X. Shang[1], A. Leskinen[1], P. Tiitta[1], E. O'Connor[2], A. Saarto[3], V. Vakkari[2,4], M. Tuononen[5],* ***M. Komppula[1]***

(1) Finnish Meteorological Institute, Atmospheric Research Centre of Eastern Finland, Yliopistonranta 8, 70211, Kuopio, Finland
(2) Finnish Meteorological Institute, Erik Palménin aukio 1, 00560 Helsinki, Finland
(3) University of Turku, Biodiversity Unit, Vesilinnantie 5, 20014, Turku, Finland
(4) North-West University, Chemical Resource Beneficiation, 2520, Potchefstroom, South Africa
(5) Vaisala Oyj, Vanha Nurmijärventie 21, 01670, Vantaa, Finland
**now at Envineer Oy, Microkatu 1, 70210, Kuopio, Finland*

Corresponding author: mika.komppula@fmi.fi

Introduction

Pollen, a major mass contributor of atmospheric primary bioaerosols [1], is closely associated with allergic diseases [2] and cloud formation processes [3]. Currently, birch pollen sensitivity affects 8–16 % of the general population [4] and it is projected that pollen sensitization in Europe alone may double by 2050 [5]. The allergic symptoms are concentration dependent [6] thus, continuous monitoring of pollen is of major importance. Continuous monitoring and accurate representation of the microphysical properties of atmospheric pollen – such as number, mass and cloud condensation nuclei (CCN) concentration – is also key to constrain climate forcing estimations and improve weather and air quality forecasts.

Near-ground pollen monitoring is performed with Hirst-type volumetric air samplers [7], hereafter, Burkard collector. Globally, this technique serves as a reference method in pollen monitoring, yet, real- or near real-time information is not feasible and recent studies show a wide discrepancy of Burkard data when compared with observations from a plethora of other instruments and measurement techniques [8].

While pollen is pacing to be one of the most important consequences of climate change for human health, polarization lidars have become a promising tool to detect pollen particles in the atmosphere. Polarization lidars which are active remote sensors present a unique opportunity to study the vertical and temporal evolution of pollen particles in the atmosphere since the non–spherical structure and irregular surface of some of the pollen types induce moderate to strong laser depolarization.

This abstract compile our previous efforts on the remote sensing of pollen particles utilizing a synergy of lidar observations and aerosol in situ instrumentation at the ACTRIS (Aerosol, Clouds, and Trace Gases Research Infrastructure) mobile station in Vehmasmäki (Kuopio), Finland (62° 44′ N, 27° 33′ E; 190 m above sea level). On site, a PollyXT, a Vaisala CL61 ceilometer and a HALO Doppler lidar are located among other aerosol and cloud in situ instruments [9]. First, we derive the characteristic particle depolarization ratio (PDR) of birch pollen particles which then allows the estimation of the microphysical properties.

Methodology

A prerequisite for the estimation of the aerosol microphysical properties is the knowledge of the characteristic PDR for each aerosol type. PDR information is also utilized in aerosol classification algorithms to aid aerosol typing efforts. In the microphysical property estimation, the characteristic PDR information is important since two or more aerosol types are most commonly mixed in the atmosphere and therefore the contribution of a specific aerosol type (e.g., birch pollen) must be estimated first in the total volume. This is done by utilizing the characteristic PDR value of the aerosol types in the mixture which primarily should be distinctive enough from each other. Therefore, we first characterize the PDR of birch pollen particles at four wavelengths (355, 532, 910, 1565 nm) utilizing observations from the three abovementioned lidars. Then, we applied the POlarization LIdar PHOtometer Networking (POLIPHON) method [10] and estimate the microphysical properties of birch pollen particles in the atmosphere. For this, the so-called conversion factors are needed which are derived through direct correlation of in situ aerosol particle distributions and lidar extinction coefficient. The methodology used to retrieve the lidar vertical

profiles of particle backscatter coefficient (β) and PDR as well as the full instrumental description and detailed methodology can be found in our recently published papers [11, 12].

Results and Discussion

A total of 102 layers were captured during the pollination seasons of 2021 and 2022 at the forest site in Vehmasmäki (Kuopio), Finland and further associated with surface pollen and PM10 concentrations estimated from the Burkard collector and a NanoScan scanning mobility particle sizer (NS) and an optical particle sizer (OPS), hereafter NS/OPS. Here, we argue that the PDR can fluctuate depending on the amount of pollen and other aerosols in the aerosol mixture. Figure 1 demonstrates that pollen concentration (contribution of other aerosols) was positively (negatively) correlated to the PDR. Where, the PDR is the mean value of the first layer in the atmosphere as described [11]. The higher the pollen concentration and the lower the contribution of other aerosols resulted to higher PDR in the pollen layer. The lower layer mean PDR values at high birch concentration regime were attributed to the presence of smoke and dust particles in the atmosphere.

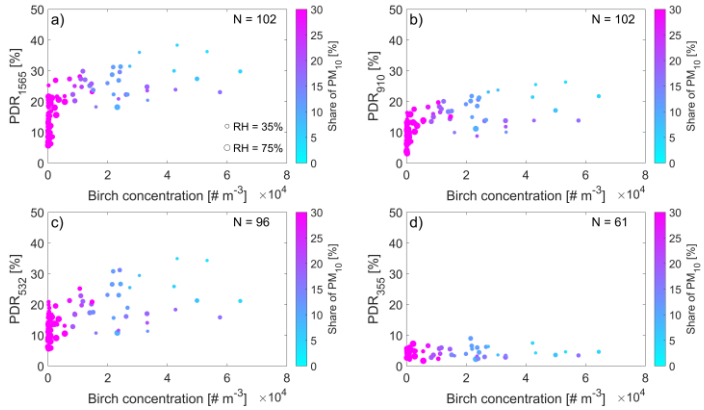

Figure 1. Wavelength dependence of the PDR at a) 1565 nm b) 910 nm c) 532 nm and d) 355 nm on the birch pollen concentration. The size of the circles indicates the relative humidity at 26 m above ground level. The colour of the circles corresponds to the share of PM10 in the PM10 plus PM_{birch} sum. The number at the top right corner corresponds to the number of layers considered at each wavelength.

To estimate the characteristic PDR or birch pollen, cases with the lowest PM_{10} share contribution (less than 10 %) to the aerosol mixture were considered. The 10 % limit was a compromise and ensured a meaningful number of cases for the calculation of birch pollen optical properties. A mean (range of) birch PDR of 5 ± 2 % (4–8), 28 ± 6 % (21–35), 23 ± 6 % (17–26), and 33 ± 4 % (27–38) at wavelengths of 355, 532, 910, and 1565 nm was estimated, respectively (Figure 2). The Backscatter-related Ångstrom Exponents, $BÅE_{355–532}$, $BÅE_{532–910}$, and $BÅE_{532–1064}$ were 0.37 ± 0.63, 0.16 ± 0.20, and 0.54 ± 0.41, respectively.

Having characterized the PDR of birch pollen, we proceeded and decomposed the lidar signal and extracted the birch backscatter coefficient (β_α) in the total β coefficient. For simplicity, we focus on the estimation of the mass concentration calculation at 910 nm and full results, including the CCN-related conversion factors and the rest of the wavelengths, can be found in [11, 12]. According to Eq. 1, the only unknown parameter is the volume-to-extinction factor, $c_{v,\alpha}$. Where, α indicates the aerosol type (e.g. birch pollen), λ the wavelength and the particle density for birch pollen is ρ = 800 kg/m^3 [13]. The volume-to-extinction factor, $c_{v,\alpha}$, has been previously retrieved using the relationship between the column volume concentration from AERONET and the extinction coefficient from the lidar for a specific aerosol type.

$$m_a = \rho \cdot c_{v,a}(\lambda) \cdot \beta_a(\lambda) \cdot LR_\alpha(\lambda) \qquad (1)$$

Nevertheless, the 15 μm upper size limitation of the AERONET inversion product may not be representative of the bigger, in size, pollen particles. Instead, the volume aerosol size distribution from ICEMET, a holographic imaging probe [14], considering the size range from 10 to 30 μm has been used. Figure 2 shows the relationship between the birch extinction coefficient at 910 nm from the CL61 ceilometer and the volume concentration from ICEMET observations.

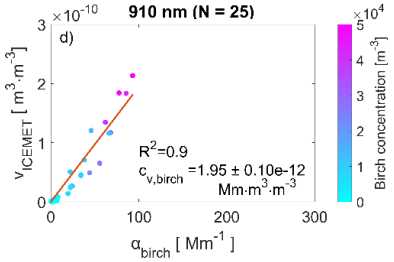

Figure 2. Relationship between birch extinction coefficient α_{birch} at 910 nm and volume concentration, v_{ICEMET} considering particles between 12 and 35 μm. Correlations are shown utilizing the mean birch extinction coefficient between 200–250 m above ground level. The slope indicates the conversion factor $c_{v,birch}$ and are also given as numbers in the panels along with the goodness of the fit expressed through R2 statistical value.

At last, Figure 3 summarizes the lidar-derived estimates of pollen mass concentration and equivalent observations from in situ instrumentation. A mixture of birch and continental pollution is assumed for the decomposition of the lidar profiles. Figures 3a-b demonstrate the *α* and PDR at 910 nm and Figure 3c shows the 2-D evolution of birch mass concentration from the lidar. Figure 3d is a comparison between Burkard, ICEMET and the lidar-derived mass concentration at 200 m (for CL61 ceilometer at 910 nm) or 400 m (for PollyXT at 532 nm).

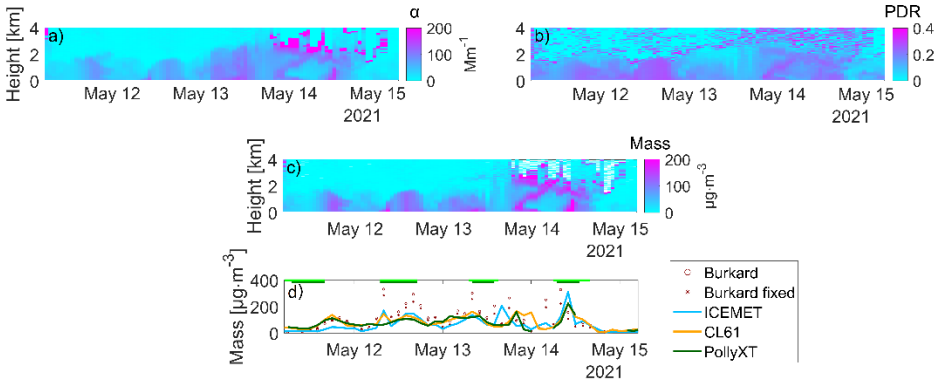

Figure 3. Timeseries of optical properties and estimated birch mass concentration between 11th of May 2021 at 05 LT and 15th of May 2021 at 05 LT at Vehmasmäki station (Kuopio) in Finland. a) Total particle extinction coefficient at 910 nm from CL61 ceilometer observations. A LR of 60 sr is used. b) PDR at 910 nm. c) Mass concentration estimated from 910 nm d) Comparison between in situ (Burkard and ICEMET) and lidar estimated mass concentrations. For the Burkard mass concentration estimation both the mean volume diameter from ICEMET (circles) and a fixed birch pollen size of 22 μm (stars) is considered. For the CL61 ceilometer observations, a mean mass concentration between 200 and 250 m above ground level is considered. For the PollyXT lidar observations, a mean mass concentration between 400 and 450 m above ground level is considered. The times that the mixing layer height was above the 400 m (200 m) height level are indicated by dark green bar (light green bars) in panel d, respectively.

It is evident that the time evolution of pollen load can be tracked using the lidar observations. This figure further confirms that 1) aerosol size distributions from ICEMET are a suitable alternative to retrieve the

needed extinction to mass conversion factor for this aerosol type, enriching the current methodology which utilizes AERONET observations only. This is validated by the similar evolution and comparable mass between the pollen sampler and ICEMET. The rather low overlap region of the lidar, which is assumed to be 200 (for CL61) or 400 m (for PollyXT) above the instrument level, is sufficient to track changes in pollen concentration at ground level. This is especially valid when the PBL is well-mixed while some discrepancy is expected during other times. Note that due to the intrinsic approach to estimate the pollen concentration in Burkard observations, the reported concentration may have resulted at any point within the 2h time frame and that may cause an additional inconsistency when compared with the rest of the instruments.

Conclusions

The pollen optical properties of birch were investigated with a synergy of three lidars and co-located in situ aerosol and pollen instruments at the rural site of Vehmasmäki (Kuopio) in Finland. The PDR was positively (negatively) correlated with the pollen concentration (share of other aerosol particles in the mixture). A higher pollen concentration and lower contribution of other aerosols resulted in a higher PDR in the pollen layer. Having the PDR of birch pollen characterized the number, mass and CCN-related estimations from lidar observations as well as aerosol typing for birch pollen is then feasible.

Furthermore, we expanded the applicability of polarization lidars to assess the microphysical properties of birch pollen utilizing a synergy of aerosol size distributions from novel in situ instrumentation. The pivotal conversion factors to turn the optical into microphysical properties in the POLIPHON method were derived from a synergy of NS, OPS, and ICEMET in situ observations. This was necessary to accurately account for birch pollen which is in the larger end of the aerosol particle sizes. The novel approach can be used as an alternative method to derive the conversion factors of other large aerosol particles, for example, volcanic ash particles and larger pollen types.

Acknowledgements

The authors gratefully acknowledge the support of the Finnish Research Impact Foundation through the Tandem Industry Academia (TIA) programme. We also acknowledge the Aerosol, Clouds and Trace Gases Research Infrastructure (ACTRIS) for providing the dataset used in this study; the dataset was produced by the Finnish Meteorological Institute and is available on https://cloudnet.fmi.fi/ (last access: 30 March 2025).

References

[1] Williams et al.: Northern Hemisphere forests at temperate and boreal latitudes are substantial pollen contributors to atmospheric bioaerosols, Forest Ecol. Manag., 401, 187–191, 2017.

[2] Kitinoja et al.: Short-term exposure to pollen and the risk of allergic and asthmatic manifestations: a systematic review and meta-analysis, BMJ Open, 10, 2020.

[3] J. Burkart, J. Gratzl, T. M. Seifried, P. Bieber, and H. Grothe: Isolation of subpollen particles (SPPs) of birch: SPPs are potential carriers of ice nucleating macromolecules, Biogeosciences, 18, 5751–5765, 2021.

[4] Biedermann et al.: Birch pollen allergy in Europe, Allergy, 74, 1237–1248, 2019.

[5] Lake et al.: Climate Change and Future Pollen Allergy in Europe, Environ. Health Perspect., 1, 385–391, 2018.

[6] Pfaar et al.: Defining pollen exposure times for clinical trials of allergen immunotherapy for pollen-induced rhinoconjunctivitis – an EAACI position paper, Allergy, 72, 713–722, 2017.

[7] Hirst, J. M.: An automatic volumetric spore trap, Ann. Appl. Biol., 39, 257–265, 1952.

[8] Maya-Manzano et al.: Towards European automatic bioaerosol monitoring: Comparison of 9 automatic pollen observational instruments with classic Hirst-type traps, Sci. Total Environ., 866, 161220, 2023.

[9] Hirsikko et al..: Observing wind, aerosol particles, cloud and precipitation: Finland's new ground-based remote-sensing network, Atmos. Meas. Tech., 7, 1351–1375, 2014,

[10] Ansmann et al.: Dust mass, cloud condensation nuclei, and ice-nucleating particle profiling with polarization lidar: updated POLIPHON conversion factors from global AERONET analysis, Atmos. Meas. Tech., 12, 4849–4865, 2019

[11] Filioglou et al.: Spectral dependence of birch and pine pollen optical properties using a synergy of lidar instruments, Atmos. Chem. Phys, 23, 9009–9021, 2023.

[12] Filioglou et al.: Lidar estimates of birch pollen number, mass, and CCN-related concentrations, Atmos. Chem. Phys., 25, 1639–1657, 2025.

[13] Gregory, P. H.: The microbiology of the atmosphere, ISBN 0249441101, 1973.

[14] Tiitta et al.: Intercomparison of holographic imaging and single-particle forward light scattering in situ measurements of liquid clouds in changing atmospheric conditions, Atmos. Meas. Tech., 15, 2993–3009, 2022.

Smoke in the Valleys, Data on the Peaks: Remote Sensing of Wildfire Aerosols in the Alps.

M.A. Posyniak[1], *J. Speidel*[1], *T. Stacewicz*[2], *H. Vogelmann*[1]

(1) Karlsruhe Institute of Technology, Institute of Meteorology and Climate Research - Atmospheric Environmental Research, Kreuzeckbahnstraße 19, 82467, Garmisch-Partenkirchen, Germany
(2) University of Warsaw, Faculty of Physics, Institute of Experimental Physics, Pasteura 5, 02-093, Warsaw, Poland
Corresponding author: michal.posyniak@kit.edu

Introduction

Optical remote sensing is one of the key methods for investigating aerosol concentration and composition. Instruments such as multiwavelength photometers and lidars are commonly used for these observations. This study presents the application of remote sensing facilities operated by the Karlsruhe Institute of Technology at Campus Alpin (Germany) to investigate aerosol optical and microphysical properties.

In March 2025, a case study was conducted following a large forest fire in South Tyrol (Italy), approximately 90 km south of Garmisch-Partenkirchen. The fire affected an area of about 100 hectares of forest near the Vinschgau municipalities of Latsch and Kastelbell.

Methodology

The remote sensing instrumentation is located both in the valley at Garmisch-Partenkirchen (734 m a.s.l.) and at high altitude on Mount Zugspitze (2962 m a.s.l.), providing a valuable vertical range for atmospheric observations.

A multiwavelength lidar system (TONI), installed at Campus Alpin in 2024, is based on a diode-pumped Nd:YAG laser operating at three wavelengths: 1064, 532 and 355 nm, with pulse energies of 90, 90, and 50 mJ respectively, and a repetition rate of 100 Hz. The system uses a 300 mm diameter telescope, enabling an overlap starting at around 250 m, making it suitable for both Planetary Boundary Layer (PBL) and free troposphere aerosol measurements. The receiver is equipped with seven channels: three elastic (1064, 532 and 355 nm), two Raman (607 and 387 nm) and two depolarisation (532 and 355 nm).

Complementing the lidar observations, two CIMEL CE318T photometers are in operation: one co-located with the lidar in the valley, and another installed on Mount Zugspitze. Both instruments are capable of solar, lunar, and sky observations. This altitudinal setup enables the distinction between aerosol properties in the PBL (typically <3 km a.s.l.) and in the free troposphere [1], thus enhancing our understanding of aerosol behaviour in complex mountainous environments.

The proximity of the photometer to the lidar enables synergistic retrieval of aerosol optical and microphysical profiles. Using different algorithms (e.g., [2], [3]), it is possible to derive detailed columnar and vertically resolved aerosol properties. The combination of lidar and photometer data provides information that cannot be obtained from either instrument alone, allowing for the retrieval of concentration profiles of fine and coarse aerosol modes [4].

Furthermore, we demonstrate the use of an alternative method for retrieving Aerosol Particle Size Distribution (APSD) profiles. This technique incorporates a predefined APSD model directly into the lidar equations and uses a minimization approach to determine the best-fit parameters by comparing measured and simulated signals [5]. Notably, this approach does not require prior knowledge of the lidar ratio [6].

Additionally, during this episode, we operated a ceilometer (CL51, Garmisch), an aerosol lidar (532 nm) at Schneefernerhaus (2650 m a.s.l., approx. 7 km from Garmisch-Partenkirchen).

Parallel to the lidar soundings, photometer measurements were conducted. Aerosol optical depth (AOD) and Ångström exponent plots from both Garmisch and Zugspitze showed an increase in optical depth throughout the day, consistent with strengthening lidar returns.

Results and Discussion

The smoke from the 6 March 2025 fire became visible at 12:30 UTC from the top of Zugspitze and began spreading across the region (Fig. 1).

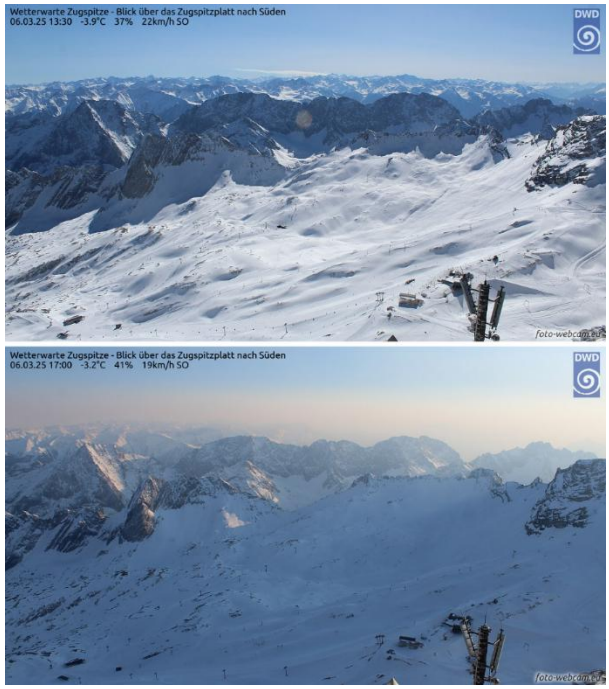

Figure 1. Photographs taken on 6 March 2025 (upper) 13:30 CET and (lower) 17:00 CET from the summit of Zugspitze looking south. Image source: www.foto-webcam.eu

Multiple aerosol layers were detected in the atmosphere using TONI lidar (Fig. 2). The layer below 1.5 km corresponded to aerosol within the PBL, while layers between 6 and 8 km were likely associated with desert dust. A pronounced aerosol layer at approximately 3 km altitude was attributed to smoke. This feature was also observed by the ceilometer in Garmisch-Partenkirchen. Additionally, night-time lidar measurements were conducted at the Schneefernerhaus observatory, confirming the presence of elevated aerosol layers.

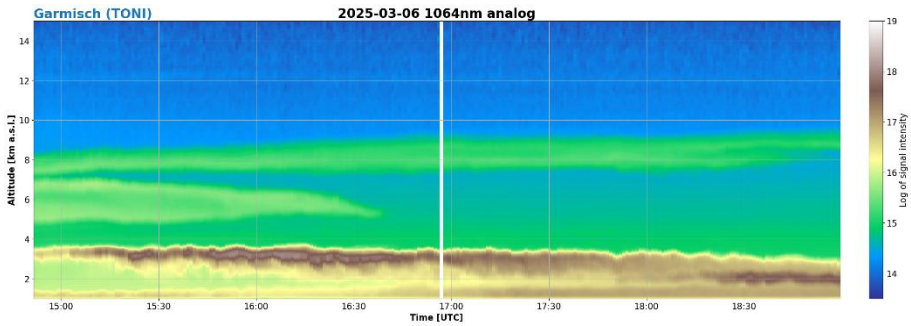

Figure 2. Logarithm of range-corrected signal registered in Garmisch-Partenkirchen on 2025-03-06 using TONI lidar.

Fig. 3 presents aerosol optical depth and Angstrom exponent registered on 6 March 2025 on Zugspitze. We observed growth of both parameters over time which may be related to higher concentration of small particles. Moreover, particle size distributions retrieved from both photometers [7] indicate a significant increase in aerosol concentration. The dominance of small particles is consistent with the typical size range of smoke aerosols. Evening observations show an overall increase in aerosol concentration, particularly in the number of small particles, as compared to larger desert dust particles, which were also present.

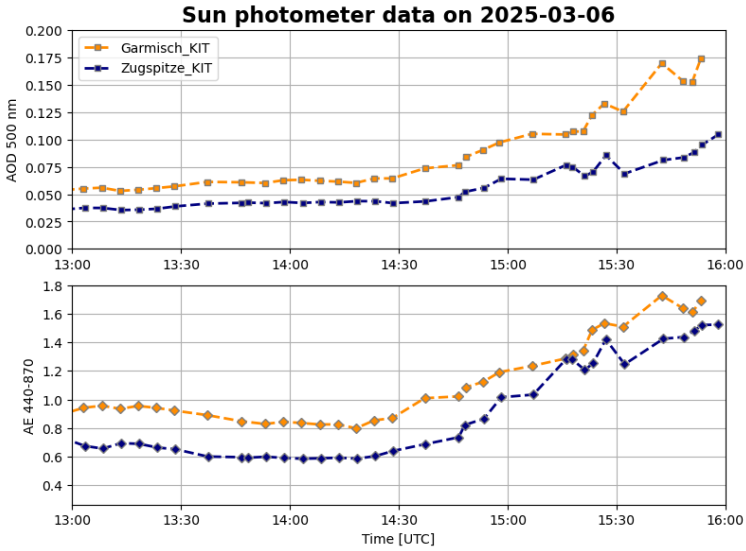

Figure 3. Aerosol optical depth at 500 nm and Ångstrom exponent (440-870 nm) measured with photometers in Garmisch-Partenkirchen and Zugspitze on 2025-03-06.

Profiles of particle sizes, particularly effective radius profiles retrieved from the lidar in Garmisch-Partenkirchen, will be presented in detail (Fig. 4). For APSD retrievals we used refractive index obtained with photometers. Below, two profiles of aerosol effective radius are presented.

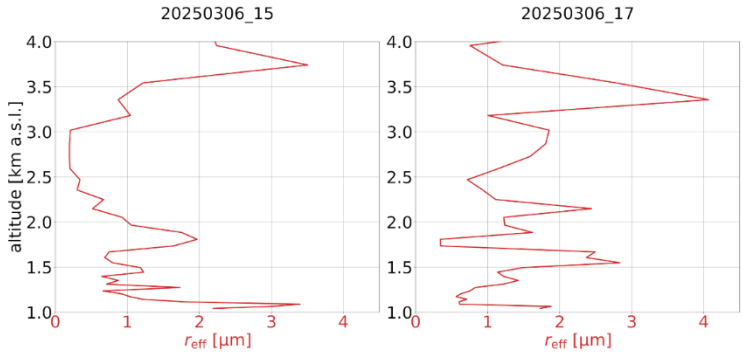

Figure 4. Effective radius of aerosol particles retrieved from lidar on 2025-03-06 at 15:00 and 17:00 UTC.

Conclusions

Although the wildfire in South Tyrol was a tragic event, requiring the evacuation of several villages, it also provided a valuable opportunity to study the transport of smoke from a forest fire in its near-source region. The unique altitudinal setup of remote sensing instruments at Campus Alpin enabled detailed vertical profiling of aerosols. The integration of multiple ground-based remote sensing systems: lidars, photometers, and ceilometer, allowed for a comprehensive analysis of aerosol properties and highlighted the potential of synergistic observations in complex mountainous environments.

Acknowledgements

This work was financed by the German Federal Ministry of Education and Research within in the project ACTRIS-D NF/TP2 FK:01LK2001B.

References

[1] Posyniak, M.A. et al.: *Experimental study of smog microphysical and optical vertical structure in the Silesian Beskids, Poland*, Atmospheric Pollution Research, 12(9), 101171, doi:10.1016/j.apr.2021.101171, 2021.

[2] Dubovik, O. et al.: *A Comprehensive Description of Multi-Term LSM for Applying Multiple a Priori Constraints in Problems of Atmospheric Remote Sensing: GRASP Algorithm, Concept, and Applications*, Frontiers in Remote Sensing, 2, 706851, doi:10.3389/frsen.2021.706851, 2021.

[3] Böckmann, C., Ritter, C., and Graßl, S.: *Improvement of Aerosol Coarse-Mode Detection through Additional Use of Infrared Wavelengths in the Inversion of Arctic Lidar Data*, Remote Sensing, 16(9), 1576, doi:10.3390/rs16091576, 2024.

[4] Lopatin, A. et al.: *Synergy processing of diverse ground-based remote sensing and in situ data using the GRASP algorithm: applications to radiometer, lidar and radiosonde observations*, Atmospheric Measurement Techniques, 14(3), 2575–2614, doi:10.5194/amt-14-2575-2021, 2021.

[5] Sitarek, S., Stacewicz, T., and Posyniak, M.: *Software for retrieval of aerosol particle size distribution from multiwavelength lidar signals*, Computer Physics Communications, 199, 53–60, doi:10.1016/j.cpc.2015.08.024, 2016.

[6] Makuch, P. et al.: *Lidar observation of aerosol transformation in the atmospheric boundary layer above the Baltic Sea*, Oceanologia, 63(2), 238–246, doi:10.1016/j.oceano.2021.01.002, 2021.

[7] Sinyuk, A. et al.: *The AERONET Version 3 aerosol retrieval algorithm, associated uncertainties and comparisons to Version 2*, Atmospheric Measurement Techniques, 13(6), 3375–3411, doi:10.5194/amt-13-3375-2020, 2020.

Decoding Urban Air Quality: A Multidimensional Exploration of Pollution Dynamics in Wrocław, Poland.

A. Drzeniecka-Osiadacz[1], *Ch. Di Marco[2], T. Sawiński[1], I. Stachlewska[3], M. Górka[1], A. Hafiz[3], P. Poczta[4], M Jabłońska[6], M. Werner[1], M. Kryza[1], K. Klejnowski[5], K. Jaworek[5], W. Bartz[1], M. Syrzycki[7], J. Bratkowski[7], S. Leeson[2], N. Mullinger[2], P. Modzel[1], M. Szczyrba[6]*

(1) Department of Climatology and Atmosphere Protection, Faculty of Earth Science and Environmental Management, University of Wrocław, Kosiby 8 Str, 521-621 Wrocław, Poland
(2) UK Centre for Ecology & Hydrology, Bush Estatem Penicuik, Midlothian, EH26 0QB, UK
(3) University of Warsaw, Faculty of Physics, Institute of Geophysics, (IGFUW), Pasteura 5, 02-093, Warsaw, Poland
(4) Laboratory of Bioclimatology, Poznan University of Life Sciences, Piatkowska 94, 60-649 Poznan, Polan
(5) The Institute of Environmental Engineering of the Polish Academy of Sciences, Zabrze, Poland
(6) University of Silesia in Katowice – University Laboratories of Atmosphere Control (UŚ ULKA)
(7) Institute of Environmental Protection - National Research Institute (IOŚ PIB)

Corresponding author: anetta.drzeniecka-osiadacz@uwr.edu.pl

Introduction

Atmospheric aerosols constitute one of the most ubiquitous yet least comprehensively characterized components of urban atmospheric contamination. Their particle-size distribution and pronounced chemical heterogeneity govern both toxicological potency and radiative climate forcing [1], while their short atmospheric residence time engenders pronounced spatio-temporal variability that often eludes conventional regulatory monitoring networks. Chronic exposure to fine particulate matter ($PM_{2.5}$) has been causally linked to elevated morbidity and mortality from cardio-respiratory diseases and neurodegenerative disorders [2]. Polish cities, such as Wrocław, suffer from recurrent winter smog episodes driven predominantly by domestic combustion of solid fossil fuels and biomass, increasingly augmented by traffic-related emissions. Robust quantification of aerosol climatic impacts and evidence-based air quality management both require a thorough understanding of emission sources, atmospheric transformation pathways, and associated feedback mechanisms. Despite advancements in air quality monitoring, traditional networks often fail to capture the spatial and temporal heterogeneity of urban pollutants. Furthermore, the mass concentration of particulate matter (PM) alone provides no information about its provenance or the physico-chemical and optical properties that govern toxicity and radiative effects. Detailed chemical and physical speciation, combined with knowledge of the spatio-temporal structure of the atmosphere, including its vertical stratification and the pollutants' properties, is therefore indispensable. Recent studies that couple high-resolution in-situ measurements with active remote-sensing techniques (e.g., lidar and sodar) have demonstrated the effectiveness of such synergistic approaches for source apportionment, boundary-layer process characterization, and the evaluation of aerosol–climate interactions [3, 4, 5, 6]. Building on this foundation, the present study adopts a multidisciplinary monitoring framework that integrates high-resolution chemical analysis and advanced remote sensing, complemented by concurrent meteorological observations. The authors argue that this approach substantially alleviates the constraints inherent in the traditional measurement methodologies employed by monitoring networks.

Methodology

From 15 November to 5 December 2022, a comprehensive field campaign was conducted at the Climatology and Atmospheric Protection Observatory in the Sępolno district of Wrocław (51.10° N, 17.10° E; 116 m a.s.l.). Air quality in this part of the city is shaped primarily by residential solid-fuel combustion and local traffic emissions. Aerosol composition was measured using a high-resolution time-of-flight aerosol mass spectrometer (HR-TOF-AMS, Aerodyne Research Inc.) operated by the UK Centre for Ecology & Hydrology; the resulting data were subsequently subjected to positive matrix factorization (PMF) source apportionment analysis. Equivalent black carbon (eBC) concentrations were determined with a seven-wavelength AE43 aethalometer. Continuous $PM_{2.5}$ and PM_{10} mass concentrations were monitored using TEOM analysers operating at 1-min resolution. A gravimetric sampler provided 24-h filter samples, which

were analysed offline for inorganic ions, organic and elemental carbon, anhydrosugars, mineralogy, and $\delta^{13}C$ isotopes.

Vertical profiling was performed using the mobile EMORAL multi-wavelength Mie–Raman–fluorescence lidar (University of Warsaw), which provided profiles at 3.75 m × 60 s resolution. A monostatic Doppler sodar supplied information on boundary-layer dynamics up to 350 m a.g.l., while a co-located automatic weather station continuously recorded standard meteorological parameters. Additionally, a hot-air balloon from the University of Silesia provided supplementary in-situ measurements of aerosols and gaseous pollutants. This integrated observational framework delivers synchronous information on aerosol chemical speciation, vertical distribution, and meteorological drivers, enabling process-level analysis of winter air-quality episodes in Wrocław.

Results and Discussion

The measurement campaign conducted in Wrocław between 15 November and 5 December 2022 coincided with typical late-autumn weather conditions in Central Europe. Meteorological conditions were relatively variable, characterized by a high prevalence of cloudy skies and intermittent periods of rainfall. Relatively low air temperatures, not exceeding 5 °C during the day and dropping as low as –8 °C at night, favored increased emissions from residential and domestic sources. Concurrently, observed changes in the atmospheric boundary layer contributed to dynamic variations in both particulate matter concentrations and the chemical composition of aerosols. Wind speeds were generally low, predominantly ranging between 0.5 and 2.0 m/s, with the lowest wind speeds (<1.0 m/s) recorded during periods of elevated particulate matter concentrations (Fig. 1).

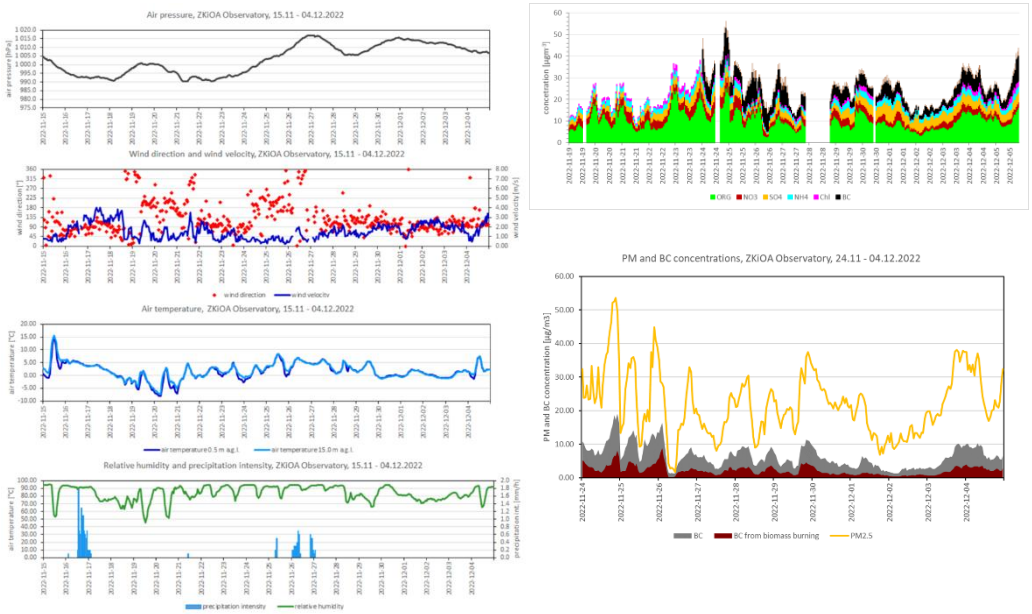

Figure 1. The main characteristics of meteorological and air quality variables during the measurement campaign.

During the measurement campaign, the atmospheric boundary layer (ABL) exhibited pronounced diurnal variability, strongly influenced by local meteorological conditions. EMORAL lidar observations showed that the daytime ABL height generally did not exceed 1500 m and frequently dropped below 200–300 m at night, promoting the accumulation of pollutants in the surface layer. Under highly stable conditions (e.g., 23–24 November), a well-defined stratified aerosol structure was observed, with multiple elevated aerosol layers forming above the primary mixing layer. Aerosol optical properties, including elevated depolarization

ratios ($\delta > 0.10$), indicated the presence of irregularly shaped particles typical of a mixture of secondary aerosols and biomass burning emissions [7; 8].

The lidar-based findings were consistent with in situ chemical measurements. The chemical composition of PM_1, determined via aerosol mass spectrometry (AMS), was dominated by organic aerosols (OA), accounting for 40–60% of the non-refractory mass fraction. Among inorganic species, sulfate and ammonium exhibited the highest contributions, while nitrate concentrations increased under high relative humidity, particularly at night, indicating active secondary aerosol formation. Chloride was also present in significant amounts and showed a strong correlation with the organic fraction, suggesting contributions from biomass and coal combustion, as well as potential emissions from waste burning. Source apportionment using Positive Matrix Factorization (PMF) identified three primary factors (Fig. 2): traffic emissions (hydrocarbon-like organic aerosol, HOA), biomass burning (BBOA), and coal combustion (CCOA), along with two secondary oxygenated organic aerosol components: less oxidized (LO-OOA) and more oxidized (MO-OOA). On average, primary components contributed slightly more than 20% of the total OA mass. The LO-OOA fraction, strongly correlated with biomass burning markers ($R^2 = 0.83$), peaked during nighttime, likely representing moderately aged solid fuel emissions. The simultaneous presence of LO-OOA and MO-OOA underscores the importance of secondary atmospheric processing, particularly under humid and weakly mixed boundary-layer conditions.

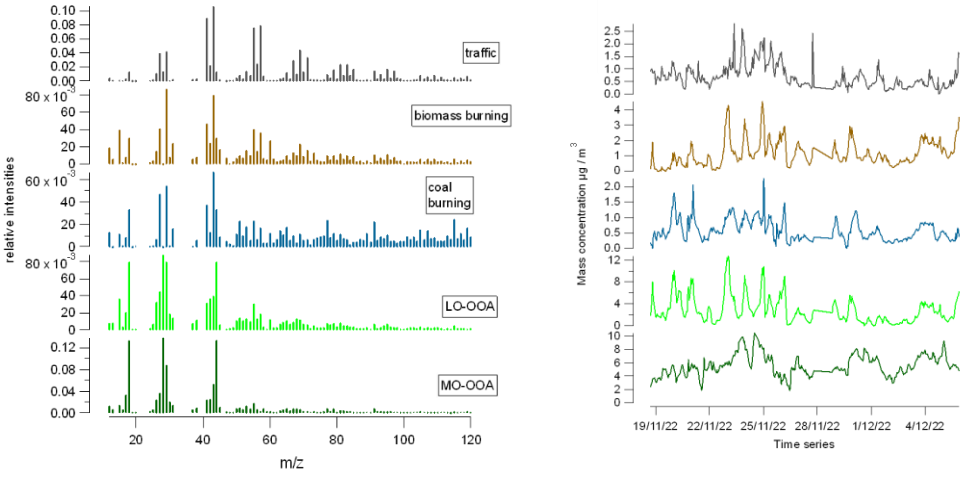

Figure 2. Source apportionment of organic aerosols

Two pollution episodes (Fig. 3) characterized by elevated aerosol concentrations were selected for detailed analysis. During the first episode (23–24 November), lidar observations revealed strong aerosol stratification within the boundary layer. Complementary sodar data confirmed the formation of a stable nocturnal inversion, which favored the accumulation of primary organic aerosol components (HOA, BBOA, CCOA) and less oxidized secondary organics (LO-OOA). Enhanced mixing during the daytime facilitated the entrainment of aged aerosols from the residual layer into the boundary layer. In contrast, the second episode (29–30 November) was characterized by lower concentrations of organic aerosols, accompanied by an increased contribution from inorganic species, particularly sulfate (SO_4^{2-}) and nitrate (NO_3^-). This pattern suggests a more significant role of secondary aerosol formation processes, consistent with the observed increase in more oxidized oxygenated organic aerosols (MO-OOA) during daytime hours. The chemical and vertical profile evolution indicates that oxidative and condensational processes dominated within a relatively shallow, well-mixed, and humid boundary layer.

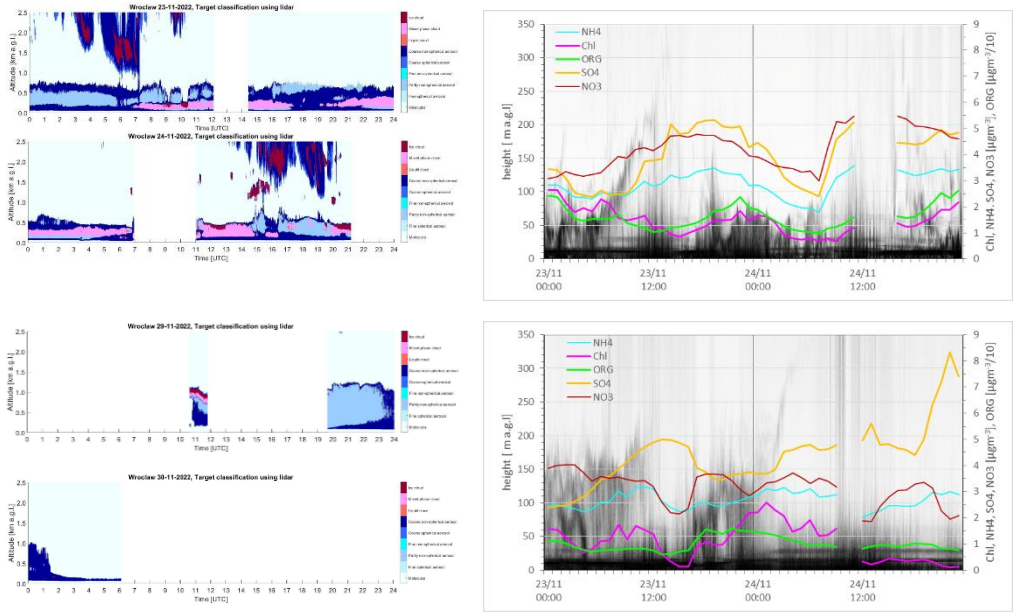

Figure 43. Epizodes characteristic: target classification based on lidar data (left), diurnal variability of aerosol types derived from AMS measurements, and lower atmospheric boundary layer structure provided by SODAR (gray area indicates the inversion layer; spiky structure denotes intense mixing within the ABL) (right)

Conclusions

The integrated observational approach combining chemical, optical, and dynamical measurements proved effective in capturing the complexity of aerosol sources and transformation processes during winter air-quality episodes in Wrocław. The findings highlight the dominant role of primary emissions under stable nocturnal conditions and the enhanced contribution of secondary aerosol formation under humid, well-mixed daytime boundary-layer regimes.

Acknowledgements

The study was supported by the European Union's Horizon 2020 research and innovation program under grant agreement No.856599; ACTRIS-PL is funded by the Ministry of Science and Higher Education of Poland under grant agreement 2024/WK/04.

References

[1] Fuzzi, S. et all., Particulate matter, air quality and climate: lessons learned and future needs, Atmos. Chem. Phys., 15, 8217–8299, https://doi.org/10.5194/acp-15-8217-2015 2015

[2] WHO. WHO global air quality guidelines: particulate matter (PM2.5 and PM10), ozone, nitrogen dioxide, sulfur dioxide and carbon monoxide. World Health Organization, 2021

[3] Stachlewska, I. S. et al. Effect of heat wave conditions on aerosol optical properties derived from satellite and ground-based remote sensing over Poland. Remote Sensing, 9(11), 1199. https://doi.org/10.3390/rs9111199, 2017

[4] Zhang, H. et al. Comparison of scanning aerosol lidar and in situ measurements of aerosol physical properties and boundary layer heights. Aerosol Research, 2(1), 135-151, https://doi.org/10.5194/ar-2-135-2024, 2024.

[5] Davulienė, L. et al. Synergic use of in-situ and remote sensing techniques for comprehensive characterization of aerosol optical and microphysical properties. Science of the Total Environment, 906, 167585. https://doi.org/10.1016/j.scitotenv.2023.167585, 2024

[6] Yavuz, V. et al. Analysing of atmospheric conditions and their effects on air quality in Istanbul using SODAR and CEILOMETER. Environmental Science and Pollution Research, https://doi.org/10.1007/s11356-021-16958-w, 2022.

[7] Tesche, M. et al. Vertically resolved separation of dust and smoke over Cape Verde using multiwavelength Raman and polarization lidars during Saharan Mineral Dust Experiment 2008. Journal of Geophysical Research: Atmospheres, , 114.D13, https://doi.org/10.1029/2009JD011862, 2009

[8] Burton, S. P., et al. Aerosol classification using airborne High Spectral Resolution Lidar measurements–methodology and examples. Atmospheric Measurement Techniques, 5.1: 73-98, https://doi.org/10.5194/amt-5-73-2012, 2012.

Synergy of lidar and hot air balloon observations: aerosol size distribution

***M. Jabłońska*[1,2]**, *I.S. Stachlewska*[3], *P. Gałka*[1], *M. Szczyrba*[1,2,3], *D. Szczepanik*[3], *H. Baars*[4], *J. Janicka*[3], *C. Böckmann*[5], *J. Janeczek*[1,2]

(1) University of Silesia in Katowice, University Laboratories for Atmosphere Survey (ULAS), Sosnowiec, Poland
(2) University of Silesia in Katowice, Institute of Earth Sciences, Będzińska 60, 41-200 Sosnowiec, Poland
(3) University of Warsaw, Faculty of Physics, Institute of Geophysics, (UW), Pasteura 5, 02-093, Warsaw, Poland
(4) Leibniz Institute for Tropospheric Research (TROPOS), Permoserstr. 15, 04318 Leipzig, Germany
(5) Institut für Mathematik der Universität Potsdam, Karl-Liebknecht-Str. 24-25, Potsdam, Germany

Corresponding author: mariola.jablonska@us.edu.pl, iwona.stachlewska@fuw.edu.pl,

Introduction

Within activities of Aerosol, Clouds and Trace-gas Research Infrastructure (ACTRIS), the ACTRIS-Poland Pilot Measurement Campaign was conducted in August 18-20, 2021 in Warsaw, Poland. During the campaign passive and active remote sensing at the ACTRIS observational platform in Warsaw (WOS, PL) were conducted. Aerosol was sampled by using a hot-air balloon being a part of the ACTRIS exploratory platform (AMP, PL). Scientific goal of this pilot study aimed at comparing the test results from the two different measurement techniques with the intention of using the obtained results to improve the models of the spread of pollutants in the troposphere.

Methodology

A dedicated field campaign was done in August 18-20, 2021 in Warsaw within the project entitled *ACTRIS-Poland Pilot Measurement Campaign* financed by the internal resources of University od Silesia in Katowice and University of Warsaw. The core measurements were done with the ACTRIS-Poland Mobile Platform (AMP) of University Laboratories for Atmosphere Survey (ULAS) at University of Silesia in Katowice (Fig.1). The ground-based atmospheric profiling was done using Mie-Raman lidar (PollyXT-UW), sunphotometer, microwave radiometer, and meteo-sensors. These observations were done at the ground and roof platforms of the Remote Sensing Laboratory (RS-Lab) of the Warsaw Observatory Station (WOS) located at the Institute of Geophysics of the Faculty of Physics at the University of Warsaw (Fig.2). The Warsaw station is the ACTRIS National Facility and provides measurements within several research networks: PollyNET, EARLINET, CLOUDNET, AERONET, PGN, and PolandAOD.

Figure 1 The instrumented air balloon platform of the ACTRIS-Poland Mobile Platform of ULAS.

Figure 2 Instrumented ground and roof platforms of Warsaw ACTRIS observational platform of University of Warsaw.

Results and Discussion

For this experiment we performed two hot-air balloon flights with takeoff location in Warsaw on two different days. The meteorological condition on the measurements days were not typical for summertime in Warsaw. Daily mean of 16.9 ºC on August 18, slightly increased to 18.6 ºC and 18.8 ºC on the two following days. In opposite, the dry conditions, with daily mean RH of 57.3 %, became wetter, to reach 61.3 % on the second day, up to 69.6 %. The winds were lowering form 3 m/s, to 2.6 m/s, and 1.9 m/s, respectively.

The mean columnar sun photometer-derived Aerosol Optical Depth (measured at daytime) at 500 nm was low of 0.17, 0.19 and 0.21, on each consecutive day, while Angstrom Exponent was of 1.1 on the first day, increased to 1.25 on the second day, reached 1.5 in the morning of the third day to rapidly decrease to 0.75 on the last day. This results are consistent with in-situ observations at the RS-Lab roof platform and the hot air balloon flights (Fig. 3).

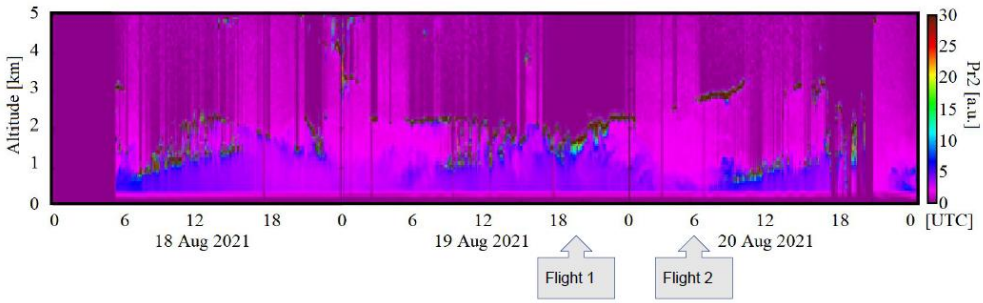

Figure 3 PollyXT-UW lidar measurements (range corrected signal at 532 nm) at WOS, PL ACTRIS observational platform with indications on times of the hot-air balloon flights of AMP, PL ACTRIS exploratory platform.

Lidar observations (Fig.3) show complicated aerosol and cloud structures throughout the whole 3-days period. Majority of aerosol load was confined to the lowermost atmosphere. Unusually strong inversion layer at ~2.5 km (persistent over the days) was captured with noon and midnight radiosoundings conducted at Legionowo WMO-12374 station located 25 km North of RS-Lab station (not shown for brevity).

The lidar-derived profiles of the aerosol backscatter coefficient (β) 532nm and 355nm, the aerosol extinction coefficient (α) at 607nm and 387nm, and the depolarization ratio (δ) at 532nm and 355nm (Fig.4) were obtained using automated online service of the PollyNET run bv the Leibniz Institute for Tropospheric Research (TROPOS). One can see significant aerosol load below 3km in β and α profiles, while negligible δ indicates spherical particles.

The obtained sets of the optical properties profiles can serve as an input for microphysical parameters retrieval. The sets of 2β+2α at different altitudes were used for deriving microphysical parameters using the SVD and Pade inversions algorithms developed at the University of Potsdam (Table 1, right subfigure).

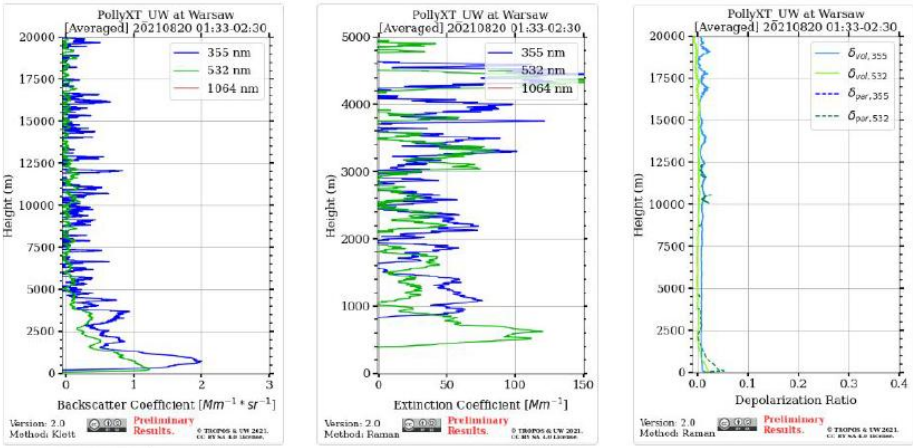

Figure 4 PollyXT-UW automated retrievals obtained from PollyNET online open-access service run at TROPOS. Profile for 1064 nm not available due to technical issues.

Here we show only one an example for a layer at 0.8-1.5km discernible in PollyXT-UW lidar data during the second hot-air balloon flight on 20 August 2021. In this layer the mean optical properties were at 532nm: β of 0.39 Mm^{-1} sr^{-1}, α of 24 Mm^{-1}, lidar ratio of 61 sr, AOD of 0.0168, and at 355nm β of 1.05 Mm^{-1} sr^{-1}, α of 53 Mm^{-1}, lidar ratio of 50 sr, AOD of 0.0371. The microphysical parameters (Table 1, right) inverted for this layer show bi-modal particle size distribution that indicates abundance of particles of small size (r_{eff} of 0.18) and larger size (r_{eff} of 0.85). Size distribution indicates likely anthropogenic pollution. Imaginary part of the refractive index indicates no absorption.

As a next step we validated this results by in-situ measurements onboard hot-air balloon (Table 1, left). More info on balloon observations is given in [1]. The size distribution (in %) of aerosol particles was derived from in situ measurements onboard the hot-air balloon and near-surface in-situ measurements at the RS-Lab roof platform (~21 m a.g.l.). This observations were compared with the size distribution derived from the PollyXT-UW lidar observations. The lidar results show good agreement with the in situ measurements. This is one example of a successful comparison between lidar based inversion results with in-situ data.

Table 1 The size distribution (in %) of aerosol particles derived from *in situ* measurements with hot-air balloon of the ACTRIS-Poland Mobile Platform (AMP, PL) of University of Silesia. Near-surface in-situ measurements were done at the RS-Lab of the ACTRIS Warsaw Observatory Station (WOS, PL) of University of Warsaw.

Size range *in situ*	RS-Lab 19 Aug	Balloon 19 Aug	Balloon 20 Aug
< 0.5 µm	91.26	94.94	94.20
0. 5 - 1.0 µm	5.90	4.19	5.06
1.0 - 2.5 µm	1.74	0.44	0.43
2.5 - 5.0 µm	0.58	0.32	0.23
5.0 - 10.0 µm	0.40	0.08	0.06
> 10 µm	0.12	0.03	0.02

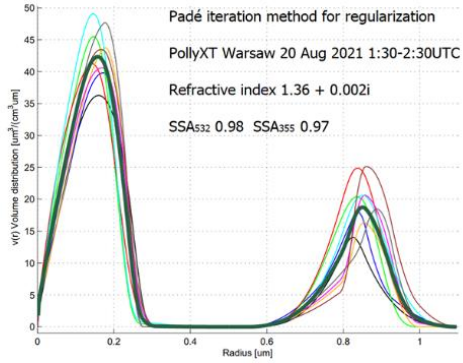

The in-situ samples of atmospheric particles collected at the roof platform and during the balloon flight were used also for detailed mineralogical analyzes that were done at the University Laboratories for Atmosphere Survey (ULAS) of University of Silesia in Katowice. The samples were analyzed using backscatter electron (BSE) imagery and Energy-dispersive X-ray (EDX) spectra to identify atmospheric particles of geogenic and anthropogenic origin [2] (examples in Fig.5).

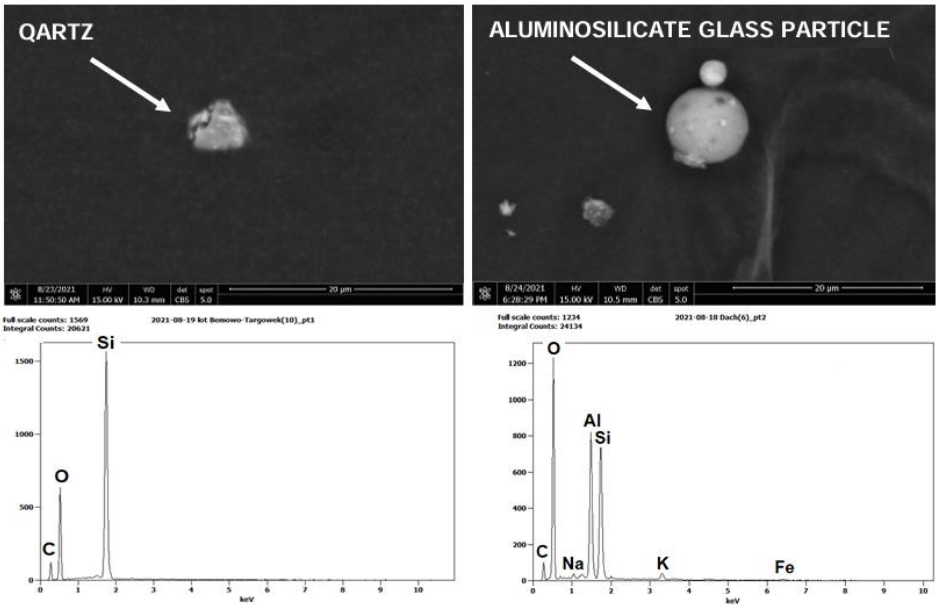

Figure 5 BSE image and EDX spectrum of identified particles from in-situ samples collected at the roof of WOS, PL and during hot-air balloon flight of AMP, PL. Mineralogical analyzes were done at ULAS of University of Silesia.

The mineralogical investigation resulted in identification of geogenic particles such as quartz, feldspar, mica and highly abundant carbonates. The anthropogenic constituents include aluminosilicate glass (fly ash), black carbon, iron oxides, and Na sulfates. Analyses revealed also the secondary particles formed in reactions between aerosols in the troposphere, e.g. needle-like, acicular crystals of Na ($^{+}$Ca) sulfates (secondary particle) formed on isometric NaCl crystals (primary particle). Iron oxides and carbonates were predominant constituents of suspended particles collected in the RS-Lab roof platform. Opposite was found for hot-air balloon samples, where the vital part play secondary particles.

Conclusions

Synergic observations with remote and in situ sensors are crucial to derive the aerosol properties, specifically the aerosol size distribution. Lidar-derived size distribution was successfully validated with in situ measured size distribution onboard a hot-air balloon. Mineral composition of particles differ significantly depending on the altitude of sampling in the lower atmosphere. Samples collected at surface (RS-Lab) are enriched in both natural (quartz, feldspars, carbonates) and anthropogenic (iron oxides, fly ash) pollutants. Samples collected at heights of 200-850 m contain sulphates and chlorides, as dominant solid phases probably originated in the atmosphere as a result of gas-to particle conversion.

Acknowledgements

The ACTRIS exploratory platform "ACTRIS-Poland Mobile Platform (AMP, PL) of University Laboratories for Atmosphere Survey (ULAS) at University of Silesia in Katowice and the ACTRIS observational platform "Warsaw Observatory Station" (WOS, PL) of the University of Warsaw are the official access providers for the Trans-national Access program (TNA) within funding of the European Commission Horizon2020 Programme, project *Solutions for Sustainable Access to Atmospheric Research Facilities* (ATMO- ACCESS); grant agreement no.101008004.

The AMP, PL and WOS, PL platforms operate within the ACTRIS-Poland funded by the Ministry of Science and Higher Education of Poland under grant agreement 2024/WK/04.

References

[1] Smołka-Danielowska, D., Jabłońska, M. & Godziek, S. (2021) *The influence of hard coal combustion in individual household furnaces on the atmosphere quality in Pszczyna (Poland)*. Minerals, vol. 11, no. 11, ISSN: 2075163X, (1).
[2] Jabłońska, M. & Janeczek, J. (2019) *Identification of industrial point sources of airborne dust particles in an urban environment by a combined mineralogical and meteorological analyses: A case study from the Upper Silesian conurbation, Poland*. Atmospheric Pollution Research, vol. 10, no. 3, pp. 980-988, ISSN: 13091042, (20).

The Dust Doctoral Network

F. Marenco[1], *V. Amiridis*[2], *M-J. Costa*[3], *K. Kandler*[4], *S. Kazadzis*[5], *M. Klose*[6], *C. Pérez García-Pando*[7,8], *C. Ryder*[9], *C. Antunes*[3,10], *S. Basart*[11], *D. Bortoli*[3], *D. Bouris*[12], *M. Brooks*[13], *J. Buters*[14], *P. Canhoto*[3], *M-E. Carra*[15], *P. Choutris*[16], *T. Christoudias*[1], *R. Clarkson*[17], *H. Dacre*[9], *O. Dubovik*[18], *K. Fragkos*[1], *D. Francis*[19], *D. Fuertes*[18], *M. Gonçalves Ageitos*[1,20], *B. Johnson*[13], *E. Llopis*[18], *S. Mallios*[2], *R. Mamouri*[21], *E. Marinou*[2], *C. Meleti*[22], *A. Pozzer*[23,1], *A. Rimell*[17], *J.Sciare*[1], *J. Shumake-Guillemot*[11], *N. Tembhekar*[17], *A. Tsekeri*[2], *A. Vogel*[17], *I. Wessels*[14], *C. Westbrook*[9], *F. Wienhold*[24], *M. Wild*[24]

(1) Cyprus Institute, Climate and Atmosphere Research Centre, Nicosia, Cyprus (CYI)
(2) National Observatory of Athens, Greece (NOA)
(3) University of Évora, Portugal (UE)
(4) Technical University of Darmstadt, Germany (TUDa)
(5) Physikalisch-Meteorologisches Observatorium Davos, World Radiation Center, Switzerland (PMODWRC)
(6) Karlsruhe Institute of Technology, Germany (KIT)
(7) Barcelona Supercomputing Centre, Spain (BSC)
(8) Catalan Institute for Research and Advanced Studies, Barcelona, Spain (ICREA)
(9) University of Reading, United Kingdom (UoR)
(10) Centro Académico Clínico do Alentejo, Portugal (C-TRAIL)
(11) World Meteorological Organisation, Switzerland (WMO)
(12) National Technical University of Athens, Greece (NTUA)
(13) Met Office, United Kingdom (MetO)
(14) Center of Allergy and Environment - Technical University of Munich, Germany (ZAUM)
(15) Ciemat - Plataforma Solar de Almería, Spain (PSA)
(16) Earnst and Young, Cyprus (EY)
(17) Rolls Royce plc, United Kingdom (RR)
(18) Generalized Retrieval of Atmosphere and Surface Properties, France (GRASP-SAS)
(19) 'The Environmental and Geophysical Sciences Lab, Khalifa University, United Arab Emirates (KU)
(20) Universitat Politècnica de Catalunya, Spain (UPC)
(21) Eratosthenes Centre of Excellence, Cyprus (ECoE)
(22) Aristotle University of Thessaloniki, Greece (AUTH)
(23) Max Planck Institute for Chemistry, Germany (MPIC)
(24) Swiss Federal Institute of Technology Zürich, Switzerland (ETHZ)

Corresponding author: f.marenco@cyi.ac.cy

Introduction

Mineral dust is a major atmospheric aerosol, and it gives us one of the most visible and detectable aspects of transboundary transport of atmospheric constituents, impacting visibility, radiation and climate [1]. This aerosol type is very often detected at some of the reference lidar sites. What is less evident are the quantitative impacts of dust on health, transportation and energy production. Atmospheric dust is not fully understood at the fundamental level (microphysical properties, dust emissions, source regions), and therefore atmospheric models fail to fully reproduce its impacts. Moreover, dust observations using ground-based instrumentation, remote sensing (lidar and others) and aircraft are abundant, but not evenly distributed; in particular they are missing near the major dust sources. The techniques and methodologies to study dust are still under development, with each giving a different picture of a phenomenon with multiple facets. For example, it is now known that super-coarse and giant dust particles [2] have gone undetected for a long time due to limitations in the measurement and modelling tools that have been in use for decades, and this misdetection alters the understanding and the prediction of a number of processes. Finally, dust affects the environment, society, and several economic sectors, with impacts on the transportation and energy sectors for example, the nature and cost of which is not fully understood and quantified. Several methodologies exist to study mineral dust, each giving its own differing picture of a complex phenomenon: numerical modelling, remote sensing, in-situ observations, laboratory research.

Table 1. Scientific facilities and spaceborne missions that Dust-DN can benefit from. Mod=Modelling; IS=atmospheric in-situ observations; RS=atmospheric remote sensing; Lab=laboratory; En=energy production facility. Grey background = facilities that include lidar

Facility	Methodology	Operator
Marenostrum 5 HPC with MONARCH + EC-EARTH model	Mod	BSC
Cyclone HPC with WRF-Chem model	Mod	CyI
HoreKa HPC with ICON-ART model	Mod	KIT
Unmanned Systems Research Laboratory	airborne IS	CyI
Cyprus Atmospheric Observatory	RS + IS	CyI
Panhellenic Geophysical Observatory of Antikythera	RS	NOA
Electron Microscopy Center	Lab	TUDa
Particle Settling Laboratory	Lab	UoR
Solar rad. and aerosol meas. facilities (incl. GAW PFR network)	RS	PMODWRC
Concentrating technologies and solar energy generation facilities	En	PSA
Évora Atmospheric Sciences Observatory	RS + IS	UÉ
Biochem lab and cell culture lab	Lab	UÉ
Solar Radiation Monitoring stations of Évora and Beja	RS	UÉ
Laboratory for controlled cell exposure to aerosol at air-liquid interface	Lab	ZAUM
Cyprus Atmospheric Remote Sensing Observatory	RS	ECoE
Earth Surface Mineral Dust Source Investigation (EMIT) mission	satellite RS	NASA
Earth Clouds, Aerosol and Radiation Explorer (EarthCARE) mission	satellite RS	ESA/JAXA

Methodology

To address some of these challenges, the first doctoral network on a European scale (to our knowledge) on the topic of dust has started its activity, bringing together expertise on mineral dust in the atmosphere, combining multidisciplinary aspects. The Dust Doctoral Network (Dust-DN) is a strategic international, interdisciplinary and intersectoral alliance of high-profile partners, able to leverage on unique state-of-the-art facilities and recent innovative spaceborne missions (including several lidar facilities and spaceborne lidar): see Table 1. Dust-DN will provide a careful blend between individual research projects and integrated combined training and networking, and a critical mass on dust-focused studies using complementary methodologies. Seventeen doctoral candidates will be exposed to differing research and working environments, multiple technologies and methodologies. They will be trained in remote sensing, the atmospheric sciences, dust science questions, transferable skills and on the partners' unique research infrastructure, enabling to tackle the bigger picture of dust challenges. The network comprises dedicated applied research projects, with direct contributions and impacts embedded with the societal and industrial sector. It involves 8 leading partners and 15 associated partners, from research, academia and industry, and representing 9 countries and the World Meteorological Organisation (Fig. 1).

The network is built around four research objectives, and seventeen PhD projects have been proposed to advance in these scientific questions (Table 2). Several of these projects are relevant to lidar research, and this is why it is useful to present the network here, where the lidar technique is used together with several other methodologies and facilities in pursuing general advances in the science of dust. Doctoral candidate DC3 will work towards a global lidar estimate of the pure-dust atmospheric component, making use of the novel EarthCARE mission [3] and ground-based lidars, and leveraging on the legacy of LIVAS; DC15 will identify the source-dependent radiative properties of dust and will make use, amongst others, of the synergistic use of solar spectral, sun photometric and lidar measurements towards aerosol classification with the GRASP algorithm; DC17 will study dust mineralogy and ice nucleation, making use of ground-

Figure 1. Dust-DN partners. The acronyms are defined in the affiliations.
Red: leading partners; white: associated partners.

based remote sensing with lidars and sunphotometers; DC7 will focus on the dust radiative effect and will make extensive use of lidar-derived profiles in combination with flux observations, in-situ sampling, and radiative modelling; DC5 will study the impact of mineral dust on aircraft engines, making use (amongst others) of ground based lidars/ceilometers and spaceborne lidars; DC10 which will improve knowledge of the scattering properties of non-spherical particles, with an aim to improve the exploitation of advanced lidar systems; DC14 will study the behavior of dust in turbulent flows, making use amongst others of extensive field campaigns that combined several in-situ observations with wind-Doppler lidar.

Conclusions

The strength of addressing the scientific questions with a doctoral network, as opposed to individual specialised projects, resides in the international, interdisciplinary and intersectoral approach, which valorises each methodology (including lidar) and the specialisations of each partner to address the thematic of atmospheric dust from several points of view. This will be reinforced through advanced training and networking opportunities for the doctoral candidates. Each of them will be supported through an individualised career development plan and a number of mobilities to be carried out during the project, and all of them will be gathered together for network-wide schools and workshops. They will also be encouraged to build team spirit through more frequent virtual networking opportunities.

Dust-DN officially started operations in November 2024, and it already attracted a lot of interest in very motivated potential doctoral candidates, having received 226 applications, some of which of a very high standard, and which could unfortunately not all be selected. Dust-DN is more than a collection of 17 very visionary PhD projects on mineral dust and it will create a dust science community that will enhance the potential of a number of unique techniques and facilities, including ground-based and spaceborne lidar. It is expected that the network will advance the science of atmospheric dust, it will further develop scientific synergies and complementarities, and it will train a cohort of dust experts of tomorrow.

Table 2. Dust-DN research objectives and PhD projects.
Grey background = projects relevant to the lidar community (see text).

Research objectives	**PhD projects**	
Understanding of the fundamentals of dust microphysical properties and processes	DC2	Dust particle shape, aspect ratio and orientation: new information from UAV campaigns
	DC4	Atmospheric Sedimentation of Non-Spherical Dust Particles: Developing knowledge for improvement of models
	DC10	New scattering database for desert dust, with realistic size, shape and refractive index measured in-situ
	DC14	Size-dependent turbulent dust transport in idealised and realistic high-resolution simulations
	DC17	Ice nucleating dust particle concentration profiling and effects on ice crystal formation
Identifying the influence of source regions on atmospheric dust properties	DC12	Modelling the effects of dust upon regional climate with constrained dust-source mineralogy
	DC13	Variability of dust composition, shape and size distribution across the Mediterranean, based on single-particle analysis
	DC15	Identification of dust properties from different sources using sun-photometry and their effects on spectral solar irradiance
	DC16	Quantification and characterisation of dust microphysical properties in the Mediterranean and Middle East, through the novel Aerotape technology
Socio-economic impacts of dust on health, aviation and energy production	DC1	Modelling impacts of aeolian dust towards air quality policy planning
	DC5	The impact of mineral dust on Aircraft Engines in the Middle East
	DC6	Modelling and assessment of the impact of atmospheric dust on solar resource for energy applications
	DC8	Assessment of the respiratory health impact of atmospheric dust
Dust in the global climate system	DC3	Global dust estimation from novel space missions
	DC7	Enhancing the understanding of dust direct radiative effect
	DC9	Modelling of dust transport processes. Bridging the gap between theory, observations, and models
	DC11	Modelling super-coarse dust and its effect upon climate

Acknowledgements
Dust-DN is funded by the European Union under the Marie Skłodowska-Curie Actions (grant agreement 101168425), and by the corresponding national agencies of the United Kingdom (UKRI) and Switzerland (SERI). Views and opinions expressed are however those of the author(s) only and do not necessarily reflect those of the European Union and Marie Skłodowska-Curie Actions (MSCA). Neither the European Union nor MSCA can be held responsible for them.

References
[1] Kok, J.F. et al, *Mineral dust aerosol impacts on global climate and climate change*, Nat. Rev. Earth Environ. 4, 71, 2023.
[2] Adebiyi, A. et al, *A review of coarse mineral dust in the Earth system*, Aeolian Research 60, 100849, 2023.
[3] Wehr T. et al, *The EarthCARE mission – science and system overview*, Atmos. Meas. Tech.,**16**, 3581–3608 2023.

Retrieval of the aerosol optical and microphysical properties derived from GRASPpac

M. Adam[1], *G.J. Vasilescu*[1]

(1) National Institute of Research and Development for Optoelectronics - INOE 2000, 409 Atomistilor Street, Magurele, 077125, Romania

Corresponding author: mariana.adam@inoe.ro

Introduction

Range Corrected Signal (*RCS*) of a CHM15k ceilometer and photometer's aerosol optical depth (*AOD*) and radiances serve as input in Generalized Retrieval of Aerosol and Surface Properties (GRASP) model [1] to retrieve the aerosol optical and microphysical properties for the year of 2024. The remote sensing measurements are taken in Măgurele, Romania (South of Bucharest) in a peri-urban region [2]. The fine mode size distribution is compared with ground-based in-situ measurements on one hand while all the (column integrated) variables are compared with AERONET retrievals. A seasonal characterization is discussed. Several studies were performed using GRASP in this configuration (GRASPpac). Roman et al. [3] compare the total volume concentration with airborne in-situ and ground-based insitu measurements, the differences found being within GRASPpac uncertainty. In the study by Titos et al. [4], in-situ measurements of backscatter and extinction coefficients at 635 nm were compared with retrievals from GRASPpac at 675 nm, while the total volume concentration retrieved from GRASPpac was compared with values derived from measured size distribution over 0.25 – 32 μm. A good agreement was found, with GRASPpac inversions yielding higher values. Salgueiro et al. [5] uses GRASPpac for some locations in order to characterize the spatial-temporal evolution of three volcanic plumes detected in the troposphere over Iberian Peninsula. Herreras et al. [6] evaluate the extinction profile accuracy by comparing the integrated aerosol extinction (*IAE*) with AERONET optical depth for specific layers (*AOD* available at three AERONET stations located at different altitudes). It was found a good agreement in general between AERONET optical depth and GRASPpac *IAE* for various layers. However, GRASPpac method overestimates the extinction at low altitudes and underestimates it at high levels.

Methodology

The input file ("sdat" file) in GRASPpac model consists of normalized *RCS* at 1064 nm over 60 altitude bins (equally spaced in logarithmic scale), L2 (or L1.5) AERONET data of *AOD* at 440 nm, 675 nm, 870 nm and 1020 nm) and AERONET almucantar data of radiances at the same wavelengths (see GRASP description on https://www.grasp-open.com/doc/). The main steps involved are provided bellow.

"sdat" file creation:

- Get almucantar data at 440 nm, 675 nm, 870 nm and 1020 nm. Data should have at least 10 measurements for each wavelength and at least one measurement in each azimuth interval. The azimuth intervals are: [2°,6°], [6°,30°], [30°,80°], >80° [3].
- Get Solar Spectral Irradiance data, used to normalize the photometer irradiances (http://doi.org/10.7289/V53776SW).
- Get L2 (or L1.5) data over ± 15 min around the mean almucantar time. Take the mean value.
- Get ceilometer *RCS* over ± 15 min around the mean almucantar time. At least half of the interval is cloud free. Take the mean *RCS* value. A moving average over seven bins (105 m) is applied. The altitude range considered is [82.5 m, 7000 m]. Finally, the 60 log scale bins are considered and *RCS* is normalized. *RCS* should be positive.

To run GRASP, we consider the Bidirectional Reflectance Distribution Function (*BRDF*) data (https://ladsweb.modaps.eosdis.nasa.gov/search/order/1/MCD43C1--61). The settings file is updated with *BRDF* data for each specific day. The settings file consists of a number of chosen parameters such as fitting parameters for model inversion and the errors associated with the input variables (https://www.grasp-open.com/doc/). The main settings (errors and Lagrange Multiplier – LM) are the following. Errors: 5 %

(irradiances), 0.005 (*AOD*), 50 % (*RCS*). LM: 0.1 (size distribution), 600 (real part of refractive index *RRI*), 10 (imaginary part of refractive index *IRI*), 1e-6 (*RCS*), 0 (*BRDF*). The particle volume size distribution (*VSD*) consists of 22 bins, over [50 nm, 15 μm] range (as for AERONET). *RRI* and *IRI* values are retrieved in the range of [1.33, 1.6] and [0.001, 0.1] respectively.

The GRASPpac output data consists of a) column integrated values: *VSD* (microphysical), *AOD*, absorption *AOD* (*AAOD*), single scattering albedo (*SSA*), *RRI*, *IRI* and lidar ratio (*LR*) (optical) and b) profiles of backscatter (β) and extinction (κ) coefficient at 1064 nm (optical). The output data for which the convergence is smaller than 5 % is dismissed. Note that the profile of the extinction coefficients is given by aerosol vertical profile (output GRASP) multiplied with *AOD*. The backscatter coefficient profile is obtained by diving the extinction coefficient to the *LR* (GRASP output). The following analyses are envisaged:

- The column integrated variables are compared with the AERONET inversion products (L1.5) (https://aeronet.gsfc.nasa.gov/). The *VSD* fine mode is compared with in-situ measurements by scanning mobility particle sizer (SMPS) (over [7.3, 307.6] nm radius), when available.
- Backscatter and extinction coefficient profiles are compared with ceilometer retrievals using the Klett-Fernald method with *AOD* constraint.
- Seasonal characterization for all variables.

Results and Discussion

Figure 1 shows an example of column integrated values and altitude profiles for 11 August 2024 07:35 UTC. Remarks: *VSD* is similar for all GRASPpac, AERONET and SMPS for fine mode while for coarse mode, GRASPpac shows an increase towards larger radius. The largest difference with AERONET is for *RRI*. The profiles show a good agreement for extinction coefficient but slightly different for backscatter (see different *LR*). Figure 2 shows the scatter plots between GRASPpac retrievals and AERONET /ceilometer retrievals. The correlation coefficients are good except for *RRI* (<0.7). H=0 (Kolmogorov-Smirnov test) means the data have the same distribution (valid only for *AOD*). Root mean square bias (*RMSB*), mean bias (*MB*) and standard deviation of the bias (*SB*) have small values which implies that the systematic and random errors between the datasets are small. Figure 3 shows the *VSD* (same events for all three methods) for three seasons. The agreement among them is good in general except the region for small size particles which cannot be retrieved by models (inversion starts at 50 nm). Interquartile range (IQR) shows more variability for SMPS data. Aerosol load is higher in Summer. GRASP retrievals show lower peak amplitude, smoother curves, narrower IQR than AERONET. Figure 4 shows the profiles for extinction and backscatter profiles (median, 25th and 75th percentiles). GRASPpac retrievals are in average smaller than ceilometer's retrievals, but within error bars. Better agreement is observed for smaller boundary layers (during Autumn and Winter). The high IQR values for extinction and backscatter coefficients (except Winter) suggests a large variability of the profiles. For the analysed data, the planetary boundary layer height reaches ~ 4 km during Summer, ~ 3.5 km during Spring, ~ 2 km during Autumn and ~ 0.6 km during Winter.

Conclusions

The retrievals of GRASPpac are in general in line with AERONET retrievals, except for *RRI*. Ground in-situ *VSD* show good agreement with models for fine mode side. The profiles of backscatter and extinction coefficients retrieved by GRASPpac are smaller than those retrieved from ceilometer using Klett-Fernald with *AOD* constraint (better agreement for small boundary layer).

Acknowledgements

This work was financed by the Core Program within the Romanian National Research Development and Innovation Plan 2022-2027, carried out with the support of MCID, project no. PN 23 05 and partly by the European Commission under the Horizon Europe – Research and Innovation Framework Programme, through the PANORAMA project under grant agreement No 101182795". Authors acknowledge AERONET-Europe/ACTRIS for calibration and maintenance services. In this work we used data form https://aeronet.gsfc.nasa.gov/ and local database for ceilometer data.

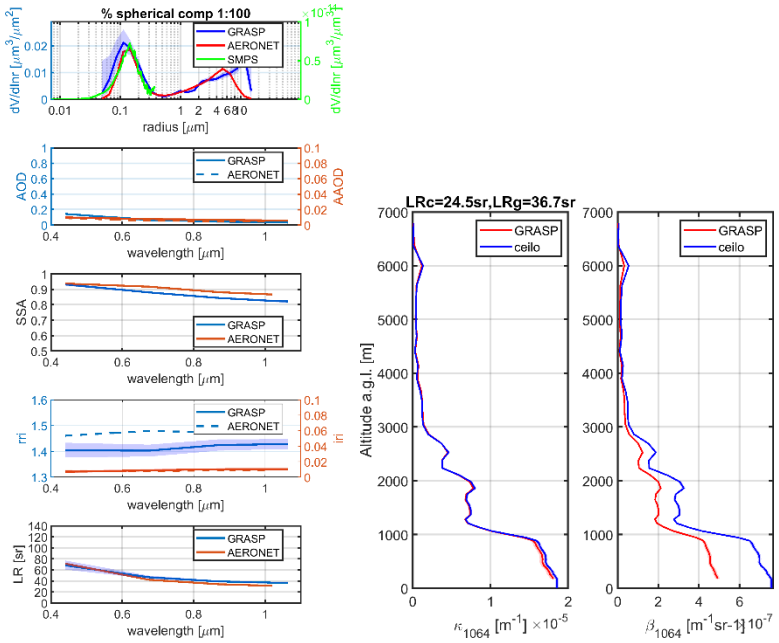

Figure 1. (left) Column integrated variables (*VSD*, *AOD*, *AAOD*, *SSA*, *RRI*, *IRI*, *LR*). (right) Backscatter and extinction coefficient profiles. Event: 11 August 2024, 07:35 UTC.

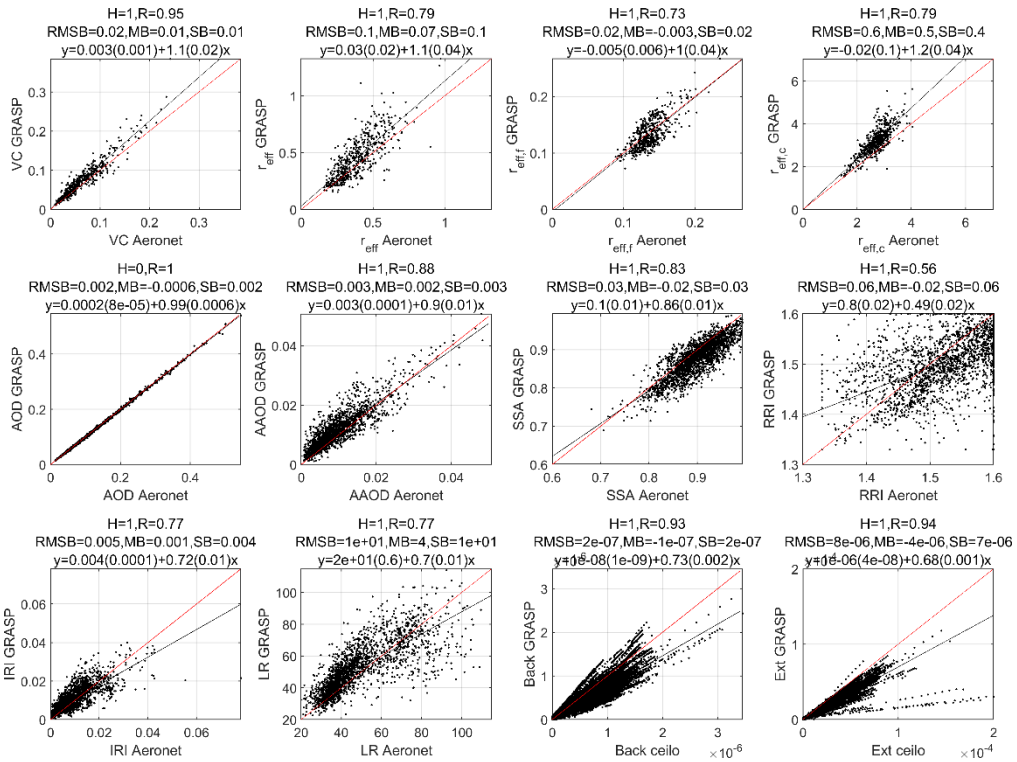

Figure 2. Scatter plots for 2024: GRASPpac versus AERONET and GRASPpac versus ceilometer (for backscatter and extinction coefficient).

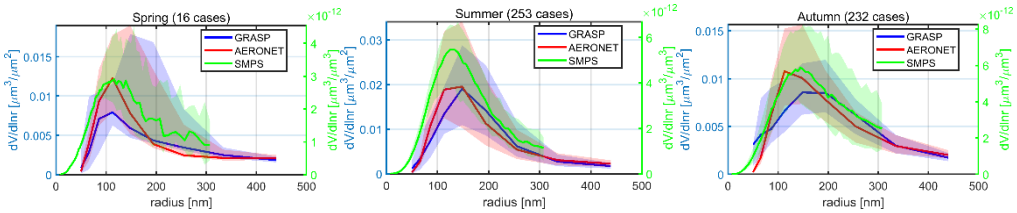

Figure 3. Seasonal *VSD* for GRASPpac, AERONET and SMPS for 2024.

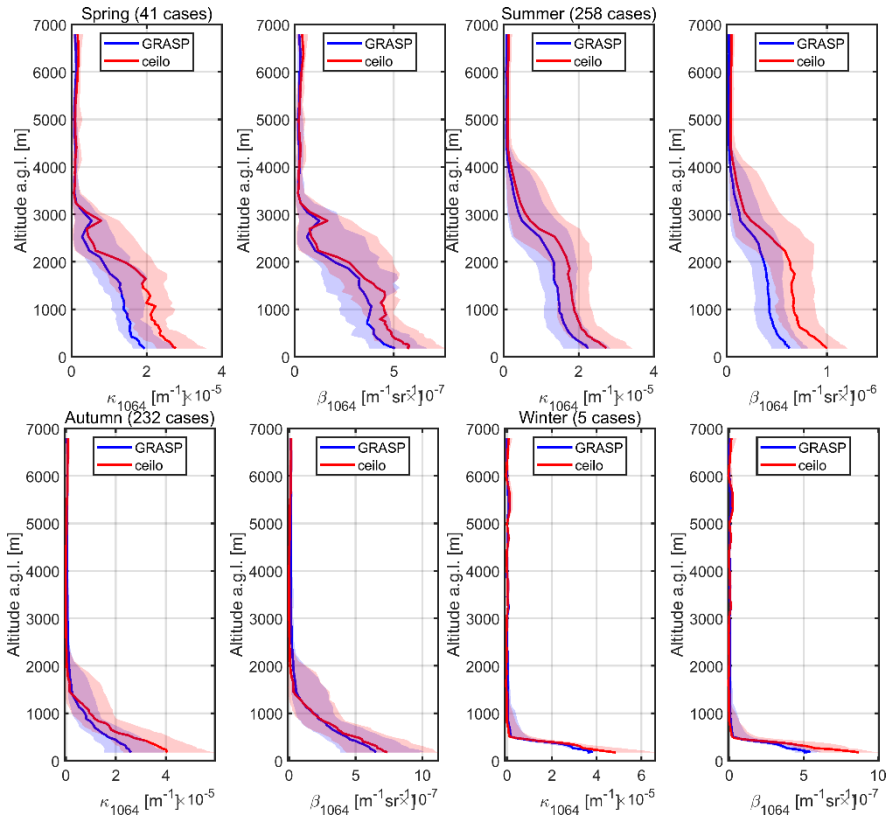

Figure 4. Seasonal means for particle extinction and backscatter coefficients for 2024.

References

[1] Dubovik, O. et al.: *A Comprehensive Description of Multi-Term LSM for Applying Multiple a Priori Constraints in Problems of Atmospheric Remote Sensing: GRASP Algorithm, Concept, and Applications*, Front. Remote Sens. 2:706851, https://doi.org/10.3389/frsen.2021.706851, 2021.

[2] Adam, M. et al.: *Towards Early Detection of Tropospheric Aerosol Layers Using Monitoring with Ceilometer, Photometer, and Air Mass Trajectories*. Remote Sens., 14, 1217, https://doi.org/10.3390/rs14051217, 2022

[3] Román, R. et al.: *Retrieval of aerosol profiles combining sunphotometer and ceilometer measurements in GRASP code*, Atmos. Res., 204, 161-177, https://doi.org/10.1016/j.atmosres.2018.01.021, 2018.

[4] Titos, G. et al.: *Retrieval of aerosol properties from ceilometer and photometer measurements: long-term evaluation with in situ data and statistical analysis at Montsec (southern Pyrenees)*, Atmos. Meas. Tech., 12, 3255–3267, https://doi.org/10.5194/amt-12-3255-2019, 2019.

[5] Salgueiro, V. et al.: *Characterization of Tajogaite volcanic plumes detected over the Iberian Peninsula from a set of satellite and ground-based remote sensing instrumentation*, Remote Sensing of Environment, 295, 113684, https://doi.org/10.1016/j.rse.2023.113684, 2023.

[6] Herreras, M. et al.: *Evaluation of retrieved aerosol extinction profiles using as reference the aerosol optical depth differences between various heights*, Atmos. Res., 230, 104625, https://doi.org/10.1016/j.atmosres.2019.104625, 2019.

Evaluation of a satellite dust optical depth product using using lidar measurements in Thessaloniki, Greece.

C. Biskas[1], *K. Michailidis*[1], *G. Peletidou*[1], *K.A. Voudouri*[2,1], *M.E. Koukouli*[1], *S. Vandenbussche*[3], *D. Balis*[1]

(1) Laboratory of Atmospheric Physics, Physics Department, Aristotle University of Thessaloniki, 54124, Greece.
(2) Institute for Astronomy, Astrophysics, Space Applications and Remote Sensing, National Observatory of Athens, 15236 Greece
(3) Royal Belgian Institute for Space Aeronomy, 3 Avenue Circulaire, 1180 Brussels, Belgium
Corresponding author: cmpiskas@physics.auth.gr

Introduction

IASI (Infrared Atmospheric Sounding Interferometer) is a spectrometer onboard the MetOp polar-orbiting satellites, first launched in 2006 by EUMETSAT. Being at an altitude of around 800km, it provides various products concerning aerosols, trace gases and clouds at a daily basis [1]. The Sahara desert is the dominant source of atmospheric dust particles in Europe, with an estimated 500 million tons annually [2], while most transport events over the Mediterranean occur during spring and summer of each year.

Monitoring such events is essential in order to study their effects on human health, weather systems and climate change. In this study, the Dust Optical Depth product of IASI is evaluated for certain dust episodes, using measurements from Thessaloniki's Lidar System (THELISYS), a member of EARLINET (European Aerosol Research LIdar NETwork) [3].

Methodology

Identifying a dust transport event requires the synergy of different instruments and methodologies. High particle depolarization ratio values retrieved by lidar, ranging from 0.2 to 0.4, are the first and primary indicator that dust particles might be present above the instrument [4]. The Laboratory of Atmospheric Physics (LAP) at the Aristotle University of Thessaloniki (AUTh) is also an AERONET (Aerosol Robotic NETwork) station. Measuring high Aerosol Optical Depth and low Angstrom Exponent values from the CIMEL sunphotometer, indicates the presence of mineral dust [5], [6]. Lastly, backward trajectory models like HYSPLIT [7] and dust forecasting models like MONARCH [8] are also used for further ensuring the presence of dust.

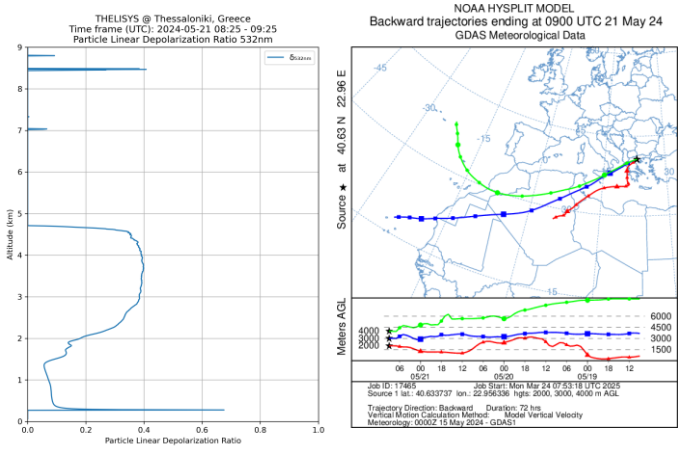

Figure 1: Dust case identification methodology. Particle depolarization ratio (left) at LAP, AUTh for 21/05/2024 provided a visible dust layer between 2 and 5km. Backward trajectory results (HYSPLIT) indicate dust transport from Sahara (right).

Once the case is identified, the dust contribution of the backscatter lidar signal is extracted using the well-established POLIPHON (Polarization Lidar Photometer Networking) method [9], which uses specific threshold depolarization ratio values. One-step POLIPHON separates the lidar signal to dust and non-dust, whereas the two-step method can also further distinguish fine and coarse dust particles.

The optical depth by lidar is calculated using Eq. 1:

$$\tau = S \int_{z_1}^{z_2} \beta \, dz \tag{1}$$

where τ is the optical depth, S the lidar ratio, β the backscatter signal and z_1, z_2 the bottom and top heights of identified layers. To calculate the optical depth of dust, the lidar ratio used is retrieved by Ramam night measurements during the events and β is the dust contribution derived by the POLIPHON method. Application of the methodology to a dust event is shown below (Fig. 3). IASI provides dust optical depth at 10μm and 550nm, using a conversion factor of 1.78 [10]. In this study, the satellite data used are provided by the Royal Belgian Institute for Space Aeronomy, as part of the Mineral Aerosol Profiling from Infrared Radiation (MAPIR), version 5.1 [11]. The dust case over Greece at 21/05/2024, shown in Figure 1, is profoundly detected by IASI (Fig. 2), with missing pixels being the result of cloudness. Once the previous methodology concerning the lidar data is completed, there are two directly comparable dust optical depth products, one from each instrument.

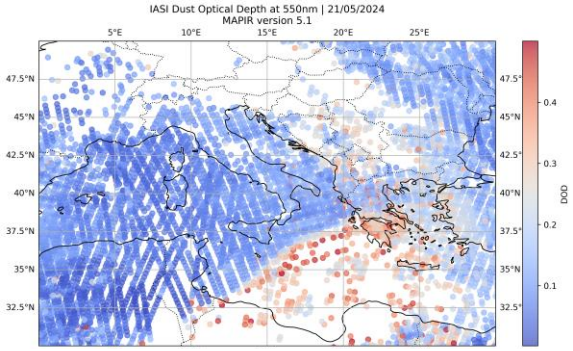

Figure 2: IASI Dust Optical Depth (DOD) retrievals for 21/05/2024. Missing pixels are the result of heavy clouds.

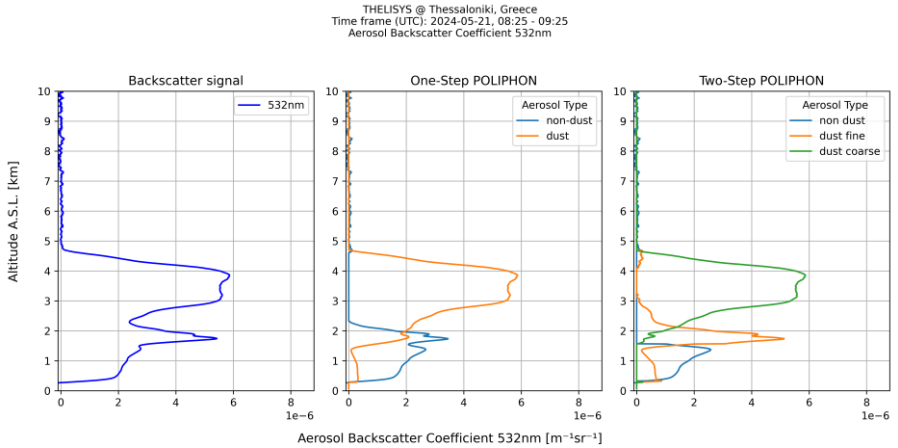

Figure 3: Application of the POLIPHON method to a Lidar backscatter profile during a dust trasport case at 21/05/2024 over LAP, AUTh.

Results and Discussion

There are certain parameters that need to be considered in order to ensure the consistency of the methodology previously described. Satellite pixels need to be relatively close to the lidar station and also present high-confidence without clouds. In addition, concerning the lidar, at least one Raman night measurement during the dust event is required, as well as no clouds between the isntrument and the dust layer. For this study, only the closest satellite pixels to the lidar station were chosen during days with no clouds and thick, well-defined dust layers above the planetary boundary layer.

In Table 1, the comparison between the IASI retrievals and different POLIPHON methods are presented for two distinct dust trasport cases over Thessaloniki, for June 2024. As far as the 1-step POLIPHON method is concerned, dust optical depth from lidar seems to be in better agreement with IASI at 550nm. Regarding the 2-step method, at 6/6/2024 IASI at 550nm provides a DOD value of about half the total lidar DOD (Fine & Coarse). However, during the second dust event, DOD at the same wavelength is much closer to the total DOD extracted by Lidar.

Table 1. Dust Optical Depth (DOD) retrievals from IASI at 10μm and 550nm. Lidar DOD is derived from the 1-step (Dust) and the 2-step (Fine and Coarse) POLIPHON method using lidar ratio values from Raman night measurements.

	IASI		Lidar		
Date	**10μm**	**550nm**	**Dust**	**Fine**	**Coarse**
06/06/2024	0.12 ± 0.02	0.21 ± 0.04	0.27 ± 0.06	0.2 ± 0.04	0.19 ± 0.04
10/06/2024	0.25 ± 0.04	0.44 ± 0.07	0.32 ± 0.05	0.1 ± 0.02	0.26 ± 0.04

Conclusions

High values of dust optical depth derived by both instruments suggest that the methodology used to identify and quantify dust provides consistent results. Although these first results are satisfying, it is evident that more dust transport cases need to be identified and included in the evaluation, in order to be able to proceed to a statistical evaluation of the various parameters affecting the comparisons (e.g. lidar ratio, conversion factors, collocation criteria).

Acknowledgements

In this work we used data form the Royal Belgian Institute for Space Aeronomy (BIRA), European Aerosol Research Lidar Network (EARLINET), Aerosol Robotic Network (AERONET) and the National Oceanic and Atmospheric Administration (NOOA).

References

[1] Blumstein, D. et al.: *IASI instrument: Technical overview and measured performances*, Proceedings of SPIE - The International Society for Optical Engineering, 5543, doi: /10.1117/12.560907, 2004.

[2] Middleton, N. and Goudie, A.: *Saharan dust: Sources and trajectories*, Transactions of the Institute of British Geographers. 26. 165 – 18, doi: /10.1111/1475-5661.00013, 2002.

[3] Pappalardo, G. et al.: *EARLINET: Towards an advanced sustainable European aerosol lidar network*, Atmospheric Measurement Techniques Discussions, doi: /10.5194/amtd-7-2929-2014, 2014.

[4] Illingworth, A. et al.: *THE EARTHCARE SATELLITE: The next step forward in global measurements of clouds, aerosols, precipitation and radiation*, Bulletin of the American Meteorological Society, 96. 1311–1332, doi: /10.1175/BAMS-D-12-00227.1, 2015.

[5] Dubovik, O. et al.: *Variability of Absorption and Optical Properties of Key Aerosol Types Observed in Worldwide Locations*, Journal of the Atmospheric Sciences. 59. 590-608, doi: /10.1175/1520-0469(2002)059<0590:VOAAOP>2.0.CO;2, 2002.

[6] Siomos, N.: *Are EARLINET and AERONET climatologies consistent? The case of Thessaloniki, Greece*, Atmospheric Chemistry and Physics Discussions, 1-29, doi: /10.5194/ acp-18-11885-2018, 2018.
[7] Stein, A.F. et al.: *NOAA's HYSPLIT atmospheric transport and dispersion modeling system*, Bulletin of the American Meteorological Society, 96, 2059-2077, doi: /10.1175/BAMS-D-14-00110.1, 2015.
[8] Nickovic, S. et al.: *Atmospheric dust modeling from meso to global scales with the online NMMB/BSC-Dust model – Part 1: Model description, annual simulations and evaluation*, Atmos. Chem. Phys., 16, 11367–11378, doi: /10.5194/acp-16-11367-2016, 2016.
[9] Mamouri, R.E. and Ansmann, A.: *Fine and coarse dust separation with polarization lidar*, Atmospheric Measurement Techniques, 7, 3717–3735, doi: /10.5194/amt-7-3717-2014, 2014.
[10] Vandenbussche, S.: *Mineral Aerosol Profiling from Infrared Radiances (MAPIR) version 5.1 File content and user information*, Royal Belgian Institute for Space Aeronomy, https://data.aeronomie.be/
[11] Vandenbussche, S. and De Maziere, M.: *Vertical Profiles of Mineral Dust Aerosols from IASI (MAPIR algorithm version 5.1)*, Royal Belgian Institute for Space Aeronomy, doi: /10.18758/72Q26UNK, 2024.

Comparison of ABLH estimates in the frame of the BELLA-ABL Campaign in Southern Italy

***D.Summa*[1]**, *A. Amodeo*[1], *B. De Rosa*[1], *P. Di Girolamo*[2], *M. Di Paolantonio*[3], *I. Gandolfi*[1], *M. Mytilinaios*[1], *I. Zaccardo*[1], *L. Mona*[1] *and G. D'Amico*[1]

[1]*CNR-Consiglio Nazionale delle Ricerche, IMAA- Istituto di Metodologie per Analisi Ambientali, 85050 Tito, Italy*
[2]*Università della Basilicata, Dipartimento di Scienze della Salute, Via dell'Ateneo Lucano 10, 85100 Potenza Italy*
[3]*CNR-ISMAR Area della Ricerca di Roma 2 – Tor Vergata Via del Fosso del Cavaliere, 100 00133 Roma*

Corresponding author: donato.summa@cnr.it

Introduction

The atmospheric boundary layer (ABL) represents the lowermost part of the atmosphere directly in contact with the Earth's surface. The estimation of its depth is of crucial importance in meteorology and for anthropogenic pollution studies. ABL height (ABLH) measurements are usually far from being adequate, both spatially and temporally. Thus, different remote sensing sources can be of great help in growing both the spatial and temporal ABLH measurement capabilities.

This work reports results from an intercomparison effort involving different sensors used to measure the atmospheric boundary layer height (ABLH). The effort was carried out in the framework of the BELLA (Boundary layer Extensive campaign with multi Instrumental Analysis see: https://ciao.imaa.cnr.it/bella-boundary-layer-extensive-campaign-with-multi-instrumental-analisys/) measurement campaign, which took place at the CNR-IMAA Atmospheric Observatory (CIAO) during April-June 2024. An additional Raman lidar system (CONCERNING see: https://web.unibas.it/lablidar/CONCERNING.html) was operated throughout the entire duration of the campaign. This system was located at the University of Basilicata in Potenza, about 7 km south-east of the CIAO site. All lidar systems involved in the measurement campaign were operated with high spatial and temporal resolution, typically 3.5 -10 m and 10 sec, respectively, with the ability to obtain vertical profiles, both in daytime and nighttime, for a variety of atmospheric components/variables, including mixing ratio of water vapor and CO_2, temperature profiles and optical properties (backscatter/extinction) of particles (aerosols and clouds). The aim of this campaign was to characterize the structure of the ABL and get estimates of the ABLH with numerous different techniques and algorithms reported in the literature. In particular, results from all techniques were compared against ABLH estimates obtained from co-located radiosonde data available on site throughout the duration of the measurement campaign.

These latter, exploiting ABLH dependence on potential temperature measurements, were used as a reference. Furthermore, ABLH estimates obtained from the different atmospheric signals measured by CONCERNING were compared with those obtained from radiosonde and Raman lidar measurements at CIAO, correctly revealing the differences associated with the different approaches and atmospheric variability. In this work our attention is focused on two specific case studies (15-16 April 2024 and 28 April-01 May 2024), with results revealing a good agreement, quantified in terms of absolute and percentage BIAS, between the different sensors and approaches.

Instrumental Set-up

Measurements carried out at the CNR-IMAA Atmospheric Observatory (CIAO) in combination with those carried out by the Raman lidar CONCERNING at the University of Basilicata represents an effective ensemble of data for the characterization of aerosol and cloud properties to reach the goals of the BELLA validation campaign.

Currently, CIAO represents one of the largest ground-based remote sensing stations in the Mediterranean basin and in Europe for meteorological and climate studies. CIAO research activity primarily

focus on long-term observations of aerosols, clouds, trace gases and greenhouse gases within the European research infrastructures ACTRIS through the use of a wide range of available instruments illustrated in Table 1.

Table 1. List of characteristic and description of instruments used during the BELLA Campaign

System Name	Characteristic and description of Instruments
Ceilometer CL51	The ceilometer Vaisala CL51 emits short light pulses at 905 nm in zenith or near zenith direction using a single-lens trans-receiver. The light backscattered from atmospheric particles (e.g.: aerosols, clouds, fog and precipitation) is received to detect the attenuated backscatter profiles. The ceilometer profiles have high vertical and temporal resolution, typically in the order of 30 m and 10 s, and a typical measurement range for clouds from 15 m to 12 km above the ground.
Fixed multi-wavelenght POLPO	The system is multi-wavelaegth Raman lidar in biaxial configuration and is based on two Nd:YAG laser sources operating at 10 Hz: one emitting radiation at 532 and 355 nm, the other emitting radiation only at 1064 nm, to avoid polarization purity loss due to the SHG and THG crystals. It provides measurements of aerosol backscatter, extinction and depolarization at 1064, 532 and 355 nm, together with water vapour mixing ratio. The system has the capability to perform measurements in both day and night configurations.
Scanning Doppler LiDAR - Halo Photonics Stream LineXR	The Doppler lidar emits laser light pulses at 1.5 μm, with low energy (~ 100 μJ) and high repetition frequency (10kHz). It provides range-resolved measurements of backscattered radiation from atmospheric aerosol/cloud particles and particles' radial velocity (i.e. the velocity component parallel to the laser beam). Range and time resolutions of the products provided are user-selectable, with minimum values in the order of 30 m and 1 s, respectively
Radiosounding systems (Raman lidar VAISALA AS13)	Balloon-based measurements of temperature, pressure, humidity and wind (speed and direction) through the troposphere and stratosphere are performed at CIAO using three different VAISALA MW41 radiosounding systems, two manual (fixed and mobile) and one equipped with an automatic launcher (VAISALA autosonde system AS13).
Ka-Band Doppler radar Metek MIRA-3	The radar has a 1 m diameter antenna emitting microwave pulses at 35.5 GHz, with a peak power of 30 kW, duration of 200 ns and repetition rate of 5 KHz. The antenna beam width is 0.6° x 0.6°, the antenna gain is 49 dBi, while the radar sensitivity is -44 dBZ (-53dbZ) at 5 km 0.1 sec (10 sec) time resolution. The Doppler velocity resolution is better than 0.05 m/s.
Lidar CONCERNING -UNIBAS	The system is capable to perform high-resolution (i.e., 10 s and 3.75 m) and accurate measurements of atmospheric temperature and water vapour, both in daytime and nighttime, based on the application of the rotational and roto-vibrational Raman lidar techniques in the UV.

All the instruments listed in the table were operational during the entire campaign, simultaneously acquiring approximately more than 2000 hours of consecutive data in different weather conditions both in daytime and nighttime.

Results and Discussion

In this section we illustrate and discuss the results obtained by comparing ABLH estimates from different sensors or model data: Raman lidars, radiosondes, a ceilometer, ECMWF ERA5 reanalysis. ABLH estimates were obtained by applying the different algorithms available on the different products obtained from the various sensors in measurement acquisition during the BELLA campaign. These estimates were also compared with the recently developed MIPA (Morphological Image Processing Approach) algorithm [1]. The different ABLH estimates were compared with each other considering as reference the one obtained exploiting ABLH dependence on potential temperature profile measurements carried out by the radiosondes (RS) launched from CIAO during the BELLA campaign.

Table 2. Algorithms used to compute ABLH during the selected period

Instruments	Algorithms	Product
Raman Lidar CIAO-POLPO	Gradient method that searches the range and overlap corrected attenuated backscatter profile for local gradient minima	Particle backscatter [m-1sr-1]
	MIPA	Range Corrected Signals, 532nm and 1064nm
Raman Lidar CONCERNING	Location of the minimum vertical gradient of specific humidity and Temperature	T(z), q(z)
Radio Sounding Vaisala	Location of the maximum vertical gradient of potential temperature T(z)	T(z), ϑ (z)

The figure below shows the scatter plot for two cases studies, of the ABLH obtained with the different methods, compared with that obtained by the Potential Temperature method. A linear fit with "0" intercept is also shown, with the relative R^2 value [2].

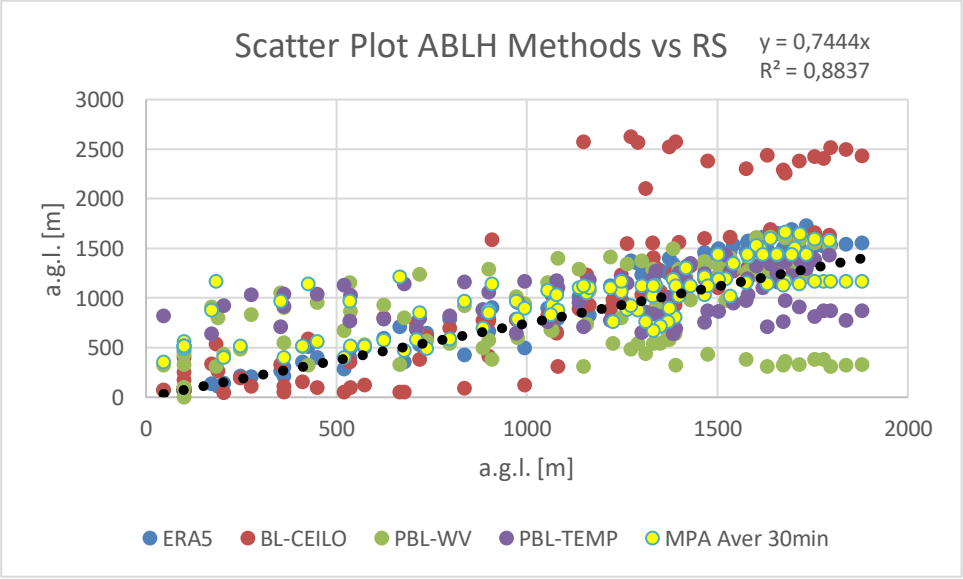

Figure 1. Scatter plots of the different methods vs ABLH from Potential Temperature.

Table 3 lists ABLH estimates from the different sensors/methodologies.

Table 3. ABLH estimates from the different sensors/methodologies

Bias [%]	Average Bias[%]	Average Std. Dev[m]	R^2
ERA5 vs RS	-11.14	11.81	0.94
Ciel. vs RS	+29.36	56.73	0.78
WV vs RS	-17.17	84.40	0.82
MIPA vs RS	19.58	116.50	0.89
Temp Lidar (CONCERNING) vs RS	22.7	42.7	0.87

Conclusions

A BELLA measurement campaign has been organized by the CNR-IMAA in collaboration with UNIBAS with the main goal to establish a comprehensive dataset for the study of the ABLH evolution and for the characterization of the most important physical and chemical processes taking place within both the ABL and the troposphere. All these sensors have been operating continuously during the campaign under different atmospheric conditions [3,4].

In Table 3, the bias values [-11;+22], standard deviation [11;116] and correlation index R^2 [0.78;0.94] of each method with respect to the radiosoundings are reported in terms of mean. All methods reveal in general a good agreement between the different sensors and approaches. The difference between the various methodologies depends fundamentally on the type of tracer (aerosol, water vapor, temperature, etc.) and on the overlap of each of the lidar systems.

These results (entirely preliminary) will be the subject of further study and discussion during the conference.

Acknowledgements

The authors acknowledge Next Generation EU Mission 4 “Education and Research” - Component 2: “From research to business” - Investment 3.1: “Fund for the realization of an integrated system of research and innovation infrastructures” - Project IR0000032 – ITINERIS. We also acknowledge the IR0000032—ITINERIS, Italian Integrated Environmental Research Infrastructures System (D.D. no. 130/2022—CUP B53C22002150006) funded by the EU—Next Generation EU PNRR-Mission 4 “Education and Research”—Component 2: “From research to business”—Investment 3.1: “Fund for the realization of an integrated system of research and innovation infrastructures”.

References

[1] Vivone, G., D’Amico G., Summa, D., Lolli, S., Amodeo, A., Bortoli D., and Pappalardo,G.: *Atmospheric boundary layer height estimation from aerosol lidar: a new approach based on morphological image processing techniques*. Atmos. Chem. Phys., 21, 4249–4265, 2021 https://doi.org/10.5194/acp-21-4249-2021

[2] Summa, D., Madonna, F., Franco, N., De Rosa B., and Di Girolamo P.: *Inter-comparison of atmospheric boundary layer (ABL) height estimates from different profiling sensors and models in the framework of HyMeX-SOP1*, Atmos. Meas. Tech., 15, 4153–4170, 2022 https://doi.org/10.5194/amt-15-4153-2022

[3] Summa, D., Vivone, G., Franco, N., D’Amico, G., De Rosa, B., and Di Girolamo, P.: *Atmospheric Boundary Layer Height: Inter-Comparison of Different Estimation Approaches Using the Raman Lidar as Benchmark*. Remote Sens. **2023**, *15*, 1381. https://doi.org/10.3390/rs15051381

[4] Di Girolamo, P., Ambrico, P. F., Amodeo, A., Boselli, A., Pappalardo, G., and Spinelli, N.: *Aerosol Observations by Lidar in the Nocturnal Boundary Layer*, Appl. Optics, 38, 4585–4595, 1999.

Combining micropulse lidar and photometer for aerosol monitoring over oceans: TRANSAMA ship-based campaign

M. F. Sanchez-Barrero[1], *P. Goloub[1], L. Blarel[1], I. Popovici[1,2], B. Torres[1], G. Dubois[1], T. Podvin[1], F. Ducos[1], M. Sicard[3], C. Skonieczny[4]*

(1) Univ. Lille, CNRS, UMR 8518 - LOA - Laboratoire d'Optique Atmosphérique, F-59000 Lille, France
(2) R&D Department, CIMEL Electronique, 75011 Paris, France
(3) Univ. La Réunion, CNRS, UMR 8105 - LACy - Laboratoire de l'Atmosphère et des Cyclones, Météo-France, 97744 Saint-Denis de La Réunion, France
(4) Univ. Paris-Saclay, CNRS, UMR 8148 - GEOPS - Laboratoire Géosciences Paris-Saclay, Institut Pierre Simon Laplace (IPSL), 91405 Orsay Cedex, France

Corresponding author: mariafernanda.sanchezbarrero@univ-lille.fr

Introduction

Aerosols significantly influence climate, air quality, and human health, with marine aerosols dominating oceanic regions that cover over 70% of the Earth's surface. Though, uncertainties persist regarding their radiative impacts. Observations from remote oceanic regions, where aerosol optical depth (AOD) is typically low, provide valuable insights into pre-industrial conditions. However, discrepancies between satellite and ground-based AOD measurements highlight the need for improved observational capabilities [1, 2].

The network MAN (Maritime Aerosol Network) [3], an initiative of the world-wide photometer network AERONET (AErosol Robotic NETwork) [4], has implemented the use of handheld photometers on-board cruise ships to cover the oceans for several years now. More recently, the advanced automated Sun-sky-lunar photometer CIMEL CE318-T has been adapted for ship-borne applications [5]. Since 2021, the CE318-T ship-adapted photometer has been continuously performing measurements aboard the research vessel (RV) Marion Dufresne, under the framework of MAP-IO (Marion Dufresne Atmospheric Program – Indian Ocean) [6], a French instrumental facility. This deployment has significantly enhanced aerosol monitoring over remote regions such as the South Indian Ocean [7].

Field campaigns employing lidars on mobile platforms (cars, aircraft, and ships) have demonstrated their potential to validate satellite observations, assess air quality in diverse terrains, and study aerosol transport over oceans. While advanced lidars systems face challenges related to environmental conditions and frequent maintenance requirements, compact automatic micropulse lidars provide a viable alternative for continuous mobile observations. When coupled with photometers, these systems achieve greater accuracy. The CIMEL CE370 lidar, successfully deployed in several field campaigns, has proven to be effective for aerosol characterization [8, 9, 10, 11].

The TRANSAMA campaign (transit to AMARYLLIS-AMAGAS oceanographic mission), conducted aboard the RV Marion Dufresne, integrated remote sensing instrumentation—including CE370 micropulse lidar and two CE318-T photometers—to investigate aerosol properties in marine environments. By addressing observational gaps, the campaign contributes to our understanding of aerosol distribution and transatlantic transport. The TRANSAMA campaign highlights the potential of synergistic observations to characterize aerosols, demonstrating their value in refining climate models and emphasizing the importance of long-term marine aerosol monitoring programs like MAP-IO. This approach opens the doors for further developments on observational strategies in remote oceanic regions.

Methodology

This study employed remote sensing instruments to investigate aerosol and atmospheric properties during the TRANSAMA campaign. A CE370 lidar, operating at 532 nm with 20 μJ pulse energy at 4.7 kHz repetition rate, provided aerosol and cloud distribution, with 15 m vertical resolution. It was paired with the CE318-T photometer, adapted for ship-borne applications with GPS and compass modules for accurate Sun-Moon tracking in motion. On the RV Marion Dufresne, a permanent photometer had been installed on the main mast since 2021 (photometer A in Fig. 1a). A second unit was temporarily placed on Deck I (photometer B in Fig. 1b) during the campaign for operational assessments and data validation (presented

in [7]). The lidar system included a laser source and acquisition/control system installed in the MAP-IO lab (Fig. 1c) and an emission/reception telescope on Deck I (Fig. 1d), housed in an enclosure.

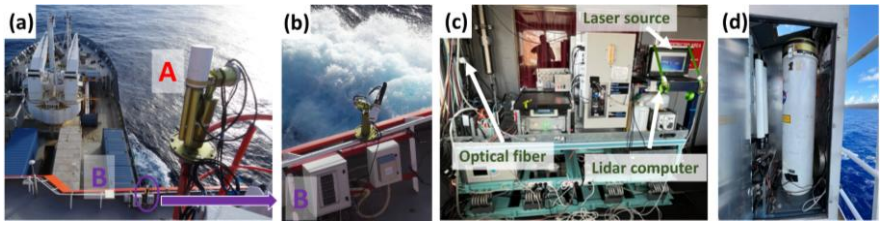

Figure 1. Remote sensing setup aboard the RV Marion Dufresne. Photometer A is on the main mast (a), Photometer B on Deck I (b), the lidar source and acquisition system in the MAP-IO lab (c), and the telescope on Deck I (d).

Lidar data processing employed range-corrected signal and normalized relative backscatter (NRB) profiles, with detection limits spanning from 350 m to 12 km by day, given by the overlap function and signal-to-noise ratio. Atmospheric structure, including the MBL (marine boundary layer), cloud and aerosol layers, were analyzed following BASIC [12] and STRAT [13] algorithms. On the other hand, photometer data followed AERONET data quality protocols [14]. A multi-factor analysis revealed significant reduction in AOD measurements at Level 1.5 when vessel motion exceeded 1.5 degrees in standard deviation. Wind speed was observed to impact the photometer A (main mast) more than the deck unit, likely due to its increased exposure to wind-induced vibrations. For quality-assured lidar and photometer data, aerosol properties were derived through the Klett-Fernald method, which calculates backscatter and extinction coefficients from lidar returns based on assumed lidar ratios. Using an iterative approach, the lidar ratio were constrained with the available AOD from photometer.

This approach permitted to study the atmospheric structure and aerosol transport during the campaign, enhancing aerosol characterization in remote oceanic regions.

Results and Discussion

The TRANSAMA campaign covered the transit of the RV Marion Dufresne from Le Port, La Réunion (20.94 °S, 55.29 °E) to Bridgetown, Barbados (AMARYLLIS-AMAGAS mission's starting point, 13.10 °N, 59.63 °W). From April 21 to May 15, 2023, aerosol properties were characterized along the transect.

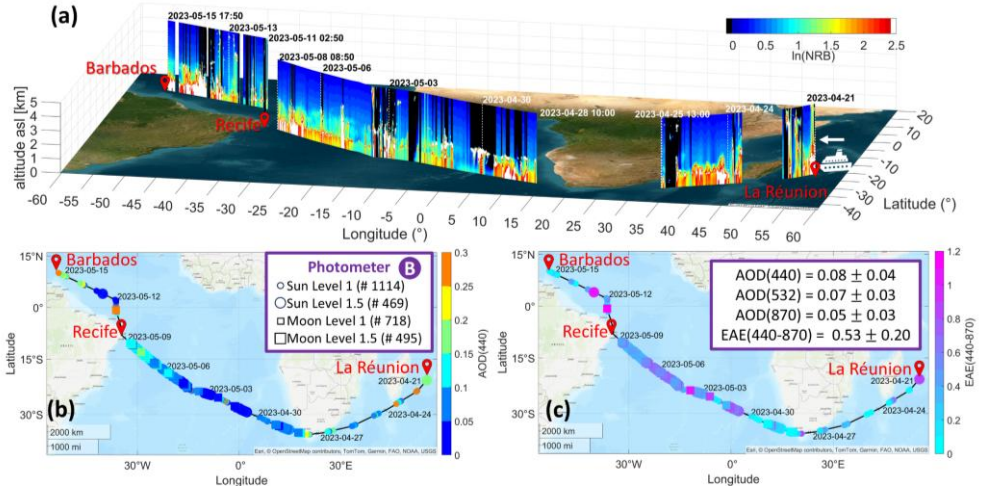

Figure 2. Spatio-temporal variability of aerosol properties measured by lidar and photometer B (deck I) during TRANSAMA. (a) The 3D variation of NRB profiles on top true color image, along with (b) AOD at 440 nm and (c) EAE at 440/870 nm on top of topographic maps are presented. Both photometer data level 1 and 1.5 are featured.

During the campaign, low aerosol loadings were predominantly observed, with mean AOD values at 440 nm of 0.08 (Fig. 2b) and EAE values at 440-870 nm of 0.53 (Fig. 2c). Both Level 1 and 1.5 of direct Sun-Moon photometer observations (photometer B) are presented, emphasizing the difficulty to achieve quality-assured data in rough seas like in presence of the Aghullas current (southwest Indian Ocean).

Lidar measurements spanned 73% of the total navigation time, generating 26,215 one-minute profiles, 53% of which were flagged as cloud-contaminated (Fig. 2a). Territorial waters of Madagascar, South Africa and Brazil were restricted for active sensing. Stacked histograms including MBL, aerosol and cloud occurrences (Fig. 3a) exposed a broad altitude range of cloud coverage, with cirrus clouds extending up to the tropopause. High-altitude cirrus (>13 km) was only detected within ±5° of the equator, consistent with a higher tropical tropopause. Cloud occurrence peaked below 2 km, coinciding with increased aerosol concentrations. The mean (median) MBL top height was found to be 0.8 ± 0.3 km (0.7 km), with no significant diurnal growth.

Despite very clean conditions were encountered in the south Atlantic Ocean with AOD values at 440 nm below 0.05 (Fig. 2b), lidar observations revealed thin aerosol layers above the MBL (Fig. 3a). These layers are unlikely to originate from the ocean, as sea spray aerosols are typically confined inside the MBL. Thus, the aerosols above the MBL are likely transported.

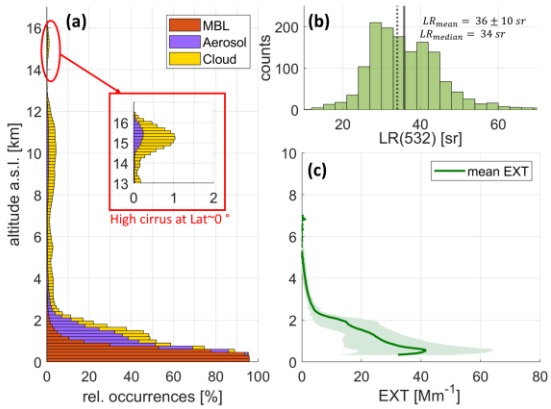

Figure 3. Atmospheric structure and aerosol properties derived from lidar. (a) Stacked histograms of MBL, aerosol and cloud layers are presented for the entire campaign (26,215 one-minute profiles), along with the derived (b) effective lidar ratios and (c) mean extinction profile from quality-assured and AOD paired lidar data.

For further analysis, quality control (Rayleigh fit procedure) was performed to the free-cloud lidar profiles with a reference zone at 5 km, applying the standard tropical atmosphere model to derive molecular coefficients. Validated profiles paired with photometer observations underwent the inversion scheme to derive effective lidar ratios (LR; Fig. 3b) and extinction (EXT) profiles (Fig. 3c). The LR presented mean (median) values of 36 ± 10sr (34 sr) in agreement with previous studies presenting mixture of marine and fine mode aerosols [15, 16]. The mean EXT profile for the overall campaign shows values of $10 - 40\ Mm^{-1}$ extending up to 2 km, consistent with the low aerosol loadings and the presence of aerosols above the MBL. Ancillary information, such as back-trajectories, revealed the origin of the persistent presence of fine aerosols, attributing it to fires in the South African savanna and likely mixed with urban aerosols.

Conclusions and perspectives

The TRANSAMA campaign demonstrated the efficacy of combining automatic micropulse lidar and photometer measurements to enhance aerosol characterization over oceans. The synergistic and continuous observations provided standard vertical-resolved aerosol properties along the transect from La Réunion Island to Barbados. While very clean conditions were identified in the South Atlantic with the photometer, lidar detected thin aerosol layers above the MBL, likely transported from wildfires in southern Africa. These

findings underscore the influence of continental emissions even in remote oceanic regions, advancing our understanding of climate processes and cloud formation in pristine conditions.

The campaign also enabled continuous assessments of instrument performance, paving the way for the planned installation of a CIMEL CE376 depolarization lidar aboard the Marion Dufresne in Spring/Summer 2025 under ACTRIS-FR/OBS4CLIM. Likewise, a dedicated data processing chain for lidar-photometer mobile observations will be implemented by the Data and Service center AERIS, contributing to ACTRIS-FR exploratory platforms. The MAP-IO program and ongoing efforts to equip research vessels with advanced Sun-sky-lunar photometers (e.g., Gaia Blu vessel) represent promising steps toward the development of an extended oceanic aerosol monitoring network. Integrating vertical-resolved lidar profiles in this network will significantly enhance our understanding of aerosol transport and dynamics, with implications for both climate modeling and satellite validation.

Acknowledgements

TRANSAMA campaign was supported by MAP-IO program, ACTRIS-FR, the laboratories LOA (Laboratoire d'Optique Atmospherique), University of Lille, LACy (Laboratoire de l'Atmosphère et des Cyclones), University of La Reunion and GEOPS (Laboratoire Géosciences Paris-Saclay), University of Paris Saclay.

MAP-IO was funded by the European Union through the ERDF programme, the University of La Réunion, the SGAR-Réunion, the Région Réunion, the CNRS, IFREMER, and the Flotte Océanographique Française.

References

[1] Koren, I. et al.: From aerosol-limited to invigoration of warm convective clouds, Science, 344, 1143–1146, https://doi.org/10.1126/science.1252595, 2014.

[2] Mallet, P.-É. et al.: Marine aerosol distribution and variability over the pristine Southern Indian Ocean, Atmospheric Environment, 182, 17–30, https://doi.org/10.1016/j.atmosenv.2018.03.016, 2018.

[3] Smirnov, A. et al.: Maritime Aerosol Network as a component of Aerosol Robotic Network, J. Geophys. Res., 114, D06204, https://doi.org/10.1029/2008JD011257, 2009.

[4] Holben, B. N. et al.: AERONET—A Federated Instrument Network and Data Archive for Aerosol Characterization, Remote Sensing of Environment, 66, 1–16, https://doi.org/10.1016/S0034-4257(98)00031-5, 1998.

[5] Yin, Z. et al.: Aerosol measurements with a shipborne Sun–sky–lunar photometer and collocated multiwavelength Raman polarization lidar over the Atlantic Ocean, Atmos. Meas. Tech., 12, 5685–5698, https://doi.org/10.5194/amt-12-5685-2019, 2019.

[6] Tulet, P. et al.: MAP-IO: an atmospheric and marine observatory program on board Marion Dufresne over the Southern Ocean, Earth Syst. Sci. Data, 16, 3821–3849, https://doi.org/10.5194/essd-16-3821-2024, 2024.

[7] Torres, B. et al.: Adaptation of the CIMEL-318T to Shipborne Use: Three Years of Automated AERONET-Compatible Aerosol Measurements Onboard the Research Vessel Marion Dufresne, EGUsphere [preprint], https://doi.org/10.5194/egusphere-2025-1356, 2025.

[8] Popovici, I. E. et al.: Description and applications of a mobile system performing on-road aerosol remote sensing and in situ measurements, Atmos. Meas. Tech., 11, 4671–4691, https://doi.org/10.5194/amt-11-4671-2018, 2018.

[9] Popovici, I. E. et al.: Mobile On-Road Measurements of Aerosol Optical Properties during MOABAI Campaign in the North China Plain, Atmosphere, 13, 21, https://doi.org/10.3390/atmos13010021, 2022.

[10] Warneke, C. et al.: Fire Influence on Regional to Global Environments and Air Quality (FIREX-AQ), JGR Atmospheres, 128, https://doi.org/10.1029/2022JD037758, 2023.

[11] Sanchez Barrero, M. F et al.: Enhancing Mobile Aerosol Monitoring with CE376 Dual-Wavelength Depolarization Lidar, Atmos. Meas. Tech., 17, 3121–3146, https://doi.org/10.5194/amt-17-3121-2024, 2024.

[12] Mortier, A. et al.: Detection and characterization of volcanic ash plumes over Lille during the Eyjafjallajökull eruption, Atmos. Chem. Phys., 13, 3705–3720, https://doi.org/10.5194/acp-13-3705-2013, 2013.

[13] Morille, Y. et al.: STRAT: An Automated Algorithm to Retrieve the Vertical Structure of the Atmosphere from Single-Channel Lidar Data, J. of Atmos. and Ocean. Tech., 24, 761–775, https://doi.org/10.1175/JTECH2008.1, 2007.

[14] Giles, D. M. et al.: Advancements in the Aerosol Robotic Network (AERONET) Version 3 database – automated near-real-time quality control algorithm with improved cloud screening for Sun photometer aerosol optical depth (AOD) measurements, Atmos. Meas. Tech., 12, 169–209, https://doi.org/10.5194/amt-12-169-2019, 2019.

[15] Duflot, V. et al.: Marine and biomass burning aerosols in the southern Indian Ocean: Retrieval of aerosol optical properties from shipborne lidar and Sun photometer measurements, J. Geophys. Res., 116, D18208, doi:10.1029/2011JD015839, 2011.

[16] Burton, S. P. et al.: Aerosol classification from airborne HSRL and comparisons with the CALIPSO vertical feature mask, Atmos. Meas. Tech., 6, 1397–1412, https://doi.org/10.5194/amt-6-1397-2013, 2013.

Arabian and Saharan Dust Optical and Microphysical Properties: Synergy of CARO Limassol Polly^{XT} Lidar, and Sun Photometer observations using GRASP algorithm.

A. Savva[1,2], *A. Nisantzi*[1,2], *F. Scarlatti*[1], *A. Lopatin*[3], *D. Hadjimitsis*[1,2] *and R.E. Mamouri*[1,2]

(1) Eratosthenes Centre of Excellence, Limassol, 3012, Cyprus
(2) Department of Civil Engineering & Geomatics, Cyprus University of Technology, Limassol, 3036, Cyprus
(3) GRASP SAS, Lille, 59800, France

Corresponding author: athina.savva@eratosthenes.org.cy

Introduction

Earth's atmospheric radiative energy budget is strongly influenced by aerosols in the atmosphere [1]. Desert dust from the Middle East and the Sahara/North Africa regions is considered one of the major types of atmospheric aerosols globally. The Eastern Mediterranean, particularly Cyprus, is influenced by the transport of air masses from the Sahara Desert and the Arabian Peninsula. Many studies have shown that some optical and microphysical characteristics of these two aerosol types differ [2]. A study by Nisantzi et al. (2015) [2] conducted in Cyprus, found that the Lidar ratio of Saharan dust is 53 ± 6 sr, while that of Middle Eastern dust was significantly lower, at 41 ± 4 sr at 532 nm. Additionally, the real part of the refractive index for Middle Eastern dust was higher, measured at 1.55, compared to 1.45 for Saharan dust in the 500–550 nm wavelengths [2]. The main objective of the present study is to investigate the optical and the microphysical characteristics of desert dust from both regions by utilizing the synergy between the Polarization Polly^{XT} Raman Lidar and the Cimel sun/sky photometer, in Limassol city of Cyprus. The analysis is performed using the Generalized Retrieval of Atmosphere and Surface Properties (GRASP) algorithm [3].

GRASP is a highly flexible inversion algorithm applicable in a variety of domains, including observations from both active and passive remote sensing methods. Developed by Dubovik et al. (2014) [3], the algorithm is based on the general principles of numerical inversion and atmospheric radiation modelling. Lopatin et al. (2013, 2021) [4, 5] first proposed the application of the GRASP algorithm, utilizing the synergy between multi-wavelength Lidar and the Aerosol Robotic Network (AERONET) sun/sky photometer observations [4,5]. Information derived from the synergy of lidar, and sun photometer is complementary: the backscatter provided by the Lidar signal enhances the columnar sensitivity of aerosol properties, while the photometer measures the quantity and microphysical properties of particulate matter, related to its source, thus providing additional constraints, crucial for lidar data quantitative interpretation. The combination of the data from these instruments provides advanced vertical profiles of the microphysical characteristics of the aerosol [4, 5, 6]. Previously it was demonstrated by Lidar and Radiometer Inversion code [6] that a combination of a three-wavelength elastic lidar with depolarization, and sun-photometric observations that aerosol can be characterized as a vertically resolved mixture of fine, coarse spherical and coarse non-spherical particles.

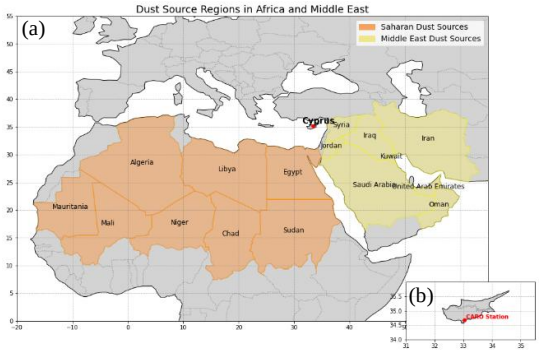

Figure 1. (a) Map of the dust source regions in Africa and Middle East. (b) Cyprus Atmospheric Remote Sensing Observatory location. It is often influenced by dust transportation from Sahara and Middle East regions.

Cyprus Atmospheric Remote Sensing Observatory (CARO), of the Eratosthenes Centre of Excellence, is the National Facility (NF) of the Republic of Cyprus for aerosol and cloud monitoring using remote sensing techniques. The station is part of the ACTRIS (Aerosols, Clouds, and Trace Gases Research Infrastructure) network, operates continuously and follows data quality assurance protocols [7]. The ground-based station (GBS) is equipped with a PollyXT (POrtabLe Lidar sYstem) a multi-wavelength Polarization Raman Lidar [8] which allows the measurement of vertical profiles of the particle backscatter coefficient (β) at wavelengths 355, 532, 1064 nm, the particle extinction coefficient (α) the volume and particle linear depolarization ratios and lidar ratios at 355 and 532 nm [9]. Additionally, the CUT-TEPAK AERONET site in Limassol hosts an AERONET Cimel sun/sky photometer operational since 2010. It performs direct and diffuse sun and sky measurements of Irradiance and AOD at eight wavelengths (340, 380, 440, 500, 675, 870, 1020 and 1640 nm), enabling the retrieval of key column properties. Microphysical parameters of the vertical column of the atmosphere can be derived by the AERONET inversion algorithm including the size distribution (dV(r)/dln(r)), the real and the imaginary part of the refractive index (η_R, η_I), the single scattering albedo (SSA) and the scattering phase function (PF) [10,11].

Data & Methodology

The methodology for retrieving the profiles of microphysical parameters of the aerosol layers is based on the application of the GRASP inversion algorithm with the synergy of lidar and sun/sky photometer measurements. The GRASP method performs a statistically optimized inversion for measurements from both instruments, using a multi-term least-squares approach and incorporating a priori information about aerosol properties [4, 5]. In Figure 2, the input and output of GRASP algorithm are presented.

Input data for GRASP algorithm:

- Lidar: Level 1b, normalized lidar signals at 355, 532, 1064 nm and volume depolarization at 355 and 532 nm [13, 14].
- Sun-photometer: Level 1.5 data of direct-sun, total optical depth (TOD) and sky radiance measurements at 340, 380, 440, 500, 675, 870, 1020, 1064 nm.

GRASP algorithm retrieves key properties of aerosol like the volume size distribution, the real and the imaginary part of the refractive index, sphericity fraction and vertical distribution profiles, that could be distinguished between several aerosol modes, thus allowing to estimate a wide variety of vertically resolved optical properties e.g. backscatter, extinction, SSA and LR.

In this study the microphysical characteristics of two desert dust events are analyzed: one originating from Sahara and the other one from Middle East, both observed in Limassol. The cases were selected to be daytime, cloud-free conditions, with large AOD load and high particle depolarization ratio values.

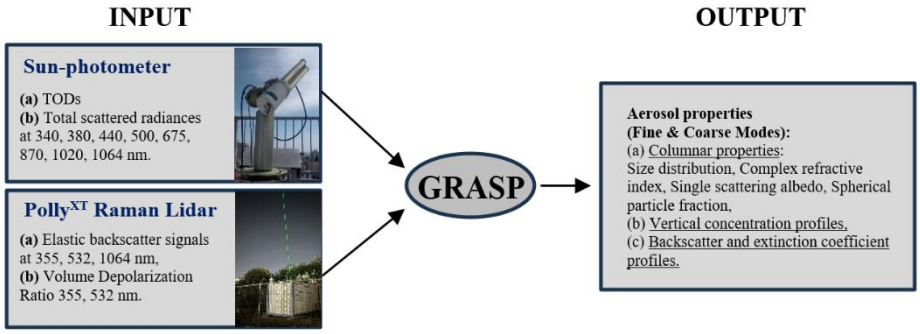

Figure 2. Input and output of GRASP algorithm.

Preliminary results and Discussion

A Sahara dust event on 02 March 2024 captured by the Polly^{XT} Lidar and CUT-TEPAK sun-photometer of CARO NF in Limassol. Figure 3 below shows the attenuated backscatter coefficient at 1064 nm and the volume depolarization ratio at 532 nm. The vertical extends of the dust layer at 6:00 – 12:00 UTC was between 2-4 km from the ground. The origin of the plume according to the HYbrid Single Particle Lagrangian Integrated Trajectory (HYSPLIT) model as shown in Figure 4 was the Saharan region of North Africa (Egypt).

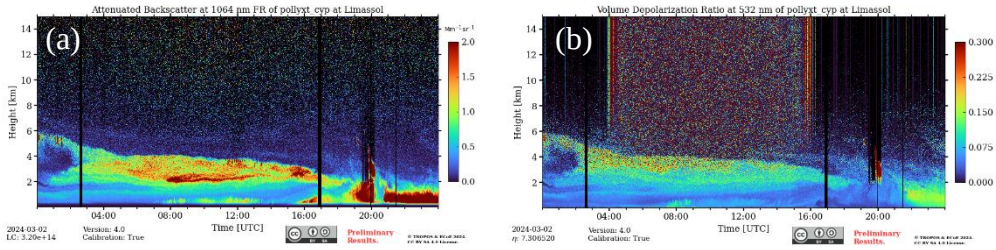

Figure 3. Time-height cross section of the (a) total attenuated backscatter coefficient at 1064nm and (b) volume depolarization ratio at 532 nm measured from CARO Polly^{XT} Lidar on 02 March 2024, over Limassol, Cyprus.

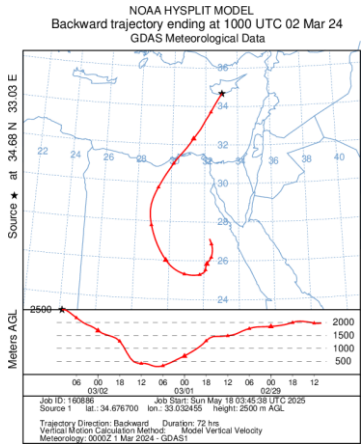

Figure 4. The 72-hour backward trajectory using the HYSPLIT model for the aerosol layer on 2 March 2024 at 10:00 UTC. The air mass originated from Sahara Desert (Egypt) and transported to Cyprus.

Figure 5 presents the GRASP single pixel approach retrieved size distribution, spectral real and imaginary part of the refractive index at 10:04:04 UTC, within ± 15 mins of the almucantar scan of sun-photometer, on 2nd March 2024. The size distribution reveals a predominance of coarse mode aerosols. The spectral variation of the refractive index reveals that fine aerosols have a moderate absorption, which decreases with increasing wavelength, with VIS region to observe the strongest absorption. Coarse-mode aerosols have stronger absorption at shorter wavelengths mostly in UV-VIS range with decline in absorption in the NIR.

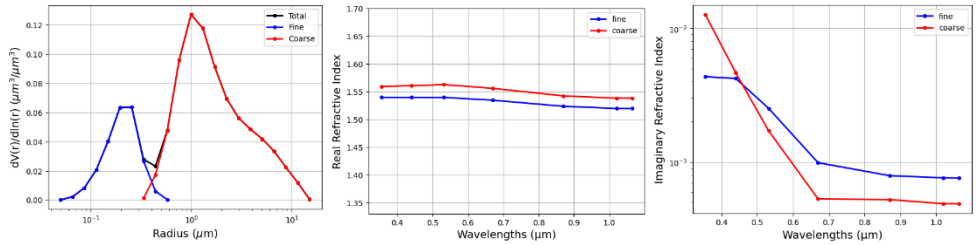

Figure 3. Size distribution, spectral real and imaginary part of refractive index, from GRASP algorithm, single pixel mode, at Limassol, Cyprus, on 02 March 2024, at 10:04:04 UTC (±15 min) UTC.

Conclusions

This study highlights the importance of the retrievals from the synergy of lidar and sun-photometer measurements applying GRASP algorithm for characterizing desert dust events over Limassol, Cyprus. The integration of these complementary datasets provides advanced outcome of vertical distribution and microphysical characteristics of atmospheric aerosols. The preliminary microphysical parameters retrieved from the GRASP algorithm for the Saharan dust case are presented in this paper, showing the difference in the microphysical characteristics of fine and coarse mode aerosols. More results from the GRASP algorithm and a comparative analysis of the characteristics of the Saharan and the Middle Eastern dust events, will be presented at the conference.

Acknowledgements

This study has been supported by the EXCELSIOR project under Grant Agreement No 857510, funding from the EU Horizon 2020, the Government of the Republic of Cyprus, and the Cyprus University of Technology. The authors also acknowledge the support received by ATARRI Horizon Europe Widespread Twinning Project under the Grant Agreement No 101160258.

References

[1] IPCC: Climate Change 2021: The Physical Science Basis, Cambridge University Press, Cambridge, United Kingdom and New York, NY, USA, 2391 pp., https://doi.org/10.1017/9781009157896, 2021.

[2] Nisantzi, A. et al.: Middle East versus Saharan dust extinction-to-backscatter ratios, Atmos. Chem. Phys., 15, 7071–7084, https://doi.org/10.5194/acp-15-7071-2015, 2015

[3] Dubovik, O. et al.: GRASP: a versatile algorithm for characterizing the atmosphere, SPIE Newsroom, https://doi.org/10.1117/2.1201408.005558, 2014.

[4] Lopatin, A. et al.: Enhancement of aerosol characterization using synergy of lidar and sun-photometer coincident observations: the GARRLiC algorithm, *Atmos. Meas. Tech.*, 6, 2065–2088, https://doi.org/10.5194/amt-6-2065-2013, 2013.

[5] Lopatin, A. et al.: Synergy processing of diverse ground-based remote sensing and in situ data using the GRASP algorithm: applications to radiometer, lidar and radiosonde observations, *Atmos. Meas. Tech.*, 14, 2575–2614, https://doi.org/10.5194/amt-14-2575-2021, 2021.

[6] Chaikovsky, A. et al.: Lidar-Radiometer Inversion Code (LIRIC) for the retrieval of vertical aerosol properties from combined lidar/radiometer data: development and distribution in EARLINET, Atmos. Meas. Tech., 9, 1181–1205, https://doi.org/10.5194/amt-9-1181-2016, 2016.

[7] ACTRIS: Aerosols, Clouds and Trace gases Research InfraStructure home page, https://www.actris.eu/, last access: 27 March 2023.

[8] Engelmann, R. et al.: The automated multiwavelength Raman polarization and water-vapor lidar PollyXT: the neXT generation, *Atmos. Meas. Tech.*, 9, 1767–1784, https://doi.org/10.5194/amt-9-1767-2016, 2016a, b.

[9] Mamouri, R.-E. et al.: Wildfire smoke triggers cirrus formation: lidar observations over the eastern Mediterranean, *Atmos. Chem. Phys.*, 23, 14097–14114, https://doi.org/10.5194/acp-23-14097-2023, 2023.

[10] Dubovik, O. and King, M. D.: A flexible inversion algorithm for retrieval of aerosol optical properties from Sun and sky radiance measurements, *J. Geophys. Res.*, 105, 673–670, https://doi.org/10.1029/2000JD900282, 2000.

[11] Dubovik, O. et al.: Application of spheroid models to account for aerosol particle nonsphericity in remote sensing of desert dust, *J. Geophys. Res.-Atmos.*, 111, D11208, https://doi.org/10.1029/2005JD006619, 2006.

[12] D'Amico, G. et al.: EARLINET Single Calculus Chain – technical – Part 1: Pre-processing of raw lidar data, Atmos. Meas. Tech., 9, 491–507, https://doi.org/10.5194/amt-9-491-2016, 2016.

[13] Mattis, I. et al.: EARLINET Single Calculus Chain – technical – Part 2: Calculation of optical products, Atmos. Meas. Tech., 9, 3009–3029, https://doi.org/10.5194/amt-9-3009-2016, 2016.

Establishing a Dual-Component ACTRIS Site in Cluj-Napoca: From Technical Integration to Scientific Potential in Aerosol and Cloud Remote Sensing

*A. Mereuță[1], **A. Radovici[1]**, H. Ștefănie[1], A. Tehei[1], A. Câțu[1], N. Ajtai[1]*

(1) Babeș Bolyai University, Faculty of Environmental Science and Engineeering, Fântânele 30, Cluj-Napoca, Romania
Corresponding author: andrei.radovici@ubbcluj.ro

Introduction

The ACTRIS-UBB project was initially planned for implementation between July 2020 and December 2023, and it became operational in November 2024. Its aim is to contribute to pan-European research on atmospheric composition and climate change. The newly operational site—Cluj Atmospheric Remote Sensing Observatory (CARO)—includes ground-based observation facilities, associated laboratories, and a data center that significantly contribute to Earth observation activities in two key areas: aerosol and cloud remote sensing.

Instrumentation and initial setup

The newly developed CARO site is located in the northwestern part of Romania, in the peri-urban area of Cluj-Napoca, the country's second-largest city. The facility (46.7678°N, 23.54006°E) is located at an altitude of 459 meters a.s.l., approximately 120 meters above the average elevation of the city. Due to local constraints, the building was designed with a longitudinal layout, and three platforms were constructed on top of each section to accommodate the research equipment (Figure 1).

Figure 1. Aerial view of the CARO facility, showing the building layout and rooftop platforms designated for remote sensing instrumentation.

The equipment installed within CARO was planned according to the labelling process agreed within the ACTRIS Preparatory Phase Project (ACTRIS-PPP).

For the aerosol remote sensing National Facility (NF), an upgraded version of the existing multiwavelength Raman and depolarization lidar system ($3\alpha + 2\beta + 2\delta$, fixed, not eye safe) was installed at the new location. A Cimel CE-318 sun photometer has been operational at a nearby facility since 2010, and a newer version—this time with lunar measurement capabilities—was acquired to retrieve essential aerosol parameters.

For the cloud remote sensing National Facility (NF), the following instruments were installed:

- Lufft CHM 15k Ceilometer – A fixed, eye-safe instrument with a measuring range of up to 15 km, used to retrieve aerosol backscatter profiles, cloud base height, aerosol layer height, cloud cover, and related parameters.

- HALO Photonics StreamLine XR Doppler Lidar – An eye-safe, scanning lidar with a range of up to 12 km, designed for the retrieval of wind profiles, planetary boundary layer (PBL) mapping, and other dynamic atmospheric structures.
- RPG-FMCW-94 Cloud Doppler Radar – A scanning radar operating over a range from 50 m to 18 km, providing measurements of radar reflectivity, liquid water content, vertical velocity, and cloud microphysical properties.
- RPG-HATPRO-G5 Microwave Radiometer – A scanning radiometer capable of continuous atmospheric profiling up to 10 km, retrieving temperature, humidity, and liquid water path.
- OTT Parsivel² Laser Precipitation Disdrometer – An optical disdrometer for surface-level measurements of precipitation, including size distribution and fall velocity of hydrometeors.
- Thies Clima Weather Station – An automatic weather station for monitoring key meteorological parameters such as temperature, relative humidity, wind speed and direction, and precipitation amount.

Additionally, supporting instruments such as a solar radiance monitoring system and an all-sky camera were installed to improve the observational capabilities. In parallel, instruments for in-situ aerosol analysis were also installed, including an Inductively Coupled Plasma Mass Spectrometer (ICP-MS) for determining the elemental composition of aerosols, an Aerosol Chemical Speciation Monitor (ACSM) for real-time measurement of aerosol chemical composition, and a Cloud Condensation Nuclei Counter (CCNC) for characterizing the cloud-forming potential of aerosols.

Opportunities and challenges

The main opportunity lies in the fact that developing a dual-component ACTRIS facility such as CARO, which integrates advanced aerosol and cloud remote sensing instruments, a detailed vertical profiling of atmospheric constituents is enabled. This supports a better understanding of aerosol–cloud interactions and contributes to reducing uncertainties in climate models. Another opportunity comes from the fact that ACTRIS NF`s are meant to follow standardized measurement techniques. On one hand, having similar equipment across sites means that potential issues are already well known in the community—so troubleshooting is faster, and know-how gets transferred more easily. On the other hand, the strict quality assurance and control protocols required by ACTRIS ensure that the produced data is reliable and easy integrated into platforms like Cloudnet, EARLINET, or AERONET. This kind of structure not only improves the quality of the research itself, but also creates a strong environment for training early-career scientists. Working with standardized tools and being part of an international network helps young researchers to grow faster in the field.

When it comes to limitations, two main aspects made the technical integration of the CARO facility more challenging than initially expected:

Due to specific legal provisions at the local level, metallic privacy panels to protect the surrounding residential properties had to be installed. While necessary from an urban planning perspective, these structures significantly limit the scanning capabilities of certain instruments. For instance, based on site-specific measurements, a minimum elevation angle of 35° was determined for the Doppler lidar, restricting its ability to perform low-angle scans. Similarly, the microwave radiometer cannot perform scans toward the north—contrary to standard operating procedures—due to the same obstruction. This limitation also affects the scanning capabilities of the cloud radar, reducing its ability to perform full azimuthal sweeps.

A second limitation came from relocating legacy equipment that had been in use at a different site. Moving the multiwavelength Raman lidar system, for instance, led to misaligned optical components after the system was completely taken apart and reassembled at the new location—a process that came with risks to its integrity and required extra time for operationalization. In addition, the sun photometer, was not reinstalled at the new site due to suboptimal sky visibility conditions. The local topography obstructs a

significant portion of the sky dome, particularly affecting photometric measurements during sunrise and sunset periods when the solar elevation is low. In the future, to optimize data collection, plans are in place to install a 355nm Raman and depolarization lidar system for continuous, cost-effective measurements. The current multi-channel Raman system will be used only for specific events of interest to the scientific community.

Observations from a Recent Atmospheric Event

Synergistic ceilometer and Doppler Wind Lidar (DWL) observations [1], [2] on March 15, 2025, revealed complex aerosol structures coinciding with forecasted dust deposition. Ceilometer backscatter (Image 2, top) showed persistent boundary layer aerosol and elevated layers, particularly when significant wet deposition was predicted (Image 2, bottom) [3]. Concurrent DWL vertical velocities (Image 2, middle) indicated sinking motion within these layers, suggesting downward transport relevant to deposition processes, alongside boundary layer turbulence.

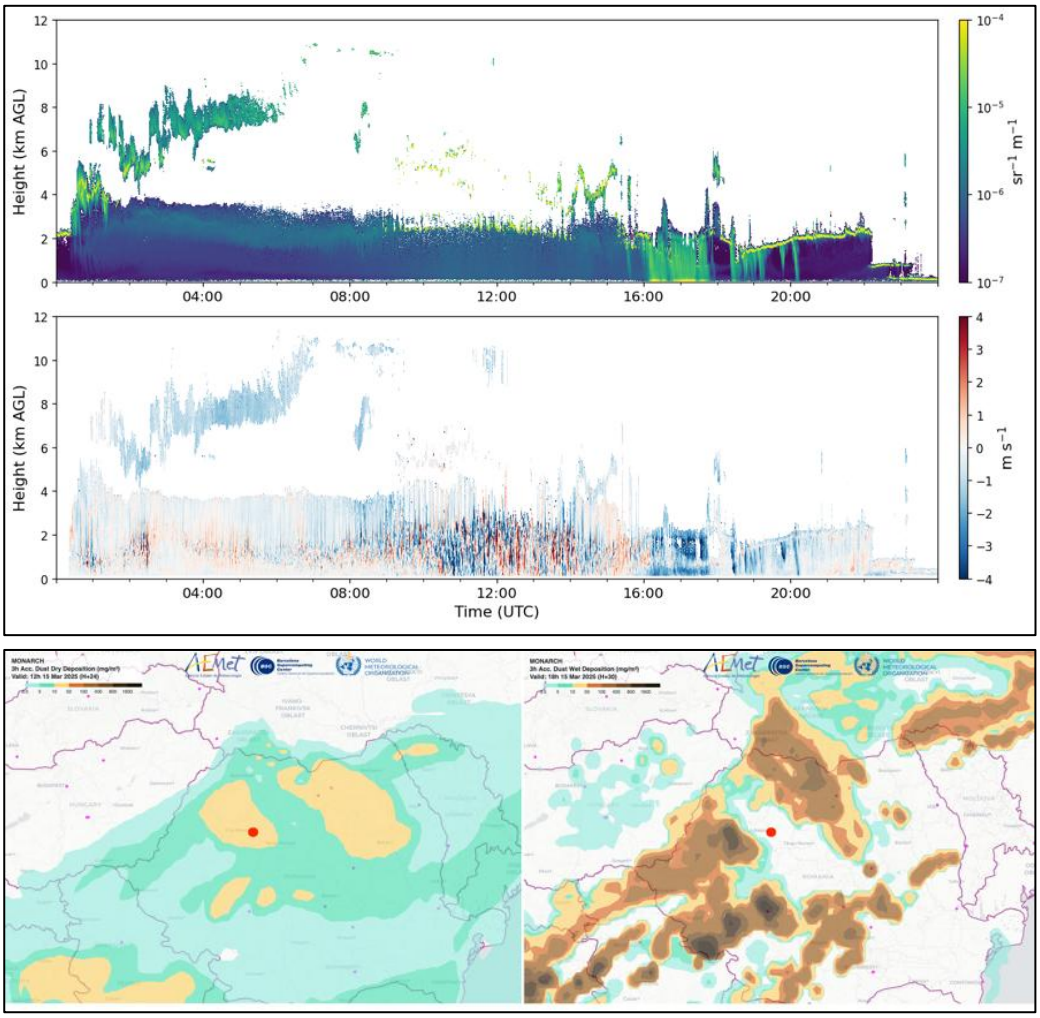

Figure 2. Attenuated backscatter coefficient (top) vs Doppler velocity (middle) vs dry & wet dust deposition (bottom) on 15.03.2025 over Cluj-Napoca, Romania

While the ceilometer-DWL synergy links aerosol structure and vertical dynamics, two key limitations hindered a complete characterization: the DWL, operating only in vertical stare mode, could not provide horizontal wind profiles needed to calculate vertical wind shear, thus limiting insights into shear-driven mixing and layer dynamics. Furthermore, the absence of simultaneous multi-wavelength polarization Raman lidar measurements prevented unambiguous aerosol typing (via depolarization) and quantitative optical profiling (extinction, lidar ratio, Ångström exponents). These represent missed opportunities for a comprehensive microphysical and dynamical assessment of aerosol evolution during this notable transport and potential wet deposition event.

Conclusions

The development of the CARO facility in Cluj-Napoca as a dual-component ACTRIS National Facility—covering both aerosol and cloud remote sensing—marks an important step forward for atmospheric research in Romania and the broader European context. Despite the technical and logistical challenges encountered the facility has successfully integrated a wide range of high-performance instruments. These include legacy systems alongside newly acquired cloud remote sensing instruments.

The prospects for resolving the technical and logistical challenges at the CARO facility are encouraging, thanks to adaptive planning and strong integration within the ACTRIS framework. Technically, issues like instrument misalignment and limited scanning angles due to local building constraints are being addressed through recalibration, optimized scanning strategies, and the planned addition of a more robust 355 nm Raman lidar system. Although sky visibility limitations prevent the use of certain instruments like the sun photometer, alternative deployment strategies are under consideration. Logistically, the use of standardized ACTRIS protocols ensures data consistency, facilitates troubleshooting, and enables collaboration across the wider research network. This ensures not only data interoperability but also supports the training and growth of early-career scientists working within a collaborative, international research environment.

Acknowledgements

The work was financed by Smart Growth, Digitization and Financial Instruments Program (PoCIDIF) 2021-2027, Action 1.3 Integration of the national RDI ecosystem in the European and international Research Space, project "Supporting the operation of facilities in Romania within the ACTRIS ERIC research infrastructure", SMIS code 309113, ctr. no. G 2024-96579/17.12.2024/390010/19.12.2024.

In this work we used data form Multiscale Online Nonhydrostatic AtmospheRe CHemistry model (MONARCH) continuously developed at the Barcelona Supercomputing Center (BSC)

References

[1] Câțu, A. (2025). UBB CHM 15k. ACTRIS Cloud remote sensing data centre unit (CLU). https://hdl.handle.net/21.12132/3.d6bf209bc48b48a4

[2] Deaconu, L. (2025). UBB HALO. ACTRIS Cloud remote sensing data centre unit (CLU). https://hdl.handle.net/21.12132/3.5d15cd3ce9c54139

[3] Klose, M. et al.: *Mineral dust cycle in the Multiscale Online Nonhydrostatic AtmospheRe CHemistry model (MONARCH) version 2.0*. Geosci. Model Dev. Discuss., pp.1-59, 2021.

The potential of the ERATOSTHENES CARO National Facility in the EMMENA region: An Holistic Approach for aerosol and cloud profiling over Limassol, Cyprus

***R. E. Mamouri*[1,2]**, *A. Nisantzi*[1,2], *H. Panahifar*[1], *G. Kotsias*[1], *M. Poutli*[1,2], *D. Hadjimitsis*[1,2], *P. Seifert*[3] *and A. Ansmann*[3],

(1) Eratosthenes Centre of Excellence, Franklin Roosevelt 82, 3012, Limassol, Cyprus
(2) Cyprus University of Technology, Department of Civil Engineering and Geomatics, Archiepiskopou Kyprianou 30, 3036, Limassol, Cyprus
(3) Leibniz Institute for Tropospheric Research (TROPOS), Permoserstraße 15, 04318, Leipzig, Germany
Corresponding author: rodanthi@eratoisthenes.org.cy

Introduction

Cyprus is strategically located in the region of the Eastern Mediterranean, the Middle East and North Africa (EMMENA). As a crossroad between Europe, Asia and Africa, it is representative of meteorological conditions and coastal areas in the EMMENA region. Therefore, Cyprus, and especially Limassol as a coastal city, can be considered an ideal natural laboratory for advanced and comprehensive field studies on climate change, aerosol-cloud-dynamics-precipitation interaction, and the weather-precipitation-dryness complex [1].

A major challenge in the global understanding of atmospheric processes is the incomplete coverage of ground monitoring stations. Although satellite missions like EarthCARE provide continuous regional-to-global observations, their data must be validated with high-resolution ground-based measurements to be effectively integrated into atmospheric models and improve climate projections. The lack of a modern supersite in the Eastern Mediterranean, one of the world's hotspots for climate change, limits the ability to monitor pollution, dust storms, and changing precipitation patterns in the region.

To address this gap, a state-of-the-art observational supersite—the Cyprus Atmospheric Remote Sensing Observatory (CARO)—has been established in Limassol. The CARO National Facility (NF) is designed to provide long-term, high-resolution profiling of atmospheric parameters including aerosol, cloud, wind, humidity, and precipitation. Its strategic role is amplified through participation in international satellite validation activities, including the CORAL project, part of the EarthCARE CAL/VAL program.

In addition, to apply a measurement–modelling synergistic approach to address key environmental and atmospheric challenges, CARO's advanced ground-based infrastructure is also leading the ATARRI project (ATmospheric and solAR Research and Innovation in the Eastern Mediterranean). ATARRI aims to strengthen scientific knowledge and innovation and increase the readiness of CARO NF towards supporting cal/val for future satellite missions, as well as supporting, dust modelling and forecasting [2], relationship between aerosol, clouds and solar radiation and modelling in urban areas and Solar energy assessment in different spatiotemporal scales [3]. Selected cases that demonstrate the complex aerosol conditions over Eastern Mediterranean will be presented as well as an intercomparison between EarthCARE products and CARO NF observations during two overpasses on 4–5 March 2025 over Cyprus.

Methodology

Due to satellite orbital constraints, perfect temporal collocation with ground-based systems is often not possible. In this study, a ±3 hour time window was used to align ground-based observations with EarthCARE overpasses. This is considered acceptable under stable nighttime conditions, particularly when dealing with elevated dust layers that evolve slowly. The comparison focused on: Layer altitude and structure, Backscatter intensity profiles, Depolarization ratio agreement, Aerosol type classification consistency.

Results and Discussion

During the EarthCARE satellite overpasses on 4 and 5 March 2025, coinciding ground-based PollyXT lidar, cloud radar and wind lidar observations were conducted at the CARO facility in Limassol, Cyprus. These observations revealed a well-defined Saharan dust layer positioned between approximately 2.2 and 5.5 km altitude. The dust layer was identified by elevated particle linear depolarization ratios (PLDRs), ranging

between 0.25 and 0.35 at 532 nm, and lidar ratios between 40 and 55 sr, values typical of non-spherical mineral dust particles. The ATLID instrument onboard EarthCARE captured backscatter and depolarization profiles at 355 nm that were highly consistent with the PollyXT measurements. The aerosol layer observed by ATLID was classified as a "dusty mix," further supporting the ground-based aerosol typing. Despite a 2–3 hour temporal offset between ATLID overpass times and PollyXT data acquisition, the observed atmospheric layers remained stable under nighttime conditions, allowing for effective comparison. This highlights the robustness of nighttime intercomparisons in validation studies.

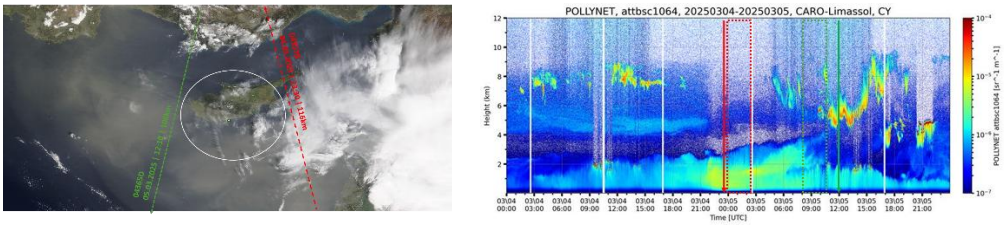

Figure 1. Time–height cross-section of attenuated backscatter at 1064 nm from the PollyXT lidar (left). The red box indicates the period 2–3 hours after the EarthCARE overpass, while the green box shows the period 2–3 hours before the overpass. The map on the left illustrates the EarthCARE overpass ground tracks relative to the CARO location.

Conclusions

The intercomparison between EarthCARE and CARO NF observations during the 4–5 March 2025 overpasses demonstrates a strong consistency in the detection and characterization of dust layers over Cyprus. The analysis highlights the effective use of depolarization measurements for aerosol typing. Despite the inherent temporal mismatches between satellite overpasses and ground-based data acquisition, the validation was feasible and robust, particularly due to the atmospheric stability during nighttime conditions. These findings reinforce the crucial role of ground-based observatories such as the CARO in satellite data validation. Situated in a strategic location between Europe, Asia, and Africa, CARO serves as a vital infrastructure for continuous monitoring of aerosol and cloud properties in the Eastern Mediterranean and Middle East region—a recognized climate-change hotspot. As a National Facility under ACTRIS, CARO contributes significantly improving atmospheric models, advancing climatological research, and strengthening our understanding of aerosol-cloud interactions in one of the world's most complex and dynamic environments.

Acknowledgements

The 'EXCELSIOR' project has received funding from the European Union's Horizon 2020 research and innovation programme under Grant Agreement No 857510, from the Government of the Republic of Cyprus through the Directorate General for the European Programmes, Coordination and Development and the Cyprus University of Technology. The authors also acknowledge the ATARRI project funded by the European Union's Horizon Europe Twinning Call (HORIZON-WIDERA-2023-ACCESS-02) under the grant agreement No 101160258 and the EVID39 CORAL project as part of the CAL/VAL EarthCARE activities

References

[1] Nisantzi A.et al.: Middle East versus Saharan dust extinction-to-backscatter ratios, Atmos. Chem. Phys., 15, 7071–7084, https://doi.org/10.5194/acp-15-7071-2015, 2015.

[2] E. di Tomaso et al., "The MONARCH high-resolution reanalysis of desert dust aerosol over Northern Africa, the Middle East and Europe (2007-2016)," Earth System Science Data, vol. 14, no. 6, pp. 2785–2816, Jun. 2022, doi:10.5194/ESSD-14-2785-2022.

[3] Theristis M, et al. "Blind photovoltaic modeling intercomparison: A multidimensional data analysis and lessons learned." Prog Photovolt Res Appl. 2023; 31(11): 1144-1157. doi:10.1002/pip.3729.

Multi-Platform Vertical Profiling of Aerosol Optical Properties Using Lidar, UAS, and Tethered Balloon at ACTRIS-PL site in Strzyżów.

K. M. Markowicz[1], *M. Broda*[1], *M. T. Chiliński*[1], *K. Nurowska*[1], *O. Zawadzka*[1], *J. Markowicz*[1], *M. Szczyrba*[1], *Iwona S. Stachlewska*[1]

(1) University of Warsaw, Faculty of Physics, Institute of Geophysics, (IGFUW), Pasteura 5, 02-093, Warsaw, Poland
Corresponding author: kmark@igf.fuw.edu.pl

Introduction

This study aims to highlight the advantages of using aerosol lidar, an unmanned aerial system (UAS), and tethered balloons in atmospheric aerosol research—particularly for obtaining information on the vertical variability of aerosol single-scattering properties in the lower troposphere ([1], [2]). The results presented in this paper were collected at the ACTRIS-PL site in Strzyżów (southeastern Poland) during the spring and summer of 2025. The tethered balloon was equipped with miniaturized instruments, including a low-cost SPS30 aerosol counter and an RS41 radiosonde, to measure aerosol single-scattering properties and atmospheric thermodynamic parameters. The aerosol sensor was calibrated to retrieve the aerosol scattering coefficient (ASC), scattering Ångström exponent (SAE), and particle effective radius (PER). Vertical profiles from the UAS, tethered balloon, and lidar observations were acquired during Canadian wildfire smoke episodes, mineral dust events, and under background conditions.

Methodology

In this study, the Raymetrics LR322-D300 Raman lidar was used. The system employs a Nd:YAG laser (Quantel CFR 400 Series) operating primarily at 532 nm, with typical pulse energies of ~90 mJ at 532 nm and ~107 mJ at 355 nm, at a repetition rate of 20 Hz. The laser beam, with a divergence of approximately 0.70 mrad (532 nm) and 0.63 mrad (355 nm), is optically expanded to reduce divergence and improve collimation. A 300 mm diameter Cassegrain telescope optimized for near-range signal collection is used, achieving full overlap at approximately 320 m above ground level. The backscattered signal is transmitted through optical components to high-sensitivity photomultiplier tubes (PMTs), operating in both analog and photon-counting modes (Licel modules). The system includes the following detection channels: elastic backscatter at 532 nm (parallel and cross-polarized), elastic backscatter at 355 nm, and Raman channels at 387 nm and 407 nm. The vertical resolution is 3.75 m. The lidar is housed in a climate-controlled enclosure suitable for continuous operation under harsh environmental conditions, with full support for remote control and automation.

Vertical profiles were also obtained using sensors mounted on a DJI Matrice 300 RTK unmanned aerial system (UAS). For this purpose, a prototype sun photometer was integrated into the platform, enabling measurements of spectral aerosol optical depth (AOD) and the Ångström exponent (AE) under clear-sky conditions. The sun photometer transmits real-time data to the ground-based radio controller. It is mounted on a custom system built on the DJI X-Port gimbal, equipped with stepper motors allowing two-axis rotation of the sensor head. Two methods are used for solar targeting: the first provides a coarse estimation based on theoretical solar geometry relative to the UAS position; the second employs a digital camera to detect the sun's image, enabling precise and rapid alignment. The optical system includes a miniature STS-VIS spectrometer (Ocean Optics), with a spectral range of 350–800 nm. The spectrometer uses a 1024-pixel CCD array, providing a spectral resolution of 1.0 nm (FWHM) with a 10 µm input slit. The field of view (FOV) is limited to 2.0° using a Gershun Tube.

To measure vertical profiles of solar (shortwave) radiation, the SP510 and SP610 sensors were used; for longwave (infrared) radiation, the SL510 and SL610 (Apogee Instruments) were employed. All sensors measuring downward irradiance were mounted on a horizontally stabilized platform to eliminate the effects of UAS tilting and orientation. Additionally, the UAS carried SPS30 and OPC-N3 sensors to measure aerosol concentrations, an AE-51 aethalometer to determine equivalent black carbon (eBC) concentrations, and a Vaisala RS41 radiosonde for thermodynamic profiling.

Independent tethered balloon soundings were also performed using the SPS30 and RS41 sensors. The SPS30, a low-cost optical particle counter, includes an LED light source, photodiode detector, and focusing optics inside a compact chamber. It calculates mass concentrations (PM_1, $PM_{2.5}$, PM_4, PM_{10}) and number concentrations for particles ≥0.3, 0.5, 1.0, 2.5, 5.0, and 10.0 µm, based on scattering intensity and embedded algorithms (proprietary). The electronics include a fast analog-to-digital converter (~1 MS/s)

and a microcontroller for signal processing. The stated measurement precision for PM_1 and $PM_{2.5}$ is ±10 µg/m³ (for concentrations up to 100 µg/m³) and ±10% for higher values. The system was tested under low-pressure conditions in a vacuum chamber, confirming that the internal fan stabilizes at 6000 RPM, indicating no need for altitude-based volume flow correction. SPS30 measurements were further processed to derive ASC, SAE, and PER, following the methodology described in [3].

Results and Discussion

A linear relationship was observed between PM_{10} concentrations measured by the SPS30 sensor and the ASC obtained from the Aurora 4000 nephelometer. The estimated ASC values represent ambient conditions, as the sampled air was neither heated nor dried prior to measurement. A high correlation coefficient (R = 0.96) and a low root mean square error (RMSE = 11.8 Mm^{-1}) were obtained, with values approaching the theoretical Rayleigh scattering limit (13.1 Mm^{-1} at 1013 hPa and 25°C). The main limitation of this approach lies not in the conversion of PM_{10} mass concentrations to optical properties, but in the relatively high noise level under clean or background conditions. For SAE, derived from Aurora 4000 data, the relationship with SPS30-based estimates was non-linear, similarly to the relationship observed for PER derived from the LAS3340 instrument. The RMSE for SAE was relatively high (0.31) and the correlation coefficient was negative (R = –0.86), indicating systematic differences in sensitivity between the instruments. In contrast, for the PER, a high positive correlation (R = 0.94) was found, with a low RMSE of 0.02 µm. Most calibration data were obtained under conditions characterized by small particle sizes and low PM_{10} concentrations**.** Preliminary UAS-based measurements of the AOD profile confirmed the expected decrease in AOD with altitude, while the AE exhibited more complex vertical variability**.**

Conclusions

Preliminary data collected during the field campaign show good agreement between the vertical profiles of the lidar backscattering coefficient and the ASC derived from SPS30 sensors mounted on both a tethered balloon and a UAS. The additional information provided by UAS and balloon profiling, when combined with lidar observations, has the potential to enhance our understanding of the impact of aerosol single-scattering properties on the net radiation budget in the lower troposphere.

Acknowledgements

This work was financed by ACTRIS-PL, which is funded by the Ministry of Science and Higher Education of Poland under grant agreement 2024/WK/04.

References

[1] Chilinski, M.T.; Markowicz, K.M.; Poczta, P.; Chojnicki, B.H.; Harenda, K.M.; Makuch, P.; Wang, D.; Stachlewska, I.S. Vertical Profiles of Aerosol Optical Properties (VIS/NIR) over Wetland Environment: POLIMOS-2018 Field Campaign. *Remote Sens.* 2024, *16*, 4580. https://doi.org/10.3390/rs16234580.

[2] Chiliński, M.T., Markowicz, K.M. & Kubicki, M. UAS as a Support for Atmospheric Aerosols Research: Case Study. *Pure Appl. Geophys.* 175, 3325–3342 (2018). https://doi.org/10.1007/s00024-018-1767-3

[3] Markowicz, K.M.; Chiliński, M.T. Evaluation of Two Low-Cost Optical Particle Counters for the Measurement of Ambient Aerosol Scattering Coefficient and Ångström Exponent. Sensors 2020, 20, 2617. https://doi.org/10.3390/s20092617.

ELC

2025